

# UC San Diego

## UC San Diego Electronic Theses and Dissertations

### Title

Experimental and Numerical Seismic Response of Offshore Wind Turbines Supported on Bucket Foundations

### Permalink

<https://escholarship.org/uc/item/9sd6m7sd>

### Author

Zayed, Muhammad

### Publication Date

2022

Peer reviewed|Thesis/dissertation

UNIVERSITY OF CALIFORNIA SAN DIEGO

Experimental and Numerical Seismic Response of Offshore Wind Turbines Supported on Bucket  
Foundations

A dissertation submitted in partial satisfaction of the requirements for the degree

Doctor of Philosophy

in

Structural Engineering

by

Muhammad Zayed

Committee in charge:

Professor Ahmed Elgamal, Chair  
Professor William Hodgkiss  
Professor Kenneth Loh  
Professor John McCartney  
Professor Benson Shing

2022

Copyright

Muhammad Zayed, 2022

All rights reserved

The Dissertation of Muhammad Zayed is approved, and it is acceptable in quality and form for publication on microfilm and electronically:

University of California San Diego

2022

# DEDICATION

*To my parents, Aida Ayoub and Ahmed Zayed*

*For their incredible nurture, great sacrifices and unconditional love.*

# EPIGRAPH

*If you want to find the secrets of the universe, think  
in terms of energy, frequency and vibration.*

– Nikola Tesla

# TABLE OF CONTENTS

<b>SIGNATURE PAGE .....</b>	<b>iii</b>
<b>DEDICATION .....</b>	<b>iv</b>
<b>EPIGRAPH .....</b>	<b>v</b>
<b>TABLE OF CONTENTS .....</b>	<b>vi</b>
<b>LIST OF FIGURES .....</b>	<b>x</b>
<b>LIST OF TABLES .....</b>	<b>xix</b>
<b>ACKNOWLEDGEMENTS.....</b>	<b>xx</b>
<b>VITA .....</b>	<b>xxiv</b>
<b>ABSTRACT OF THE DISSERTATION.....</b>	<b>xxxii</b>
<b>Chapter 1 Introduction .....</b>	<b>1</b>
1.1 Extended abstract .....	1
1.2 Motivation.....	3
1.3 Research goals .....	6
1.4 Dissertation outline .....	7
<b>Chapter 2 Literature review on bucket foundation for offshore wind applications ...</b>	<b>11</b>
2.1 Introduction.....	11
2.2 Offshore wind .....	12
2.3 Foundations for offshore wind turbines.....	15
2.4 Use of Bucket foundation for offshore wind applications .....	16
<b>Chapter 3 1-g shake table testing of bucket foundation wind turbine: Model preparation, experimental procedures, and data processing.....</b>	<b>29</b>
3.1 Introduction.....	29
3.2 Shake table test facility .....	29
3.3 Soil stratum model .....	30
3.4 Bucket foundation wind turbine model.....	31
3.5 Instrumentation .....	32
3.6 Test motions.....	33
3.7 Data processing.....	34
3.8 Modal testing and system identification .....	36
3.8.1 Fixed base configuration of the test model .....	36

3.8.2	Soil-structure interaction effects .....	36
3.9	Acknowledgement .....	40
<b>Chapter 4</b>	<b>Shake table testing - Results and discussion .....</b>	<b>71</b>
4.1	Introduction.....	71
4.2	Results of test H5 .....	72
4.2.1	Shaking event acceleration .....	72
4.2.2	Soil response .....	72
4.2.3	Tower response .....	73
4.2.4	Moment-rotation response of bucket foundation.....	74
4.2.5	Pore pressure response inside and outside bucket foundation .....	76
4.3	Observations from additional tests.....	80
4.4	Summary and conclusions .....	82
4.5	Acknowledgement .....	83
<b>Chapter 5</b>	<b>Calibration of finite element model of bucket foundation wind turbine .</b>	<b>111</b>
5.1	Numerical modelling .....	111
5.1.1	Computational framework .....	111
5.1.2	Soil-Bucket interface .....	113
5.1.3	Model configuration and calibration.....	114
5.2	Experimental and numerical results.....	115
5.2.1	Soil response in the far-field .....	116
5.2.2	Response of bucket foundation and tower .....	119
5.3	Summary and conclusions .....	122
5.4	Acknowledgement .....	123
<b>Chapter 6</b>	<b>Seismic response of 3.45 MW utility-scale offshore wind turbine with bucket foundation in sand .....</b>	<b>143</b>
6.1	Design for fundamental frequency.....	143
6.1.1	Fixed-base structure .....	144
6.1.2	Flexible-base structure .....	145
6.1.3	Design for stability under operational wind loading.....	148
6.2	Seismic response .....	150
6.2.1	Model configuration.....	150
6.2.2	Results and discussion .....	151
6.3	Summary and conclusions .....	155



6.4	Acknowledgement .....	156
<b>Chapter 7</b>	<b>Parametric study on seismic response of 3.45 MW offshore wind turbine with bucket foundation .....</b>	<b>176</b>
7.1	Selection of bucket foundation dimensions .....	176
7.1.1	Design for fundamental frequency.....	176
7.1.2	Design for stability under operational wind loads .....	178
7.2	Influence of soil stiffness .....	179
7.3	Influence of ground motion .....	181
7.3.1	Earthquake motions .....	181
7.3.2	Earthquake intensities .....	182
7.4	Influence of soil permeability .....	182
7.5	Influence of bucket size .....	184
7.5.1	Similar bucket diameter (effect of skirt length).....	184
7.5.2	Similar skirt length (effect of bucket diameter).....	185
7.5.3	Similar fundamental frequency (different size).....	185
7.6	Influence of damping .....	186
7.7	Summary and Conclusions .....	188
7.8	Acknowledgement .....	191
<b>Chapter 8</b>	<b>Shake table testing: A high-resolution vertical accelerometer array for tracking shear wave velocity .....</b>	<b>218</b>
8.1	Abstract.....	218
8.2	Introduction.....	219
8.3	Shear wave velocity tracking framework .....	221
8.4	Estimation of $V_s$ from recorded dynamic signals.....	221
8.5	Analytical $V_s$ evaluation approaches.....	222
8.6	Experimental application of the $V_s$ tracking framework .....	223
8.6.1	Shake table and laminar container .....	223
8.6.2	Model 1 preparation and experimental procedures.....	224
8.6.3	Vertical accelerometer array and data acquisition .....	225
8.6.4	Representative results and interpretation .....	226
8.6.5	Implementation of the $V_s$ tracking framework .....	228
8.7	Additional application of the $V_s$ tracking framework .....	230
8.7.1	Model 2 preparation and test configuration .....	230

8.7.2	Recorded acceleration and excess pore pressure .....	231
8.7.3	Tracking of Vs during seismic excitation .....	231
8.8	Acknowledgement .....	232
<b>Chapter 9</b>	<b>Asymmetric Input Motion for Accumulation of Lateral Ground Deformation in Laminar Container Shake Table Testing .....</b>	<b>258</b>
9.1	Abstract .....	258
9.2	Introduction.....	259
9.3	Conceptual framework of asymmetric base excitation.....	261
9.4	Experimental implementation.....	262
9.5	Experimental procedures .....	263
9.5.1	shake table and laminar soil container .....	263
9.5.2	Model preparation.....	264
9.5.3	Test description.....	265
9.6	Experimental response and discussion.....	266
9.6.1	Soil acceleration and pore pressure response.....	266
9.6.2	Lateral soil deformation.....	267
9.6.3	Evaluation of shear stress-strain histories.....	268
9.7	Forward and backward accumulation of deformation .....	269
9.8	Acknowledgement .....	269
<b>Chapter 10</b>	<b>Summary and conclusion.....</b>	<b>291</b>
10.1	Seismic response of bucket foundation for offshore wind turbines.....	291
10.2	A high-resolution vertical accelerometer array for tracking shear wave velocity .....	295
10.3	Asymmetric input motion for accumulation of lateral ground deformation in laminar container shake table testing.....	296
10.4	Recommendations for future research .....	296
10.4.1	Physical modeling.....	296
10.4.2	Numerical modeling.....	297
<b>REFERENCES</b>	.....	<b>298</b>

# LIST OF FIGURES

Figure 2-1: Average wind speed on the coastal zone of the United States (from <a href="https://www.energy.gov/eere/articles/computing-america-s-offshore-wind-energy-potential">https://www.energy.gov/eere/articles/computing-america-s-offshore-wind-energy-potential</a> ).....	22
Figure 2-2: Locations of U.S. offshore wind pipeline activity and call area as of March 2019 (After Musial <i>et al.</i> 2017).....	23
Figure 2-3: Types of OWT foundations at relatively shallow waters (up to 50 m).....	24
Figure 2-4: Schematic of a) offshore bucket foundation-supported wind turbine and b) bucket foundation with inner compartments .....	25
Figure 2-5: Water depths for various offshore wind plants in the U.S. (After Musial <i>et al.</i> 2019).....	26
Figure 2-6: Enlarged view for location and water depth of U.S. East Coast offshore wind pipeline activity and call areas as of March 2019 (After Musial <i>et al.</i> 2019) .....	27
Figure 2-7: The 2018 Modified Mercalli Intensity (MMI) hazard maps of the conterminous United States showing estimates of earthquake shaking in terms of 2% probability of exceedance in 50 years (After Petersen <i>et al.</i> 2020).....	28
Figure 3-1: Laminar soil container placed on shake table at the UC San Diego Powell Laboratory .....	46
Figure 3-2: Illustrative images showing a) placement of the EPDM liner inside the laminar soil container, b) dry pluviation of sand inside the laminar container, c) compaction of the soil inside the container, d) sand cone test for determination of sand relative density .....	47
Figure 3-3: Top view of the laminar soil container: a) before, and b) after saturating the sand stratum.....	48
Figure 3-4: Bucket foundation wind turbine CAD drawing and details for manufacturing .....	49
Figure 3-5: Illustrative images showing a) 3-dimensional CAD model of the scaled bucket foundation with wind turbine, b) model after fabrication, a) bottom view of bucket foundation with honeycomb shaped compartments showing pore pressure transducers installed inside the bucket, b) pore pressure transducers installed outside the bucket foundation, b) side view of bucket foundation .....	50
Figure 3-6: Illustrative images showing a) placement of bucket foundation inside the laminar soil container by overhead crane, b) installation of bucket foundation into saturated sand stratum under its own weight, c) driving bucket foundation into saturated sand by suction, and d) de-attaching suction hoses from bucket foundation after model installation.....	51
Figure 3-7: Testing configuration and instrumentation layout (dimensions shown in mm).....	52

Figure 3-8: Layout of pore pressure transducers (PP#) around the front and back sides of the bucket foundation .....	53
Figure 3-9: Bucket foundation after being installed in the saturated sand with instrumentation attached to it .....	54
Figure 3-10: Schematic illustrating a) calculation of lateral force on bucket foundation and lateral displacement of bucket foundation relative to the surrounding soil, and b) elastic and rigid components of lateral tower total displacement .....	55
Figure 3-11: View of bucket foundation wind turbine model with fixed-base configuration before performing modal analysis for system identification .....	56
Figure 3-12: Typical time histories and the corresponding Fourier transforms of tower accelerations for hammer excitation of the fixed-base bucket foundation model .....	57
Figure 3-13: Normalized transfer function for fixed-base model (between A25 as input and A30 as output) .....	58
Figure 3-14: Time histories of soil accelerations for test WN1 .....	59
Figure 3-15: Frequency spectrum of the recorder soil accelerations for test WN1 .....	60
Figure 3-16: Normalized transfer function between lowermost and uppermost recorded soil accelerations for test WN1 .....	61
Figure 3-17: Evolution of $V_s$ with time for test WN1 .....	62
Figure 3-18: Tower acceleration time histories and the corresponding frequency spectra for test WN 1 .....	63
Figure 3-19: Normalized transfer function between A08 (i.e., soil near the bucket foundation) and A30 (i.e., top of the tower) for test WN1 .....	64
Figure 3-20: Time histories of lateral soil acceleration in north and south arrays for test WN2 .....	65
Figure 3-21: Frequency spectra of lateral soil acceleration in north and south arrays for test WN2 .....	66
Figure 3-22: Transfer function between uppermost and lowermost soil acceleration records for test WN2 .....	67
Figure 3-23: Change in soil $V_s$ with time during test WN2 .....	68
Figure 3-24: Time histories of lateral tower acceleration for test WN2 .....	69
Figure 3-25: Transfer function between acceleration records at the tower top (A30) and soil top near the bucket foundation (A08) for test WN2 .....	70
Figure 4-1: Acceleration time history and corresponding frequency spectrum of shake table input excitation for test H5 .....	84
Figure 4-2: Time histories of lateral soil acceleration along north and south arrays for test H5 .....	85

Figure 4-3: Frequency spectra of lateral soil acceleration along north and south arrays for test H5.....	86
Figure 4-4: Change in soil $V_s$ with time during test H5 .....	87
Figure 4-5: Time histories of lateral soil displacement relative to laminar container base for H5.....	88
Figure 4-6: Time histories of soil excess pore pressure for test H5.....	89
Figure 4-7: Time histories and corresponding frequency spectra of lateral tower accelerations for test H5 .....	90
Figure 4-8: Time histories of lateral tower displacement relative to lateral soil displacement at the foundation level (LP05) for test H5.....	91
Figure 4-9: Time histories of tower bending moment for test H5 .....	92
Figure 4-10: Time history of a) vertical displacement of bucket foundation, b) rotation of bucket foundation, and c) bending moment at tower bottom (i.e., the bucket top) for test H5.....	93
Figure 4-11: Plot of a) bucket moment vs. bucket rotation for test H5, and b) one loop of bucket moment vs. bucket rotation for test H5 (between 3.25 and 4 seconds) .....	94
Figure 4-12: Schematic illustrating bucket foundation rotation at each of the five points marked in Figure 4-10 and Figure 4-11 .....	95
Figure 4-13: Vertical bucket displacement vs. bucket rotation for Test H5.....	96
Figure 4-14: Time histories of EPP at bucket foundation a) north and b) south edges for test H5.....	97
Figure 4-15: EPP ratio around bucket foundation vs. bucket rotation for test H5 between 3.25 and 4 seconds.....	98
Figure 4-16: EPP ratio around bucket foundation vs. top bucket moment for test H5 between 3.25 and 4 seconds .....	99
Figure 4-17: EPP ratio around bucket foundation vs. bucket rotation for the entire shaking duration of test H5 .....	100
Figure 4-18: EPP ratio around bucket foundation vs. top bucket moment for the entire shaking duration of test H5.....	101
Figure 4-19: EPP ratio around bucket foundation vs. vertical bucket displacement at each edge, test H5 between 3.25 and 4 sec.....	102
Figure 4-20: EPP ratio around bucket foundation vs. vertical bucket displacement at each edge, for the entire shaking duration of test H5 .....	103
Figure 4-21: EPP ratio around bucket at south edge vs. at north edge for H5 a) between 3.25 and 4 seconds, b) entire shaking.....	104
Figure 4-22: Plot of bucket moment vs. bucket rotation for a) test H2, b) test H8 and c) test H10 .....	105

Figure 4-23: Average of vertical bucket displacement vs. bucket rotation (left column) and vertical bucket displacement time histories (right column) for a) test H2, b) test H8 and c) test H10 .....	106
Figure 4-24: EPP ratio around bucket foundation vs. top bucket moment for the entire shaking duration of test H2.....	107
Figure 4-25: EPP ratio around bucket foundation vs. top bucket moment for the entire shaking duration of test H10.....	108
Figure 4-26: EPP ratio around bucket at south edge vs. at north edge for a) test H2, and b) test H10.....	109
Figure 4-27: Variation of maximum suction level with maximum bucket moment and maximum bucket rotation for different tests .....	110
Figure 5-1: a) Soil-structure element connectivity, b) Schematic of 8-node u-p brick elements with zeroLength elements, and c) different soil-structure interface boundary surfaces defined for bucket foundation, where 1) outer skirt surface, 2) inner skirt surface, 3) bucket tip surface, and 4) bucket lid bottom surface .....	126
Figure 5-2: Elastic no-tension model adopted for interface normal stiffness .....	127
Figure 5-3: Elastic perfectly plastic model adopted interface tangential stiffness .....	127
Figure 5-4: Finite Element Model: a) 3D half-mesh of the bucket foundation wind turbine model, and b) enlarged view of bucket foundation mesh.....	128
Figure 5-5: H5 shaking event a) acceleration time history of input excitation, numerical and experimental time histories of b) excess pore pressure, c) soil acceleration, d) acceleration spectra at different depths of the sand model in the far-field .....	129
Figure 5-6: H10 shaking event a) acceleration time history of input excitation, numerical and experimental time histories of b) excess pore pressure, c) soil acceleration, d) acceleration spectra at different depths of the sand model in the far-field .....	130
Figure 5-7: H5 shaking event a) shear stress and strain time histories at different depths, b) shear stress-strain response at depth 1.23m.....	131
Figure 5-8: H10 shaking event a) shear stress and strain time histories at different depths, b) shear stress-strain response at depth 1.23m .....	132
Figure 5-9: N3 shaking event a) acceleration time history of input excitation, numerical and experimental time histories of b) excess pore pressure, c) soil acceleration, d) acceleration spectra at different depths of the sand model in the far-field .....	133
Figure 5-10: T3 shaking event a) acceleration time history of input excitation, numerical and experimental time histories of b) excess pore pressure, c) soil acceleration, d) acceleration spectra at different depths of the sand model in the far-field .....	134
Figure 5-11: N3 shaking event a) shear stress and strain time histories at different depths, b) shear stress-strain response at depth 1.23m .....	135
Figure 5-12: T3 shaking event a) shear stress and strain time histories at different depths, b) shear stress-strain response at depth 1.23m .....	136

Figure 5-13: Experimental and numerical tower response in H5 shaking event: a) displacement, b) acceleration, c) frequency spectra, d) bucket moment and rotation time histories, and e) bucket moment-rotation hysteresis.....	137
Figure 5-14: Experimental and numerical tower response in H10 shaking event: a) displacement, b) acceleration, c) frequency spectra, d) bucket moment and rotation time histories, and e) bucket moment-rotation hysteresis.....	138
Figure 5-15: FE deformed mesh contours for vertical displacement (scale factor = 2) showing bucket rotation at 3.4 seconds of the H10 shaking event.....	139
Figure 5-16: Time histories of excess pore pressure around bucket in H10 shaking event for the a) north side and b) south side .....	140
Figure 5-17: Experimental and numerical tower response in N3 shaking event: a) displacement, b) acceleration, c) frequency spectra, d) bucket moment and rotation time histories, and e) bucket moment-rotation hysteresis.....	141
Figure 5-18: Experimental and numerical tower response in T3 shaking event: a) displacement, b) acceleration, c) frequency spectra, d) bucket moment and rotation time histories, and e) bucket moment-rotation hysteresis.....	142
Figure 6-1: Schematic of OWT with bucket foundation .....	161
Figure 6-2: 3D view of the FE half-mesh employed in modeling 3.45 MW utility-scale OWT with bucket foundation.....	162
Figure 6-3: Plot of transfer function between tower top and bucket acceleration at mid skirt height for low amplitude shaking .....	163
Figure 6-4: Bucket response under effects of quasistatic operational wind loads; a) moment-rotation ( $K_{RR}$ is the foundation secant rotational stiffness) and b) lateral force-displacement ( $K_{LL}$ are the foundation secant translational stiffness) .....	164
Figure 6-5: Schematic of the base-springs model (for natural frequency calculations) .....	165
Figure 6-6: Plot of quasistatic monotonic moment-rotation relationship of bucket foundation in undrained conditions (combined with 5.8 MN vertical dead load of the superstructure).....	166
Figure 6-7: Plot of (a) acceleration time history at the model base and near surface in the far field (Figure 6-2), and (b) the corresponding acceleration response spectrum .....	167
Figure 6-8: Plots of a) acceleration time histories at different heights along the OWT structure .....	168
Figure 6-9: Plots of b) frequency spectra of accelerations at different heights along the OWT structure, and c) transfer function between acceleration at tower top and soil-bucket acceleration at mid skirt height.....	169
Figure 6-10: Plot of time histories of bucket moment (top plot), bucket rotation (middle plot) and near field $r_u$ at mid skirt height (bottom plot) with operational wind load effects.....	170

Figure 6-11: Plot of bucket moment-rotation response during shaking with operational wind load effects.....	171
Figure 6-12: Bucket moment-rotation response at different time instances .....	172
Figure 6-13: Time histories of bucket moment (top plot), bucket rotation (middle plot) and near field $r_u$ at mid skirt height (bottom plot) for OWT without operational wind load effects.....	173
Figure 6-14: Plots of a) acceleration time histories, and b) frequency spectra of accelerations at different heights along OWT structure using SDOF structure .....	174
Figure 6-15: Comparison between moment, rotation and near field (i.e., beside the bucket) excess PP response for MDOF and SDOF structures .....	175
Figure 7-1: Change of a) bucket rotation, b) bucket lateral displacement, and c) structure fundamental frequency with bucket diameter and skirt length under monotonic quasi-static operational wind loads ( $D_r = 75\%$ ) .....	198
Figure 7-2: Change of a) bucket rotation, b) bucket lateral displacement, and c) structure fundamental frequency with bucket diameter and skirt length under monotonic quasi-static operational wind loads ( $D_r = 90\%$ ) .....	199
Figure 7-3: Demonstration of the first six vibration mode shapes evaluated using base-spring model for B4 in sand of $D_r = 75\%$ .....	200
Figure 7-4: Variation of natural frequencies for different models ( $D_r = 75\%$ ) .....	201
Figure 7-5: Plot of transfer function between tower top and bucket acceleration at mid skirt height under low amplitude shaking for B4 in sand with $D_r$ of a) 75% and b) 90% .....	202
Figure 7-6: Plot of moment-rotation relationship of bucket foundation in drained quasistatic monotonic loading (combined with 5.8 MN vertical dead load of the superstructure) for c) B4 in sand with $D_r$ of 75% and 90%, and d) different buckets in sand of $D_r$ of 75%.....	203
Figure 7-7: Time histories of bucket moment (top plots), rotation (middle plots) and excess PP response (bottom plots) for B4 in sand with $D_r$ of a) 75% and b) 90% under E50-I and E50-II motions (Table 7-5).....	204
Figure 7-8: a) Time history plots of B4 bucket rotation (top plot) and near field $r_u$ (bottom plot) for different $D_r$ , and change of permanent bucket rotation at end of shaking with b) sand relative density and c) maximum near field $r_u$ under E50 motions (Table 7-5) .....	205
Figure 7-9: Acceleration time histories (top plots) and the corresponding response spectra (bottom plots) for B4 with 90% relative density at model base (left column) and near surface (right column) for the different employed earthquake input motions: E50-II, N38 and T31 (Table 7-5) .....	206
Figure 7-10: Time histories of bucket moment (top plots), bucket rotation (middle plots) and $r_u$ (bottom plots) for B4 with 90% relative density due to the different earthquake motions.....	207



Figure 7-11: Time histories of bucket rotation (top plot) and near-field $r_u$ (bottom plots) for B4 with 75% and 90% $D_r$ due to the different earthquake motions: E50-I, N28 and T16 (for 75% $D_r$ ), and E50-II, N38 and T31 (for 90% $D_r$ ) .....	208
Figure 7-12: Time histories of a) bucket rotation (top plot) and near field $r_u$ (bottom plots), and b) bucket moment for B4 with 90% relative density under motions E75, N50 and T50 .....	209
Figure 7-13: Change of residual/permanent B4 bucket rotation with maximum near-field $r_u$ (representing different $D_r$ values) towards end of shaking under different earthquake motions (Table 7-5).....	210
Figure 7-14: Time histories of bucket moment (top plots), bucket rotation (middle plots) and near field $r_u$ (bottom plots) for B4 under E50 motions with different soil permeability ( $k$ ) .....	211
Figure 7-15: Change of permanent bucket rotation towards end of shaking with soil permeability for B4 in different $D_r$ values using E50 motions.....	212
Figure 7-16: Time histories of bucket moment (top plots), rotation (middle plots) and excess PP response (bottom plots) for B4 in sand with $D_r$ of 100% under E50 motion.....	213
Figure 7-17: Time histories of bucket moment (top plots), bucket rotation (middle plots) and $r_u$ (bottom plots) for different buckets with 90% relative density under E50-II motion .....	214
Figure 7-18: FE deformed mesh contours for vertical displacement (scale factor = 2) showing the permanent bucket rotation at end of shaking (time = 35 seconds) for bucket a) B1 and b) B4 (Table 7-3) in 90% $D_r$ sand of permeability of 1E-4 m/s due to E50-II motion.....	215
Figure 7-19: Change of residual/permanent bucket rotation at end of shaking with the OWT fundamental frequency for different buckets (B1 through B8) with sand $D_r$ of 75% and 90% under E50 motions (Table 7-5) .....	216
Figure 7-20: Plots of a) soil acceleration time histories below the bucket at mid skirt height, b) the corresponding response spectra, c) time histories of bucket moment, and d) time histories of bucket rotation (top plot) and near field $r_u$ (bottom plot) for different damping coefficients .....	217
Figure 8-1: A schematic of accelerometer array for tracking of shear wave propagation velocity .....	237
Figure 8-2: Laminar soil container with internal dimensions of 3.9 m x 1.8 m x 1.8 m (Length x Width x Height), placed on shake table at the UC San Diego Powell Laboratory.....	238
Figure 8-3: a) Placing the EPDM liner inside the soil container, b) Soil hopper with a screen attached, c) additional sieves placed inside the soil container, and d) dry sand pluviation into water.....	239
Figure 8-4: Testing configuration and instrumentation layout of model 1 (dimensions shown in mm).....	240

Figure 8-5: Error in the evaluated shear wave velocity due to one time-step error, for sampling rate of 25,600 samples/second .....	241
Figure 8-6: Acceleration time history of the shake table input excitation for model 1 .....	242
Figure 8-7: Model 1 acceleration time histories at different depths .....	243
Figure 8-8: Time histories of excess pore pressure ratio at different depths in model 1 .....	244
Figure 8-9: Lateral displacement profile of the laminar container relative to displacement at depth 2.75 m, at selected time instants in model 1, along with the corresponding accelerometers .....	245
Figure 8-10: Cross-correlation between A08 and A09 accelerations (model 1) for two time windows centered at 3 seconds (i.e., at the beginning of shaking) and 21 seconds (i.e., towards end of shaking).....	246
Figure 8-11: Enlarged view of the cross-correlation between A08 and A09 accelerations (model 1) for different time windows centered at 3, 12, 16 and 21 seconds.....	247
Figure 8-12: Time histories of $V_s$ as well as the corresponding acceleration (A09, A10 and A11) and EPP ratio within the base dense layer in model 1 .....	248
Figure 8-13: Time histories of $V_s$ as well as the corresponding acceleration (A06, A07, A08 and A09) and EPP ratio within the loose and dense layers in model 1 .....	249
Figure 8-14: Time histories of $V_s$ as well as the corresponding acceleration (A03, A04, A05 and A06) and EPP ratio within the loose layer in model 1 .....	250
Figure 8-15: Time histories of $V_s$ and the corresponding acceleration (A01, A02 and A03) within the crust layer in model 1 .....	251
Figure 8-16: Evolution of $V_s$ during shaking at different locations along depth of model 1 .....	252
Figure 8-17: Model 2 layout of accelerometers and nearby pore pressure transducers (dimensions shown in mm), as well as input shake table motion and final lateral displacement profile of the laminar container .....	253
Figure 8-18: Model 2 time histories of acceleration at different depths, and the corresponding histories of EPP ratio .....	254
Figure 8-19: Cross-correlation between A5 and A6 accelerations (model 2) for two time windows centered at 3 seconds (i.e., at the beginning of shaking) and 13 seconds (i.e., towards end of shaking).....	255
Figure 8-20: Enlarged view of the cross-correlation between A5 and A6 accelerations (model 2) for different time windows centered at 3, 6, 8 and 13 seconds.....	256
Figure 8-21: Model 2 evolution of shear wave velocity during shaking at different locations along depth .....	257
Figure 9-1: Asymmetric motion example for the forward increments scenario .....	273
Figure 9-2: Idealized representative asymmetric acceleration base excitation signals.....	274
Figure 9-3: Input motion displacement, velocity, and acceleration (first 20 of 30 seconds in total).....	275

Figure 9-4: Enlarged view for two cycles of the input motion .....	276
Figure 9-5: Velocity and displacement time histories for Rinaldi and SKR records (After Kalkan and Kunnath 2006).....	277
Figure 9-6: Velocity and displacement records of Station 12 during 1982 Lulong earthquake (After Iwan <i>et al.</i> 1984) .....	278
Figure 9-7: Laminar Soil Container Placed on Shake Table at the UC San Diego Powell Laboratory.....	279
Figure 9-8: a) Placing the EPDM liner inside the soil container, b) Soil hopper with a screen attached to it, c) additional set of sieves placed inside the soil container and d) sand pluviation.....	280
Figure 9-9: Testing configuration and instrumentation layout (dimensions shown in mm).....	281
Figure 9-10: Command and feedback signals of the input motion (first 20 of 30 seconds in total).....	282
Figure 9-11: Enlarged view of the command and feedback signals of the input excitation showing two cycles.....	283
Figure 9-12: Representative acceleration and pore water pressure response during shaking along the north instrumentation array.....	284
Figure 9-13: Lateral relative displacement along the laminar container height .....	285
Figure 9-14: Soil container before and after the shaking event .....	286
Figure 9-15: Accumulated lateral displacement profiles at different cycles during the shaking event .....	287
Figure 9-16: Shear stress and strain time histories at 0.75 m, and 1 m depth.....	288
Figure 9-17: Shear stress-strain response during shaking event (within the saturated medium-dense stratum) .....	289
Figure 9-18: Command and feedback of input motion for the two preliminary shaking tests and lateral deformation of soil container .....	290

# LIST OF TABLES

Table 2-1: Offshore wind projects with bucket foundations (After BOEM 2021a).....	21
Table 3-1: Geotechnical properties of F-65 Ottawa sand (After Bastidas 2016a).....	42
Table 3-2: Properties of sand stratum for the shake table test .....	43
Table 3-3: Properties of the prototype and the scaled model.....	44
Table 3-4: Description of shake table test motions.....	45
Table 5-1: Calibrated parameters for PDMY02 soil model.....	124
Table 5-2: PIMY model parameters employed for bucket foundation to represent aluminum material .....	125
Table 6-1: Properties of the prototype and the scaled model.....	158
Table 6-2: Parameters of PDMY02 and PIMY models for full-scale case.....	159
Table 6-3: Natural frequencies and mode shapes of fixed-base and flexible base 3.45 MW OWT .....	160
Table 7-1: Description of different bucket models B1 through B8 .....	192
Table 7-2: Parameters of PDMY02 and PIMY models for full-scale cases .....	193
Table 7-3: Rotational and translational stiffness as well as natural frequencies ( $f_n$ ) of 3.45 MW OWT bucket foundation for different buckets (B1 through B8) evaluated under operational wind loads in sand with $D_r$ of 75% and 90% .....	194
Table 7-4: Safety factors against bearing capacity and overturning failure modes for different buckets .....	195
Table 7-5: Description of the modified earthquake motions .....	196
Table 7-6: Damping ratios at the first 6 modes of vibration for different Rayleigh damping coefficients (highlighted cells are the target damping ratios for the first and third modes).....	197
Table 8-1: Geotechnical properties of F-65 Ottawa sand (After Bastidas 2016a).....	234
Table 8-2: Properties of sand strata for model 1 .....	235
Table 8-3: Properties of sand strata for model 2.....	236
Table 9-1: Geotechnical properties of F-65 Ottawa sand (After Bastidas 2016b) .....	271
Table 9-2: Properties of the two sand strata.....	272

## ACKNOWLEDGEMENTS

I would like to thank Professor Ahmed Elgamal for his support, guidance and encouragement throughout this work.

For me, the PhD journey was not straightforward, and it would not have been possible without the valuable contributions and the great help I received from my professors, colleagues, friends and family members. I would like to express my sincere gratitude to Dr. Kyungtae Kim and Dr. Ismaail Ghaaowd who helped guiding me through many of the aspects related to experimental work, physical modeling and shake table testing (including but not limited to instrumentation, sensor assembly and calibration as well as data acquisition) at the University of California San Diego (UCSD). Moreover, I would like to thank Mr. Athul Parayancode for his significant help and the great discussions we had while conducting the physical and numerical modeling work. In addition, I would like to recognize the useful insights and support provided by Dr. Jinchu Lu, Dr. Zhijian Qui, Dr. John Li, Dr. Ahmed Ebeido, Dr. Abdullah Almutairi and Dr. Lan Luo. The experimental work reported in this dissertation was conducted at the Structural Engineering laboratories of UCSD with assistance graciously provided by Dr. Christopher Latham, Mr. Andrew Sander, Mr. Mike Sanders, Mr. Abdullah Hamid and Mr. Darren Mckay.

Part of the presented research was conducted under grant OISE 1445712 from the National Science Foundation, funding from the California Department of Transportation as well as the Trent R. Dames and William W. Moore graduate fellowship from the American Society of Civil Engineers (ASCE) and the CalGeo Graduate Student Fellowship. Furthermore, I appreciate the pressure-transducer partial contribution made by Kyowa Electronic Instruments Co., LTD.

The time I spent on research was only part of the PhD journey. I have learned a lot from the classes I have completed and the other ones I was assigned as teaching assistant at UCSD. For that, I would like to say “Thank you” to Professors John McCartney, Michael Todd, J.S. Chen, Joel Conte, William Hodgkiss, Benson Shing and Kenneth Loh. The classes also gave me the chance to make a wonderful friendship with two amazing people, Dr. Manuel Vega, Ms. Yuhan Shi and Ms. Kristina Koharchik – thank you for everything.

On the non-academic and non-technical level, I enjoyed the extra curriculum work and activities I did at UCSD. I was fortunate to serve as a Principal member of the ASCE Geo-Institute and CalGeo Student Chapters at UCSD. In this regard, I would like to thank Ms. Radhavi Samarakoon, Dr. Lan Luo, Dr. Fatemah Behbehani, Ms. Mahta Movasat, Mr. Jeffery Newgard, Dr. Wenyong Rong, Dr. Leticia Nocko, Dr. Tugce Baser, Dr. Yewei Zheng, Ms. Carolina Jauregui, Dr. Morgan Funderburk and Dr. Patrick Hughes. Moreover, being part of the Structural Engineering Department representation at the UCSD Graduate Student Associate (GSA) and the Student Workers Union was a privilege through which I have learned a lot. In addition, mentoring a group of undergraduate engineering students at part of the Jacobs Undergraduate Mentorship Program (JUMP) was a great and enjoyable experience.

On the other hand, I would like to extend my thanks to my coworkers at DNV Energy Systems USA, particularly Mrs. Cory Gessert, Mrs. Claire Haack, Mr. Matt Rogers and Mr. Eric Ntambakwa. Being part of the North America Civil Engineering Section at DNV for the past two and half years has been wonderful experience during which I have learned a lot not only about onshore and offshore wind engineering but also solar and renewable energy.

Finally, to my parents, Dr. Aida Ayoub and Mr. Ahmed Zayed, my sister and brother, Dr. Ghady and Mr. Mostafa, I would have never been able to reach this far without your support and love – Thank you for everything!

The content of this dissertation being prepared to be and has been published in few journals that are listed in the following paragraphs, authored by the dissertation author, Dr. Ahmed Ebeido, Mr. Athul Prabhakaran, Dr. Kyungtae Kim, Dr. Zhijian Qiu, and Professor Ahmed Elgamal.

The discussion carried out in chapters 3 and 4 is currently being prepared to be published as a journal paper tentatively in the ASTM Geotechnical Testing Journal or the ASCE Journal of Geotechnical and Geoenvironmental Engineering. The proposed title of this paper is “Shake table testing of bucket foundation for offshore wind applications”. The dissertation author is the primary author of this paper with Dr. Kyungtae Kim, Mr. Athul Prabhakaran, and Professor Ahmed Elgamal as coauthors.

The content of chapters 5 and 6 is currently being prepared to be published as a journal paper tentatively in the ASCE Journal of Geotechnical and Geoenvironmental Engineering or the Soil Dynamics and Earthquake Engineering Journal. The proposed title of this paper is “Computational modeling of bucket foundation seismic response for utility-scale offshore wind turbine using experimental data”. The dissertation author is the primary author of this paper with Dr. Kyungtae Kim, Mr. Athul Prabhakaran, and Professor Ahmed Elgamal as coauthors.

The parametric study presented in chapter 7 is currently being prepared to be published as a journal paper tentatively in the ASCE Journal of Geotechnical and Geoenvironmental Engineering or the Soil Dynamics and Earthquake Engineering Journal. The proposed title of this paper is “Seismic response of bucket foundation utility-scale wind turbine: Effects of bucket size,

soil stiffness and permeability”. The dissertation author is the primary author of this paper with Dr. Kyungtae Kim, and Professor Ahmed Elgamal as coauthors.

The approach developed in chapter 8 has been published as a journal paper in the ASTM Geotechnical Testing Journal, Volume 44, Issue number 4, with a publication date 28<sup>th</sup> of July 2020. The title of this paper is “Shake table testing: A high-resolution vertical accelerometer array for tracking shear wave velocity”. The dissertation author is the primary author of this paper with Dr. Ahmed Ebeido, Mr. Athul Prabhakaran, Dr. Kyungtae Kim, Dr. Zhijian Qiu, and Professor Ahmed Elgamal as coauthors.

The contents of chapter 9 have been published as a journal paper in the Canadian Geotechnical Journal, Volume 58, Issue number 2, with a publication date 14<sup>th</sup> of April 2020. The title of this paper is “Asymmetric input motion for accumulation of lateral ground deformation in laminar container shake table testing”. The dissertation author is the primary author of this paper with Dr. Ahmed Ebeido, Mr. Athul Prabhakaran, Dr. Zhijian Qiu, and Professor Ahmed Elgamal as coauthors.

I wrote this for my own pleasure and to record experiences I shall never forget. At UCSD, I have had good times, hard times, but never bad times. Thank you UCSD for being like home!

March 2022



# VITA

## Education

- 2015 –2022      *Doctor of Philosophy, Structural Engineering*  
University of California San Diego, United States
- 2011 –2014      *Master of Science, Structural Engineering*  
Ain Shams University, Cairo, Egypt
- 2005 –2010      *Bachelor of Science, Civil Engineering*  
Ain Shams University, Cairo, Egypt

## Research Experience

*Sep 2015 – June 2019*

### **PhD Student**

*University of California San Diego, Structural Engineering Department  
La Jolla, California, United States*

- Conducting 1-g shake table testing to study the seismic response of bucket foundations for offshore wind turbines.
- Instrumentation and testing of pile foundation in a large-scale liquefaction-induced lateral spreading experiment at NEES-UCSD shake table.
- Fabricating laminar soil container for dynamic centrifuge testing.
- Tested dynamic response of pile group in centrifuge shake table testing.
- Developing low-cost pressure sensors for monitoring excess pore pressure in soil during seismic excitation.
- Developing new approach for tracking evolution of shear wave velocity in saturated soil during seismic excitation, using a newly developed framework.
- Investigating use of asymmetric base excitation for simulating near-fault ground motions with accumulation of lateral deformation in large-scale shake table testing, for applications on modeling liquefaction-induced lateral spreading mechanism.
- Modeling and calibrating finite element model for wind turbines including soil-structure interaction, using experimental data collected from field measurements and shake table testing for wind turbine models.

*Jul 2018 – Aug 2018*

### **Visiting Graduate Student**

*Asia-Pacific-Euro Summer School on Smart Structures Technology  
Harbin Institute of Technology and University of Qingdao, China*

- Conducted 3 experimental and analytical projects on: 1) system identification of pedestrian bridge, 2) damage detection, 3) computer vision for crack detection and classification, as part of the research activities during the summer school.

*Jan 2012 – Jun 2014*

**Research Assistant**

*Soil Mechanics and Foundation Engineering Research Unit,  
Ain Shams University, Cairo, Egypt*

- Analytically modeling soil-pile interaction to develop partial safety factors for limit state design approach, as part of the work done for updating the design code of practice from working stress design to limit state design.
- Conducting laboratory and in-situ testing for soils and foundations, e.g., Standard Penetration Test, Pressure Meter Test and low-strain Pile Integrity Test.
- Modeling and designing shallow and deep foundations, as well as earth retaining structures.
- Preparing geotechnical reports.

**Teaching Experience**

*Winter 2020, Spring 2019, Winter 2019 & Fall 2017 & Fall 2020*

**Teaching Assistant**

*University of California San Diego, Structural Engineering Department*

- Advanced Structural Dynamics (Prof. Michael Todd)- 21 students.
- Structural Dynamics (Prof. Michael Todd)- 61 students.
- Earthquake Engineering (Prof. Ahmed Elgamal)- 46 students.
- Finite Elements in Solid Mechanics I (Prof. Shabnam Semnani) – 40 students

*Jul 2014 – Aug 2015*

**Assistant Lecturer**

*Ain Shams University, Structural Engineering Dep., Cairo, Egypt*

- Foundation Engineering (Prof. Fathalla El-Nahhas) - three sections, 55 students/each.

*Jan 2012 – Jun 2014*

**Teaching Assistant**

*Ain Shams University, Structural Engineering Dep., Cairo, Egypt*

- Geotechnical Engineering I (Prof. Yasser El-Mossallamy) - 3 sections, 55 students/ea.
- Geotechnical Engineering II (Prof. Mohamed Mansour) - 2 sections, 55 students/ea.

*Oct 2010 – Jan 2012*

**Teaching Assistant**

*Future University in Egypt, Al Tagamoa El Khames, Cairo, Egypt*

- Construction Project Management || Geotechnical Engineering I || Structural Analysis I

**Professional Experience**

*Jul 2019– Present*

**Civil/Geotechnical Engineer**

*DNV GL Energy USA, Inc. – San Diego office*

- Review of design drawings and calculations for Wind and Solar Energy foundations structural support systems, to support project financing.
- Evaluation of pre-market design concepts for Wind and Solar Energy structural support systems.
- Evaluation and root cause analyses of Wind and Solar Energy system structural failures.
- Observation and documentation of Wind and Solar Energy construction.
- Conducting liquefaction analyses for shallow and deep foundation used with energy structures.
- Conducting site response analyses,
- Conducting Probabilistic Seismic Hazard Analyses (PSHA).
- Supervising construction works in wind and solar energy projects.

*Oct 2011– June 2015*

**Geotechnical Engineer**

*El-Mossallamy Engineering Consultancy (Yasser El-Mossallamy, PhD)*

*Heliopolis, Cairo, Egypt*

- Conducted numerical modeling, analysis and design of deep excavation, slope stability, earth-retaining structures (R.C., gravity and pile walls) as well as shallow and deep foundations (pile foundations and piled-rafts).
- Supervised in-situ boreholes, standard penetration tests, cone penetration tests and pressure-meter tests.
- Planned and supervised rehabilitation and repair works of shallow foundations.

*Jan 2012 – Jun 2014*

**Geotechnical/Laboratory Engineer (Part-time)**

*Soil Mechanics and Foundation Engineering Research Unit,*

*Ain Shams University, Cairo, Egypt*

- Analytically modeled pile-soil-interaction to develop partial safety factors for limit state design approach, as part of the work done for updating the design code of practice from working stress design to limit state design.
- Conducted laboratory and in-situ testing for soils and foundations, e.g., Standard Penetration Test, Pressure Meter Test and low-strain Pile Integrity Test.
- Modeled and designed shallow and deep foundations, as well as earth retaining structures.
- Prepared geotechnical reports.

**Internship**

*Nov 2010 – Aug 2011*

**Structural Engineering Intern**

*ECCP (General Contractor), Obour City, Cairo, Egypt*

- Performed analysis and design of reinforced concrete and steel structures.

*Aug 2009 – Aug 2009*

**Environmental Engineering Intern**

*Schlumberger, Matrouh, Egypt*

- Involved in oil & gas exploration field measurements in Western Desert, Egypt.

*Jun 2009– Jul 2009*

**Structural Engineering Intern**

*Dar Group (Dar Al-Handasah, Shair and Partners), Cairo, Egypt*

- Conducted numerical modeling, analysis and design of reinforced concrete and structures as well as retaining walls for underground subway station.

**Training & Certifications**

Feb 2021 **Professional Civil Engineer (Geotechnical focus) – License Number 92454**

Board for Professional Engineers in California, USA.

Fall 2017 **Equity, Diversity and Inclusion in Postsecondary Education Training**

UC San Diego Extension, California, USA.

Aug 2017 **LabVIEW Core 1 & 2 Training**

National Instruments, California, USA.

## **Honors & Awards**

Fall 2020 Recipient of the CalGeo Scholarship.

Jun 2019 Recipient of the ASCE Dams and Moore Fellowship.

May 2019 Grant: ISSMGE Foundation Grant.

Apr 2019 Fund: UC San Diego Graduate Student Association Travel Fund.

Nov 2018 Award: ISSMGE Bright Spark Lecture Award – GeoMEast Congress.

Oct 2018 Fund: UC San Diego Jacobs School of Engineering Travel Grant.

Aug 2018 Scholar of the *Asia-Pacific-Euro Summer School (APESS) Graduate Student Program on Smart Structures Technology*, Harbin and Qingdao, China.

Jun 2018 Fund: UC San Diego Jacobs School of Engineering Travel Grant.

2006 - 2010 Academic Honor – Ain Shams University.

## **Professional Affiliation/Association**

- Licensed Professional Engineer in California (License Number 92454)
- American Society of Civil Engineers (ASCE) & Geo-Institute, *member*
- California Geotechnical Engineering Association (CalGeo), *member*
- Deep Foundation Institute (DFI), *member*
- Earthquake Engineering Research Institute (EERI), *member*
- International Society of Ocean and Polar Engineering (ISOPE), *member*
- International Society of Soil Mechanics and Geotechnical Engineering (ISSMGE)
- Structural Engineering Association of San Diego (SEAOSD), *member*

## **Outreach & Leadership and Mentorship Experience**

*Academic Years 2017-18 & 2018-19*

**Graduate Student Mentor**

*IDEA Center, Jacobs Schools of Engineering, UC San Diego*

Mentored undergraduate engineering students for two years, as part of Jacobs Undergraduate Mentor Program (JUMP) for first-generation college students.

***Academic Years 2017-18 & 2018-19***

**Mentor for GeoWall Team**

*Jacobs Schools of Engineering, UC San Diego*

Mentored UC San Diego GeoWall undergrad team for the National and PSWC GeoWall competitions.

***Academic year 2018/19***

**Graduate Student Association (GSA) Council Member**

*UC San Diego*

Representing graduate students at Structural Engineering Department to represent interests and concerns of graduate and professional students, aiming to enrich their life and advance their interests academically, socially and politically.

***Academic year 2018/19***

**Diversity Advisory Council (DAC) Member**

*Graduate Student Association, UC San Diego*

Addressing issues pertaining to equity and diversity in the campus community as well as issues for underrepresented minorities across campus.

***Nov 2016 – Mar 2017***

**Organization Committee Member**

*Earthquake Engineering Research Institute (EERI), San Diego, CA*

*2<sup>nd</sup> Workshop on Geotechnical Earthquake Engineering*

Planned and organized (with a team) the workshop that aimed to Honor Lifetime Achievements & Contributions of Prof. Kenji Ishihara. The workshop theme was “*Dealing with The Consequences of Liquefaction*”.

## **Publications**

### ***Journal Publications***

**Zayed, M., Ebeido, A., Prabhakaran, A., Qiu, Z., and Elgamal, A. (2021).** "Asymmetric input motion for accumulation of lateral ground deformation in laminar container shake table testing." *Canadian Geotechnical Journal* 58 (2):210-223.

**Zayed, M., Ebeido, A., Prabhakaran, A., Kim, K., Qiu, Z., and Elgamal, A. (2020).** "Shake Table Testing: A High-Resolution Vertical Accelerometer Array for Tracking Shear Wave Velocity." *Geotechnical Testing Journal* 44 (4).

El-Mossallamy, Y. M., Tawfik, M. M., and **Zayed, M. (2017).** *Application of ultimate limit state design for axially loaded single piles in Egyptian geotechnical practice.* *HBRC Journal*, 13(2), 181-189.

**Zayed, M., Kim, K., Prabhakaran, A., and Elgamal, A. (2022).** *Shake table testing of bucket foundation for offshore wind applications.* *ASTM Geotechnical Testing Journal or ASCE Journal of Geotechnical and Geoenvironmental Engineering.* (***In progress***)

**Zayed, M., Kim, K., Prabhakaran, A., and Elgamal, A. (2022).** *Computational Modeling of Bucket Foundation Seismic Response for Utility-Scale Offshore Wind Turbine Using Experimental Data.* *ASCE Journal of Geotechnical and Geoenvironmental Engineering or Soil Dynamics and Earthquake Engineering Journal.* (***In progress***)

**Zayed, M., Kim, K., and Elgamal, A. (2022).** *Seismic Response of Bucket Foundation Utility-Scale Offshore Wind Turbine: Effects of Bucket Size, Soil Stiffness and Permeability.* *ASCE Journal of Geotechnical and Geoenvironmental Engineering or Soil Dynamics and Earthquake Engineering Journal.* (***In progress***)

### ***Conference Proceedings***

**Zayed, M., Kim, K., & Elgamal, A. (2019).** *Shake Table Testing for Suction Bucket Foundation Wind Turbine Seismic Response.* *Proceedings of the 29<sup>th</sup> International Ocean and Polar Engineering Conference (ISOPE-2019), Honolulu, Hawaii, June 16-21.*

**Zayed, M., Kim, K., & Elgamal, A. (2019).** *Seismic Response of Suction Caisson - 1g Shake Table Test.* *Paper will be Proceedings of the 7<sup>th</sup> International Conference on Earthquake Geotechnical Engineering, Rome, Italy, June 17-20.*

**Zayed, M., Elgamal, A., Saudi, G., Abd el-aal, K. A. & El-Zahaby, K. (2018).** *Response of A 850 KW Wind Turbine Including Soil-Structure Interaction During Seismic Excitation.* *Proceedings of the 2<sup>nd</sup> GeoMEast International Congress and Exhibition on Sustainable Civil Infrastructures, Egypt, Nov. 24-28 (Vol. I, pp. 114-125).*

Ebeido, A., Elgamal, A. & **Zayed, M. (2019).** *Large Scale Liquefaction-Induced Lateral Spreading Shake Table Testing at the University of California San Diego.* *Paper will be presented at the Geo-Congress 2019, Philadelphia, Pennsylvania, March 24-27.*

Ebeido, A., Elgamal, A. & **Zayed**, M. (2018). *Pile response during liquefaction-induced lateral spreading: 1-g shake table tests with different ground inclination*. Physical Modelling in Geotechnics: (ICPMG 2018), London, United Kingdom, July 17-20.

Ebeido, A., **Zayed**, M., Kim, K., Wilson, P. & Elgamal, A. (2018). *Large Scale Geotechnical Shake Table Testing at the University of California San Diego*. Proceedings of the 2<sup>nd</sup> GeoMEast International Congress and Exhibition on Sustainable Civil Infrastructures, Egypt, Nov. 24-28 (Vol. I, pp. 101-113).

**Zayed**, M., Luo, L., Kim, K., McCartney, J., & Elgamal, A. (2017). *Development and performance of a laminar container for seismic centrifuge modeling*. Paper presented at the 3<sup>rd</sup> International Conference on Performance-Based Design in Earthquake Geotechnical Engineering, Vancouver, BC, Canada, July 16-19.

**Zayed**, M. (2014). *Towards Limit State Design for Axially Loaded Piles in Egyptian Geotechnical Practice*. Paper presented at the 8<sup>th</sup> African Young Geotechnical Engineers Conference, Stellenbosch, Western Cape, South Africa; Sep. 2014.

#### ***Invited Lectures***

*Seismic Response of Bucket Foundation for Offshore Wind Turbines: 1-g Shake Table Test*. ISSMGE Bright Spark Lecture During the Young Geotechnical Engineers Session, 2<sup>nd</sup> GeoMEast Congress and Exhibition, Cairo, Egypt, November 26.

#### ***Magazine Articles***

Tugce Baser, Yewei Zheng & Muhammad **Zayed** (2017): *Lessons Learned from Geo-Legends (Tien Wu, PhD, Hon.M.ASCE)*. GEOSTRATA Magazine - 08/2017: pages 24-31; Geo-Institute of ASCE.



# **ABSTRACT OF THE DISSERTATION**

Experimental and Numerical Seismic Response of Offshore Wind Turbines Supported on Bucket Foundations

by

Muhammad Zayed

Doctor of Philosophy in Structural Engineering

University of California San Diego, 2022

Professor Ahmed Elgamal, Chair

Bucket foundations have proven to be an efficient cost-effective option for a wide range of offshore applications. Motivated by the strong growth in offshore wind energy, this dissertation aims to investigate the seismic response of bucket foundations. A scaled soil-structure model of a 3.45 Megawatt (MW) utility-scale Offshore Wind Turbine (OWT) was tested on medium-size 1-g shake table. A preliminary testing phase resulted in developing new approaches for: i) tracking shear wave velocity variation within the ground during seismic excitation, and ii) generating accumulated ground deformation via asymmetric base shaking. Thereafter, the OWT model was

subjected to a series of harmonic and earthquake-like excitations. From the collected data, key features of the overall system response were gleaned. Utilizing the experimental data, a nonlinear finite element (FE) model was calibrated to simulate the observed seismic response. The developed FE model was then extended to investigate the seismic behavior of a representative utility-scale OWT in sands under earthquake motions, combined with operational wind load effects. A parametric study is conducted to investigate influence of: i) soil stiffness and strength, ii) ground motion characteristics, iii) soil permeability, iv) bucket size, and v) damping on the OWT seismic response. The results suggest that: i) the near field pore water pressure build-up and bucket rotation are correlated, ii) ground motion characteristics have direct impact on the permanent bucket rotation, iii) lower soil permeability results in larger rotation due to the higher near field pore water pressure build-up, iv) permanent bucket rotation tends to reach a maximum and a minimum at the lower and upper bounds of soil permeability, respectively, reflecting the fully drained and undrained conditions, v) the difference in permanent bucket rotation between undrained and drained conditions tends to decrease with increasing soil stiffness, vi) Within the range of investigated scenarios, an essentially linear correlation was noted between the OWT fundamental frequency and the permanent bucket rotation, and vii) viscous damping at higher frequencies might have a significant effect on the bucket moment rotation response. As such, the gained insights provide guidance for seismic design of bucket foundation offshore wind turbines.

# Chapter 1

## Introduction

*Success is not final. Failure is not fatal. It is the courage  
to continue that counts.*

– Winston Churchill

### 1.1 Extended abstract

Bucket foundations have proven to be an efficient cost-effective option for a wide range of offshore applications. Motivated by the strong growth in offshore wind energy, this dissertation aims to investigate the seismic response of bucket foundations. In order to generate quantitative response data sets, a scaled soil-structure model of a 3.45-Megawatt (MW) utility-scale Offshore Wind Turbine (OWT) was tested on medium-size 1-g shake table. Harmonic and earthquake-like excitations were imparted, and different types of model response were recorded. The model was subjected to a total of 18 shaking events, and the response was observed and documented. From this data, key characteristics of the system bucket foundation and the overall wind turbine system response were gleaned. Utilizing the experimental data, a nonlinear finite element (FE) model was calibrated to simulate the observed seismic response. The developed FE model was then extended to investigate the seismic behavior of a representative utility-scale OWT in sands under different earthquake motions, combined with operational wind load effects. A parametric study is conducted to investigate influence of: i) soil stiffness and strength, ii) ground motion characteristics, iii) soil

permeability, iv) bucket size, and v) damping on the OWT seismic response. The results suggest that: i) the near field pore water pressure build-up and bucket rotation are correlated, ii) ground motion characteristics have direct impact on the permanent bucket rotation with the latter mainly depending on the resulting near field pore water pressure response, iii) lower soil permeability results in larger rotation due to the higher near field pore water pressure build-up, iv) permanent bucket rotation tends to reach a maximum and a minimum at the lower and upper bounds of soil permeability, respectively, reflecting the fully drained and undrained conditions, v) the difference in permanent bucket rotation between undrained and drained conditions tends to decrease with increasing soil stiffness, vi) a linear correlation can be expressed between the OWT fundamental frequency and the permanent bucket rotation, and vii) viscous damping at higher frequencies might have a significant effect on the bucket moment rotation response. As such, the gained insights provide guidance for seismic design of bucket foundation offshore wind turbines.

As a main element of preparation for the OWT testing scope, preliminary efforts included the investigation of data collected from shake table tests to develop a technique for estimating changes in soil shear wave velocity ( $V_s$ ) during seismic excitation. Since the change in soil stiffness is related to  $V_s$ , the developed technique can be used to monitor changes in soil stiffness and soil shear modulus during seismic excitation. Supported by pore water pressure measurements, data sets from different medium and large-scale 1-g shake table tests were used to develop and verify the technique. Using the developed technique, evolution of  $V_s$  with time can be observed at different depths within the tested soil model. Results from this technique are found to capture loss of soil stiffness and strength due to liquefaction, which is reflected by the drop in  $V_s$  as it approaches zero. Such evidence of liquefaction was confirmed by the corresponding records of excess pore water pressure. The results showed that soil liquefaction starts at the top part of loose

sand layers, and then propagates downwards. An isolation mechanism above the liquefiable layer was observed using the developed technique, where the top crust stratum moves essentially as a rigid block following the underlying liquefiable layer.

Furthermore, a novel approach for generating accumulated ground deformations in shake table testing was developed. This approach employs asymmetric inertial loading that results in a biased dynamic one-dimensional shear state of stress. As such, the proposed approach allows for further insights into the soil cyclic response and pore water pressure build-up, with deformations accumulating in a preferred direction. In order to permit a virtually unlimited number of such loading cycles, focus is placed on motions that do not cause the shake-table actuator to accumulate displacement, in view of its possible limited stroke. Using this approach, representative experimental response is outlined and discussed. In addition to liquefaction-induced lateral spreading, this asymmetric shaking approach might be beneficial for a wide class of earthquake engineering shake table testing applications.

## **1.2 Motivation**

Offshore wind industry started in 1990s and has been growing in scale ever since (Rodrigues *et al.* 2015, Ogden 2021). However, in recent years, growth has accelerated. From being 1% of global installations by capacity in 2009, offshore wind has grown to over 10% in 2019. The global offshore wind market grew on average by 24% each year since 2013, bringing the total installations to 29.1 Gigawatt (GW), which accounted for 5% of total global wind capacity as the end of 2019. The top five offshore wind markets in total installations are: the UK, Germany, China, Denmark and Belgium. Expectations are set for the global offshore wind market to reach a 70 GW milestone by 2030 (Gordon 2020).

North America has a 30 Megawatt (MW) offshore wind capacity currently (early 2021) in operation in the US, making it the only region with commercial offshore wind outside Europe and Asia. However, the US offshore wind sector made significant progress to accelerate deployment and construction of new offshore wind projects (AWEA 2020) . The total offshore wind procurement targets increased from 9.1 GW in 2018 to 25.4 GW in 2019, after New York and New Jersey upgraded their offshore targets. More states are deciding on their offshore wind targets, which will eventually increase the national US offshore wind target for 2020. According to the Global Wind Energy Council (GWEC), a total of 23 GW of offshore wind is predicted to be built in the East Coast region of the US by 2026. The U.S. National Renewable Energy Lab (NREL) revealed that offshore wind resources in 26 states would have the wind resources to meet at least 20% of their electricity needs, with many states having sufficient offshore wind resources to meet 100% of their needs.

The 12 MW Dominion Virginia demonstration project was successfully installed in June 2020 as the first offshore wind project to be approved by the Bureau of Ocean Energy Management (BOEM) and installed in U.S. federal waters (Musial *et al.* 2019). On the state level, the East Coast cluster consisting of Maine, Connecticut, Massachusetts, New York, New Jersey, Delaware, Maryland, Virginia and North Carolina is driving strong demand for offshore wind energy with the total announced offshore procurement targets reaching 28 GW as of 2019 (AWEA 2020). As for the West coast, California passed Senate Bill 100 (i.e., The 100 Percent Clean Energy Act of 2018), making it the largest state to establish a 100% electrical renewable energy goal, and setting a carbon-free target year of 2045 (Musial *et al.* 2019). In 2019, BOEM received 14 nominations from companies interested in commercial wind energy leases in three proposed call areas off

central and northern California. Musial *et al.* (2019) pointed out these three call areas altogether could support an offshore wind generating capacity of up to 8.4 GW.

Thanks to recent developments and expansion in offshore wind, the cost of electricity generated by offshore wind has dropped from about 255 United States Dollar (USD) per Megawatt-hour (MWh) in 2012 to about 85 USD per MWh in early 2021, and it is expected to reach 58 USD per MWh by 2025 (AWEA 2020). Among the expenses comes the costs of support structure. For offshore wind plants in shallow water (up to 30-meter water depth), cost of support structures represents about 20-30% of the capital cost and 12-25% of the life-cycle cost (Musial and Ram 2010, Versteijlen *et al.* 2011). Furthermore, the foundation construction costs about 60% of the total installation expenses for offshore wind plants (Wang *et al.* 2018). Types of support structure for an Offshore Wind Turbine (OWT) depends mainly on water depth, turbine size and the soil conditions. Monopiles and gravity foundations are the most used type of support structures for the majority of wind turbines in shallow water (Houlsby and Byrne 2000).

Bucket foundation is a relatively new type of foundation that has been used for offshore structures for about 30 years (Houlsby *et al.* 2005). The latter study revealed that bucket foundation was initially introduced as anchors, mainly in clays, and has been used as foundations for offshore platforms. Past research revealed that bucket foundation is an economically attractive alternative for offshore wind farms (Jalbi *et al.* 2018).

Earlier experimental and numerical research has been conducted to investigate the performance and capacity of bucket foundation. However, most of the focus in the existing research was placed on the performance of the bucket foundation in terms of rotation and settlement under the prevalent wind and wave lateral cyclic loading (Zhang *et al.* 2007, Foglia and

Ibsen 2014b, Nielsen 2016, Zhu *et al.* 2019, Fugro 2020, Yin *et al.* 2020, Barari *et al.* 2021, Stapelfeldt *et al.* 2021).

### 1.3 Research goals

Motivated by the potential growth in the U.S. offshore wind market, the research presented in this dissertation aims to address the seismic response of bucket foundations for offshore wind applications. As such, a scaled model of a wind turbine with bucket foundation was tested in a saturated medium dense sand stratum on a 1-g shaking table. The shake table was used to generate cyclic and earthquake-like excitations and the corresponding model responses were recorded. Different harmonic excitations and scaled earthquake records were used to conduct a total of 18 shake table tests. Results of these tests were useful to shed highlight on a number of main response characteristics of the bucket foundation-supported wind turbine model. In addition, the collected data were used to calibrate a three-dimensional finite element model with soil-structure interaction effects that was further used to investigate seismic response of a utility scale 3.45 MW OWT.

Moreover, testing approaches and data collected as part of the overall shake table investigation framework were used to develop:

i) A new technique for estimating changes in shear wave velocity ( $V_s$ ) during seismic excitation. Since any change in soil stiffness is associated with changes in soil  $V_s$ , the developed technique can be used to monitor changes in soil stiffness and soil shear modulus during seismic excitation. Supported by pore water pressure measurements, data sets from different large-scale 1-g shake table tests were used to develop and verify the technique. Using the developed technique, evolution of  $V_s$  with time can be displayed at different depths within the tested soil model. Results from the developed technique are found to capture loss of soil strength and stiffness due to



liquefaction, which is reflected as a dramatic drop in  $V_s$  towards zero. This liquefaction is further confirmed by the corresponding records of excess pore water pressure. Results showed that soil liquefaction starts at the top part of loose sand layers, and thereafter the layer liquefies from the top to downwards. As such, soil liquefaction has been noted to highly interrupt shear wave propagation while traveling through the liquefied layer. An isolation mechanism above the liquefiable layer can be observed using the developed technique, where the top crust layer behaves essentially as a rigid block above the underlying liquefiable layer.

ii) A new approach for generating accumulated ground deformations. The latter approach uses asymmetric inertial loading that results in a biased dynamic one-dimensional shear state of stress. As such, the proposed approach allows for further insights into the soil cyclic response and pore pressure build-up, with deformations accumulating in a preferred direction. In order to permit a virtually unlimited number of such loading cycles, focus is placed on motions that do not cause the shake-table actuator to accumulate displacement, in view of its possible limited stroke. Using this approach, representative experimental response is outlined and discussed. This experimental response can be used for calibration of numerical models to emulate the observed permanent strain accumulation profile and associated mechanisms. In addition to liquefaction-induced lateral spreading, this asymmetric shaking approach might be beneficial for a wide class of earthquake engineering one-dimensional and multi-dimensional shake table testing applications.

## **1.4 Dissertation outline**

The dissertation contains a total of 10 chapters and two appendices, related to the topics described in Section 1.3. A brief description for each chapter is provided below.

Chapter 2 presents a literature review about OWT foundations and use of bucket foundation for offshore wind applications. It also contains a review of earlier and current research related to bucket supported OWTs.

Chapter 3 presents a detailed description of model preparation for shake table testing and includes a comprehensive description of the bucket foundation wind turbine model from CAD modeling to manufacturing. This chapter also includes a description and results of modal testing that was conducted to verify the fundamental frequency of the bucket foundation-supported wind turbine model. Further details about the employed sand and the testing facility are also incorporated. In addition, special data processing approaches are described.

Chapter 4 presents the shake table testing observations regarding excess pore water pressure response of the bucket foundation wind turbine model. Records of pore pressure transducers around the bucket are discussed. In the context of the collected data, the relations between generation of negative excess pore pressure (i.e., suction) and bucket moment and rotation are investigated. In addition, the main response characteristics of the test model in terms of lateral accelerations, vertical displacements, overturning moments, and rotations are presented. The content of chapters 3 and 4 is currently being prepared to be published as a journal paper tentatively in the ASTM Geotechnical Testing Journal or the ASCE Journal of Geotechnical and Geoenvironmental Engineering. The proposed title of this paper is “Shake table testing of bucket foundation for offshore wind applications”.

Chapter 5 presents development and calibration procedures of a three-dimensional numerical model, where the data collected from 1-g shake table testing were used to calibrate and the numerical model. Full description of the numerical model and the computational platform are provided in detail.

Chapter 6 presents seismic response of an idealized 3.45 MW utility scale OWT founded on bucket foundation, in which the numerical model calibrated in Chapter 6 is employed and extended. Results from numerical analysis show various response types of the utility scale wind turbine and the supported bucket foundation under various earthquake excitations. The content of chapters 5 and 6 is currently being prepared to be published as a journal paper tentatively in the ASCE Journal of Geotechnical and Geoenvironmental Engineering or the Soil Dynamics and Earthquake Engineering Journal. The proposed title of this paper is “Computational modeling of bucket foundation seismic response for utility-scale offshore wind turbine using experimental data”.

Chapter 7 presents results of a parametric study conducted to investigate effects of bucket size, soil stiffness, soil permeability, damping parameters, as well as earthquake excitation on seismic response of the soil-bucket-structure system. This chapter is currently being prepared to be published as a journal paper tentatively in the ASCE Journal of Geotechnical and Geoenvironmental Engineering or the Soil Dynamics and Earthquake Engineering Journal. The proposed title of this paper is “Seismic response of bucket foundation utility-scale wind turbine: Effects of bucket size, soil stiffness and permeability”.

Chapter 8 describes a new technique that was developed to track changes in soil shear wave velocity ( $V_s$ ) during seismic excitation. The developed technique can be used to monitor changes in soil stiffness and soil shear modulus during seismic excitation. Supported by pore water pressure measurements, data sets from different large-scale 1-g shake table tests were used to verify the developed technique. Evolution of  $V_s$  with time can be displayed at different depths within the tested soil model. Contents of this chapter are published as a journal paper in the ASTM

Geotechnical Testing Journal, Volume 44, Issue number 4, with a publication date 28<sup>th</sup> of July 2020.

Chapter 9 presents a new approach for generating accumulated lateral ground deformations in shake table testing. The latter approach uses asymmetric inertial loading that results in a biased dynamic one-dimensional shear state of stress. As such, the proposed approach allows for accumulation of lateral deformations in a preferred direction, with further insights into the soil cyclic response and pore pressure build-up. Using this approach, representative experimental responses are outlined and discussed. Contents of this chapter are published as a journal paper in the Canadian Geotechnical Journal, Volume 58, Issue number 2, with a publication date 14<sup>th</sup> of April 2020.

Chapter 10 includes a summary of the dissertation as well as conclusions drawn from the conducted research, and recommendations for future research.

Appendix A and Appendix B include plots of different mode responses measured from the shake table tests. Content of the appendices is directly related to Chapter 3 and Chapter 4.

## **Chapter 2**

# **Literature review on bucket foundation for offshore wind applications**

*In the middle of each difficulty lies an opportunity.*

– Albert Einstein

### **2.1 Introduction**

Use of wind energy is increasing rapidly worldwide, with, exceeding the 650 Gigawatt (GW) mile stone in 2019 with an increase of about 10% compared to 2018 (REN21 2019, AWEA 2020). China and the U.S. remain the world's largest onshore wind markets, together accounting for more than 60% of new installed capacities in 2019. The United States (U.S.) Department of Energy set a goal to have 20% of the national end-use electricity demand generated by wind energy in 2030, and 35% by 2050 (Wiser *et al.* 2015). With over 60,000 wind turbines operating across 41 states and two territories in 2019, there are about 110 GW of operating wind capacity in the U.S. representing about a 7.3% share of the total utility-scale electricity generation facilities (AWEA 2020).

## 2.2 Offshore wind

The offshore wind industry started in the 1990s and has been growing in scale ever since (Rodrigues *et al.* 2015, Ogden 2021) . In recent years, however, growth has accelerated. From being 1% of global wind installations by capacity in 2009, offshore wind has grown to over 10% in 2019. A record 6.1 GW new capacity of offshore wind was added globally in 2019 accounting for a share of about 10% of new wind installations (AWEA 2020). The global offshore wind market grew on average by 24% each year since 2013, bringing the total installations to 29.1 GW, which accounted for 5% of total global wind capacity by end of 2019 (IRENA 2019). Europe remains the largest offshore market as end of 2019, making up 75% of total global offshore wind installation (Lee and Zhao 2020). However, Asia showed significant increase in the offshore wind market with China taking the lead followed by Taiwan, Vietnam, Japan and South Korea. Currently, the top five offshore wind markets in total installations are: the UK, Germany, China, Denmark and Belgium (Cozzi and Wanner 2019). Expectations are set for the global offshore wind market to reach 70 GW milestones by 2030 (Gordon 2020).

The United States has set a target to deploy 30 GW of offshore wind by 2030 (Pryor *et al.* 2021). U.S. data showed that 28 states with a coastal boundary use 78% of the nation's electricity. Out of these 28 states, only 6 have a sufficient land-based wind energy resource to meet more than 20% of their electricity requirements through wind power (Lindenberg *et al.* 2009). Musial (2007) revealed that: i) shallow water offshore potential (less than 30 m in depth) is included in the wind resource mix, ii) 26 of the 28 states would have the wind resources to meet at least 20% of their electricity needs, and iii) many states have sufficient offshore wind resources to meet 100% of their electricity needs.

Musial and Ram (2010) indicated that the U.S. offshore wind energy resources can significantly increase the wind industry's contribution to the nation's clean energy portfolio. The United States is fortunate to have large and accessible offshore wind energy resources. Figure 2-1 shows the average wind speed on the coastal zones of the United States. This figure indicates that wind speeds tend to increase significantly with distance from land-based sites. The National Renewable Energy Laboratory estimates that U.S. offshore winds have a gross potential generation capacity four times greater than the nation's present electricity capacity (Jonkman *et al.* 2009).

In North America, the first test OWT that was a 1/8 geometric scale of a 6-Megawatt (MW) wind turbine was installed off the coast of Maine in 2013. The first commercial wind project was connected to the grid in Rhode Island in 2016 (PowerTechnologies 2021). As of the end of 2019, North America has 30 MW offshore wind currently in operation in the US, making it the only region with commercial offshore wind outside Europe and Asia (Lee and Zhao 2020). However, the latter study indicated that the US offshore wind sector made significant progress to accelerate deployment and construction of new offshore wind projects.

The total offshore wind procurement in the U.S. targets increase from 9.1 GW in 2018 to 25.4 GW in 2019 after New York and New Jersey upgraded their offshore targets (AWEA 2020). More states are deciding on their offshore wind target estimates which will eventually increase the national US offshore wind capacity for 2020. So far, a total of six states have selected locations for more than 6 GW of offshore wind plants through state-issued solicitations as of end of 2020 (Lee and Zhao 2020). The US offshore industry is now moving on a phase of project construction planning and execution as more than 15 offshore wind plants are expected to be built by 2030 (Musial *et al.* 2020). According to the Global Wind Energy Council (GWEC, 2020), a total of 23 GW of offshore wind is predicted to be built in the East Coast region of the US by 2026.

The 12 MW Dominion Virginia demonstration project was successfully installed in June 2020 as the first offshore wind project to be approved by the Bureau of Ocean Energy Management (BOEM) and installed in federal U.S. waters (Musial *et al.* 2019). Lee and Zhao (2020) revealed that the level of offshore wind development activity in the US market remains impressively high. As of the end of 2019, BOEM has auctioned 16 active commercial leases for offshore wind development that are expected to produce about 23 GW of generating capacity (AWEA 2020). On the state level, Figure 2-2 shows locations of U.S. offshore wind pipeline activity and call areas as of March 2019. Musial *et al.* (2019) revealed that the East Coast cluster consisting of Maine, Connecticut, Massachusetts, New York, New Jersey, Delaware, Maryland, Virginia, and North Carolina is driving strong demand for offshore wind energy with the total announced offshore procurement targets reaching 28 GW as of 2019. As for the West coast, California passed Senate Bill 100 (i.e., The 100 Percent Clean Energy Act of 2018), making it the largest state to establish a 100% electrical renewable energy goal, and setting a carbon-free target year of 2045 (Musial *et al.* 2019). In 2019, BOEM received 14 nominations from companies interested in commercial wind energy leases within three proposed call areas off central and northern California (BOEM 2021b). Altogether, these three call areas could support an offshore wind generating capacity of up to 8.4 GW (AWEA 2020). Full details about the current and future potential growth of offshore wind in the U.S. market are provided by (Musial *et al.* 2019).

Thanks to recent developments and expansion in offshore wind industry, the cost of electricity generated by offshore wind has experienced a rapid decline. IRENA (2019) and Musial *et al.* (2019) showed that the average cost of electricity generated from offshore wind dropped from about 255 USD per Megawatt-hour (MWh) in 2012 to about 85 USD per MWh in 2021, and it is expected to reach about 58 USD per MWh by 2025.



## 2.3 Foundations for offshore wind turbines

Among the expenses comes cost of the support structure. For offshore wind plants in shallow water (up to 30-meter water depth), support structures represent about 20-30% of the capital and 12-25% of the life-cycle expenses (Musial and Ram 2010, Versteijlen *et al.* 2011) . Wang *et al.* (2018) revealed that the foundation installation costs about 60% of the total for offshore wind plants. Therefore, an easy to install support system that is also cost-efficient is preferred by the offshore wind industry.

Type of support structure for an OWT depends mainly on water depth, soil stratigraphy, wind turbine size, and economic, environmental, and sometimes political policies (Houlsby and Byrne 2000) . The main types of foundations used with OWTs installed in relatively shallow waters (water depth between 0 to 50 m) are sketched in Figure 2-3. Monopiles and gravity foundations are the most used type of support structures for the majority of wind turbines in shallow water. A brief description of each type follows:

- Gravity-based foundations are designed to have sufficient dead load (i.e., weight) to prevent the foundation from potential uplift, excessive tilting and sliding, while ensuring that the total vertical stresses are within the allowable soil bearing capacity. The gravity dead load is typically provided by a large mass of reinforced concrete.
- Monopiles are the second most widely used foundation type for OWTs after gravity base. A monopile typically is a large diameter hollow steel pile installed in the seabed. The monopile diameter varies depending on soil type and stiffness requirements of the wind turbine. However, it is usually equal to or slightly larger than the lowermost diameter of the wind turbine tower (Liingaard 2006). Lateral inertial and external forces resulting from

a wind turbine and its tower are resisted by lateral soil earth pressure on the monopile, while vertical load components are mainly resisted by side friction along the monopile embedment depth. Depending on water depth, local soil conditions, and rated capacity of the OWT, design length of the monopile can range between 20 and 60 m, with about 50% of the length embedded in the seabed (Liingaard 2006). Monopiles are manufactured onshore then transported to their designated locations where they are usually installed as driven piles via hydraulic or vibratory hammers (Leite 2015).

- Tripod foundation can be considered as the extension of monopiles, where three monopiles are driven in the seabed instead of one. The main design criterion for pile of tripod foundations is usually axial bearing capacity rather than lateral resistance (Liingaard 2006).
- Bucket foundation has been recently used for offshore wind applications, mainly adopted from the offshore oil and gas industry (Houlsby *et al.* 2005). Description and use of bucket foundation for OWTs are detailed in the following section.

As the rated capacity and size of OWTs rapidly increase, the demand for more economic, reliable, and robust supporting structures increases. The next generation of turbines promises larger rotors and lower specific power ratings suited for U.S. offshore markets. Specific examples of next generation turbines (Jiang 2021) include the 14 MW Siemens Gamesa SG 14-222 DD, the Vestas V236-15 MW and the GE Haliade-X 14 MW turbines.

## **2.4 Use of Bucket foundation for offshore wind applications**

Bucket foundation is a hollow cylindrical shaped structure that is closed from the top by a flat lid and open from the bottom. Figure 2-4.a shows schematic of an offshore bucket foundation-

supported wind turbine with the main components illustrated. Bucket foundation can have compartments inside formed by a honeycomb shape (Wang *et al.* 2017a) as shown in Figure 2-4.b.

Houlsby *et al.* (2005) considered the bucket foundation, being a relatively new type of foundation used for offshore structures for about 30 years. It was initially introduced as anchors, mainly in clay, and has been used as foundations for offshore platforms. Houlsby and Byrne (2000) revealed that bucket foundation is an economically attractive alternative for offshore wind farms. Moreover, Byrne *et al.* (2002) reported that loading regimes for OWTs are different in several aspects from those of offshore platforms for the oil and gas industry. As such, the existing design criteria for offshore platforms cannot be used directly for OWTs. Foglia and Ibsen (2014a) emphasized that more research should be directed to the behavior of mono bucket foundations under predominant overturning loads and dynamic soil structure interaction.

Currently, bucket foundation is considered to be an efficient alternative for OWTs, which can conceptually cover ranges of water depths of up to 30 m (Houlsby *et al.* 2005, Byrne and Houlsby 2006, Zhang *et al.* 2015). The latter studies pointed out that bucket foundation is preferable for installation in medium stiff clays and fine to medium sands. Moreover, it is not suitable for subsurface conditions with cobbles, boulders, coarse gravel layers or soft soils. Finally, bucket foundations have less negative acoustic effects than monopiles due to the lower noise inducing activities during installation (BOEM 2021a).

The first bucket foundation was installed in Frederikshavn, Denmark in late 2003, with a 3 MW wind turbine prototype in normal operation (Ibsen and Brincker 2004). Furthermore, In March 2009, DONG Energy successfully installed a prototype of a monopod bucket foundation at the Horns Rev 2 Offshore Wind Farm, Denmark (Bakmar *et al.* 2009). Ding *et al.* (2011) reported

that the first OWT with large-scale top-bearing bucket foundation has been installed in China in 2010. Table 2-1 summarizes some information about offshore wind projects that utilize bucket foundations. Few offshore wind farms employed multiple buckets (i.e., bucket jacket foundations) with diameters and lengths between 7 m and 11 m in water depths between 19 m and 45 m (BOEM 2021a).

Recent research on bucket foundations showed that it is a promising solution as supporting structure for OWTs (Houlsby *et al.* 2005, Achmus *et al.* 2013, Foglia and Ibsen 2014a). Byrne *et al.* (2002) claimed that the installation method of bucket foundation (by suction) is cheaper, simpler and quicker than other types of foundations. In addition, they illustrated that bucket foundations can be removed completely from the seabed by the end of lifetime of the wind turbine. As such, the relatively lightweight and easy transportation as well as installation convenience of the bucket foundation makes it an economic alternative as support structure for OWTs (Wang *et al.* 2017b).

Experimental work has been conducted to investigate the vertical, lateral and combined loading capacity of bucket foundations (Villalobos *et al.* 2005, Zhang *et al.* 2007, El Wakil 2010, Villalobos *et al.* 2010, Hung and Kim 2012, El Wakil 2013, Li *et al.* 2014, Li *et al.* 2015, Chen *et al.* 2016, Wang *et al.* 2017a), and under cyclic loading (Foglia and Ibsen 2014b, Nielsen 2016, Fugro 2020). Houlsby *et al.* (2006) conducted lateral cyclic quasi-static and dynamic loading on a bucket foundation installed in sand and reported adequate stiff response under low amplitude cycles with gradual loss of stiffness at larger amplitudes. This study showed that bucket foundations installed in sand can generate a considerable ultimate tensile resistance. Moreover, it revealed that use of bucket foundations in dense sand can result in about 40% cost reduction compared to installation in soft clay.

Few researchers investigated the performance of bucket foundations under seismic loading numerically (Kourkoulis *et al.* 2014, Zafeirakos and Gerolymos 2014, Athanasiu *et al.* 2015), and experimentally by means of dynamic centrifuge modeling (Yu *et al.* 2014, Choo *et al.* 2015, Wang *et al.* 2015, Wang *et al.* 2017a, b), 1-g shake table testing (Yamazaki *et al.* 2003) or field investigations (Houlsby and Byrne 2000, Houlsby *et al.* 2005, Houlsby *et al.* 2006). A review of recent advancements in bucket foundation research was reported by (Wang *et al.* 2018). Most of the focus in the reported studies was placed on performance of the bucket foundation in terms of rotation and settlement under lateral and cyclic loading.

As mentioned earlier, the U.S. offshore wind market is growing rapidly with many plants (Figure 2-2) moving from the planning phase to design and construction. Musial *et al.* (2017) reported water depths for various offshore wind projects in the U.S., as illustrated in Figure 2-5. It can be noted that majority of the U.S. offshore wind plants are located in zones with water depth less than 45 m, especially on the East Coast (Figure 2-6). As such, bucket foundation appears to be a promising and competitive, to be used in many of the U.S. offshore wind plants.

Figure 2-7 presents the 2018 Modified Mercalli Intensity (MMI) hazard map of the U.S. showing estimates of earthquake shaking in terms of 50% probability of exceedance in 50 years (Petersen *et al.* 2020). It may be noted that the U.S. East Coast offshore wind cluster lies in a zone of moderate to medium hazard, while locations of offshore wind plants off the California coast are located in a high hazard zone. Therefore, it is critical to consider seismic hazard in design of all offshore wind plants at the United States.

The research presented in this dissertation aims to investigate the seismic response of bucket foundations for offshore wind applications. As such, a scaled model of a wind turbine with

bucket foundation was tested in a saturated medium-dense sand stratum. Testing was conducted on a 1-g shaking table using a laminar soil container. The shake table was used to generate harmonic and earthquake-like excitations and different types of model responses were recorded. Harmonic excitations and scaled earthquake records were used to conduct a total of 18 shake table tests. Results of shake table tests were used to shed light on a number of main response characteristics of the bucket foundation-supported wind turbine model. In addition, the collected data were used to calibrate a three-dimensional finite element model with soil-structure interaction effects that was further used to investigate seismic response of a utility scale 3.45 MW OWT.

Table 2-1: Offshore wind projects with bucket foundations (After BOEM 2021a)

<b>Project</b>	<b>Country</b>	<b>Water Depth(m)</b>	<b>Bucket Diameter(m)</b>	<b>Skirt length(m)</b>
Qidong City (nearshore test facility)	China	15	30	7.2
Xiangshui	China	8-12	30	12
Frederikshavn	Denmark	1-4	12	6
Horns Rev 2	Denmark	9-17	12	6
Wilhelmshaven	Germany	18	16	15
Dogger Bank	UK	18	14	8
East Anglia One North (design stage)	UK	33-59	25-35	-

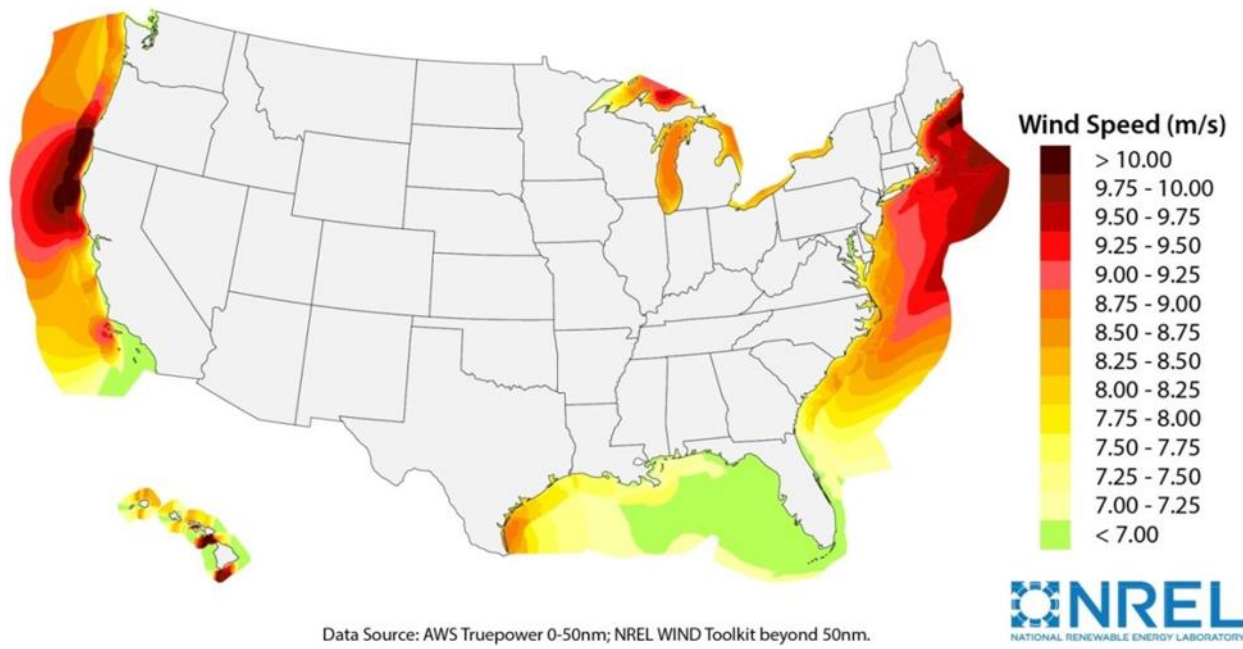


Figure 2-1: Average wind speed on the coastal zone of the United States (from <https://www.energy.gov/eere/articles/computing-america-s-offshore-wind-energy-potential>)



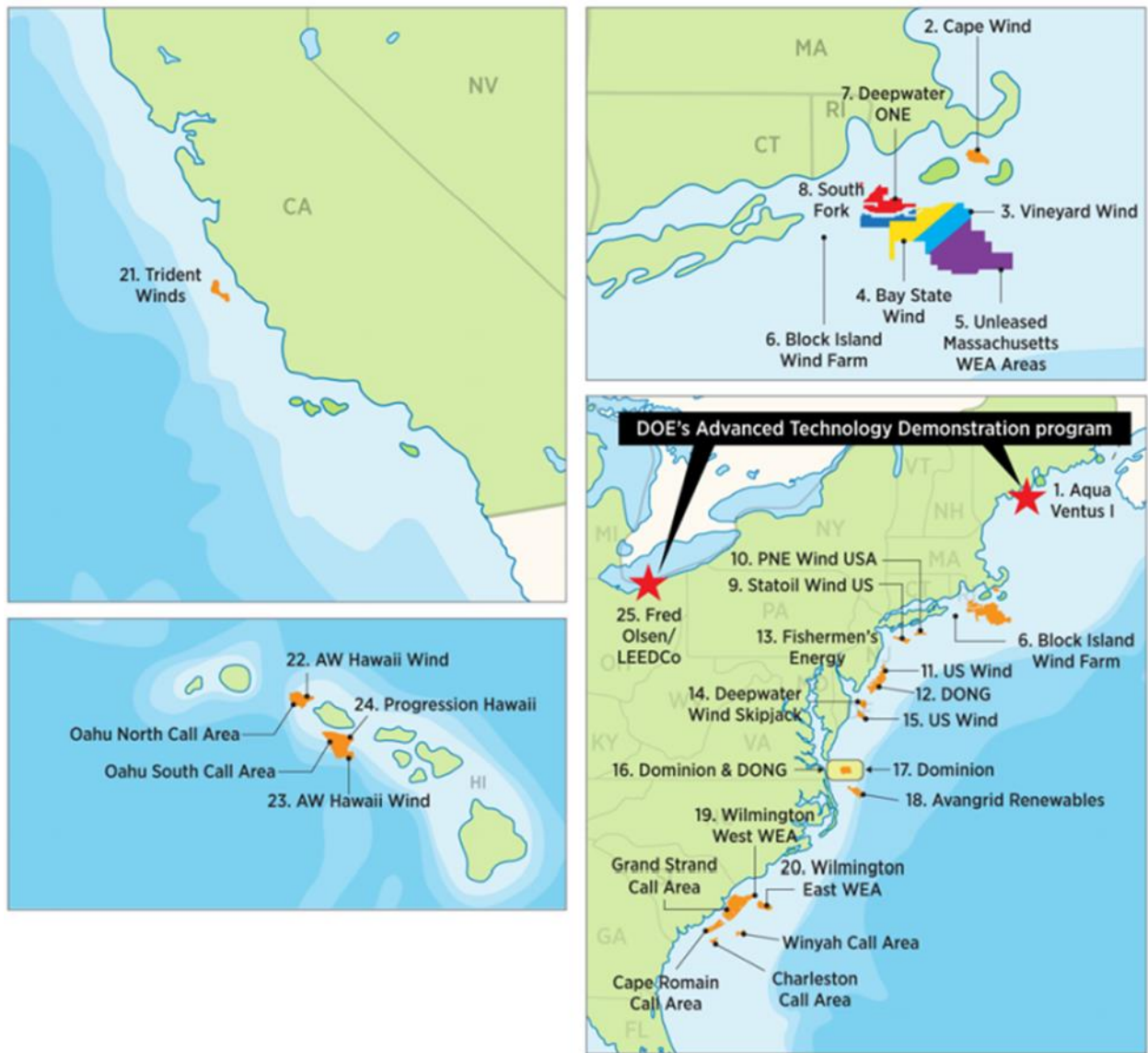


Figure 2-2: Locations of U.S. offshore wind pipeline activity and call area as of March 2019 (After Musial *et al.* 2017)

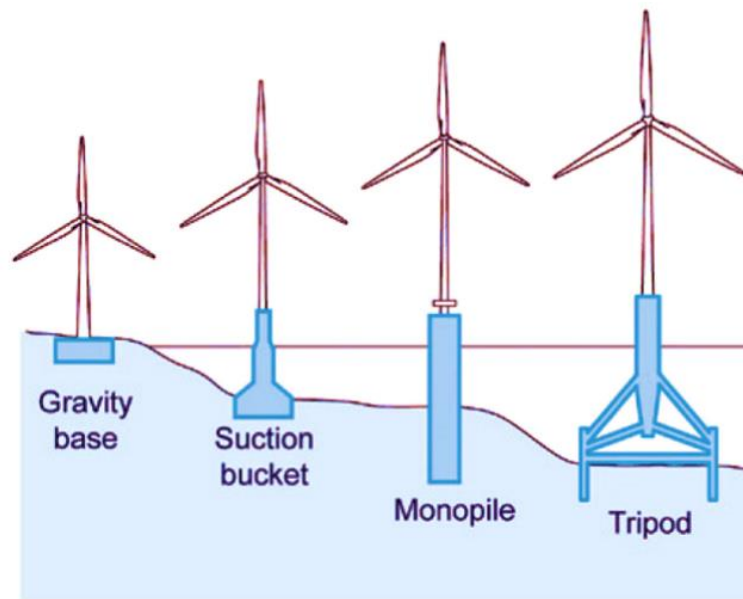


Figure 2-3: Types of OWT foundations at relatively shallow waters (up to 50 m)

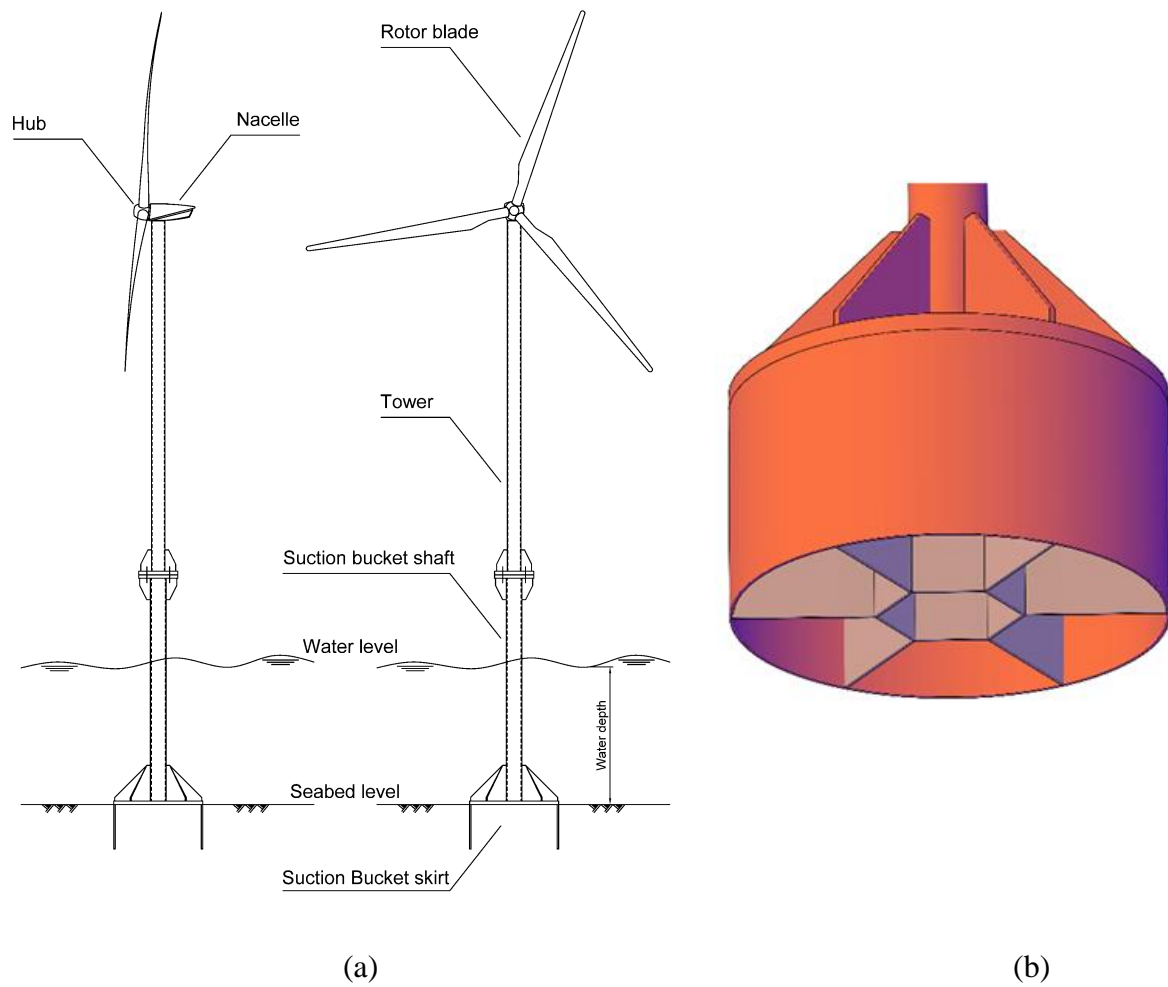


Figure 2-4: Schematic of a) offshore bucket foundation-supported wind turbine and b) bucket foundation with inner compartments

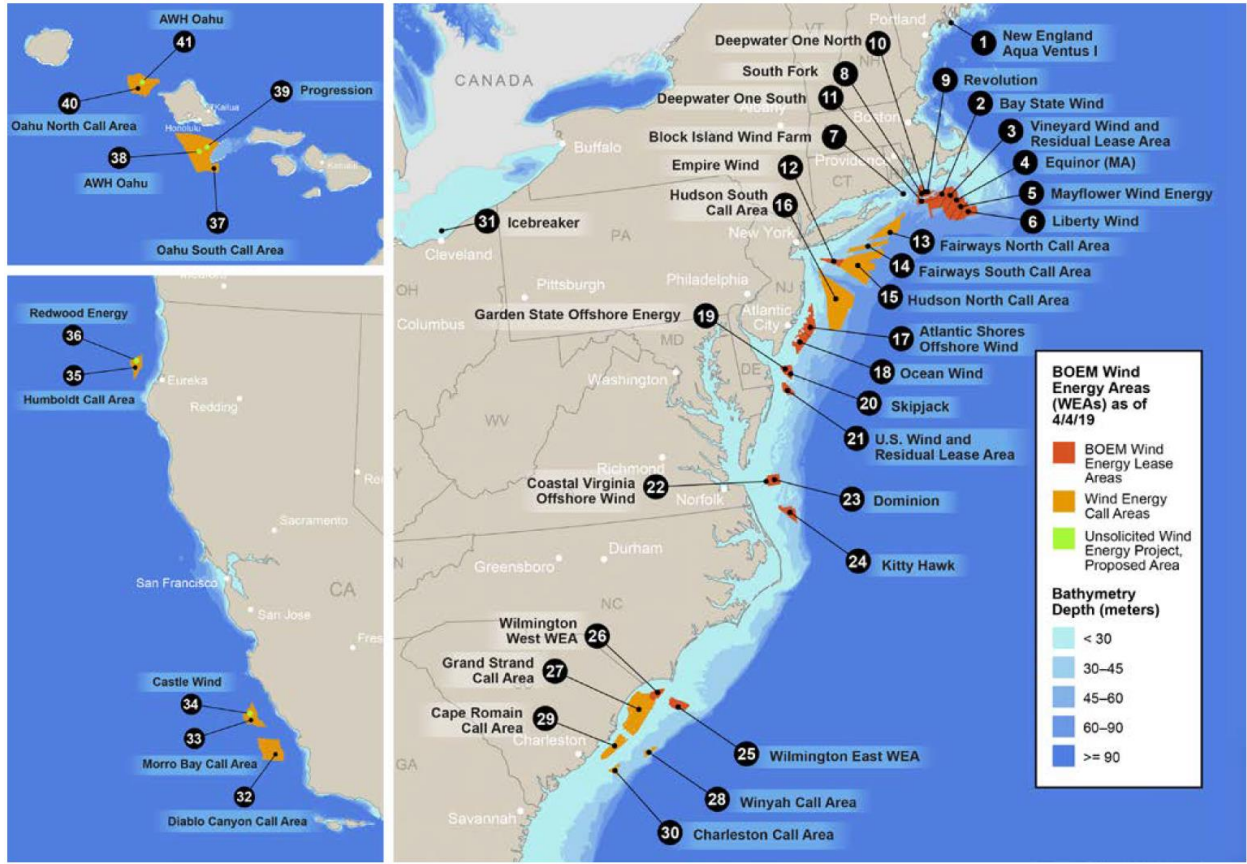


Figure 2-5: Water depths for various offshore wind plants in the U.S. (After Musial *et al.* 2019)

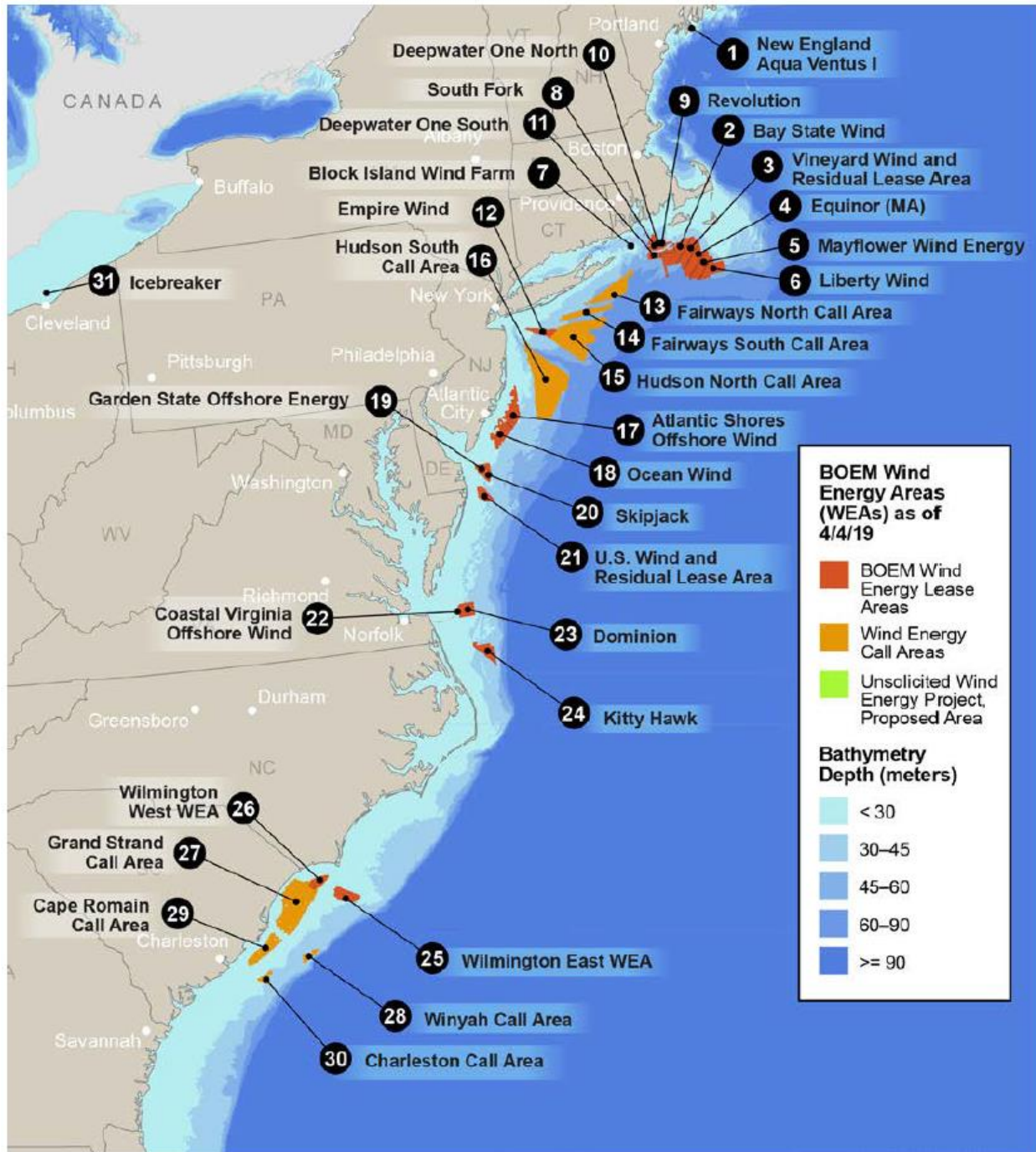


Figure 2-6: Enlarged view for location and water depth of U.S. East Coast offshore wind pipeline activity and call areas as of March 2019 (After Musial *et al.* 2019)

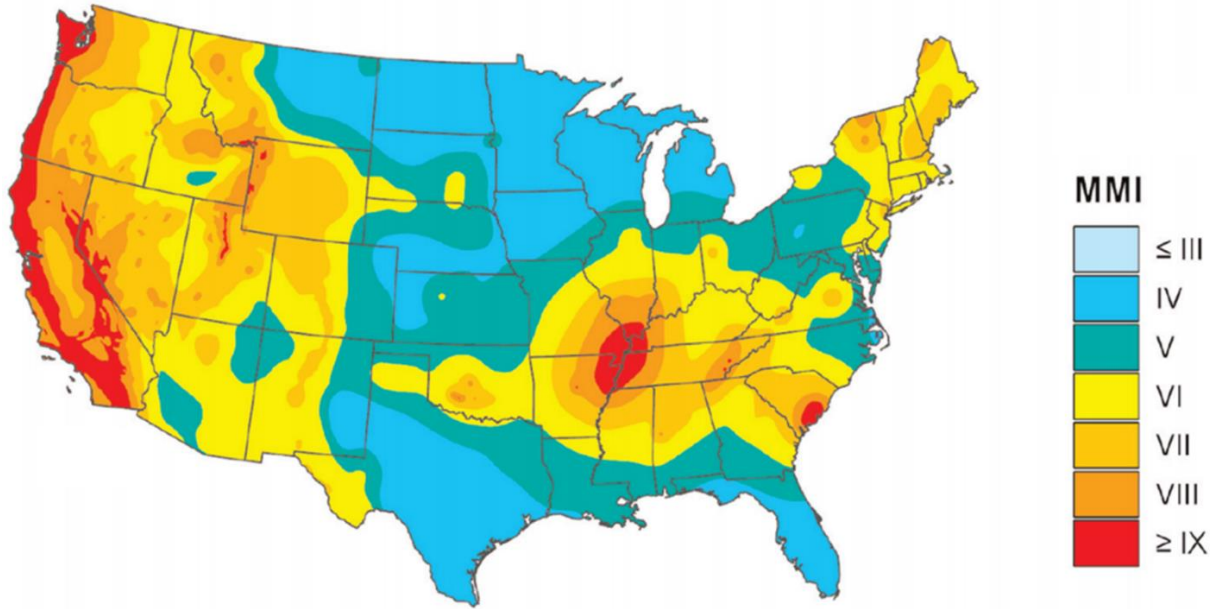


Figure 2-7: The 2018 Modified Mercalli Intensity (MMI) hazard maps of the conterminous United States showing estimates of earthquake shaking in terms of 2% probability of exceedance in 50 years (After Petersen *et al.* 2020)

## **Chapter 3**

# **1-g shake table testing of bucket foundation wind turbine: Model preparation, experimental procedures, and data processing**

*A problem well-stated is a problem half-solved.*

– Charles Kettering

### **3.1 Introduction**

This chapter presents a description of model preparation for shake table testing and includes full details about the bucket foundation wind turbine model, from Computer-Aided Design (CAD) modeling to manufacturing. Also included, are results of modal testing that was conducted to document the fundamental frequency of the bucket foundation-supported wind turbine model. Further details about the employed sand and the testing facility are presented as well. In addition, the data processing approaches are described.

### **3.2 Shake table test facility**

The experimental work in this study was conducted at the Powell Laboratory uniaxial shake table facility, located at the University of California San Diego (UCSD). The shake table platform

has dimensions of 4.9 m by 3.1 m, with a real-time three-variable digital controller. A maximum nominal shaking force of 490 kN (110 kips) can be imparted by the shake table actuator. The table platform can hold models that weigh up to 350 kN (80 kips). Maximum table displacement is  $\pm 150$  mm with a maximum nominal operating frequency of 20 Hz. Performance and construction of this Powell laboratory shake table are detailed in Magenes (1989b), and Trautner *et al.* (2018).

A laminar container with internal dimensions of 3.9 m x 1.8 m x 1.8 m (L x W x H) was constructed at UCSD using 28 structural steel frames arranged in stacks (Ashford and Jakrapiyanun 2001). The laminar container was designed to be used with dry and saturated soil models and is built to exhibit minimal lateral boundary effects; simulating a 1D shear stress-strain wave propagation state (Chang and Hutchinson 2012, Chang and Hutchinson 2013, Ebeido *et al.* 2018b). Figure 3-1 shows the laminar container attached to the shake table, with the bucket foundation wind turbine model placed inside.

### **3.3 Soil stratum model**

Ottawa F-65 sand (Table 3-1) was used to prepare the soil model. A 60 MIL thick Ethylene Propylene Diene Monomer (EPDM) rubber liner was placed to hold soil and water inside the laminar container (Figure 3-2-a). The tested soil model consisted of one saturated medium dense sand layer. Building the medium dense 1.5 m sand model (Figure 3-7) was accomplished in 6 lifts. To ensure uniformity of the soil model, each lift was pluviated inside the container as shown in Figure 3-2-b. Thereafter, each lift, of about 0.25 m in thickness, was compacted using a plate compactor (Figure 3-2-c).

By monitoring weight of each sand batch being placed inside the container and knowing volume of the sand layer, average relative density ( $D_r$ ) was estimated to be about 80%. The  $D_r$  was



later estimated as well via sand cone testing as shown in Figure 3-2-d. After construction, the whole sand layer was saturated with water carefully dripped into the container by means of Poly-Vinyl Chloride (PVC) pipes and hoses. The final water table was at 5 cm above the soil top surface (Figure 3-3). Table 3-2 summarizes properties of the sand stratum.

### **3.4 Bucket foundation wind turbine model**

The tested model represents a scaled prototype of a 3.5-Megawatt (MW) wind turbine. Following type III of similitude for shaking table tests on soil-structure-fluid models in a 1-g gravitational field (Iai and Sugano 1999), a scaled model of the wind turbine with bucket foundation was designed using a scaling factor of 1:32. Figure 3-4 presents the Computer-Aided Design (CAD) drawings used for model manufacturing. A three-dimensional view of the CAD model and image of the model after manufacturing are shown in Figure 3-5-a and Figure 3-5-b, respectively.

Table 3-3 presents the main properties of the bucket foundation wind turbine prototype and of the corresponding scaled model. The model total tower height is 3.4 m and the top mass is 50 kg. All the components of the prototype tower head (nacelle, hub, rotor, blades) are simply represented by a lumped mass at the model tower top. For the scaled model, the top tower mass was back calculated to achieve the target fundamental frequency of the model. Aluminum material was used to manufacture the model, while the top lumped mass was made of steel.

The bucket foundation skirt is designed to be 0.25 m in length  $L$  and 0.5 m in diameter  $d$ , in order to keep the same  $L/d$  ratio of 0.5 for both the prototype and the model. Dimensions of the laminar soil container were considered while designing the test model to minimize boundary effects. The bucket foundation was designed with a total of six inner compartments as shown in

Figure 3-5-c (Wang *et al.* 2017a). For installation purposes, a total of six openings were included in the top lid plate, with one opening in each compartment (Figure 3-5).

To install the model in saturated soil inside the laminar container, the bucket and the connected shaft were lifted by means of an overhead crane (Figure 3-6-a). Thereafter, the bucket foundation was left to sink in the saturated soil under its own weight until refusal (Figure 3-6-b). At this point, hoses were connected to openings in the top lid plate, and suction pressure was applied using a vacuum pump to drain the trapped water between the bucket skirt and the topsoil surface, until the bucket was fully driven into the saturated sand (Figure 3-6-c). Full contact was assured between bucket lid and soil by visually inspecting the suction openings after de-attachment of the hoses (Figure 3-6.d).

### **3.5 Instrumentation**

Figure 3-7 presents the configuration and dimensions of the tested 1.5 m high soil stratum with bucket foundation model installed, as well as instrumentation types and locations. Three instrumentation arrays were installed inside the laminar container while building the model. The north (i.e., leftmost) and south (i.e., rightmost) arrays represented far field arrays, and each had 4 pairs of accelerometers (A#) and pore pressure (PP#) transducers, while the middle array, below the bucket foundation, had 3 pairs of accelerometers and PP transducers. Just after building the model, PP06 malfunctioned, and it did not work in all tests. Special care was exercised in the vicinity of the deployed sensors hung inside the soil container by means of geogrid strips (Figure 3-2-d) to avoid potential damage to the instrumentation and/or the cables.

In order to monitor pore pressure response around the bucket, fourteen small-size pore pressure (PP#) transducers were deployed to measure excess pore water pressure inside and outside

the bucket foundation during shaking. Seven PP transducers were installed at the north (i.e., front) side of the bucket, and the other seven PP transducers were installed at the south side. Figure 3-8 demonstrates locations of the deployed pore pressure transducers around the bucket. Installing the latter transducers was possible by means of stainless-steel tubes that were fixed from the inside and outside of the bucket (Figure 3-5-c and Figure 3-5-d).

Four linear potentiometers (LP#) were connected to the tower and the top mass to measure lateral displacements. In addition to the linear potentiometers, a total of six accelerometers were attached to the tower and top mass to monitor lateral vibration. Moreover, six linear variable differential transducers (LVDT#) were installed to measure settlement of the soil surface near the bucket foundation and in the far field. In addition, two more LVDTs were installed on the bucket foundation top lid to record vertical displacement at its two edges (i.e., north edge and south edge) as shown in Figure 3-9.

### **3.6 Test motions**

Eighteen shake table tests were conducted. The model was excited by two white noise motions (i.e., WN1 and WN2) to characterize the system dynamic properties in terms of fundamental frequency of the soil model and the soil-foundation-structure system, as well as shear wave velocity of the soil stratum. In addition to white noise, two types of motions were used as input excitation for the shake table: harmonic motions and scaled earthquake motions. Details of excitation frequency and amplitude of harmonic and white noise motions as well as Peak acceleration scale factor of earthquake motions are summarized in Table 3-4.

### 3.7 Data processing

Measured displacements and strains are used to calculate resultant bending moment and rotation at top surface center point of the bucket foundation model. Lateral forces acting on the bucket foundation model are calculated via summing lateral forces along the tower as follows:

$$F_{lateral-bucket} = \sum_i a_i m_i \quad (3.1)$$

where  $a_i$  is acceleration at location  $i$  along the tower, and  $m_i$  is lumped mass at location  $i$ .

Lateral displacement of the bucket foundation relative to the surrounding soil is calculated by double integrating acceleration records of A07 and A25 to get total displacements at these two locations. The integrated displacement from A07 may be considered to represent lateral soil displacement while the integrated displacement at A25 (top of the bucket foundation) represents lateral displacement of the bucket foundation. Subtracting the two displacements results in lateral displacement of the bucket foundation relative to the surrounding soil. Figure 3-10-a shows a schematic of this process illustrating the calculation of lateral force and lateral relative displacement of the bucket foundation.

In test H10 (Table 3-4), strain gauges at the tower base (SG005) malfunctioned and did not record any data. Thus, bending moment at tower base  $M_{base}$  (at location of SG005) was calculated using acceleration data as follows:

$$M_{base} = F_{lateral(i)} d_i = \sum_i a_i m_i z_i \quad (3.2)$$

where  $z_i$  is the vertical distance between lateral force  $F_i$  and location of SG005.

Moreover, instrumentation LVDT13 and LVDT14 reached their maximum stroke during shaking in test T3 (Table 3-4). As a result, rotation of bucket foundation was not possible to be inferred from these transducers. Alternatively, rotation was calculated from strain data combined with tower lateral displacement data. Figure 3-10-b shows schematic of total lateral displacement  $\delta_T$  which consists of i) elastic deformation component  $\delta_e$ , and ii) rigid body rotation component of tower displacement  $\delta_r$ , such that:

$$\delta_T = \delta_e + \delta_r \quad (3.3)$$

where  $\delta_T$  is measured at different location along the tower height via linear potentiometers transducers (LP#) previously presented in Figure 3-7. Rearranging (3.3), the rigid body rotation deformation component  $\delta_r$  can be calculated as:

$$\delta_r = \delta_T - \delta_e \quad (3.4)$$

with elastic deformation component  $\delta_e$  calculated from strain data as follows:

$$\delta_e = \iint \frac{\varepsilon}{r_{tower}} dz^2 \quad (3.5)$$

where  $\varepsilon$  is the strain measured along the tower axis (i.e.,  $z$  direction), and  $r_{tower}$  is radius of tower section. Thus, the elastic component  $\delta_e$  and subsequently the rigid body rotation component  $\delta_r$  can be calculated at different elevations along the tower. As such, tower rigid body location can be calculated using  $\delta_r$  at two locations along the height. Rigid body rotation of the tower may be assumed equal to bucket foundation rotation, since the connection between bucket foundation and wind turbine tower is designed and manufactured to be practically rigid.

## 3.8 Modal testing and system identification

### 3.8.1 Fixed base configuration of the test model

Aiming to confirm the fundamental frequency of bucket foundation wind turbine model (with fixed-base configuration) prior to placing it in the laminar soil container, the model was rigidly attached to the concrete floor of the testing facility by means of lateral steel beams as shown in Figure 3-11. Thereafter, the model was excited by a hammer hit near the base and the recorded accelerations were used to estimate the fundamental frequency of this fixed-base model.

The transfer function  $H(f)$  between an input signal  $x(t)$  and an output signal  $y(t)$  for a linear system can be defined as (Lutes and Sarkani 2004):

$$H(f) = \frac{Y(f)}{X(f)} \quad (3.6)$$

where  $X(f)$  and  $Y(f)$  are Fourier transform of the input and output signals, respectively.

Time histories and Fourier transforms of the recorded tower accelerations are presented in Figure 3-12. A transfer function between A30 (output) and A25 (input) was estimated as shown in Figure 3-13. The maximum amplification is observed to occur at a frequency of about 1.57 Hz which is in good agreement with the design fundamental frequency for fixed-base model of 1.6 Hz (previously summarized in Table 3-3).

### 3.8.2 Soil-structure interaction effects

In order to characterize dynamic properties of the test model in terms of fundamental frequencies of soil model and soil-foundation-structure system, as well as shear wave velocity of

soil stratum, the test model was excited by two white noise motions (i.e., WN1 and WN2). Test WN1 was conducted as the first shake table test after building the test model, while test WN2 was conducted after test H8. In both white noise tests, the test model was excited using acceleration amplitude of about 0.03g (in RMS sense) with frequency range between 0.1 and 30 Hz. The low amplitude of 0.03g (in root mean square sense) was selected to ensure low-strain conditions and the system can be assumed to remain essentially in the linear elastic range.

Using results of white noise shaking, fundamental frequency of soil stratum can be estimated using Fourier transform of uppermost and lowermost acceleration records within the soil stratum. Knowing fundamental frequency  $f_s$  of soil stratum, an crude estimate for shear wave velocity  $V_s$  can be calculated using (Dobry *et al.* 1976):

$$V_s = \frac{4H_s}{T_s} = 4H_s f_s \quad (3.7)$$

where  $H_s$  is height of soil stratum (i.e., distance between two accelerometers) and  $T_s$  is fundamental period of soil stratum ( $T_s = 1/f_s$ ).

The above procedures are implemented in the following chapter using data from different shake table tests to evaluate fundamental frequency of the soil stratum, and soil-foundation-structure model. Moreover, an estimate for average soil  $V_s$  is evaluated using (3.7), knowing the fundamental frequency of the soil stratum. The following subsections highlight main findings from test WN1 and WN2. Full results of both tests are presented in APPENDIX A.

### 3.8.2.1.1 Test WN1

No appreciable increase in the pore water pressure was observed either in the soil arrays or around the bucket foundation, with excess pore pressure (EPP) ratio  $r_u$  (defined as recorded excess pore water pressure  $u_e$  divided by initial effective vertical stress  $\sigma'_{vo}$ ) less than 0.1. The recorded lateral displacements along the laminar soil container were found to be quite low as well (i.e., less than 1 mm).

Figure 3-14 shows time histories of the north and south accelerometer arrays during the test, while Figure 3-15 shows the corresponding frequency spectra. The two arrays show consistent recorded accelerations, except A15 that shows lower amplitude compared to A07. The frequency spectra presented in Figure 3-15 show consistent observations with the recorded accelerations. It may be noticed that the largest acceleration amplification in the soil model occurs at frequencies between 6 and 8 Hz. Figure 3-16 shows a transfer function between the topmost and bottom soil accelerations estimated using (3.6). From Figure 3-16, it can be observed that the most significant amplification for both arrays occurs at about 8 Hz, which can be considered as the fundamental frequency  $f_s$  of the soil model. Soil shear wave velocity  $V_s$  is then calculated using (3.7) and found to be about 48 m/s.

Zayed *et al.* (2020) developed a new approach to track the changes in  $V_s$  during seismic excitation. This approach is implemented with the north array recorded accelerations and the evolution of  $V_s$  with time during test WN 1 is presented in Figure 3-17. The resulting  $V_s$  fluctuates between 38 and 52 m/s with an average of about 48 m/s, which is in a good agreement with the estimated  $V_s$  using (3.7) (i.e., 48 m/s).



Propagation of accelerations along the tower height is presented in Figure 3-18 with the corresponding frequency spectra. The tower base acceleration A25 (i.e., bottom plot in Figure 3-18) shows a consistent frequency spectrum with soil top accelerations A08 and A16. Maximum tower acceleration at the tower top was about 0.12g. A change in the frequency content along the tower height can be observed where the tower acted as a low-pass filter and the high-frequencies were filtered out in the top part of the tower. The fundamental frequency of the soil-foundation-structure system can be estimated using (3.6) treating A08 (i.e., soil acceleration near the bucket foundation) as the system input and A30 (i.e., tower top) as the system output. The normalized transfer function of the soil-foundation-structure system is shown in Figure 3-19, where it can be noticed that the maximum amplification occurs at about 1.4 Hz. As such, the soil-foundation-structure system has a fundamental frequency that is 10% less than the frequency of the fixed-base configuration for the same structure (1.4 Hz vs. 1.57 Hz), which illustrates how the system becomes more flexible when accounting for soil-structure interaction effects.

#### **3.8.2.1.2 Test WN2**

After conducting tests H1 through H8, a second white noise test was run to assess any changes in the dynamic properties of the test model. Test WN2 used the same shake table input motion used in test WN1 as a broadband excitation to examine any changes in the fundamental frequency of soil stratum and the soil-bucket-wind turbine system, as well as any changes in soil  $V_s$  that might have occurred after exposing the test model to few shaking events. Figure 3-22 presents a normalized transfer function between lowermost (as input) and uppermost (as output) acceleration records for both far field arrays in the soil stratum. The largest amplitude can be observed between 7 and 9 Hz for both arrays, with mean value of about 8 Hz. Comparing the latter

plot with the similar plot of test WN1 in Figure 3-16, it can be concluded that the fundamental frequency of soil stratum did not experience significant change and it is essentially the same.

Moreover,  $V_s$  was tracked during shaking (Zayed *et al.* 2020) as show in Figure 3-23, where  $V_s$  ranged between 36 and 50 m/s with an average value of about 44 m/s. The latter value of  $V_s$  is still in good agreement with  $V_s$  measured in test WN1 (Figure 3-17). Figure 3-25 illustrates the transfer function between the acceleration record of A08 (i.e., soil acceleration near the bucket foundation as an input) and the uppermost acceleration record of the wind turbine tower (A30). Response can be noticed to be amplified at a frequency of about 1.4 Hz, which is similar to that of test WN01. Thus, fundamental frequency of the soil-bucket-wind turbine system did not change after it was exposed to shaking events of tests H1 through H8.

### **3.9 Acknowledgement**

The research described in this paper was partially funded by the National Science Foundation grant OISE-1445712 as well as the Trent R. Dames and William W. Moore graduate student fellowship from the American Society of Civil Engineers (ASCE). Testing was conducted at the Powell laboratories, University of California San Diego, with assistance provided by Dr. Christopher Latham, Mr. Andrew Sander, Mr. Mike Sanders, Mr. Abdullah Hamid and Mr. Darren Mckay.

The discussion carried out in chapters 3 and 4 is currently being prepared to be published as a journal paper tentatively in the ASTM Geotechnical Testing Journal or the ASCE Journal of Geotechnical and Geoenvironmental Engineering. The proposed title of this paper is “Shake table testing of bucket foundation for offshore wind applications”. The dissertation author is the primary

author of this paper with Dr. Kyungtae Kim, Mr. Athul Prabhakaran, and Professor Ahmed Elgamal as coauthors.

Table 3-1: Geotechnical properties of F-65 Ottawa sand (After Bastidas 2016a)

<b>Property</b>	<b>Description</b>
Mineralogy	Quartz, 99.7%
Grain shape	Rounded
Specific gravity, $G_s$	2.65
Coefficient of uniformity ( $C_u$ )	1.63
$D_{30}$ (mm)	0.17
$D_{50}$ (mm)	0.2
$D_{60}$ (mm)	0.22
Coefficient of curvature ( $C_c$ )	0.97
Maximum and minimum voids ratio $e_{max}$ , $e_{min}$	0.83, 0.51
Minimum and maximum mass density $\rho_{min}$ , $\rho_{max}$ (kg/m <sup>3</sup> )	1440, 1760

Table 3-2: Properties of sand stratum for the shake table test

<b>Property</b>	<b>Soil model</b>
Water/soil condition	Saturated
Thickness (m)	1.45
Bulk unit weight $\gamma_{\text{bulk}}$ (kg/m <sup>3</sup> )	1,780
Dry unit weight $\gamma_{\text{dry}}$ (kg/m <sup>3</sup> )	1,685
Overall relative density $D_r$ (%)	80

Table 3-3: Properties of the prototype and the scaled model

Quantity	Unit	Full scale (Prototype)	Scaled model (Type III)
Rotor, Nacelle Assembly mass* (m <sub>RNA</sub> )	kg	195,000	50
Tower height	m	66.5	2.1
Tower diameter (top/bottom)	m	3.26 / 4.5	7.6
Tower wall thickness (top/bottom)	cm	1.6 / 3	0.3
Tower mass	kg	150,000	3.9
Tower discretization (beam-column elements)	-	20	21
Shaft height	m	40	1.3
Shaft diameter (top/bottom)	m	4.5 / 5.5	8.9
Shaft wall thickness	cm	4 / 5.8	0.55
Shaft mass	kg	235,000	4.95
Shaft discretization (beam-column elements)	-	12	13
Bucket diameter (d)	m	12	0.5
Bucket lid average thickness	cm	8	1.3
Skirt length (L)	m	8	0.25
Skirt wall average thickness	cm	8	0.3
Tower, shaft and bucket material	-	Steel	Aluminum
Young's modulus of tower, shaft and bucket	GPa	200	72
Mass density of tower, shaft and bucket	kg/m <sup>3</sup>	7,850	2,650
Fundamental frequency**	Hz	0.29	1.6

\* RNA mass is calculated to have model fundamental frequency of 1.6 Hz

\*\* Fundamental frequency is for the fixed base condition of the prototype and the scaled model

Table 3-4: Description of shake table test motions

#	Event type	Test	Shake table motion description		Test I.D. ***
			Frequency (Hz)	Amplitude (g)	
1	White noise	WN1	0.1-30**	0.03 (RMS*)	D1RI
2	Harmonic	H1	4	0.05	D1R02
3		H2	1.4	0.05	D2R01
4		H3	4	0.1	D1R03
5		H4	3	0.1	D1R05
6		H5	1.2	0.1	D2R02
7		H6	4	0.2	D1R04
8		H7	3	0.2	D1R06
9		H8	1.4	0.2	D2R03
10	White noise	WN2	0.1-30**	0.03 (RMS*)	D1RII
11	Harmonic	H9	1	0.3	D2R05
12		H10	1	0.3	D2R06
13	Scaled earthquake record	T1	1995 Kobi earthquake (Takatori station) Peak acceleration scaled to:	25%	D1R09
14		T2		50%	D1R12
15		T3		75%	D1R13
16	Scaled earthquake record	N1	1994 Northridge earthquake (14145 Mulholland Dr. station) Peak acceleration scaled to:	25%	D1R07
17		N2		50%	D1R08
18		N3		75%	D1R10

\* RMS: root mean square

\*\* Frequency range of the applied white noise

\*\*\* Test I.D. is used for data achieving purposes



Figure 3-1: Laminar soil container placed on shake table at the UC San Diego Powell Laboratory





(a)



(b)



(c)



(d)

Figure 3-2: Illustrative images showing a) placement of the EPDM liner inside the laminar soil container, b) dry pluviation of sand inside the laminar container, c) compaction of the soil inside the container, d) sand cone test for determination of sand relative density



(a)



(b)

Figure 3-3: Top view of the laminar soil container: a) before, and b) after saturating the sand stratum

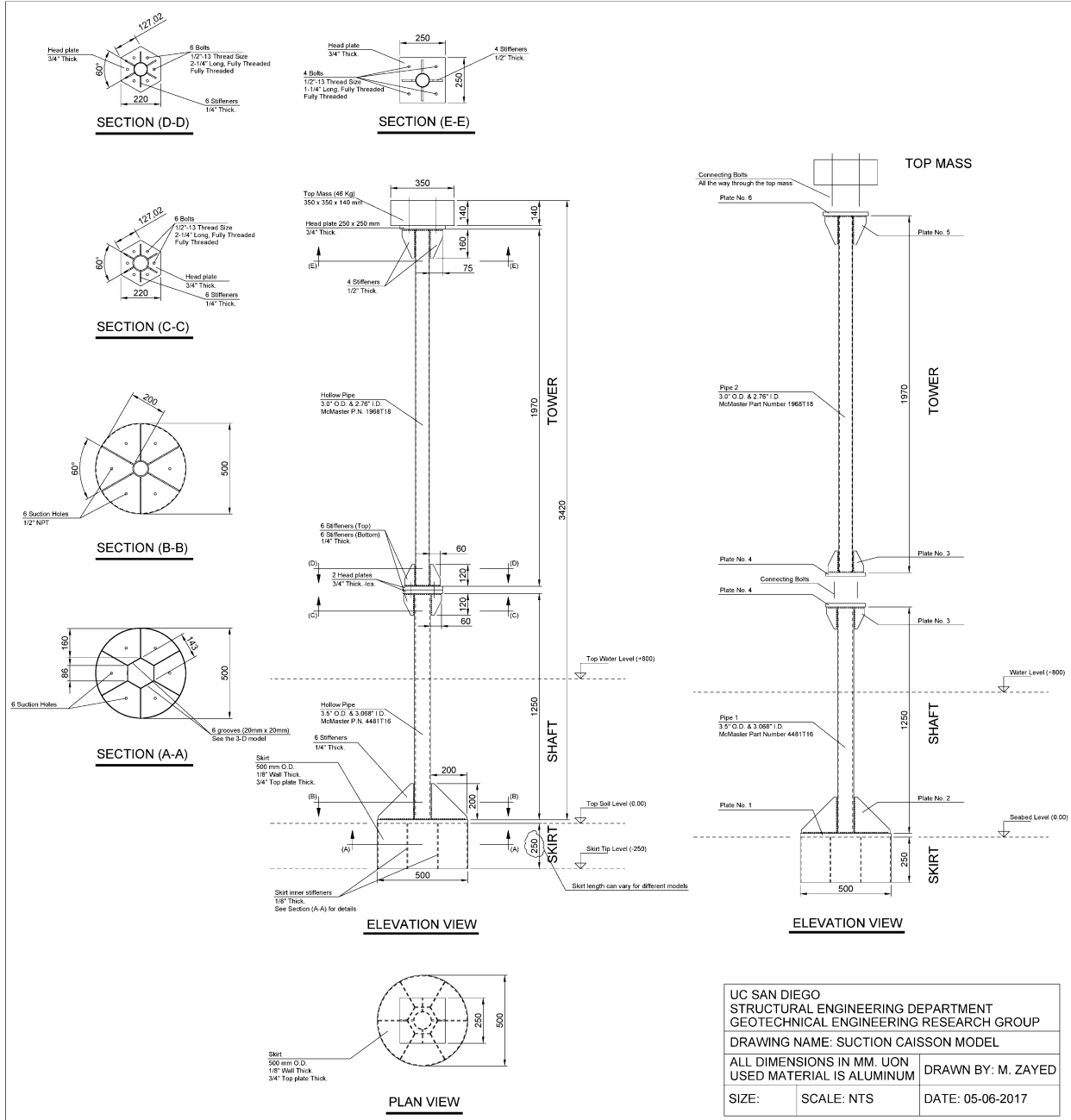
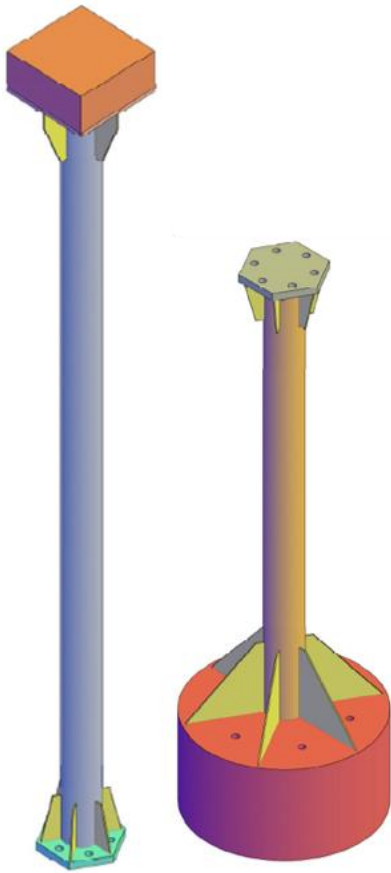
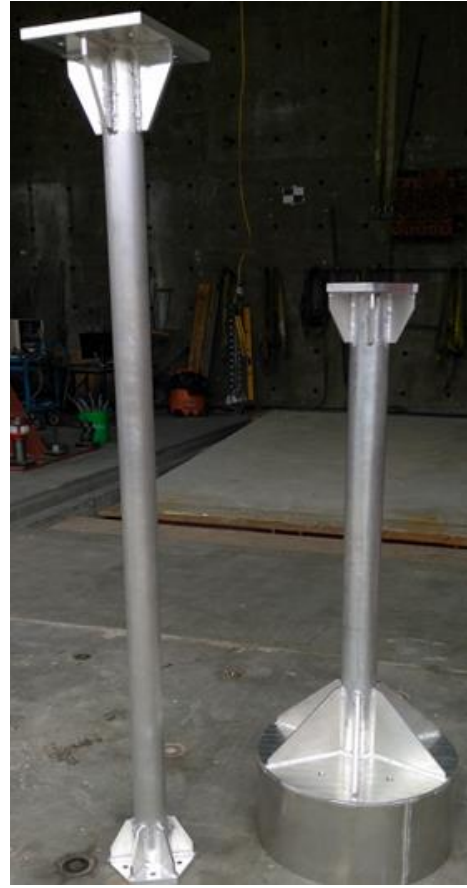


Figure 3-4: Bucket foundation wind turbine CAD drawing and details for manufacturing



(a)



(b)



(c)



(d)

Figure 3-5: Illustrative images showing a) 3-dimensional CAD model of the scaled bucket foundation with wind turbine, b) model after fabrication, a) bottom view of bucket foundation with honeycomb shaped compartments showing pore pressure transducers installed inside the bucket, b) pore pressure transducers installed outside the bucket foundation, b) side view of bucket foundation



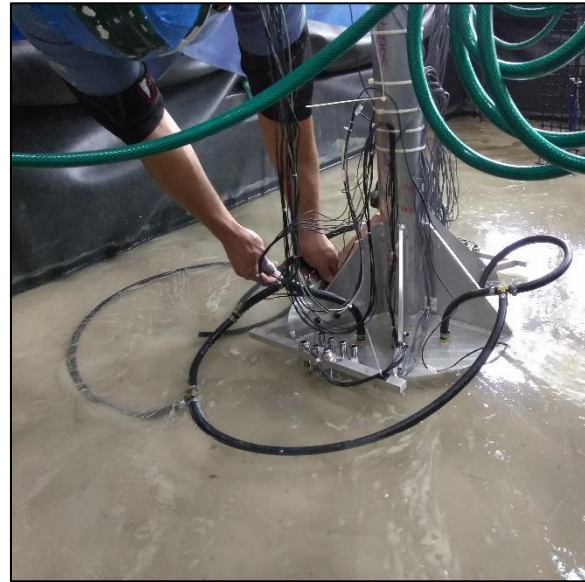
(a)



(b)



(c)



(d)

Figure 3-6: Illustrative images showing a) placement of bucket foundation inside the laminar soil container by overhead crane, b) installation of bucket foundation into saturated sand stratum under its own weight, c) driving bucket foundation into saturated sand by suction, and d) de-attaching suction hoses from bucket foundation after model installation

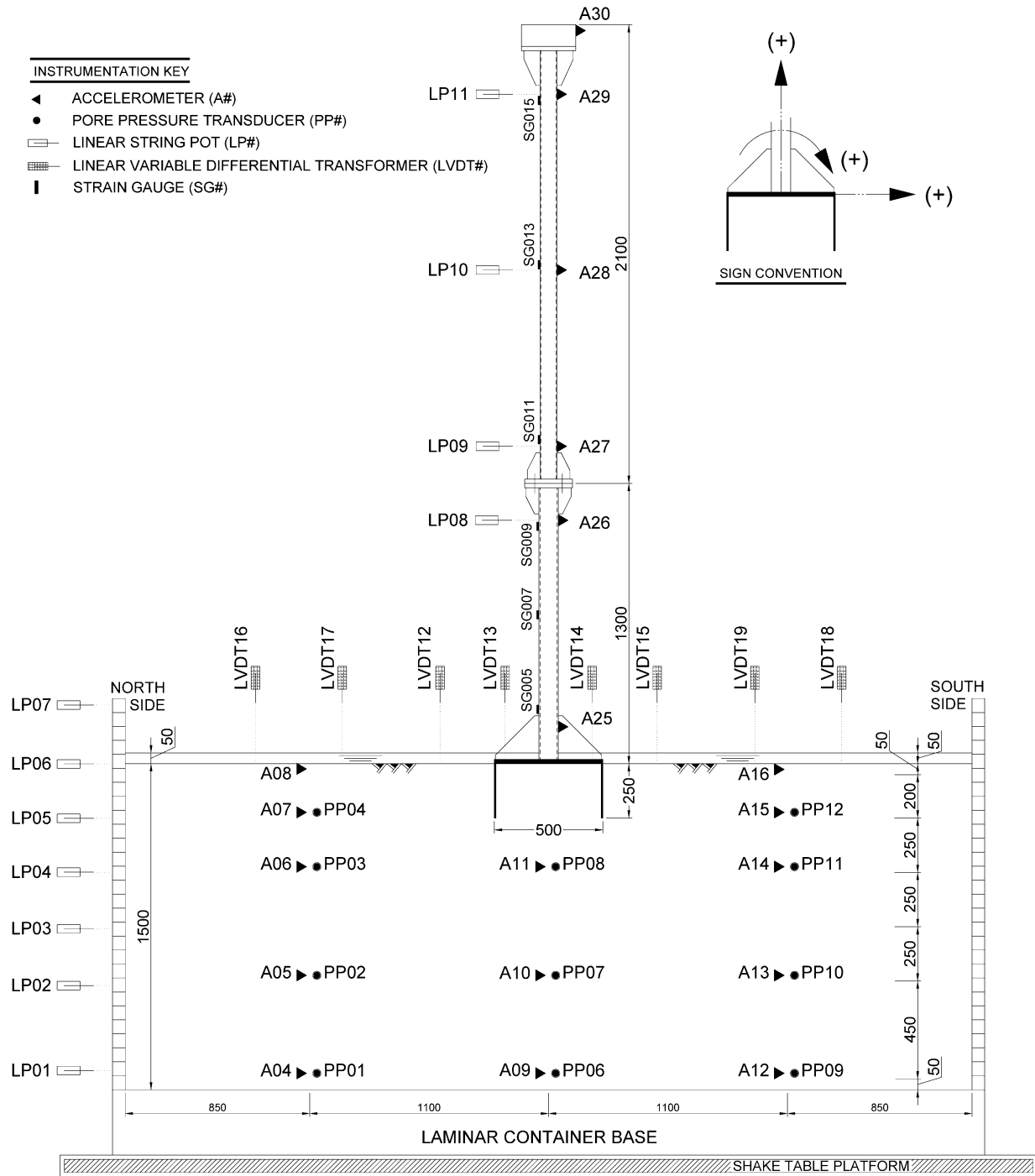


Figure 3-7: Testing configuration and instrumentation layout (dimensions shown in mm)

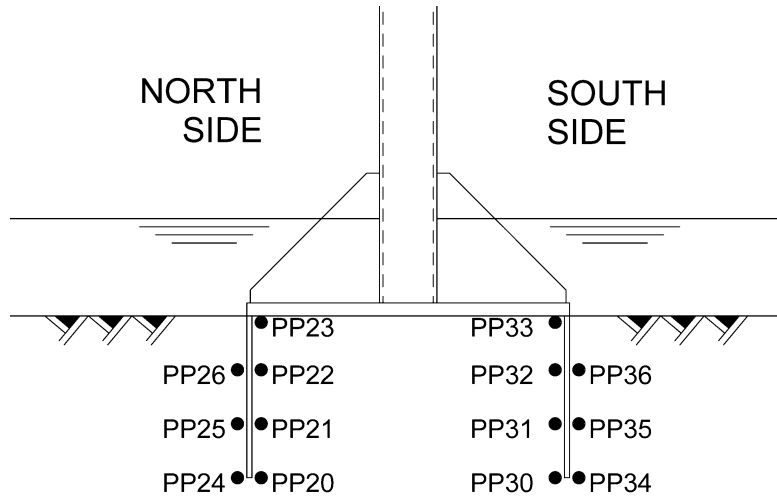


Figure 3-8: Layout of pore pressure transducers (PP#) around the front and back sides of the bucket foundation



Figure 3-9: Bucket foundation after being installed in the saturated sand with instrumentation attached to it



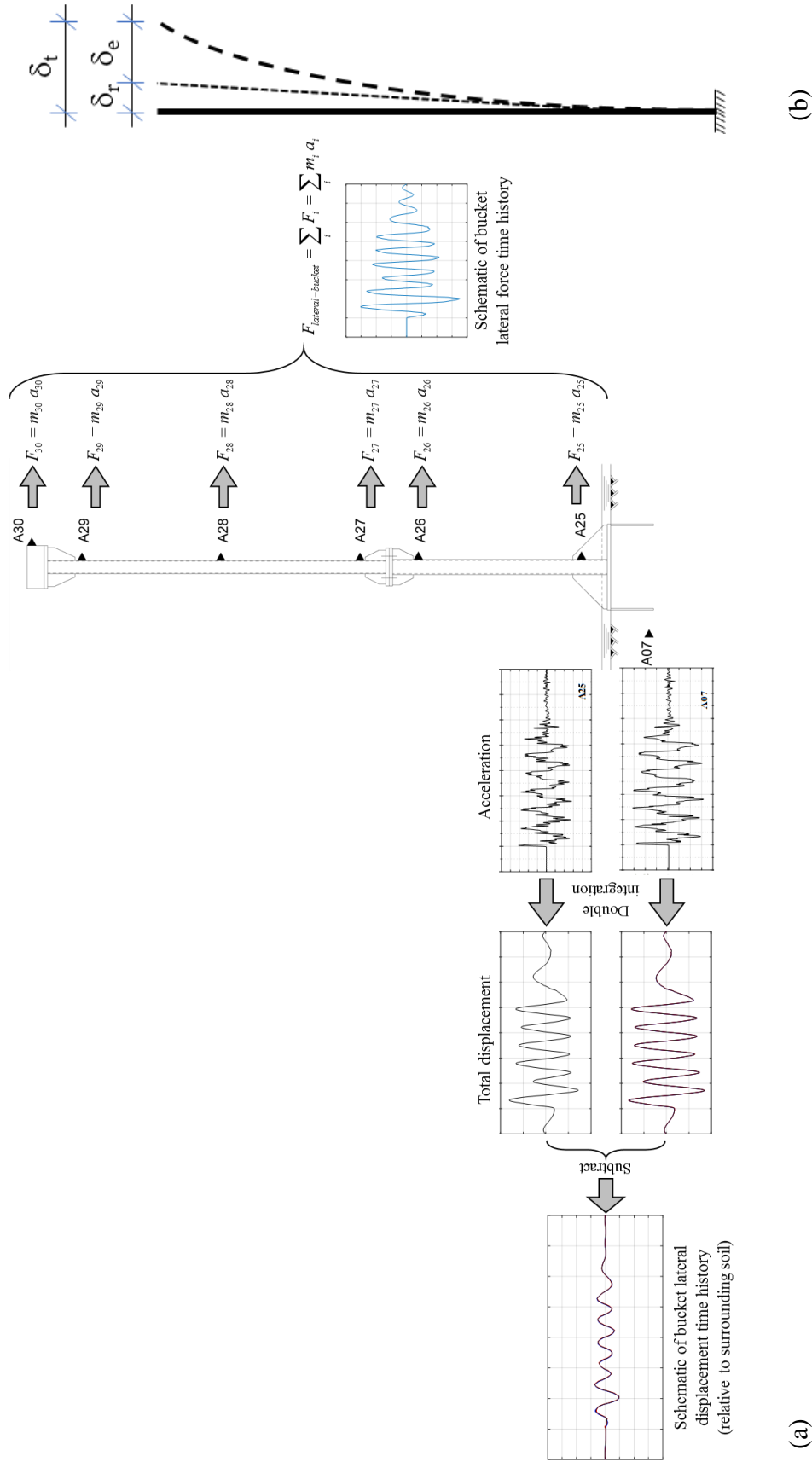


Figure 3-10: Schematic illustrating a) calculation of lateral force on bucket foundation and lateral displacement of bucket foundation relative to the surrounding soil, and b) elastic and rigid components of lateral tower total displacement



Figure 3-11: View of bucket foundation wind turbine model with fixed-base configuration before performing modal analysis for system identification

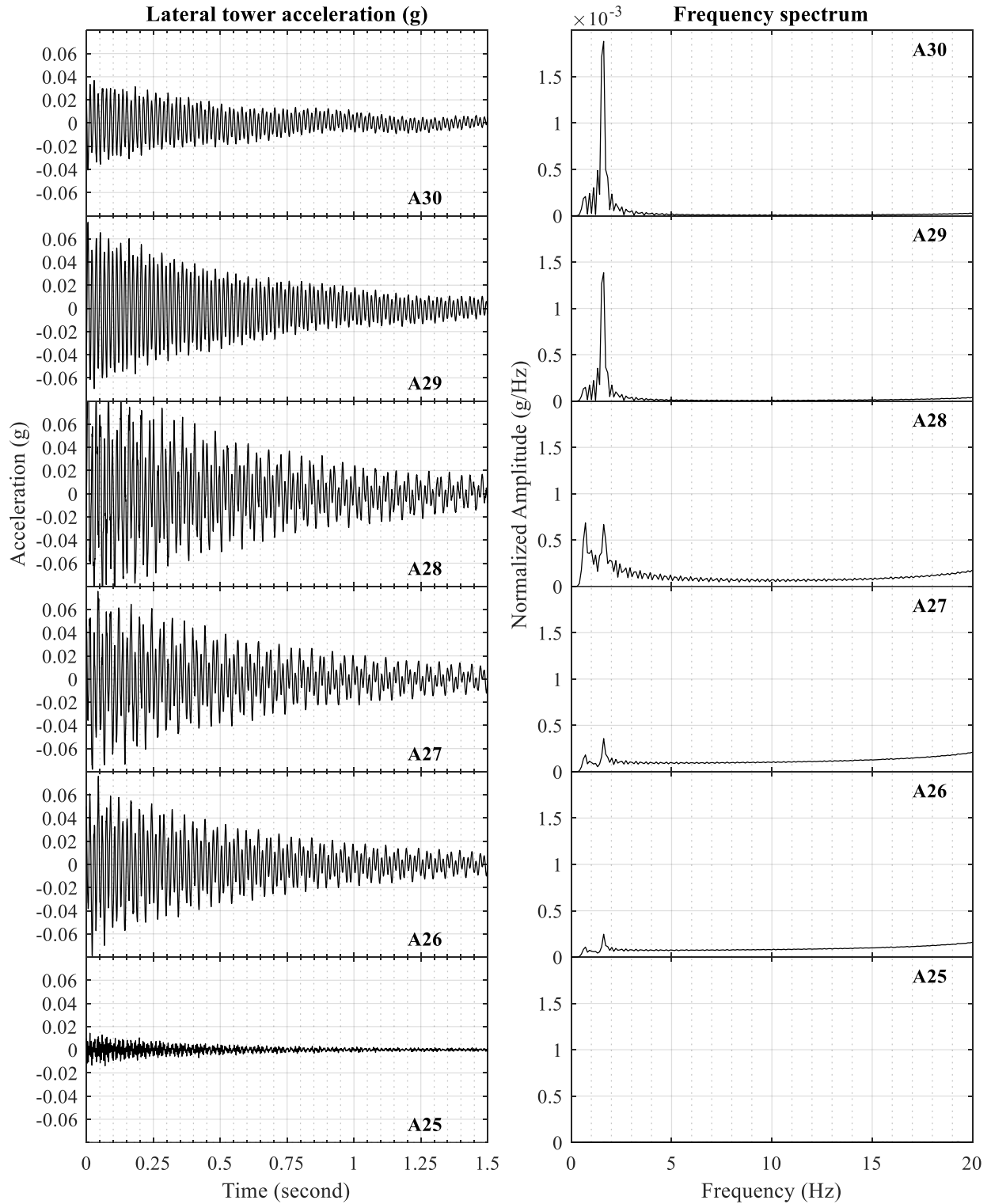


Figure 3-12: Typical time histories and the corresponding Fourier transforms of tower accelerations for hammer excitation of the fixed-base bucket foundation model

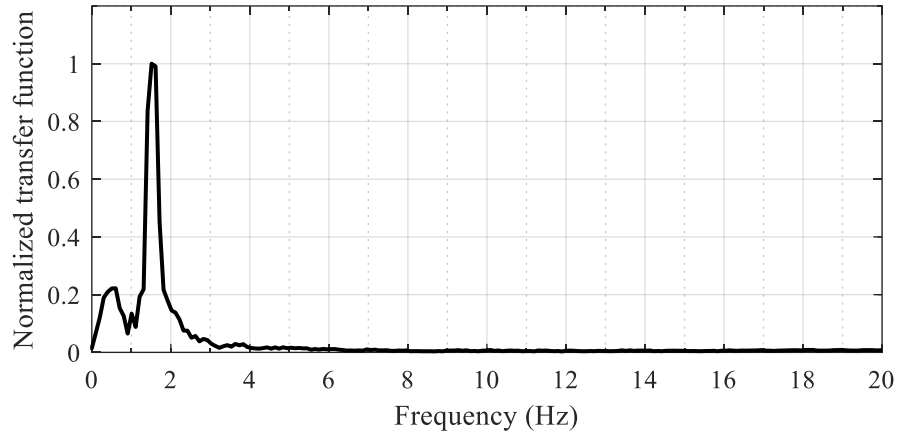


Figure 3-13: Normalized transfer function for fixed-base model (between A25 as input and A30 as output)

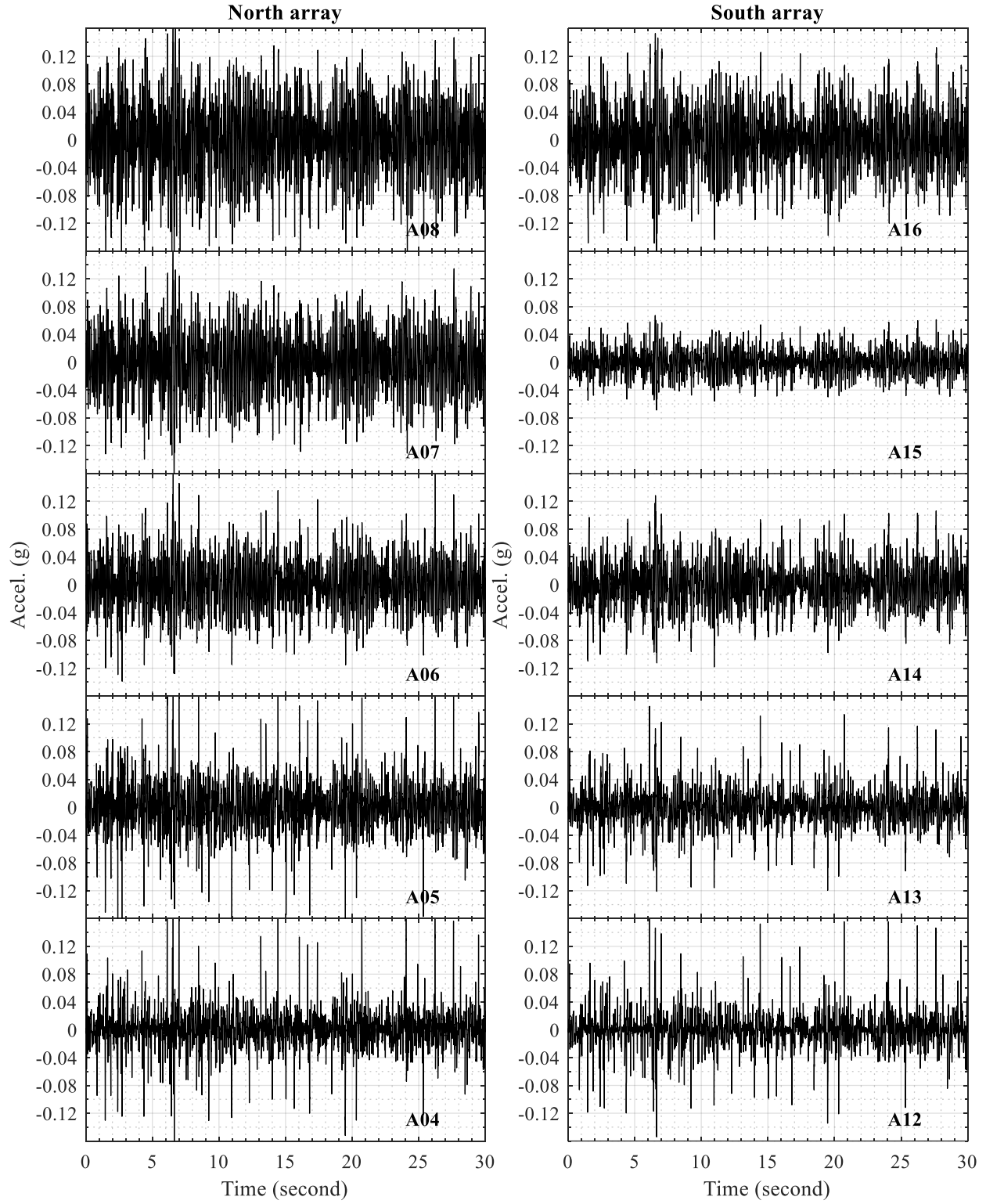


Figure 3-14: Time histories of soil accelerations for test WN1

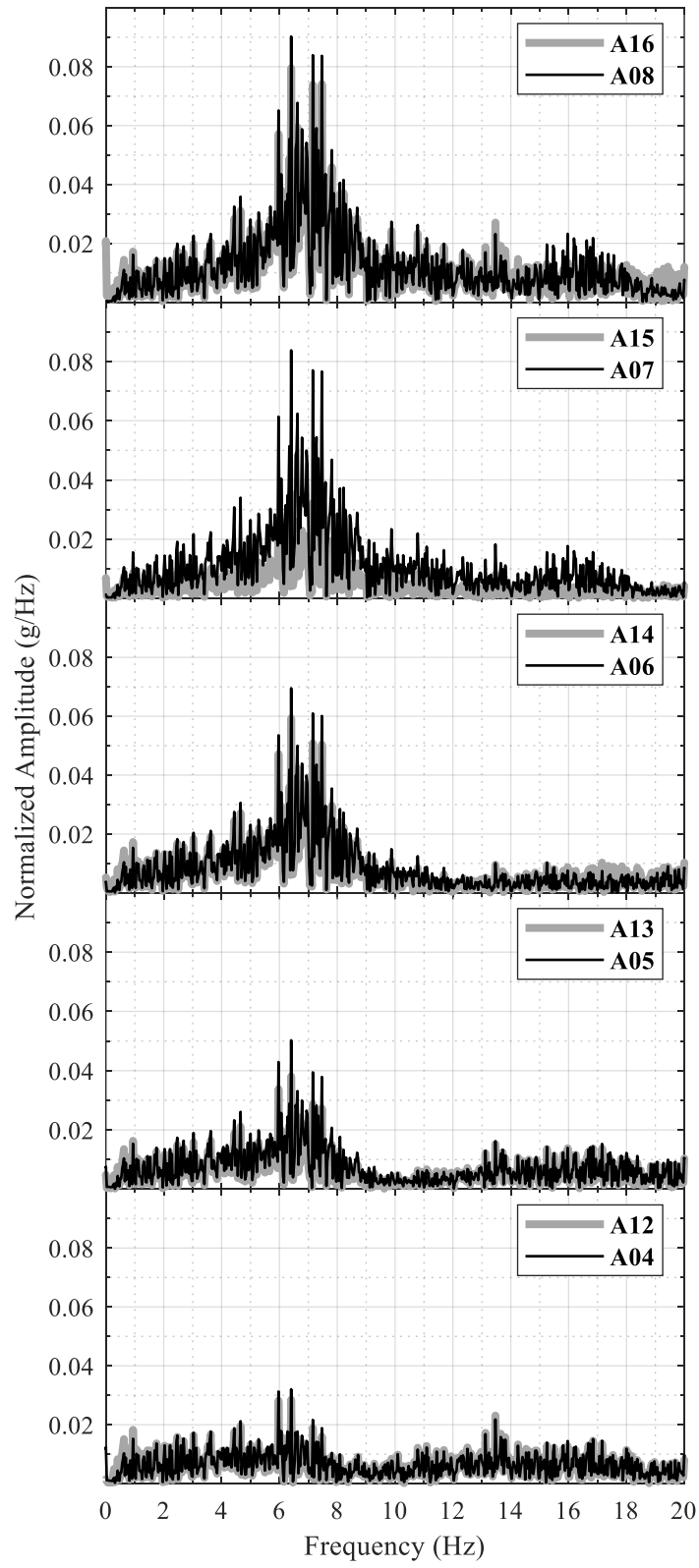


Figure 3-15: Frequency spectrum of the recorder soil accelerations for test WN1

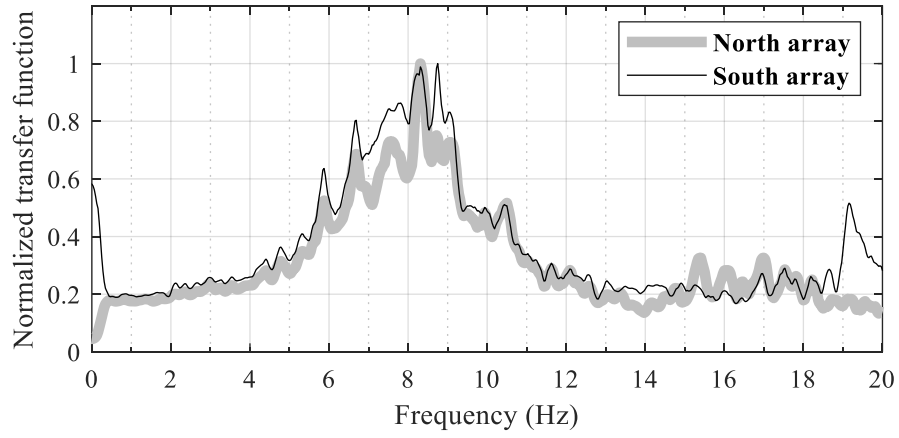


Figure 3-16: Normalized transfer function between lowermost and uppermost recorded soil accelerations for test WN1

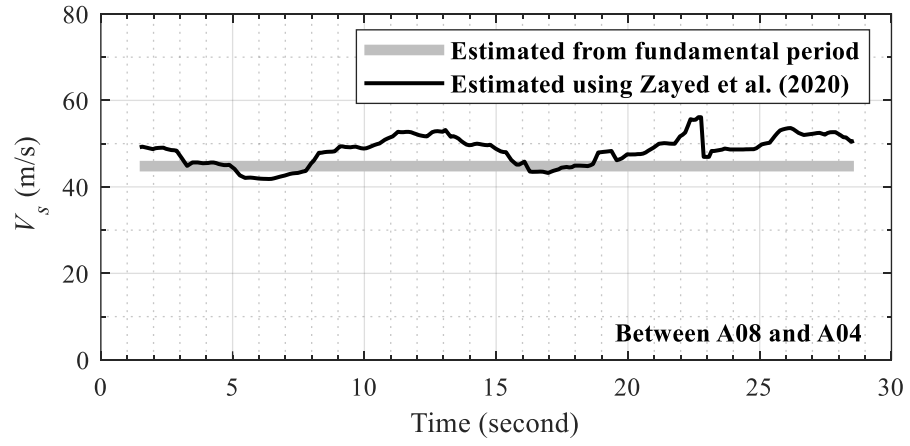


Figure 3-17: Evolution of  $V_s$  with time for test WN1



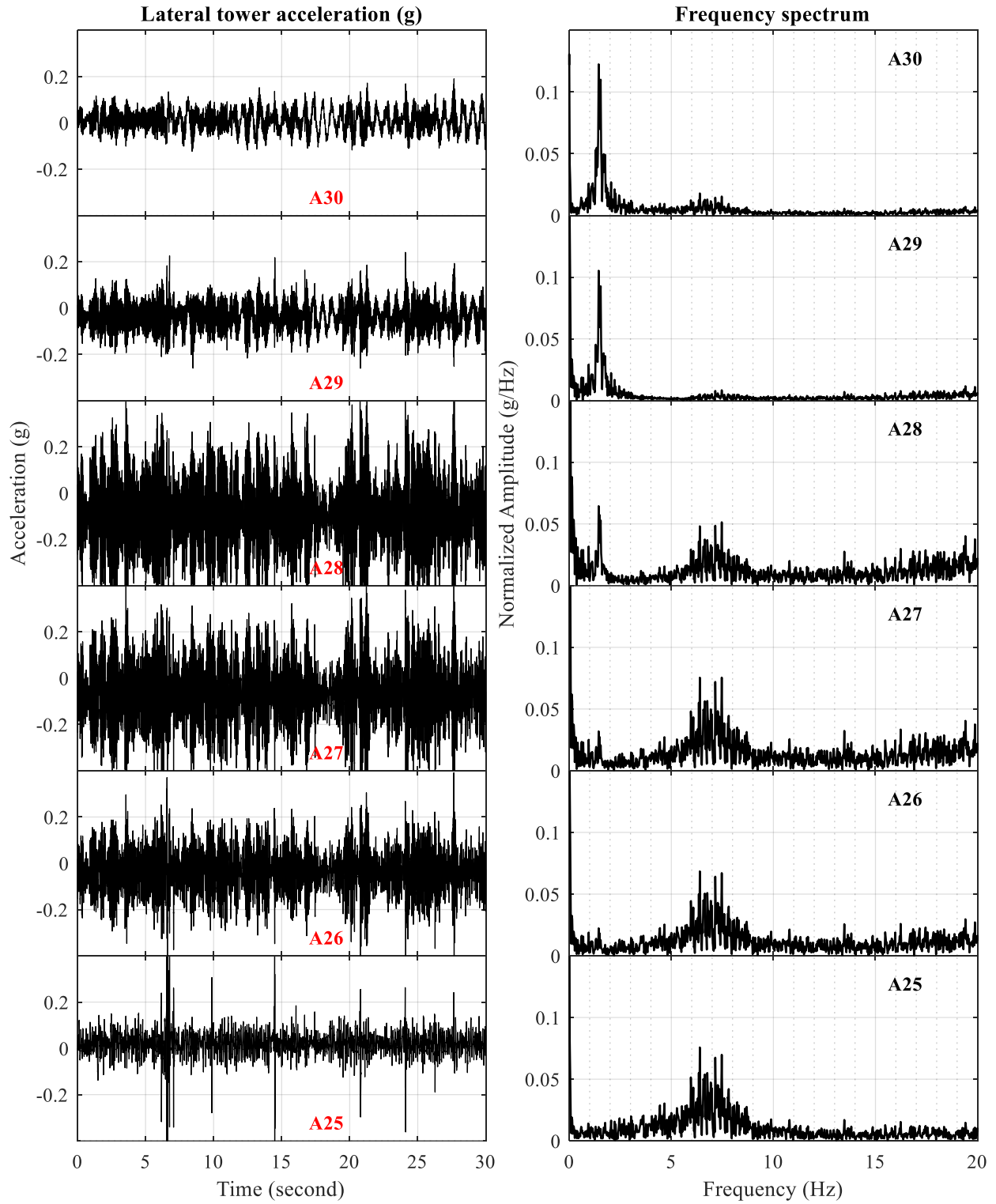


Figure 3-18: Tower acceleration time histories and the corresponding frequency spectra for test WN 1

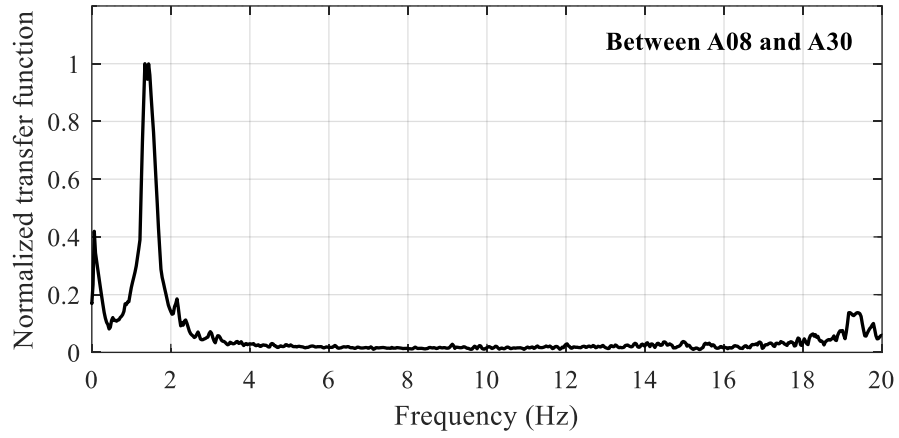


Figure 3-19: Normalized transfer function between A08 (i.e., soil near the bucket foundation) and A30 (i.e., top of the tower) for test WN1

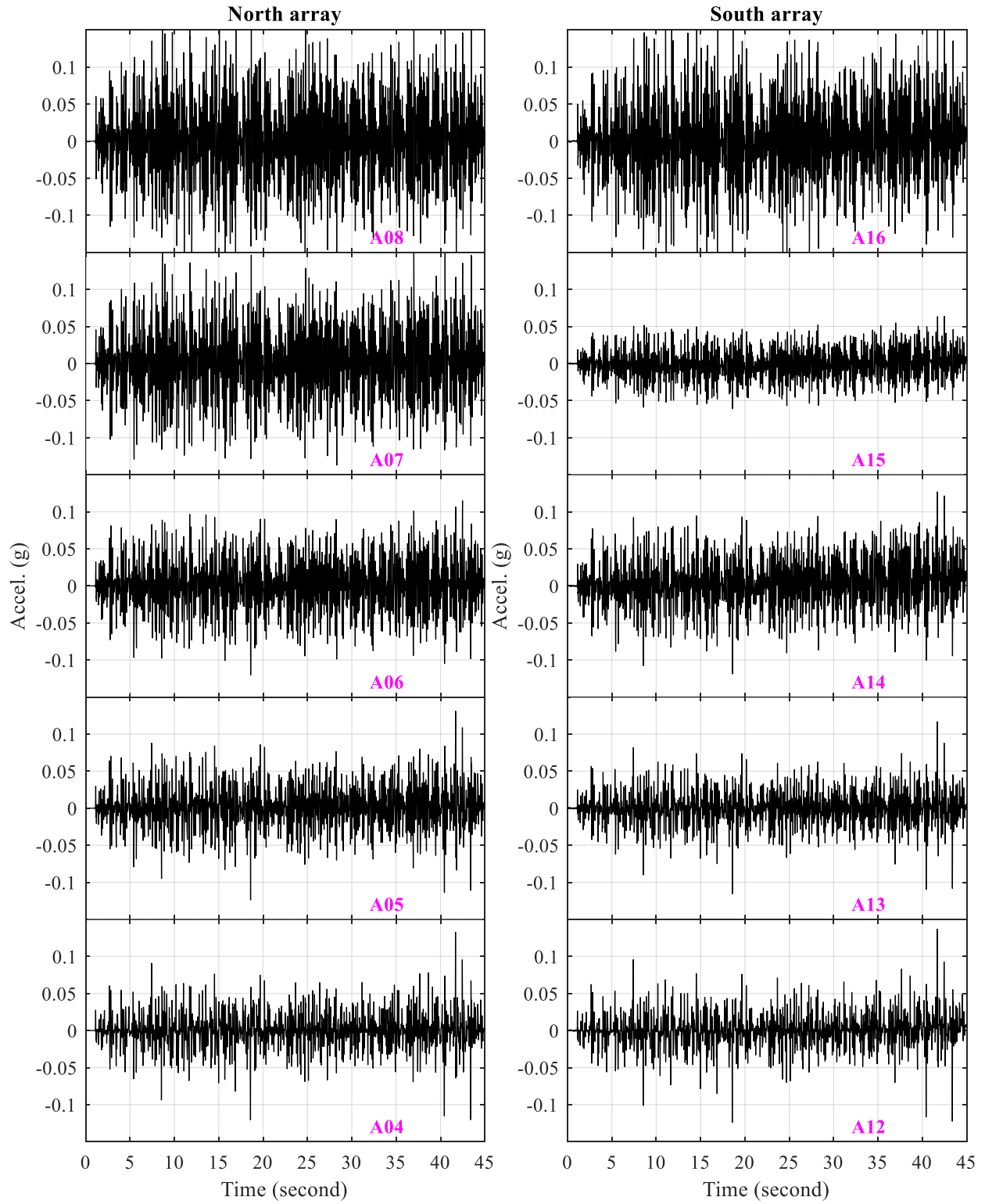


Figure 3-20: Time histories of lateral soil acceleration in north and south arrays for test WN2

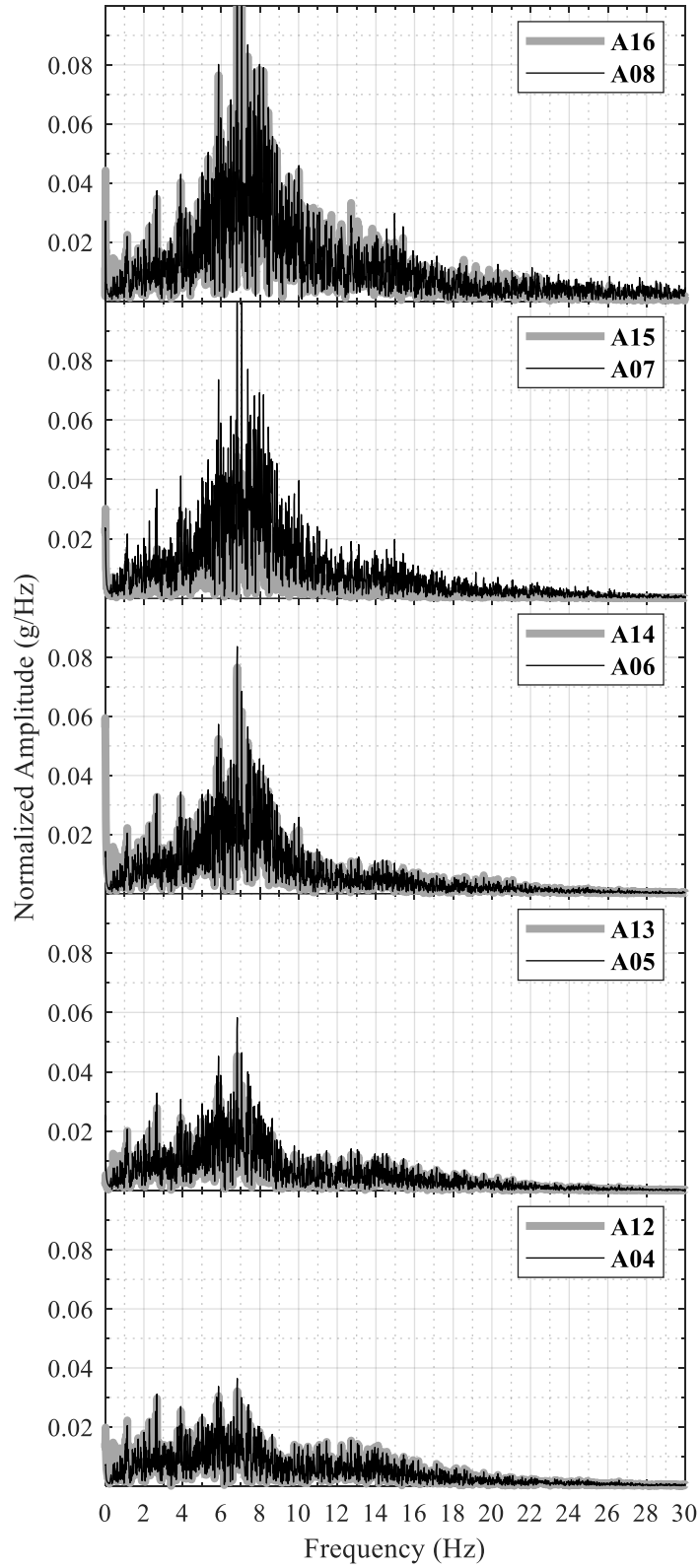


Figure 3-21: Frequency spectra of lateral soil acceleration in north and south arrays for test WN2

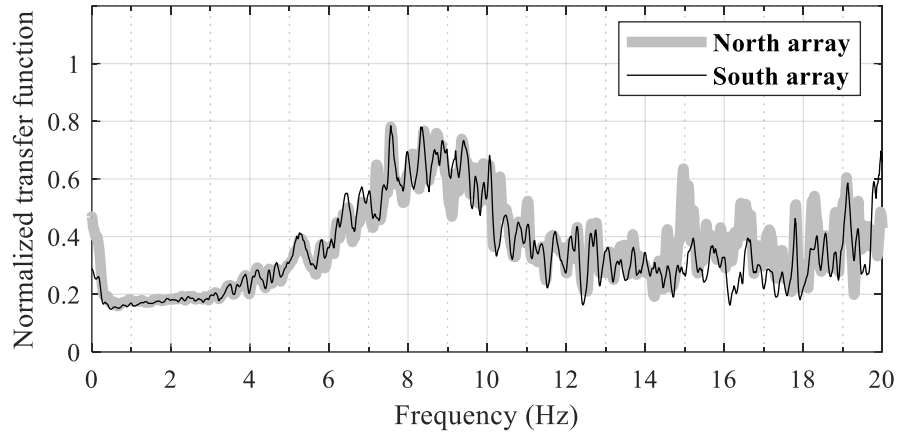


Figure 3-22: Transfer function between uppermost and lowermost soil acceleration records for test WN2

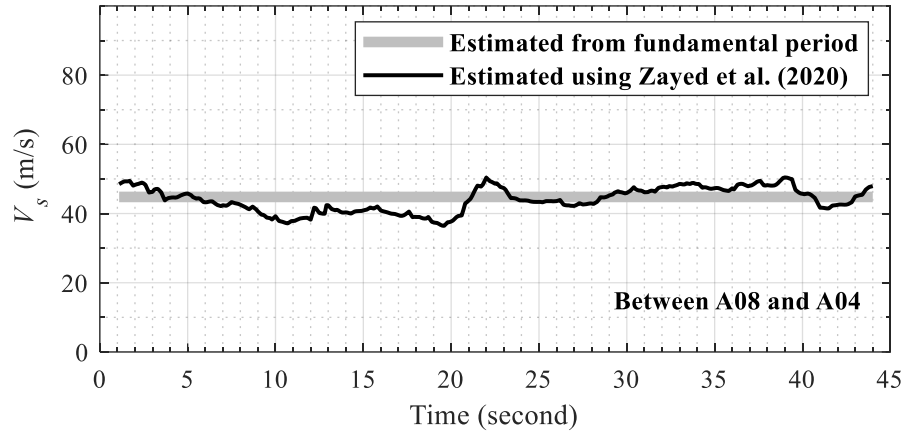


Figure 3-23: Change in soil  $V_s$  with time during test WN2

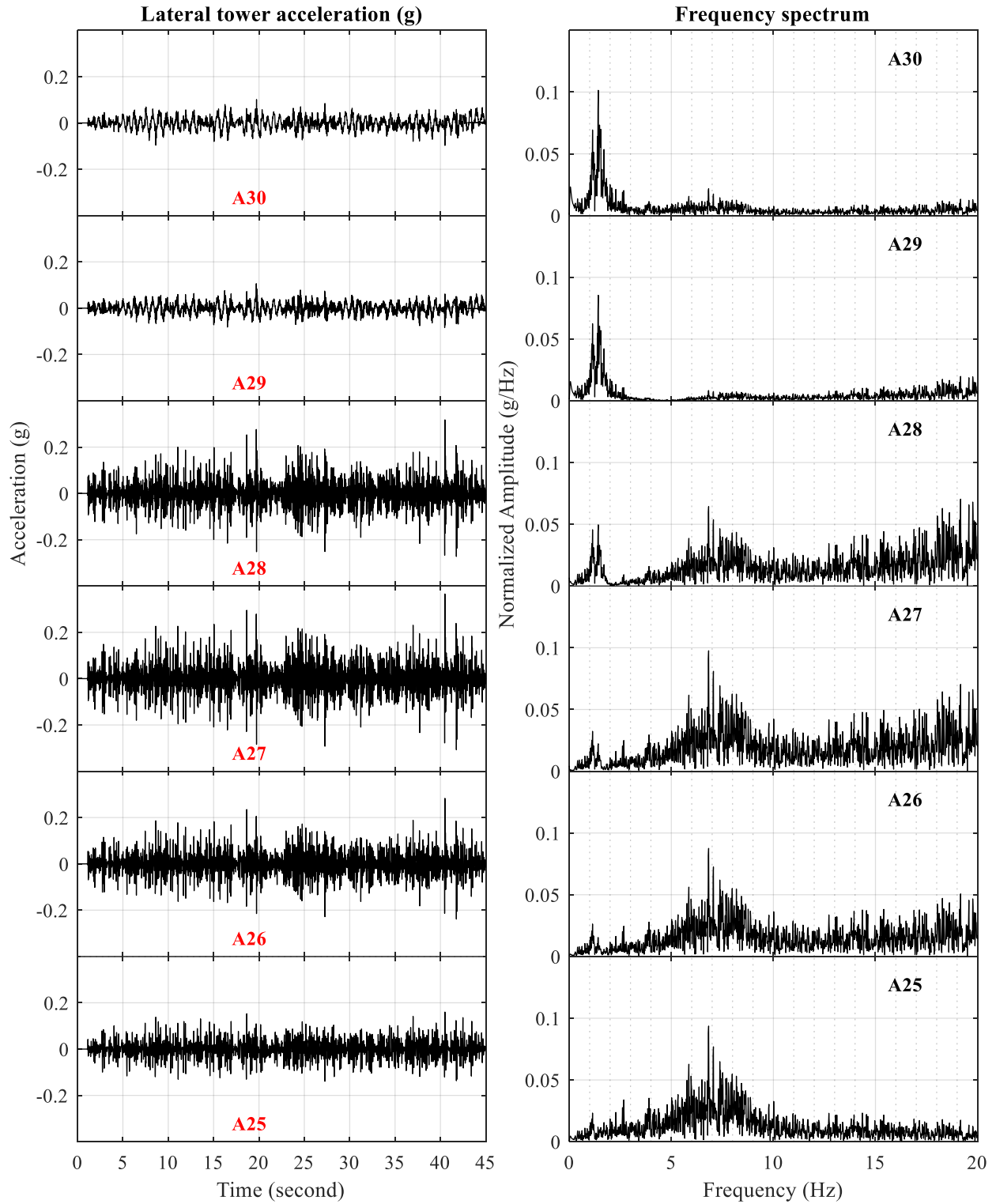


Figure 3-24: Time histories of lateral tower acceleration for test WN2

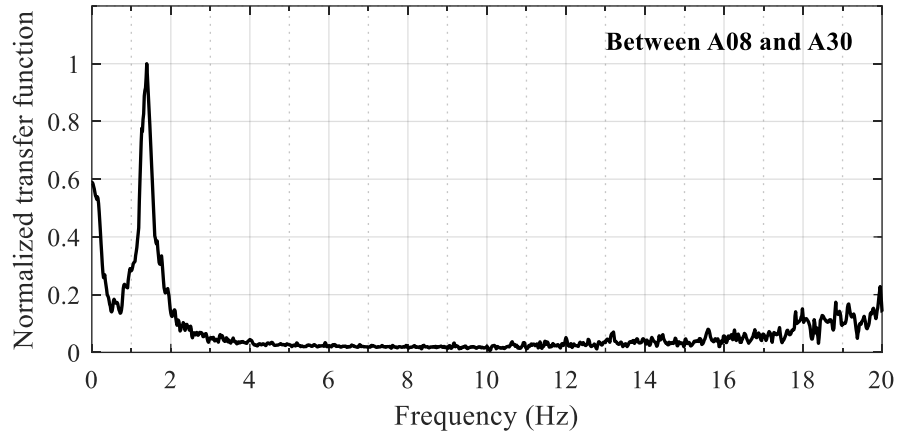


Figure 3-25: Transfer function between acceleration records at the tower top (A30) and soil top near the bucket foundation (A08) for test WN2



# Chapter 4

## Shake table testing - Results and discussion

*Don't let the perfect be the enemy of the good.*

– Gretchen Rubin Voltaire

### 4.1 Introduction

This chapter primarily presents representative experimental results, highlighting response of the soil model, wind turbine bucket foundation, as well as pore pressure (PP#) around the bucket. In the context of the collected data, the relations between generation of negative excess pore pressure (i.e., suction) and bucket moment and rotation are investigated. In addition, response characteristics of the test model in terms of lateral accelerations, vertical displacements, overturning moments, and rotations are illustrated. Results of test H5 are presented in detail followed by a discussion in which additional findings from tests H2, H8 and H10 are summarized. Similar cyclic pore pressure trends were noticed during these tests with peak shaking amplitudes of 0.05 g to 0.3 g, and excitation frequency that ranged between 1 Hz and 1.4 Hz (i.e., near or at soil-foundation system fundamental frequency). APPENDIX A and APPENDIX B provide detailed results of each test.

## 4.2 Results of test H5

### 4.2.1 Shaking event acceleration

Under displacement-control mode, the shake table was used to generate a 7-second long input excitation as shown in Figure 4-1. This motion consisted of 6 cycles with a target 0.1g in peak amplitude and 1.2 Hz in frequency. From Figure 4-1, the shake table response can be noticed to include some superimposed high frequency components, mainly in the range of about 5 to 8 Hz. This high frequency is due to friction in the shake table bearings as discussed by Trautner *et al.* (2018). Similar observation was reported by Brennan *et al.* (2005) who described such superfluous frequencies as higher harmonic components of the main input frequency. The latter study concluded that loading applied by a shake table actuator is not necessarily single frequency and higher harmonics of the main shaking frequency can exist, that are real loading components and not noise. Therefore, presence of this high frequency response influences the outcomes, and should not be filtered out.

### 4.2.2 Soil response

Soil acceleration time histories and the corresponding frequency spectra are presented in Figure 4-2 and Figure 4-3, respectively. These figures indicate that the soil model shows amplification at a frequency of about 7 Hz. Using (3.7), soil average shear wave velocity  $V_s$  can be estimated as 42 m/s. Using the approach developed by Zayed *et al.* (2020), Figure 4-4 shows that  $V_s$  changes between 40 and 50 m/s during shaking, with an overall average of about 47 m/s. The latter value is found to be in a good agreement with the  $V_s$  estimate of (3.7).

Figure 4-5 presents time histories of lateral soil displacement relative to the container base. It can be seen that a positive permanent displacement occurred early in the shaking phase, with maximum values between 2 and 3 mm near top of the soil stratum (where the bucket foundation is located). Figure 4-6 shows excess pore pressure (EPP) ratio  $r_u$  (defined as recorded excess pore water pressure  $u_e$  divided by initial effective vertical stress  $\sigma'_{v0}$ ) with values between -0.1 and 0.1, which indicate a relatively small change in pore pressures.

### 4.2.3 Tower response

Lateral acceleration time histories along the wind turbine tower and the corresponding frequency spectra are shown in Figure 4-7. It can be noticed that the input excitation frequency is maintained in the tower response. From the spectra plots of Figure 4-7, a clear amplification at the excitation frequency may be observed along the tower from about 0.07 g at tower base (A25) to about 0.24 g at tower top (A30). This amplification can be explained by the fact that the excitation frequency (about 1.2 Hz) is near the fundamental frequency of the soil-foundation-structure system (about 1.4 Hz). Moreover, acceleration time histories at the tower top (i.e., A29 and A30) show a smooth free vibration phase after the shaking stopped. As such, the tower acted as low-pass filter, damping out high-frequencies, with response of the lumped mass at the tower top predominantly at the main excitation frequency of 1.2 Hz. As presented in Figure 4-8, lateral displacements along the tower relative to the foundation base are found to reach as much as 6 mm. Time histories of bending moment along the tower as obtained from strain gauges are shown in Figure 4-9.

#### 4.2.4 Moment-rotation response of bucket foundation

Figure 4-10-a presents the vertical displacement time histories of the bucket foundation during shaking. A maximum upward and downward displacement of about 4 mm and 2 mm, respectively, can be observed, with an average residual downward displacement of about 0.5 mm. A clear cyclic rotation behavior can be observed in Figure 4-10-a as the two edges of the bucket cycle upward and downward in opposite direction. Using this vertical displacement data, the resulting bucket rotation is shown in Figure 4-10-b, which reveals maximum and residual rotations of about 0.012 (about 0.7 degrees) and 0.002 radians (about 0.1 degrees), respectively.

As the tower vibrates (Figure 4-7), it exerts inertial lateral forces along its height that accordingly result in overturning moment on the bucket foundation. The extent of overturning moment varies with amplitude of the lateral tower accelerations, with much contribution resulting from the lumped mass at the tower top. Figure 4-10-c displays bending moment time history at the tower base (location of SG005), showing a maximum value of about 0.5 kNm. Since the junction between bucket and wind turbine tower is designed with reinforcing stiffeners as a rigid connection, bending moment at SG005 (Figure 4-10-c) can be assumed to represent the bucket overturning moment. It may be noted that this bucket moment is generally symmetric in amplitudes during shaking. The 5 time instants highlighted in Figure 4-10-b and Figure 4-10-c will be useful in the following sections to demonstrate various response mechanisms of the bucket foundation.

Moment-rotation loops of the bucket foundation are shown in Figure 4-11-a, and the following observations may be noted:

- As the amplitude of lateral tower acceleration increases (Figure 4-7), the lateral inertial forces and the resulting overturning moments gradually increase, with the moment-rotation loops getting larger in size.
- First half cycle of the recorded vertical bucket displacement at the beginning of shaking (Figure 4-10-a) shows noisy response making the very first part of moment-rotation loops somewhat irregular as shown in Figure 4-11-a. Thus, rotational stiffness (defined as overturning moment divided by rotation) of the bucket foundation is not accurately represented during the first half cycle of shaking.
- However, it may be observed that the moment-rotation plot generally shows stiffer response at lower levels of rotation with less hysteresis. At large rotation amplitudes, the cycles can be seen to have a characteristic shape that will be examined closely by isolating one cycles in a separate plot.

As such, the loading cycle between 3.25 and 4 seconds is presented in Figure 4-11-b in which the marked points with associated numbers 1 to 5 correspond to the same points previously marked in Figure 4-10-b and Figure 4-10-c. Figure 4-12 shows schematics of bucket foundation illustrating its rotations for the cycle presented in Figure 4-10 and Figure 4-11. From point 1 to point 2, the bucket rotates counterclockwise (sign convention presented in Figure 4-12) from a small value of rotation (near horizontal position) to about 0.01 radian (i.e., about 0.6 degrees) with the same slope for the most part. Initial stiff unloading behavior may be noted as the bucket rotates clockwise from point 2 towards point 3, followed by a more flexible response while the response gets stiffer during opposite loading towards point 4. Unloading from point 4 to point 5 shows similar initial unloading stiffness followed by more flexible response as the bucket reaches near-horizontal position at point 5.

In addition, vertical average displacement of the bucket is displayed against rotation in Figure 4-13. This figure shows that average positive displacement values of the bucket are associated with larger rotation amplitudes.

#### **4.2.5 Pore pressure response inside and outside bucket foundation**

Pore Pressure (PP) transducers installed inside and outside the bucket foundation were used to examine the change in  $r_u$  during shaking. Figure 4-14-a and Figure 4-14-b show  $r_u$  time histories for both north and south sides of the bucket, respectively. A strong dilative response can be noticed in all PP sensors (Figure 4-14-a), with the dilation spikes stronger inside bucket inside (PP20 and PP21) compared to the outside (PP24 and PP25). It can also be noted that  $r_u$  below the bucket lid reaches one, as well as within the soil near the bucket tip (PP20). Similar observations can be concluded from Figure 4-14-b, indicating matching EPP response at both north and south edges of the bucket.

##### **4.2.5.1 Variation of bucket EPP with bucket rotation**

In order to investigate the contribution of suction (i.e., negative excess pore pressure) inside the bucket in resisting overturning moments resulting from lateral inertial forces, the one loop presented in Figure 4-11-b is further examined and in light of the  $r_u$  values around the bucket. Figure 4-15 illustrates how  $r_u$  changes with bucket rotation for all PP transducers around the bucket. For PP20 (north side inside bucket tip), as the bucket rotates counterclockwise from point 1 to point 2 (Figure 4-12),  $r_u$  decreases from about 1.5 to about -0.4, which indicate transition from contractive to dilative response during this quarter cycle. On the other side (bucket tip at south

side), the south edge of the bucket experiences maximum rotation with PP30 showing one-way increase in suction as  $r_u$  changes from about -0.5 to about -2.2.

As the bucket rotates back (clockwise) during the half cycle between point 2 and point 3 (Figure 4-12),  $r_u$  shows slight contractive response (i.e., slight increase in  $r_u$ ) as the bucket rotation is restored from about -0.01 radian to near zero. A stronger dilation can be seen during the following quarter cycle between point 3 and point 4 with  $r_u$  reaching about -1.8. The latter quarter cycle (i.e., 3<sup>rd</sup> quarter between 3 and 4) is the part where the north side of the bucket experiences the maximum rotation (Figure 4-12). That explains the suction peak of PP20 at point 4.

On the south side of the bucket, PP30 shows strong contraction during the 2<sup>nd</sup> quarter cycle (between 2 and 3) as the bucket restores its rotation from about -0.001 to nearly zero, with  $r_u$  changing from about -2.2 at point 2 to about +1.7 at point 3. Thereafter, the bucket continues its clockwise rotation for a quarter cycle to point 4 (3<sup>rd</sup> quarter), with PP30 reverting to dilative response and dropping from +1.7 to about zero at point 4. The last quarter cycle from point 4 to point 5 represents the bucket restoring its rotation back to near horizontal position (i.e., about zero rotation).

The above discussions indicate that point 2 represents the bucket experiencing its maximum rotation counterclockwise while maximum clockwise rotation is represented by point 4. Same trends can be noticed for all time histories of  $r_u$  (Figure 4-15), where all PP records in the north side mostly follow PP20 trends, and PP30 leading the trends for all PP in the south side. In addition, it can be noted that the largest exceedance of  $r_u = 1$  occurs at the inside uppermost and lowermost transducers (i.e., PP20 and PP23, as well as PP30 and PP33).

#### 4.2.5.2 Variation of bucket EPP with bucket moment

Additional observations can be drawn when plotting bucket EPP ratios against bucket moment for the same cycle, as shown in Figure 4-16. Similar to Figure 4-15, exceedance of  $r_u = 1$  is noted to occur at the inside uppermost and lowermost PP transducers. The latter two figures suggest strong correlation between bucket  $r_u$  and bucket moment as well as bucket rotation since the maximum suction is noticed to occur at the maximum bending moment and maximum rotation (point 2 and point 4 for maximum counterclockwise and clockwise rotation, respectively).

Full versions of Figure 4-15 and Figure 4-16 for the entire shaking duration are presented in Figure 4-17 and Figure 4-18, respectively. Same patterns of the former figures are repeated with smaller and larger loops indicating characteristic trends for the relationship between bucket EPP and its rotation as well as its moment.

#### 4.2.5.3 Variation of bucket EPP with bucket vertical displacement

Figure 4-19 shows the change in  $r_u$  with vertical bucket displacement expressed in terms of LVDT13 record for PP20 through PP26 (north side) and LVDT14 for PP30 to PP36 (south side), for the same cycle between 3.25 and 4 seconds. The latter figure reveals that the dilative response (reduction in  $r_u$  values) at the north edge (i.e., PP20 and PP24), while the bucket experiences maximum counterclockwise rotation at point 2 (Figure 4-12), is associated with downward movement (negative value) of that edge (i.e., penetration of north tip into sand). Similar reduction in  $r_u$  can be observed at PP30 and PP34 as bucket reaches its maximum clockwise rotation towards point 4 (Figure 4-12) while south edge penetrates the soil (1 mm downward/negative displacement).



The above discussion suggests that at maximum rotation one bucket tip moves upward while the other moves downward and further penetrates the soil which results in dilation associated with lower levels of suction. As such, suction is generated not only at the tip that experiences uplift, but also the other tip that encounters downward movement (i.e., penetration) in soil. The suction generated at the latter end is noticed to be quite less than the suction generated at the uplifting tip.

Figure 4-20 shows the full version of Figure 4-19 where  $r_u$  is displayed against vertical bucket displacement for the entire shaking duration. Identical trends in Figure 4-20 can be seen at both edges of the bucket. In addition, it can be noted that the difference between maximum uplift  $r_u$  and maximum penetration  $r_u$  is largest at the inside bucket tips (i.e., PP20 and PP30) as well as outside top PP transducers (i.e., PP26 and PP36).

#### **4.2.5.4 Relationship between bucket EPP at both sides**

Based on their pore pressure measurements inside bucket foundation during installation, Houslyby *et al.* (2006) revealed there is a strong correlation between excess pore pressures at both sides. To investigate the latter observation during seismic excitation,  $r_u$  for all PP transducer at north edge are plotted against  $r_u$  for all PP transducers at south edge for the cycle between 3.25 and 4 seconds, as presented in Figure 4-21-a and for the entire shaking duration in Figure 4-21-b. The latter figures confirm the earlier observation that suction is generated not only at the tip that experiences uplift, but also the other tip that experiences downward movement (i.e., penetration) into the soil. It can be noted that (Figure 4-21-a) points 2 and 4 of PP20/PP30 (bottom left) plot show large suction at the uplifting tip while the penetrating tip shows  $r_u$  values near zero, yet it experience dilative response as  $r_u$  decreases for both PP transducers. As such, the above discussion

suggests that the suction generated at the penetrating end is noticed lower than the suction generated at the uplifting tip.

### **4.3 Observations from additional tests**

In this section, results from tests H2, H8 and H10 (Table 3-4) are summarized and the similarities to test H5 are illustrated.

Figure 4-22 shows moment-rotation plots for tests H2, H8 and H10 in which the response can be seen to be more nonlinear as the amplitude of shaking increase from H2 towards H10 (Table 3-4). Due to the very low levels of vertical displacement incurred in test H2, a noisy response can be observed in the moment-rotation response (Figure 4-22-a), which can be attributed to low signal to noise ratio in records of LVDT13 and LVDT14. On the other hand, test H10 (Figure 4-22-c) showed a smooth moment-rotation response that has the same characteristics discussed in the previous sections for H5. From Figure 4-22-b (test H8), it can be observed that the bucket exhibits hardening response towards peak rotation. Similar observation can be seen in Figure 4-22-c of test H10.

Similar to Figure 4-13, concave trends between average of bucket vertical displacement and its rotation can be noted in the left column plots of Figure 4-23-a and Figure 4-23-b for tests H2 and H8, respectively. On the other hand, Figure 4-23-c of test H10 does not show similar concave trend as H2 or H8. The right column plots of Figure 4-23 show the corresponding vertical bucket displacement time histories. From these plots, it can be noticed that the bucket exhibits less cyclic response vertical displacement (average line) compared to Figure 4-10 of test H5. Test H10 (Figure 4-23-c) shows larger average one-way upward or uplift movement. Furthermore, north and south bucket vertical displacement in H5, H8 and H10 (Figure 4-10 and Figure 4-23) have larger

upward (i.e., positive) component than downward (i.e., negative), while it is the opposite in H2. The latter observation might be caused by the relatively large level of overturning moment (i.e., about 1.1 kNm) resulting from inertial lateral forces compared to about 0.5 kNm in test H5, which ultimately resulted in larger peak rotation in test H10 (about 0.05 radian) compared to all tests.

In addition, it can be noticed that Figure 4-24 of test H2 has similar EPP-moment response to that of test H5 previously illustrated in Figure 4-18. However, test H2 shows lower levels of  $r_u$  and moments compared to test H5. The latter observation matches the fact that H5 is of stronger amplitude compared to H2 (0.05 g vs. 0.1 g). On the other hand, Figure 4-25 for test H10 shows larger  $r_u$  and moments compared to test H5, while maintaining the same trends of  $r_u$  against bucket moment. Figure 4-26-a and Figure 4-26-b describe the relationship between  $r_u$  for all PP transducer at north edge against the corresponding  $r_u$  at south edge for tests H2 and H10, respectively. Both figures show same trends as in Figure 4-21-b, with the response being of lower amplitude (i.e., lower  $r_u$  values) for test H2 and higher (i.e., larger  $r_u$  values) for test H10.

Moreover, Figure 4-27 illustrates the change in maximum suction level (defined as maximum negative value of  $r_u$  among PP20 and PP30 records) with maximum bucket moment as well as maximum bucket rotation for the discussed tests. From this figure, it may be noticed that the maximum suction level can be approximated to vary linearly with maximum bucket moment for the range of investigated results, while it has a more non-linear trend for variation of maximum suction level with maximum bucket rotation.

The discussed results may be considered to represent partially drained conditions for bucket foundation where soil permeability is expected to have influence on the bucket foundation seismic response as well as the overall system response. The sand used in all tests of this study has

a permeability coefficient of about 0.01 cm/second (El Ghoraiby *et al.* 2020). Data collected from shake table tests presented in this study can be valuable for calibration a numerical model that can be further used to investigate influence of soil permeability on the system response and to perform parametric studies on size and geometry of the bucket foundation.

#### **4.4 Summary and conclusions**

A set of shake table tests of an idealized offshore wind turbine model with bucket foundation in sand is described. Results from four tests are discussed. These tests used harmonic input excitation motions that were selected to have main frequency at or near the fundamental frequency of the soil-foundation-structure system, with acceleration amplitudes ranging from 0.05 g to 0.3 g. Special attention was given to install small-size pore pressure transducers around the bucket from inside and outside to record pore pressure variation during shaking.

System response was recorded including far-field and near-field soil acceleration, displacement, pore water pressure as well as tower acceleration, displacement, moments and rotations. Suction pressure was noted to be generated not only at the uplifting tip of bucket foundation but also at the penetrating tip with lower suction levels at the penetrating tip. Characteristic trends between moment and bucket EPP records were observed in all tests as well as between bucket rotation and bucket EPP. A distinctive butterfly shaped trend was noted between bucket EPP generated at the uplifting tip and that generated at the penetrating tip. From the obtained data, a generally linear trend was observed between the maximum mobilized suction EPP and the maximum bucket moment, within the investigated results.

The collected data from shake table testing will serve in further chapters as a basis to develop a calibrated numerical tool to investigate utility-scale seismic response scenarios. In these

simulations, influence of soil permeability is among the primary concerns. As such, a parametric study on size and geometry of the bucket foundation is conducted using the calibrated model.

## **4.5 Acknowledgement**

The research described in this section was partially funded by the National Science Foundation grant OISE-1445712 as well as the Trent R. Dames and William W. Moore graduate student fellowship from the American Society of Civil Engineers (ASCE). Testing was conducted at the Powell laboratories, University of California San Diego, with assistance provided by Dr. Christopher Latham, Mr. Andrew Sander, Mr. Mike Sanders, Mr. Abdullah Hamid, and Mr. Darren Mckay.

The discussion carried out in chapters 3 and 4 is currently being prepared to be published as a journal paper tentatively in the ASTM Geotechnical Testing Journal or the ASCE Journal of Geotechnical and Geoenvironmental Engineering. The proposed title of this paper is “Shake table testing of bucket foundation for offshore wind applications”. The dissertation author is the primary author of this paper with Dr. Kyungtae Kim, Mr. Athul Prabhakaran, and Professor Ahmed Elgamal as coauthors.

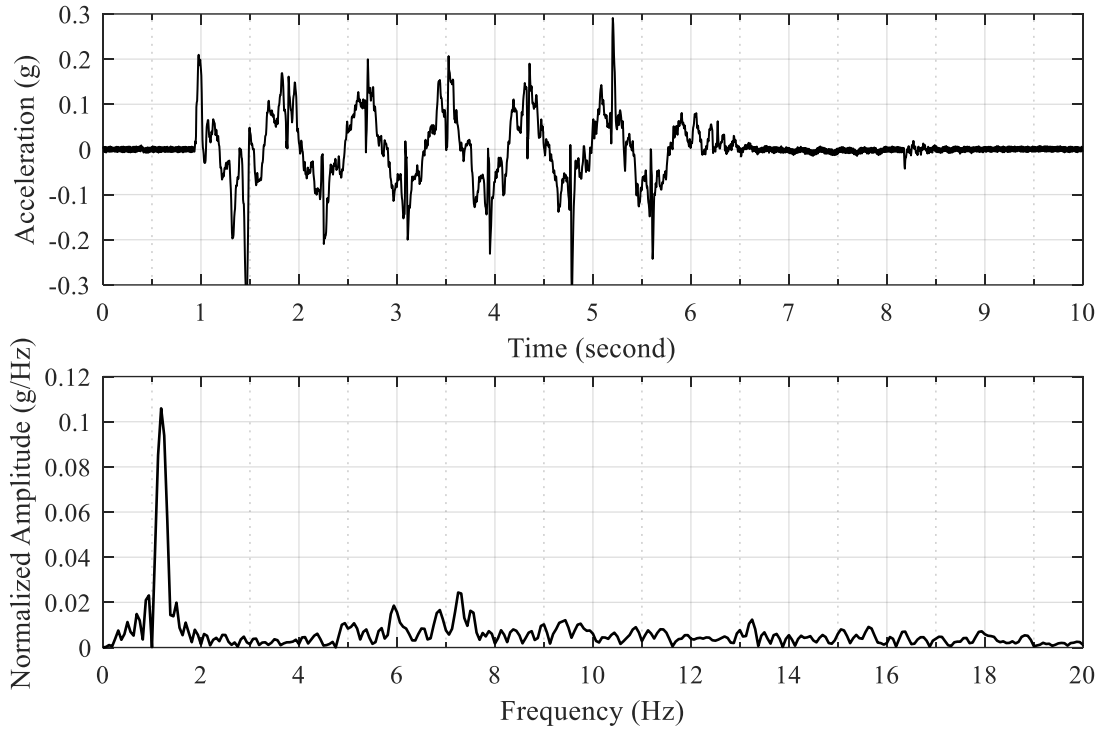


Figure 4-1: Acceleration time history and corresponding frequency spectrum of shake table input excitation for test H5

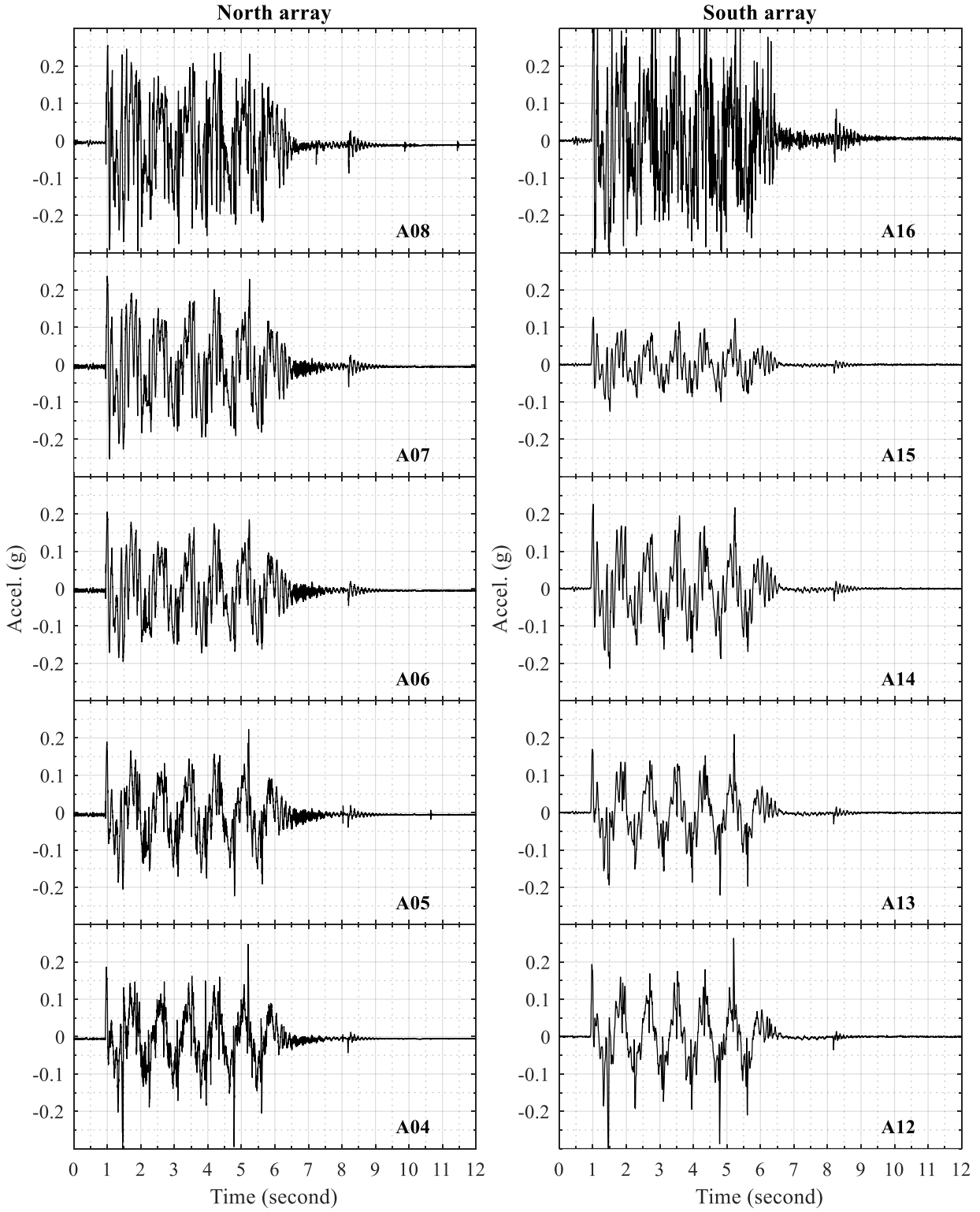


Figure 4-2: Time histories of lateral soil acceleration along north and south arrays for test H5

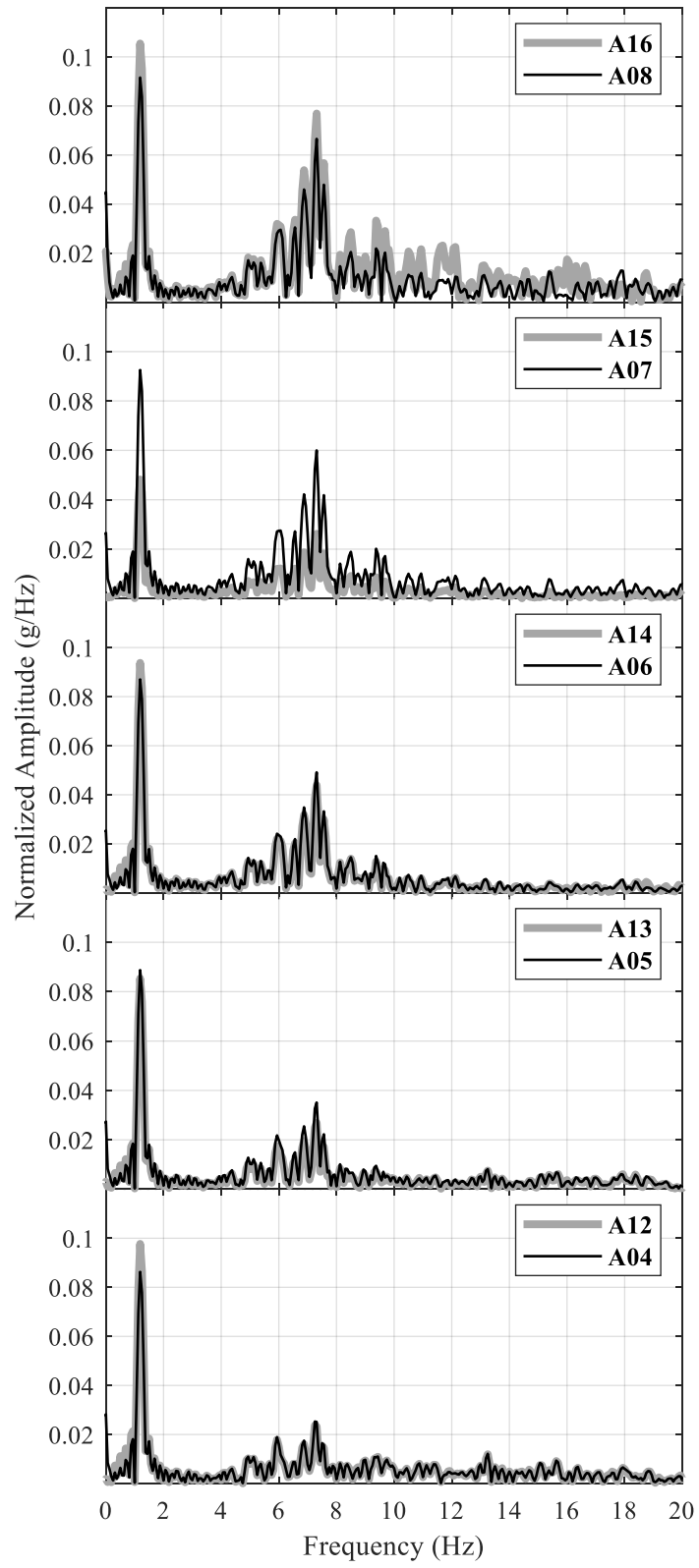


Figure 4-3: Frequency spectra of lateral soil acceleration along north and south arrays for test H5



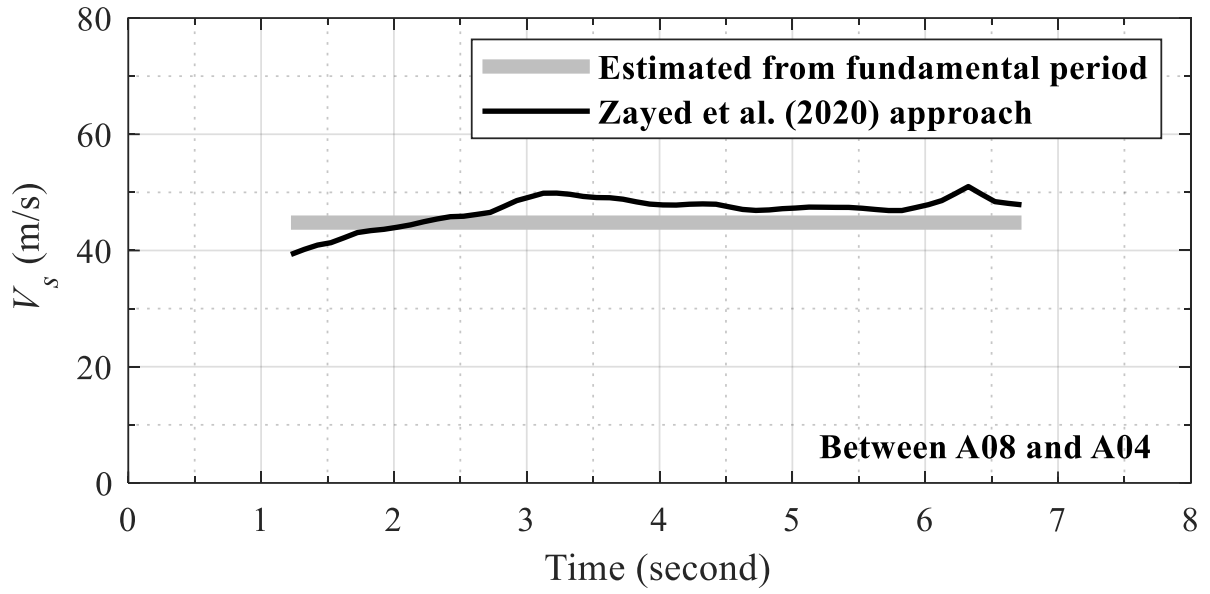


Figure 4-4: Change in soil  $V_s$  with time during test H5

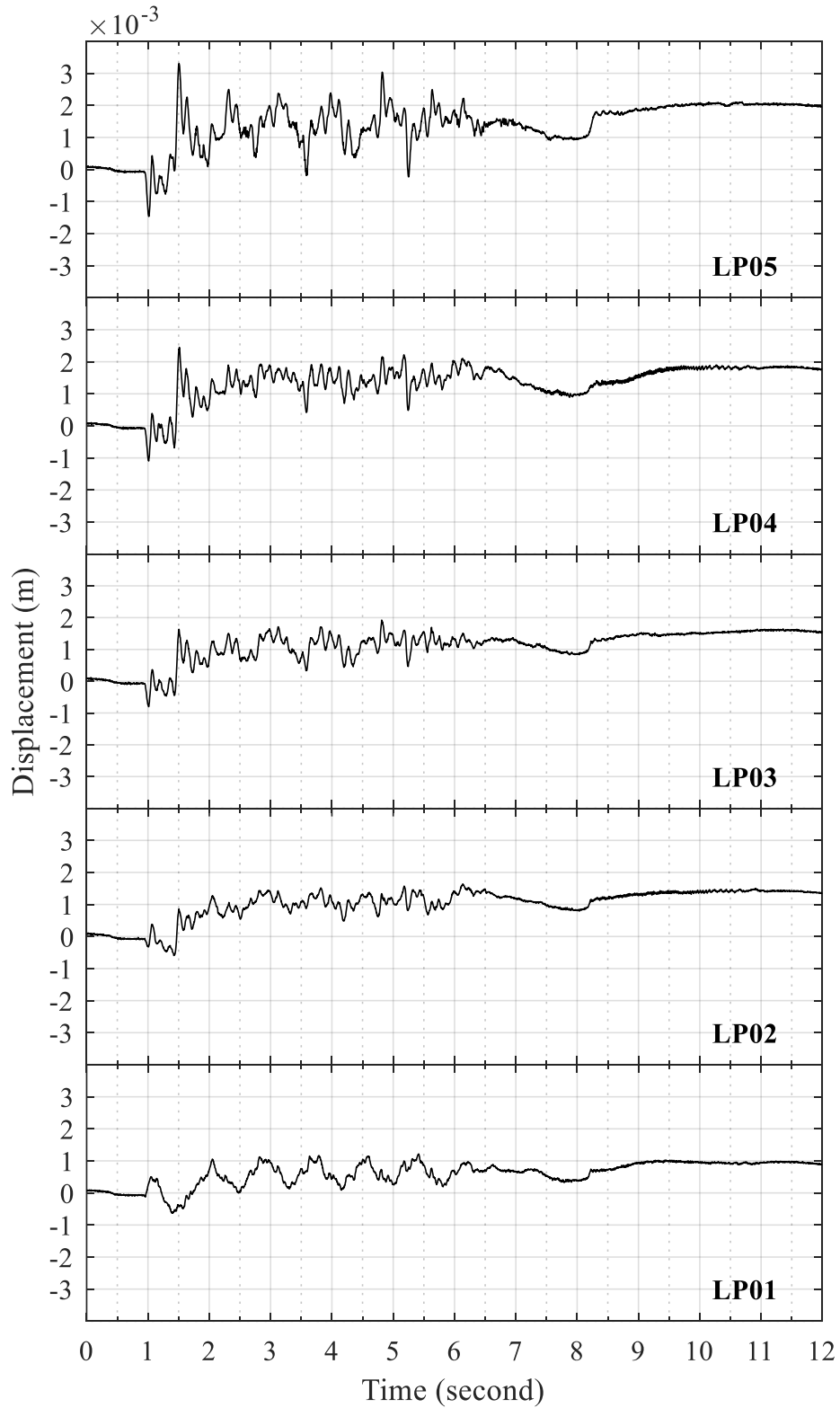


Figure 4-5: Time histories of lateral soil displacement relative to laminar container base for H5

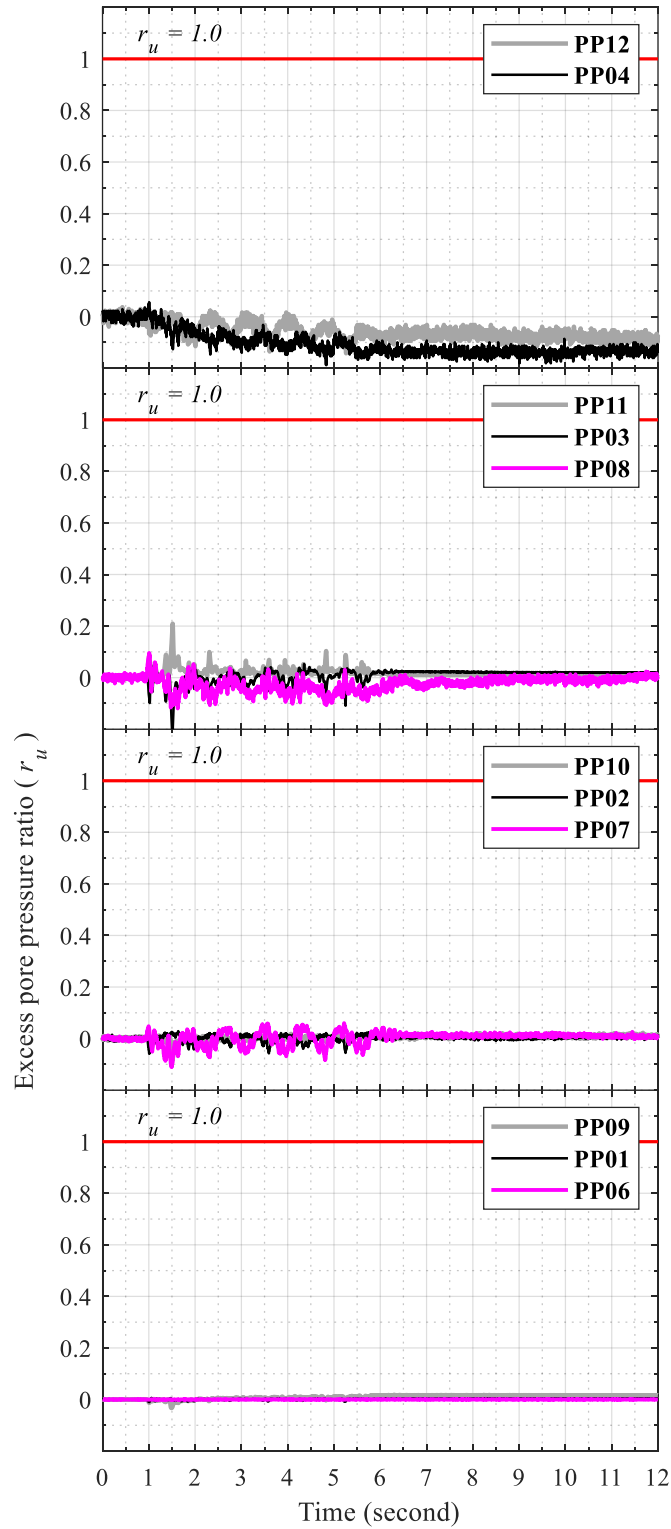


Figure 4-6: Time histories of soil excess pore pressure for test H5

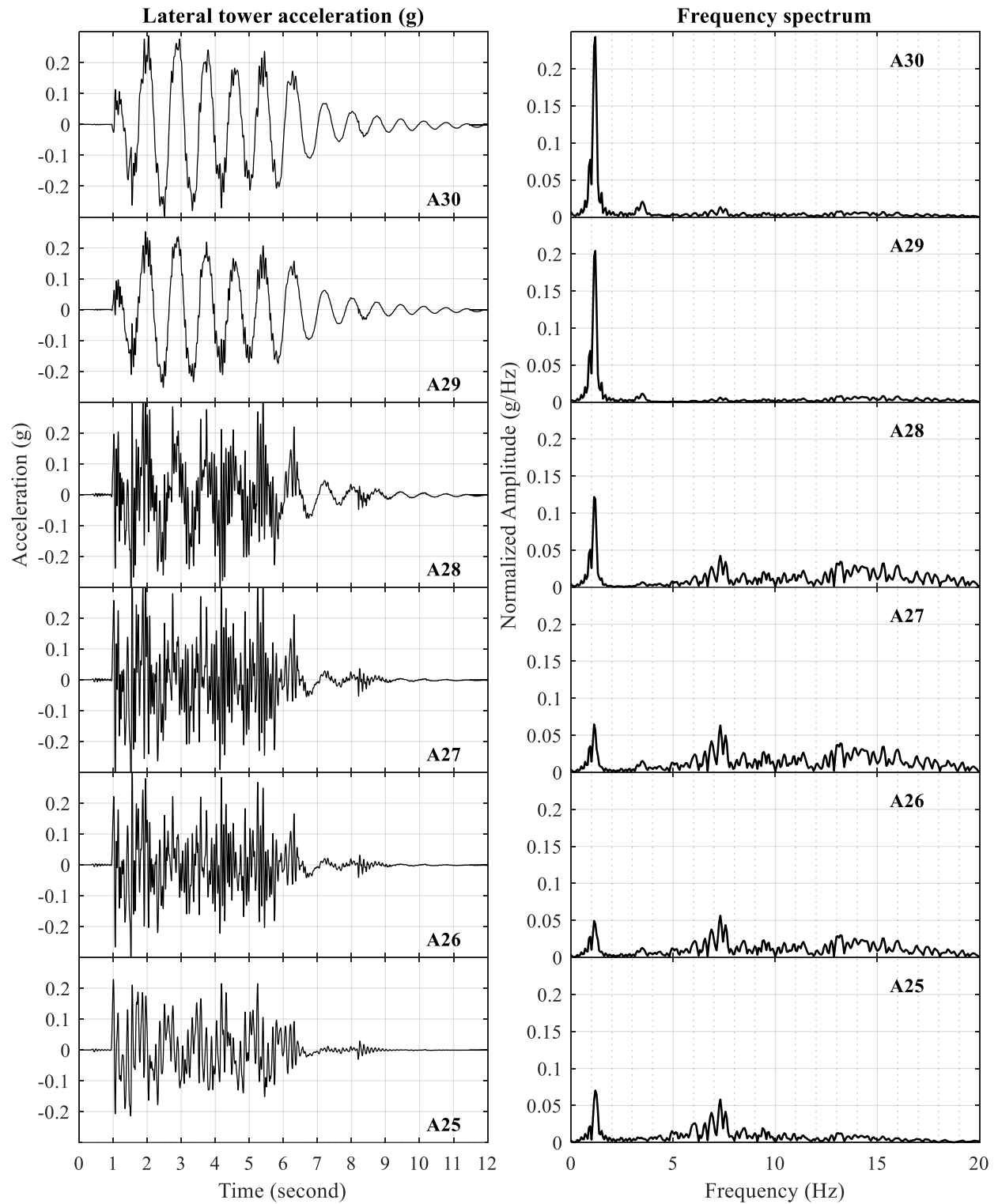


Figure 4-7: Time histories and corresponding frequency spectra of lateral tower accelerations for test H5

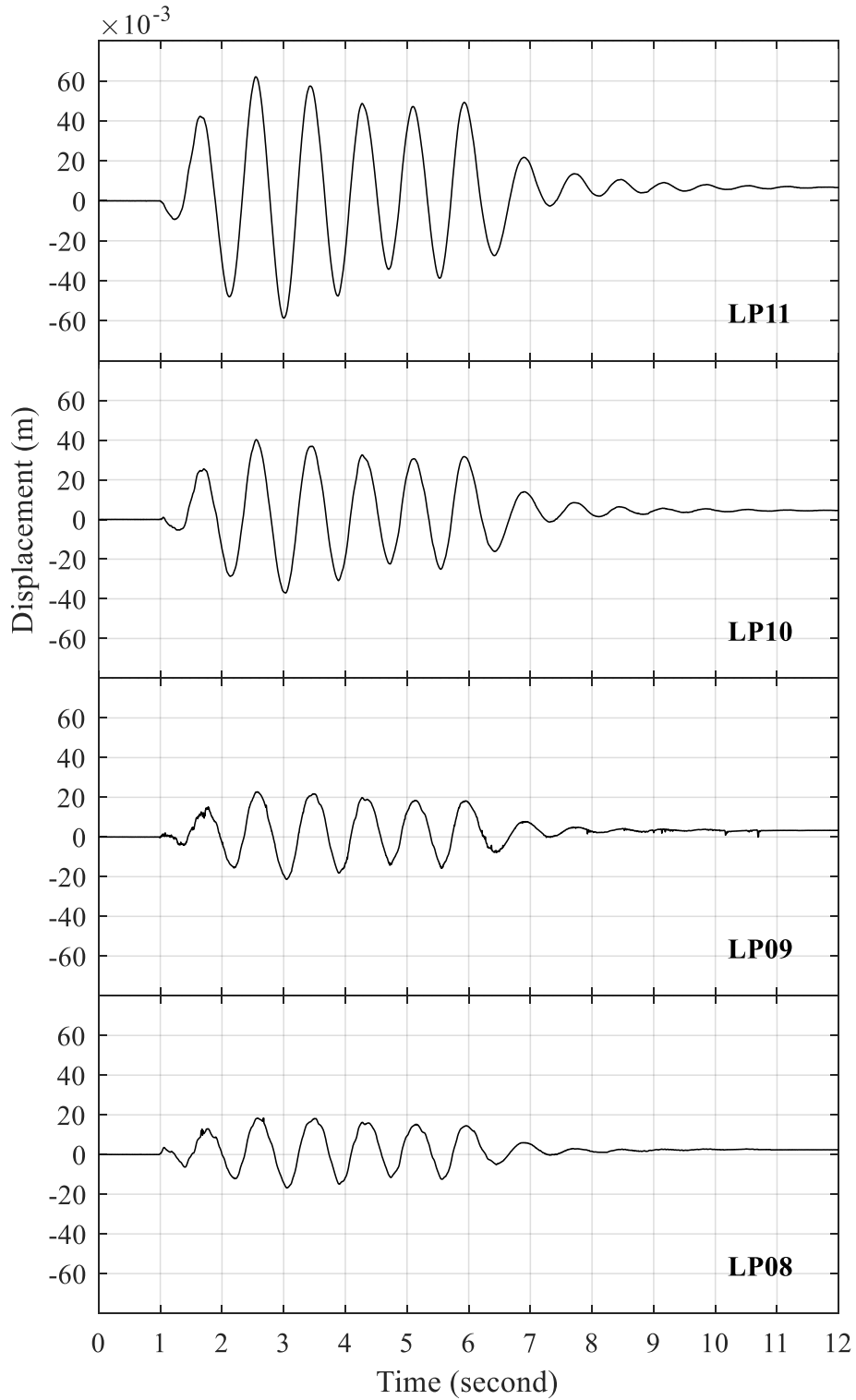


Figure 4-8: Time histories of lateral tower displacement relative to lateral soil displacement at the foundation level (LP05) for test H5

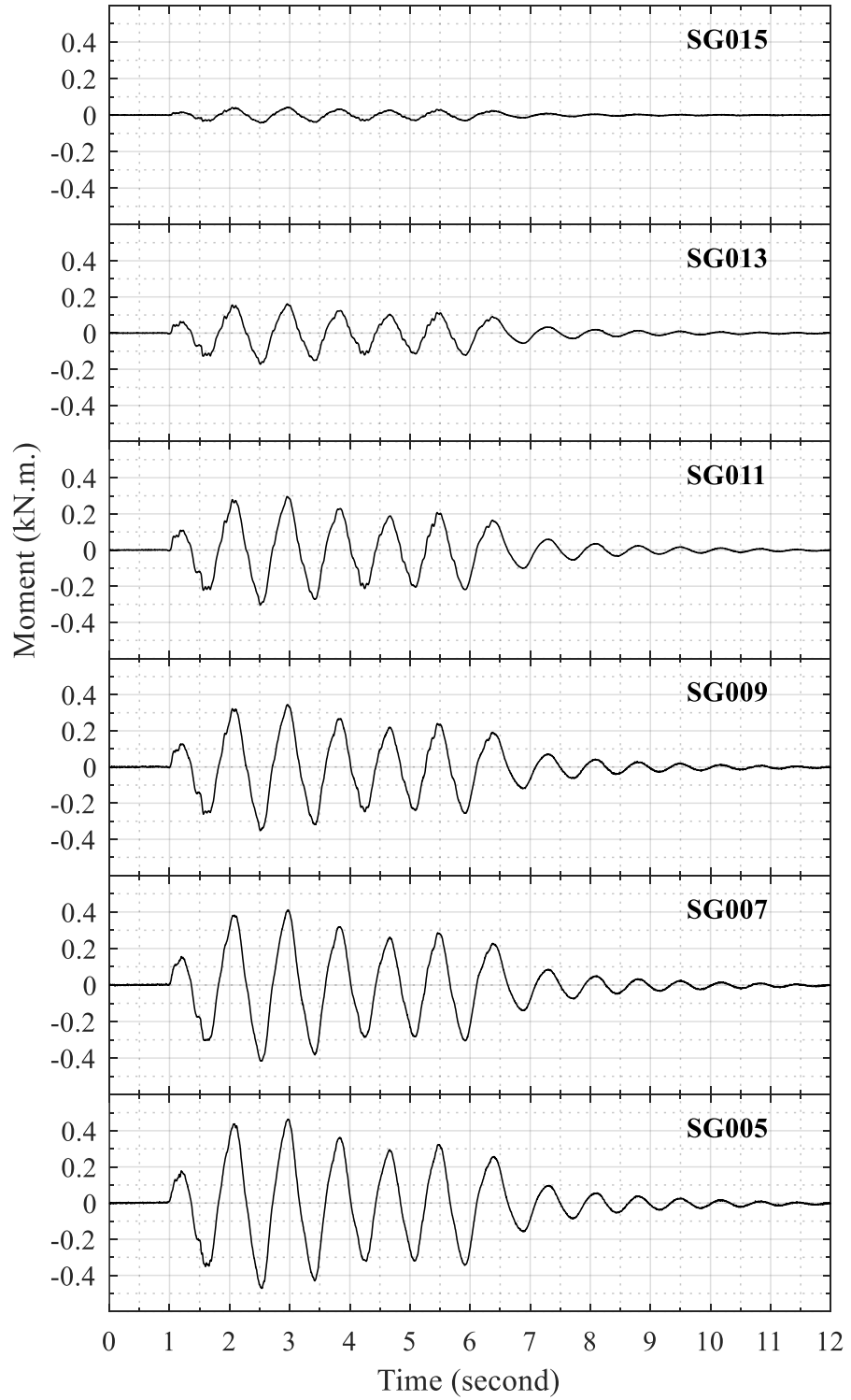


Figure 4-9: Time histories of tower bending moment for test H5

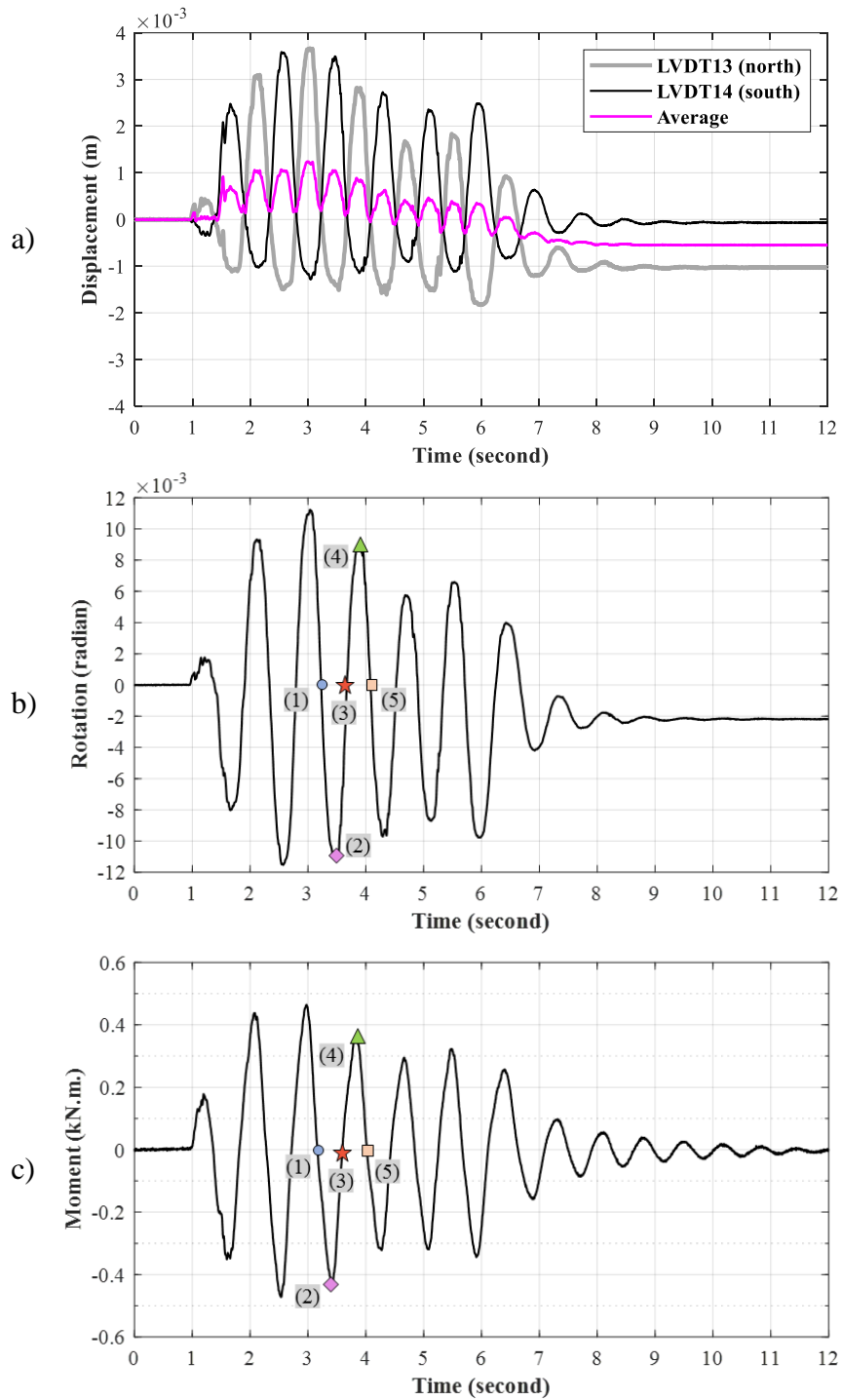


Figure 4-10: Time history of a) vertical displacement of bucket foundation, b) rotation of bucket foundation, and c) bending moment at tower bottom (i.e., the bucket top) for test H5

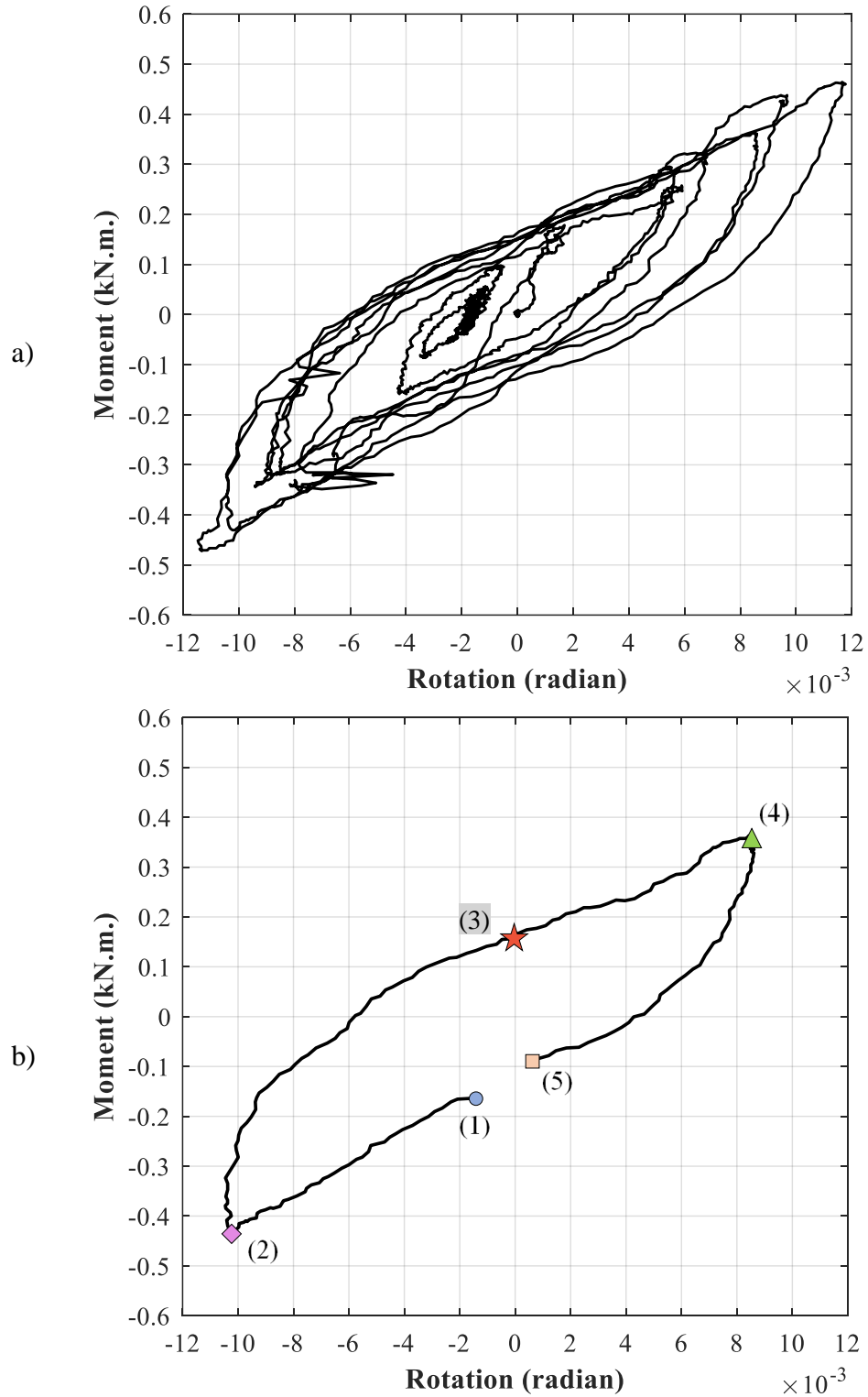


Figure 4-11: Plot of a) bucket moment vs. bucket rotation for test H5, and b) one loop of bucket moment vs. bucket rotation for test H5 (between 3.25 and 4 seconds)



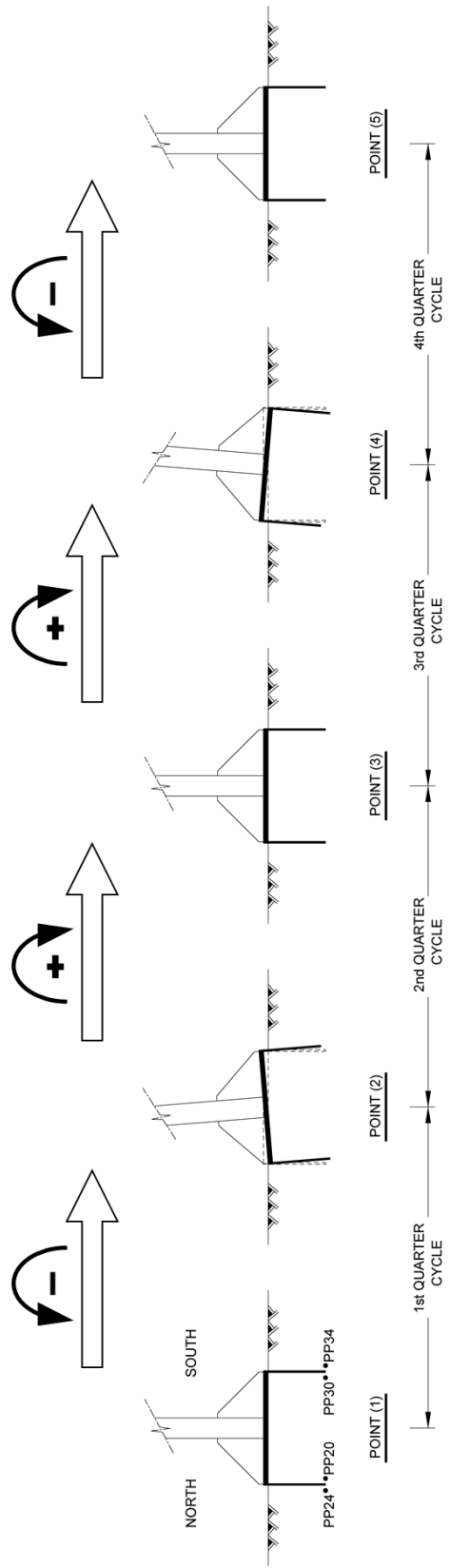


Figure 4-12: Schematic illustrating bucket foundation rotation at each of the five points marked in Figure 4-10 and Figure 4-11

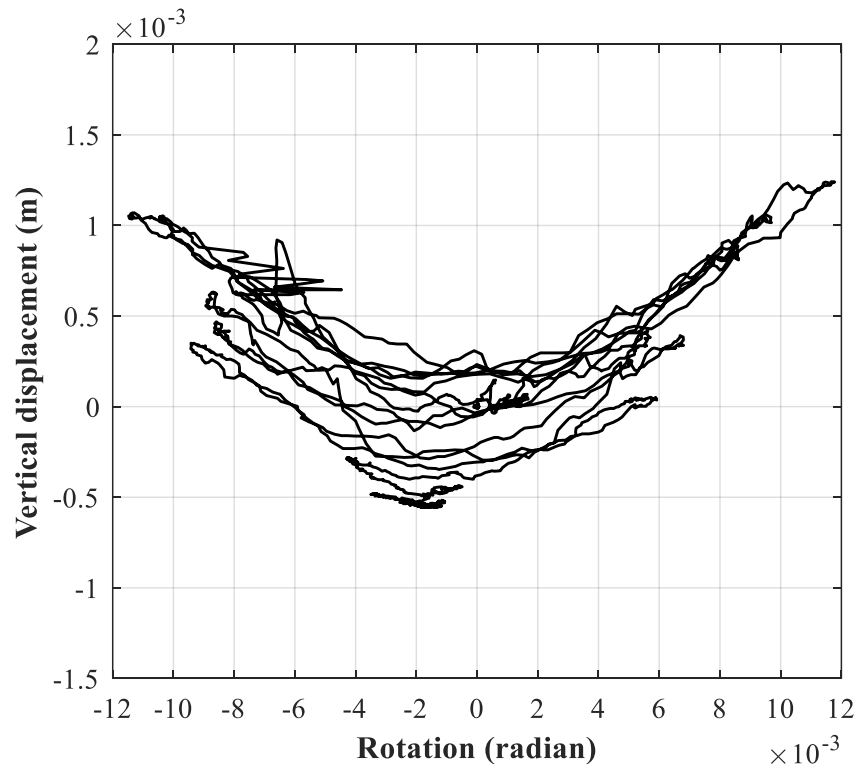
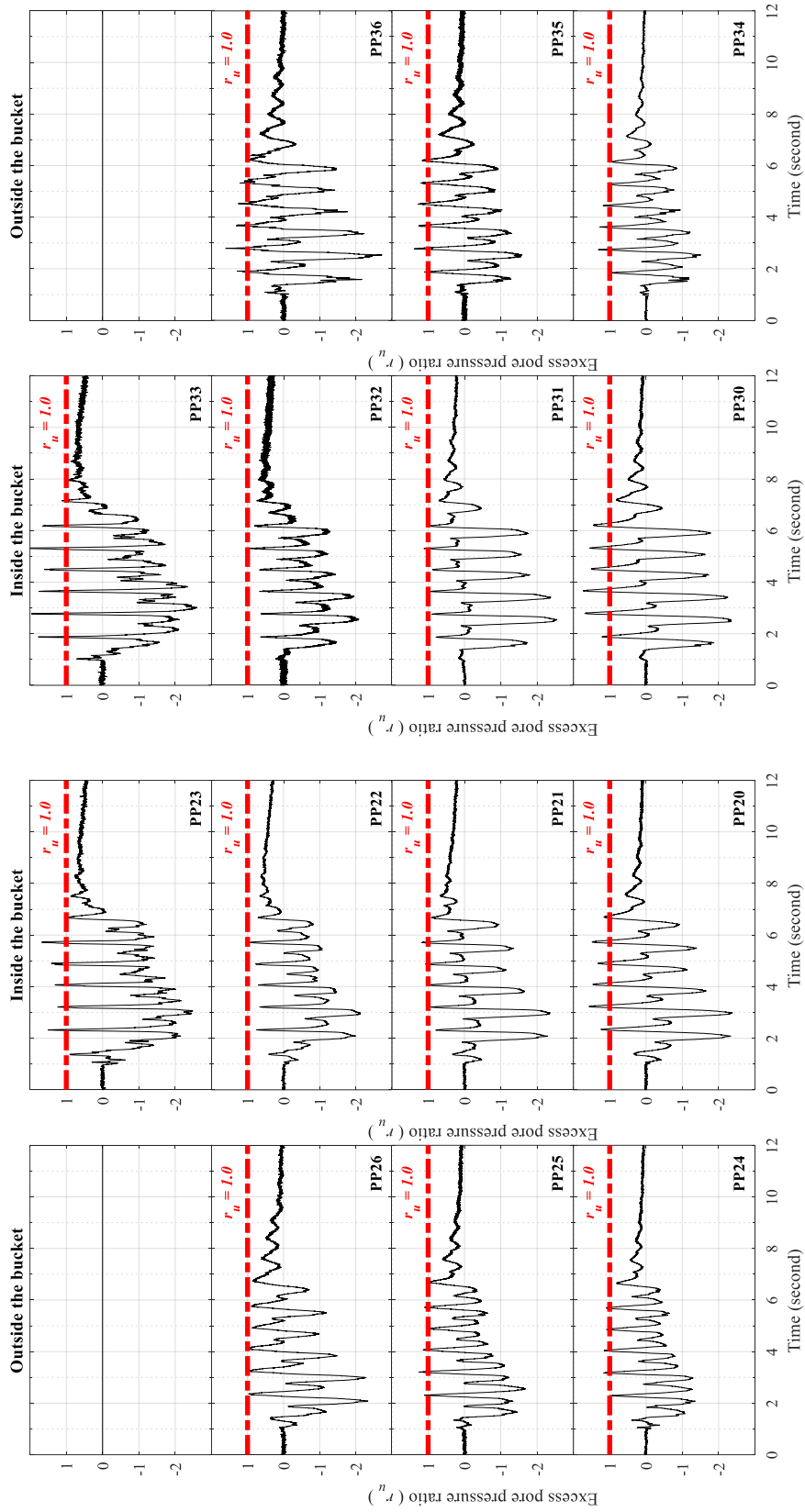
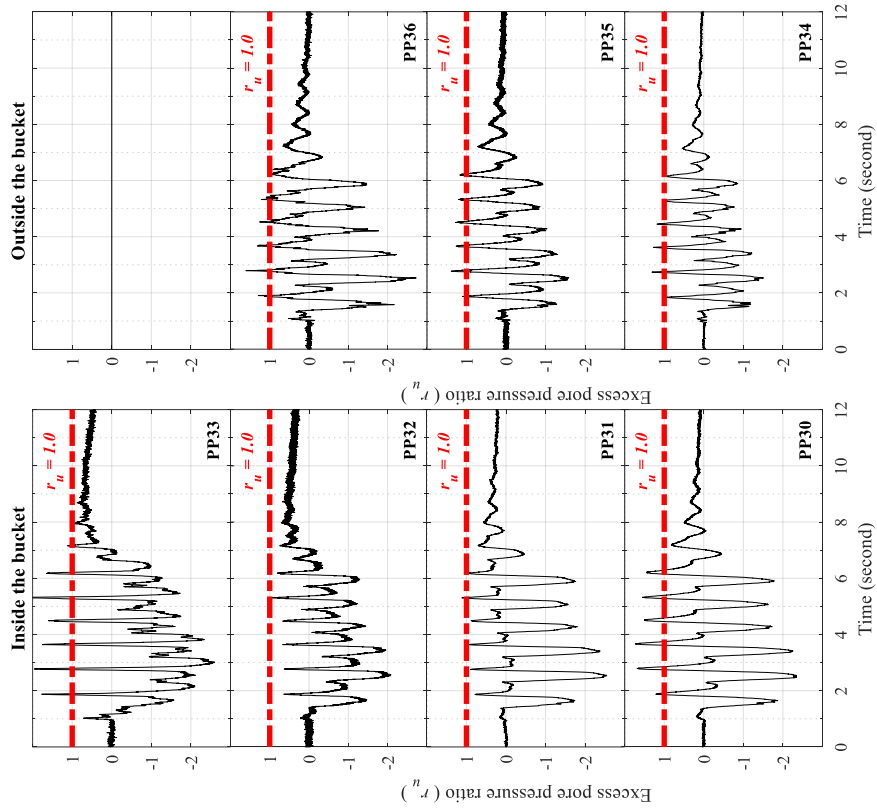


Figure 4-13: Vertical bucket displacement vs. bucket rotation for Test H5



(a)



(b)

Figure 4-14: Time histories of EPP at bucket foundation a) north and b) south edges for test H5

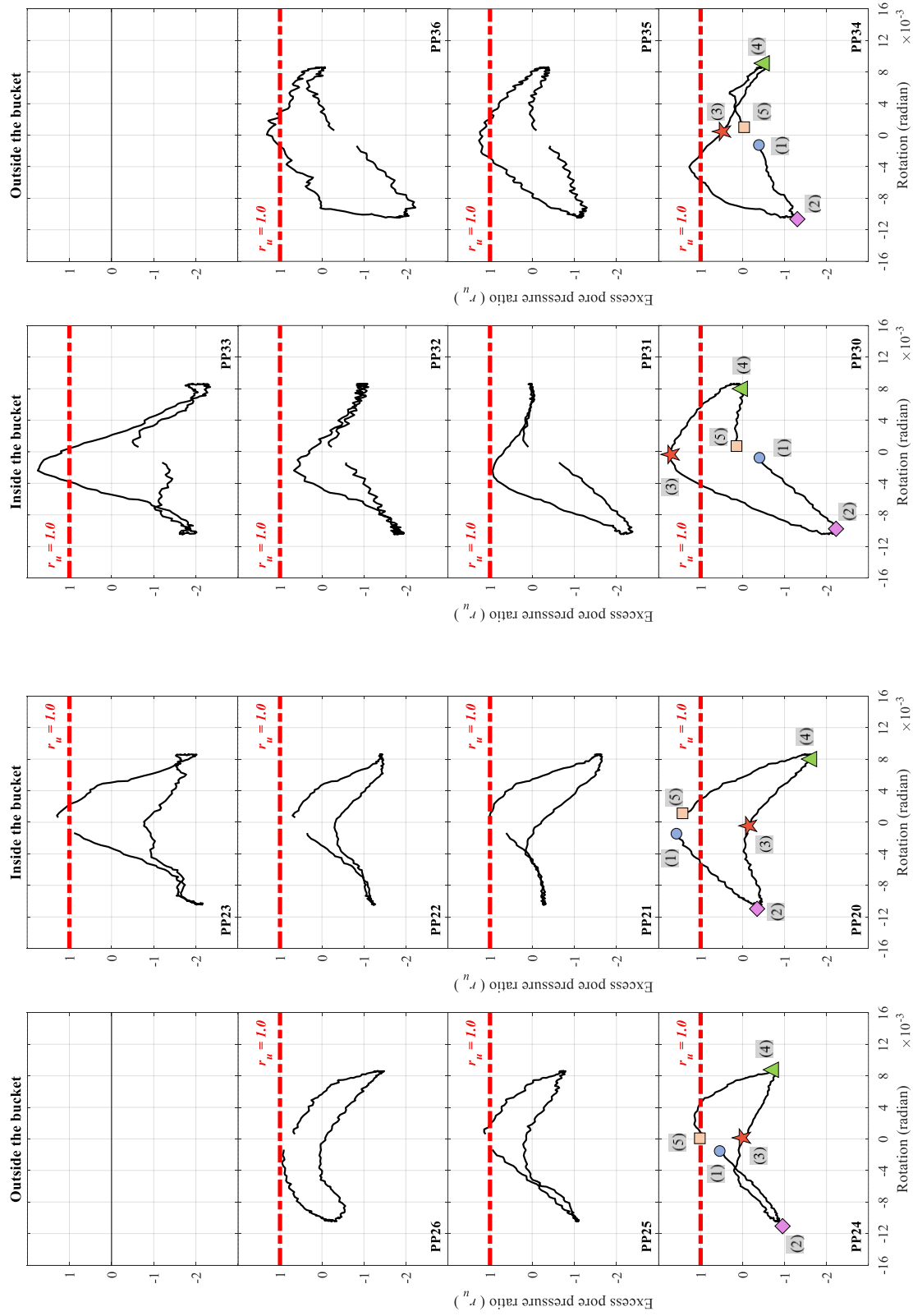


Figure 4-15: EPP ratio around bucket foundation vs. bucket rotation for test H5 between 3.25 and 4 seconds

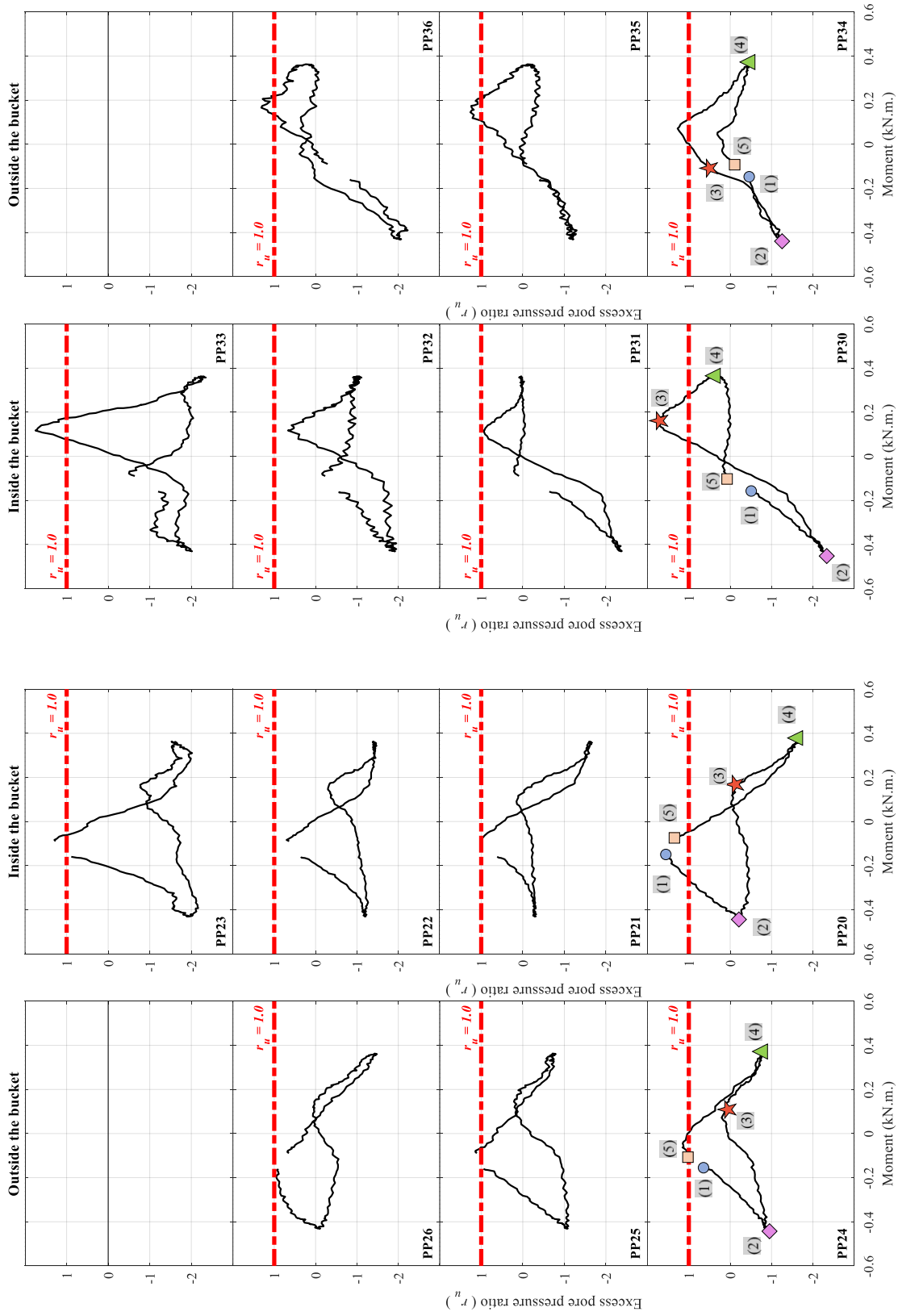


Figure 4-16: EPP ratio around bucket foundation vs. top bucket moment for test H5 between 3.25 and 4 seconds

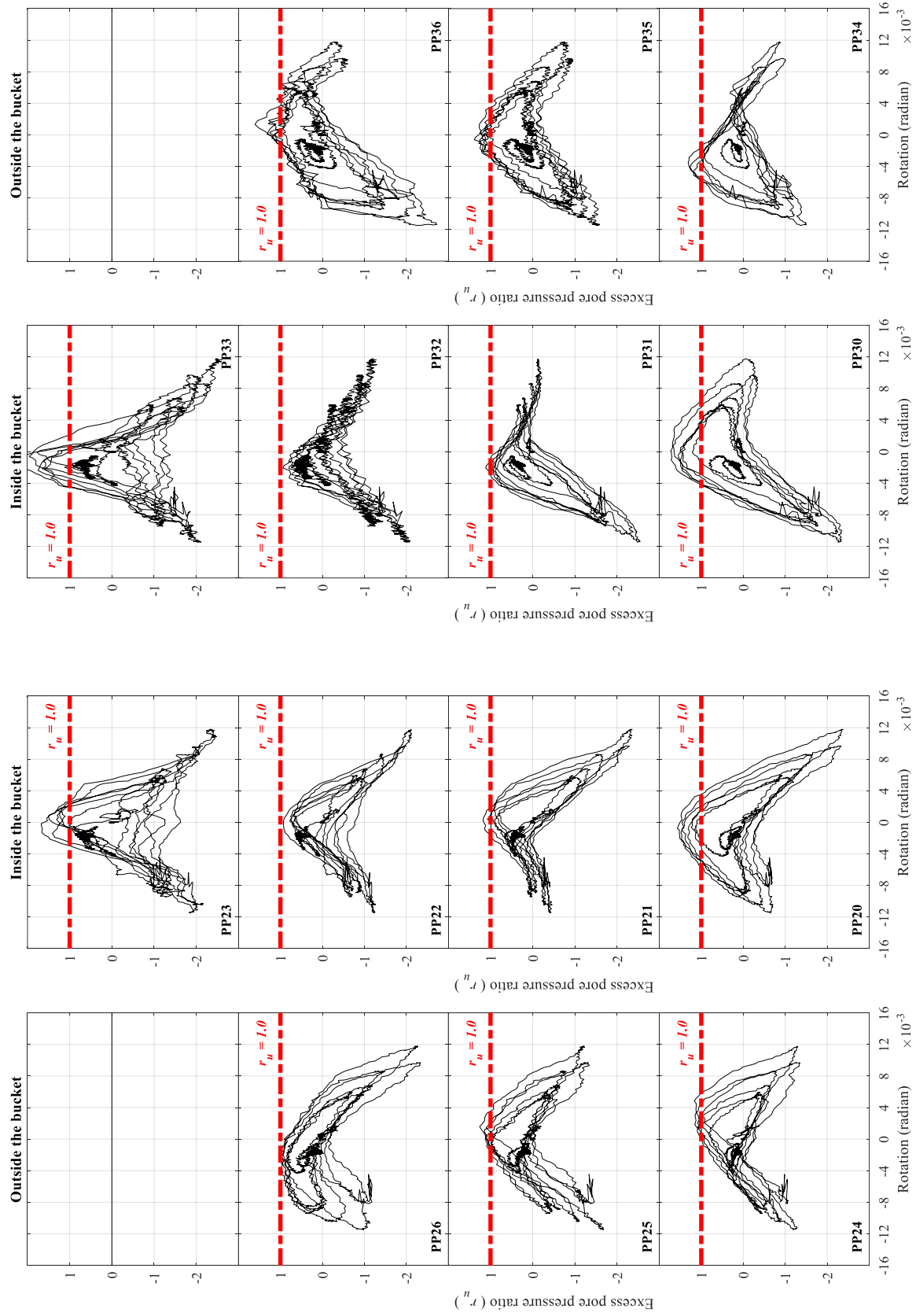


Figure 4-17: EPP ratio around bucket foundation vs. bucket rotation for the entire shaking duration of test H5

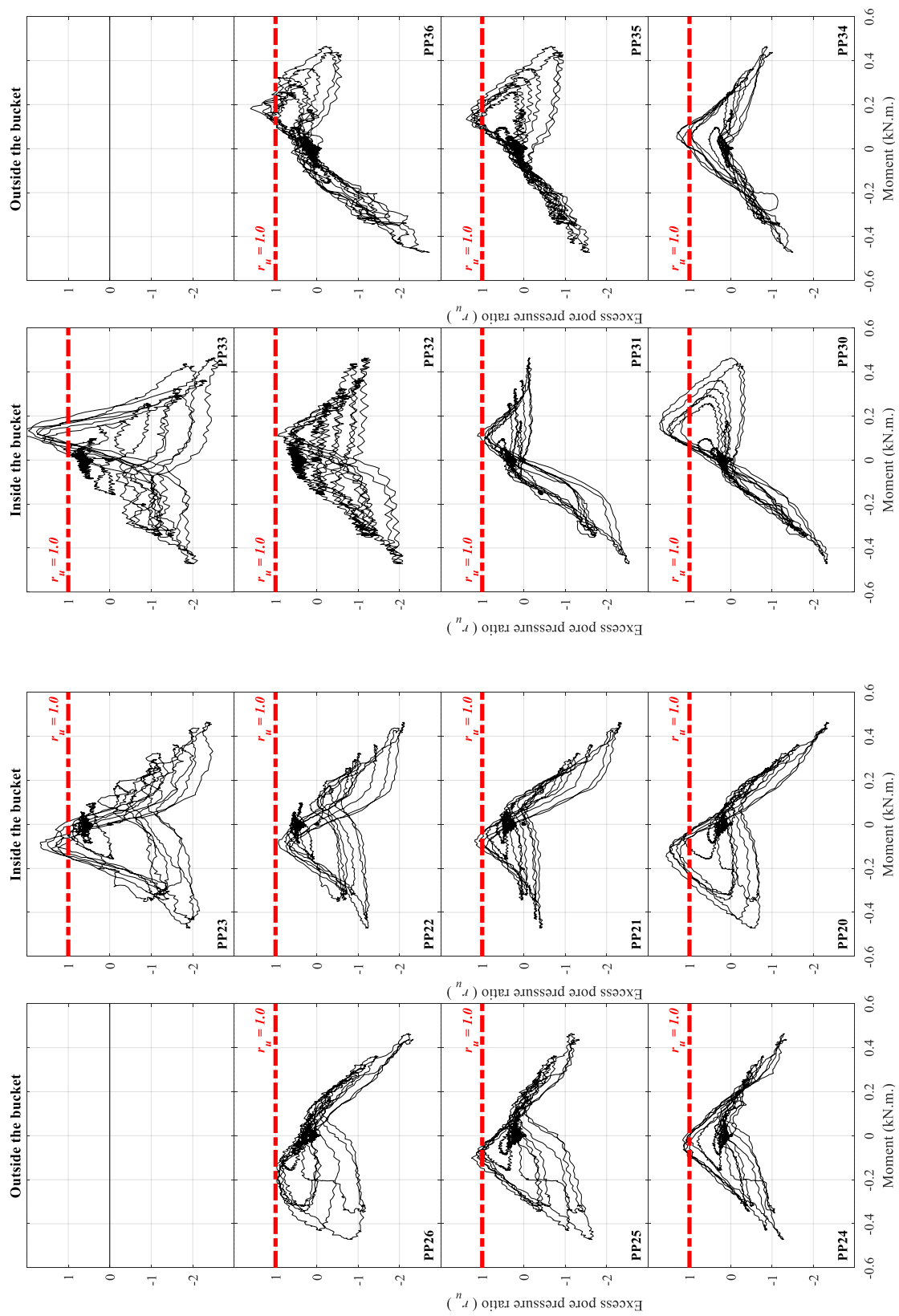


Figure 4-18: EPP ratio around bucket foundation vs. top bucket moment for the entire shaking duration of test H5

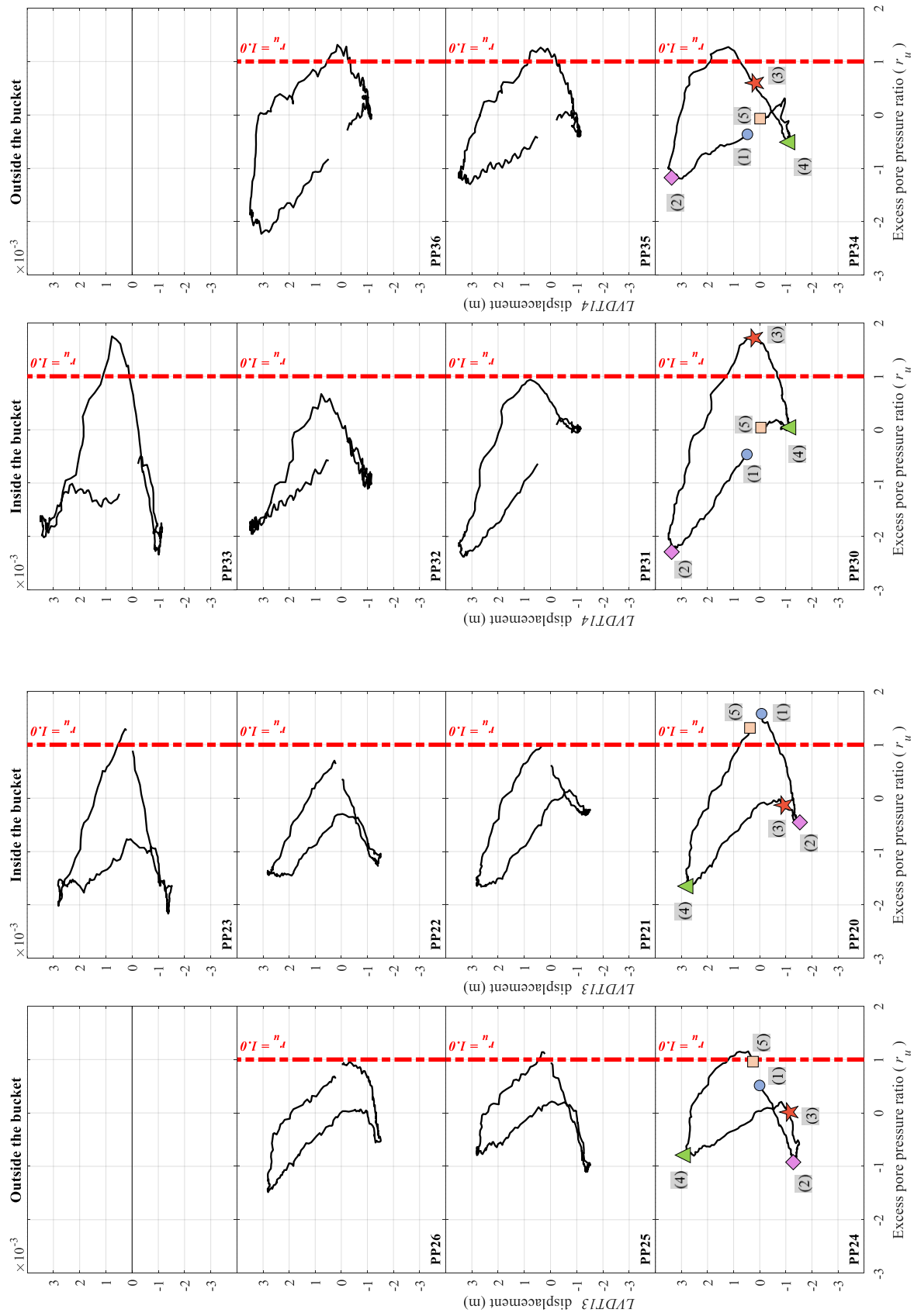


Figure 4-19: EPP ratio around bucket foundation vs. vertical bucket displacement at each edge, test H5 between 3.25 and 4 sec



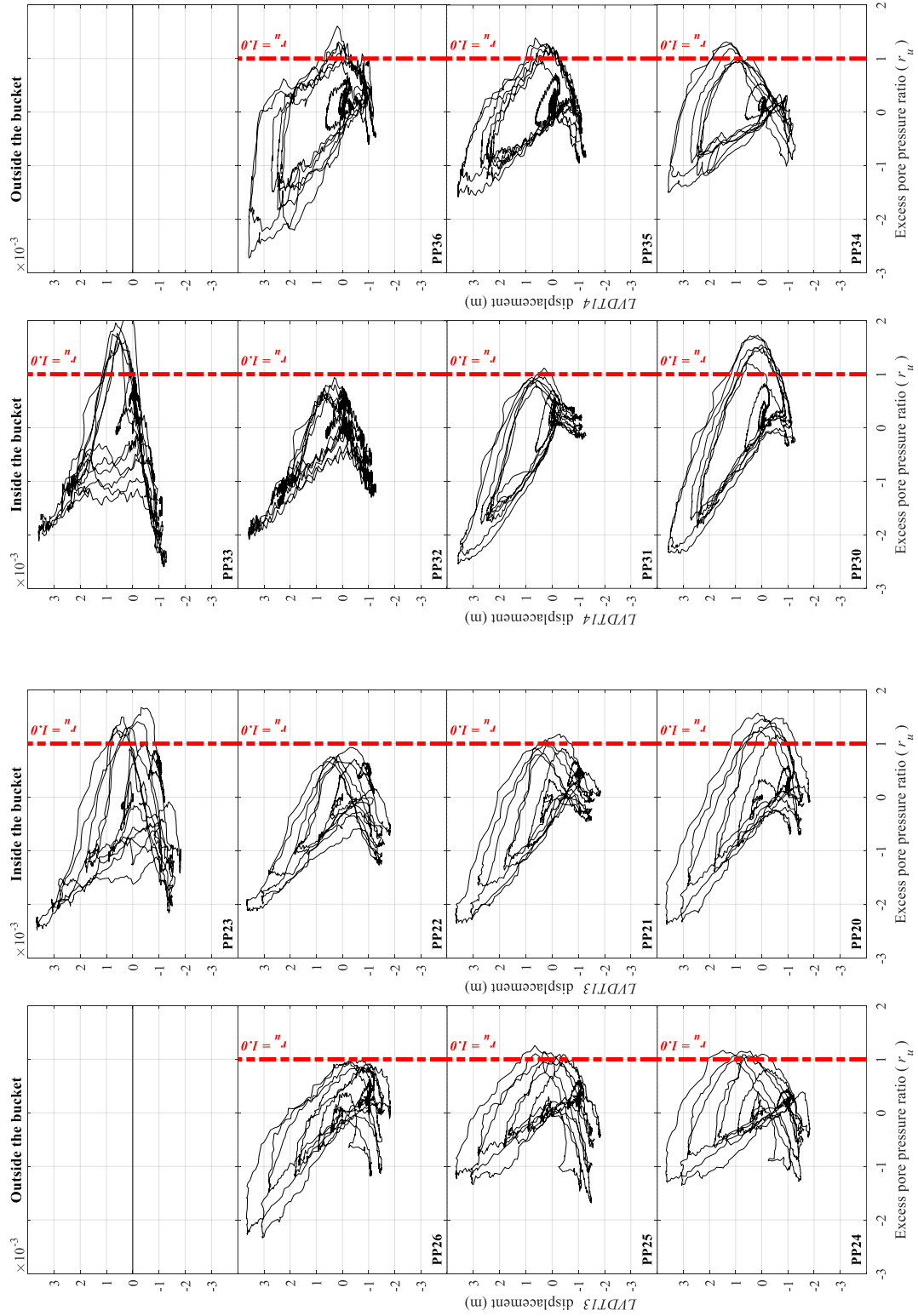
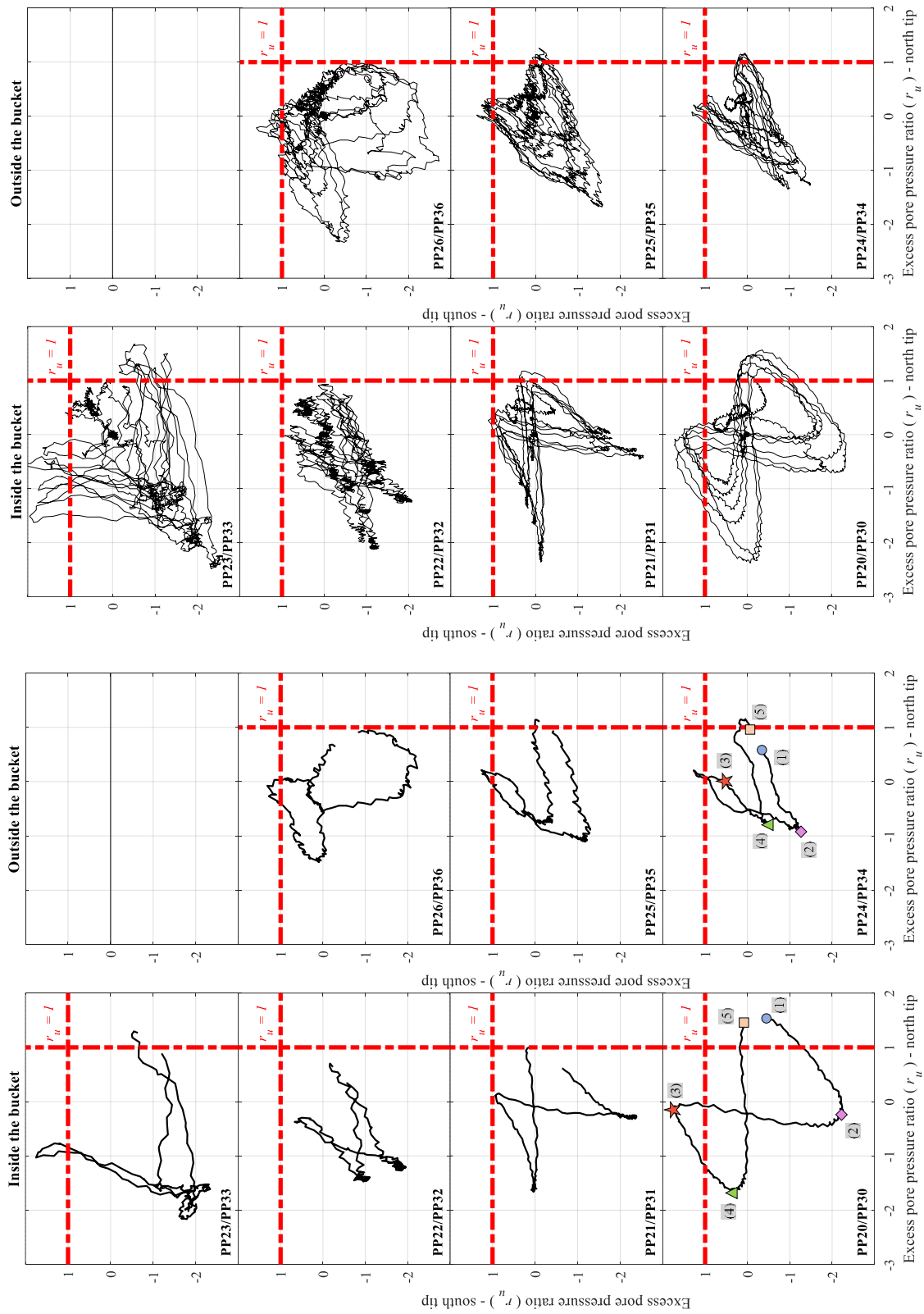


Figure 4-20: EPP ratio around bucket foundation vs. vertical bucket displacement at each edge, for the entire shaking duration of test H5



(a)

(b)

Figure 4-21: EPP ratio around bucket at south edge vs. at north edge for H5 a) between 3.25 and 4 seconds, b) entire shaking

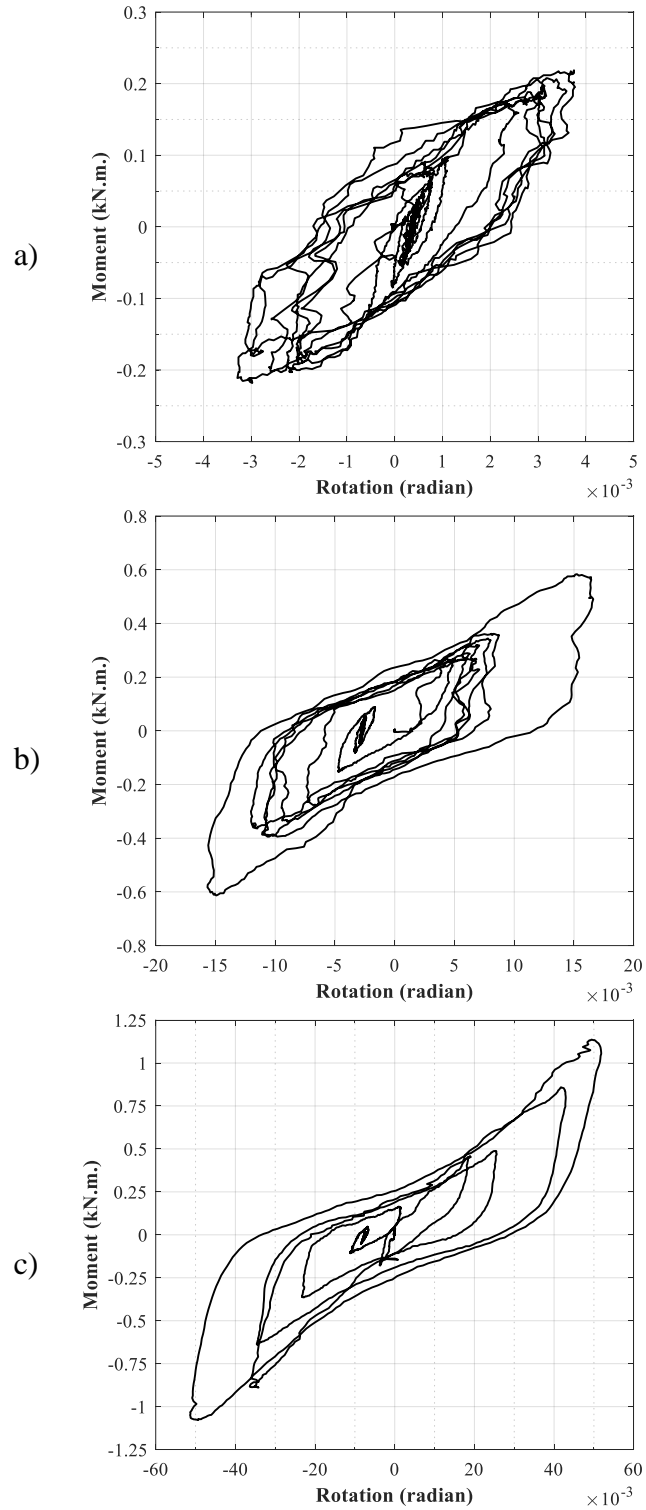


Figure 4-22: Plot of bucket moment vs. bucket rotation for a) test H2, b) test H8 and c) test H10

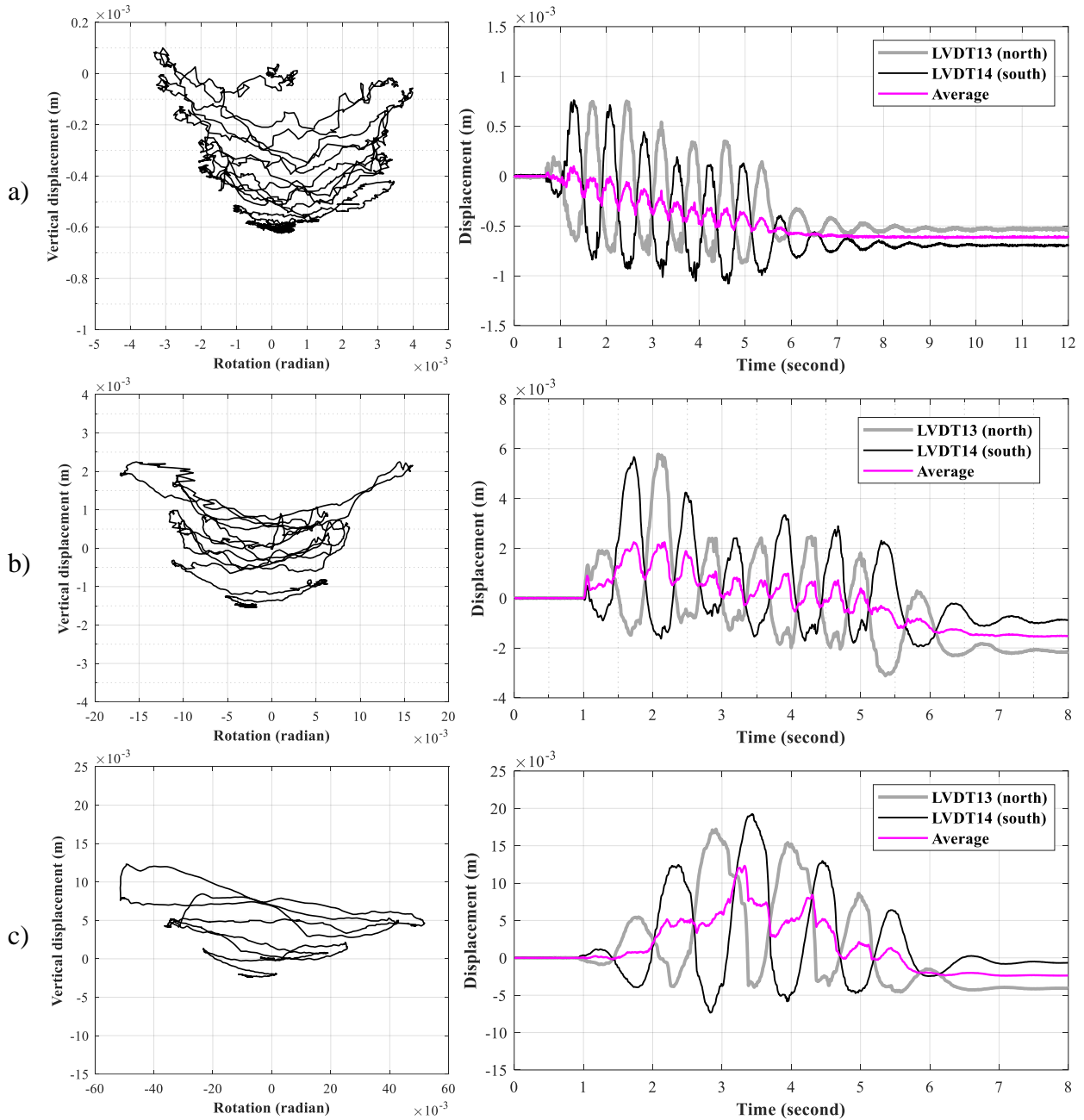


Figure 4-23: Average of vertical bucket displacement vs. bucket rotation (left column) and vertical bucket displacement time histories (right column) for a) test H2, b) test H8 and c) test H10

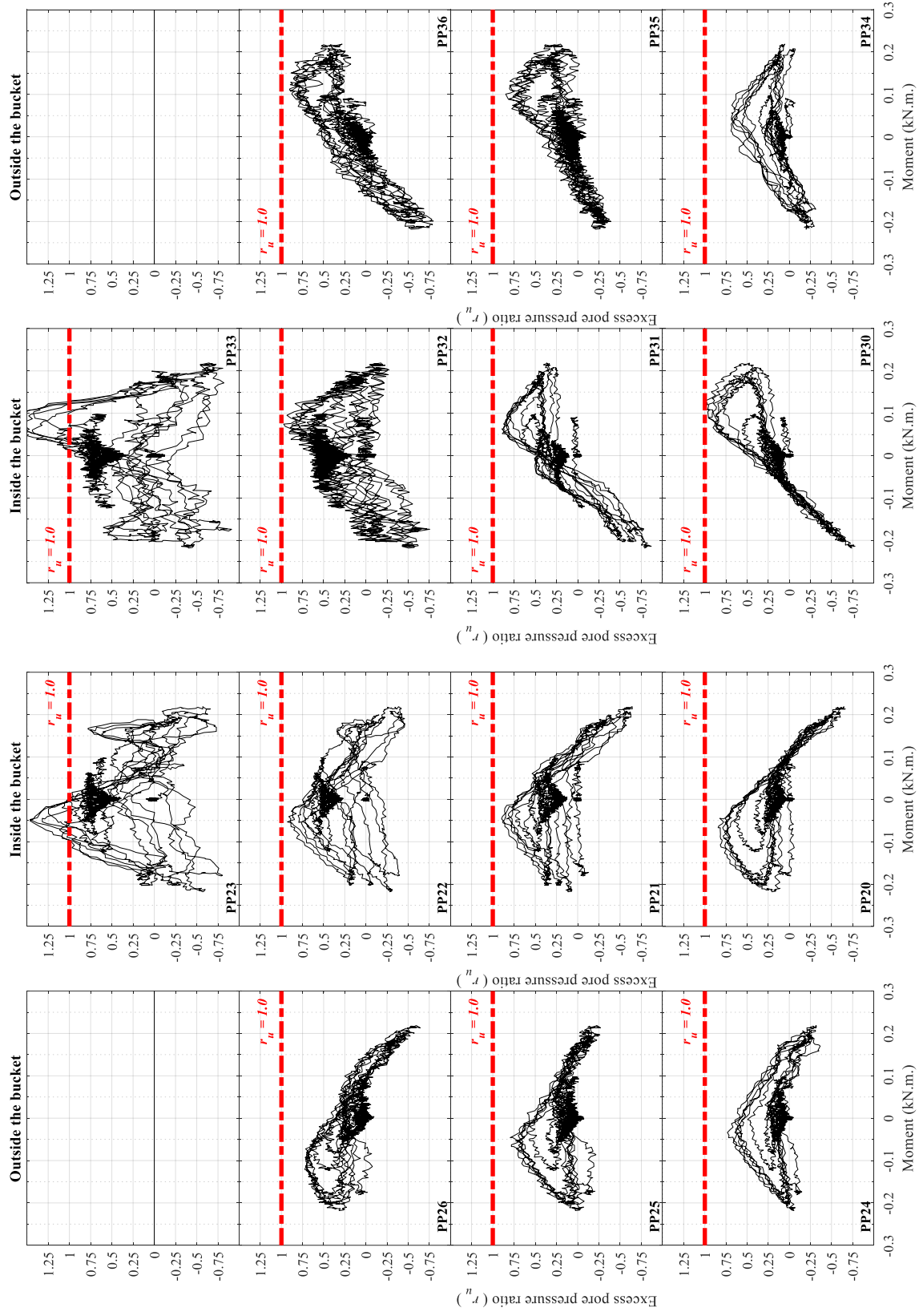


Figure 4-24: EPP ratio around bucket foundation vs. top bucket moment for the entire shaking duration of test H2

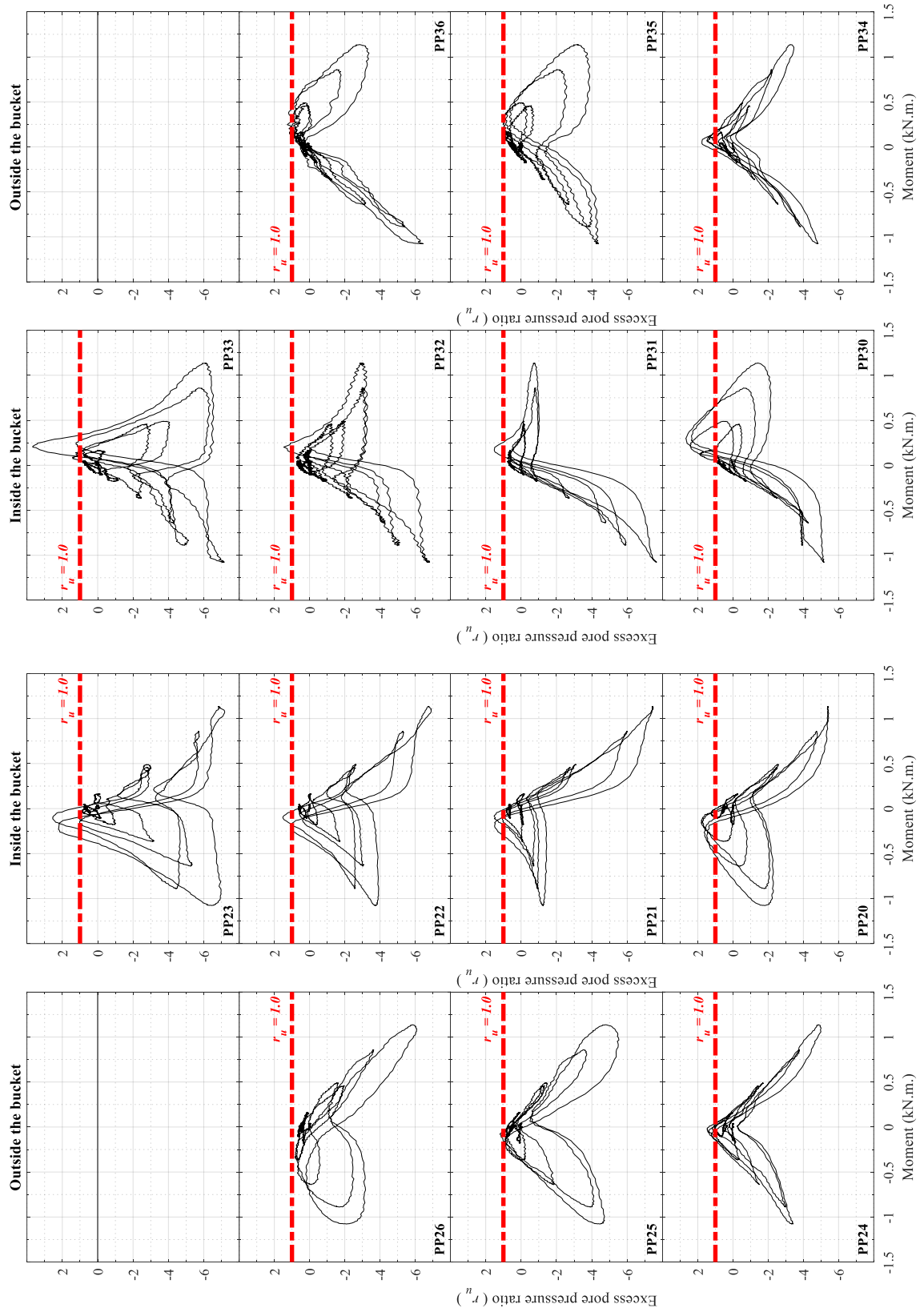
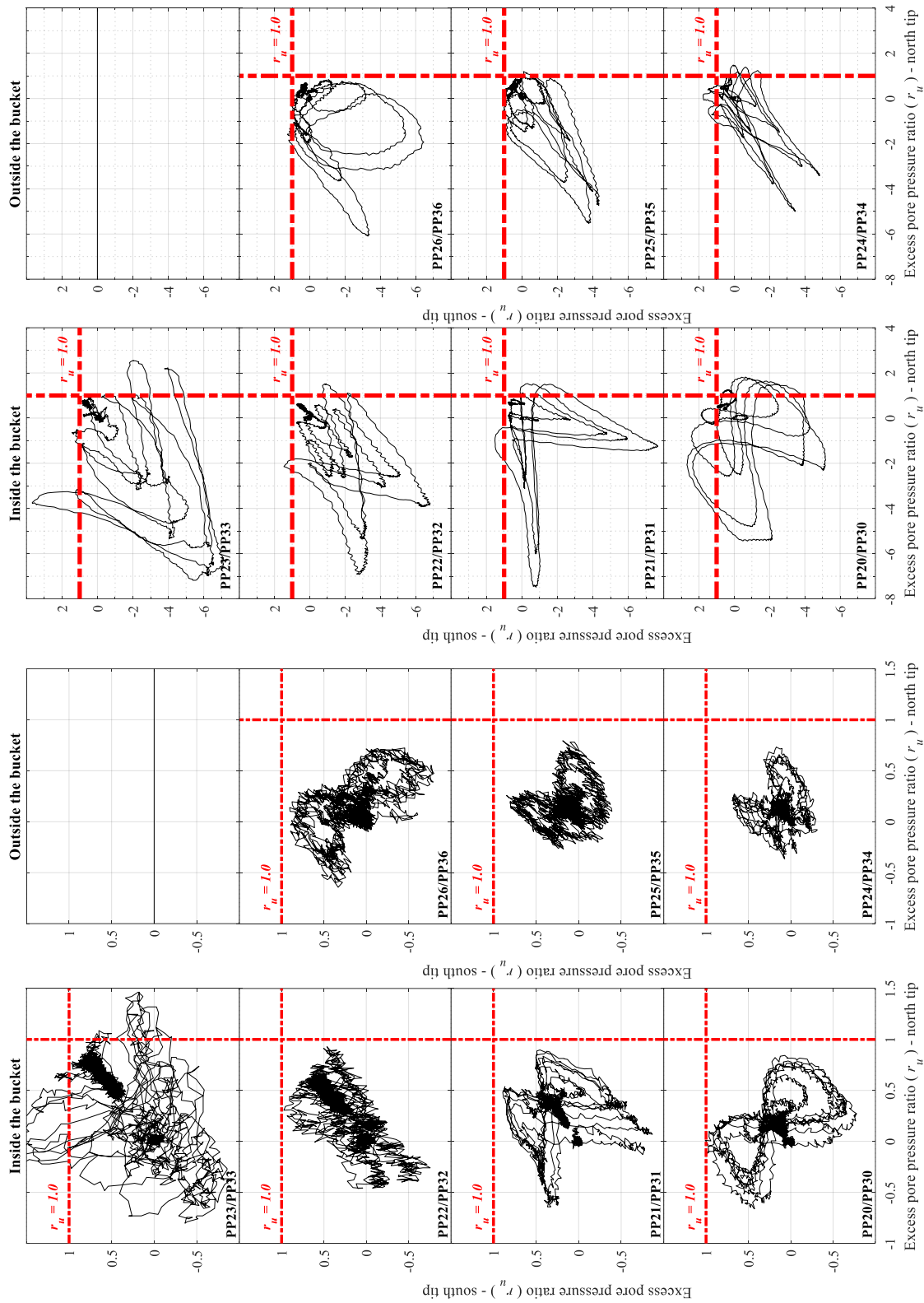


Figure 4-25: EPP ratio around bucket foundation vs. top bucket moment for the entire shaking duration of test H10



(a)

(b)

Figure 4-26: EPP ratio around bucket at south edge vs. at north edge for a) test H2, and b) test H10

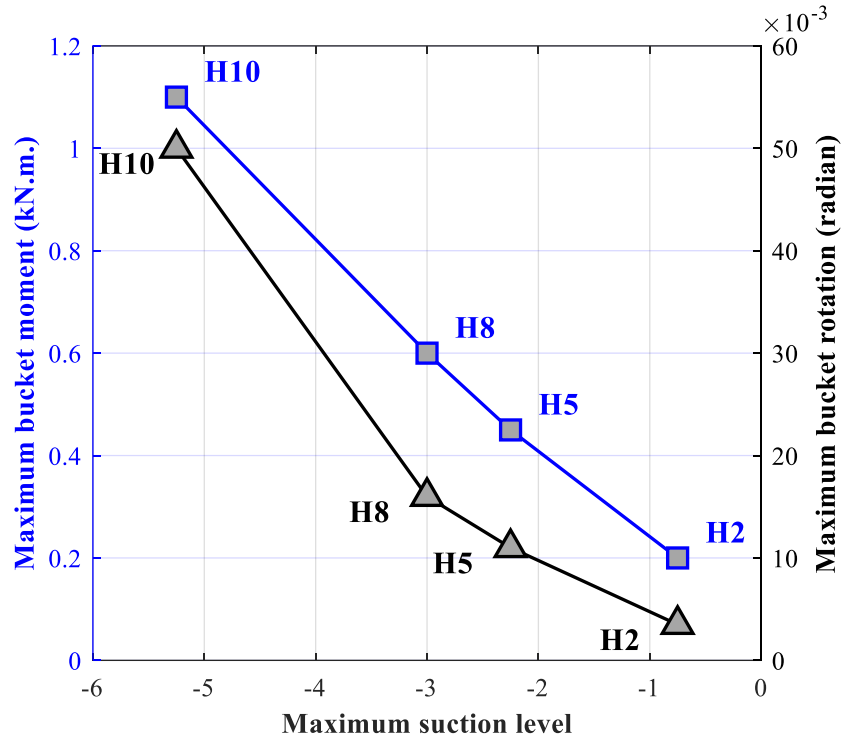


Figure 4-27: Variation of maximum suction level with maximum bucket moment and maximum bucket rotation for different tests



# Chapter 5

## Calibration of finite element model of bucket foundation wind turbine

*All models are wrong, but some are useful.*

– George Box

### 5.1 Numerical modelling

Utilizing the data collected from shake table testing, a three-dimensional (3D) finite element (FE) continuum model was developed and calibrated to simulate the dynamic response of the tested soil-bucket-structure system. The developed FE framework is further used to investigate the seismic response of a utility-scale Offshore Wind Turbine (OWT) idealized model and the consequences of strong shaking on the salient characteristics of the resulting structural response.

#### 5.1.1 Computational framework

The Open System for Earthquake Engineering Simulation (OpenSEES) framework (<http://opensees.berkeley.edu>) (McKenna *et al.* 2010) was employed to conduct the nonlinear soil-bucket-structure system analyses subjected to seismic excitation. OpenSEES is developed by the Pacific Earthquake Engineering Research (PEER) Center and is widely used for simulation of geotechnical systems and soil-foundation-structure interaction applications (Yang and Elgamal

2002, Su *et al.* 2017, Qiu *et al.* 2020). The OpenSEES elements and materials used in this FE model are briefly described below.

3D solid-fluid brick elements following the  $u-p$  formulation (Chan 1988) were employed for simulating the saturated soil and bucket foundation response, where  $u$  is displacement of the soil skeleton and  $p$  is pore-water pressure. Implementation of this  $u-p$  element is based on the following assumptions: a) small deformation and rotation, b) solid and fluid density remain constant in time and space, c) porosity is locally homogenous and constant with time, d) soil grains are incompressible and e) soil and fluid phases are accelerated equally. Hence, soil layers represented by these fully coupled elements account for deformations and changes in pore-water pressure during seismic excitation. The constitutive models (Parra-Colmenares 1996, Yang and Elgamal 2002, Elgamal *et al.* 2003) employed in this study were developed based on the multi-yield surface plasticity theory. In these models, the shear stress-strain backbone curve is represented by the hyperbolic relationship. As such, soil and bucket foundation are simulated by the implemented OpenSEES materials (Yang 2000) PressureDependMultiYield02 (PDMY02) and PressureIndependMultiYield (PIMY), respectively. Both models have been calibrated in earlier studies (Khosravifar *et al.* 2018) to capture the established guidelines on soil dynamic response and liquefaction triggering (Idriss and Boulanger 2008).

The FE matrix equation of the bucket-soil-structure system is integrated in the time domain using a Trapezoidal Rule with the second-order Backward Difference Formula (TRBDF2) integrator scheme (Bathe 2007). This integrator attempts to conserve energy and momentum in the model. The equation is solved using the modified Newton-Raphson approach with Krylov subspace acceleration. A relatively low level of viscous Rayleigh damping was employed to supplement energy dissipation from the non-linear hysteresis response and to enhance numerical

stability (Su *et al.* 2017). For that purpose, the mass and stiffness proportional terms were defined to provide viscous damping ratio of about 2% at the first structure fundamental frequency (i.e., 1.56 Hz). The latter damping is in good agreement with the measured values at the fundamental frequency of 1.67 Hz for a spinning 65 kW wind turbine reported by Prowell *et al.* (2014). Other researchers have reported a similar value of damping ratio for the first mode of vibration of an OWT (Devriendt *et al.* 2014, Arany *et al.* 2016).

The analysis is conducted in a staged fashion as follows:

1. Gravity was applied to activate the initial static state for the soil domain only with a) linear elastic properties (Poisson's ratio of 0.499), b) nodes on both longitudinal boundaries of the model were fixed against transverse translation, c) nodes were fixed along the base against vertical translation, and d) water table was specified at the topsoil surface. At the end of this stage, the soil static stress state is imposed.
2. Soil and bucket properties were updated from elastic to plastic according to Table 5-1 and Table 5-2.
3. The elastic beam-column elements of the shaft and tower were added. Thereafter, and prior to shaking stage, self-weight of the structure and any additional loads are applied.

Update permeability of soil and bucket brick elements as per Table 5-1 and Table 5-2 and apply shaking acceleration at the model base.

### **5.1.2 Soil-Bucket interface**

The 3D brick elements representing the soil are connected to the bucket elements at the outer and inner surfaces using zeroLength elements and equalDOF translation constraints. The zeroLength elements are employed to connect the soil node and the bucket node in the 3 directions.

Figure 5-1-a and Figure 5-1-b show schematics of the zeroLength elements and equalDOF configuration used with the two 8-node brick  $u-p$  elements representing soil and bucket. The interface connectivity was employed at the inner and outer surfaces of the bucket, the bucket tip surface as well as the bottom surface of the bucket lid, as illustrated in Figure 5-1-c. Stiffness of the zeroLength elements employed in the axial direction is represented by the OpenSEES elastic no-tension material (Figure 5-2), while the two tangential directions utilized elastic perfectly plastic material (Figure 5-3) to provide yield shear force in each element according to the bucket-soil interface friction angle and adhesion. As such, the yield shear force is limited by  $F = (c_A + \sigma' \tan \delta) \cdot A_{\text{int}}$ , where  $A_{\text{int}}$  is the surface area of each node on the interface surface,  $c_A$  is the soil-bucket adhesion,  $\delta$  is the soil-bucket friction angle, and  $\sigma'$  is the lateral effective stress at the interface node.

### 5.1.3 Model configuration and calibration

A 3D FE mesh is developed to represent the model wind turbine bucket foundation and soil configuration tested on the shake table. Due to symmetry, a half mesh is modeled as shown in Figure 5-4. The bucket foundation shaft and wind turbine tower are modeled using linear elastic beam-column elements. The shaft is rigidly connected to the bucket lid and the diagonal base stiffeners at the bucket lid are modeled using elastic-beam elements. Soil and bucket are both modeled using 8-node  $u-p$  brick elements with the OpenSEES PressureDependMultiYield02 material assigned to soil elements while PIMY used for bucket elements to represent steel material (mainly linear response). Based on the above, the FE mesh for the bucket-soil system was generated comprising 7,780 nodes, 6,730 brick elements, 83 beam-column elements, 783

zeroLength elements and 552 equalDOF constraints. Both zeroLength elements and equalDOF constraints are employed to model the soil-bucket interface (Figure 5-1-c).

Soil is modeled as a saturated medium-dense sand layer. The water table was prescribed at the topsoil surface. Results of the far-field instrumentation arrays were employed to calibrate a 3D shear beam model of saturated sand utilizing the OpenSEES PDMY02 constitutive material. The values for soil permeability reported by El Ghoraiby *et al.* (2020) for Ottawa F-65 sand were used. Far-field instrumentation records from various shaking events were utilized to calibrate the remaining parameters of the PDMY02 soil model. Calibration of contraction and dilation parameters was performed through an iterative process with consideration and priorities to capture the experimentally interpreted shear stress-strain response. The calibrated PDMY02 parameters are listed in Table 5-1. In order to simulate one-dimensional wave propagation in 3D space, elements on the model exterior boundary at the same elevation were assumed to have the same displacement using the equalDOF constraints. The acceleration time histories recorded at the base of the shake table laminar container were applied to the base nodes in the numerical simulations.

## **5.2 Experimental and numerical results**

The response of the shear beam model as well as the soil-bucket-structure system was numerically simulated in OpenSEES version 2.5.0 and analyzed in terms of excess pore pressures, lateral displacements and accelerations of soil, in addition to lateral displacements, accelerations and bending moments of the tower as well as rotation of the bucket foundation. The numerical results are then compared with the 1-g shake table experimental measurements during different shaking events. This section illustrates representative results and comparisons of response

characteristics for harmonic shaking events H5, H10 as well as earthquake motions N3 and T3 (Table 3-4).

### **5.2.1 Soil response in the far-field**

Nonlinear site response in the far-field (without the influence of the structure) was simulated numerically first using a single soil column subjected to base accelerations recorded in the shake table test. The results were compared to the far-field instrumentation arrays measurements (e.g., embedded in the soil model halfway between the structure and the laminar container boundary), where structure and boundary effects were assumed to be minimal. In addition, the system identification technique proposed by (Elgamal *et al.* 1996a, Elgamal *et al.* 1996b) is used to illustrate the corresponding experimental shear stress-strain response within the saturated medium-dense sand stratum. For that purpose, displacement sensor records were used to obtain both the shear stress and the shear strain time histories. Absolute acceleration was computed by double differentiation of the corresponding absolute displacement time history. Thereafter, first-order linear interpolation between displacements was adopted to evaluate shear strains. The interpolation scheme yields second-order accurate shear stress and strain estimates (Zeghal *et al.* 1995) and has been implemented in 1-g shake table testing studies by Zayed *et al.* (2021).

#### **5.2.1.1 Harmonic Excitation: H5 and H10 shaking events**

Figure 5-5-a shows acceleration time history of the input excitation for test H5. Moreover, a comparison between the numerically computed and the experimentally measured excess pore water pressure (Figure 5-5-b), lateral displacement (Figure 5-5-c) and acceleration (Figure 5-5-d) time histories is presented at different depths within the saturated sand stratum. It can be noted that

the nonlinear simulations are able to reasonably capture the far-field response trends for excess pore pressure, lateral soil displacement (Figure 5-5-c), and acceleration (Figure 5-5-d).

Similarly, the numerical model is able to reasonably capture the experimental response in Test H10 as presented in Figure 5-6. However, Figure 5-6-b shows that the strong dilative tendency in the excess pore pressure experimental response (i.e., negative spikes) is not well-captured by the numerical model. The latter can be explained by the relatively strong shaking amplitude level of H10 shaking (i.e., about 0.3g), and the relative density change due to densification from prior shaking. The PDMY02 constitutive material does not update the soil properties due to shaking-induced densification. As such, capturing the dilation spikes and drops in excess pore pressure becomes challenging after the initial one or two cycles that might have caused substantial densification. In addition, the densification and the associated change of soil properties that occur from one shaking to the next can also affect soil and system response. This can be considered as one of few possible explanations for the observed difference between numerical and experimental results. Similar observations were reported for dense sand strata by Karimi and Dashti (2016). These effects might play more significant and substantial role in case of loose sand model. However, densification of the modeled medium dense sand stratum that occurs within the same shaking or from one test to the next is not considered as significant. For the purpose of this study, a single set of material parameters are used to model the medium dense sand stratum in all shaking tests.

Figure 5-7-a and Figure 5-8-a display the numerical and experimental time histories of shear stress and strain at depths of about 0.6 m, 0.9 m and 1.2 m along the saturated sand stratum, for tests H5 and H10, respectively. Minimal accumulation of shear strain can be noted at the end of shaking. Figure 5-7-b and Figure 5-8-b present comparison between the numerical and

experimental shear stress-strain hysteresis response at depth of about 1.2 m. These comparisons indicate that numerical simulations adequately capture the overall experimental soil shear stress-strain response in the far-field.

### **5.2.1.2 Earthquake records: N3 and T3 events**

Shaking events N3 and T3 represent the 1994 Northridge earthquake (14145 Mulholland Dr record, Component N09E) and the 1995 Kobe earthquake (Takatori record, Component 90), respectively, both with amplitude scaling of 75%. Figure 5-9-a and Figure 5-10-a show the measured shake table acceleration time histories for N3 and T3, respectively, that are used as the input excitation at the numerical model base. The same model utilized for test H10 was employed in the numerical simulations of tests N3 and T3. Plots of Figure 5-9 present a comparison between the numerical and experimental excess pore water pressure (Figure 5-9-b), lateral displacement (Figure 5-9-c) and acceleration (Figure 5-9-d) time histories at different depths within the saturated sand stratum during test N3. Similarly, Figure 5-10 shows the corresponding comparison for test T3.

Time history of model base acceleration (i.e., A12) for event N3 (Figure 5-9-d) can be noted to have a wider frequency content than A12 of event T3 (Figure 5-10-d). The latter figures might also indicate that the measured acceleration records are reasonably well-replicated by the nonlinear numerical simulations. However, the numerical surface acceleration A14 is noted to have larger amplification than the experimental values between 3 Hz and 5 Hz, for both events N3 and T3. Although the experimental trends are well captured in both events, it is observed that the numerical simulations over-predicted the far-field soil excess pore pressures and lateral soil displacements in T3 (Figure 5-10-b and Figure 5-10-c) when compared with N3 (Figure 5-9-b and



Figure 5-9-c) in which trends of the far-field excess pore pressures and lateral displacements are more reasonably captured.

Comparisons between numerical and experimental time histories of shear stress and strain at various depths are presented in Figure 5-11-a and Figure 5-12-a for events N3 and T3, respectively. From Figure 5-12-a (event T3), it can be noticed that the numerical model over-predicted the residual shear strain while being captured more closely in Figure 5-11-a (event N3). Moreover, the stress-strain hysteresis presented in Figure 5-11-b (event N3) shows a somewhat stronger dilative response than the experimental observations. Despite the difference in the residual shear strain, the hysteresis presented in Figure 5-12-b (event T3) might indicate a better overall match between the numerical and experimental stress-strain.

Ramirez *et al.* (2018) reported that a key challenge in the calibration of PDMY02 parameters was to reproduce, with a single set of parameters, the experimental soil response at different shaking amplitudes and frequency contents. For the purpose of the current study, the comparisons presented in Figure 5-5 through Figure 5-12 indicate that the same PDMY02 soil model parameters (originally calibrated for event H10) illustrate that the model is reasonably able to reproduce the overall dynamic soil response using a single set of parameters for different shaking events with different amplitude and frequency content. However, more attention is paid in this study to the soil-foundation-structure interaction response as discussed in the following sections.

## **5.2.2 Response of bucket foundation and tower**

After calibrating the shear beam soil model, the calibrated parameters (Table 5-1) were employed in the soil-bucket FE mesh (Figure 5-4). The bucket foundation was modeled using the

PIMY material model. Physical and mechanical properties of aluminum are employed to define the PIMY material model parameters for modeling the bucket foundation as presented in Table 5-2. In addition, bucket shaft and tower were modeled as elastic beam-column elements to represent properties of hollow circular section (Table 3-3). Section properties of shaft and tower are defined based on outer diameter of 89 mm and 76 mm, respectively, and wall thickness of about 5.5 mm and 3 mm, respectively. Elastic and bulk moduli of 72 GPa and 27 GPa, respectively, are used to define the elastic beam-column material. The connection between the shaft and the tower is considered to be rigid (achieved in the laboratory by means of bolts) and thus modeled numerically as a single 6-DoF node shared between two different beam-column elements. The distributed mass of shaft and tower is modeled as lumped masses at the connecting nodes while the top mass was included at the topmost node. Table 3-3 summarizes properties of the tested model. Dynamic response of the tower in terms of lateral displacement and lateral acceleration as well as moment-rotation response of the bucket foundation for different shaking events are presented in the following subsections.

#### **5.2.2.1 Harmonic Excitation: H5 and H10 shaking events**

Lateral displacement and lateral acceleration of the tower during H5 shaking event are shown in Figure 5-13-a and Figure 5-13-b, respectively, while Figure 5-13-c depicts the corresponding frequency spectra of the tower acceleration. Figure 5-13-b shows that the numerical simulations overestimated the acceleration amplitude at the tower bottom while reasonably capturing the tower top acceleration as well as the tower lateral displacement (Figure 5-13-a). The difference between the numerical and experimental peak frequencies is found to be about 1% (Figure 5-13-c). As such, a good match can be noted between the experimental and numerical bucket moment (i.e., bending moment at the tower base) as shown in Figure 5-13-d. However, the

experimental data showed larger damping towards the end of shaking resulting in the numerical model slightly overestimating the moment (also can be noted in the tower top acceleration presented in Figure 5-13-b). On the other hand, the numerical model underestimated the residual bucket rotation as shown in Figure 5-13-d. An overall comparison between the numerical and experimental bucket moment-rotation hysteresis is presented in Figure 5-13-e. Similar comparisons for test H10 are presented in Figure 5-14. The deformed FE mesh with contours for vertical displacement showing the maximum bucket rotation (at about 3.4 seconds) is presented in Figure 5-15 where a gap can be noticed at the soil-bucket interface below the lid.

Figure 5-16 shows the measured excess pore pressure response around the bucket compared to the numerical response results. This figure indicates that the numerical model is able to reasonably replicate the general trends of dilation and contraction spikes of the measured excess pore pressure, particularly near the inner bucket tip (i.e., PP20 and PP30).

#### **5.2.2.2 Earthquake records: N3 and T3 events**

Figure 5-17 and Figure 5-18 present tower and bucket response time histories for shaking events N3 and T3, respectively. For tower acceleration, the numerical results for event N3 (Figure 5-17-b) indicate good agreement with the experimental data, particularly when comparing their frequency spectra as shown in Figure 5-17-c. On the other hand, Figure 5-17-a shows that the numerical model overestimated the residual lateral tower displacements towards the end of shaking, while the maximum lateral displacement at the tower top is reasonably captured. As such, the numerically calculated residual bucket rotation towards the end of shaking is noted to be larger than the experimentally observed value (Figure 5-17-d). Nevertheless, the bucket moment is reasonably reproduced by the numerical model. Figure 5-17-e shows the overall bucket moment-

rotation response of the numerical model compared with the experimental observations.

For event T3, good agreement can be noticed between the numerical and experimental results of lateral tower displacement (Figure 5-18-a) and acceleration (Figure 5-18-b). In addition, comparison between acceleration frequency spectra presented in Figure 5-18-c shows that the numerical model was able to reproduce the same frequency content as that measured experimentally. However, the model overestimated the peak amplitude frequencies. Figure 5-18-d compares the experimental and numerical bucket moment and rotation time histories, and Figure 5-18-e compares the overall moment-rotation response.

The comparison of Figure 5-17 to Figure 5-18 for events N3 and T3 might indicate that a better match between the numerical and experimental results was obtained for event T3 when compared to N3. This may be attributed to the fact that the two shaking events have different excitation amplitude and frequency content (Figure 5-9 and Figure 5-10) and the effect of prior shaking in soil densification, while single set of properties was utilized for both models, as discussed in earlier sections.

### **5.3 Summary and conclusions**

Motivated by the current expansion of offshore wind projects in seismically active zones, a shaking table experiment was conducted on a scaled wind turbine model to: i) identify and document seismic response of a supporting bucket foundation, and ii) calibrate a numerical model. The laboratory model was tested in a laminar soil container on a 1-g shake table. The experimental data was used to calibrate a 3D FE model. A comparison between the experimental response and the numerical results was presented. Pore pressure response inside and around the bucket as well as the foundation moment and rotation response were analyzed.

The numerical framework and the insights derived from this study are of general relevance to bucket foundation seismic response for offshore wind applications. The calibrated FE model was able to reasonably capture the main response characteristics of the tested soil and wind turbine bucket foundation in terms of excess pore pressure, lateral acceleration and displacement, as well as bucket moment and rotation.

In the following chapters, the calibrated model is further extended to investigate response of a bucket foundation 3.45 MW utility-scale OWT, and a parametric study is conducted to shed highlight on effects of soil stiffness, soil permeability, ground motion, bucket size, and damping on the overall seismic response.

## **5.4 Acknowledgement**

The research described in this chapter was partially funded by the National Science Foundation grant OISE-1445712 as well as the Trent R. Dames and William W. Moore graduate student fellowship from the American Society of Civil Engineers (ASCE). Testing was conducted at the Powell laboratories, University of California San Diego, with assistance provided by Dr. Christopher Latham, Mr. Andrew Sander, Mr. Mike Sanders, Mr. Abdullah Hamid and Mr. Darren Mckay. The authors also would like to graciously thank Dr. Jinchi Lu, Dr. Zhijian Qui and Dr. John Li for their useful insights.

The content of chapters 5 and 6 is currently being prepared to be published as a journal paper tentatively in the ASCE Journal of Geotechnical and Geoenvironmental Engineering or the Soil Dynamics and Earthquake Engineering Journal. The proposed title of this paper is “Computational modeling of bucket foundation seismic response for utility-scale offshore wind turbine using experimental data”. The dissertation author is the primary author of this paper with Dr. Kyungtae Kim, Mr. Athul Prabhakaran, and Professor Ahmed Elgamal as coauthors.

Table 5-1: Calibrated parameters for PDMY02 soil model

<b>Model parameter</b>	<b>Value</b>
Mass density, $\rho$ (kg/m <sup>3</sup> )	1,780
Reference shear modulus, $G_r$ (MPa)	7
Reference bulk modulus, $B_r$ (MPa)	14.5
Peak friction angle, $\varphi$ (degrees)	35
Phase transformation angle, $\varphi_{PT}$ (degrees)	23
Peak shear strain, $\gamma_{max}$ (%)	10
Reference mean effective confining pressure, $p'$ (kPa)	101
Pressure dependent coefficient, $n$	0.5
Contraction coefficient $c_1$	0.01
Contraction coefficient $c_2$	0.5
Contraction coefficient $c_3$	0
Dilation coefficient $d_1$	0.16
Dilation coefficient $d_2$	3
Dilation coefficient $d_3$	0
Number of yield surfaces, $NYS$	20
Shear strength at zero confinement, $c$ (kPa)	0.1
Permeability, $k$ (m/s)	1E-4

Table 5-2: PIMY model parameters employed for bucket foundation to represent aluminum material

<b>Model parameter</b>	<b>Value</b>
Mass density, $\rho$ (kg/m <sup>3</sup> )	2,700
Reference shear modulus, $G_r$ (GPa)	27
Reference bulk modulus, $B_r$ (GPa)	72
Cohesive strength, $c$ (GPa)	100
Peak friction angle, $\varphi$ (degrees)	60
Peak shear strain, $\gamma_{\max}$ (%)	10
Reference mean effective confining pressure, $p'$ (kPa)	101
Pressure dependent coefficient, $n$	0
Number of yield surfaces, $NYS$	20
Permeability, $k$ (m/s)	1E-20

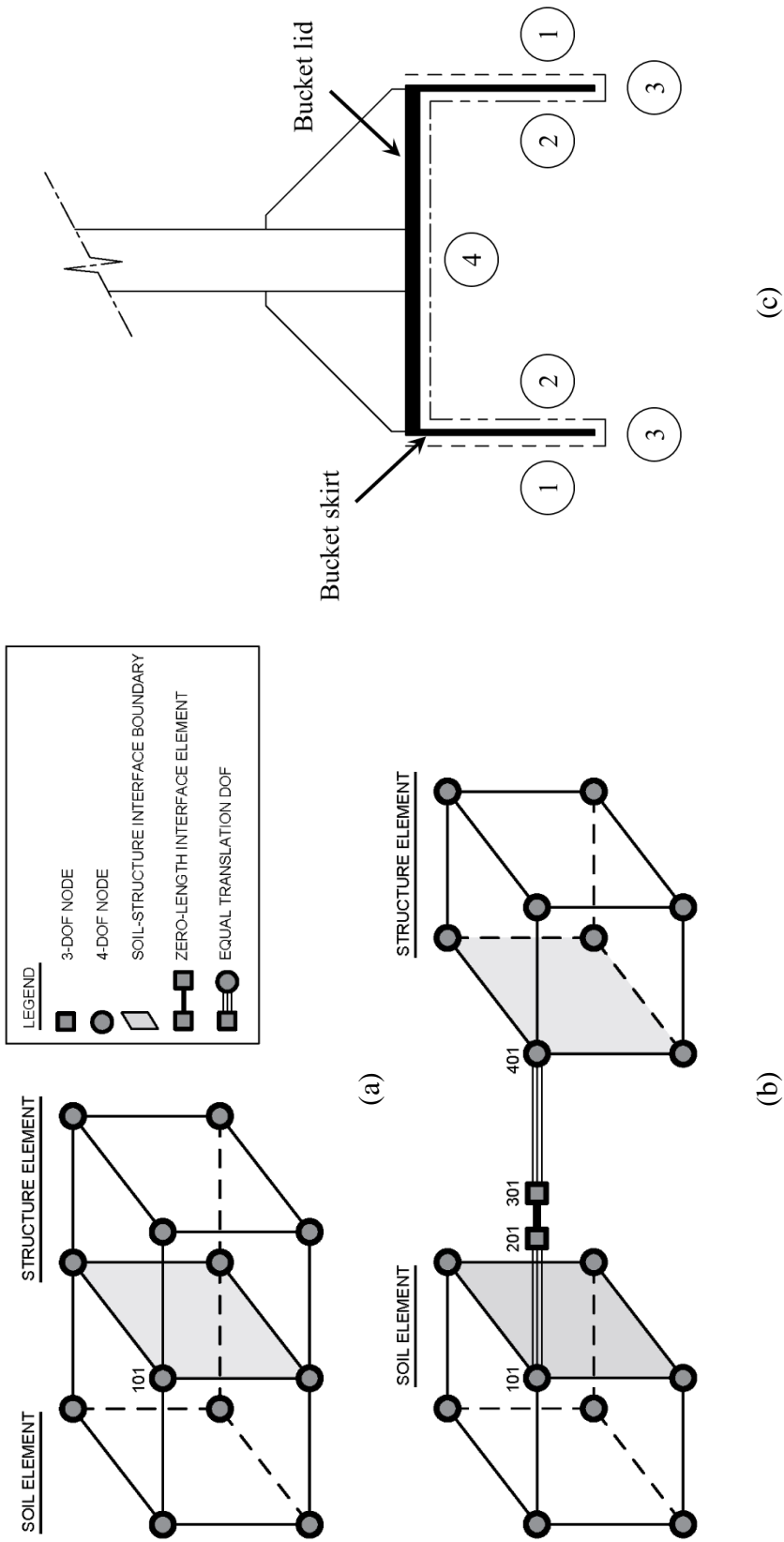


Figure 5-1: a) Soil-structure element connectivity, b) Schematic of 8-node u-p brick elements with zeroLength elements, and c) different soil-structure interface boundary surfaces defined for bucket foundation, where 1) outer skirt surface, 2) inner skirt surface, 3) bucket tip surface, and 4) bucket lid bottom surface



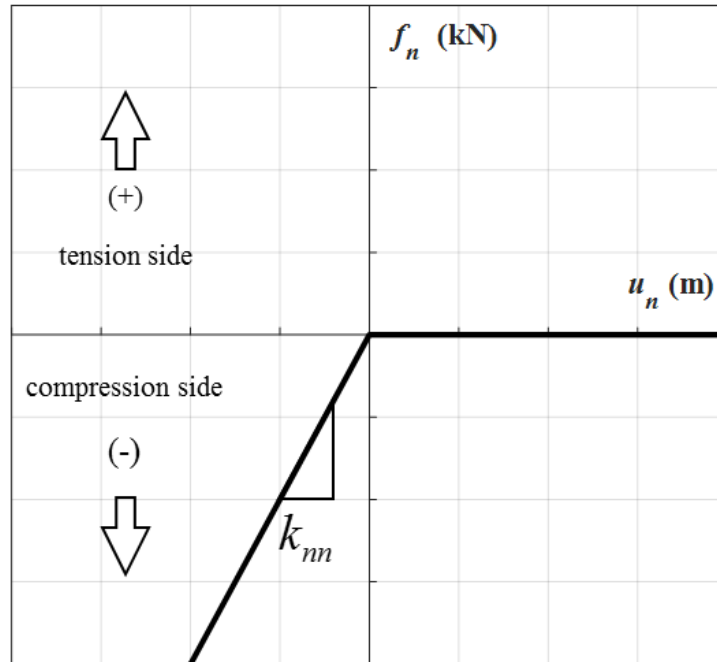


Figure 5-2: Elastic no-tension model adopted for interface normal stiffness

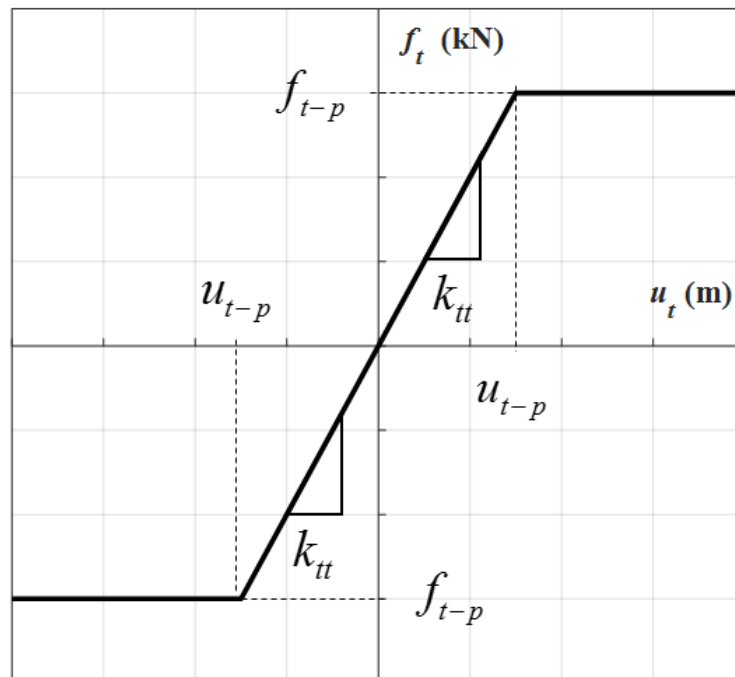
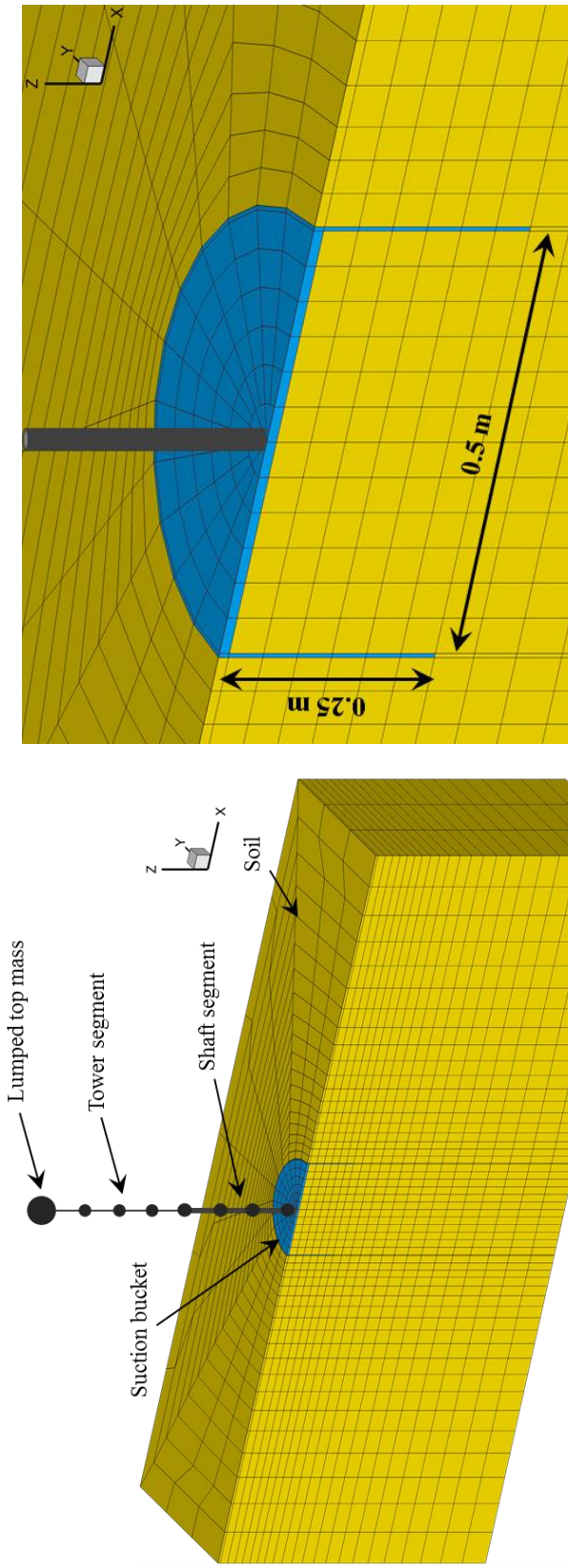


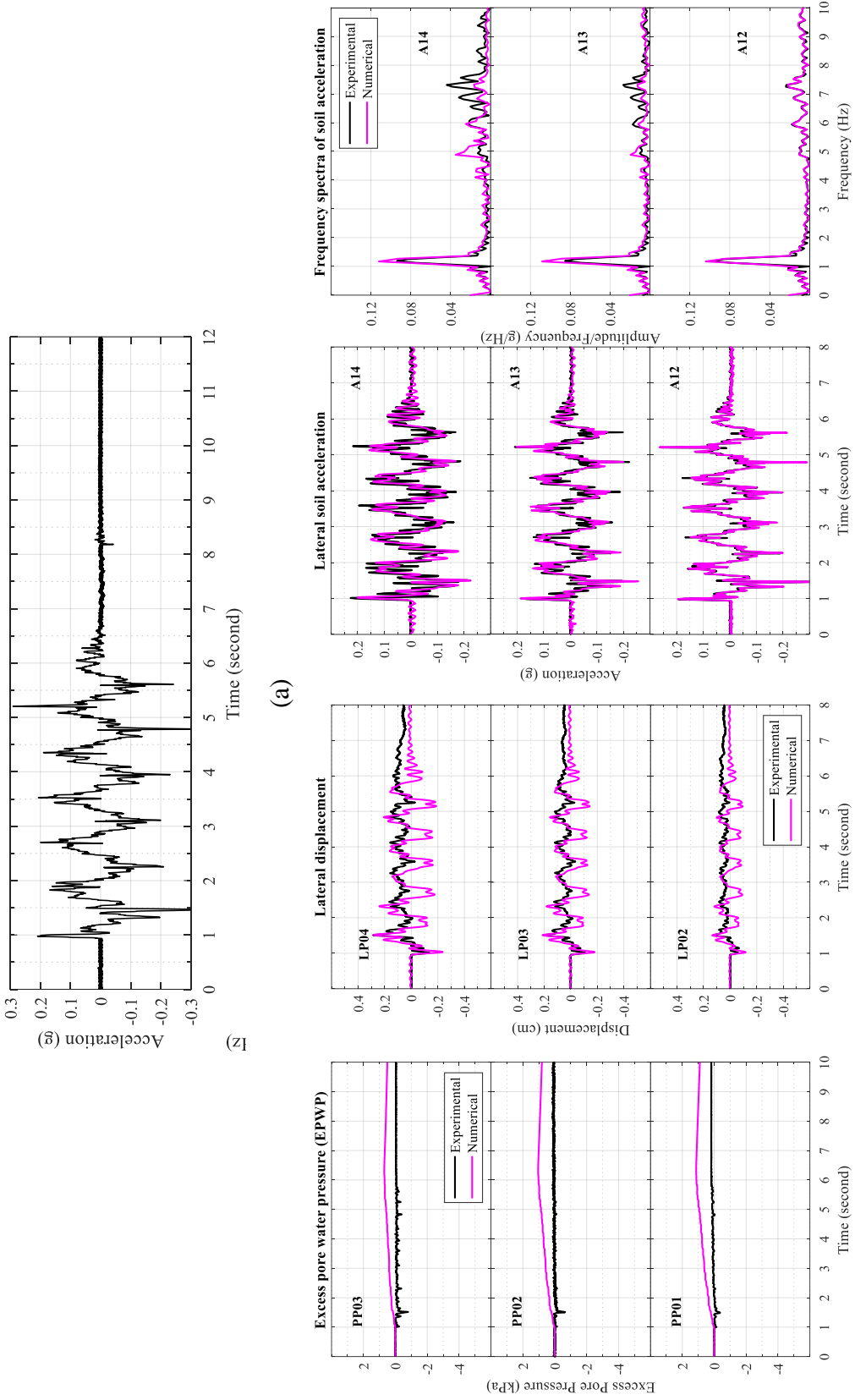
Figure 5-3: Elastic perfectly plastic model adopted interface tangential stiffness



(a)

(b)

Figure 5-4: Finite Element Model: a) 3D half-mesh of the bucket foundation wind turbine model, and b) enlarged view of bucket foundation mesh



(a) (b) (c) (d)

Figure 5-5: H5 shaking event time history of input excitation, numerical and experimental time histories of b) excess pore pressure, c) soil acceleration, d) acceleration spectra at different depths of the sand model in the far-field

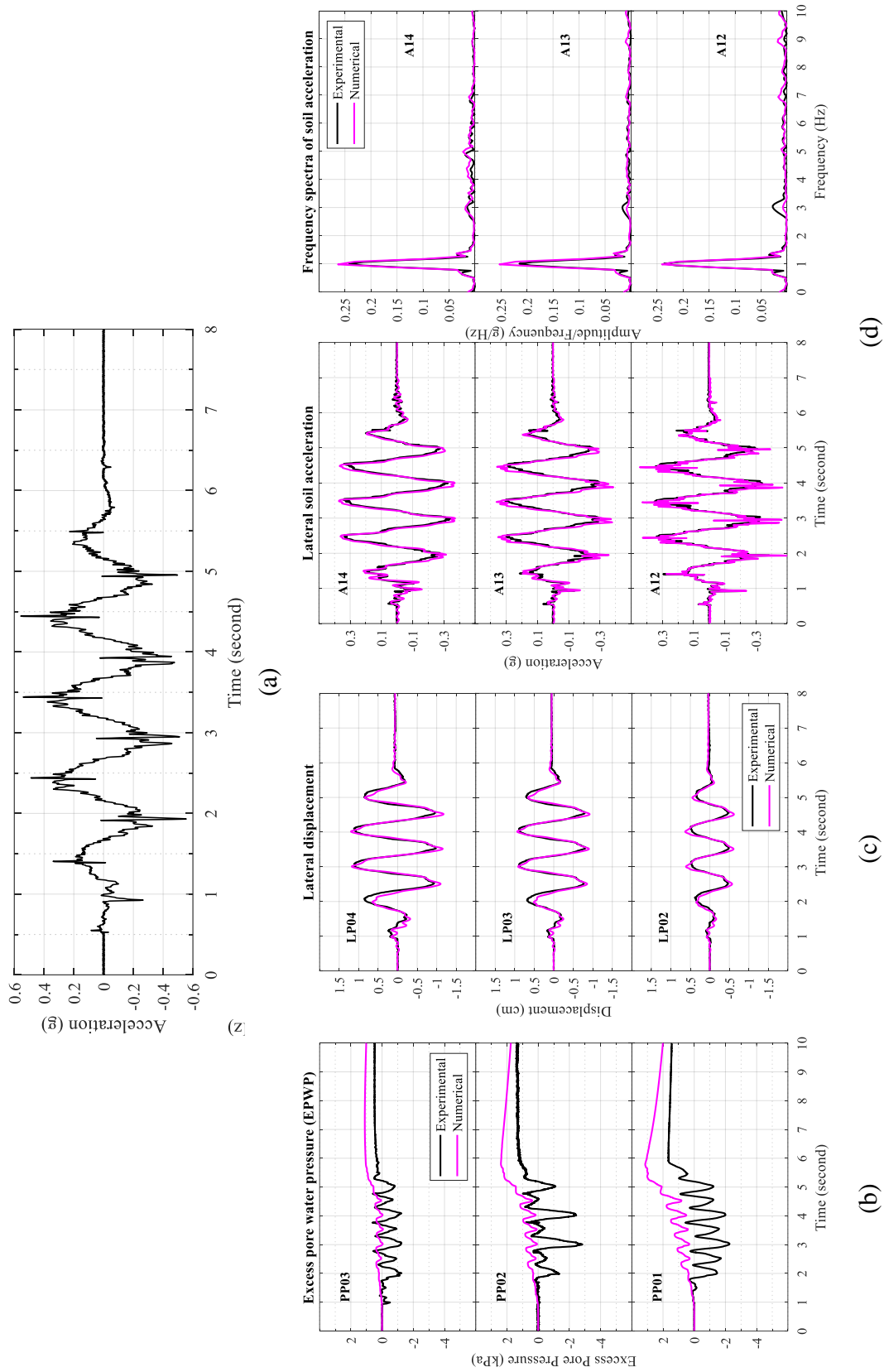
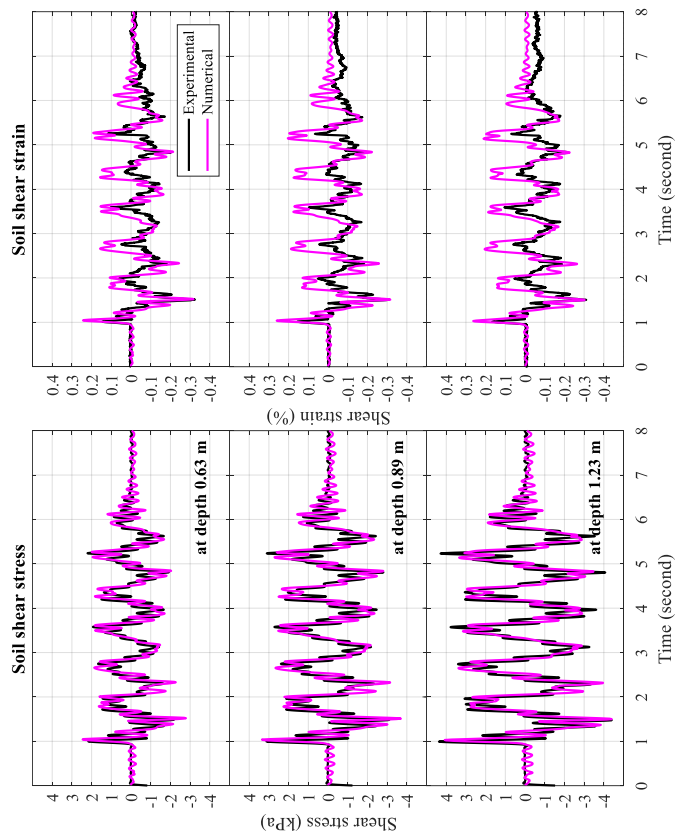
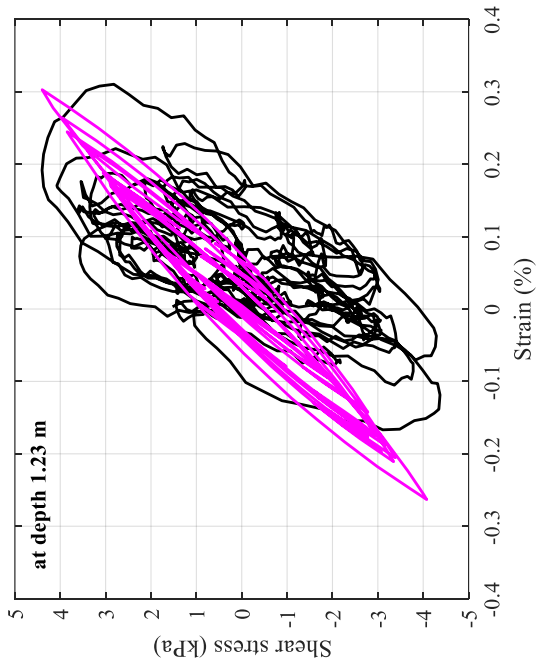


Figure 5-6: H10 shaking event a) acceleration time history of input excitation, numerical and experimental time histories of b) excess pore pressure, c) soil acceleration, d) acceleration spectra at different depths of the sand model in the far-field

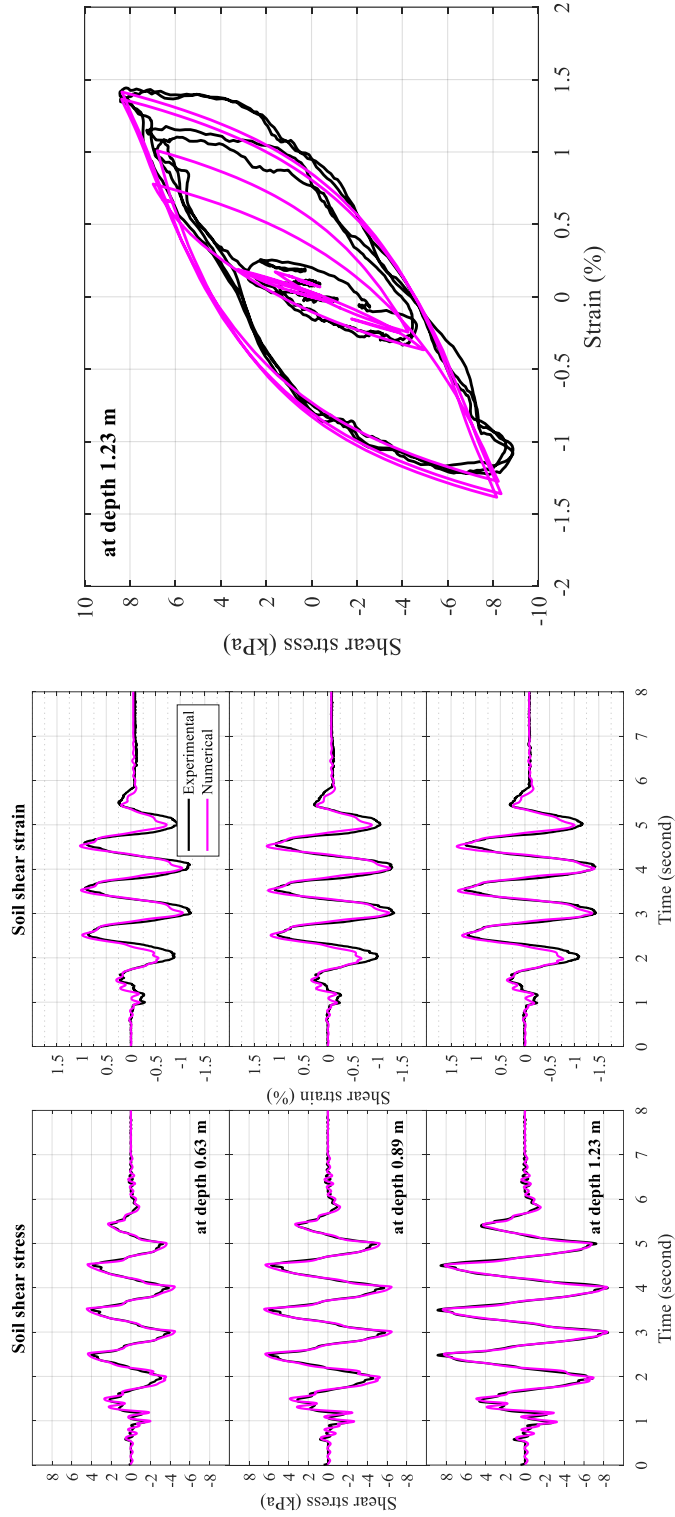


(a)

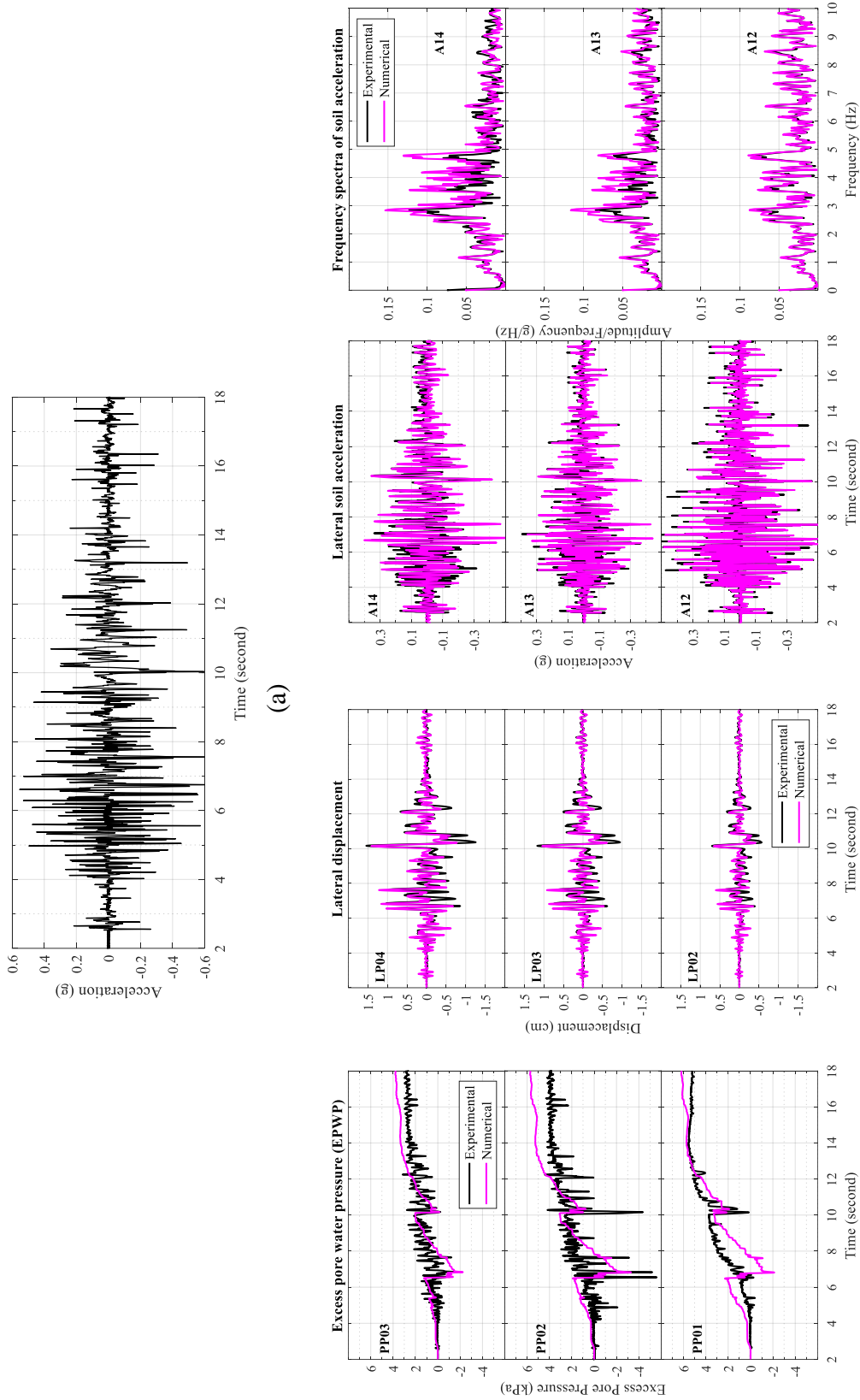


(b)

Figure 5-7: H5 shaking event a) shear stress and strain time histories at different depths, b) shear stress-strain response at depth 1.23m



(a) H10 shaking event a) shear stress and strain time histories at different depths, b) shear stress-strain response at depth 1.23m



(a) (b) (c) (d)

Figure 5-9: N3 shaking event a) acceleration time history of input excitation, numerical and experimental time histories of b) excess pore pressure, c) soil acceleration, d) acceleration spectra at different depths of the sand model in the far-field

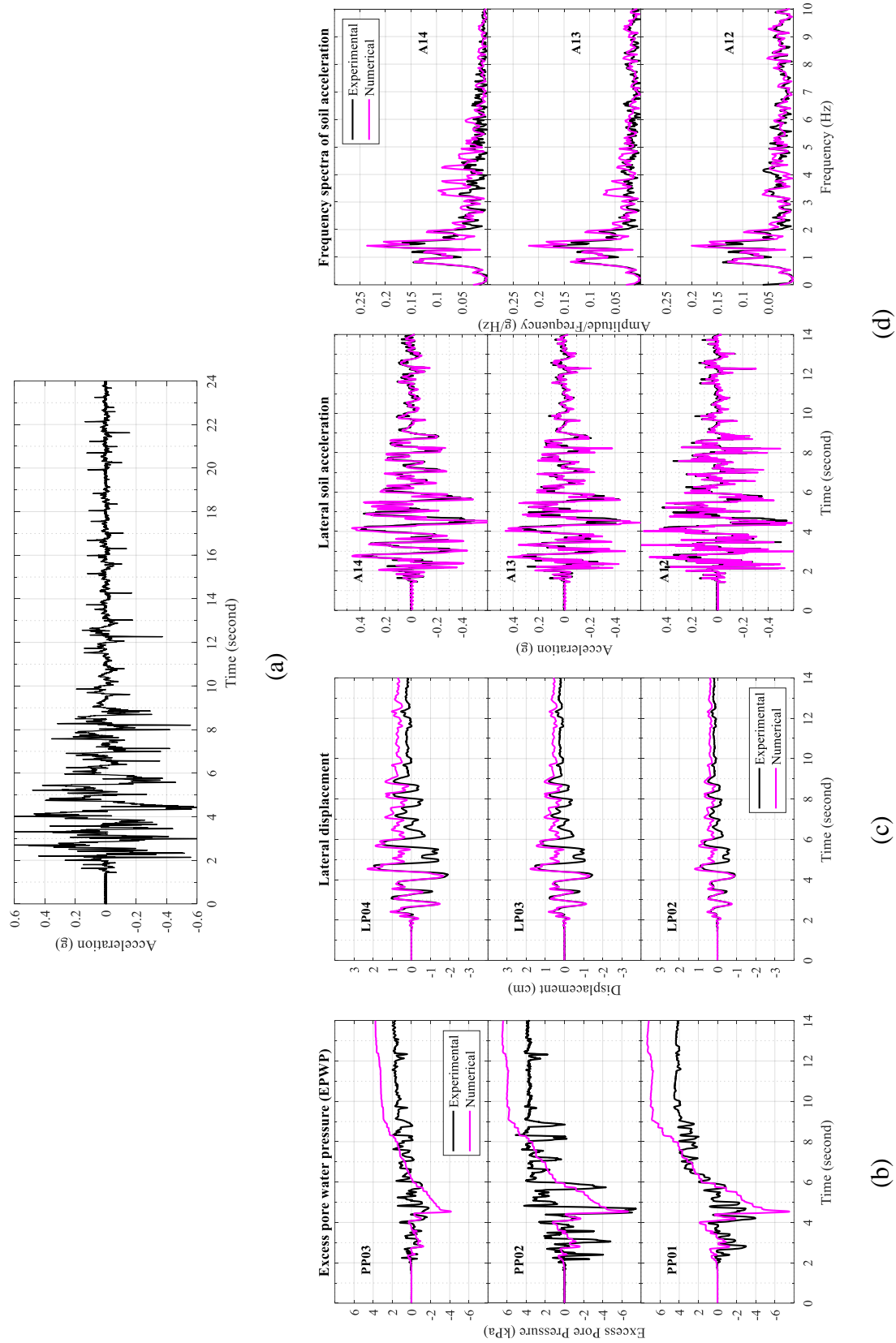
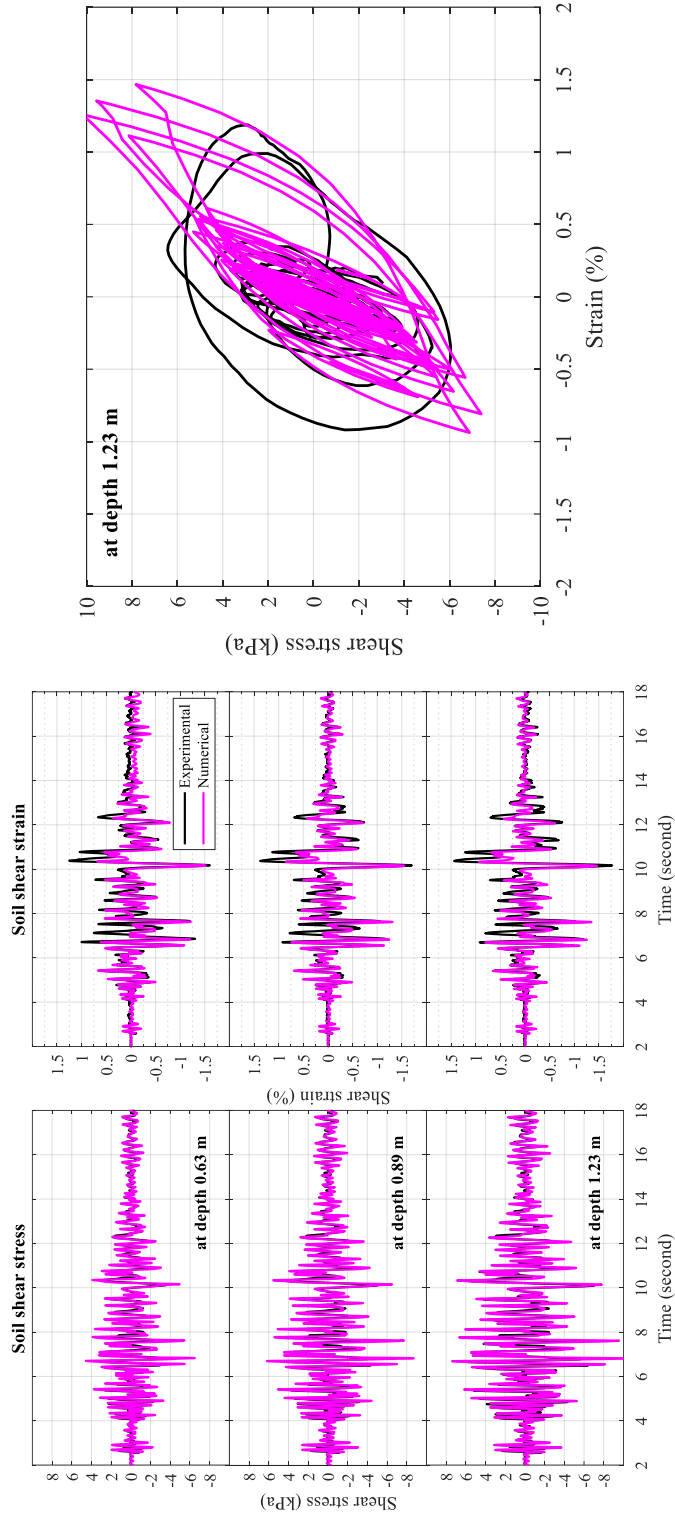


Figure 5-10: T3 shaking event a) acceleration time history of input excitation, numerical and experimental time histories of b) excess pore pressure, c) soil acceleration, d) acceleration spectra at different depths of the sand model in the far-field

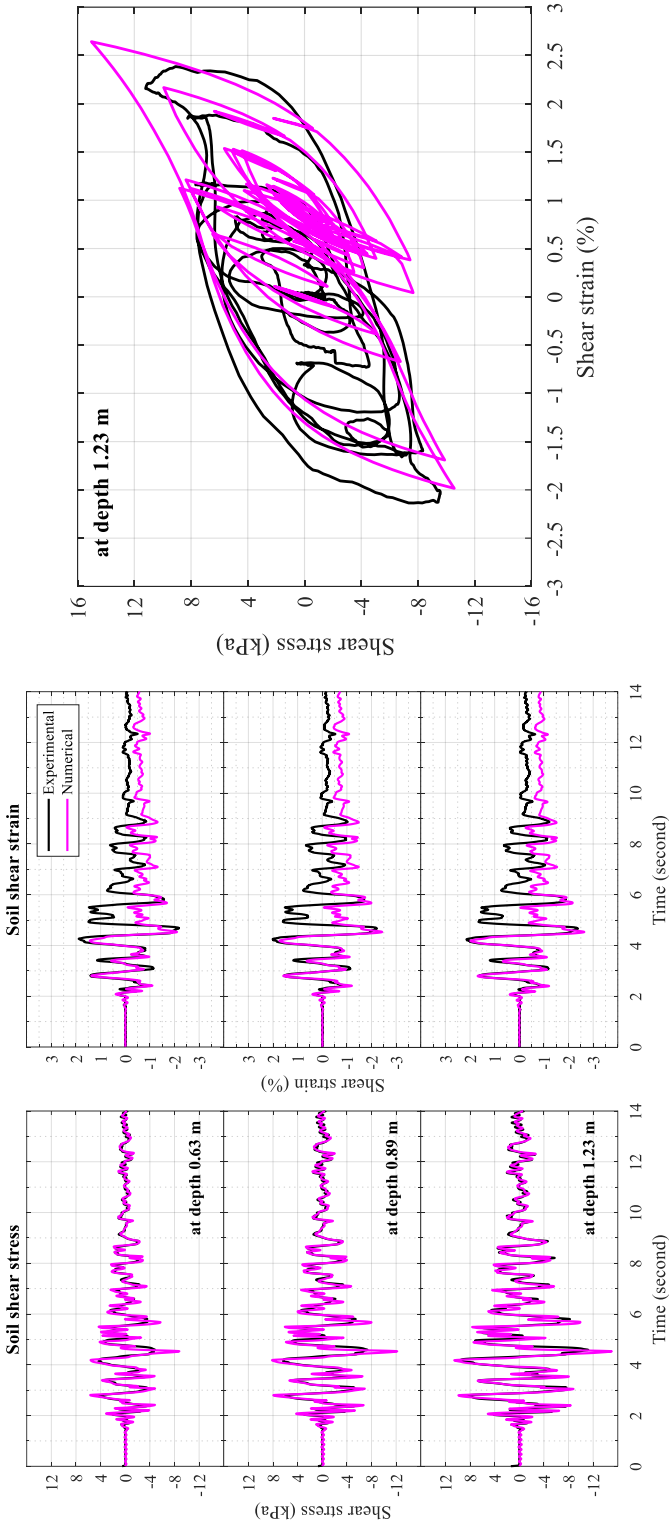




(a)

(b)

Figure 5-11: N3 shaking event a) shear stress and strain time histories at different depths, b) shear stress-strain response at depth 1.23m



(a)

(b)

Figure 5-12: T3 shaking event a) shear stress and strain time histories at different depths, b) shear stress-strain response at depth 1.23m

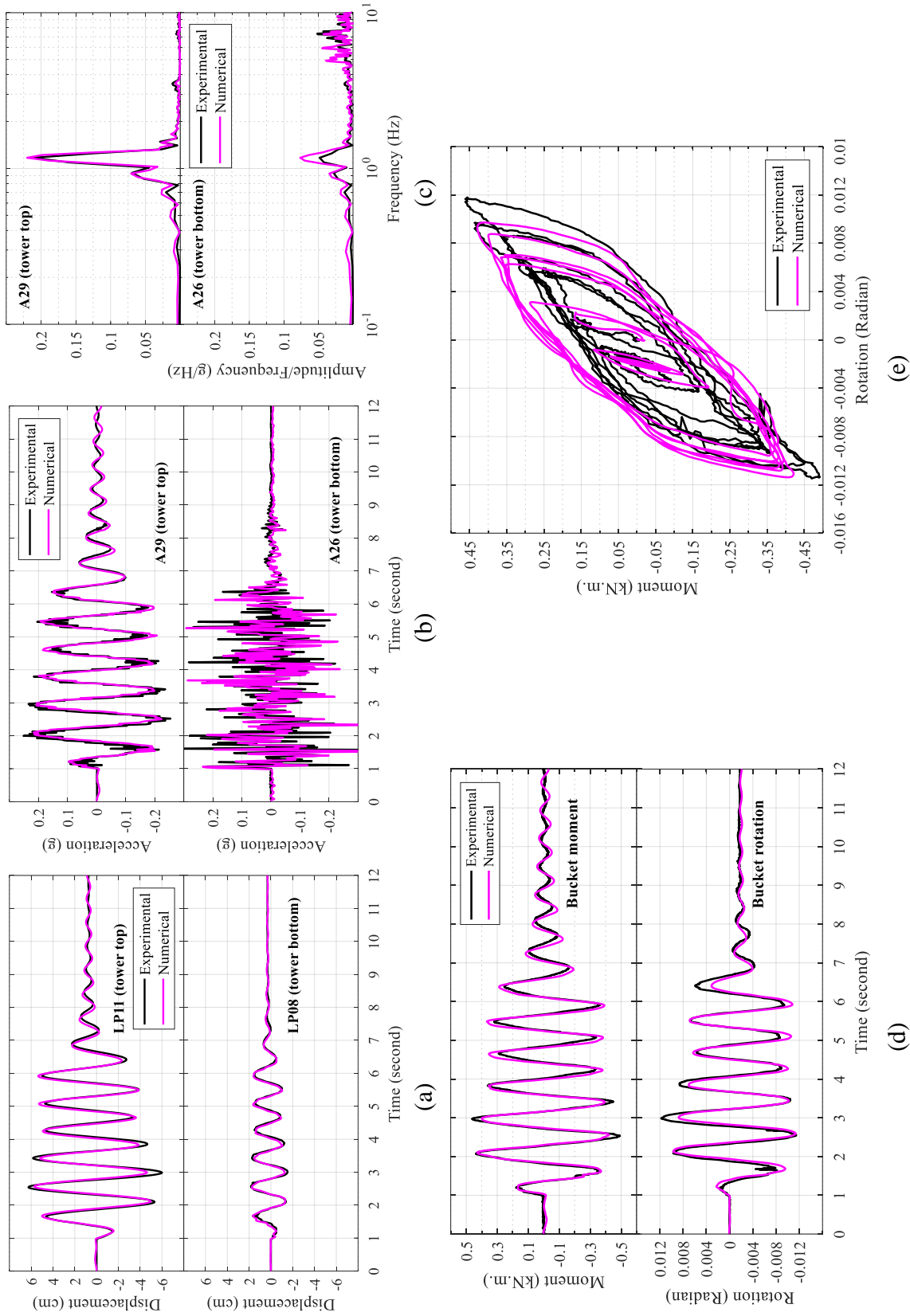


Figure 5-13: Experimental and numerical tower response in H5 shaking event: a) displacement, b) acceleration, c) frequency spectra, d) bucket moment and rotation time histories, and e) bucket moment-rotation hysteresis

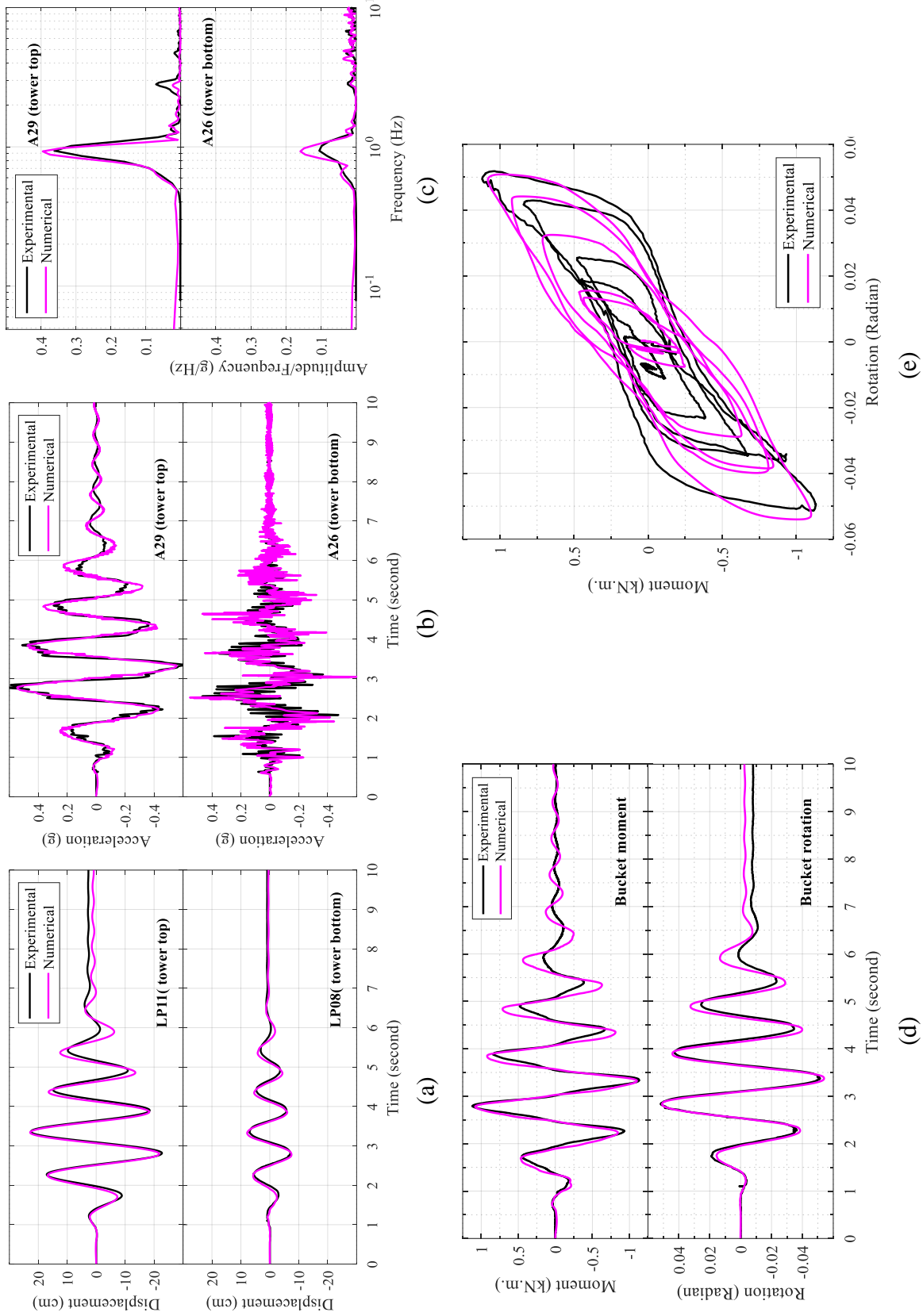


Figure 5-14: Experimental and numerical tower response in H10 shaking event: a) displacement, b) acceleration, c) frequency spectra, d) bucket moment and rotation time histories, and e) bucket moment-rotation hysteresis

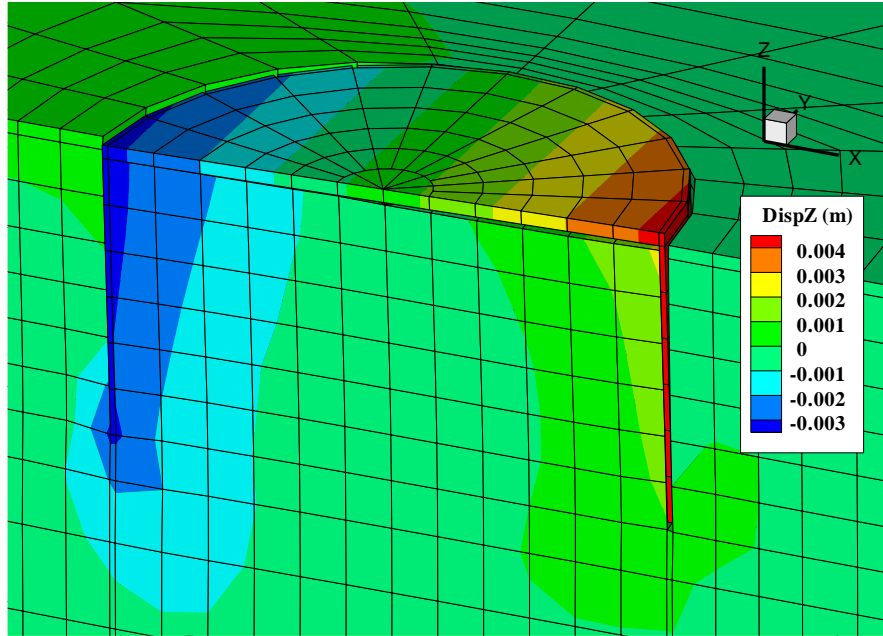
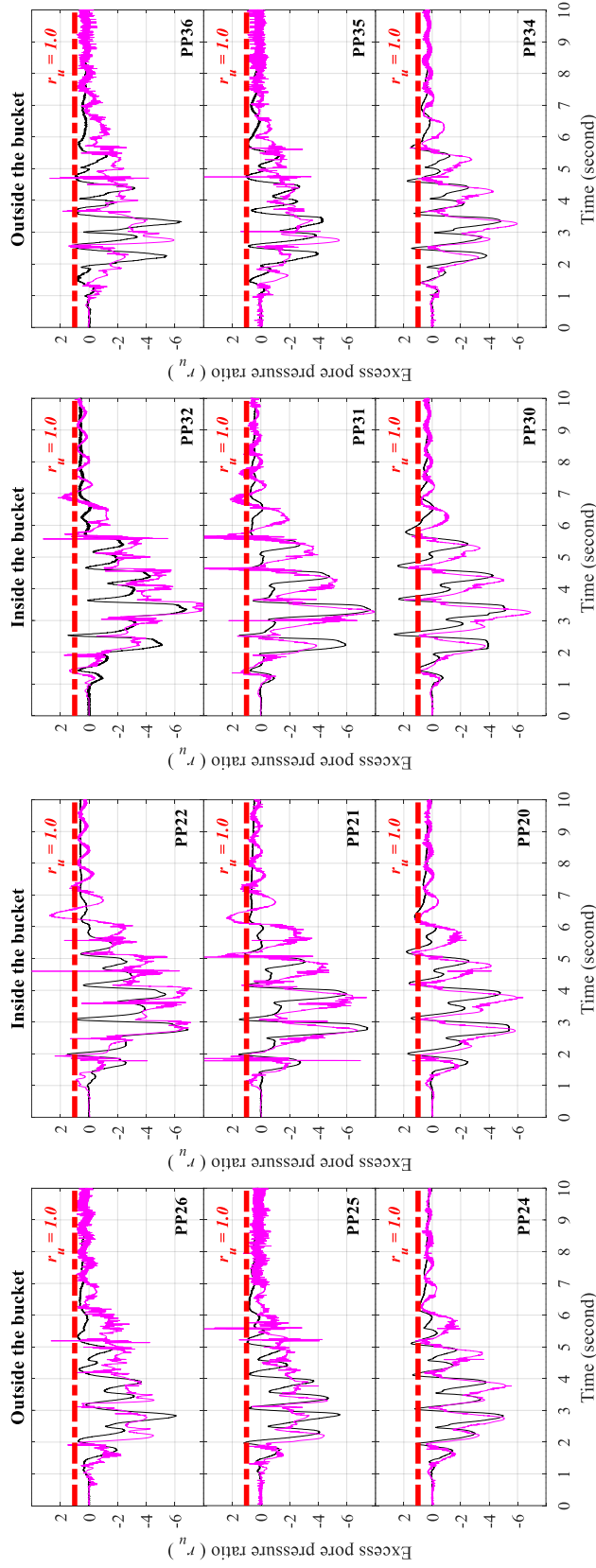
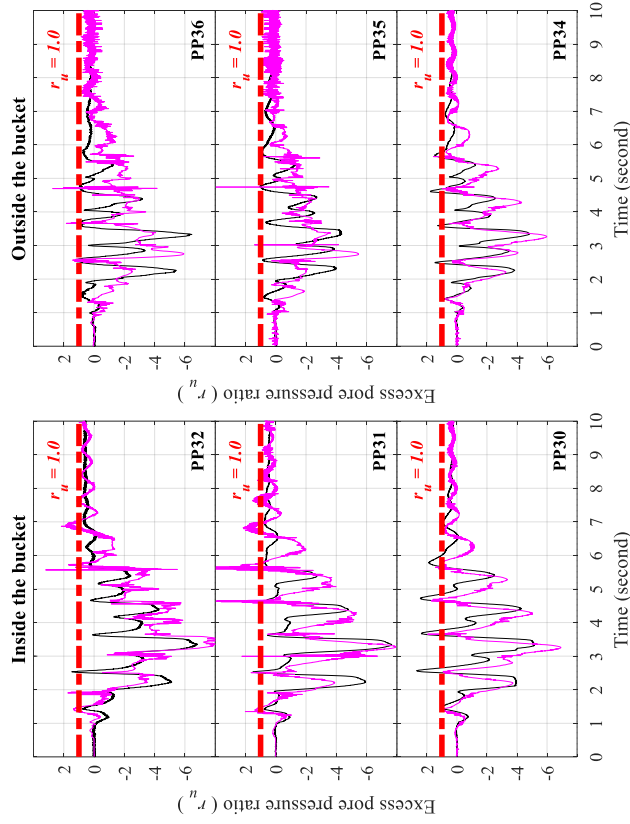


Figure 5-15: FE deformed mesh contours for vertical displacement (scale factor = 2) showing bucket rotation at 3.4 seconds of the H10 shaking event



(a)



(b)

Figure 5-16: Time histories of excess pore pressure around bucket in H10 shaking event for the a) north side and b) south side

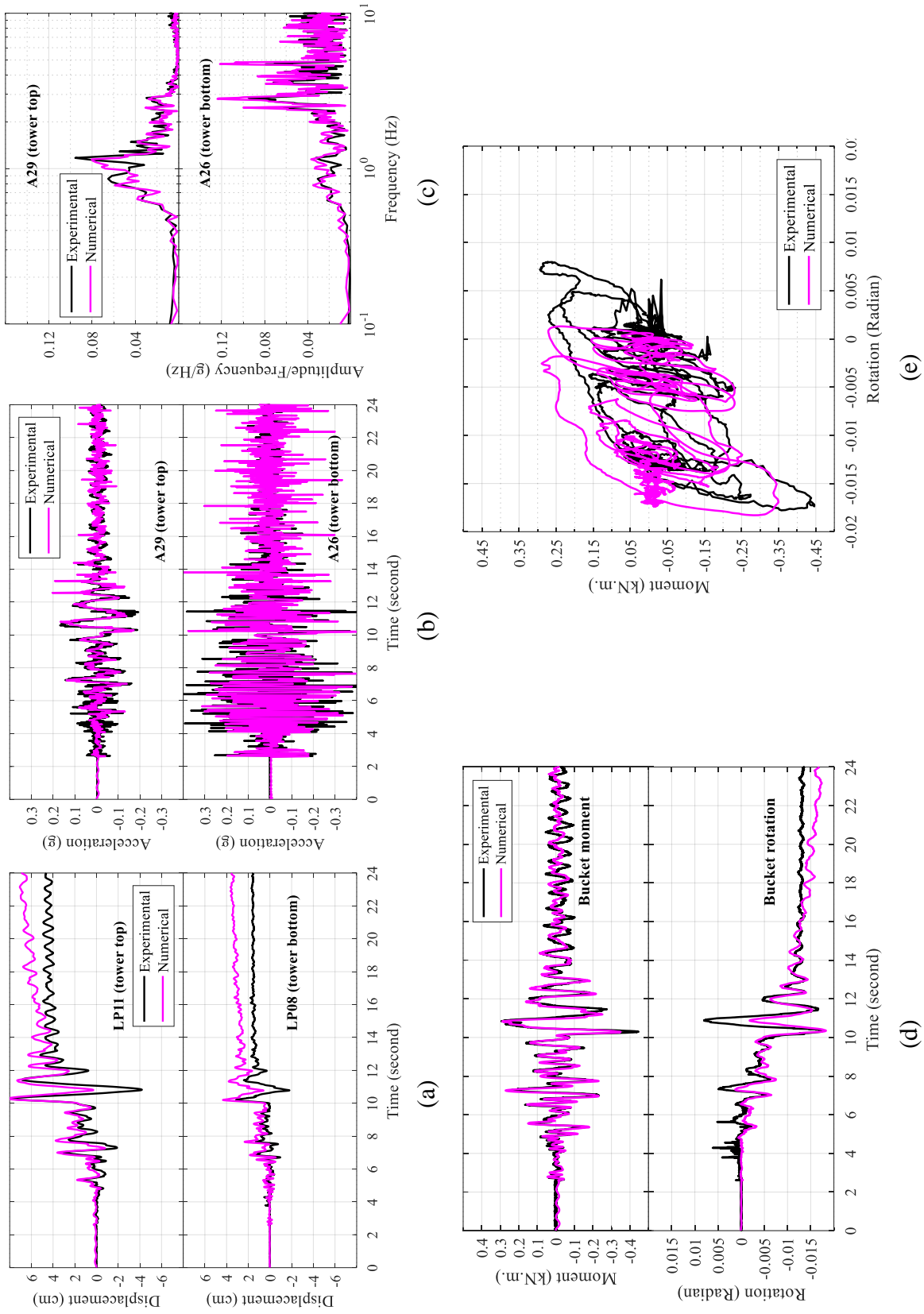


Figure 5-17: Experimental and numerical tower response in N3 shaking event: a) displacement, b) acceleration, c) frequency spectra, d) bucket moment and rotation time histories, and e) bucket moment-rotation hysteresis

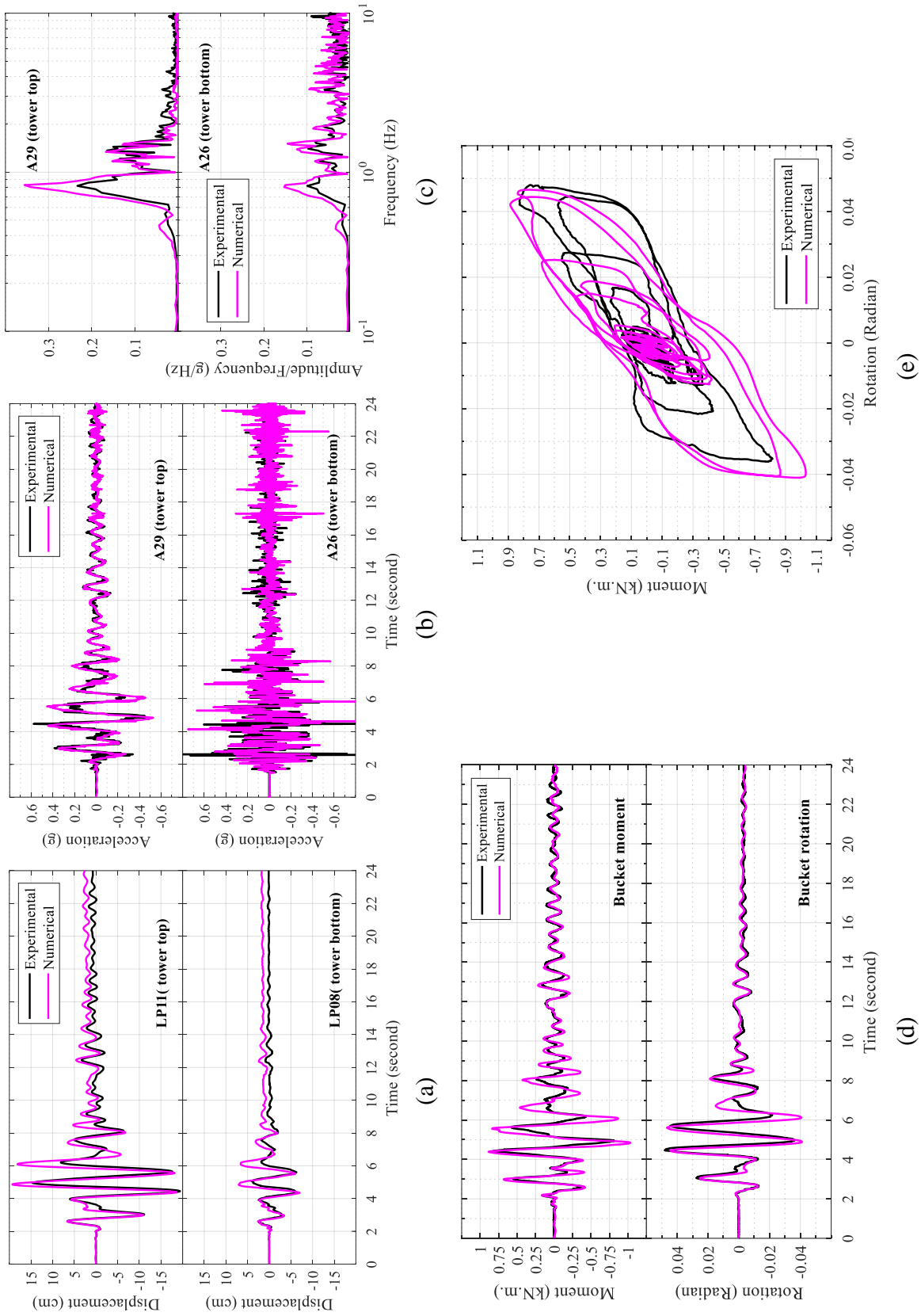


Figure 5-18: Experimental and numerical tower response in T3 shaking event: a) displacement, b) acceleration, c) frequency spectra, d) bucket moment and rotation time histories, and e) bucket moment-rotation hysteresis



## Chapter 6

# Seismic response of 3.45 MW utility-scale offshore wind turbine with bucket foundation in sand

*It gets easier. Every day it gets a little easier. But you got to do it every day. That's the hard part. But it does get easier.*

– Out to Sea, BoJack Horseman: Season 2, Episode 12

In this chapter, the calibrated numerical model of Chapter 5 is extended to investigate the seismic response of a utility-scale OWT with bucket foundation. The OWT simulated in this study is an idealized representation of the Vestas V117-3.45 MW turbine (Vestas 2021). In light of the current advancements in OWTs, the selected turbine is considered medium in size and capacity. The OWT is assumed to be placed at a location with water depth of 25 m. Further details about properties of the soil, foundation and the structure are presented in the following sections.

### 6.1 Design for fundamental frequency

In this section, dimensions of the bucket foundation and the connected shaft are determined by two steps: 1) assuming fixed base structure to roughly estimate the shaft diameter and wall thickness, and 2) assuming bucket foundation dimensions and confirm that that the flexible base structure meets the fundamental frequency criterion specified by the turbine manufacturer.

### 6.1.1 Fixed-base structure

The modeled V117-3.45 MW OWT structure consists of four main components (Figure 6-1): 1) the rotor-nacelle assembly (RNA), 2) tower, 3) shaft and 4) bucket foundation. The RNA is modeled as lumped top head mass ( $m_{RNA}$ ) while tower and shaft masses are lumped at the connecting nodes (Figure 6-2). Main properties of the OWT are summarized in Table 6-1 as provided by the publicly available data from the turbine manufacturer and the information reported by ENERGINET (2015).

Arany *et al.* (2016) indicated that OWTs of similar size would have permissible interval for the fundamental frequency of the combined turbine-foundation structure between 0.255 Hz and 0.285 Hz (typically specified by the turbine manufacturer). These lower and upper bounds are specified to ensure separation from the turbine's rotational frequency (1P) and its blade passing frequency (3P) range. As such, the target fundamental frequency of the combined turbine-foundation structure lies in the gap between 1P and 3P. This is the typical design practice for bottom fixed OWT and is commonly referred to as soft-stiff structures (van der Tempel and Molenaar 2002).

From Figure 6-1, total shaft height can be calculated knowing the distance between Mean Sea Level (MSL) and seabed (water depth assumed to be 25 m), and the height of the External Working Platform (EWP) above MSL ( $H_p$ ). The EWP is illustrated in Figure 6-1 at the interface between tower and shaft. To estimate  $H_p$ , the ENERGINET (2015) report specifies minimum of 20 m between MSL and lower blade tip (i.e., the distance referred to as gap in Figure 6-1). On the other hand, the turbine manufacturer typically specifies the minimum clearance between the EWP and the lower blade tip. In this study, the gap and minimum clearance are assumed as 20 m and 5

m, respectively. As such, distance  $H_p$  is considered as 15 m and total shaft height (i.e., sum of water depth and  $H_p$ ) of 40 m is utilized.

Knowing properties of the wind turbine (Table 6-1) and the shaft height, thickness of shaft wall can be computed to achieve a target fundamental frequency for the fixed-base OWT structure. DNV/Risø (2002) indicates that the fundamental frequency of OWT is typically reduced by 1% to 5%, when the assumption of fixed-base tower is replaced by a flexible base stiffness. In other words, the fixed-base tower can be assumed to have fundamental frequency that is 1.01 to 1.05 times that of a tower with flexible base.

As such, fundamental frequency of the equivalent fixed-base tower is targeted as 0.29 Hz (about 2% larger than the upper bound of the permissible frequency interval 0.255 Hz to 0.285 Hz). An eigen frequency analyses is conducted with the OWT modeled as a Multi-Degree of Freedom (MDOF) structure by lumping the discretized tower and shaft masses at the connecting nodes. Tower and shaft are modeled as elastic beam-column elements using the discretization, dimensions and material properties summarized in Table 6-1. Using an iterative process of eigen frequency analysis and considering a tapered shape for the shaft with top and bottom diameters of 4.5 m and 5.5 m, respectively, the target fundamental frequency can be achieved when utilizing top and bottom shaft wall thicknesses of 4 cm and 5.8 cm, respectively. The resulting total mass of the shaft is about 235 tons (Table 6-1). The 2<sup>nd</sup> and 3<sup>rd</sup> natural frequencies of the fixed-base OWT are 2.0 and 5.59 Hz, respectively.

### **6.1.2 Flexible-base structure**

In this section, two approaches are introduced to validate the fundamental frequency requirement of the flexible base OWT.

### 6.1.2.1 3D FE continuum model

To estimate the fundamental frequency of the OWT soil-foundation-structure system, a FE model is developed where both soil and bucket are modeled as 3D brick elements (Figure 6-2). For that purpose, a bucket foundation of diameter  $d = 12$  m (i.e., about 2 times the bottom shaft diameter), skirt length  $L = 8$  m as well as led and skirt average wall thickness of 8 cm is selected. Figure 6-2 shows the 3D FE discretization of the soil-foundation-structure system half mesh for the prototype scale of V117-3.45 MW OWT. Soil is modeled to represent saturated sand with relative density of about 90% while bucket foundation is represented by properties of structural steel material (Table 6-2).

The minimum wavelength to be propagated within the considered mesh was initially estimated based on small-strain shear wave velocity of the soil profile ( $V_s$ ) and the maximum frequency content of the ground motion (selected as 10 Hz in this study). The maximum element size (along the height) at different depths required to allow this wave propagation was then calculated by dividing the minimum wavelength by a factor of 4 (Kuhlemeyer and Lysmer 1973). The latter element size was further divided by 5 to allow for soil softening (Karimi and Dashti 2016). Finer elements were used near the foundation to better capture the soil-bucket interaction. Based on the above, the FE mesh for the bucket-soil system was generated comprising 24,304 nodes, 20,808 brick elements, 166 beam-column elements, 1,227 zeroLength elements and 818 equalDOF constraints. Both zeroLength elements and equalDOF constraints are employed to model the soil-bucket interface (previously illustrated in Figure 5-1-c).

A low amplitude motion is employed at the 3D FE continuum model base (Figure 6-2) resulting in Peak Ground Acceleration (PGA) of about 0.07g near the ground surface. Figure 6-3 shows transfer function between tower top and soil-bucket acceleration from which peak

amplification at frequencies 0.267, 1.733 and 5.13 Hz can be observed. As such, the OWT with bucket foundation (flexible-base conditions) achieves the fundamental frequency turbine manufacturer requirement (0.255 Hz to 0.275 Hz).

### 6.1.2.2 Base-springs model

Using the 3D FE model, operational loads due to normal wind conditions are calculated and applied as a lateral force  $F_L$  and an overturning moment  $M_o$  at the shaft-tower interface node (Figure 6-2). In addition to wind load action, structural self-weight is applied as vertical forces at the connecting nodes with a total value of  $F_v$ . Under those operational wind loads, the rotational and lateral stiffness of the foundation can be calculated (Figure 6-4) and incorporated in a base-springs model (Figure 6-5) instead of the fixed-base condition. The fundamental frequency of the base-springs model can be evaluated by conducting eigen analysis using base rotational and lateral stiffness.

Typically, the operational wind loads would be defined in a site-specific foundation load document provided by the turbine manufacturer for each project depending on actual wind speed data. In this study, operational wind loads are calculated following the approach proposed by Arany *et al.* (2017) assuming rated wind speed (i.e., wind speed at which the wind turbine generates constant power) and yearly average wind speed at hub height of 8 m/s (Vestas 2021). As such, the calculated load values for  $F_L$  and  $M_o$  are about 400 kN and 36 MNm, respectively, while self-weight total force  $F_v$  is 5.8 MN. The latter loads are applied in the 3D FE continuum model (Figure 6-2) as quasi-static forces over five time-steps and assumed to be maintained for long duration such that the assumption of drained conditions is valid (pore pressure has no contribution to the response). Modeling operational loads as quasi-static forces is considered to be a simplified

approach in which the dynamic force due to rotor and tower vibrations is neglected (De Risi *et al.* 2018).

Applying the operational wind loads ( $F_L$ ,  $M_o$  and  $F_V$ ) at the shaft-tower interface node (Figure 6-2), the computed bucket rotational and lateral displacement are presented in Figure 6-4. At the considered operational wind loads, the secant rotational  $K_{RR}$  and lateral stiffness  $K_{LL}$  are evaluated as 80.9 GNm/rad and 364 MN/m, respectively (Figure 6-4). These rotational and lateral stiffnesses are further utilized in a MDOF with base-springs model (Figure 6-5) to estimate natural frequencies of the OWT (Bhattacharya 2019). A fundamental frequency of 0.279 Hz was calculated, which is about 4% less compared to the corresponding fixed-base structure. Furthermore, the 2<sup>nd</sup> and 3<sup>rd</sup> natural frequencies of the flexible-base OWT are 1.866 and 5.06 Hz, respectively. The corresponding mode shapes are presented in Table 6-3. The latter values are about 5%, 7% and 12% different from those obtained using 3D FE continuum model.

Arany *et al.* (2016) proposed a simplified approach for estimating OWT fundamental frequency via adding 25% of tower mass to RNA lumped mass to represent the OWT as a Single-Degree of Freedom (SDOF) instead of a MDOF structure. The latter approach is employed with the base-springs model and resulted in a fundamental frequency of about 0.28 Hz, which is in good agreement with the previously evaluated values. Comparisons between SDOF and MDOF system responses are presented in chapter 7.

### **6.1.3 Design for stability under operational wind loading**

Current design guidelines and recommended practice for onshore wind turbine foundations (ASCE/AWEA 2011, DNV-GL 2018) include analytical methods with minimum required safety factors ( $SF_{min}$ ) to check the foundation stability against bearing capacity ( $SF_{min} = 3$ ), overturning ( $SF_{min} = 1.5$ ) and sliding failures ( $SF_{min} = 1.5$ ). No similar design guidelines are currently available

for bucket foundation design to date. This section provides a reference to check bucket foundation stability against bearing capacity overturning failure modes.

Wang *et al.* (2019) indicated that bucket foundation ultimate bearing capacity ( $q_{ult-bucket}$ ) in undrained dense sand can be estimated as expressed in (6.1), where  $q_{ult-surface}$  is the ultimate bearing capacity of equivalent circular surface footing of the same diameter,  $L$  is skirt length and  $d$  is bucket diameter. The general bearing capacity expression (6.2) proposed by Meyerhof (1963) can be applied to estimate  $q_{ult-surface}$ , where  $\gamma'$ ,  $N_\gamma$  and  $S_\gamma$  are effective unit weight of soil, bearing capacity factor and shape factor, respectively. Using the charts provided in the latter study, the factors  $N_\gamma$  and  $S_\gamma$  are estimated as 52 and 0.6, respectively (friction angle of 38.5 degrees as presented in Table 6-2). As such,  $q_{ult-surface}$  and  $q_{ult-bucket}$  are calculated as 2,300 kPa and 3,700 kPa, respectively. Under operational wind loads, the maximum contact stress between soil and bucket is estimated as 560 kPa, resulting in safety factor of about 6.6 against bearing capacity failure (i.e., 3,700/560).

$$\frac{q_{ult-bucket}}{q_{ult-surface}} = 1 + 0.89 \left( \frac{L}{d} \right) \quad (6.1)$$

$$q_{ult-surface} = \frac{1}{2} \gamma' d N_\gamma S_\gamma \quad (6.2)$$

On the other hand, ultimate overturning moment of the bucket foundation is assessed numerically in undrained conditions using the 3D FE continuum model in which an increasing quasi-static monotonic moment is applied at the bucket top. In addition, a total downward vertical force of 5.8 MN is pre-applied at the bucket top to represent dead load of the super-structure. The resulting moment-rotation relationship is plotted in Figure 6-6, from which the ultimate

overturning moment capacity can be considered as 250 MNm. As such, the total overturning moment on bucket top due to operational wind loads (i.e., 52 MNm) results in safety factor of about 4.8 (i.e., 250/52). Therefore, the bucket foundation provides an adequate safety margin for bearing capacity and overturning stability under operational wind loading.

## 6.2 Seismic response

The 3D FE mesh developed in Figure 6-2 is employed in this section to investigate seismic response of the utility-scale 3.45 MW OWT by applying ground motion at the model base.

### 6.2.1 Model configuration

Detailed description of the model was provided in earlier section. Additional model configuration related to damping and pre-shaking loading conditions are presented in this section.

De Risi *et al.* (2018) indicated that sources of damping for OWT include aerodynamic (generally lower than 3.5%), hydrodynamic (generally lower than 0.15%), structural (varying from 0.2% to 0.3%) and soil damping. Arany *et al.* (2017), and Bhattacharya (2019) recommended using total damping between 2% and 8% for the first mode of vibration of OWT under operational loads. In this study, a Rayleigh damping model is adopted with constant damping ratio of about 2% for the 1<sup>st</sup> and 3<sup>rd</sup> vibration modes. As such, mass and stiffness proportional damping coefficients of 0.067 and 0.0011, respectively, were employed in the FE numerical simulations. The latter coefficients correspond to damping ratios of about 1%, 3%, 5% and 8% for the 2<sup>nd</sup>, 4<sup>th</sup>, 5<sup>th</sup> and 6<sup>th</sup> vibration modes, respectively (Table 6-3).

Accounting for effects of operational wind loads is a more realistic scenario to consider when assessing seismic performance of OWTs rather than events such as storms or hurricanes (De Risi *et al.* 2018). As such, and prior to applying the seismic excitation at the model base,



operational loads due to normal wind conditions are calculated and applied as lateral force  $F_L$  and overturning moment  $M_o$  at the shaft-tower interface (Figure 6-2). The analysis is conducted in a staged fashion (Qiu *et al.* 2020). Water table was specified at the topsoil surface. Although the OWT bucket foundation is assumed to be located at a water depth of 25 m, it was noted that no apparent difference would result from modeling water at the mudline (i.e., topsoil surface) instead since both approaches would yield the same effective soil stresses, as long as the negative excess pore pressure does not reach cavitation point.

## 6.2.2 Results and discussion

In this section, modified motion of the 1940 Imperial Valley Earthquake El Centro station acceleration record NS component with 0.5 amplitude scaling is applied as input excitation at the FE model base. Foundation tilting is one of the critical aspects for OWT serviceability limits (Bhattacharya 2019). Design standards and guidelines for OWT such as and DNV/Risø (2002), DNV (2004), DNV-GL (2018) recommend that tolerance for total rotation at seabed should not exceed 0.5 degrees (about  $9E-3$  radians). Therefore, special attention is paid to bucket moment-rotation response. Unless otherwise noted, all pore pressure responses discussed in the following sections are presented at the mid skirt height (i.e., at depth  $L/2$  from ground surface).

Figure 6-7-a and Figure 6-7-b show time history and response spectrum of the input acceleration at model base and near surface at mid skirt height. Acceleration time histories along the OWT super-structure (i.e., shaft and tower) are presented in Figure 6-8. Amplification can be noticed when comparing shaft base with mid tower accelerations. The Fourier amplitude frequency spectra shown in Figure 6-9-a indicate that contribution of higher frequencies increases as the acceleration propagates upward between shaft base and near tower top. A de-amplification is observed in the acceleration response near the tower top with higher frequencies filtered out. The

transfer function between shaft base and tower top accelerations plotted in Figure 6-9-b shows that four frequencies of 0.268 Hz, 1.7 Hz and 5 Hz were amplified by the super-structure. The latter frequencies are found to be in a good agreement with the first three natural frequencies of the bucket foundation OWT structure as evaluated in previous sections (Table 6-3).

Figure 6-10 middle and top plots show times histories of bucket rotation and moment. It can be noticed that the latter plots start with the initial operational moment and the corresponding rotation. As shaking evolves, the bucket starts to accumulate rotation in one direction until about 28 seconds which represents end of forced vibration. Bucket moment consists of the operational (i.e., initial) moment that is applied prior to shaking and the moment due to vibration of the super-structure masses. The latter component is summation of the moments resulting from inertial forces due to lateral acceleration exerted during shaking on the distributed masses along the shaft and the tower (lateral inertial force = mass x acceleration). Thereafter, oscillations of the moment time history that occur towards the end of shaking (i.e., after 30 seconds) are due to free vibration of the super-structure and do not result in significant rotation accumulation. In addition, it can be noticed that the most significant accumulation of bucket rotation corresponds to the instants when moment experienced largest changes or oscillations. Permanent residual rotation of about  $7E-3$  radians was accumulated by the end of shaking.

Figure 6-10 also shows excess pore pressure (PP) ratio  $r_u$  time history at mid skirt height in the far field, near field and below bucket. It can be noticed that  $r_u$  reached a maximum of about 0.25 and 0.4 in the far field and near field, respectively, while it was about 0.8 below the bucket. Stronger dilative and contractive spikes can be noticed in the below bucket  $r_u$  record when compared to the far and near field. The observed dilative response may be attributed to the suction mechanism resulting from rocking and cyclic rotation of the bucket foundation during shaking.

A correlation can be observed in Figure 6-10 between the instant during which the below bucket  $r_u$  experienced strong dilation and when bucket moment showed large oscillations (along with permanent accumulation of rotation). Around 3 seconds, the below bucket  $r_u$  showed a strong dilative spike when the bucket experienced strong cyclic moment response. Similar observation can be noted around 15 and 28 seconds. In addition, it can be noticed that most of rotation accumulation occurred before 20 seconds when cyclic moment response was the largest, whereas the below bucket excess PP response was mostly dilative with  $r_u$  generally below 0.5. On the other hand, the near-field excess PP (outside the bucket) generally showed contractive response (i.e., soil softening) with  $r_u$  increasing to about 0.3 at 20 seconds. Although the below bucket  $r_u$  kept increasing after 20 seconds to a maximum value of 0.8, no significant accumulation in bucket rotation was noted. This can be attributed to the fact that the inertial loads were lower in this particular shaking event and the near-field excess PP response did not show significant increase after 20 seconds (i.e., end of shaking).

The above discussion suggests that bucket rotation might be influenced by the near field pore pressure build-up characteristics, along with the strong dilative response that might occur below the bucket (induced by the suction mechanism). In this regard, an increase in pore pressure outside the bucket in the near field would result in soil softening due to reduction in effective stress, which subsequently leads to degradation in the foundation rotational stiffness and thereafter rotation accumulation. On the other hand, the strong dilative response (i.e., increase in effective stresses) observed below the bucket is deemed to be helpful in improving the overall rotational stiffness of the foundation.

Bucket moment-rotation response is plotted in Figure 6-11 from which the rotation accumulation can be noticed as shaking evolves. This is further illustrated by Figure 6-12 in which selected cycles of moment-rotation response are shown at different time instants.

#### **6.2.2.1 Role of operational wind loads**

Figure 6-13 illustrates bucket foundation response where operational wind loads are neglected. Although starting with an initial value of zero, time history of bucket moment appears to be of similar characteristic to the case in which wind loads are considered (Figure 6-10). However, the dilative response can be noticed to be weaker than that of Figure 6-10. The latter observation might indicate that the strong dilative response presented in Figure 6-10 is driven by the sustained wind load effect. Similar to bucket moment, the rotation starts with an initial zero value. Cyclic bucket rotation can be observed, where the rotation experienced in one cycle is fully recovered during the following one. As such, negligible residual rotation is accumulated at the end of shaking. Similar observations were reported for OWT bucket foundation in clay (Kourkoulis *et al.* 2014).

#### **6.2.2.2 Role of tower inertial loading**

As indicated earlier, the fundamental frequency of the OWT bucket foundation can be achieved using single mass lumped at the tower top (SDOF model) where 25% of tower mass is added to the RNA mass. Figure 6-14-a shows acceleration response of the OWT where the super-structure is modeled as a SDOF. Compared to Figure 6-8 (i.e. MDOF model), a significant reduction in the super-structure accelerations can be noticed, with maximum acceleration at tower top of about 0.05 g (vs 0.4 g for the MDOF model).

Comparison between the corresponding frequency spectra presented in Figure 6-9-a for MDOF and Figure 6-14-b for SDOF indicate that the latter does not have the same amplification at frequencies between 1 and 5 Hz. Consequently, the SDOF model resulted in less inertial forces (top lumped mass  $\times$  acceleration) and moment, as illustrated in top plot of Figure 6-15. As a result, the below bucket excess PP response had no significant dilation spikes (bottom plot of Figure 6-15). Moreover, the middle graph of Figure 6-15 indicates an increase of about 50% in the accumulated rotation when accounting for tower inertial effects (i.e., MDOF) compared to SDOF structure.

As such, modeling the OWT as a SDOF via a single mass at the tower top might not result in accurate seismic response due to the associated crude representation of the inertial forces. Instead, modeling the tower as discrete masses at the connecting nodes yields a more realistic representation of the super-structure and is shown to result in more accumulated rotation at the end of shaking when compared to the crude SDOF model, which can be critical to the OWT serviceability limit

### **6.3 Summary and conclusions**

In this chapter, the calibrated model (of chapter 5) is further extended to investigate the seismic response of a utility-scale 3.45 MW OWT with bucket foundation in dense saturated sand ( $D_r = 90\%$ ). Pore pressure response below and around the bucket as well as the foundation moment and rotation response are analyzed. In addition, effects of wind and inertial loading on seismic response of the soil-bucket-structure system are examined. The numerical framework and the insights derived from this study are of general relevance to bucket foundation seismic response for offshore wind applications. Specific observations and conclusions include:

- Accounting for operational wind loads on wind turbines during seismic loading is considered to result in a more realistic response scenario. The initial bucket rotation due to operational wind loads might further result in rotation accumulation during earthquake shaking. No appreciable rotation accumulation resulted in the case of wind loads neglected, which might significantly underestimate the actual system response
- During seismic excitation, acceleration at the tower top can be of lower amplitude and of different frequency bandwidth than that along the tower.
- Modeling the OWT as a SDOF via a single lumped mass at the tower top might not result in accurate seismic response due to inaccurate representation of the inertial forces. Instead, modeling the tower as discrete masses at the connecting nodes yields a more realistic representation of the super-structure response. The MDOF model resulted in more accumulated rotation at the end of shaking when compared to the SDOF model, which can be critical to the OWT serviceability limit.
- A correlation between the near field pore pressure build-up and the bucket rotation can be observed, resulting in foundation stiffness degradation due to soil softening associated with excess pore pressure build-up.

In the following chapter, a parametric study is conducted to assess effect of bucket size on the soil-foundation-structure natural frequencies as well as the overall dynamic and seismic response. Moreover, effects of soil stiffness (i.e., relative density) and permeability as well as ground motion and damping are investigated.

## **6.4 Acknowledgement**

The research described in this chapter was partially funded by the National Science Foundation grant OISE-1445712 as well as the Trent R. Dames and William W. Moore graduate

student fellowship from the American Society of Civil Engineers (ASCE). Testing was conducted at the Powell laboratories, University of California San Diego, with assistance provided by Dr. Christopher Latham, Mr. Andrew Sander, Mr. Mike Sanders, Mr. Abdullah Hamid, and Mr. Darren Mckay. The authors also would like to graciously thank Dr. Jinchu Lu, Dr. Zhijian Qui, and Dr. John Li for their useful insights.

The content of chapters 5 and 6 is currently being prepared to be published as a journal paper tentatively in the ASCE Journal of Geotechnical and Geoenvironmental Engineering or the Soil Dynamics and Earthquake Engineering Journal. The proposed title of this paper is “Computational modeling of bucket foundation seismic response for utility-scale offshore wind turbine using experimental data”. The dissertation author is the primary author of this paper with Dr. Kyungtae Kim, Mr. Athul Prabhakaran, and Professor Ahmed Elgamal as coauthors.

Table 6-1: Properties of the prototype and the scaled model

Quantity	Unit	Full scale (Prototype)
Rotor, Nacelle Assembly mass* ( $m_{RNA}$ )	kg	195,000
Tower height	m	66.5
Tower diameter (top/bottom)	m	3.26 / 4.5
Tower wall thickness (top/bottom)	cm	1.6 / 3
Tower mass	kg	150,000
Tower discretization (beam-column elements)	-	20
Shaft height	m	40
Shaft diameter (top/bottom)	m	4.5 / 5.5
Shaft wall thickness	cm	4 / 5.8
Shaft mass	kg	235,000
Shaft discretization (beam-column elements)	-	12
Bucket diameter (d)	m	12
Bucket lid average thickness	cm	8
Skirt length (L)	m	8
Skirt wall average thickness	cm	8
Tower, shaft and bucket material	-	Steel
Young's modulus of tower, shaft and bucket	GPa	200
Mass density of tower, shaft and bucket	kg/m <sup>3</sup>	7,850
Fundamental frequency (fixed base)	Hz	0.29

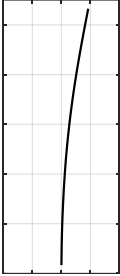
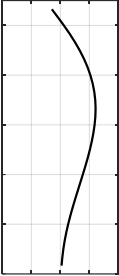
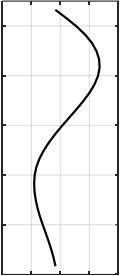
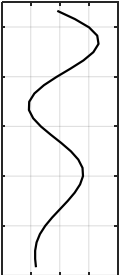
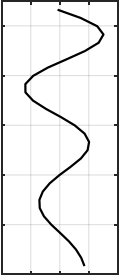
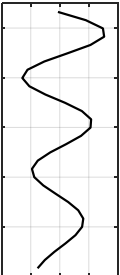


Table 6-2: Parameters of PDMY02 and PIMY models for full-scale case

Model parameter	Full-scale prototype	
	PDMY02* (sand)	PIMY (bucket)
Material	Sand with $D_r$ of 90%	Steel
Mass density, $\rho$ (kg/m <sup>3</sup> )	2,150	7,850
Reference shear modulus, $G_r$ (MPa)	215	80,000
Reference bulk modulus, $B_r$ (MPa)	1,000	140,000
Peak friction angle, $\phi$ (degrees)	38.5	60
Phase transformation angle, $\phi_{PT}$ (degrees)	26	-
Peak shear strain, $\gamma_{max}$ (%)	10	
Reference mean effective confining pressure, $p'$ (kPa)	101	
Pressure dependent coefficient, $n$	0.5	0
Contraction coefficient $c_1$	0.003	-
Contraction coefficient $c_2$	5	-
Contraction coefficient $c_3$	0	-
Dilation coefficient $d_1$	0.5	-
Dilation coefficient $d_2$	3	-
Dilation coefficient $d_3$	0	-
Number of yield surfaces, $NYS$	20	
Shear strength at zero confinement, $c$ (kPa)	1	-
Cohesive strength, $c$ (GPa)	-	100
Permeability, $k$ (m/s)	1E-4	1E-20

\* Properties are selected to represent very dense sand with relative density of 90% (Elgamal *et al.* 2003, Mazzoni *et al.* 2006)

Table 6-3: Natural frequencies and mode shapes of fixed-base and flexible base 3.45 MW OWT

Mode			1 <sup>st</sup>	2 <sup>nd</sup>	3 <sup>rd</sup>
f <sub>n</sub> (Hz)	Fixed base		0.29	2	5.59
	Flexible base	Base-springs model	0.279	1.866	5.06
		Low amplitude shaking	0.269	1.730	5.13
Mode shape (Using base-springs model)					
Damping ratio, ζ (%)			2*	1	2*
Mode			4 <sup>th</sup>	5 <sup>th</sup>	6 <sup>th</sup>
f <sub>n</sub> (Hz)	Fixed base		11.4	19.2	28.8
	Flexible base	Base-springs model	9.7	14.8	22
		Low amplitude shaking	10.3	Not identified	Not identified
Mode shape (Using base-springs model)					
Damping ratio, ζ (%)			3	5	8

\* Target damping ratio at the 1<sup>st</sup> and 3<sup>rd</sup> fixed base natural frequencies

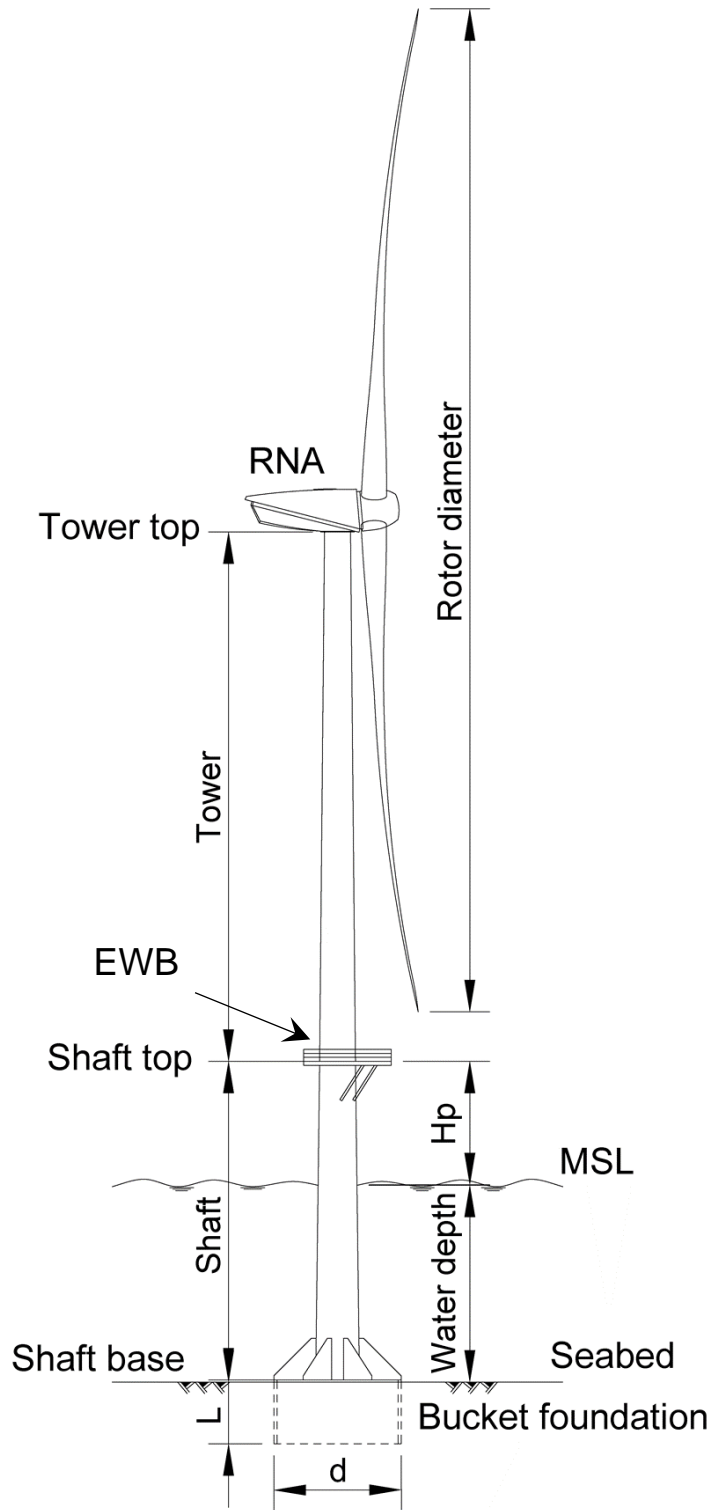


Figure 6-1: Schematic of OWT with bucket foundation

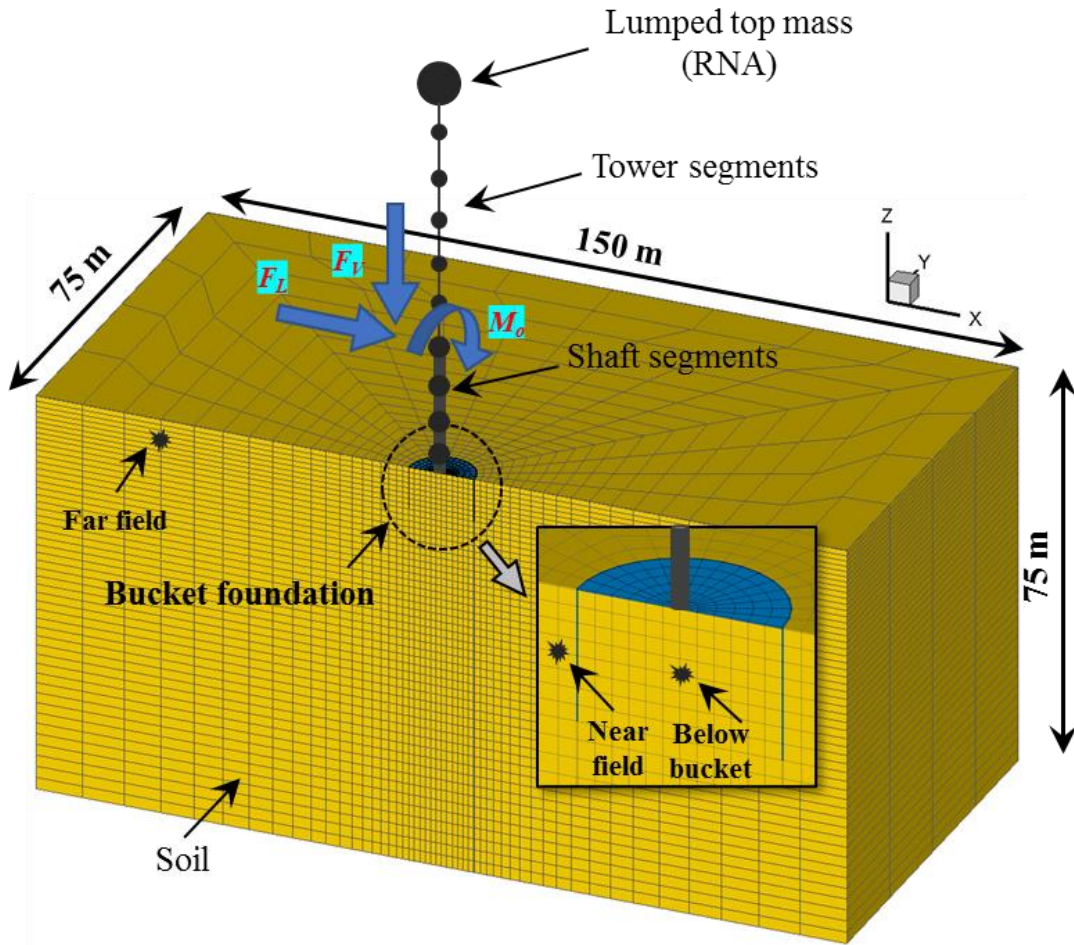


Figure 6-2: 3D view of the FE half-mesh employed in modeling 3.45 MW utility-scale OWT with bucket foundation

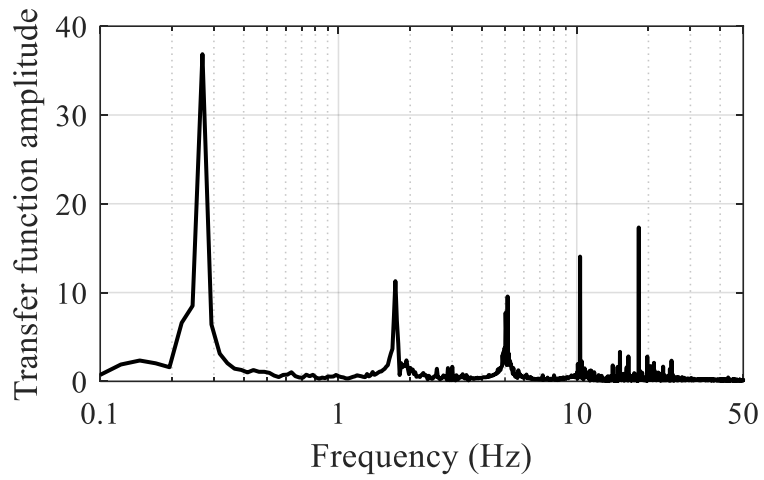
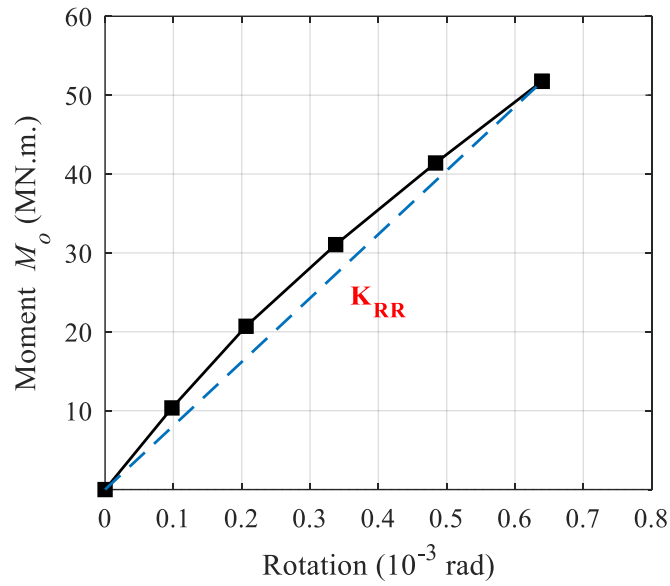
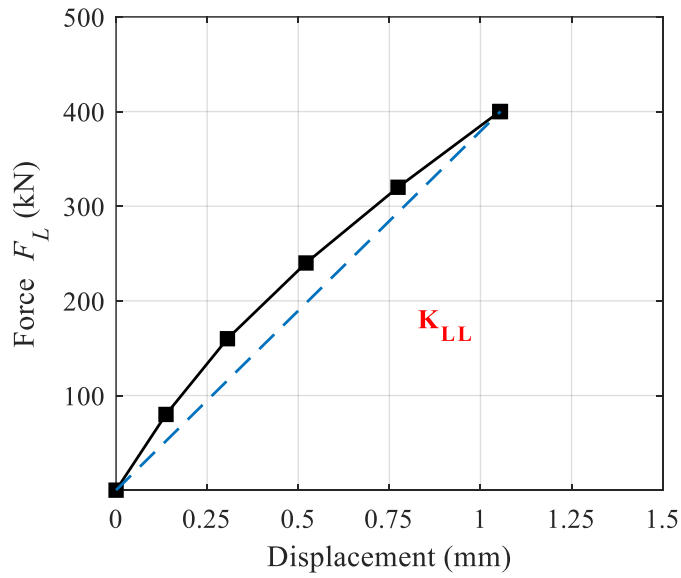


Figure 6-3: Plot of transfer function between tower top and bucket acceleration at mid skirt height for low amplitude shaking



(a)



(b)

Figure 6-4: Bucket response under effects of quasistatic operational wind loads; a) moment-rotation ( $K_{RR}$  is the foundation secant rotational stiffness) and b) lateral force-displacement ( $K_{LL}$  are the foundation secant translational stiffness)



Figure 6-5: Schematic of the base-springs model (for natural frequency calculations)

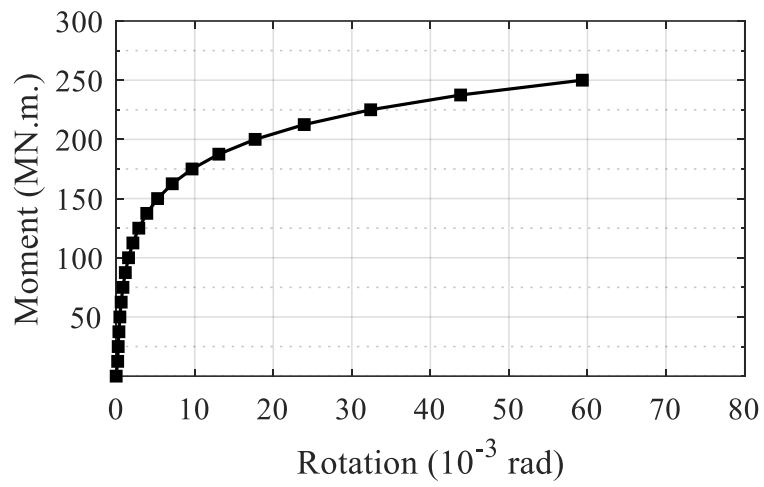
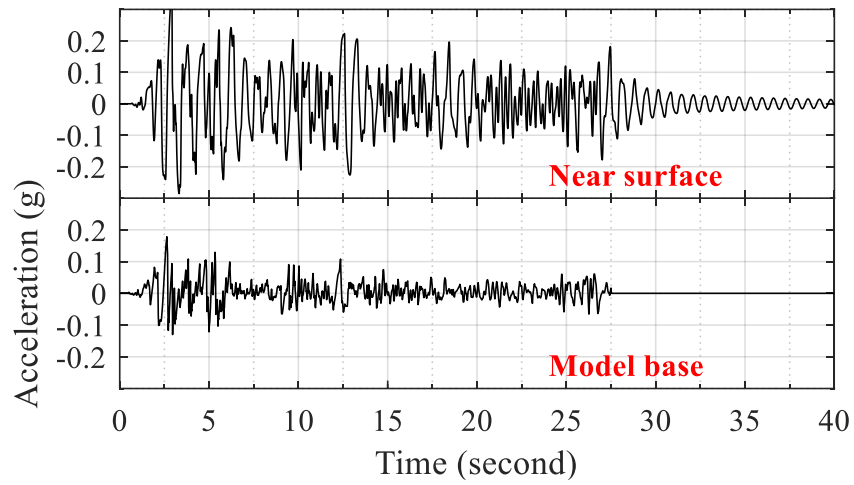
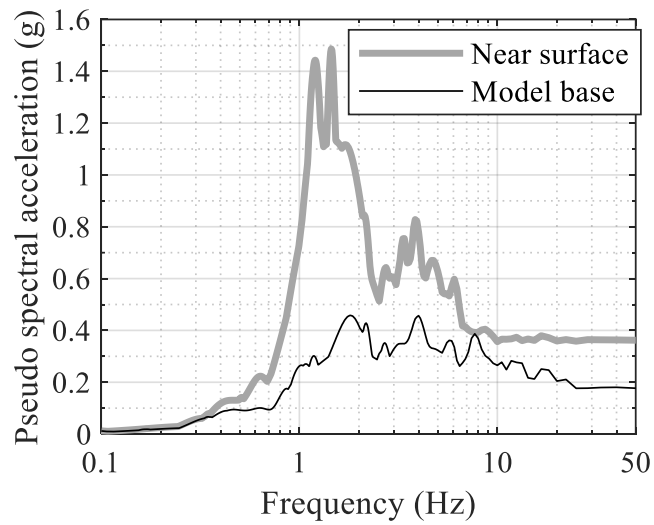


Figure 6-6: Plot of quasistatic monotonic moment-rotation relationship of bucket foundation in undrained conditions (combined with 5.8 MN vertical dead load of the superstructure)





(a)



(b)

Figure 6-7: Plot of (a) acceleration time history at the model base and near surface in the far field (Figure 6-2), and (b) the corresponding acceleration response spectrum

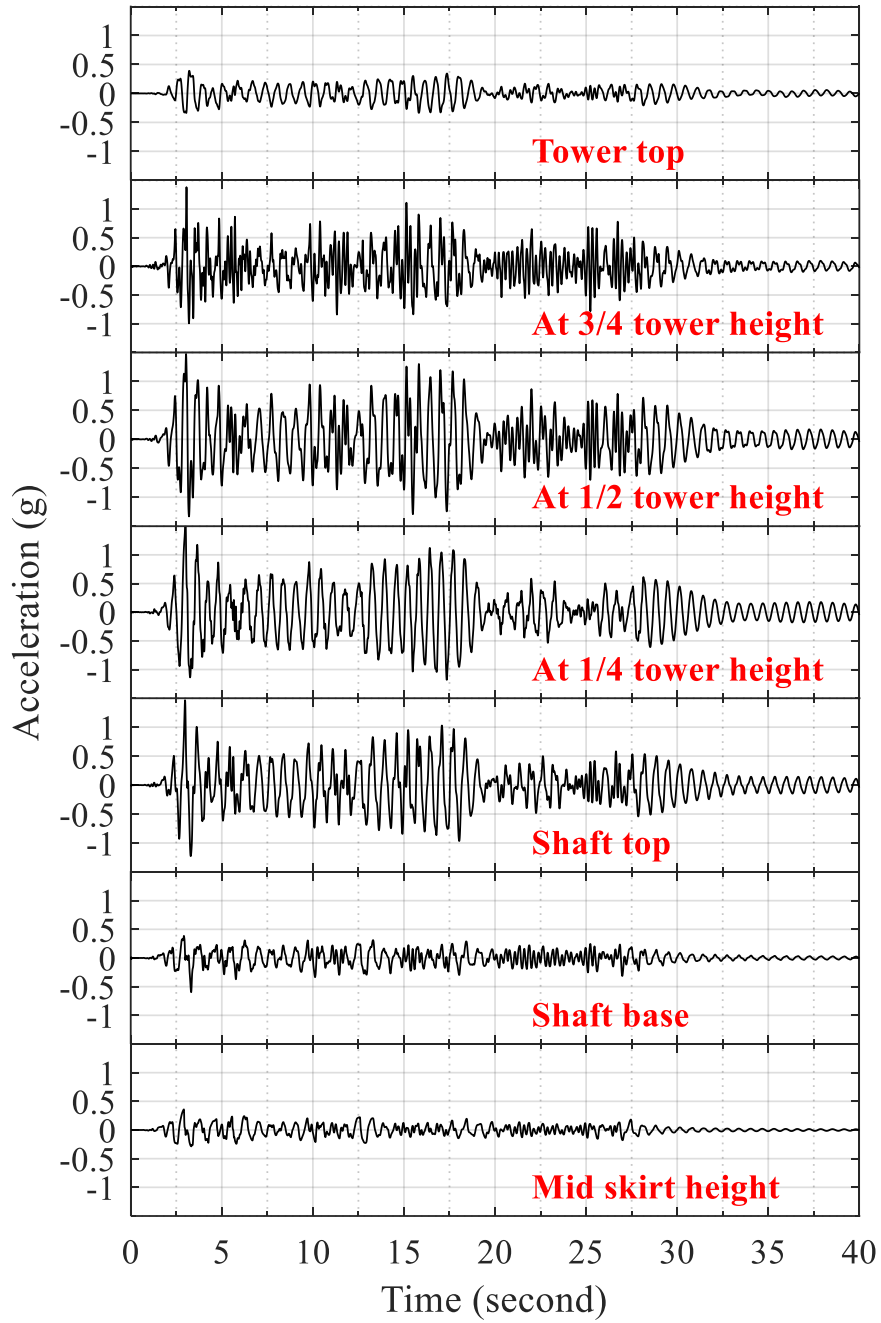
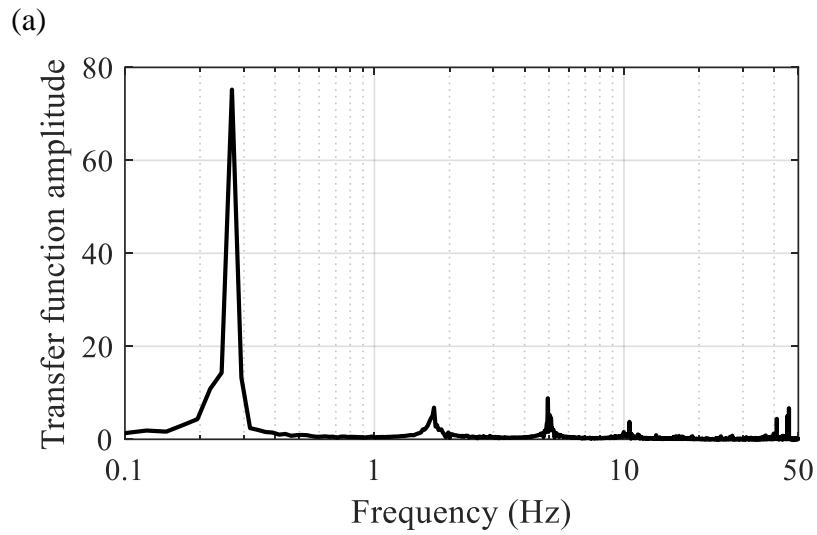
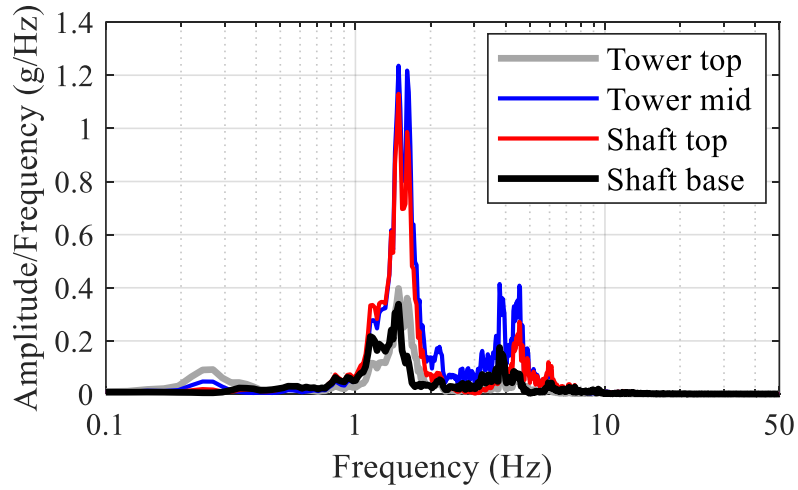


Figure 6-8: Plots of a) acceleration time histories at different heights along the OWT structure



(b)

Figure 6-9: Plots of b) frequency spectra of accelerations at different heights along the OWT structure, and c) transfer function between acceleration at tower top and soil-bucket acceleration at mid skirt height

With operational wind load effects

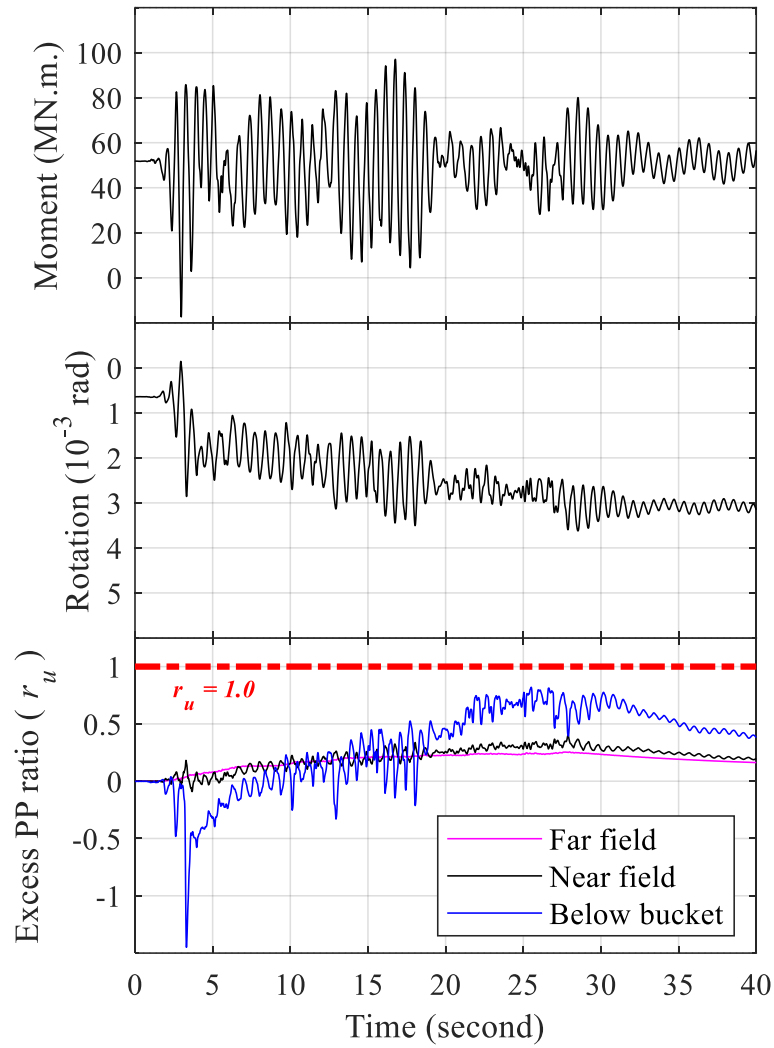


Figure 6-10: Plot of time histories of bucket moment (top plot), bucket rotation (middle plot) and near field  $r_u$  at mid skirt height (bottom plot) with operational wind load effects

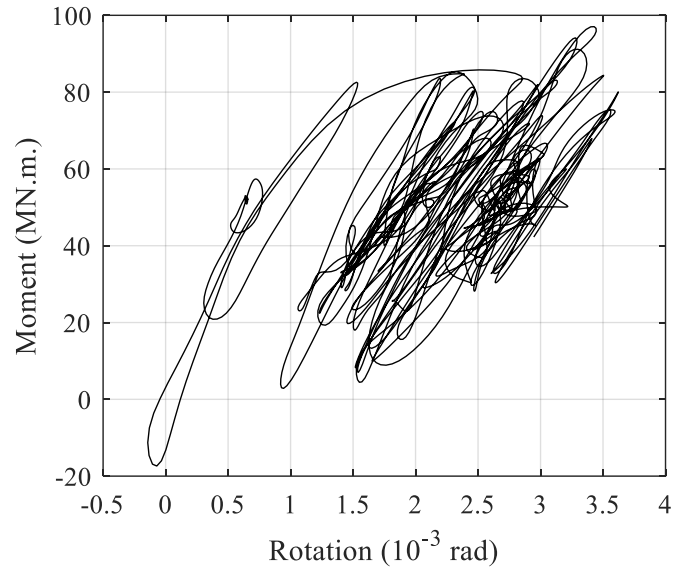


Figure 6-11: Plot of bucket moment-rotation response during shaking with operational wind load effects

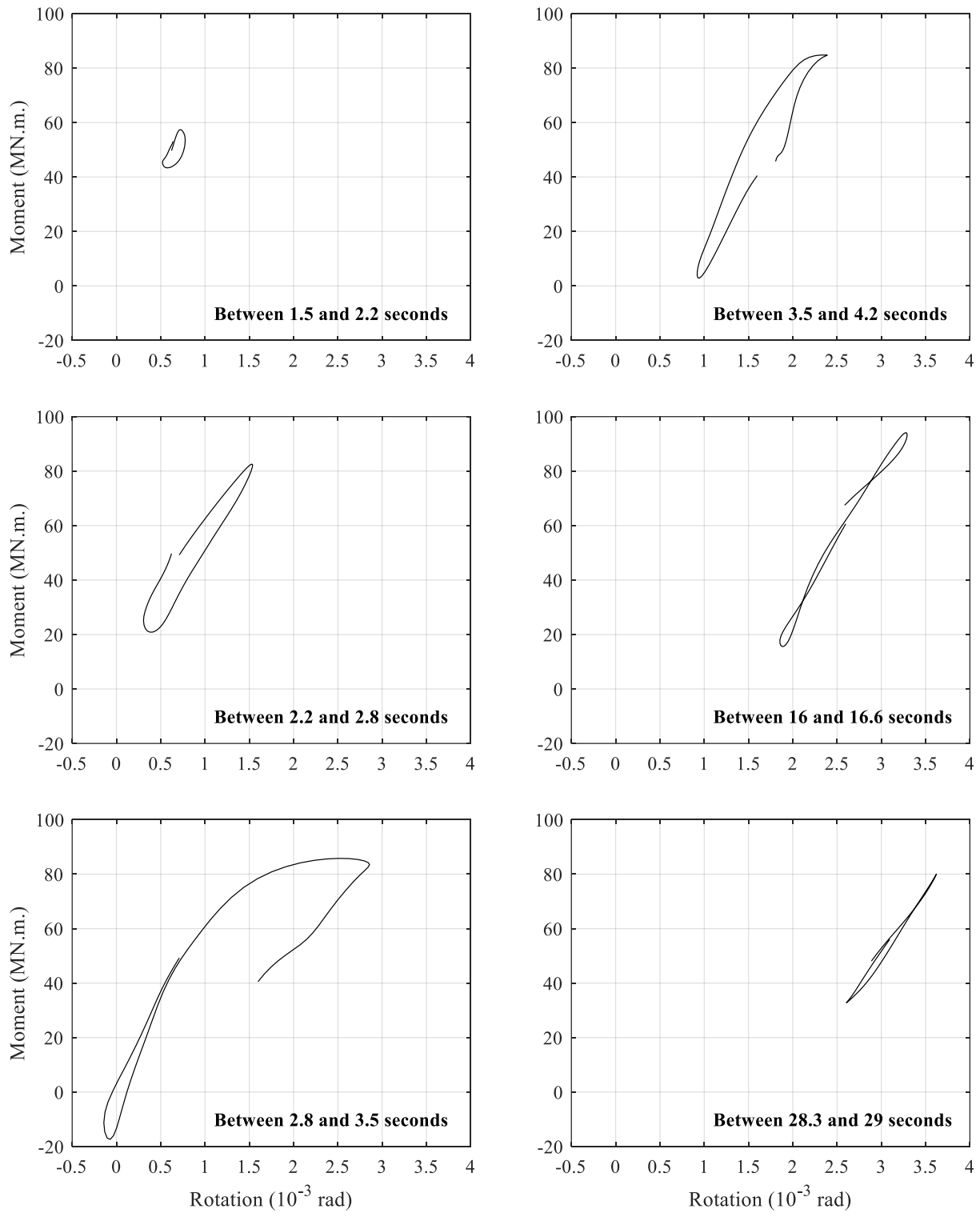


Figure 6-12: Bucket moment-rotation response at different time instances

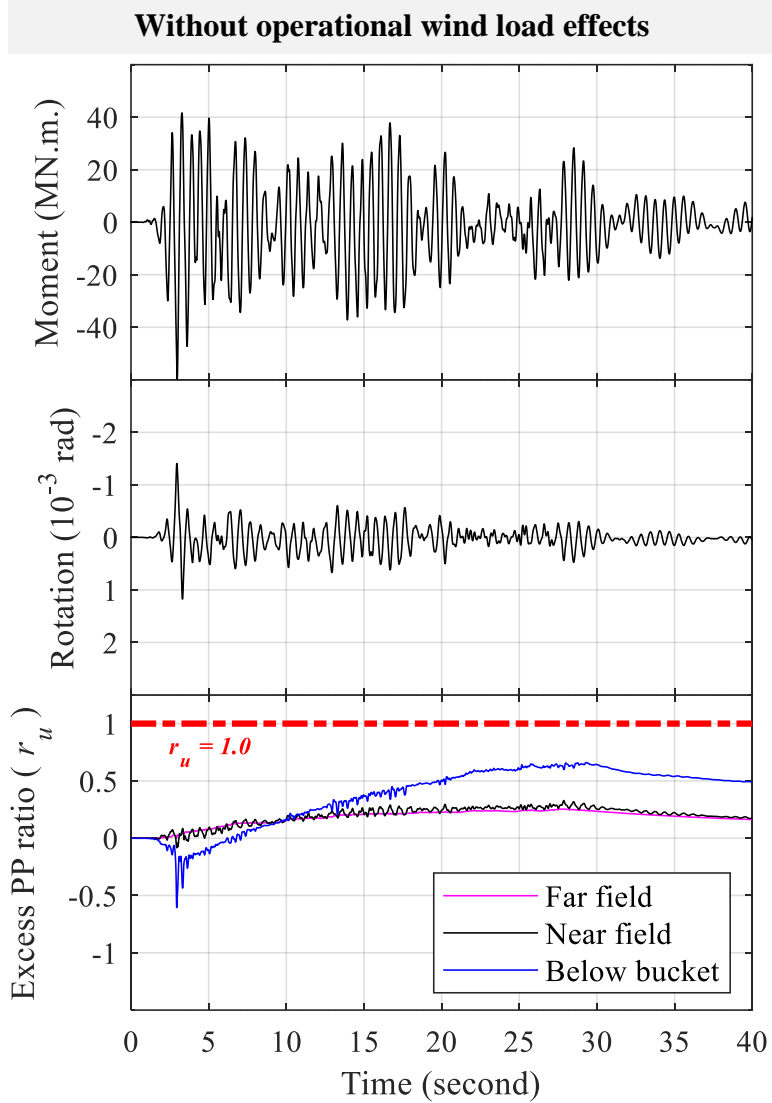
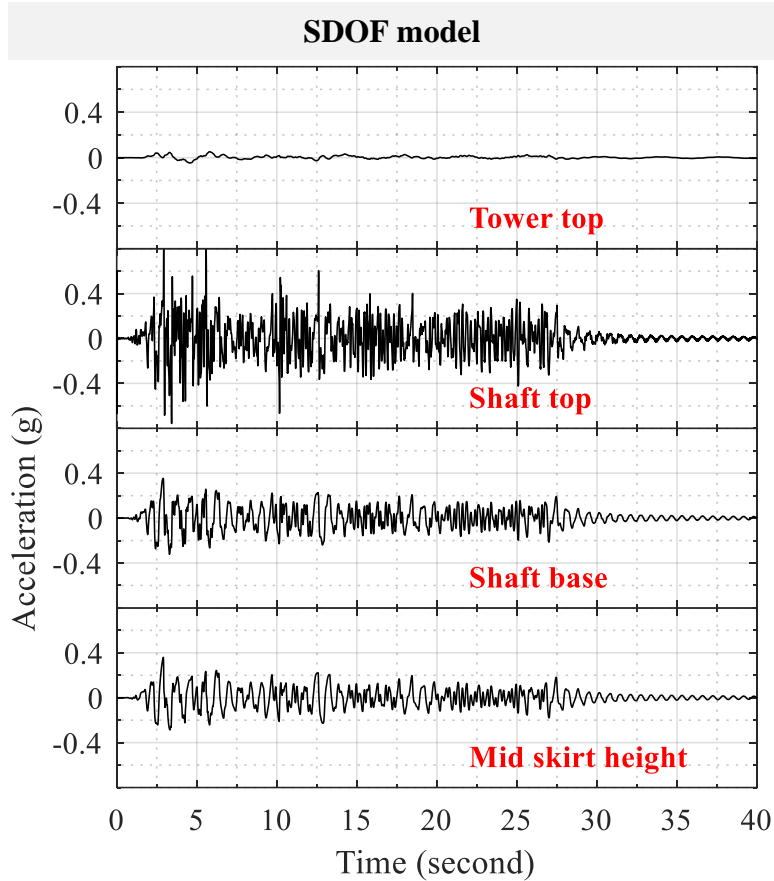
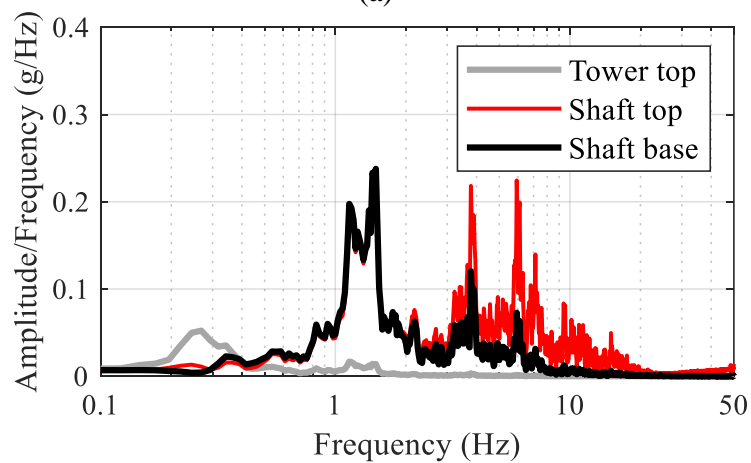


Figure 6-13: Time histories of bucket moment (top plot), bucket rotation (middle plot) and near field  $r_u$  at mid skirt height (bottom plot) for OWT without operational wind load effects



(a)



(b)

Figure 6-14: Plots of a) acceleration time histories, and b) frequency spectra of accelerations at different heights along OWT structure using SDOF structure



### Comparison between MDOF and SDOF

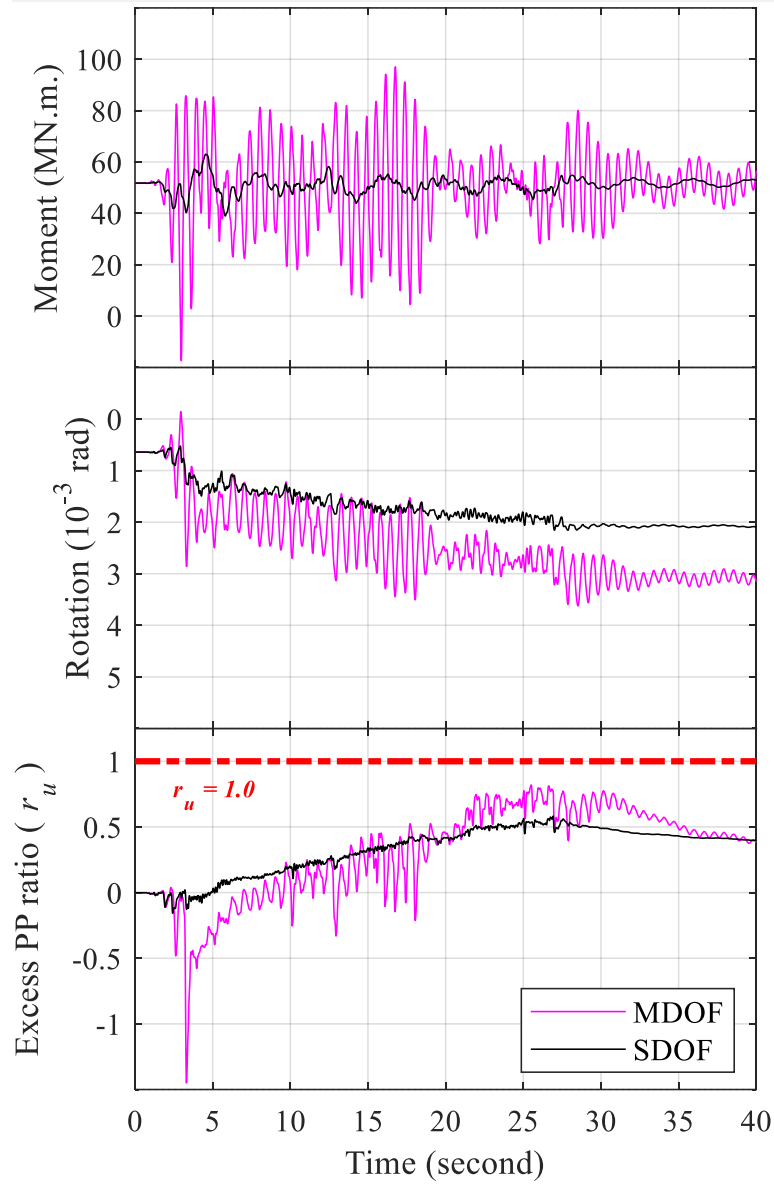


Figure 6-15: Comparison between moment, rotation and near field (i.e., beside the bucket) excess PP response for MDOF and SDOF structures

# Chapter 7

## Parametric study on seismic response of 3.45 MW offshore wind turbine with bucket foundation

*Sometimes science is more art than science, Morty. A lot of people don't get that.*

– Rick and Morty: Season 1, Episode 6

In this chapter, a parametric study is conducted to examine effects of soil stiffness, ground motion, soil permeability, bucket size and damping parameters on seismic response of the bucket foundation OWT. Prior to the parametric study, selection of bucket foundation dimensions is presented and discussed in light of achieving the natural frequency and stability requirements.

### 7.1 Selection of bucket foundation dimensions

#### 7.1.1 Design for fundamental frequency

Main properties of the OWT prototype are summarized in Table 6-1. Chapter 6 provided detailed description of the procedures to assess bucket foundation dimensions in order to meet the fundamental frequency requirement provided by the turbine manufacturer. Arany *et al.* (2016) indicated that OWTs of similar size would have a permissible interval for the fundamental frequency of the combined turbine-foundation structure between 0.255 Hz and 0.285 Hz (typically specified by the turbine manufacturer).

In the current study, distance  $H_p$  (Figure 6-1) is considered as 15 m and total shaft height (i.e., sum of water depth and  $H_p$ ) of 40 m is utilized. Using shaft top and bottom diameters of 4.5 m and 5.5 m, respectively, with top and bottom shaft wall thicknesses of 4 cm and 5.8 cm, respectively, a fixed-base fundamental frequency of 0.29 Hz (~ about 20% larger than 0.285 Hz) was achieved. Following the approach presented in Chapter 6, operational loads due to normal wind conditions represented by lateral force  $F_L$  and overturning moment  $M_o$  at shaft top (i.e., tower base) are estimated as 400 kN and 36 MNm, respectively, while self-weight total force  $F_V$  is 5.8 MN (Figure 6-2).

To investigate effect of bucket size on the OWT fundamental frequency, a total of 8 bucket models (B1 through B8) were generated each with different bucket diameter  $d$  and skirt length  $L$ . Two diameters of 12 m and 14 m are considered, each with four different  $L$  of 5 m, 6 m, 7 m, and 8 m (Table 7-1). The 3D FE continuum model developed in Section 6.1.2.1 was modified for each bucket model (B1 through B8). Soil is modeled to represent saturated sand with relative density of 75% while bucket foundation is represented by properties of structural steel material (Table 7-2). Operational wind loads are applied at the shaft-tower interface nodes and the maximum computed bucket rotation and lateral displacement are plotted in Figure 7-1-a and Figure 7-1-b, respectively, for different models ( $D_r$  of 75%).

Similar to Figure 6-4 (chapter 6), secant rotational and lateral stiffness of bucket foundation can be evaluated using those computed rotations and displacements. Natural frequencies of the flexible-base OWT can be calculated by conducting eigen frequency analysis of the base-springs model (Figure 6-5) while employing the bucket rotational and lateral stiffnesses.

Figure 7-1-c presents the fundamental frequency for different bucket dimensions with sand  $D_r$  of 75% where the highlighted zone denotes the permissible interval frequency range for the

combined OWT bucket foundation structure. Similar to Figure 7-1, Figure 7-2 shows the corresponding plots for buckets in sand with  $D_r$  of 90%. It can be noticed that sand of higher relative density resulted in less deformation and accordingly larger fundamental frequency (i.e., stiffer structure). Table 7-3 summarizes the corresponding rotational and translational stiffnesses as well as the first six natural frequencies for each model with sand  $D_r$  75% and 90%, while Figure 7-3 depicts a set of representative mode shapes. Figure 7-4 shows variation of the natural frequencies for different models compared with the fixed base condition ( $D_r$  of 75%). It can be noticed that the difference between natural frequency between fixed-base and three-springs models is the smallest at the fundamental frequency, and gets larger for higher modes.

To further validate the fundamental frequency of the soil-foundation-structure system, low amplitude motion is employed in the 3D FE continuum model base (Figure 6-2) resulting in Peak Ground Acceleration (PGA) of about 0.07 g near ground surface. Transfer function between tower top and soil-bucket acceleration for  $D_r$  of 75% and 90% are presented in Figure 7-5-a and Figure 7-5-b, respectively. These figures show that peak amplification occurs at frequencies that are in good agreement with those evaluated using the base-springs model (Table 7-3).

### **7.1.2 Design for stability under operational wind loads**

A detailed discussion for the stability design of bucket foundation under operational wind loads is presented in Section 6.1. Based on this discussion, the bearing capacity factor  $N_\gamma$  is estimated as 40 and 66 for  $D_r$  of 75% (friction angle = 36.5°) and 90% (friction angle = 38.5°), respectively, whereas  $S_\gamma$  is calculated as 0.6. As such,  $q_{ult-bucket}$  is evaluated as 2,240 kPa and 3,700 kPa for bucket B4 with  $D_r$  of 75% and 90%, respectively. For bucket B4 under operational wind loads, the maximum contact stress between soil and bucket (idealized as solid caisson) is estimated

as 560 kPa, resulting in a safety factor of about 4 (i.e., 2,240/560) and 6.6 (i.e., 3,700/560) against bearing capacity failure for  $D_r$  of 75% and 90%, respectively.

On the other hand, ultimate overturning moment of the bucket foundation is assessed numerically using the 3D FE continuum model in which an increasing quasi-static monotonic moment is applied at the bucket top while having total downward vertical force of 5.8 MN (pre-applied) to represent dead load of the super-structure. Each load step was maintaining for long duration such that the assumption of drained conditions is valid (pore pressure has no contribution to the response). The resulting moment-rotation relationship for B4 is shown in Figure 7-6-a, from which the ultimate overturning moment capacity for  $D_r$  of 75% and 90% can be considered as 200 MNm and 250 MNm, respectively. As such, the total moment on bucket top due to operational wind loads (i.e., 52 MNm) has a safety factor against overturning of about 3.8 and 4.8 for  $D_r$  of 75% and 90%, respectively.

The typical minimum safety factor against bearing capacity and overturning failure modes considered in design standards is 3.0 and 1.5, respectively. Therefore, bucket B4 with  $D_r$  of 75% and 90% is shown to provide an adequate safety margin for bearing capacity and overturning stability under operational wind loading. In Figure 7-6-b, different bucket models (B1 through B8) are employed to illustrate effect of bucket size on the drained overturning moment capacity. Table 7-4 summarizes safety factors for different bucket models in sand with  $D_r$  of 75% and 90%. This table shows that all bucket models provide adequate safety margins.

## **7.2 Influence of soil stiffness**

To investigate effect of soil stiffness, additional models with  $D_r$  of 80%, 90% and 100% are analyzed (Table 7-2). In this section, modified motion of the 1940 Imperial Valley Earthquake

El Centro station acceleration record NS component with 0.5 amplitude scaling is applied as input excitation at the FE model base (Figure 6-2). Only bucket model B4 is considered in this section.

Figure 7-7-b shows moment, rotation and  $r_u$  time histories for bucket installed in sand with  $D_r$  of 90%. Compared to 75%  $D_r$  (Figure 7-7-a), stiffer soil results in larger bucket moment, smaller permanent rotation and less pore pressure build-up. Unlike 75%  $D_r$ , far and near field  $r_u$  showed different build-up trends compared to the below bucket record. Moreover, stronger dilative response can be noticed for  $D_r$  of 90% below bucket  $r_u$  records.

Most of the permanent rotation in Figure 7-7-b is noticed to accumulate before 20 seconds when cyclic moment response was the largest, despite the strong dilative response (induced by the suction mechanism) observed in the below bucket  $r_u$  record. On the other hand, the near field  $r_u$  generally showed contractive response (i.e., soil softening) increasing to about 0.3 at 20 seconds. Although the below bucket  $r_u$  kept increasing after 20 seconds to a maximum value of 0.8, no significant accumulation in bucket rotation was noted. This can be attributed to the fact that the near field excess PP response did not show significant increase after 20 seconds. The latter observations might enforce the earlier suggestion of bucket rotation dependency on pore pressure build-up characteristics, particularly the near field  $r_u$  response. Nevertheless, the strong dilative response (i.e., soil stiffening due to increase in effective stresses) observed below the bucket might be considered helpful in improving the overall rotational stiffness of the foundation.

In this regard, an increase in pore pressure outside the bucket in the near field would result in soil softening due to reduction in effective stress, which subsequently leads to degradation in the foundation rotational stiffness and thereafter rotation accumulation. To further investigate the latter observation, Figure 7-8-a presents time histories of B4 bucket rotation and near field  $r_u$  for four different  $D_r$  values (Table 7-2). Consistent increase in the accumulated bucket rotation can be

noticed with decreasing  $D_r$  due to the stronger pore pressure build-up (i.e., larger  $r_u$  value). As such, the change of permanent bucket rotation is plotted with  $D_r$  and the maximum near field  $r_u$  as shown in Figure 7-8-b and Figure 7-8-c, respectively.

### **7.3 Influence of ground motion**

In addition to E50, motions N28 and T16 are modified after the 1994 Northridge earthquake (14145 Mulholland Dr., Beverly Hills station record - Component N09E) and the 1995 Kobe earthquake (Takatori station record – Component 90). In this section, only bucket model B4 is considered with  $D_r$  of 75% and 90%. Table 7-5 summaries the employed amplitude scale factor for each earthquake record with  $D_r$  of 75% and 90%.

#### **7.3.1 Earthquake motions**

In this section, all motions are scaled to result in similar Peak Ground Acceleration (PGA) at the top free-field ground surface in the FE model. As such, the OWT bucket foundation would be exposed to different excitations all with the same PGA.

For  $D_r$  of 90%, motions E50-II, N38 and T31 (Table 7-5) resulted in surface PGA of about 0.36 g (Table 7-5) with surface acceleration time histories and response spectra shown in Figure 7-9. Comparison between bucket response under different motions is presented in Figure 7-10, from which it can be noticed that the permanent rotation toward the end of shaking was essentially the same for all motions. While the below bucket  $r_u$  responses are different, the similarity in permanent rotation might be partially attributed to the resemblance of the near field  $r_u$  records.

Similar observations were noticed for E50-I, N28 and T16 motions with  $D_r$  of 75%. Figure 7-11 combines time histories of bucket rotation and near field  $r_u$  for  $D_r$  of 75% and 90%. The latter

figure shows that T16 with  $D_r$  of 75% and E50-II with  $D_r$  of 90% result in similar maximum near field  $r_u$  and similar permanent bucket rotation. This suggests a possible correlation between near field  $r_u$  and bucket rotation, which might be useful not only for different soil stiffness but also for different ground motions.

### **7.3.2 Earthquake intensities**

Figure 7-12 shows comparison of bucket response for E75, N50-I and T50 motions with  $D_r$  of 75%. The latter motions were scaled such that the resulting near field  $r_u$  is of similar maximum value. As such, N50-I and T50 resulted in similar permanent rotation. Yet, larger rotation was accumulated for E75, particularly after 25 seconds. The latter can be explained by the larger bucket moment values in the E75 record after 25 seconds (Figure 7-12 right column). Projecting maximum near field  $r_u$  and the corresponding permanent rotation for different motions on Figure 7-8-c (originally generated for bucket B4 with different  $D_r$  using E50 motions), Figure 7-13 for bucket B4 demonstrates that all points are in good agreement with the trend line.

## **7.4 Influence of soil permeability**

The above discussed results are for B4 bucket model with soil permeability of 1E-4 m/s. In this section, additional permeability values are considered: 1E-2 m/s and 1E-6 m/s, while maintaining all other model parameters (e.g., soil properties, bucket size, ground motion and damping coefficients) unchanged. Thus, differences in the computed response were solely due to permeability effects, in order to highlight its significance. Permeability coefficients of the order of 1E-2 m/s, 1E-4 m/s and 1E-6 m/s represent values for gravel, sand and silt, respectively, as recommended in the OpenSEES manual (Mazzoni *et al.* 2006) and calibrated by Yang and Elgamal (2002). Results of the numerical simulations for bucket B4 are presented in Figure 7-14-a and



Figure 7-14-b for three different  $k$  values with  $D_r$  of 75 % using E50-I motion (left column) and 90 % using E50-II motion (right column), respectively.

For  $D_r$  of 75%, model  $k_3$  with lowest permeability of 1E-6 m/s (silt range) resulted in larger PP build-up with  $r_u$  reaching unity at about 20. The gravel-like permeability of 1E-2 m/s (i.e.,  $k_1$ ) resulted in insignificant PP build-up with maximum  $r_u$  value of about 0.1. As such, model  $k_3$  resulted in the largest permanent rotation as illustrated in the middle plot of Figure 7-14-a. All models showed similar bucket moment response (top plot). On the other hand, stiffer soil with  $D_r$  of 90% (Figure 7-14-b) resulted in larger bucket moments and slower rate of PP build-up. Despite the different near field  $r_u$  trends for each  $k$  value, all models with  $D_r$  of 90% resulted in similar permanent rotations demonstrating that permeability had a diminished influence on permanent rotation the bucket installed in sands with very large  $D_r$ .

The change in B4 permanent bucket rotation with permeability for different  $D_r$  values using E50 motions is presented in Figure 7-15. The latter figure enforces the earlier observation that permeability would have more significant effect on rotation response of buckets installed in sands with low  $D_r$ , while the influence might be of less significance for stiffer sand (larger  $D_r$ ). In this regard, it was noticed that lower permeability would result in larger rotation due to the higher pore-pressure build-up, and vice versa. Furthermore, permanent bucket rotation can be noticed to stabilize and reach a plateau for each  $D_r$  at the lower and upper ends of the investigated permeability range, reflecting the fully undrained and drained conditions, respectively. The observed transition in the permanent rotation between drained and undrained conditions can represent the partially drained case.

In addition, it can be noticed that the effect of partially drained conditions tends to diminish with larger  $D_r$  values. Except for  $D_r$  of 100%, the fully undrained conditions (i.e., small  $k$  values)

show larger permanent rotation compared to drained scenarios. On the other hand, fully undrained conditions result in less accumulated rotation for 100%  $D_r$ . The latter can be explained by the pure dilative response (no contraction tendency with  $c$  parameters set as zero in Table 6-2) of the sand with  $D_r$  of 100% as shown in Figure 7-16.

## 7.5 Influence of bucket size

Effects of bucket size are investigated via examining response of different buckets (B1 through B8) in sand with  $D_r$  of 90% and permeability of 1E-4 m/s due to E50-II motion. Figure 7-17 illustrates comparison between different bucket responses for three scenarios as follows:

### 7.5.1 Similar bucket diameter (effect of skirt length)

To examine effect of skirt length  $L$ , models B1 and B4 (all with  $d$  of 12 m) and  $D_r$  of 90% are analyzed (Figure 7-17-a). Both models resulted in similar near field  $r_u$  build-up with maximum value of about 0.4 (bottom plot of Figure 7-17-a). Model B4 with longer skirt shows less rotation accumulation at end of shaking (middle plot of Figure 7-17-a), which can be attributed to the associated increase in rotational stiffness (Table 7-3). Nevertheless, lower moment demands for B1 (shorter skirt) can be observed when compared with B4 (top plot of Figure 7-17-a). Deformed mesh and permanent at end of shaking and the corresponding bucket rotation for B1 and B4 are shown in Figure 7-18. From the latter figure, a larger separation gap can be observed for B1 between bucket lid and the underlying soil compared to B4. The latter might explain the stronger oscillation in  $r_u$  and rotation time histories of B1 compared to B4.

### 7.5.2 Similar skirt length (effect of bucket diameter)

Effects of bucket diameter can be examined when comparing response of models B1 and B5 with  $d$  of 12 m and 14 m, respectively ( $L = 5$  m). As presented in Figure 7-17-b, both models showed very similar near field  $r_u$  response. However, moment demands on B5 are slightly larger compared to B8 (top plot of Figure 7-17-b). Subsequently, larger rotation was accumulated for B1 as shown in Figure 7-17-b middle plot.

### 7.5.3 Similar fundamental frequency (different size)

Although having different bucket size, B4 ( $d = 12$  m,  $L = 8$  m) and B6 ( $d = 14$  m,  $L = 6$  m) have similar natural frequency of about 0.278 Hz (Table 7-3 for  $D_r$  of 90%). A comparison between bucket responses of B4 and B6 is shown in Figure 7-17-c, from which it can be noticed that both models show almost identical bucket rotation and near field  $r_u$  time histories. Moment demands on both buckets can be observed to have a large degree of similarity with B4 having slightly larger peaks (top plot of Figure 7-17-c).

In spite of having different dimensions, the similarity in responses of B4 and B6 indicates that the OWT bucket foundation seismic response correlates with the fundamental frequency of the combined soil-foundation-structure system (for soil of the same permeability and  $D_r$ ). As such, increasing the fundamental frequency would result in reducing the permanent rotation due to the associated increase in the foundation rotational stiffness which contributes to decreasing the rotation accumulation during the shaking phase. The latter observation can be further confirmed by the earlier comparison between B1 and B4 (Figure 7-17-a).

Despite having larger  $r_u$  and rotation accumulation, similar observations were noticed for model with  $D_r$  of 75%. The permanent bucket rotation at the end of shaking is shown for models B1 through B8 in Figure 7-19 where different buckets are represented by their corresponding fundamental frequency (Table 7-3). This figure show results for  $D_r$  of 75% and 90%. A nearly linear trend of permanent rotation within the investigated range of fundamental frequencies can be established for bucket models with same  $D_r$ . It can be noticed that the fitted trend lines for different  $D_r$  tend to converge at larger bucket size (i.e., larger fundamental frequency), which might indicate that effect of soil stiffness tends to diminish at the larger bucket sizes (i.e., stiffer foundation). The latter can be explained by the fact that at fixed-base conditions with fundamental frequency of about 0.29 Hz, soil stiffness does not affect the system natural frequencies. Furthermore, the ratio between the permanent rotation at  $D_r$  of 75% to that of 90% ranges between 1.5 to 2 for lower and upper bounds of the investigated fundamental frequencies (i.e., 0.255 Hz and 0.285 Hz), respectively.

## 7.6 Influence of damping

In this section, effects of changing the Rayleigh damping coefficients in the numerical model are investigated. Bucket B4 in sand of 75%  $D_r$  with E50-I motion is considered in this section. As indicated earlier, the previous analysis is based on selecting Rayleigh damping mass ( $a_m$ ) and stiffness ( $a_k$ ) proportional coefficients such that damping ratio of about 2% is employed for the 1<sup>st</sup> and 3<sup>rd</sup> vibration modes, respectively, of the OWT bucket foundation structure. The latter model is represented herein by D2. Three additional models (D1, D3 and D4) with different mass and stiffness proportional coefficients ( $a_m$  and  $a_k$ ) were selected such that the damping ratio for the first vibration mode is maintained the same (about 2%). Table 7-6 shows the employed

mass and stiffness coefficients for each model and the corresponding damping ratios for the first 6 vibration modes. Model D1 was selected to have mass proportional damping only ( $a_k = 0$ ) while D4 has a stiffness coefficient only ( $a_m = 0$ ). The D3 model has larger  $a_k$  and lower  $a_m$  compared to D2 (i.e., the original model). From Table 7-6, it can be noticed that the value of  $a_m$  decreases (while  $a_k$  increases) when moving from D1 to D4 and damping ratios for higher (2<sup>nd</sup> to 6<sup>th</sup>) modes increase as a result. With  $a_m$  coefficient only, model D1 is noticed to have the lowest damping ratios for higher modes while D4 being with zero  $a_m$  has the largest ratios.

Figure 7-20-a and Figure 7-20-b show time histories of soil acceleration and the corresponding response spectra below the bucket at mid skirt height. It can be noticed that model D1 showed significantly larger spectral acceleration for frequencies between 6 Hz and 100 Hz when compared to other models. This can be explained by the significantly low higher modes damping ratios (less than 1%) for model D1 when compared to D2 through D4 (Table 7-6). As such, the accelerations along the OWT shaft and tower in D4 were of lower amplitude which resulted in less moment demands on the bucket foundation compared to the other models, as illustrated in Figure 7-20-c. As a result, model D4 showed the lowest accumulated bucket rotations (Figure 7-20-d). Although the difference in the bucket moment demands between D1 through D3 is not significantly large, the top plot of Figure 7-20-d demonstrates that D3 showed about one third the residual/permanent rotation of D1 at the end of shaking. The latter can be explained by the bottom plot of Figure 7-20-d where  $r_u$  at mid skirt height for D3 shows maximum of about 0.4 while D1 reached one. Similar observations were noted in previous sections about the effect of pore pressure build-up on the accumulation of bucket rotations.

The results discussed in this section indicate that damping of the higher modes might have significant effect on the bucket moment rotation response. Larger damping of the higher modes

would result in lower pore pressure build-up which leads to less degradation in the foundation rotational stiffness. On the other hand, the damped higher modes would result in lower moment demands on the bucket foundation as the propagated accelerations along the OWT structure would have less contribution from the higher modes. Therefore, employing realistic damping ratios can be crucial to the OWT seismic response. Overdamping would lead to unconservative response while underestimating the damping might result in unrealistic increase in the foundation deformation that might be attributed to larger excess pore pressure build-up.

## 7.7 Summary and Conclusions

As an extension to the work conducted in the previous chapter, a parametric study is conducted to investigate influence of: i) soil stiffness, ii) ground motion, iii) soil permeability and iv) bucket size, on the bucket foundation OWT seismic response. The numerical framework and the insights derived from this study are of general relevance to bucket foundation seismic response for offshore wind applications. Specific observations and conclusions include (strictly within limits of the scope of the conducted investigations):

- A correlation between the near field pore pressure build-up and the bucket rotation can be observed, resulting in foundation stiffness degradation due to soil softening associated with excess pore pressure build-up.
- Ground motion characteristics have a direct impact on the permanent bucket rotation with the latter also depending on the resulting near field pore pressure response.
- Soil permeability can be of much significance to the bucket moment-rotation response. In this regard, it was noticed that: i) at lower values of  $D_r$ , lower permeability would result in larger rotation due to the greater excess pore-pressure build-up, and ii) For very high  $D_r$ ,

lower permeability can result in relatively less rotation due to stronger dilative response which results in larger contribution of the suction mechanism to the overall bucket foundation response (as well as minimal excess pore pressure build-up in the free-field).

- For a given bucket size, permanent bucket rotation tends to stabilize at the lower and upper ends of the soil permeability range, reflecting the fully undrained and drained conditions, respectively.
- The observed change in permanent rotation between drained and undrained conditions represents the partially drained scenarios.
- The difference in permanent bucket rotation between undrained and drained conditions tends to decrease with increasing soil stiffness.
- Buckets with different dimensions with essentially identical fundamental frequency of the combined OWT-foundation system, will result in similar seismic response.
- Within the range of investigated scenarios, an essentially linear correlation was noted between the OWT fundamental frequency and the permanent bucket rotation.
- For ground motions similar to 1940 Imperial Valley (El Centro record), 1994 Northridge (Mulholland Drive record), and 1995 Kobe (Takatori record) earthquakes scaled to PGA of about 0.3 g (for medium dense sand -  $D_r$  75%) and 0.4 g (for very dense sand -  $D_r$  90%):
  - i. The investigated 3.45 MW OWT with bucket foundation of diameter  $d$  12 m and skirt length  $L$  8 m (model B4) showed adequate response under combined operational wind and earthquake loading in medium-dense and very dense saturated sands, with overall rotation not exceeding the serviceability limit of 0.5 degrees.

- ii. On the other hand, bucket foundation of diameter  $d$  12 m and skirt length  $L$  5 m (model B1) showed inadequate response in medium dense and very dense saturated sands with permanent rotation exceeding the serviceability limit.
- iii. For this bucket (B1 of  $d = 12$  m and  $L = 5$  m) to meet the rotation serviceability limit:
  - 1. A necessary increase in skirt length of about 60% would be required in medium dense sand (about 20% in very dense sand).
  - 2. Alternatively, an increase in bucket diameter of about 17% in medium dense sand (about 9% in very dense sand) would be mandatory to meet the rotation serviceability limit.
  - 3. Further increase in bucket dimensions would be necessary to withstand stronger ground motions.
- Damping of the higher modes might have significant effect on the bucket moment rotation response, such that:
  - i. Larger damping of the higher modes would result in lower pore pressure build-up which leads to less degradation in the foundation rotational stiffness. On the other hand, the damped higher modes would result in lower moment demands on the bucket foundation as the propagated accelerations along the OWT structure would have less contribution from the higher modes.
  - ii. Therefore, employing realistic damping ratios can be crucial to the OWT seismic response. Overdamping would lead to unconservative response while underestimating the damping might result in unrealistic increase in the foundation deformation that might be attributed to larger excess pore pressure build-up.



Further studies may be conducted to assess effect of a layered soil profile on the overall seismic response. Furthermore, comparison between bucket foundation and monopile for the same OWT can be investigated as part of future research.

## **7.8 Acknowledgement**

The research described in this chapter was partially funded by the National Science Foundation grant OISE-1445712 as well as the Trent R. Dames and William W. Moore graduate student fellowship from the American Society of Civil Engineers (ASCE). Testing was conducted at the Powell laboratories, University of California San Diego, with assistance provided by Dr. Christopher Latham, Mr. Andrew Sander, Mr. Mike Sanders, Mr. Abdullah Hamid and Mr. Darren Mckay. The authors also would like to graciously thank Dr. Jinchu Lu, Dr. Zhijian Qui, and Dr. John Li for their useful insights.

The parametric study presented in chapter 7 is currently being prepared to be published as a journal paper tentatively in the ASCE Journal of Geotechnical and Geoenvironmental Engineering or the Soil Dynamics and Earthquake Engineering Journal. The proposed title of this paper is “Seismic response of bucket foundation utility-scale wind turbine: Effects of bucket size, soil stiffness and permeability”. The dissertation author is the primary author of this paper with Dr. Kyungtae Kim, and Professor Ahmed Elgamal as coauthors.

Table 7-1: Description of different bucket models B1 through B8

		<b>Bucket length <math>L</math> (m)</b>			
		<b>5</b>	<b>6</b>	<b>7</b>	<b>8</b>
<b>Bucket diameter <math>d</math> (m)</b>	<b>12</b>	B1	B2	B3	B4
	<b>14</b>	B5	B6	B7	B8

Table 7-2: Parameters of PDMY02 and PIMY models for full-scale cases

Model parameter	PDMY02* (Sand soil)				PIMY (Steel)
	75%	80%	90%	100%	
Relative density, $D_r$ (%)	75%	80%	90%	100%	-
Mass density, $\rho$ (kg/m <sup>3</sup> )	2,100				7,850
Reference shear modulus, $G_r$ (MPa)	130	160	215	290	80,000
Reference bulk modulus, $B_r$ (MPa)	260	420	1,000	1,350	140,000
Peak friction angle, $\varphi$ (degrees)	36.5	37	38.5	40	60
Phase transformation angle, $\varphi_{PT}$ (degrees)	26				-
Peak shear strain, $\gamma_{max}$ (%)	10				
Reference mean effective confining pressure, $p'$ (kPa)	101				
Pressure dependent coefficient, $n$	0.5				-
Contraction coefficient $c_1$	0.013	0.008	0.003	0	
Contraction coefficient $c_2$	5				
Contraction coefficient $c_3$	0				
Dilation coefficient $d_1$	0.3	0.38	0.5	0.6	
Dilation coefficient $d_2$	3				
Dilation coefficient $d_3$	0				
Number of yield surfaces, $NYS$	20				
Shear strength at zero confinement, $c$ (kPa)	1				-
Cohesive strength, $c$ (GPa)	-				100
Permeability, $k$ (m/s)	1E-4				1E-20

\* Properties are selected to represent dense sand with  $D_r$  of 75%, 80%, 90% and 100% (Elgamal *et al.* 2003, Mazzoni *et al.* 2006)

Table 7-3: Rotational and translational stiffness as well as natural frequencies ( $f_n$ ) of 3.45 MW OWT bucket foundation for different buckets (B1 through B8) evaluated under operational wind loads in sand with  $D_r$  of 75% and 90%

		Fixed base	d = 12 m				d = 14 m				
			L=5 m "B1"	L=6 m "B2"	L=7 m "B3"	L=8 m "B4"	L=5 m "B5"	L=6 m "B6"	L=7 m "B7"	L=8 m "B8"	
<b><math>D_r = 75\%</math></b>	$K_{RR}$ (GNm/rad)	-	23.8	37.2	50.9	66.3	46.9	63.1	80.4	98.8	
	$K_{LL}$ (MN/m)	-	129	183	232	281	270	339	403	465	
	Natural frequency ( $f_n$ )	1 <sup>st</sup>	0.29	0.262	0.27	0.274	0.277	0.273	0.278	0.279	0.28
		2 <sup>nd</sup>	2	1.65	1.74	1.8	1.84	1.8	1.84	1.87	1.89
		3 <sup>rd</sup>	5.5	4.42	4.67	4.83	4.95	4.85	4.98	5.08	5.15
		4 <sup>th</sup>	11.4	8.35	8.61	8.99	9.29	9.19	9.53	9.78	9.97
		5 <sup>th</sup>	19.2	12.9	13.48	13.91	14.29	14.20	14.69	15.06	15.43
6 <sup>th</sup>	28.8	20.29	20.84	21.24	21.56	21.41	21.85	22.20	22.51		
<b><math>D_r = 90\%</math></b>	$K_{RR}$ (GNm/rad)	-	30.4	47	62.3	80.9	56.4	74.9	94.9	117	
	$K_{LL}$ (MN/m)	-	190	267	308	364	400	459	533	609	
	Natural frequency ( $f_n$ )	1 <sup>st</sup>	0.29	0.2667	0.273	0.277	0.279	0.276	0.279	0.28	0.282
		2 <sup>nd</sup>	2	1.71	1.79	1.83	1.87	1.83	1.86	1.89	1.91
		3 <sup>rd</sup>	5.5	4.63	4.85	4.95	5.06	4.99	5.09	5.16	5.22
		4 <sup>th</sup>	11.4	8.66	9.18	9.41	9.66	9.68	9.89	10.1	10.2
		5 <sup>th</sup>	19.2	13.43	14.05	14.5	14.85	14.77	15.25	15.63	16
6 <sup>th</sup>	28.8	20.77	21.32	21.76	22	21.96	22.34	22.82	22.95		

Table 7-4: Safety factors against bearing capacity and overturning failure modes for different buckets

	Failure mode	d = 12 m				d = 14 m			
		L=5 m "B1"	L=6 m "B2"	L=7 m "B3"	L=8 m "B4"	L=5 m "B5"	L=6 m "B6"	L=7 m "B7"	L=8 m "B8"
$D_r = 75\%$	Bearing capacity	3.6	3.7	3.9	4	6.2	6.3	6.5	6.7
	Overturning	1.7	2.2	2.9	3.8	2.4	3.1	4.1	5.3
$D_r = 90\%$	Bearing capacity	6.5	6.7	6.9	7.2	11.1	11.4	11.8	12.1
	Overturning	2.2	2.9	3.6	4.8	2.9	3.8	5.1	6.3

Table 7-5: Description of the modified earthquake motions

ID	Moment Magnitude (M <sub>w</sub> )	Epicenter distance (km)	Earthquake	Station (component)	Amplitude scale factor of base motion	Surface motion PGA (g)
E50-I*	6.9	13	1940 Imperial Valley	El Centro (NS)	0.5	0.29
E50-II**					0.5	0.36
E75†					0.75	0.45
N28*	6.7	12.7	1994 Northridge	14145 Mulholland Drive (N09E)	0.28	0.28
N38**					0.38	0.35
N50†					0.5	0.45
T16*	6.9	1.5	1995 Kobe	Takatori (90)	0.16	0.28
T31**					0.31	0.36
T50†					0.5	0.68

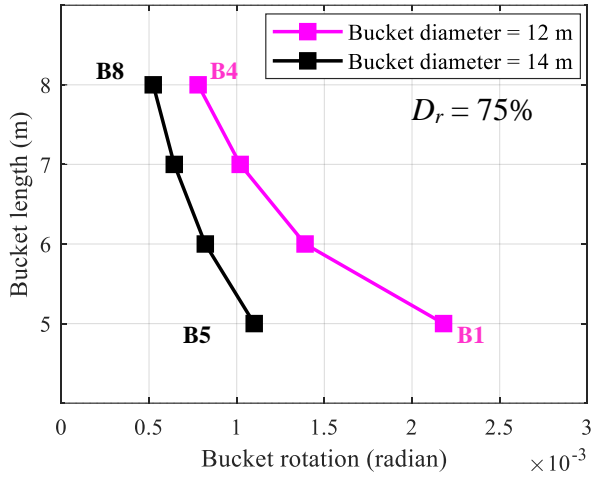
\* Motions employed with  $D_r$  of 75%

\*\* Motions employed with  $D_r$  of 90%

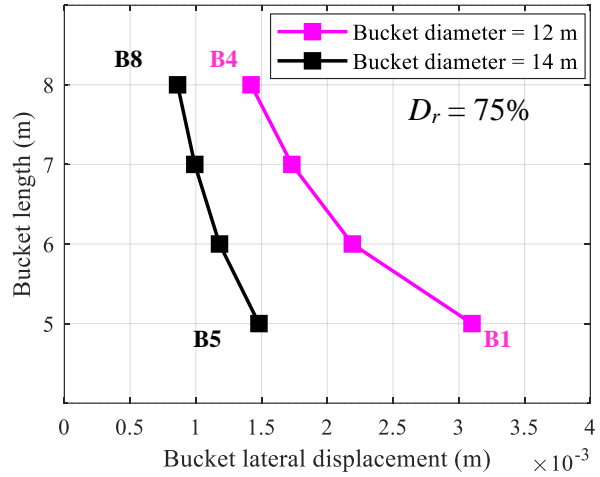
† Motions employed with  $D_r$  of 90% resulting in similar maximum near field  $r_u$  (Figure 7-12)  
 Same color rows indicate motions of similar ground surface PGA

Table 7-6: Damping ratios at the first 6 modes of vibration for different Rayleigh damping coefficients (highlighted cells are the target damping ratios for the first and third modes)

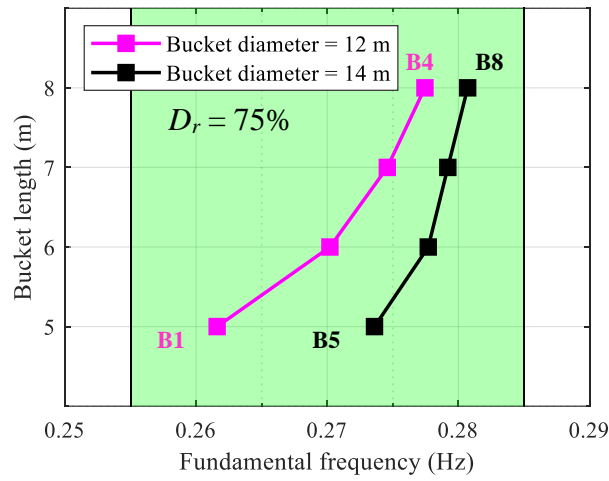
Mode	$f_n$ (Hz)	$\xi$ (%)			
		<b>D1</b> $a_m = 0.07$ $a_k = 0$	<b>D2</b> $a_m = 0.067$ $a_k = 0.0011$	<b>D3</b> $a_m = 0.05$ $a_k = 0.007$	<b>D4</b> $a_m = 0$ $a_k = 0.023$
1 <sup>st</sup>	0.278	2	2	2	2
2 <sup>nd</sup>	1.84	0.3	1	4.3	13
3 <sup>rd</sup>	4.95	0.1	2	10	36
4 <sup>th</sup>	9.29	0.06	3	20.5	67
5 <sup>th</sup>	14.29	0.04	5	31.5	103
6 <sup>th</sup>	21.56	0.03	7.5	47	156



(a)



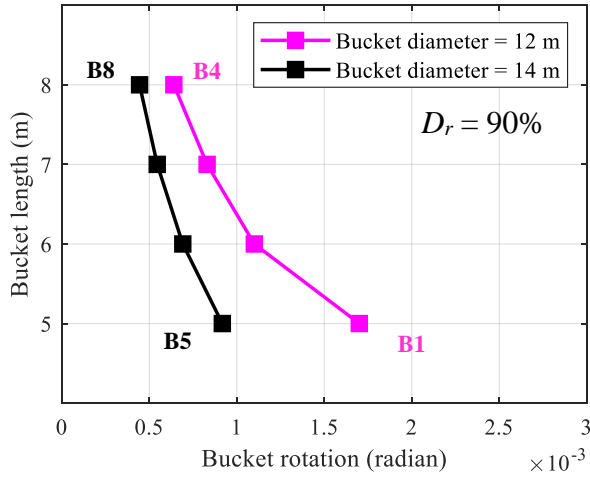
(b)



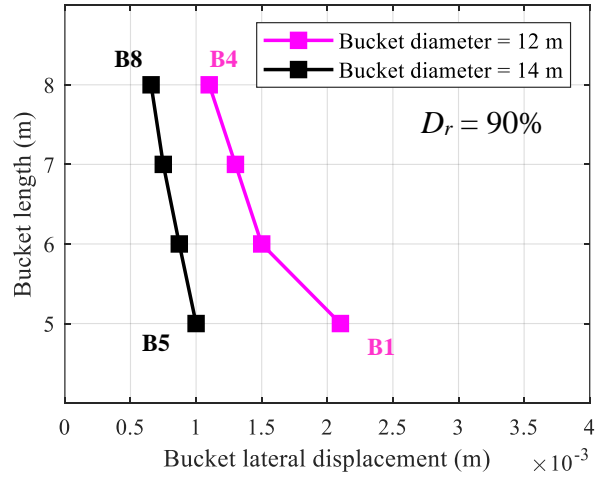
(c)

Figure 7-1: Change of a) bucket rotation, b) bucket lateral displacement, and c) structure fundamental frequency with bucket diameter and skirt length under monotonic quasi-static operational wind loads ( $D_r = 75\%$ )

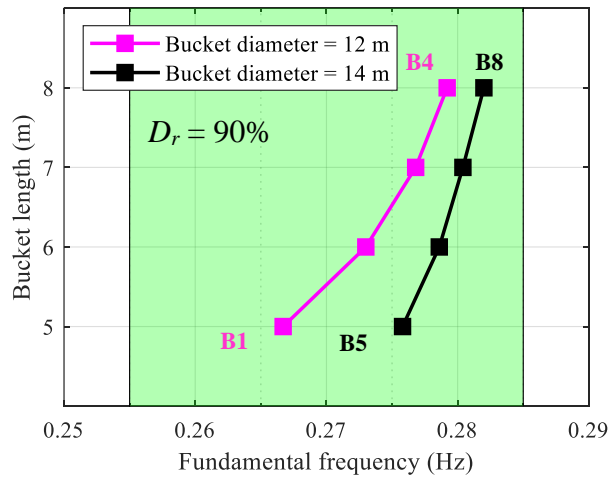




(a)



(b)



(c)

Figure 7-2: Change of a) bucket rotation, b) bucket lateral displacement, and c) structure fundamental frequency with bucket diameter and skirt length under monotonic quasi-static operational wind loads ( $D_r = 90\%$ )

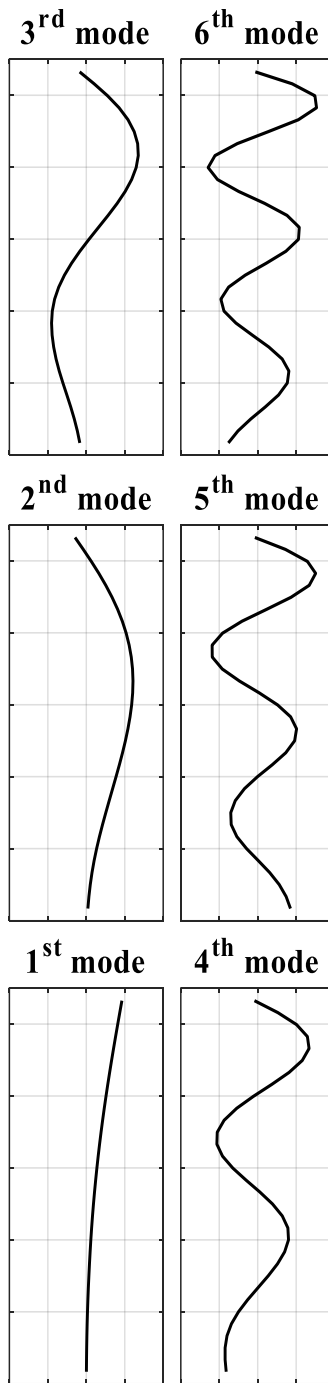


Figure 7-3: Demonstration of the first six vibration mode shapes evaluated using base-spring model for B4 in sand of  $D_r = 75\%$

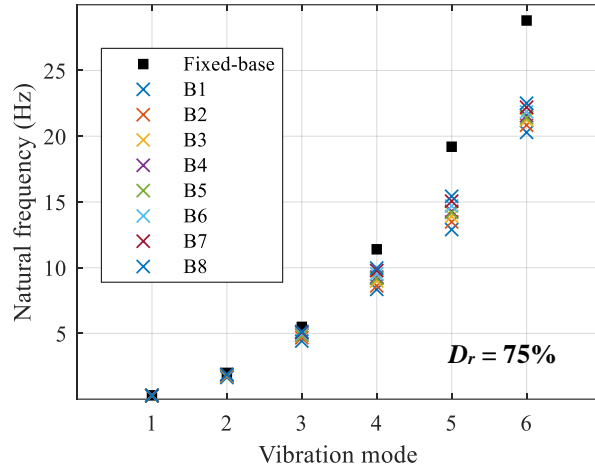


Figure 7-4: Variation of natural frequencies for different models ( $D_r = 75\%$ )

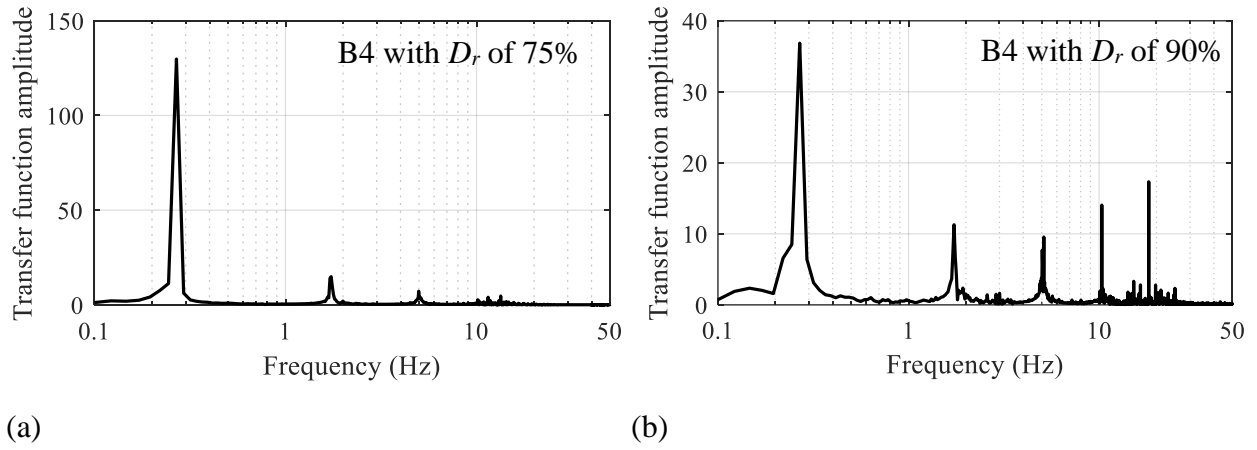
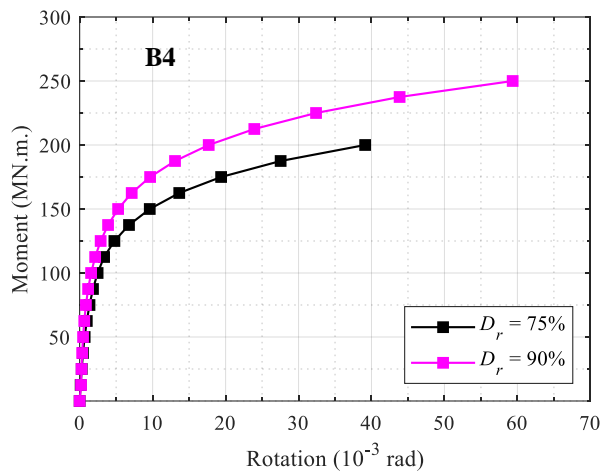
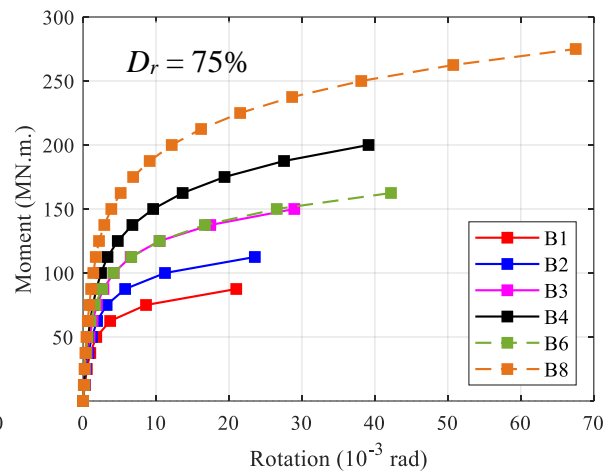


Figure 7-5: Plot of transfer function between tower top and bucket acceleration at mid skirt height under low amplitude shaking for B4 in sand with  $D_r$  of a) 75% and b) 90%



(c)



(d)

Figure 7-6: Plot of moment-rotation relationship of bucket foundation in drained quasistatic monotonic loading (combined with 5.8 MN vertical dead load of the superstructure) for c) B4 in sand with  $D_r$  of 75% and 90%, and d) different buckets in sand of  $D_r$  of 75%.

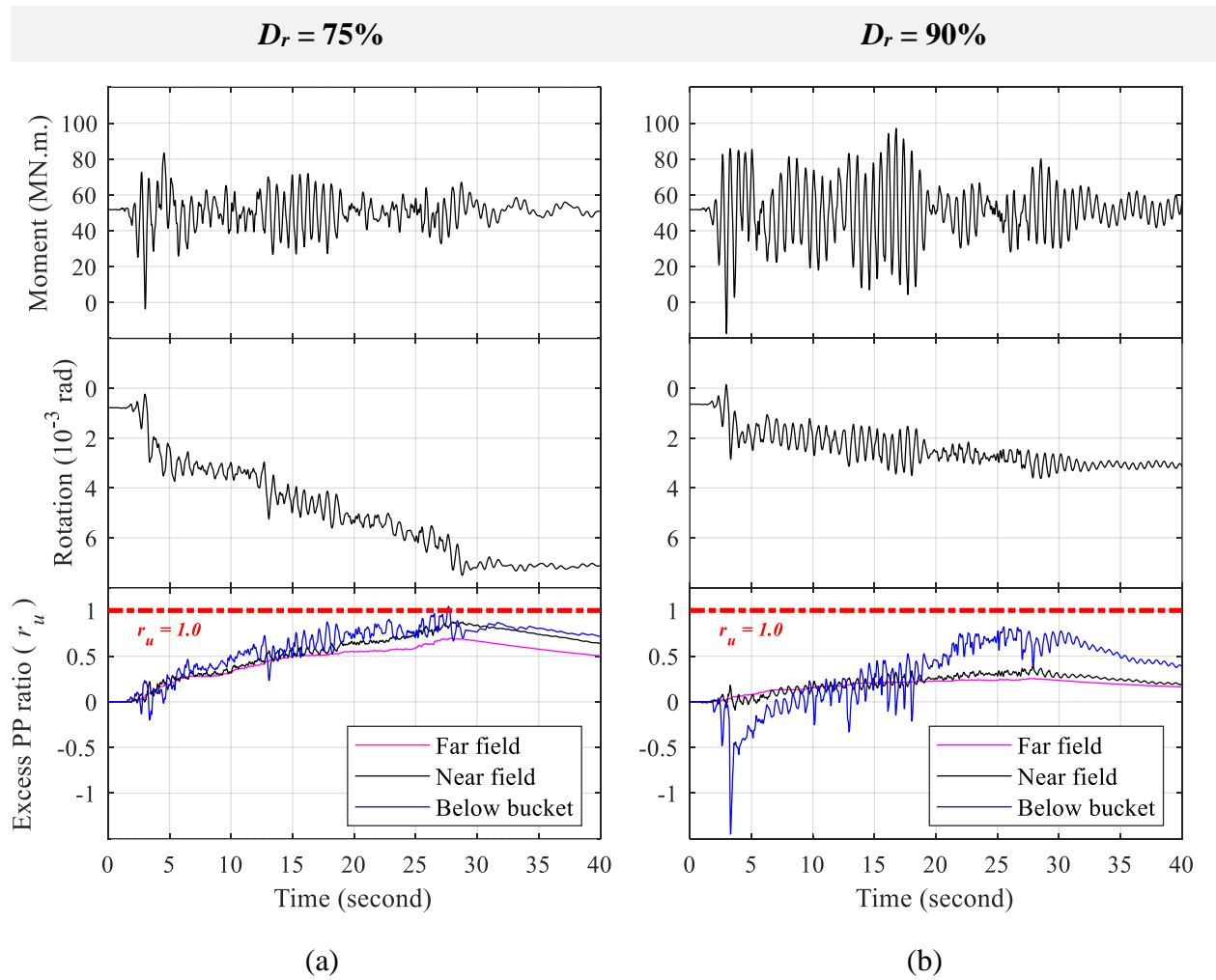
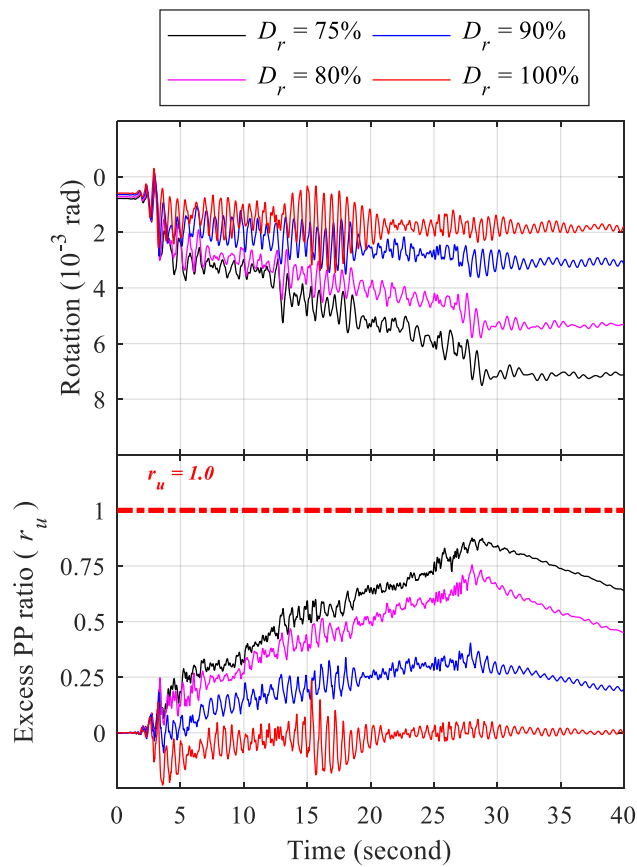
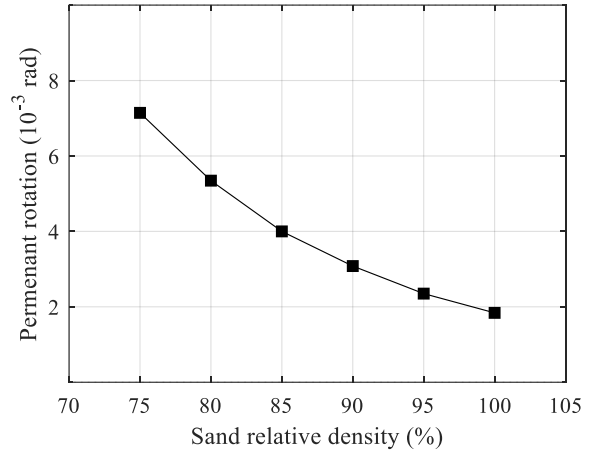


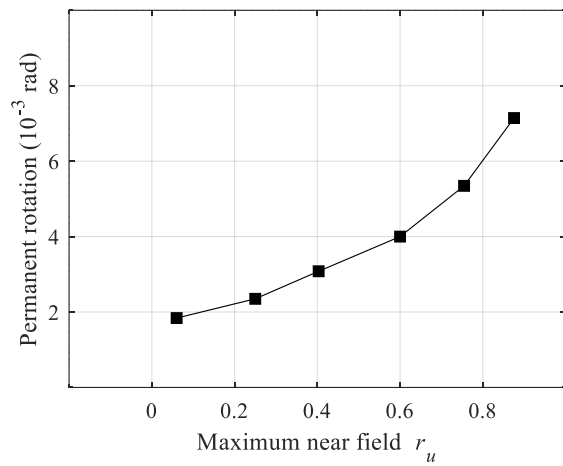
Figure 7-7: Time histories of bucket moment (top plots), rotation (middle plots) and excess PP response (bottom plots) for B4 in sand with  $D_r$  of a) 75% and b) 90% under E50-I and E50-II motions (Table 7-5)



(a)



(b)



(c)

Figure 7-8: a) Time history plots of B4 bucket rotation (top plot) and near field  $r_u$  (bottom plot) for different  $D_r$ , and change of permanent bucket rotation at end of shaking with b) sand relative density and c) maximum near field  $r_u$  under E50 motions (Table 7-5)

$D_r = 90\%$

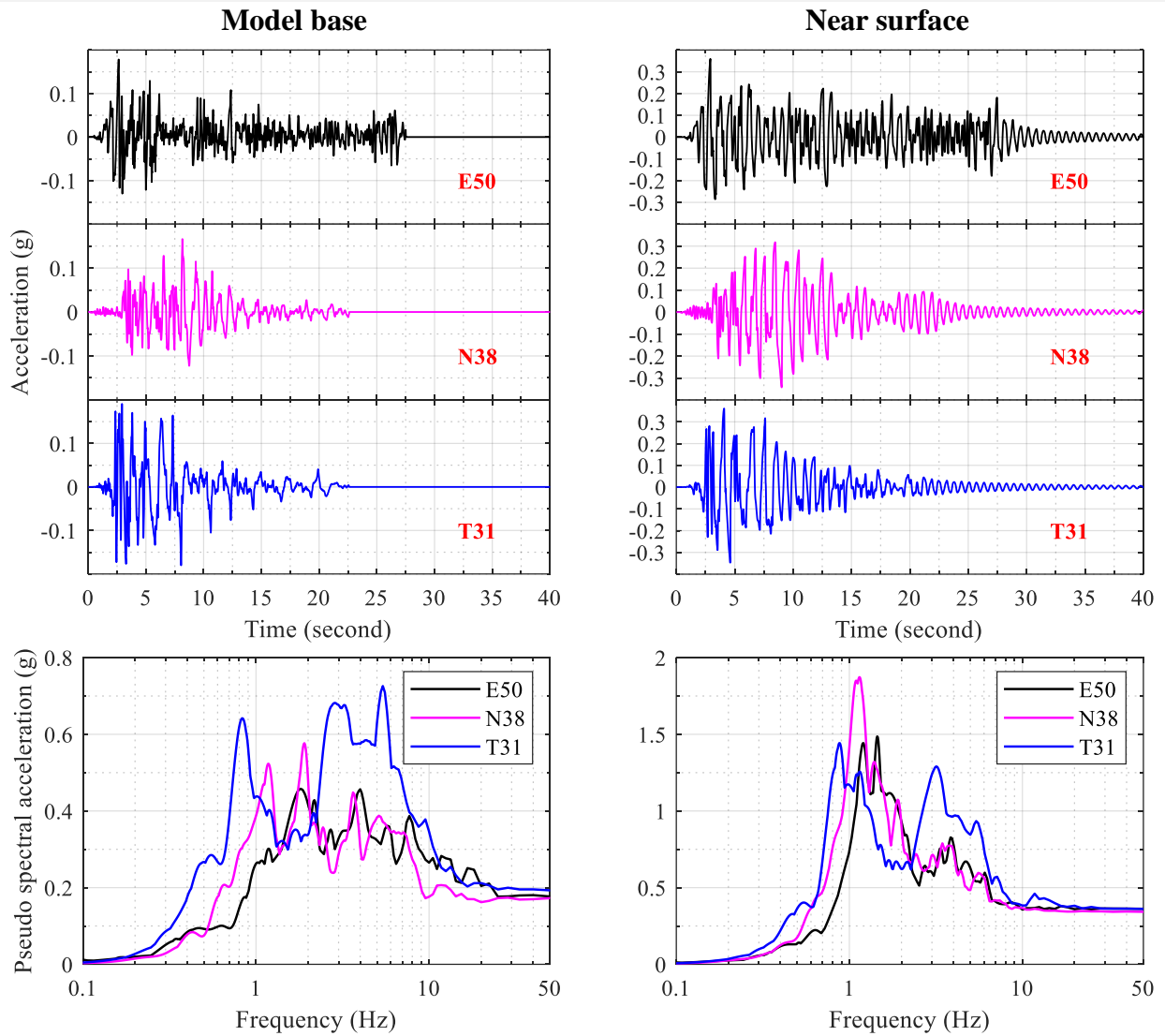
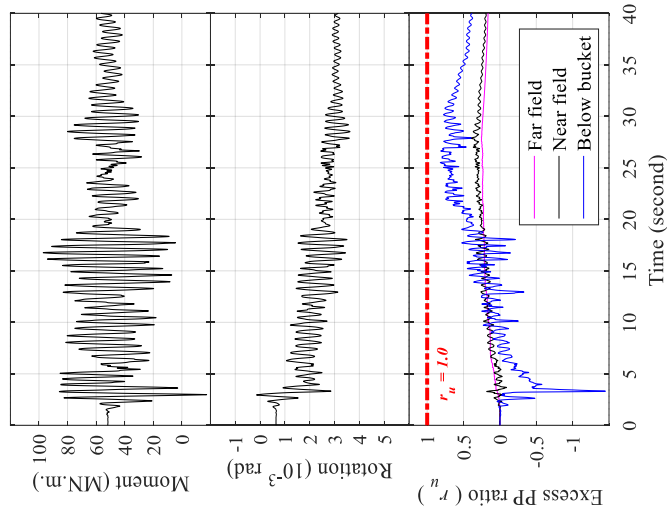


Figure 7-9: Acceleration time histories (top plots) and the corresponding response spectra (bottom plots) for B4 with 90% relative density at model base (left column) and near surface (right column) for the different employed earthquake input motions: E50-II, N38 and T31 (Table 7-5)

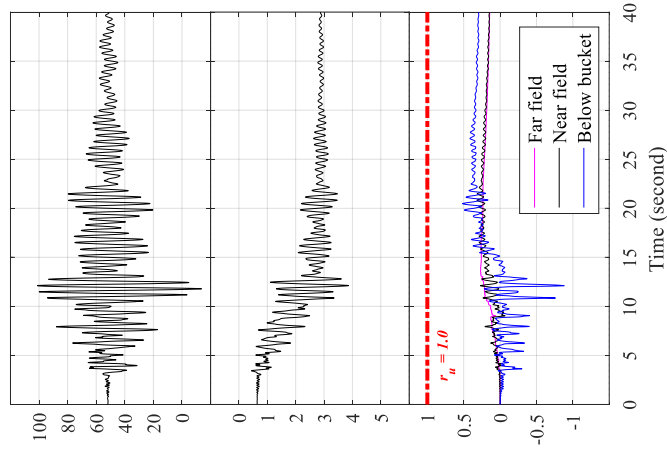


$D_r = 90\%$

(a) E50-II earthquake



(b) N38 Earthquake



(c) T31 Earthquake

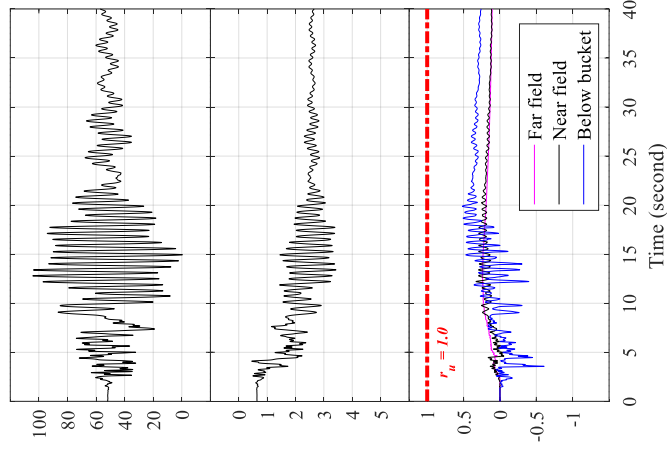


Figure 7-10: Time histories of bucket moment (top plots), bucket rotation (middle plots) and  $r_u$  (bottom plots) for B4 with 90% relative density due to the different earthquake motions

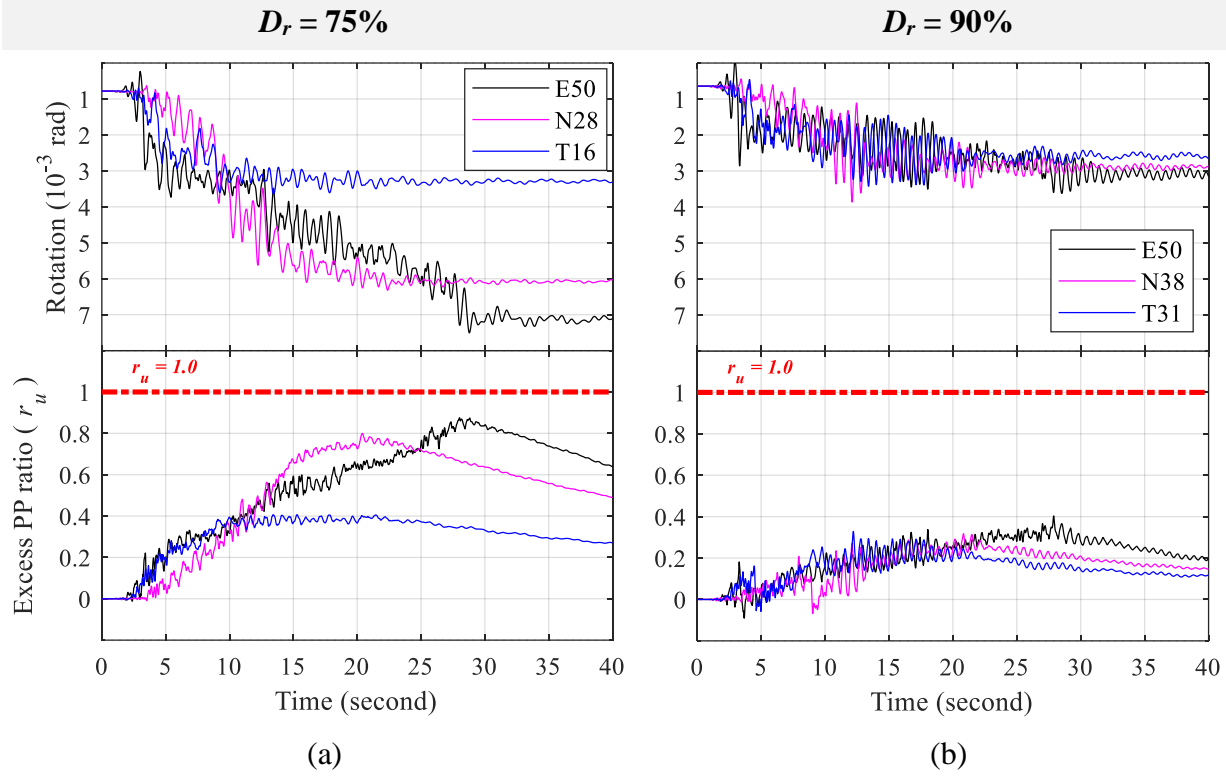


Figure 7-11: Time histories of bucket rotation (top plot) and near-field  $r_u$  (bottom plots) for B4 with 75% and 90%  $D_r$  due to the different earthquake motions: E50-I, N28 and T16 (for 75%  $D_r$ ), and E50-II, N38 and T31 (for 90%  $D_r$ )

$D_r = 90\%$

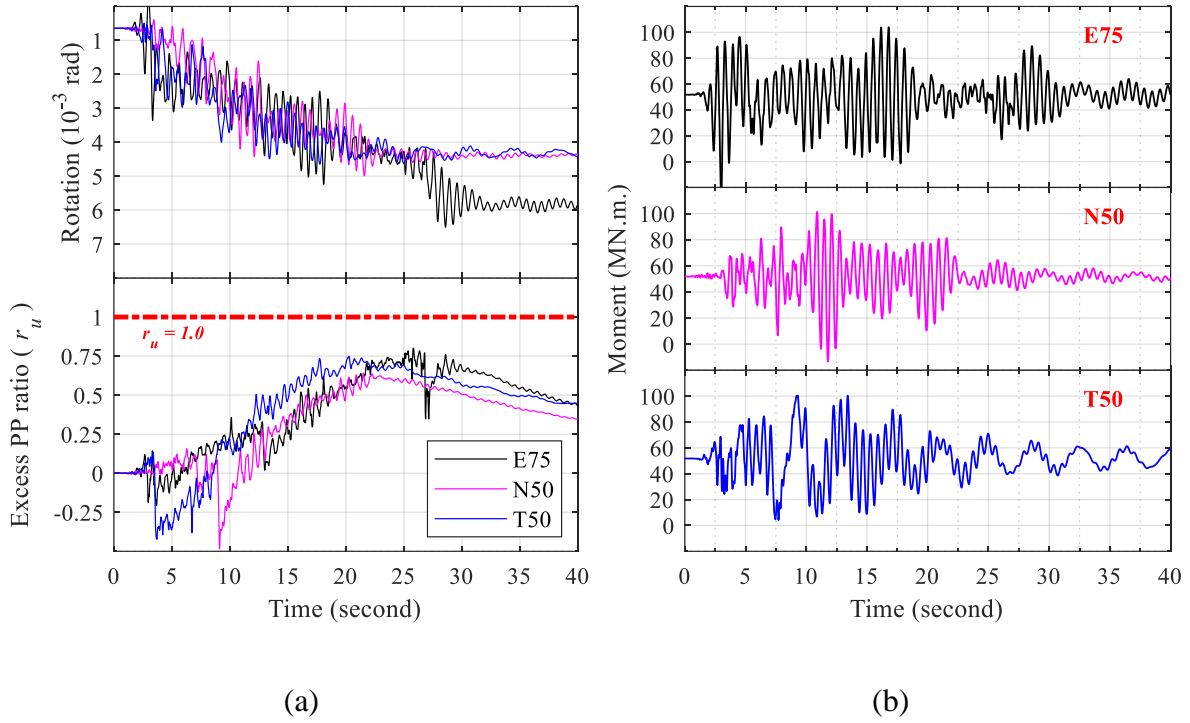


Figure 7-12: Time histories of a) bucket rotation (top plot) and near field  $r_u$  (bottom plots), and b) bucket moment for B4 with 90% relative density under motions E75, N50 and T50

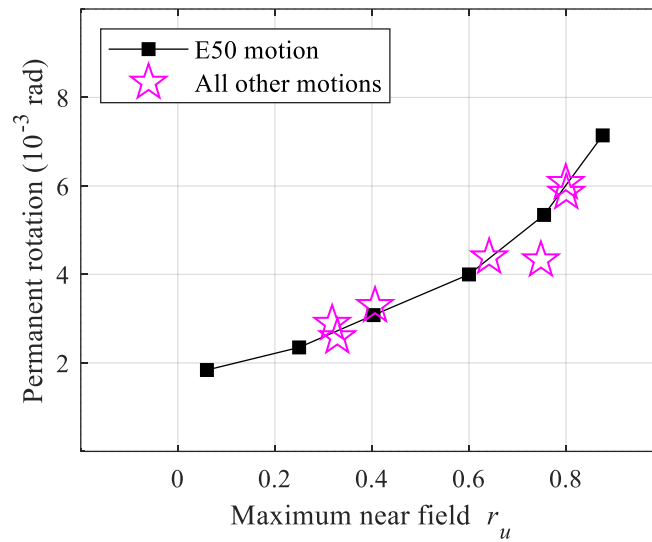


Figure 7-13: Change of residual/permanent B4 bucket rotation with maximum near-field  $r_u$  (representing different  $D_r$  values) towards end of shaking under different earthquake motions (Table 7-5)

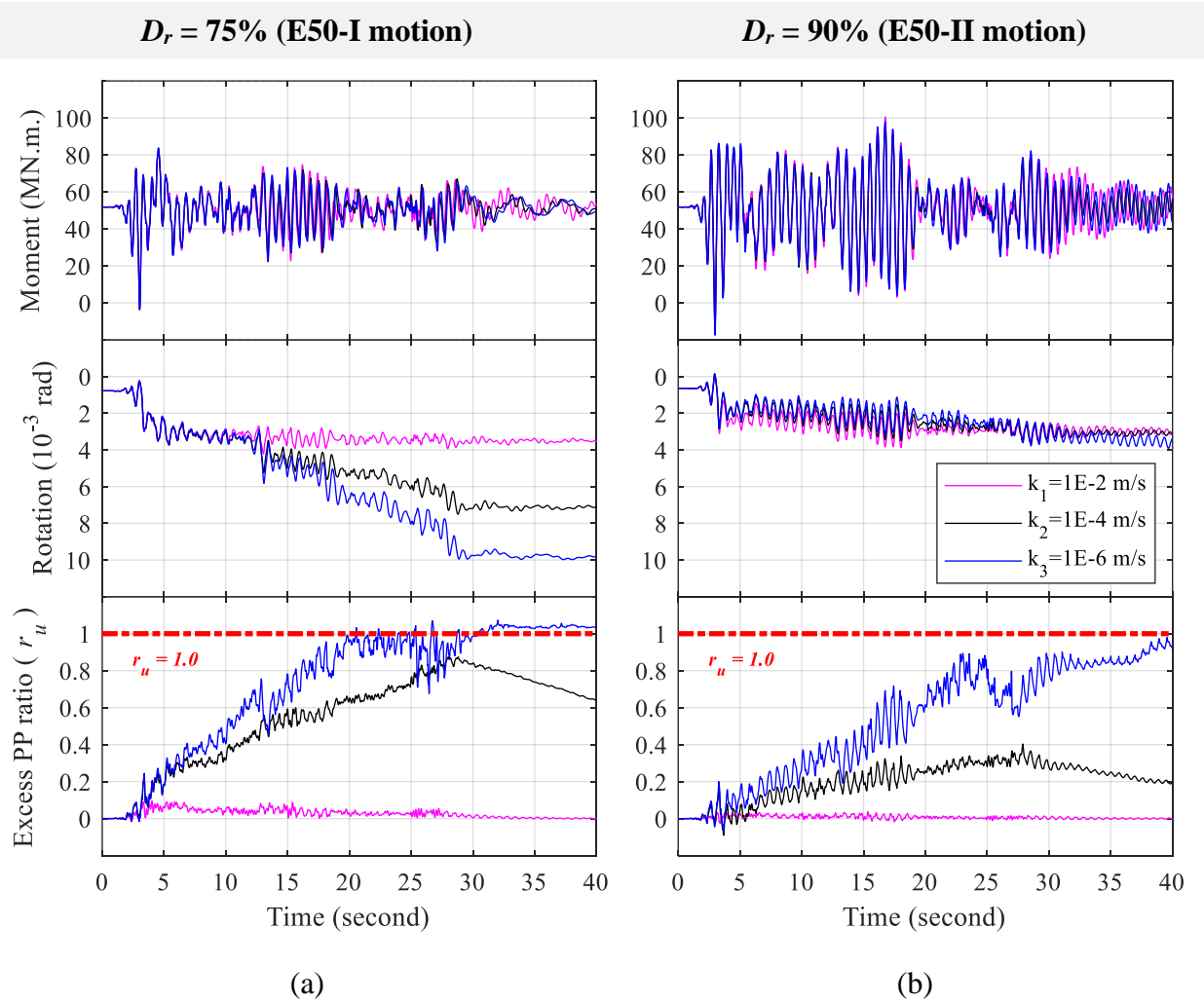


Figure 7-14: Time histories of bucket moment (top plots), bucket rotation (middle plots) and near field  $r_u$  (bottom plots) for B4 under E50 motions with different soil permeability ( $k$ )

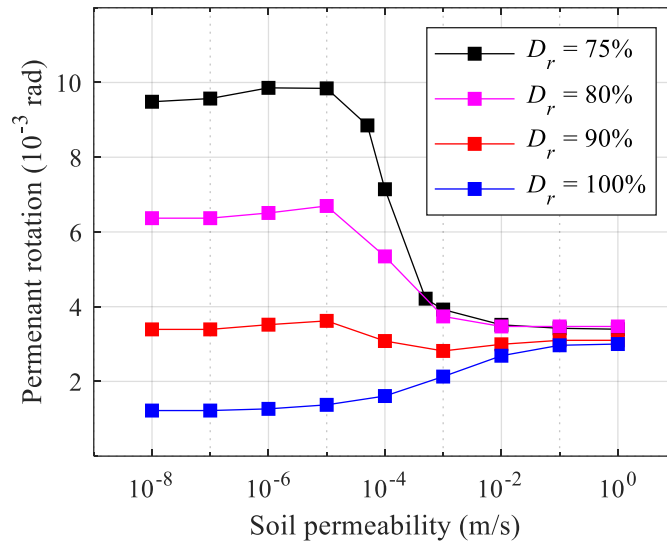


Figure 7-15: Change of permanent bucket rotation towards end of shaking with soil permeability for B4 in different  $D_r$  values using E50 motions

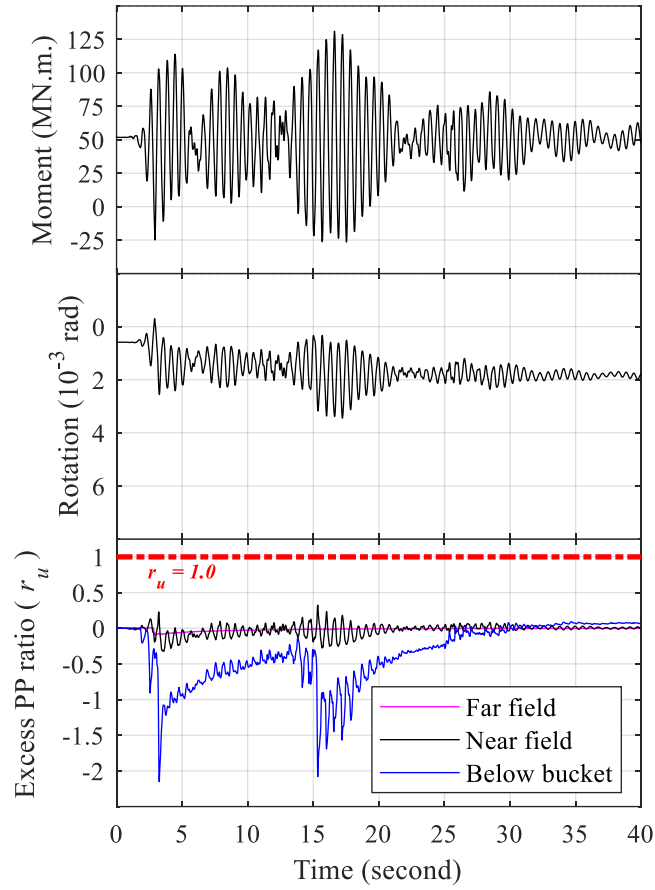


Figure 7-16: Time histories of bucket moment (top plots), rotation (middle plots) and excess PP response (bottom plots) for B4 in sand with  $D_r$  of 100% under E50 motion

$D_r = 90\%$

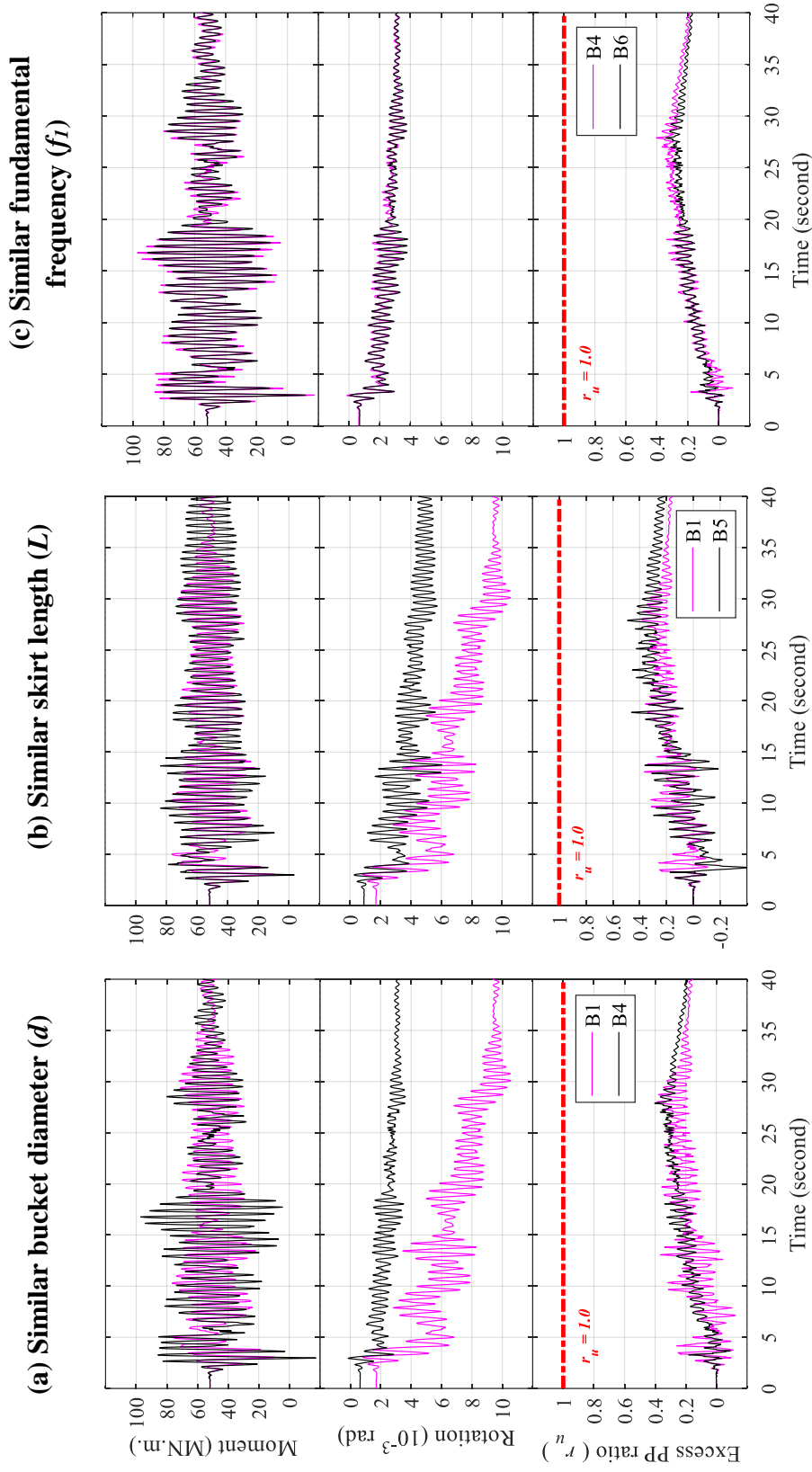
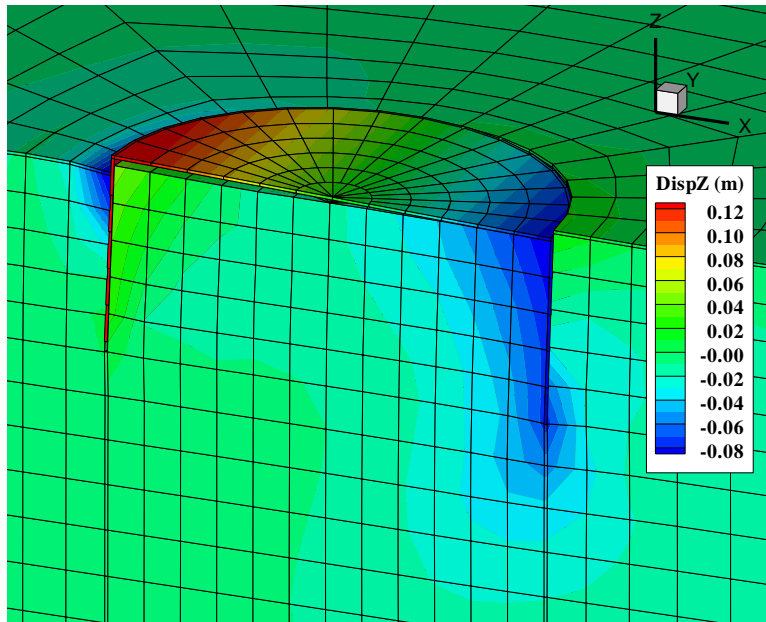
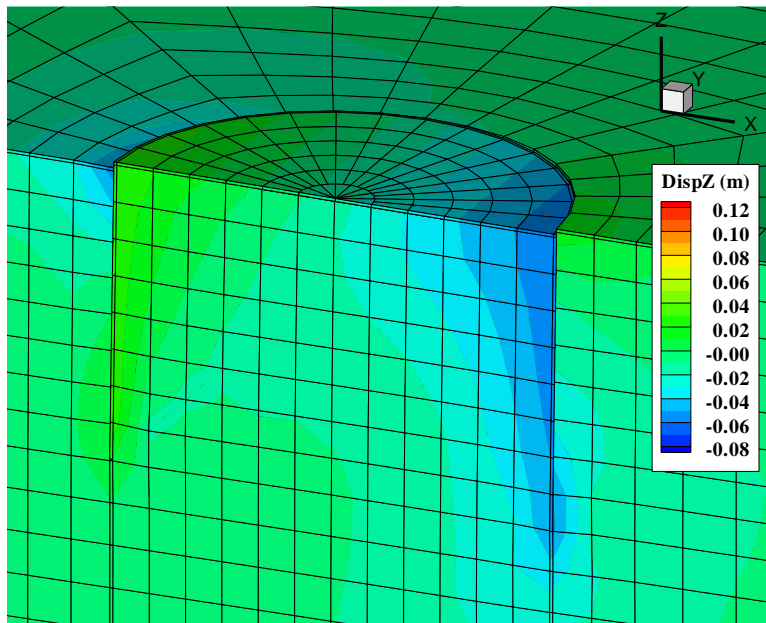


Figure 7-17: Time histories of bucket moment (top plots), bucket rotation (middle plots) and  $r_u$  (bottom plots) for different buckets with 90% relative density under E50-II motion





(a)



(b)

Figure 7-18: FE deformed mesh contours for vertical displacement (scale factor = 2) showing the permanent bucket rotation at end of shaking (time = 35 seconds) for bucket a) B1 and b) B4 (Table 7-3) in 90%  $D_r$  sand of permeability of  $1E-4$  m/s due to E50-II motion

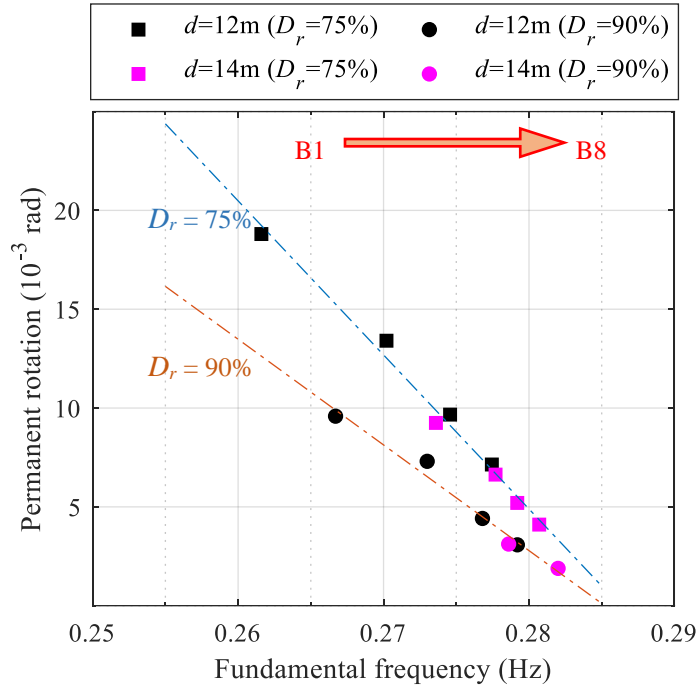


Figure 7-19: Change of residual/permanent bucket rotation at end of shaking with the OWT fundamental frequency for different buckets (B1 through B8) with sand  $D_r$  of 75% and 90% under E50 motions (Table 7-5)

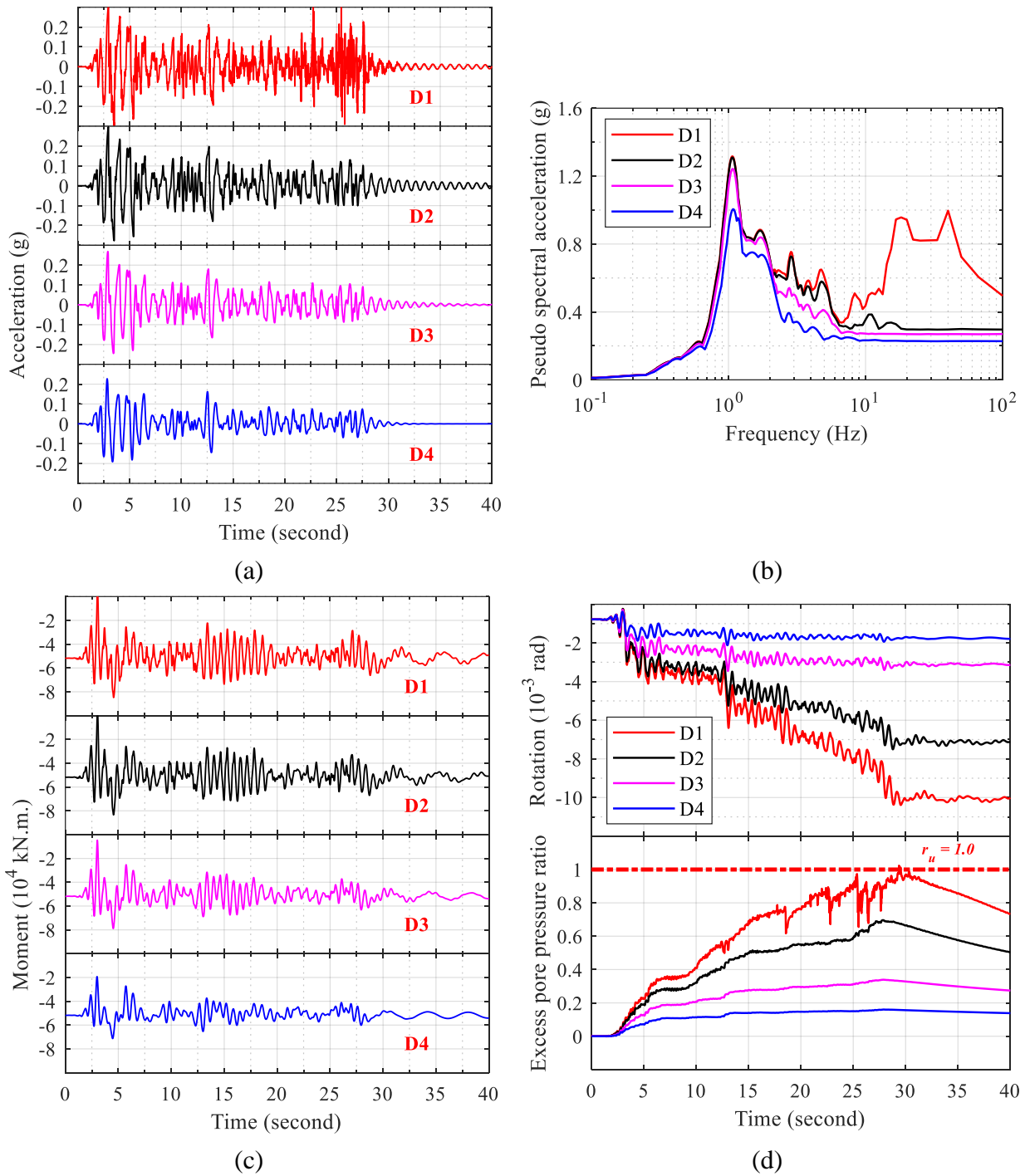


Figure 7-20: Plots of a) soil acceleration time histories below the bucket at mid skirt height, b) the corresponding response spectra, c) time histories of bucket moment, and d) time histories of bucket rotation (top plot) and near field  $r_u$  (bottom plot) for different damping coefficients

## Chapter 8

# Shake table testing: A high-resolution vertical accelerometer array for tracking shear wave velocity

*In a dark place we find ourselves, and a little more  
knowledge lights out way.*

– Star Wars Episode III: Revenge of the Sith

### 8.1 Abstract

Dynamic ground and ground-structure responses are heavily dependent on the soil shear wave velocity. During seismic excitation, soil stiffness inferred from the shear wave velocity ( $V_s$ ) might change significantly and affect the overall system response. In this study, an instrumentation and analysis framework were developed to allow for continuous estimation of  $V_s$  during dynamic/seismic excitation. The framework is presented along with representative applications during shake table testing of saturated sand strata. For that purpose, results from two different 1-g shake table tests conducted in a laminar soil container are examined and analyzed. In this context, evolution of the soil  $V_s$  profile during the shaking event is tracked and documented. The experimental setup, test procedure, and test results are described. Time histories of  $V_s$  at different depths within the sand strata are discussed. Overall, the developed techniques can be conveniently included in routine 1-g and centrifuge shake table experimentation efforts, when properly accounting for the difference between size of 1 g and centrifuge models.

## 8.2 Introduction

Local site conditions strongly influence the level of seismic ground excitation during an earthquake, and site characterization is an important element of an earthquake-response assessment framework. Ground stiffness profile is among the properties that have significance in determining the ground response. In this regard, soil shear wave velocity ( $V_s$ ) and shear modulus ( $G$ ) are main parameters. From  $V_s$ , shear modulus is derived, as expressed in (8.1), as one of the most important soil properties in geotechnical earthquake engineering and dynamic soil-structure-interaction analyses.

$$G_{\max} = \rho V_s^2 \quad (8.1)$$

where  $G_{\max}$  is the initial shear modulus and  $\rho$  is the soil mass density.

In the laboratory, bender elements were used in small-scale tests to evaluate  $V_s$  profiles (Shirley and Hampton 1978, Brignoli *et al.* 1996, Arulnathan *et al.* 1998, Pennington *et al.* 2001, Leong *et al.* 2005, Lee and Huang 2007). Furthermore, centrifuge modelers developed a number of techniques to measure  $V_s$  (Gohl and Finn 1991, Ismail and Hourani 2003, Fu *et al.* 2004, Brandenberg *et al.* 2006, Rammah *et al.* 2006, Fu *et al.* 2008, Kim and Kim 2010, Ghayoomi and McCartney 2011, El-Sekelly *et al.* 2012, El-Sekelly *et al.* 2013, El-Sekelly *et al.* 2014). Arulnathan *et al.* (2000) and Ghosh and Madabhushi (2002) used a miniature air hammer to generate shear waves at the base of different model soil profiles for sand and for organic soil. The propagated shear waves were recorded using a vertical array of accelerometers positioned at various depths that ranged between 2 and 4 meters (prototype scale). For the latter experiments, either an air

hammer or bender elements were embedded in the soil while building the model soil profile in order to generate the shear waves.

In large-scale shake table tests (Koga and Matsuo 1990, Lin and Wang 2006),  $V_s$  was measured before and after the imparted shaking event, where hammer excitation at the surface of the model soil profile was used to generate small-strain shear wave while the downward propagating wave is picked up by accelerometers placed along the depth of the model. More recently, in centrifuge shaking table testing, Lee *et al.* (2012) developed a bender element measurement system that was used to track the change of  $V_s$ : i) during shaking in a dense sand model, and ii) during the post shaking phase of excess pore pressure dissipation in a loose sand model. In the field, deployed seismic downhole arrays have been used to evaluate shear wave propagation characteristics, and variation of  $V_s$  with depth and time (Beeston and McEvelly 1977, Katayama *et al.* 1990, Shakal and Petersen 1992, Elgamal *et al.* 1995, Zeghal *et al.* 1995, Elgamal *et al.* 1996a, Wang *et al.* 2001).

In this study, similar to the in-situ downhole array studies, a framework is developed for tracking the evolution of  $V_s$  during large strain shake-table dynamic excitation. This framework employs accelerometers that are placed horizontally (one at each depth such that accelerometers are perpendicular to the shear wave propagation direction) and does not require additional instrumentation such as an air hammer or bender elements that usually require a pair to be installed at each depth. In the following sections, the details are provided, along with representative applications during 1-g shake table tests involving loose and dense saturated sand strata.

### 8.3 Shear wave velocity tracking framework

Aiming to track the propagation of shear waves within the soil strata during ground motion, an array of closely spaced accelerometers (e.g., spacing in the range of 0.2 m to 0.5 m) is placed vertically within the soil profile (Figure 8-1). Closely spaced accelerometers allow for high spatial resolution while tracking the change in  $V_s$  with time during the ground excitation phase. With such close spacing between accelerometers, the relatively small travel time of the propagated shear waves between each two accelerometers is expected to place high demand on the sampling rate and the employed data acquisition software and hardware, as explained below.

### 8.4 Estimation of $V_s$ from recorded dynamic signals

Figure 8-1 shows a schematic representation of the accelerometer array and the one-dimensional shear wave propagation mechanism. The shear wave velocity ( $V_s$ ) between any two accelerometers spaced at a distance  $d$ , is estimated by measuring the time  $\tau_d$  required for the wave to travel between the sensors (i.e., travel time):

$$V_s = \frac{d}{\tau_d} \quad (8.2)$$

The data acquisition system used for measuring  $V_s$  must provide a sampling rate that is (Arulnathan *et al.* 2000): i) more than twice the highest frequency in the generated waves to avoid aliasing, and ii) high enough that the sampling time step ( $t_s$ ) combined with the expected travel time ( $\tau_d$ ) avoid low resolution error in the calculated  $V_s$  estimate. The error band,  $\Delta V_s$  in the measured  $V_s$  due to the employed sampling time step ( $t_s$ ) can be expressed as (Elgamal *et al.* 1995):

$$\Delta V_s = \frac{V_s t_s}{\tau_d} \quad (8.3)$$

According to (8.2), an increase in travel time during any seismic excitation (e.g., shaking) event denotes a decrease in  $V_s$ , which in turn reflects reduction in the shear modulus ( $G$ ), due to mechanisms caused by either: i) large shear strains that occur during the seismic event (Seed *et al.* 1986), and/or ii) reduction in effective confinement (Afifi and Richart 1973) as a result of pore water pressure generation during the event. On the other hand, between any two seismic events, the change in the soil mass density (8.1) as well as the restoration of confinement due to pore water pressure dissipation results in increase in  $V_s$ .

## 8.5 Analytical $V_s$ evaluation approaches

A number of researchers (Gohl and Finn 1991, Kita *et al.* 1992, Arulnathan *et al.* 2000, Brandenburg *et al.* 2006, Da Fonseca *et al.* 2008, Murillo *et al.* 2009, Kim and Kim 2010, Ghayoomi and McCartney 2011, Lee *et al.* 2012) employed the Peak-to-Peak method to evaluate  $V_s$  travel time in geotechnical centrifuge models. In this approach, the first strong peak is detected in the time history of the two selected accelerometers. Thus, the time difference based on peak arrival can be calculated. Other researchers (Kawaguchi *et al.* 2001, Zhou and Chen 2007, El-Sekelly *et al.* 2014) relied on first arrival for evaluating  $V_s$ . Alternatively, the cross-correlation approach (Madera 1970) was employed (Chang *et al.* 1991, Zeghal and Elgamal 1994a, Elgamal *et al.* 1995) to calculate an average  $V_s$  over a given time window.

In this study, the travel time  $\tau_d$  between any two accelerometers is estimated via the cross-correlation approach. This approach provides a quantitative measure of similarity of two signals



as a function of the time lag in one relative to the other. As such, the cross-correlation function between two acceleration time histories  $a_i(t)$  and  $a_j(t)$  recorded at locations  $i$  and  $j$  (Figure 8-1), may be expressed as (Bendat and Piersol 1980):

$$c_{a_i a_j}(\tau = m t_s) = \frac{\frac{1}{N-m} \sum_{n=1}^{N-m} a_i(n t_s) a_j[(n+m) t_s]}{\sqrt{\frac{1}{N} \sum_{n=1}^N a_i^2(n t_s)} \sqrt{\frac{1}{N} \sum_{n=1}^N a_j^2(n t_s)}}, \quad m = 0, 1, 2, \dots, N-1 \quad (8.4)$$

in which  $t_s$  is time step of the digital data,  $\tau = m t_s$  is the time delay, and  $N t_s$  is acceleration record length. A major peak of the cross-correlation function is reached at a time delay  $\tau = \tau_d$ , where  $\tau_d$  is the travel time of seismic waves from station  $i$  to station  $j$ .

In the above, the cross-correlation function is calculated over a pre-defined time window of short duration. This window is systematically shifted along the time span of the recorded accelerations (Elgamal *et al.* 1996a), allowing for continuous evaluation of  $\tau_d$  estimates throughout the shaking event.

## 8.6 Experimental application of the Vs tracking framework

### 8.6.1 Shake table and laminar container

The experimental work in this study was conducted at the Powell Laboratory shake table facility (Magenes 1989b, Trautner *et al.* 2018), located at the University of California San Diego (UCSD). A laminar container with internal dimensions of 3.9 m x 1.8 m x 1.8 m (Length x Width x Height) was constructed at UCSD using 28 structural steel frames arranged in stacks (Ashford

and Jakrapiyanun 2001). The laminar container was designed to reduce boundary effects, simulating a 1D shear stress-strain state of wave propagation (Chang and Hutchinson 2013). Aiming to enhance its capabilities, the container has been recently extended to a 2.9 m height instead of 1.8 m, by inclusion of 16 additional steel frames (Ebeido 2020). Figure 8-2 shows the extended laminar container attached to the Powell Laboratory shake table.

### **8.6.2 Model 1 preparation and experimental procedures**

Ottawa F-65 sand (Table 8-1) was used to build the soil model. An Ethylene Propylene Diene Monomer (EPDM) rubber liner was placed inside the laminar container to hold soil and water (Figure 8-3a). The model consisted of two saturated layers with an upper crust stratum (Figure 8-4). Construction of the soil model was accomplished in three phases. The first consisted of building a 1.0 m dense sand base stratum. Using a plate compactor, this base layer was densified in lifts, each of about 0.25 m in thickness. By monitoring weight of each lift and knowing volume of the sand layer, overall relative density ( $D_r$ ) was estimated at about 90%. After construction, this base layer was saturated with water carefully flowing into the container by means of perforated plastic pipes placed at the base of the container.

Next, the middle layer was constructed by pluviating the sand into the container from a hopper (Figure 8-3b) at a constant falling height and a steady flow rate, in an effort to build a relatively uniform deposit. To further promote uniformity of this middle stratum, the sand was pluviated through an additional set of sieves that was placed inside the soil container (Figure 8-3c). The pluviating process was always conducted while keeping the water table above the top sand surface. The distance between the top water surface and the top sand surface was kept in the range of 0.25-0.40 m, while the distance between the additional set of sieves and the top water surface

was kept around 0.8-1.0 m. After building the middle loose sand layer, its average  $D_r$  was estimated to be about 35%.

The final phase of model construction involved pluviation and compaction of the top crust stratum using the plate compactor. Upon completing the model,  $D_r$  of this crust layer was estimated at about 80%. As such, ground water table was 0.55 m below the soil surface (Figure 8-4). The 3-layer soil profile was selected to allow for measuring different values and capturing different change in  $V_s$  for different soils. Table 8-2 summarizes properties of the different sand layers.

### **8.6.3 Vertical accelerometer array and data acquisition**

For the purpose of this study, data from a high-resolution vertical array placed at a distance of about 0.75 m away from the container boundary (Figure 8-4) was employed. Eleven accelerometers (A#) of type 393B04 manufactured by *PCB Piezotronics, Inc.* were used for the downhole array and spaced mostly at 0.25 m. Along with the accelerometers, 11 small-size pore pressure transducers (PP#) of type BPR-A-S manufactured by *Kyowa Electronic Instruments Co., LTD* were placed nearby (Figure 8-4).

The collected data was acquired and saved at a sampling rate of 25600 sample/second/channel. On this basis, error in  $V_s$  due to time step size (8.3) is displayed in Figure 8-5. For instance, the resolution band ( $V_s \pm \Delta V_s$ ) using the aforementioned sampling rate is found to be 49-51 m/s and 146-153 m/s for  $V_s$  equal to 50 m/s and 150 m/s, respectively.

## 8.6.4 Representative results and interpretation

### 8.6.4.1 Initial shear wave velocity prior to the shaking event

Prior to running the shake table test, a low level (0.03 g peak input amplitude) white noise was generated at the base of the container. Due to limitations in shake table fidelity at this low level of shaking, an external dynamic excitation source was attached to the shake table platform. This external source was employed, as the mechanical properties and control system of the shake table do not allow to generate the desired low-level of acceleration amplitude. As such, the initial average shear wave velocity ( $V_{so}$ ) of the soil model was estimated (Table 8-2). Values reported in Table 8-2 represent average  $V_{so}$  within each stratum evaluated between the lowermost and uppermost accelerometers within each stratum.

### 8.6.4.2 Shaking event accelerations

Under displacement-control mode, the shake table was used to generate a 25-second long input excitation as shown in Figure 8-6. This motion consisted of 15 cycles including 3 initial cycles ramping up to the desired peak amplitude and 3 cycles ramping down at the end of the motion. It might be noticed that the input excitation exhibits a level of asymmetry in terms of positive and negative acceleration peaks. Furthermore, the table response can be seen to include some superimposed high frequency noise (Figure 8-6), due to superfluous friction in the shake table bearings as discussed by Trautner *et al.* (2018).

Figure 8-7 shows time histories of the 11-accelerometer array during the shaking event. The following observations may be noted in the recorded response:

1. Characteristics of the input excitation are manifested in the base dense layer and maintained up to A8. This response changes starting at the lower boundary of the loose layer (A7 and A6) with a change in the frequency content where the loose layer acted as a low-pass filter and the high-frequencies were filtered out.

2. In the dry crust above the liquefied loose sand stratum (A1-A3), a clear decay in amplitude is observed. Liquefaction in the loose sand and associated loss of stiffness and strength resulted in this base-isolation effect (Kokusho 2014, Bouckovalas *et al.* 2016).

#### **8.6.4.3 Pore water pressure response**

Figure 8-8 shows the recorded response in terms of Excess Pore Pressure (EPP) ratio ( $r_u = u_e/\sigma'_{vo}$  where  $u_e$  is recorded EPP and  $\sigma'_{vo}$  is initial effective vertical stress). In the dense base stratum, maximum  $r_u$  was less than 1, as the soil experienced relatively gradual EPP build-up. All pore pressure transducers in the middle loose layer (PP03-PP07) showed a sharper rate of EPP increase and evidence of liquefaction as  $r_u = 1.0$  was reached.

#### **8.6.4.4 Lateral soil deformation**

Figure 8-9 shows lateral displacement profiles of the laminar container at selected time instants during the shaking event. From these displaced configurations, it can be noted that deformation was minimal within the crust layer above the water table. In the underlying saturated soil, the middle loose layer follows a deformation trend that is steeper than that of the underlying dense layer. This is an outcome of the tendency for larger deformation within the liquefied looser layer, compared to that of the denser layer below.

### 8.6.5 Implementation of the $V_s$ tracking framework

The logic of a moving time window with overlap was used with the recorded accelerations (Figure 8-7) to evaluate shear modulus variation with time (Elgamal *et al.* 1996a). Following this logic, a 2-second moving time window with a step of 0.1 second is used herein to estimate the travel time between any two accelerometers for each moving time window via cross-correlation. Thereafter,  $V_s$  is estimated using the distance between the two accelerometers (i.e., 10 values of  $V_s$  are estimated during every second of dynamic response). The window size of 2 seconds includes about 1.5 cycle (Figure 9-6) with 51200 data points, allowing for reasonable accuracy in the resulting  $V_s$  estimates (Figure 8-5). Selection of 2 seconds for the window size was made after a sensitivity analysis was conducted and it was concluded that 2 second is sufficient for the purpose of moving window with sampling rate of 25,600 sample/second.

Figure 8-10 shows a sample cross-correlation (8. 4) evaluated between A8 and A9 acceleration records of model 1 at early shaking (i.e., at 3 seconds) and towards the end of shaking (i.e., at 21 seconds). An enlarged view of the latter cross-correlation is presented in Figure 8-11 to further show the evolution of time delay ( $\tau$ ) with shaking. From Figure 8-11, it can be noted that the peak of the cross-correlation occurs at later times (i.e., larger time delays) as the shaking evolves, which reflects an increase in the travel time ( $\tau_d$ ) and consequently reduction in  $V_s$ , as explained in the following sections.

#### 8.6.5.1 Evolution of $V_s$ in the base dense sand layer

Within this stratum, Figure 8-12 illustrates the acceleration and EPP responses, in addition to the computed  $V_s$  evolution with time. As can be seen, the acceleration time histories do not show

significant amplification or change in frequency content within this layer. In general, the estimated  $V_s$  is larger at the deeper location, in accordance with the corresponding higher confinement. Starting values are about 80 % of the earlier low amplitude estimates (Table 8-2), due to the higher levels of shaking. In view of pore-pressure build-up, the calculated  $V_s$  estimates are seen to gradually decrease, eventually becoming about 70 % of their starting values.

#### **8.6.5.2 Evolution of $V_s$ in the loose layer**

With the rapid increase in EPP towards liquefaction, Figure 8-13 shows that  $V_s$  drops dramatically within the middle loose layer, as well as the topmost part of the base dense layer (between A8 and A9). At the dense-loose strata interface (between A8 and A9),  $r_u$  values were as high as 0.8, with starting  $V_s$  at about 120 m/s, gradually dropping to as little as 30 m/s near the end of shaking (rebounding to about 60 m/s by the end of shaking as shaking amplitudes diminish).

Within the loose layer (between A6, A7 and A8 in Figure 8-13),  $V_s$  started at about 100 m/s at the beginning of shaking and gradually decreased to as low as essentially zero, reflecting the liquefaction induced loss of soil stiffness. The latter observation is in agreement with the corresponding EPP values that indicate liquefaction ( $r_u = 1$ ).

From Figure 8-13, it can be noted that the time at which  $V_s$  approaches zero occurs earlier at shallower depths. Similar observation can be seen in Figure 8-14, where  $V_s$  drops earlier near the top of the loose layer (between A3 and A4) compared to the locations at mid-depth (between A5 and A6).

### **8.6.5.3 Evolution of $V_s$ in the crust layer**

Acceleration histories and evolution of  $V_s$  within the crust layer is illustrated in Figure 8-15. It can be noticed that main characteristics of the acceleration response (frequency content and amplitude) are maintained among A1, A2 and A3. Within the crust layer (between A2 and A3), the starting  $V_s$  was about 200 m/s, thereafter, rapidly fluctuating between 150 and 350 m/s. Later at about 6 seconds, the  $V_s$  suddenly shows a dramatic increase essentially approaching infinity. A similar trend in  $V_s$  was observed between A1 and A2 as well. The estimated  $V_s$  approaching infinity is a consequence of an estimated zero time-delay between the two correlated acceleration signals. Such zero time-delay indicates perfectly in-phase propagation between the two acceleration signals. Essentially, it indicates that the crust layer was moving as a rigid body following the displacement of the top part of middle liquefied layer as shown earlier in Figure 8-9.

The overall evolution of  $V_s$  at different depths within the soil model is summarized in Figure 8-16. Within the loose layer, reduction in stiffness from the top downwards is evident. Furthermore, the relatively mild variation in  $V_s$  within the base dense layer verses the sharp decrease within the liquefied loose layer can be observed.

## **8.7 Additional application of the $V_s$ tracking framework**

### **8.7.1 Model 2 preparation and test configuration**

Results from an additional shake table test (Ebeido 2020) are discussed in this section. Model 2 (Figure 8-17), mildly inclined at 4 degrees to simulate lateral spreading, was also tested at the Powell Laboratory using the same laminar soil container. Table 8-3 summarizes properties of the sand layers. The shake table was used to generate a 14-second long sinusoidal motion, 0.15g



in amplitude with a 2 Hz fundamental frequency, as shown in Figure 8-17. Full details of the experimental setup are reported in Ebeido (2020). Due to presence of the pile, the overall response is not purely driven by the 1-dimensional vertical shear wave propagation mechanism. Nevertheless, salient insights were drawn from the analysis as presented below.

### **8.7.2 Recorded acceleration and excess pore pressure**

Acceleration and EPP ratio time histories in Model 2 are presented in the left and right columns of Figure 8-18, respectively. The asymmetry, in terms of positive versus negative acceleration response, is indicative of the recorded accumulation of downslope lateral deformations (Figure 8-17) during the shaking event (Zeghal and Elgamal 1994a). This response is most prominent at the lower boundary of the middle looser layer (A4 and A5). The acceleration spikes in the negative direction denote tendency for dilation during the large downslope shear strain excursions. Similar to model 1, significant attenuation in accelerations is observed in the dry crust above the liquefied sand stratum (A1-A3). As discussed earlier, liquefaction of the medium-dense middle layer (Figure 8-18) and associated loss of stiffness and strength results in this base-isolation effect.

In the pore pressure response (right column of Figure 8-18), it can be seen that the rate of EPP build-up is slower at larger depths. Liquefaction ( $r_u = 1$ ) is reached at the upper locations and approached eventually deeper in the ground with progress of the dynamic excitation.

### **8.7.3 Tracking of Vs during seismic excitation**

A sample cross-correlation evaluated between A5 and A6 acceleration records of model 2 is illustrated in Figure 8-19, at early shaking (i.e., at 3 seconds) and towards the end of shaking

(i.e., at 13 seconds). Similar to model 1, the enlarged view presented in Figure 8-20 shows that the peak of the cross-correlation occurs at later times (i.e., larger time delays) as the shaking evolves, which reflects an increase in the travel time ( $\tau_d$ ) and consequently reduction in  $V_s$ .

Figure 8-21 shows evolution of  $V_s$  at different locations in model 2. Similar to Figure 8-16, a relatively milder variation in  $V_s$  is observed within the upper zone of the-dense layer (between A5-A6) versus the sharp drop in  $V_s$  within the overlying medium-dense layer (between A3-A4 and A4-A5). In addition, an early drop in  $V_s$  to zero at shallow depth can be observed. The rapid reduction in  $V_s$  between A3 and A4, and the more gradual between A5 and A6, mirror the EPP trends at these locations (Figure 8-18 and Figure 8-21). As observed in the response model 1,  $V_s$  in the crust layer fluctuates and approaches infinity (i.e., zero-time lag), indicative of the essentially rigid body motion (Figure 8-17) within this upper crust zone.

## **8.8 Acknowledgement**

The research described in this chapter was partially funded by the California Department of Transportation (Caltrans) and the National Science Foundation grant OISE-1445712 Testing was conducted at the Powell laboratories, University of California San Diego, with assistance provided by Dr. Christopher Latham, Mr. Andrew Sander, Mr. Mike Sanders, Mr. Abdullah Hamid, and Mr. Darren Mckay.

The approach developed in chapter 8 has been published as a journal paper in the ASTM Geotechnical Testing Journal, Volume 44, Issue number 4, with a publication date 28<sup>th</sup> of July 2020. The title of this paper is “Shake table testing: A high-resolution vertical accelerometer array for tracking shear wave velocity”. The dissertation author is the primary author of this paper with

Dr. Ahmed Ebeido, Mr. Athul Prabhakaran, Dr. Kyungtae Kim, Dr. Zhijian Qiu, and Professor Ahmed Elgamal as coauthors.

Table 8-1: Geotechnical properties of F-65 Ottawa sand (After Bastidas 2016a)

<b>Property</b>	<b>Description</b>
Mineralogy	Quartz, 99.7%
Grain shape	Rounded
Specific gravity, $G_s$	2.65
Coefficient of uniformity ( $C_u$ )	1.63
Coefficient of curvature ( $C_c$ )	0.97
Maximum and minimum void ratio $e_{max}, e_{min}$	0.83, 0.51
Minimum and maximum mass density $\rho_{min}, \rho_{max}$ ( $kg/m^3$ )	1440, 1760

Table 8-2: Properties of sand strata for model 1

	<b>Dense layer</b>	<b>Loose layer</b>	<b>Crust layer</b>
Soil condition	Saturated	Saturated	Moist
Thickness (m)	1.0	1.35	0.55
Total unit weight $\gamma_{\text{total}}$ (kN/m <sup>3</sup> )	20	19	17
Dry unit weight $\gamma_{\text{dry}}$ (kN/m <sup>3</sup> )	17	15	16
Relative density $D_r$ (%)	90	35	78
Initial average shear wave velocity $V_{so}$ (m/s)	176	102	85

Table 8-3: Properties of sand strata for model 2

	<b>Dense layer</b>	<b>Loose layer</b>	<b>Crust layer</b>
Soil condition	Saturated	Saturated	Moist
Thickness (m)	1.5	0.7	0.7
Total unit weight $\gamma_{\text{total}}$ (kN/m <sup>3</sup> )	20	19	17
Dry unit weight $\gamma_{\text{dry}}$ (kN/m <sup>3</sup> )	16.6	15.6	16.7
Relative density $D_r$ (%)	82	53	84

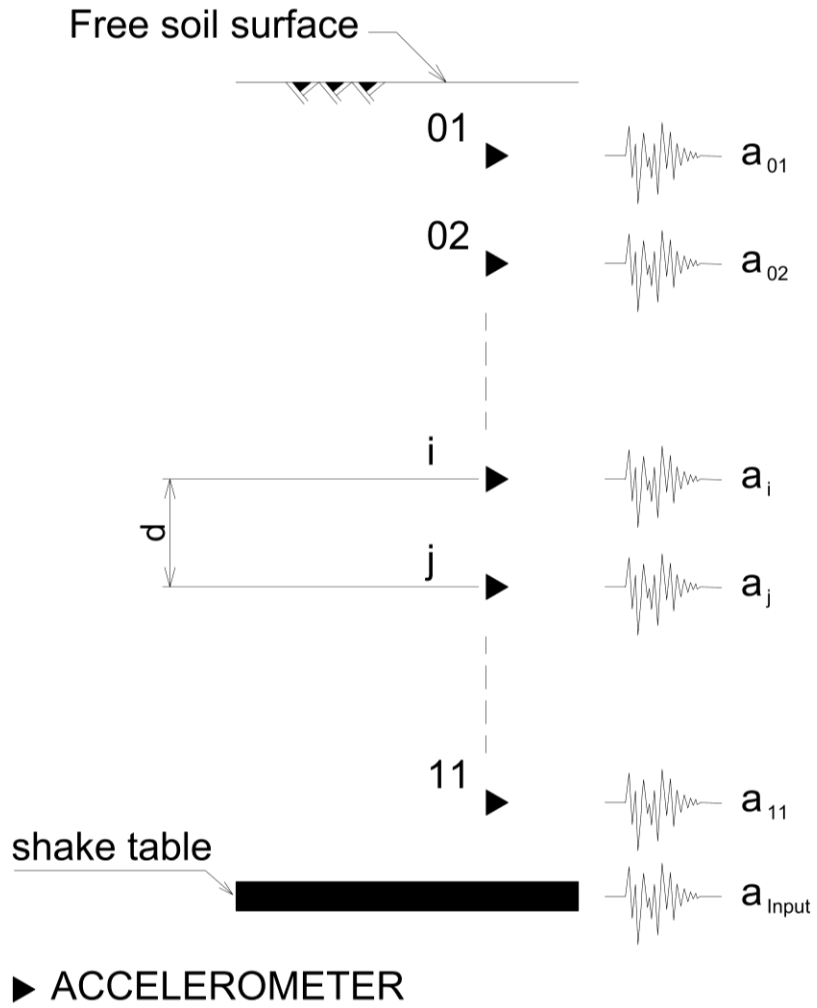


Figure 8-1: A schematic of accelerometer array for tracking of shear wave propagation velocity



Figure 8-2: Laminar soil container with internal dimensions of 3.9 m x 1.8 m x 1.8 m (Length x Width x Height), placed on shake table at the UC San Diego Powell Laboratory





a)



b)



c)



d)

Figure 8-3: a) Placing the EPDM liner inside the soil container, b) Soil hopper with a screen attached, c) additional sieves placed inside the soil container, and d) dry sand pluviation into water

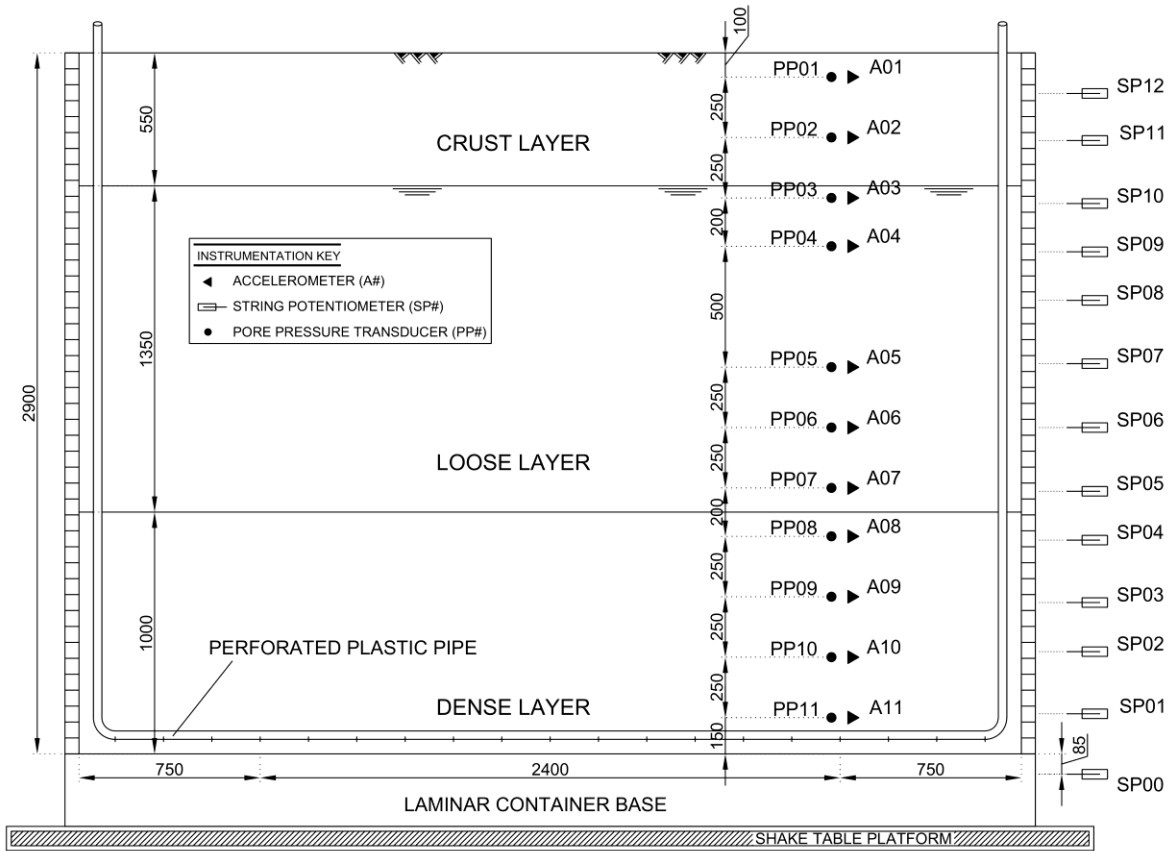


Figure 8-4: Testing configuration and instrumentation layout of model 1 (dimensions shown in mm)

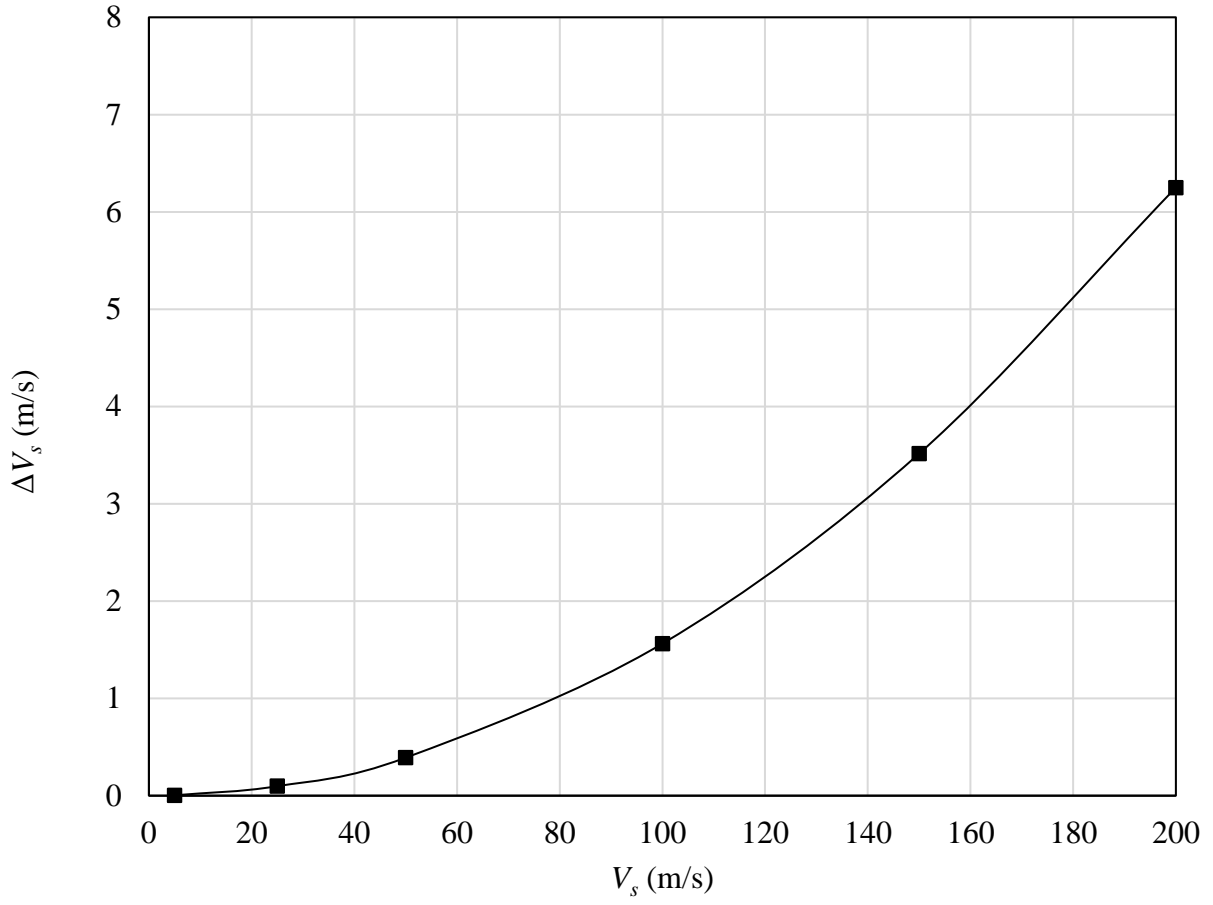


Figure 8-5: Error in the evaluated shear wave velocity due to one time-step error, for sampling rate of 25,600 samples/second

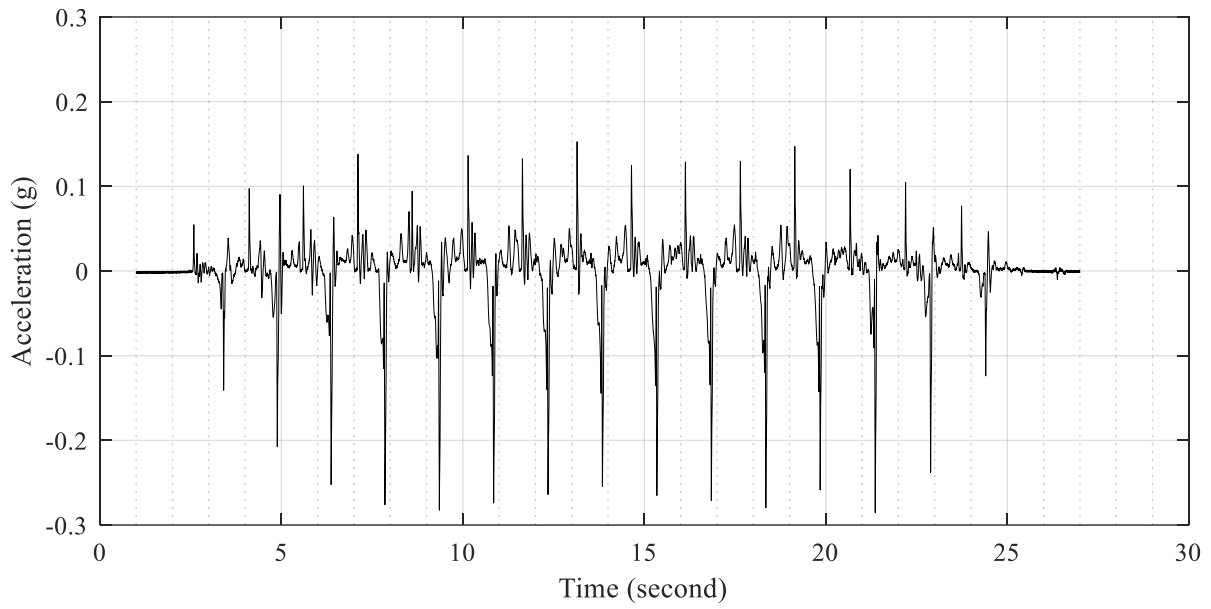


Figure 8-6: Acceleration time history of the shake table input excitation for model 1

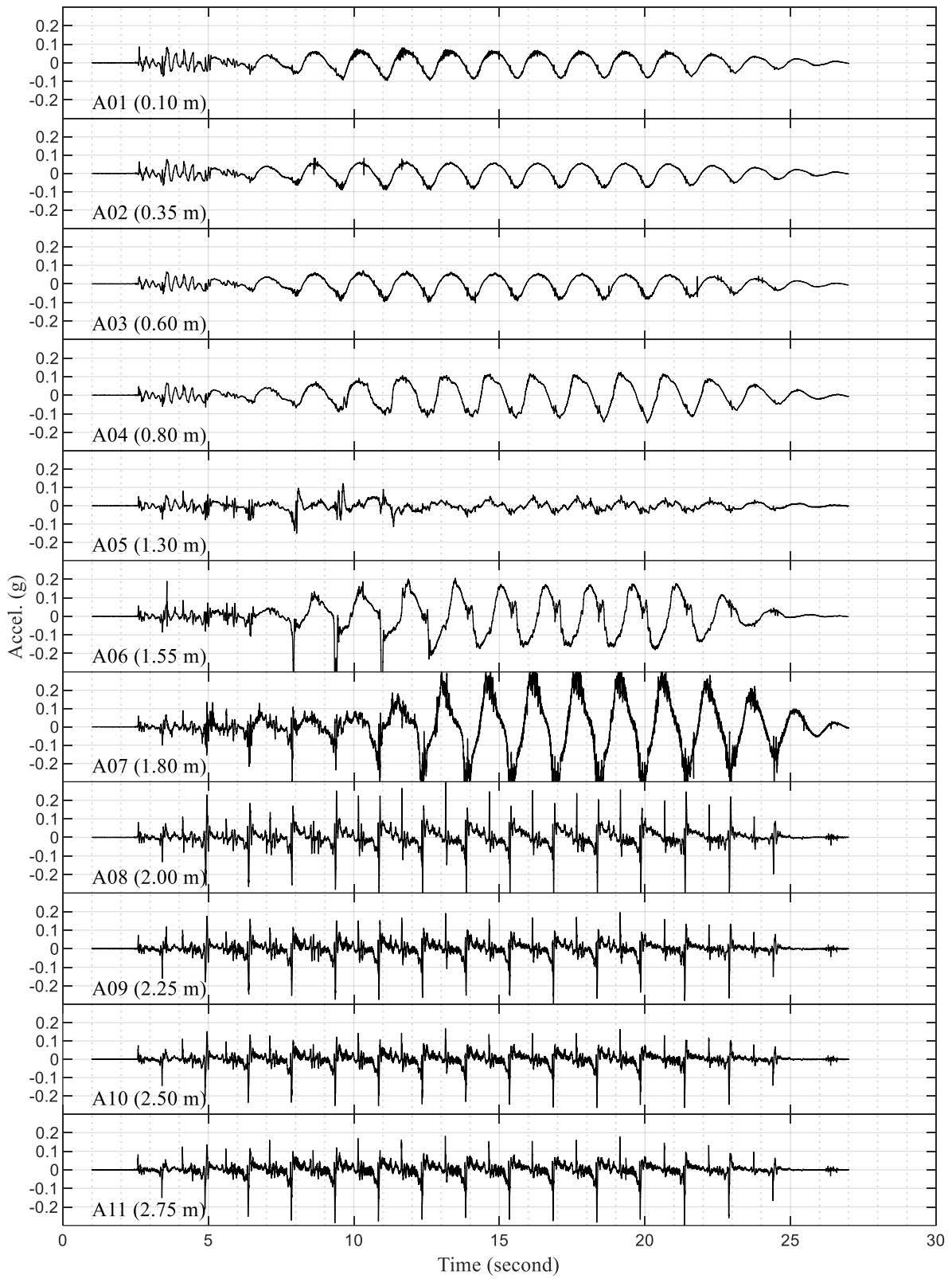


Figure 8-7: Model 1 acceleration time histories at different depths

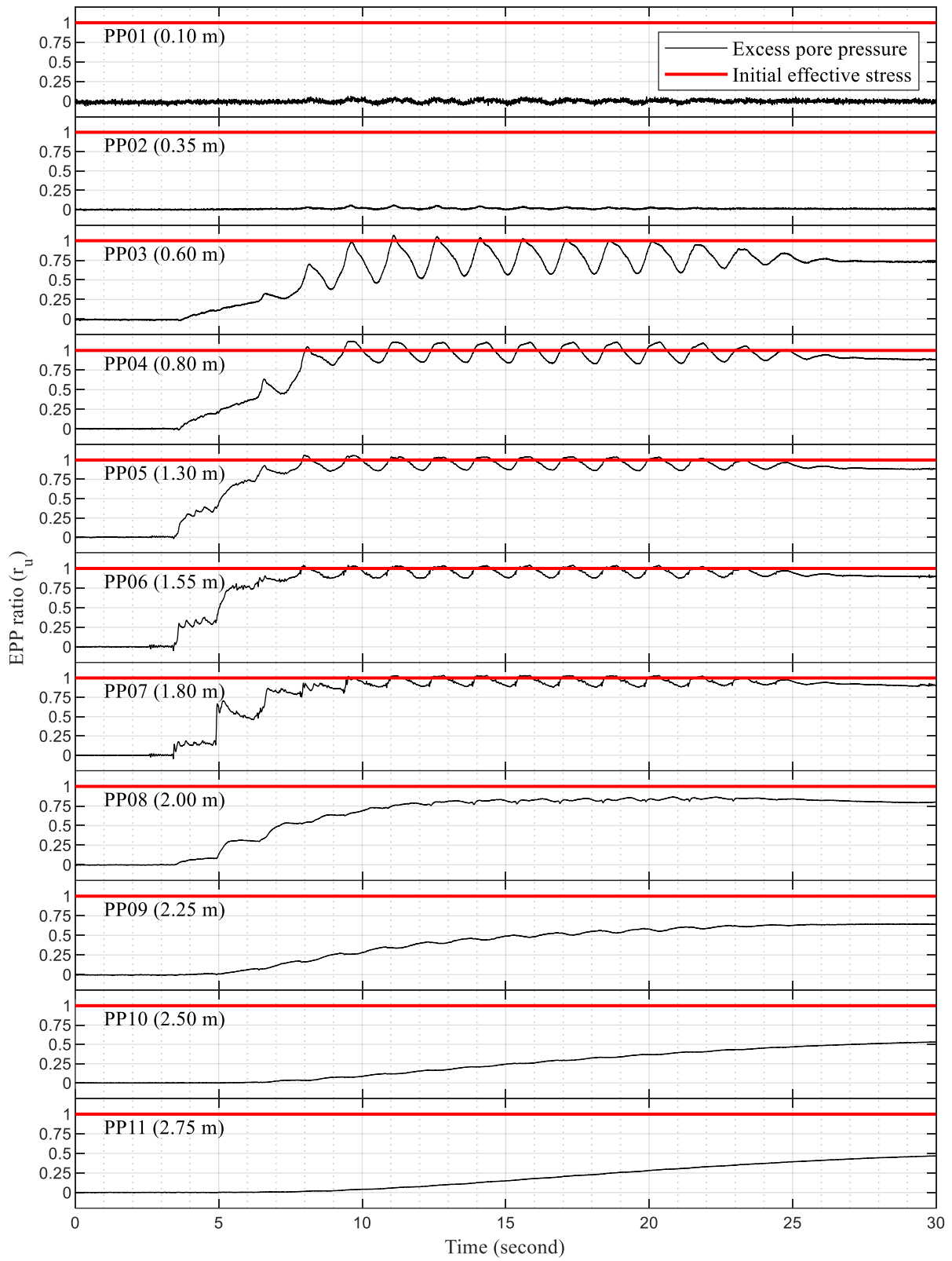


Figure 8-8: Time histories of excess pore pressure ratio at different depths in model 1

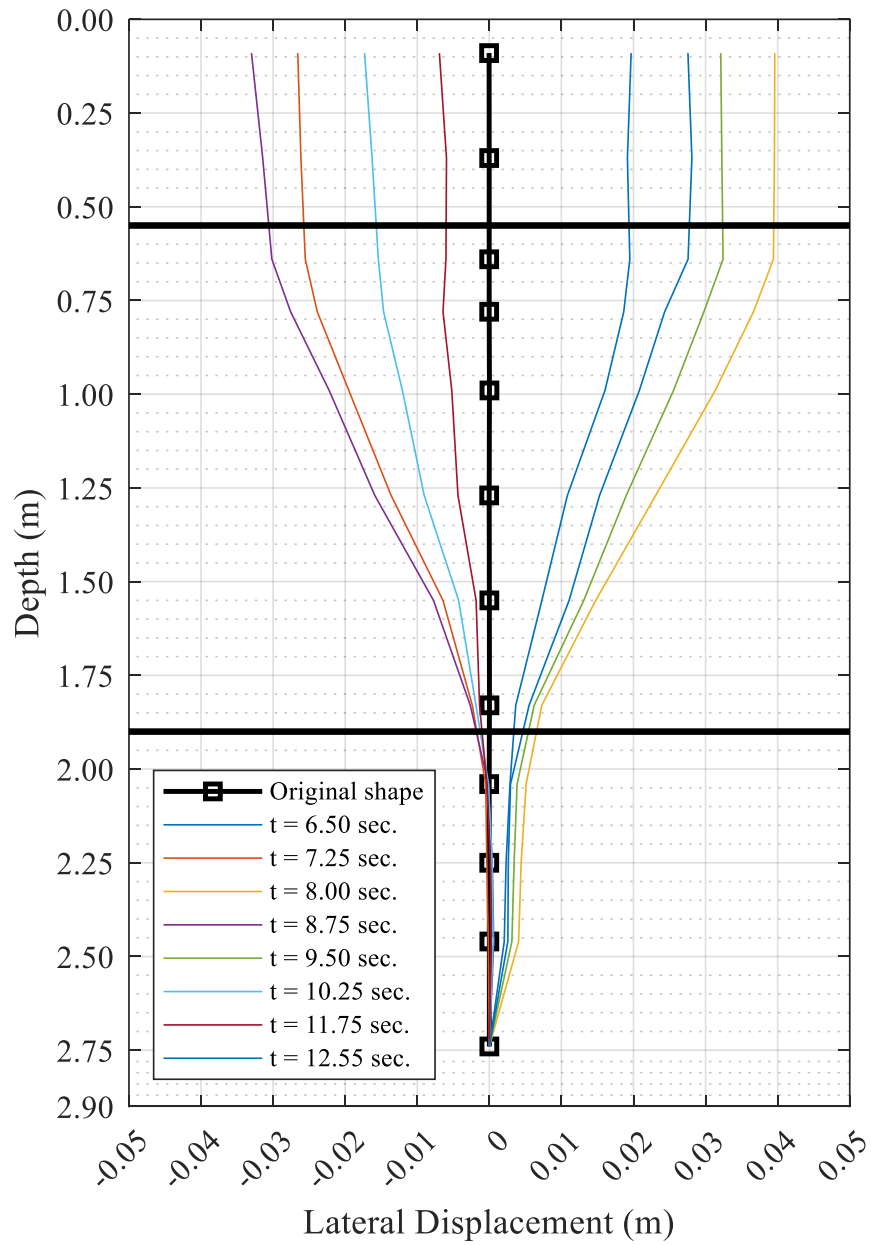


Figure 8-9: Lateral displacement profile of the laminar container relative to displacement at depth 2.75 m, at selected time instants in model 1, along with the corresponding accelerometers

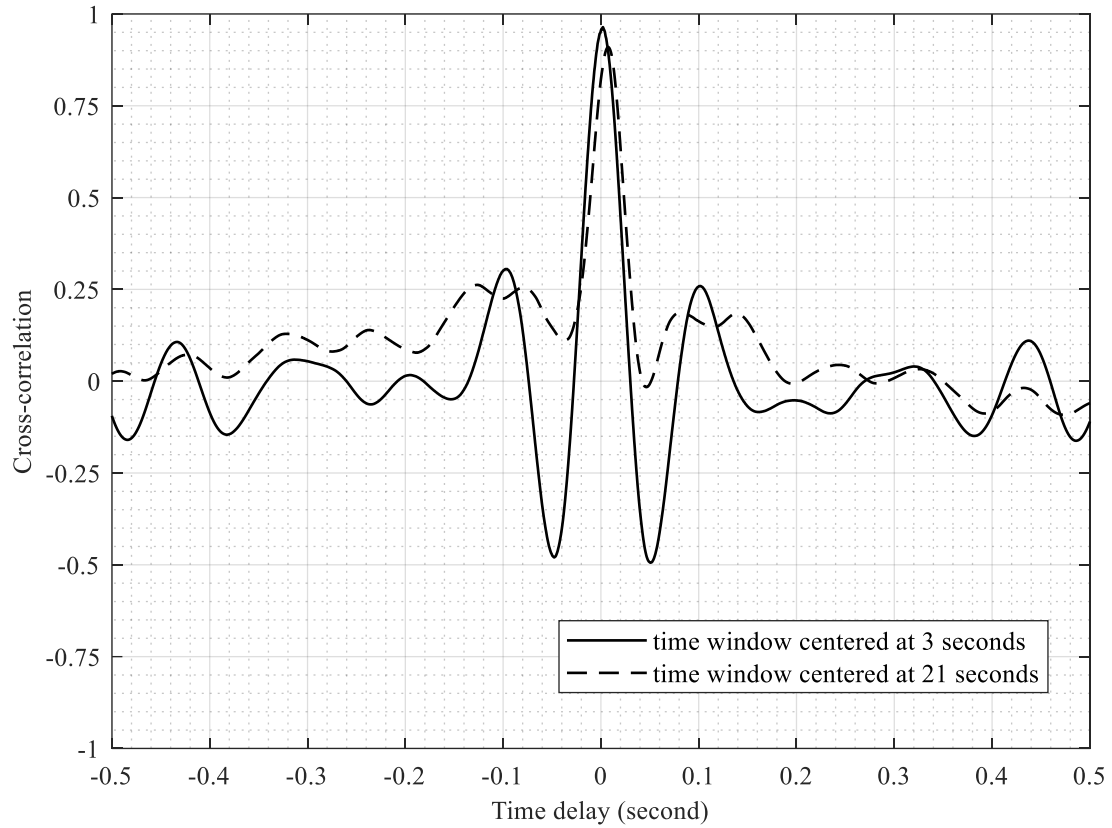


Figure 8-10: Cross-correlation between A08 and A09 accelerations (model 1) for two time windows centered at 3 seconds (i.e., at the beginning of shaking) and 21 seconds (i.e., towards end of shaking)



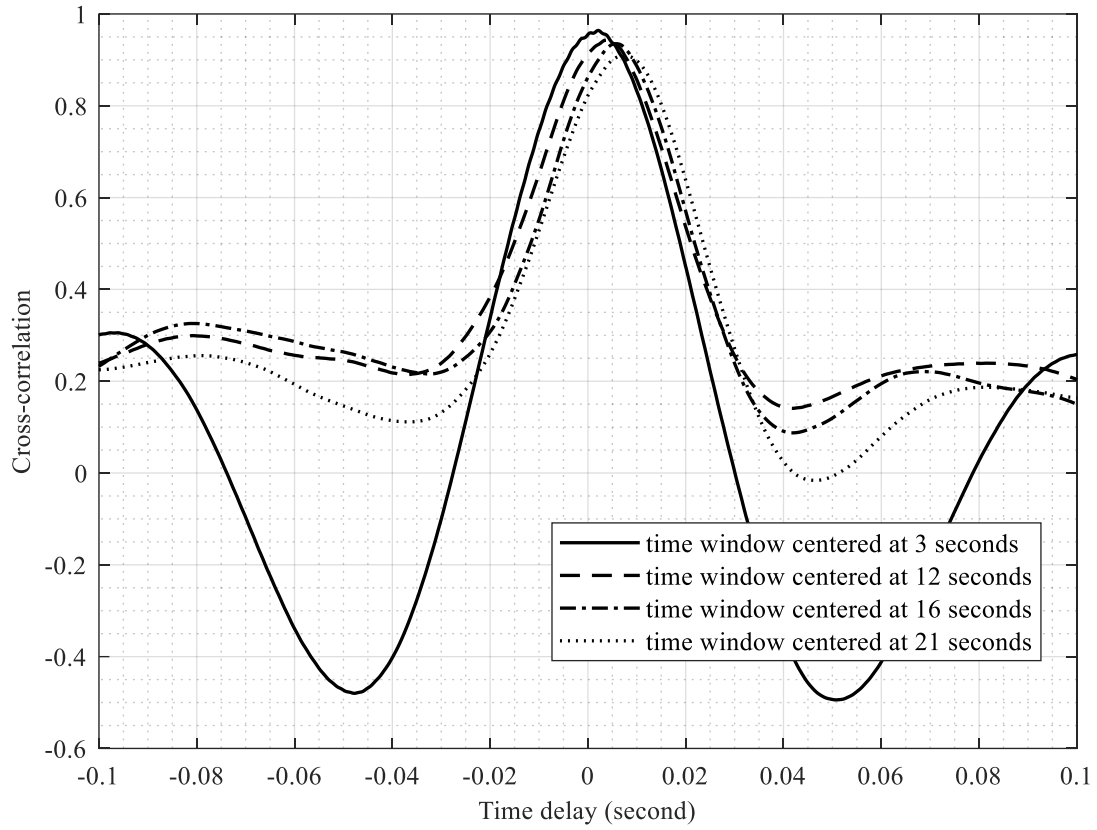


Figure 8-11: Enlarged view of the cross-correlation between A08 and A09 accelerations (model 1) for different time windows centered at 3, 12, 16 and 21 seconds

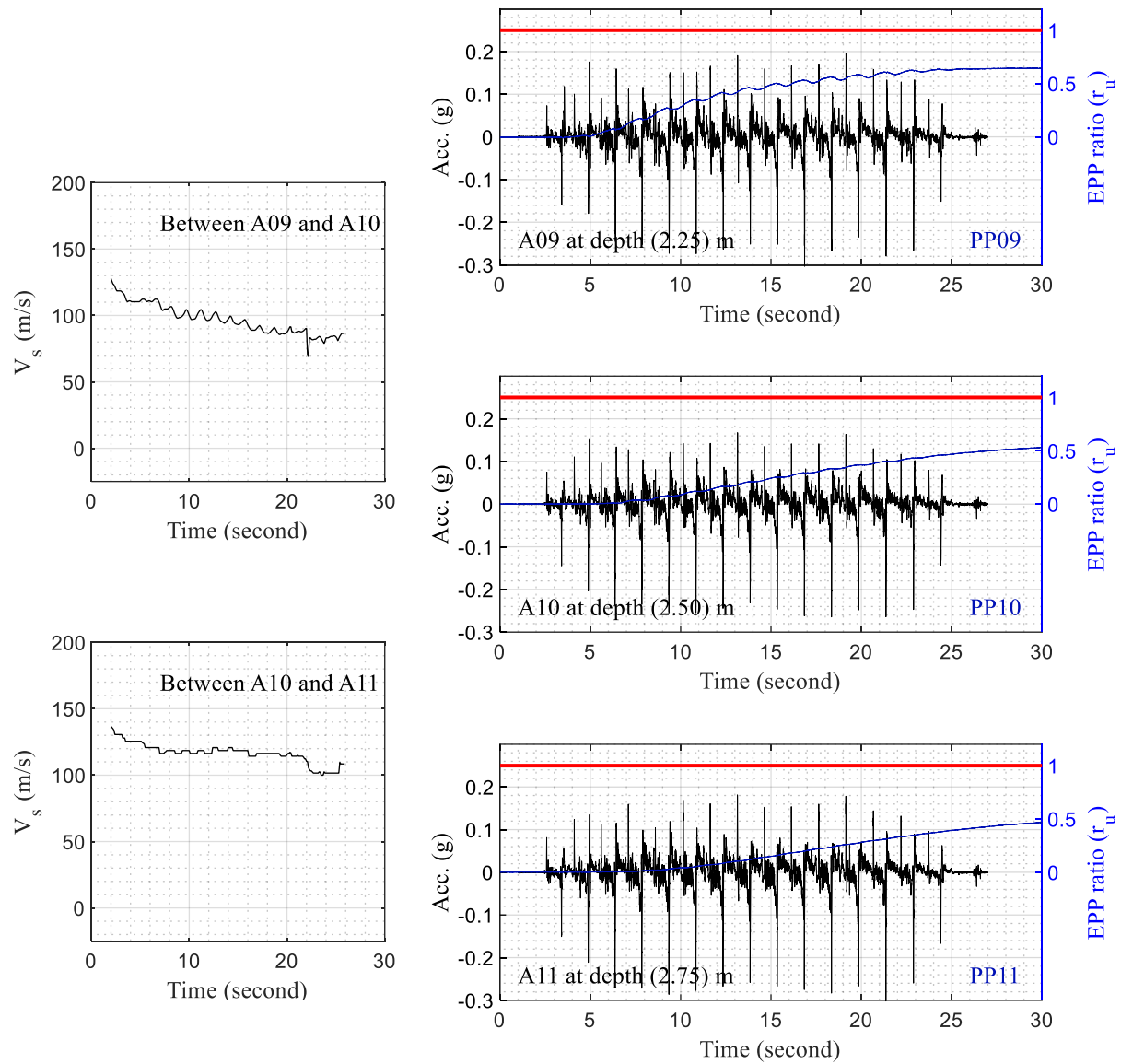


Figure 8-12: Time histories of  $V_s$  as well as the corresponding acceleration (A09, A10 and A11) and EPP ratio within the base dense layer in model 1

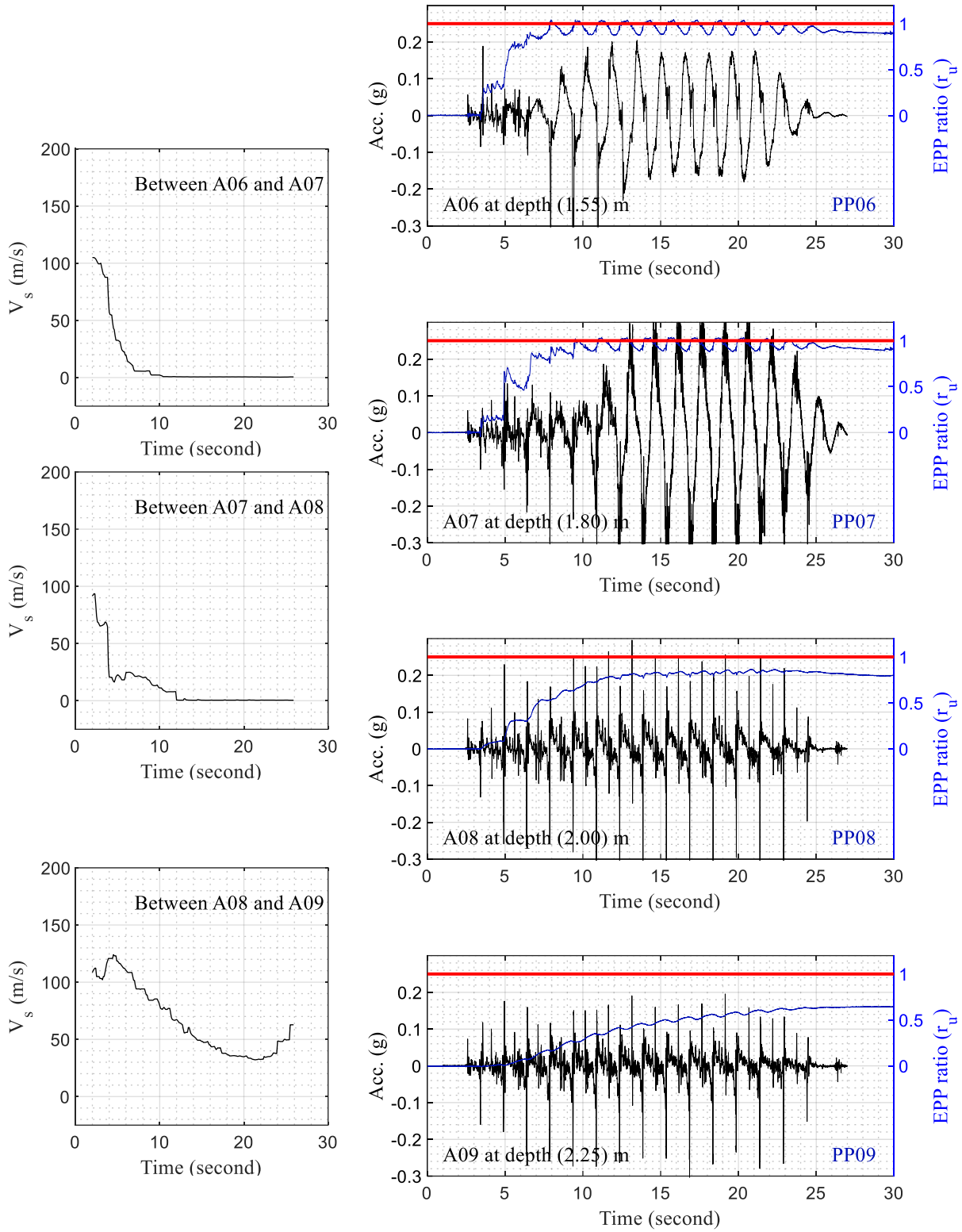


Figure 8-13: Time histories of  $V_s$  as well as the corresponding acceleration (A06, A07, A08 and A09) and EPP ratio within the loose and dense layers in model 1

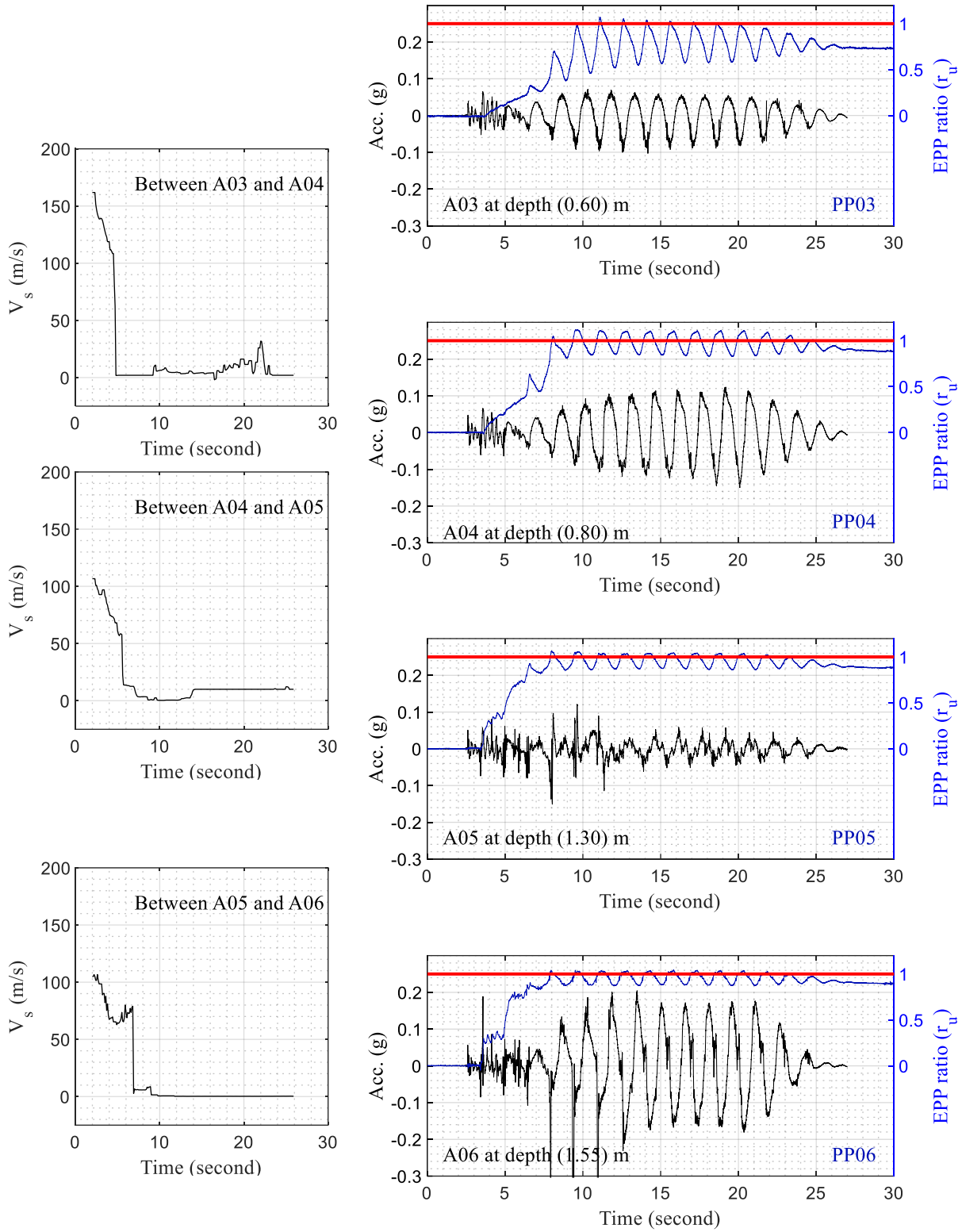


Figure 8-14: Time histories of  $V_s$  as well as the corresponding acceleration (A03, A04, A05 and A06) and EPP ratio within the loose layer in model 1

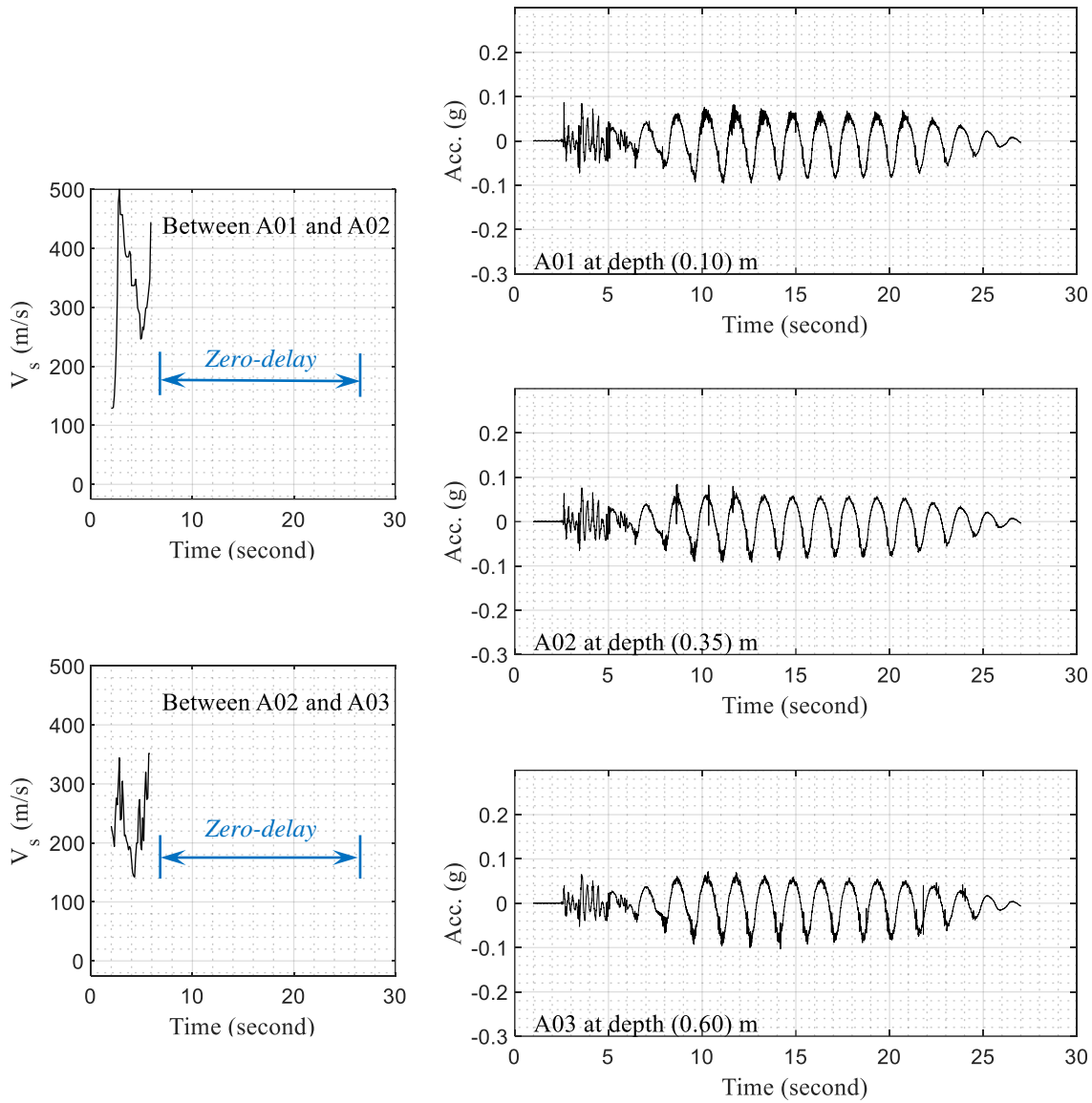


Figure 8-15: Time histories of  $V_s$  and the corresponding acceleration (A01, A02 and A03) within the crust layer in model 1

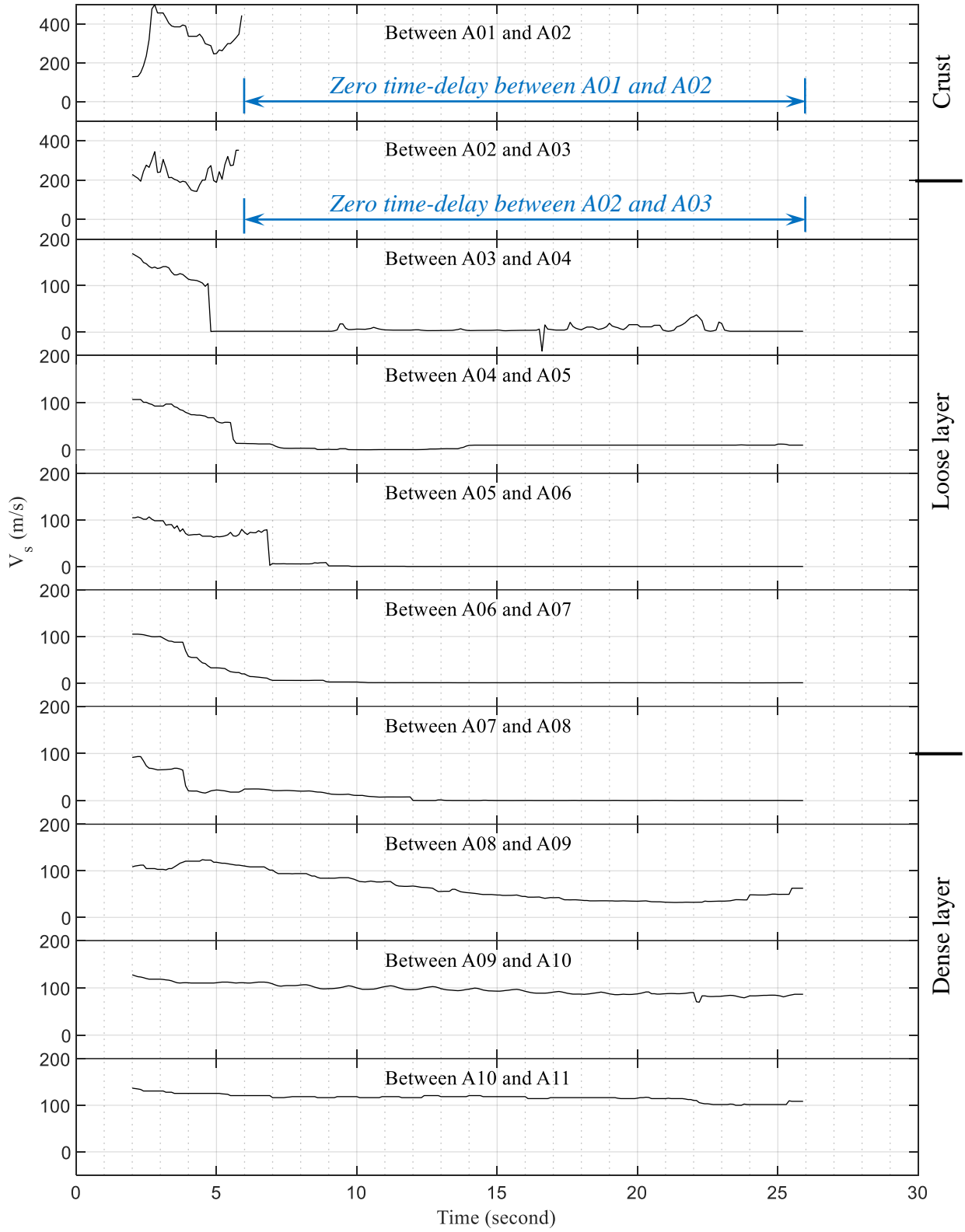


Figure 8-16: Evolution of  $V_s$  during shaking at different locations along depth of model 1

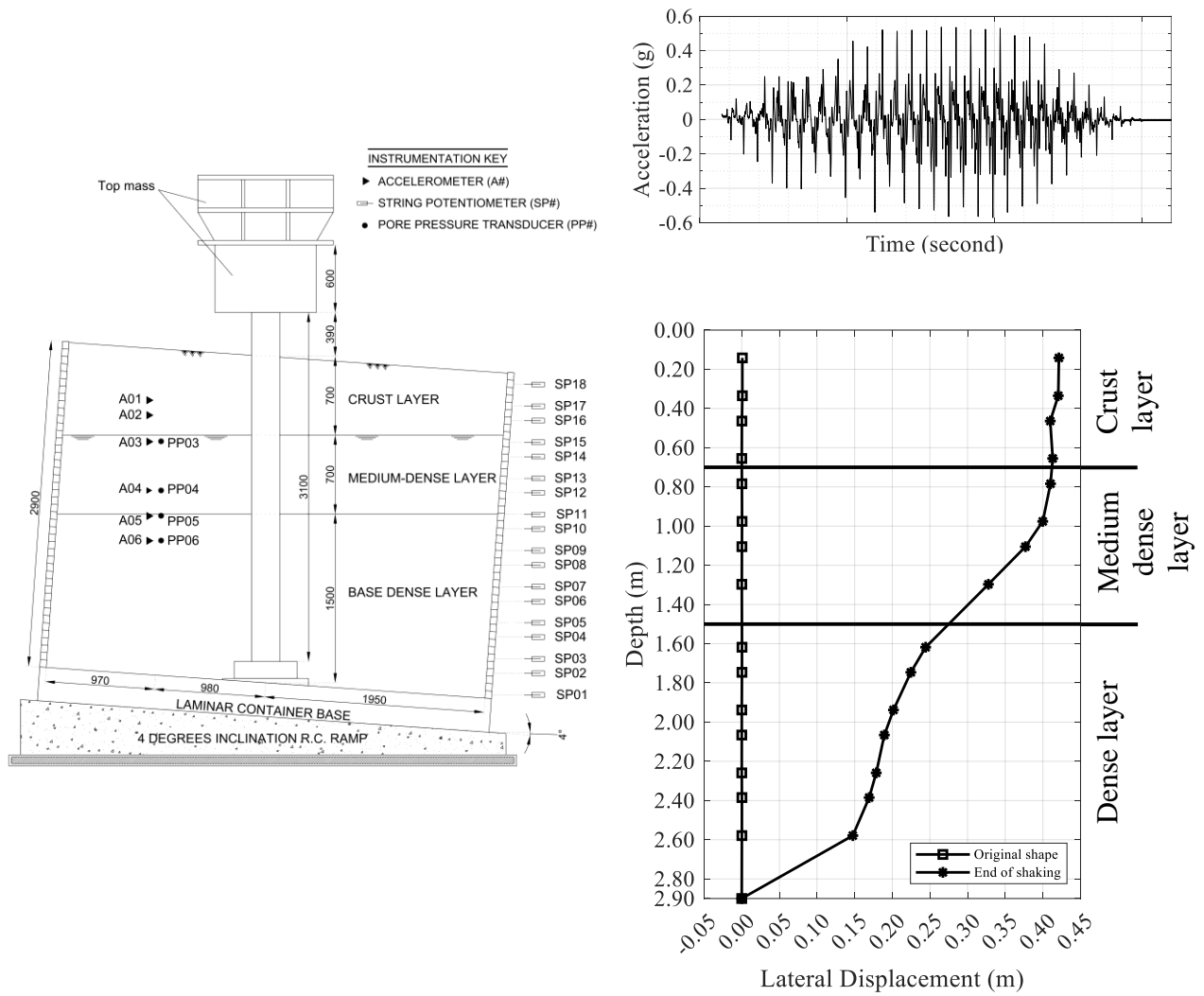


Figure 8-17: Model 2 layout of accelerometers and nearby pore pressure transducers (dimensions shown in mm), as well as input shake table motion and final lateral displacement profile of the laminar container

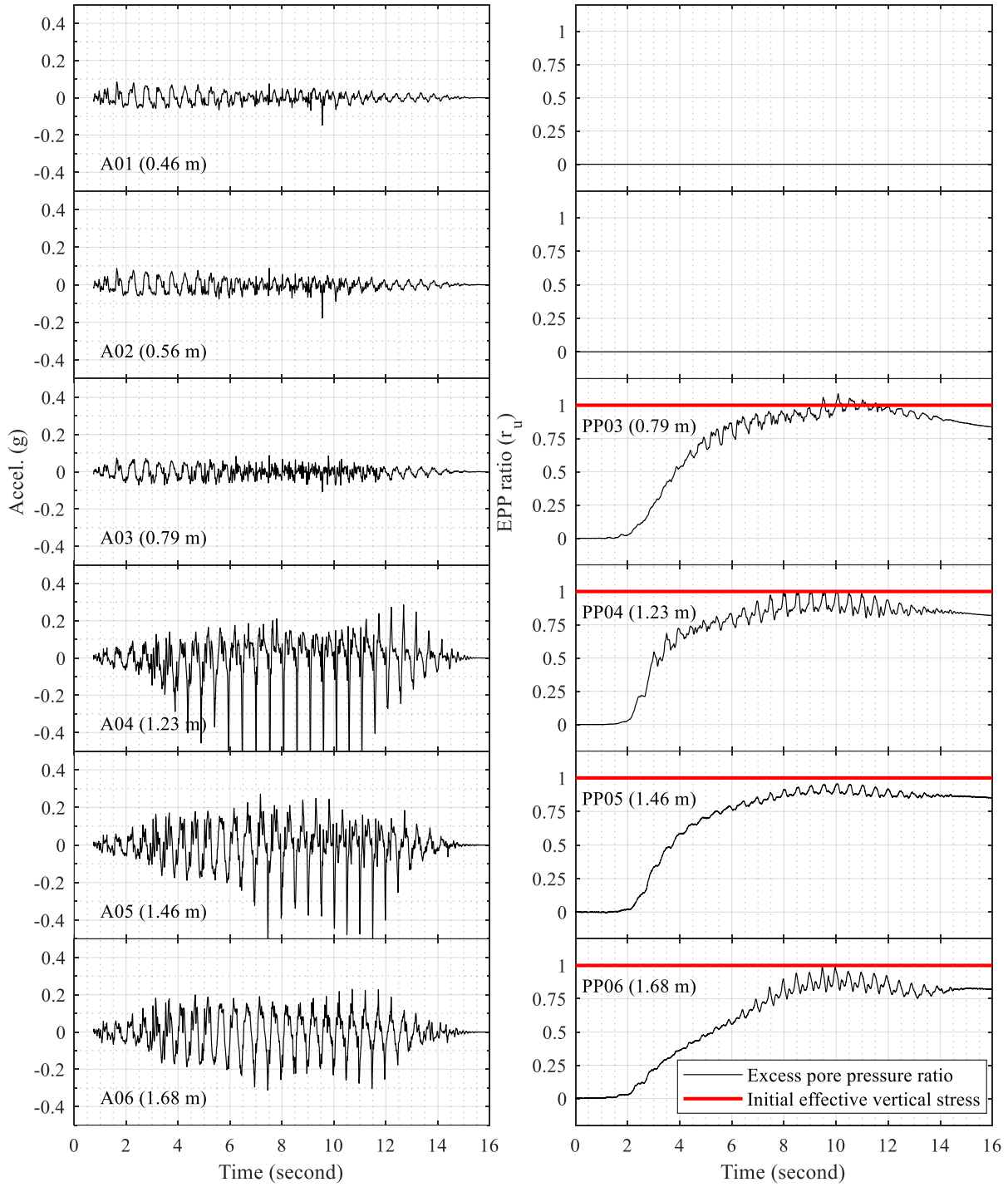


Figure 8-18: Model 2 time histories of acceleration at different depths, and the corresponding histories of EPP ratio



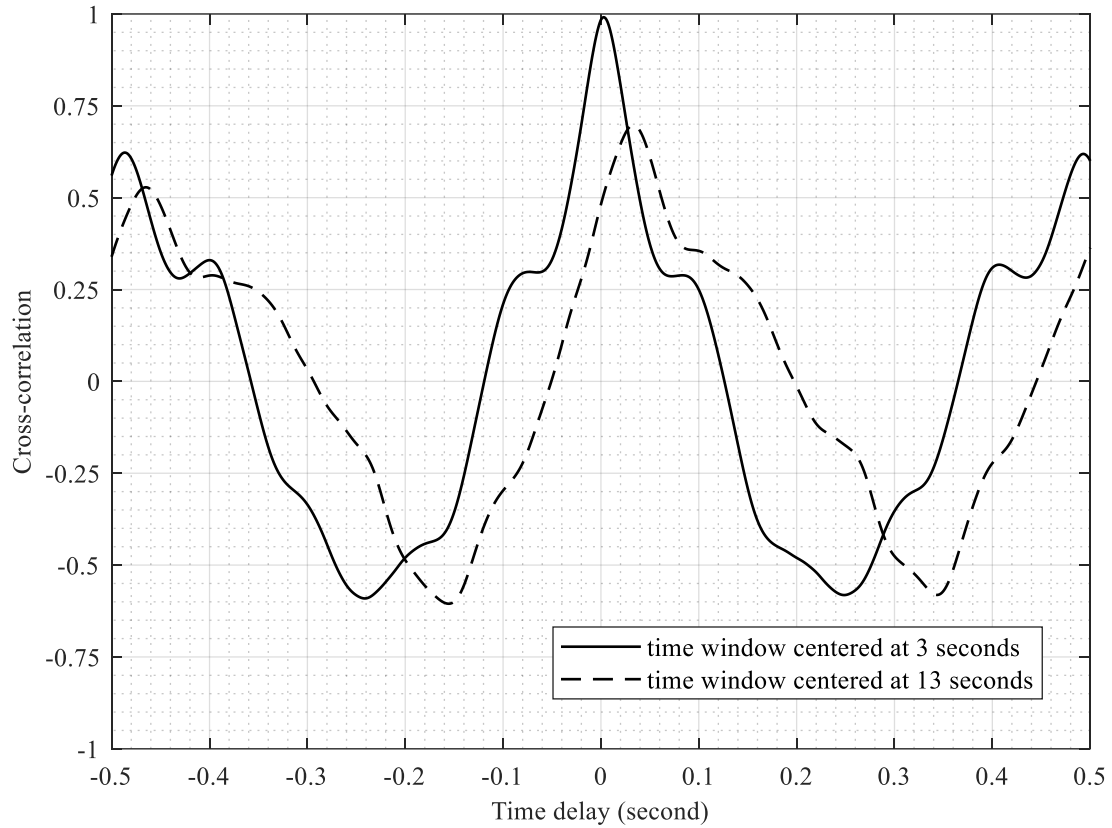


Figure 8-19: Cross-correlation between A5 and A6 accelerations (model 2) for two time windows centered at 3 seconds (i.e., at the beginning of shaking) and 13 seconds (i.e., towards end of shaking)

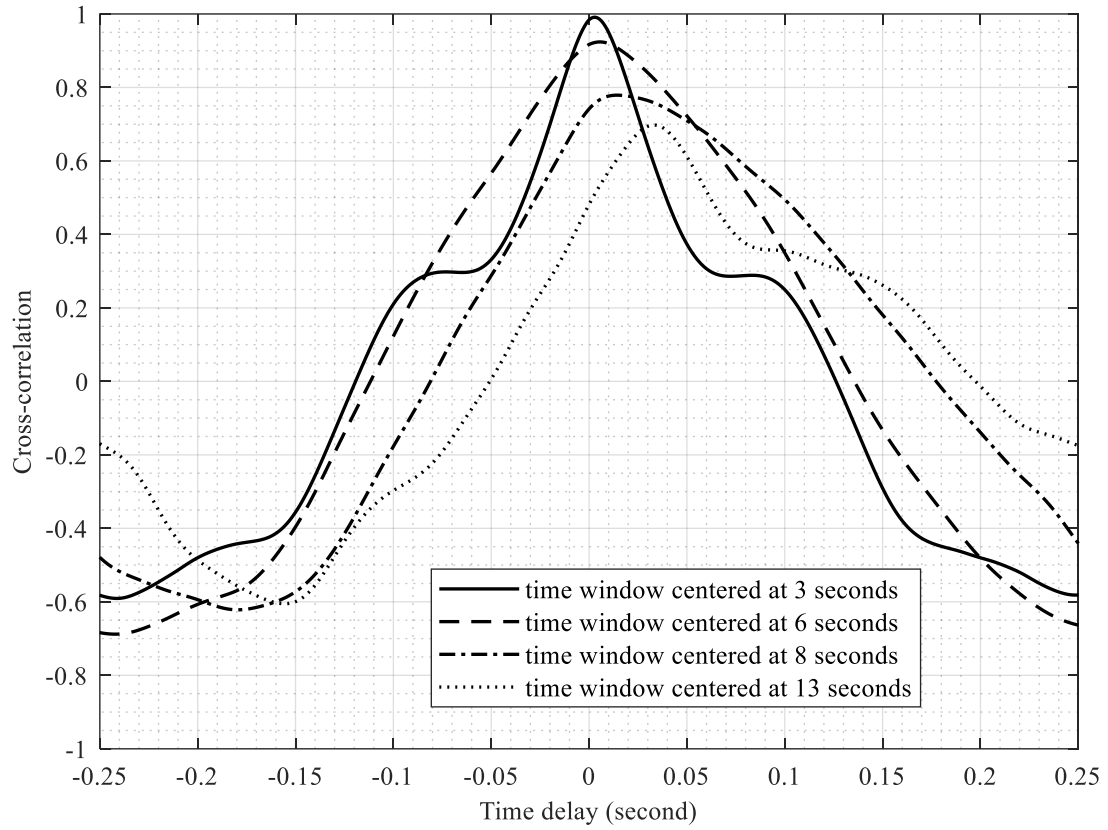


Figure 8-20: Enlarged view of the cross-correlation between A5 and A6 accelerations (model 2) for different time windows centered at 3, 6, 8 and 13 seconds

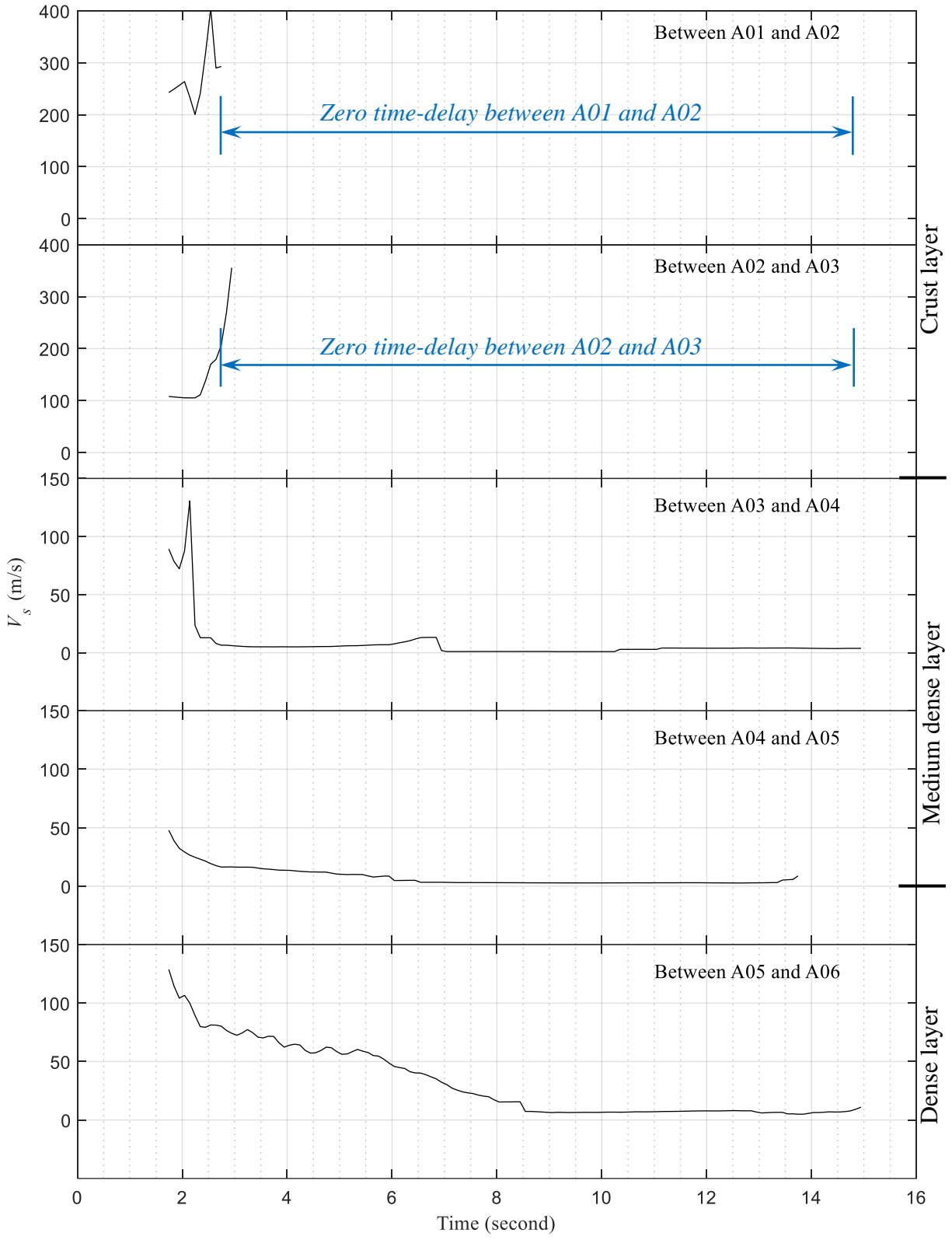


Figure 8-21: Model 2 evolution of shear wave velocity during shaking at different locations along depth

## Chapter 9

# Asymmetric Input Motion for Accumulation of Lateral Ground Deformation in Laminar Container Shake Table Testing

*I have not failed. I have just found 10,000 ways that  
won't work.*

– Thomas A. Edison

### 9.1 Abstract

Due to seismic response, accumulation of permanent ground deformation (lateral spreading) is an important mechanism of much practical significance. Such deformations typically occur near a ground slope, behind retaining structures such as sheet-pile and quay walls, and in mildly sloping ground. In conducting a shake table test, the generation of permanent deformations further elucidates the underlying mechanisms and allows for related ground-foundation-structure response insights. In this paper, an approach for development of accumulated ground deformations is presented, in which asymmetric inertial loading results in a biased dynamic one-dimensional shear state of stress. As such, the proposed approach allows for further insights into the soil cyclic response and pore pressure build-up, with deformations accumulating in a preferred direction. In order to permit a virtually unlimited number of such loading cycles, focus is placed on motions

that do not cause the shake-table actuator to accumulate displacement, in view of its possible limited stroke. Using this approach, representative experimental response is outlined and discussed. This experimental response can be used for calibration of numerical models to emulate the observed permanent strain accumulation profile and associated mechanisms. In addition to liquefaction-induced lateral spreading, this asymmetric shaking approach might be beneficial for a wide class of earthquake engineering shake table testing applications.

## 9.2 Introduction

Liquefaction-induced lateral ground deformation due to earthquake excitation is a main mechanism that results in major damage to embedded structures and foundation systems worldwide (Andrus and Youd 1987, Sims and Garvin 1995, Cetin *et al.* 2004, Sonmez *et al.* 2008, Cubrinovski *et al.* 2012, Tokimatsu *et al.* 2012). Using the extensive data compiled for the 1964 Niigata and 1983 Nihonkai-Chubu earthquakes in Japan (Hamada *et al.* 1986), Bartlett and Youd (1995) identified two general types of lateral deformations: (1) lateral spread in a level ground towards a free face or near quay wall, sheet pile wall or yielding retaining structure, and (2) lateral spread down a mild ground inclination where a free face is absent. In addition to the above two types of lateral spreads, permanent coseismic lateral displacement has been documented from records of near-fault ground motion (Iwan *et al.* 1984, Iwan *et al.* 1985, Hall *et al.* 1995, Elnashai *et al.* 2010, Vigny *et al.* 2011).

Due to the scarcity of instrumented sites and well documented field case histories, physical model experiments have been of much value in elucidating the associated response mechanisms. In the context of physical modeling, permanent ground deformation was reproduced by sloping ground configurations (Madabhushi *et al.* 2001, Haigh and Madabhushi 2002, Brandenberg *et al.*

2005, 2007a, b, Carey *et al.* 2018, Manzari *et al.* 2018), and by presence of yielding retaining structures such as sheet piles or quay walls (Sato 1997, Ghalandarzadeh *et al.* 1998, Horikoshi *et al.* 1998, Lee 2005, Motamed and Towhata 2009, Motamed *et al.* 2009, Motamed *et al.* 2013, Tang *et al.* 2014). Researchers at Rensselaer Polytechnic Institute (RPI), developed and employed a mildly inclined laminar container configuration as an innovative technique to emulate the mechanism of liquefaction-induced lateral spreading in scenarios of gentle ground slopes. Since then, a large number of investigations over a span of more than 20 years have adopted this valuable testing technique in centrifuge testing (Dobry 1994, Taboada 1995, Elgamal *et al.* 1996b, Taboada-Urtuzuastegui and Dobry 1998, Abdoun and Dobry 2002, Abdoun *et al.* 2003, Abdoun *et al.* 2005, Gonzalez *et al.* 2009), as well as in 1-g shake table experimentation (Elgamal *et al.* 2006, Thevanayagam *et al.* 2009, Dobry *et al.* 2010, Chang and Hutchinson 2013). In this testing configuration, dominance of the simple shear state of stress facilitated extraction of the underlying stress-strain response and potential progression towards liquefaction as recorded by pore-pressure transducers (Elgamal *et al.* 1996b, Taboada-Urtuzuastegui and Dobry 1998, Dobry *et al.* 2010).

The stress-states reproduced in the above-mentioned experimental studies provided a wealth of data that has been used to glean insights about the shear deformation accumulation mechanisms (Zeghal *et al.* 1999, Carey *et al.* 2018, Zeghal *et al.* 2018). As a contribution to this line of research, a technique is proposed herein for accumulation of deformations in laminar container testing, without imposing an inclination on the tested geometric configuration. This technique does not replicate any of these stress-states, but simply relies on asymmetric base excitation (positive versus negative) to generate higher inertial lateral forces and deformations in a prescribed preferred direction (analogous to downslope motion). As such, the proposed technique provides additional insights about the mechanisms of cyclic shear strain accumulation, not

manifested in conventional symmetric loading situations. These insights can be of much value in calibration of numerical models in terms of capturing the observed levels of cycle-by-cycle shear deformations, and the associated excess-pore pressure buildup characteristics.

Simplifications and advantages of this asymmetric motion approach stem from: i) conducting the laminar container test without an underlying ramp, potentially leading to significant savings in expenses and time, particularly for large-scale 1-g testing scenarios, ii) aligning the shaking direction with the horizontal layering of the ground strata, iii) ability to tailor the input shake table excitation so as to impose arbitrary levels of symmetric as well as biased accumulated displacement, which can even alternate between forward and backward deformations during the same shaking event, and iv) possible implementation of this approach in multi-directional loading environments, thus generating more complex stress-path scenarios that might be of interest for the purposes of numerical model calibration. In the following sections, the proposed technique is presented, along with experimental results to illustrate the outcomes.

### **9.3 Conceptual framework of asymmetric base excitation**

In geotechnical earthquake engineering, asymmetric acceleration and resulting downslope deformations are conceptually displayed in the Newmark sliding block waveform (Kramer 1996). Aiming to generate biased accumulated permanent ground deformation, an approach of asymmetric base excitation is discussed herein in the context of uni-directional 1-Degree of Freedom (DOF) shaking (but equally applicable for multi-directional 6-DOF scenarios). The asymmetric base excitation induces seismic inertial forces that are larger in the forward direction for instance, leading to a corresponding gradual accumulation of ground deformation. As such, cyclic loading of this type will allow accumulation of permanent deformations in the forward

direction on a cycle-by-cycle basis. In each cycle, the full stroke of the shake table actuator may be fully utilized in order to maximize the input shaking amplitude.

In general, any asymmetric input acceleration waveform will result in an accumulation of deformations. When a long stroke actuator is available, more versatility is allowed in tailoring the input acceleration. For instance, Figure 9-1 shows an asymmetric acceleration signal (Ebeido 2019) with the actuator moving from one end of its stroke to the other (a total of 1.2 m in the UC San Diego outdoor shake table facility <http://nheri.ucsd.edu>), generating sustained levels of imposed lateral acceleration that is superposed on the otherwise harmonic excitation.

If needed (due to limited actuator stroke), returning the actuator to its initial starting position (on a cycle-by-cycle basis) will allow for application of a virtually unlimited number of loading cycles. As such, Figure 9-2 shows examples of asymmetric base acceleration, depicting different waveforms of the resulting actuator displacement.

It is worth noting that the presented examples in Figure 9-2 for instance, can be further tailored to impose different levels of asymmetry in each loading cycle. As such, the recorded response might encompass a broader range of response scenarios with different levels of accumulated cyclic strains for the purpose of subsequent numerical model calibration.

## **9.4 Experimental implementation**

Figure 9-3 displays the employed asymmetric shake table base excitation, tailored such that the displacement returns back to its original position, on a cycle-by-cycle basis. Figure 9-4 shows an enlarged view for one cycle of the asymmetric base excitation presented in Figure 9-3. From Figure 9-4, it can be observed that the velocity at the beginning of each cycle is ramping up



and reaching a peak value. During this velocity build-up phase, the acceleration increases slightly, and the displacement increases in amplitude (Figure 9-4). Thereafter, the velocity undergoes a sudden drop in amplitude, associated with the large biased instant of negative acceleration. To complete the cycle, the table displacement is prescribed to gradually return back to zero, allowing potentially for an unlimited number of cycles to be applied. As such, in each cycle, the base excitation is designed to have a large acceleration peak, in one direction, with much lower peaks in the other direction.

It is of interest to note that velocity pulses of analogous shape have been noted (Iwan *et al.* 1984, Hall *et al.* 1995, Kalkan and Kunnath 2006) in the records of near-fault ground motions, such as those of Rinaldi, 1994 Northridge earthquake, Sakarya-SKR, 1999 Kocaeli earthquake (Figure 5) and Station 12, 1982 Lulong earthquake (Figure 9-6). Hall *et al.* (1995) discuss many earthquake records that displayed velocity pulses and resulted in considerable permanent ground deformation (e.g.,  $M_w$  7.2 Landers earthquake – Lucerne station,  $M_w$  6.7 Northridge earthquake– Rinaldi receiving station,  $M_w$  6.6 Superstition Hills earthquake– Parachute test site).

## **9.5 Experimental procedures**

### **9.5.1 shake table and laminar soil container**

The experimental work in this study was conducted at the Powell Laboratory shake table facility, located at the University of California San Diego (UCSD). The uniaxial shake table platform has dimensions of 4.9 m by 3.1 m, with a real-time three-variable digital controller. The shake table actuator has a maximum nominal shaking force of 490 kN (110 kips). The table platform can hold models that weight up to 350 kN (80 kips). Maximum table displacement is

±150 mm with a maximum nominal operating frequency of 20 Hz. Performance and construction of the Powell laboratory shake table are detailed in Magenes (1989a), and Trautner *et al.* (2018).

A laminar container with internal dimensions of 3.9 m x 1.8 m x 1.8 m (Length x Width x Height) was constructed at UCSD using 28 structural steel frames arranged in stacks (Ashford and Jakrapiyanun 2001). The laminar container was designed to be used with dry and saturated soil models and exhibits minimal boundary effects; simulating a one-dimensional (1D) shear stress-strain wave propagation state (Chang and Hutchinson 2012, Chang and Hutchinson 2013, Ebeido *et al.* 2018a). Aiming to enhance its capabilities, the container has been recently extended to a 2.9 m height instead of 1.8 m, by inclusion of 16 additional steel frames (Ebeido 2019). Figure 9-7 shows the extended laminar container attached to the Powell Laboratory shake table.

### **9.5.2 Model preparation**

Ottawa sand F-65 (Table 9-1) was used to prepare the soil model. A.60 MIL thick Ethylene Propylene Diene Monomer (EPDM) rubber liner manufactured by *Field Lining Systems, Inc.* was placed to hold soil and water inside the laminar container (Figure 9-8a). Construction of the soil model (Figure 9-9) was accomplished in two phases. The first consisted of building a 1.3 m high very dense sand base stratum (Table 9-2). This base layer was placed and compacted in lifts, each of about 0.25 m in thickness, using a plate compactor. Special care was exercised in the vicinity of the deployed sensors, hung inside the soil container by means of geogrid strips (Figure 9-8c and Figure 9-9), to avoid potential damage to the instrumentation and/or the cables.

By monitoring weight of each sand batch being placed inside the container and knowing volume of the sand layer, average relative density ( $D_r$ ) was estimated to be about 90%. Conducted sand cone tests resulted in a similar estimate as well. After construction, this base layer was

saturated with water, carefully and slowly dripped into the container by means of perforated Poly-Vinyl Chloride (PVC) pipes that were placed at the container base before building the soil model. Such technique allows for water saturation and minimizes the chance of air bubbles being trapped within the soil model. After saturation, a number of white noise motions of 0.03g acceleration amplitude were imparted on the dense layer to further promote removal of any trapped air bubbles (none were observed).

Building the upper 1.7 m high medium dense layer (Figure 9-9) constituted the second phase of model construction. Sand was pluviated into the container from a hopper equipped with sieves (Figure 9-8b) at a constant falling height and flow rate, in an effort to build a relatively uniform deposit. To further promote uniformity of this upper stratum, an additional set of sieves was placed inside the soil container as shown in Figure 9-8c. The pluviation process was conducted while keeping the water table above the top sand surface at all times (Figure 9-8d). The distance between the top water surface and the top sand surface was kept in the range of 0.25 m-0.40 m. After building the upper medium dense sand layer, water table was lowered to 0.3 m below the topsoil surface (resulting in an un-saturated 0.3 m upper crust). Average relative density ( $D_r$ ) was found to be about 65% (Table 9-2).

### **9.5.3 Test description**

The free field soil response due to the imparted base excitation was recorded using three vertical arrays of accelerometers and pore pressure transducers as shown in Figure 9-9. At the same elevations, the outer laminates were instrumented with string potentiometers to measure lateral displacement. Number of accelerometers (A#) varied for each array from 4 to 11, vertically spaced, to record seismic wave propagating from the base all the way upwards to the soil top

surface. Additionally, small-size pore pressure transducers (PP#) of type BPR-A-S manufactured by *Kyowa Electronic Instruments Co., LTD* were placed in each array, near the accelerometers.

The shake table was used to generate one dimensional asymmetric motion as presented in Figure 9-3 and Figure 9-4. The motion consisted of 20 cycles (about 30 seconds), with a uniform peak acceleration of about 0.6g and peak displacement amplitude of 0.05 m. Figure 9-10 shows the actual command and feedback signals in terms of displacement, velocity and acceleration for the base excitation as recorded by the shake table controller data acquisition system at a sampling frequency of 256 sample/second/channel.

An enlarged view of the shake table response is further presented in Figure 9-11, from which it can be noticed that the shake table reasonably achieved the target displacement as well as the target velocity. The acceleration response is somewhat noisy due to friction in the shake table bearings as discussed in Trautner *et al.* (2018), Zayed *et al.* (2020).

## **9.6 Experimental response and discussion**

### **9.6.1 Soil acceleration and pore pressure response**

Figure 9-12 displays representative results of the recorded lateral acceleration and pore pressure along the north instrumentation array (Figure 9-9) Attenuation in acceleration amplitude is clear starting from the depth of 0.85 m (A107, at base of medium dense layer) and above. Such attenuation is associated with pore pressure (right column in Figure 9-12) achieving the level of liquefaction by the first half of the 1<sup>st</sup> cycle and the 3<sup>rd</sup> cycle, at the base and top of the liquefiable layer, respectively. Because of liquefaction, the acceleration record at the free surface (A111) displays the lowest amplitudes. A comparison between the acceleration records within the

liquefiable layer (A107 and A109) with those in the very dense layer (A101 and A103) indicates that the liquefiable layer acted as a band pass filter upon liquefaction, filtering out some high frequency content.

By the end of shaking, high excess pore pressures prevailed with liquefaction reaching a depth of about 2.0 m. Pore pressure transducers within the upper portion of the dense layer (i.e., PP105), show consistent and clear cycle by cycle pore pressure build-up, eventually reaching the level indicative of liquefaction. As such, pore pressure records show that liquefaction has occurred within the medium dense layer as well as the top of the very dense layer. Similar observations concerning evidence of liquefaction at the top of a dense sand stratum overlain by a looser layer were reported in a number of earlier studies (Fiegel and Kutter 1994, Byrne *et al.* 2004, Zayed *et al.* 2020).

## **9.6.2 Lateral soil deformation**

Time histories of the container lateral displacement are presented in Figure 9-13. Maximum permanent displacement of about 0.17 m was recorded at the top of the container. Figure 9-14 shows the container configuration before and after the shaking event. The cyclic accumulation of lateral deformation can be viewed in the form of the profiles presented in Figure 9-15. During the 1<sup>st</sup> and 2<sup>nd</sup> cycles, the laminar container accumulated a relatively small level of permanent lateral deformation. Thereafter, the soil model started to accumulate larger levels of biased permanent deformation, on a cycle-by-cycle basis.

From the soil profile displaced configurations (Figure 9-15), it can be noted that deformation was minimal above the water table, within the top crust stratum. In the underlying saturated soil, the upper medium dense layer follows a deformation trend that is steeper than that

of the underlying very dense layer. This is simply an outcome of the tendency for larger deformation within the upper saturated medium dense layer, compared to that of the underlying denser stratum.

Finally, some slippage may be observed as well at the very base of the soil model. This slippage occurred between the lowermost laminate and the base of the container. Due to the smooth nature of the EPDM liner, low friction was generated between the base of the laminar container and the liner, resulting in such slippage at the base of the container.

### **9.6.3 Evaluation of shear stress-strain histories**

The system identification technique proposed by Elgamal *et al.* (1996b) is used to illustrate the corresponding shear stress strain response within the medium dense liquefied sand stratum. For that purpose, displacement records were used to obtain both the shear stress and the shear strain time histories. Absolute acceleration was computed by double differentiation of the corresponding absolute displacement time histories. Thereafter, first order linear interpolation between accelerations was employed to estimate shear stresses, and second order interpolation between displacements was used to evaluate shear strains. These interpolation schemes yield second-order accurate shear stress and strain estimates (Zeghal *et al.* 1995).

On this basis, Figure 9-16 displays shear stress-strain time histories at the depths of 0.75 m, and 1.00 m, in the vicinity of peak accumulated shear strain along the soil profile. Strain accumulation and dilative spikes in the stress time histories can be observed as a consequence of those in the recorded acceleration (Figure 9-12).

Figure 9-17 presents the corresponding shear stress-strain response. The initial high shear modulus is visible at the very first cycle, followed by significant softening due to the liquefaction-induced strength degradation. Cycle-by-cycle accumulation of shear strains is seen thereafter (about 0.5% per cycle). In each cycle, a slight instantaneous regain in shear strength may be noted due to the tendency for dilation at large shear strain excursions (Zeghal and Elgamal 1994b).

## **9.7 Forward and backward accumulation of deformation**

An illustration of versatility in controlling the direction of deformations is shown in Figure 9-18. During a preliminary trial test, asymmetric motion presented in the upper row (Figure 9-18) was used to accumulate permanent lateral deformation of about 0.15 m in the forward direction. Adequate time was allowed after this shaking event for pore pressure dissipation. Thereafter, in the same test model, a different asymmetric motion was employed aiming to restore the accumulated lateral deformation of the container towards its original undeformed shape, as shown in the lower row of Figure 9-18. As such, the outcomes presented in Figure 9-18 further illustrate that the asymmetric base excitation can be tailored to allow for accumulation of lateral deformation arbitrarily in the forward or backward directions as desired.

## **9.8 Acknowledgement**

The research described in this chapter was partially funded by the California Department of Transportation (Caltrans) and the National Science Foundation grant OISE-1445712 Testing was conducted at the Powell laboratories, University of California San Diego, with assistance provided by Dr. Christopher Latham, Mr. Andrew Sander, Mr. Mike Sanders, Mr. Abdullah Hamid and Mr. Darren Mckay.

The contents of chapter 9 have been published as a journal paper in the Canadian Geotechnical Journal, Volume 58, Issue number 2, with a publication date 14<sup>th</sup> of April 2020. The title of this paper is “Asymmetric input motion for accumulation of lateral ground deformation in laminar container shake table testing”. The dissertation author is the primary author of this paper with Dr. Ahmed Ebeido, Mr. Athul Prabhakaran, Dr. Zhijian Qiu, and Professor Ahmed Elgamal as coauthors.



Table 9-1: Geotechnical properties of F-65 Ottawa sand (After Bastidas 2016b)

<b>Property</b>	<b>Description</b>
Mineralogy	Quartz, 99.7%
Grain shape	Rounded
Specific gravity, $G_s$	2.65
Coefficient of uniformity ( $C_u$ )	1.61
Coefficient of curvature ( $C_c$ )	0.96
Maximum and minimum voids ratio $e_{max}$ , $e_{min}$	0.853, 0.503
Maximum and minimum mass density $\rho_{min}$ , $\rho_{max}$ ( $kg/m^3$ )	1430, 1763

Table 9-2: Properties of the two sand strata

<b>Property</b>	<b>Base very dense sand layer</b>	<b>Top medium dense sand layer</b>
Thickness (m)	1.3	1.7
Bulk unit weight $\gamma_{\text{bulk}}$ (kg/m <sup>3</sup> )	2090	2010
Dry unit weight $\gamma_{\text{dry}}$ (kg/m <sup>3</sup> )	1730	1645
Relative density $D_r$ (%)	90	65

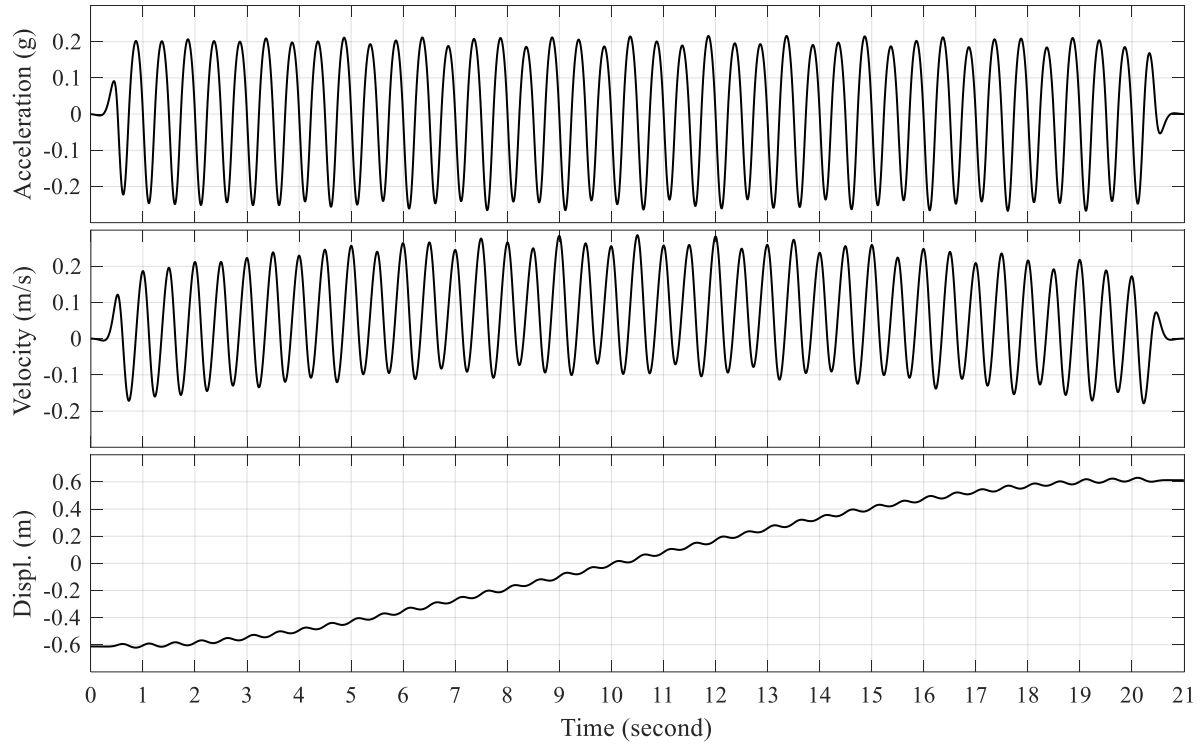


Figure 9-1: Asymmetric motion example for the forward increments scenario

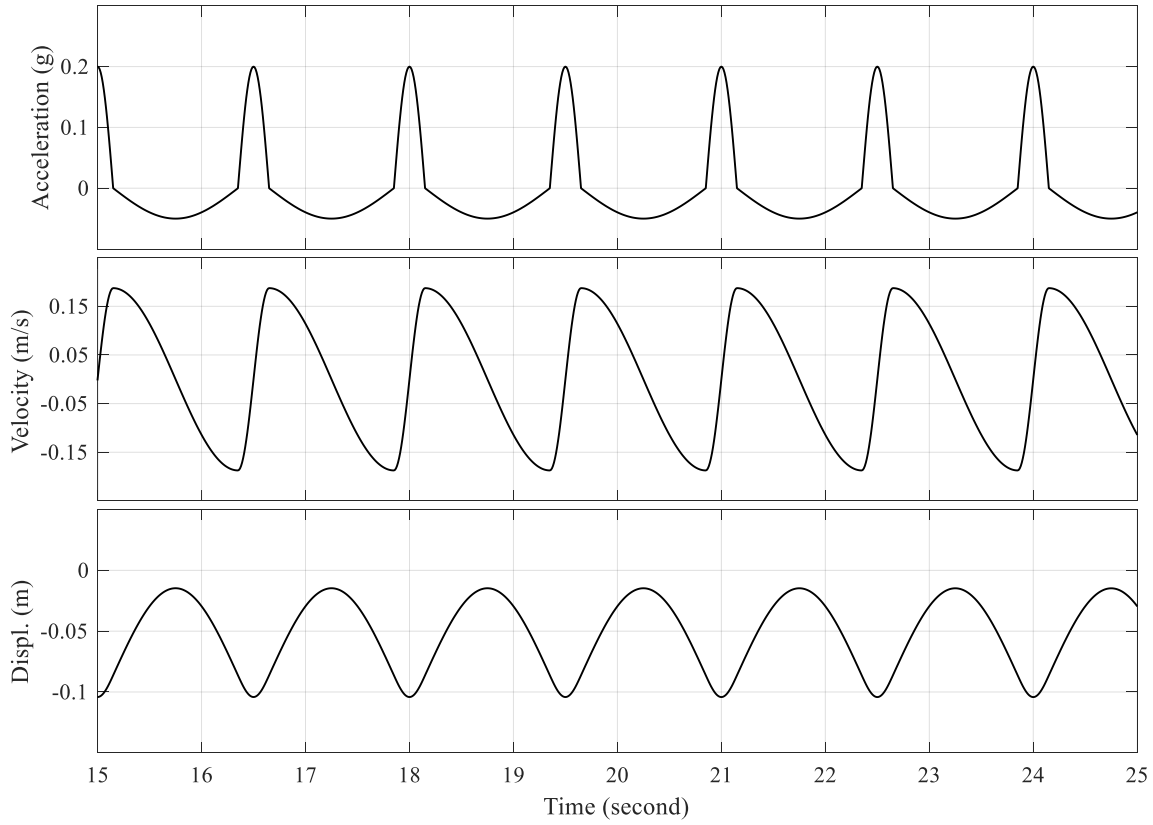
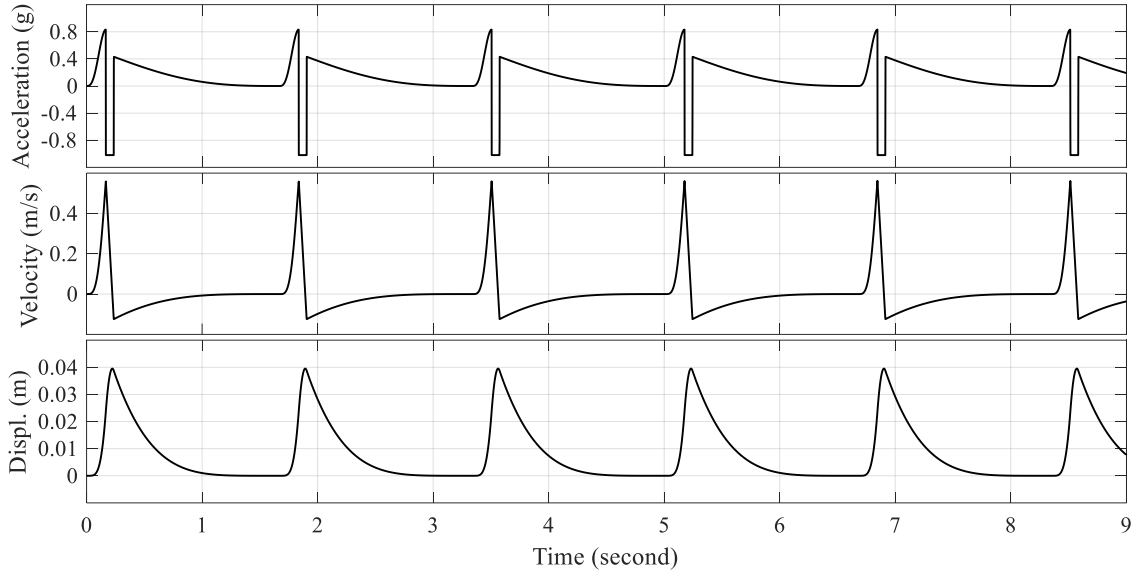


Figure 9-2: Idealized representative asymmetric acceleration base excitation signals

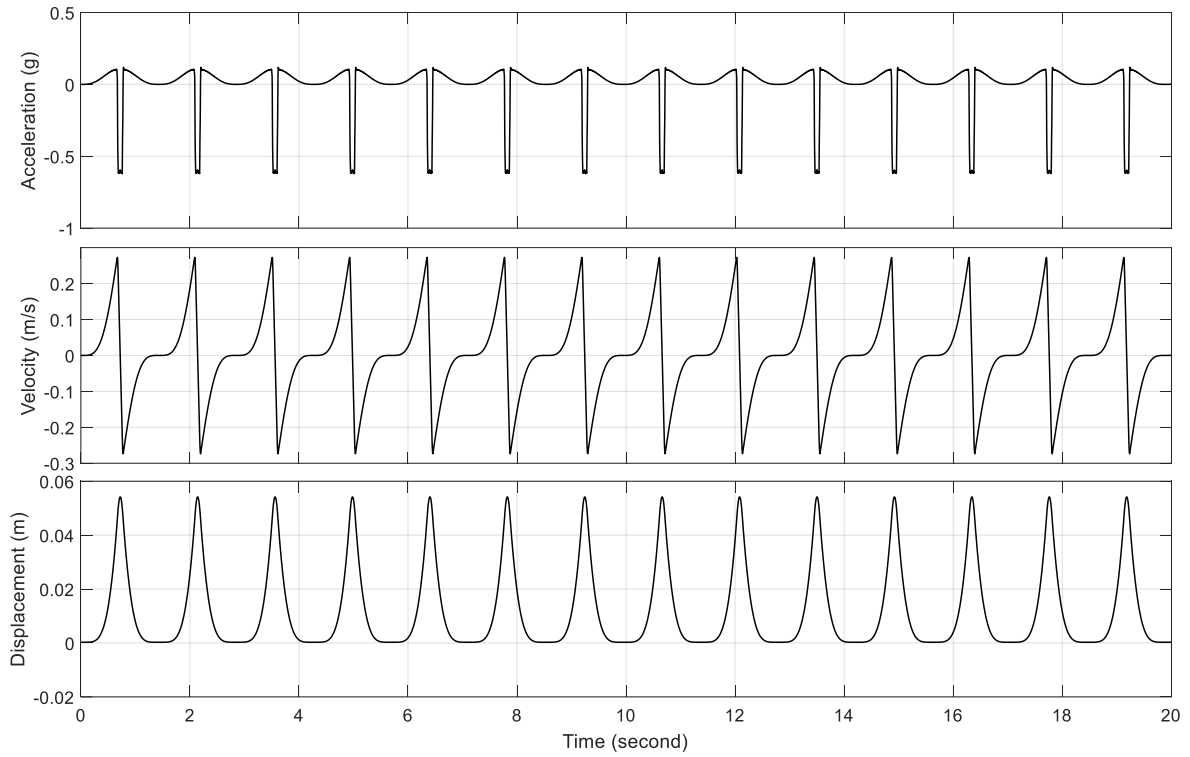


Figure 9-3: Input motion displacement, velocity, and acceleration (first 20 of 30 seconds in total)

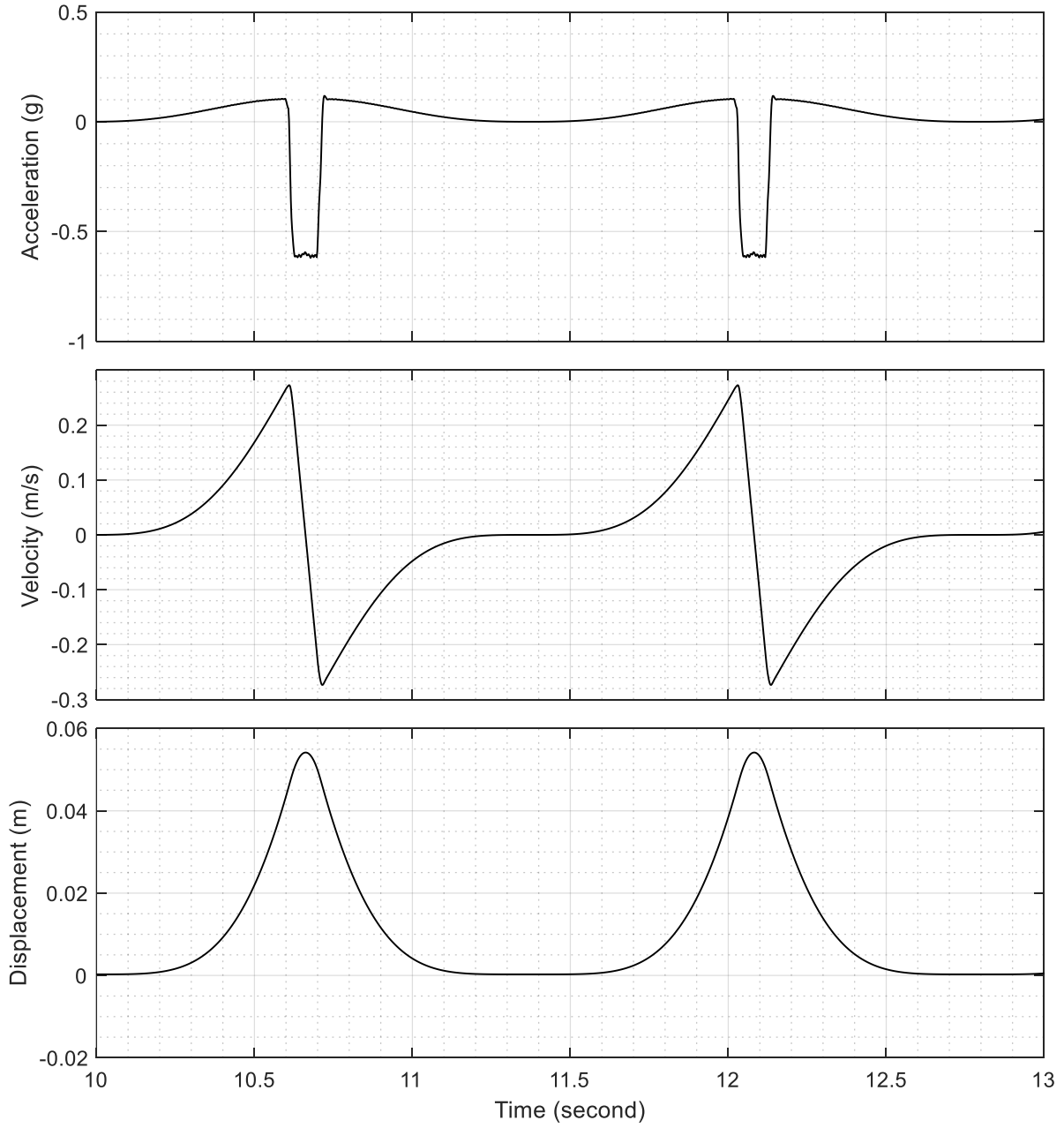


Figure 9-4: Enlarged view for two cycles of the input motion

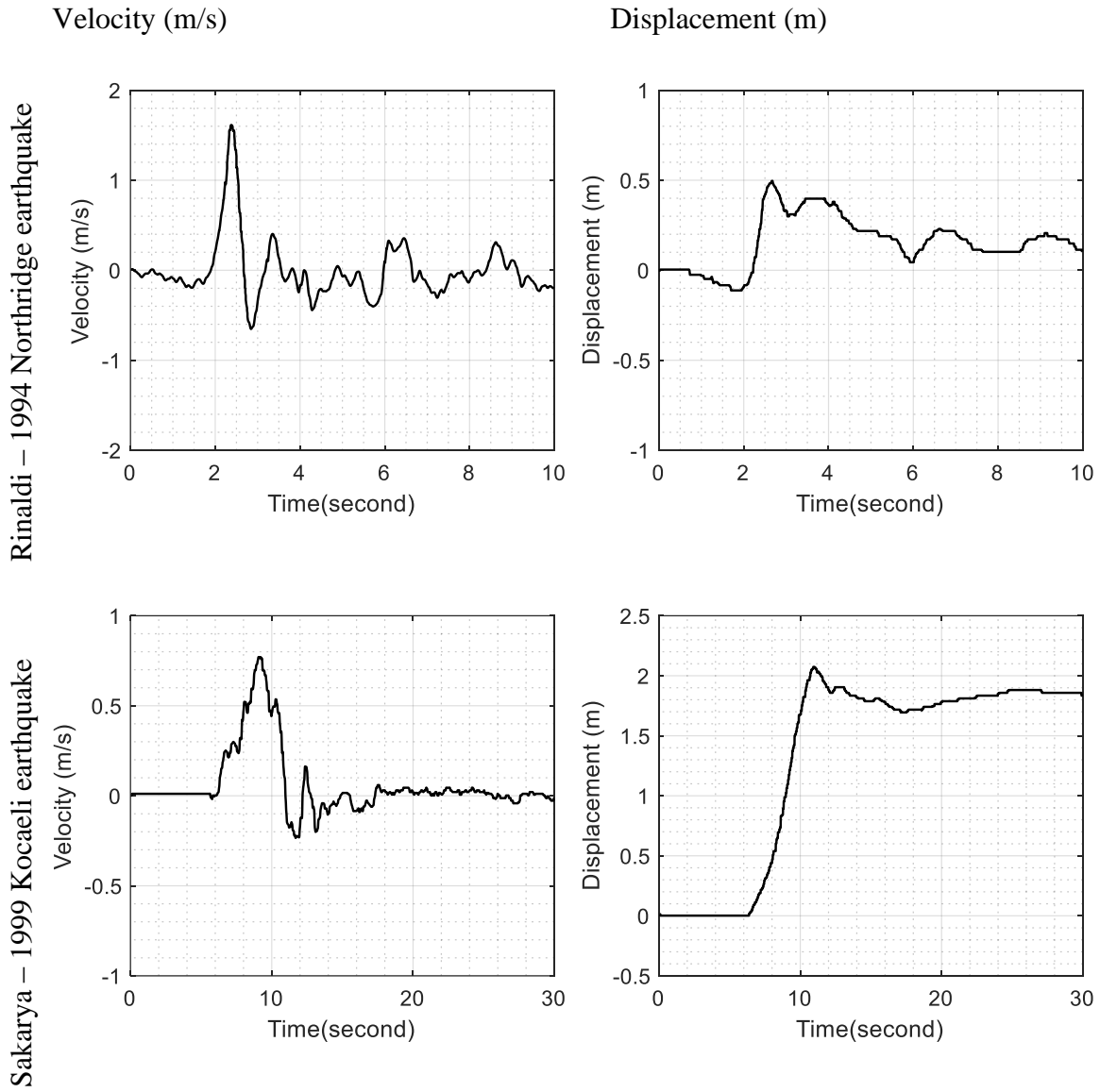


Figure 9-5: Velocity and displacement time histories for Rinaldi and SKR records (After Kalkan and Kunnath 2006)

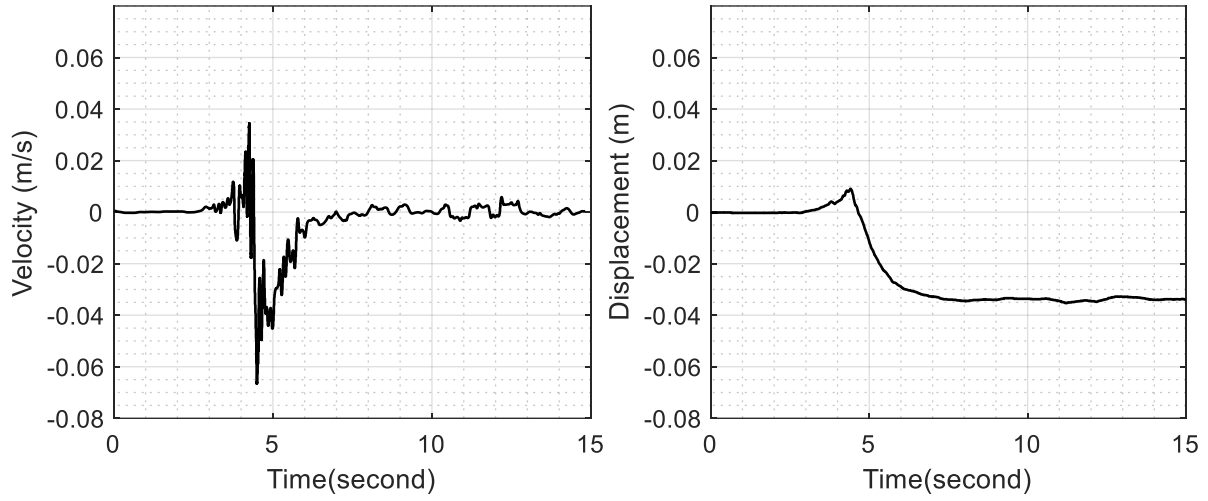


Figure 9-6: Velocity and displacement records of Station 12 during 1982 Lulong earthquake  
(After Iwan *et al.* 1984)





Figure 9-7: Laminar Soil Container Placed on Shake Table at the UC San Diego Powell Laboratory



(a)



(b)



(c)



(d)

Figure 9-8: a) Placing the EPDM liner inside the soil container, b) Soil hopper with a screen attached to it, c) additional set of sieves placed inside the soil container and d) sand pluviation

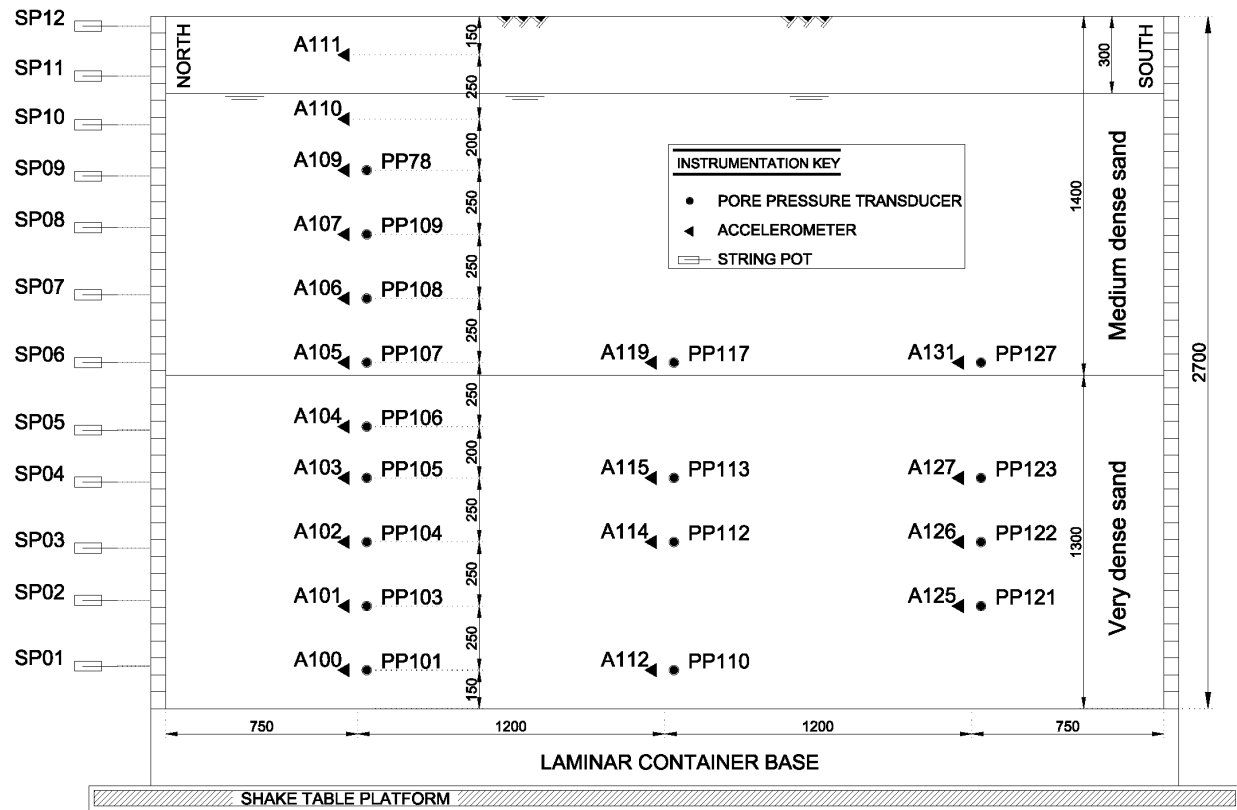


Figure 9-9: Testing configuration and instrumentation layout (dimensions shown in mm)

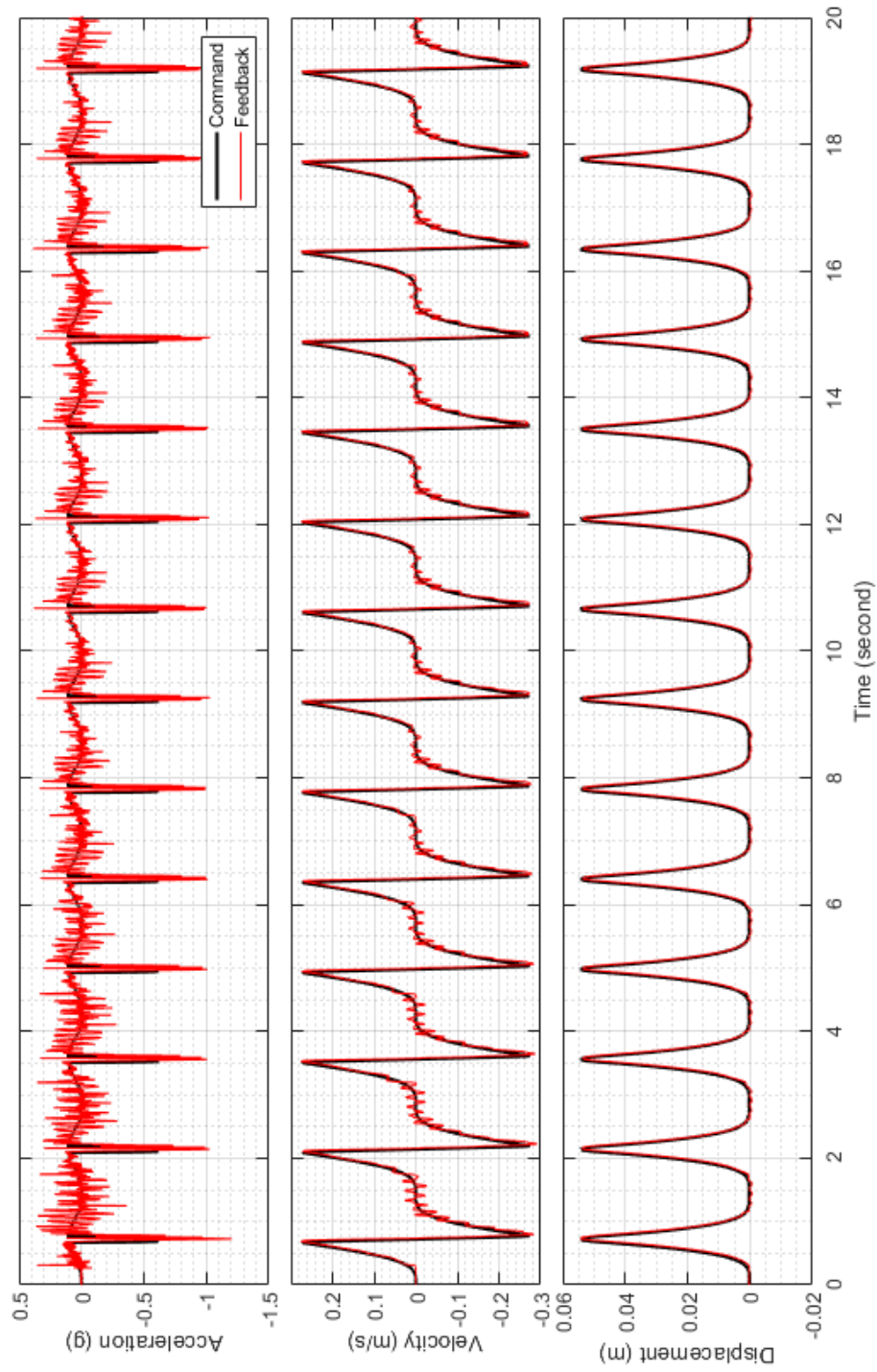


Figure 9-10: Command and feedback signals of the input motion (first 20 of 30 seconds in total)

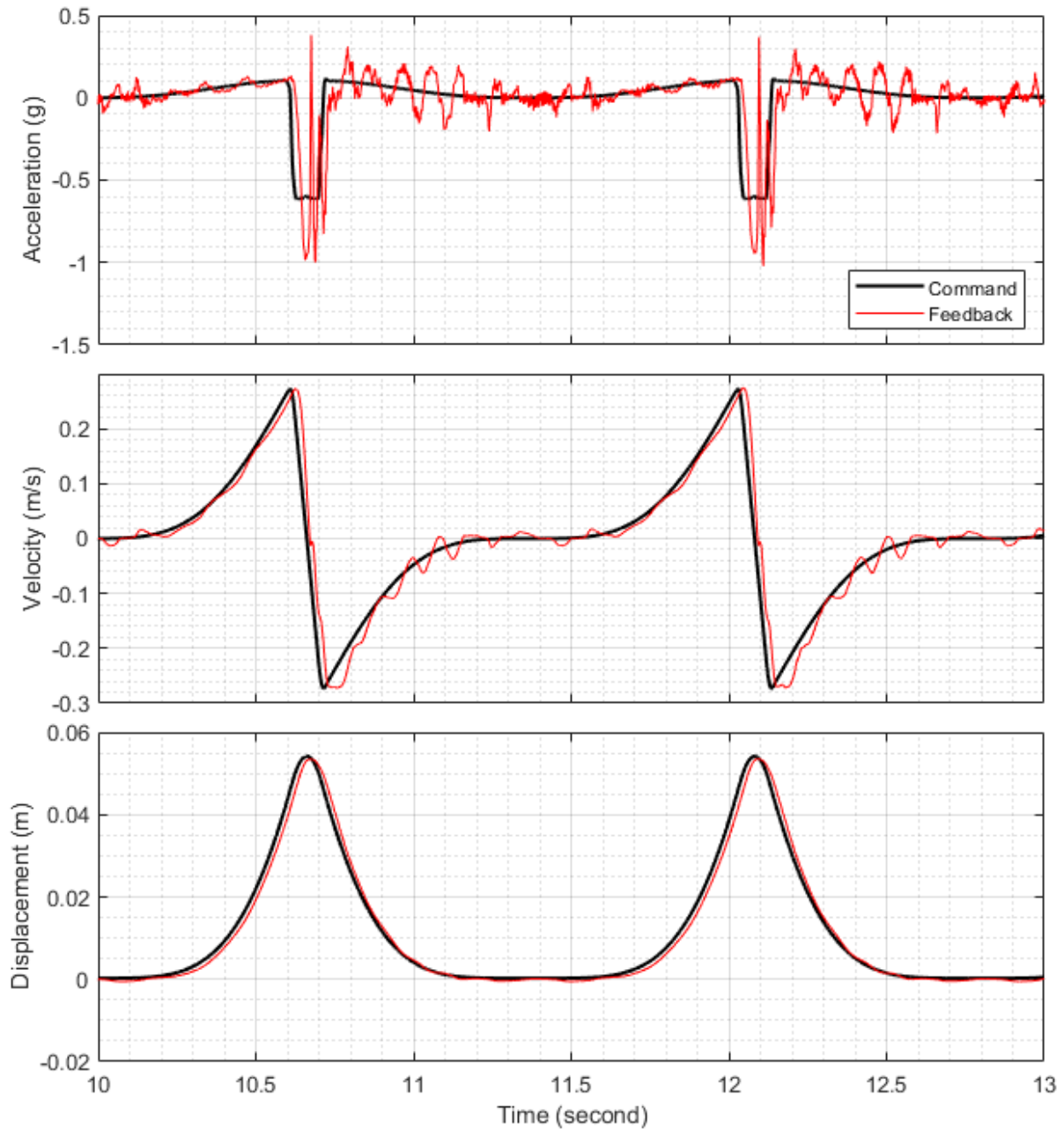


Figure 9-11: Enlarged view of the command and feedback signals of the input excitation showing two cycles

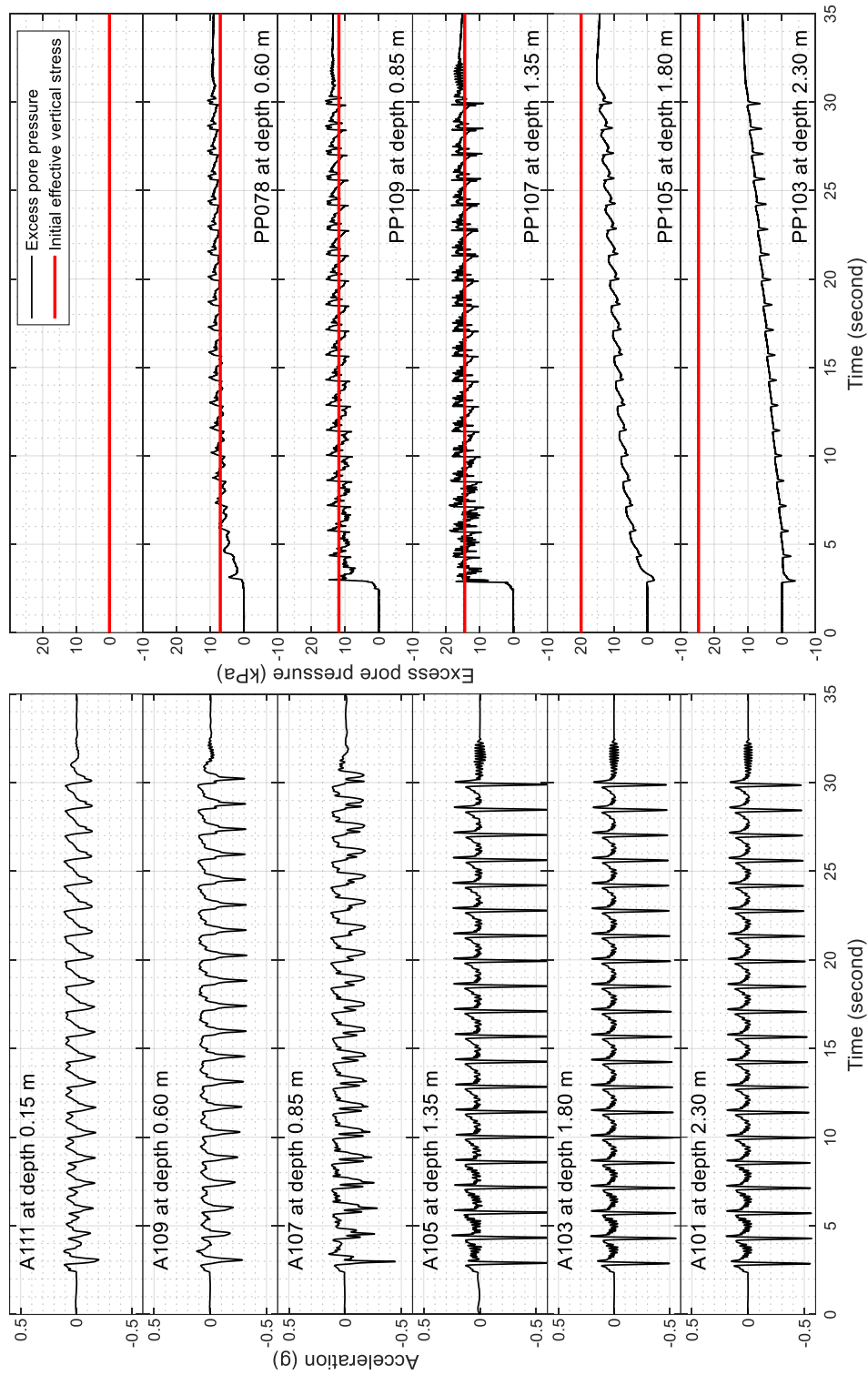


Figure 9-12: Representative acceleration and pore water pressure response during shaking along the north instrumentation array

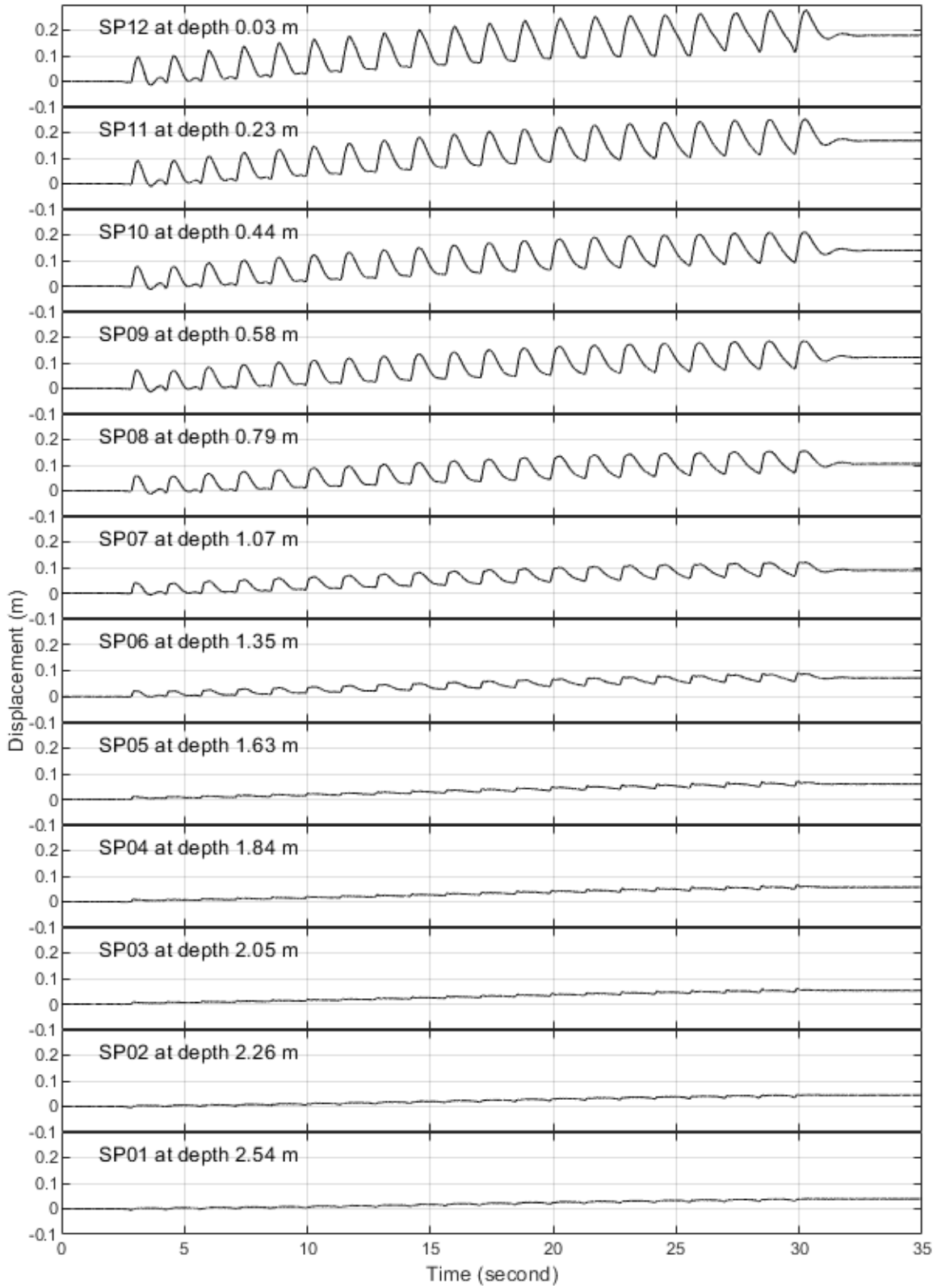


Figure 9-13: Lateral relative displacement along the laminar container height



Figure 9-14: Soil container before and after the shaking event



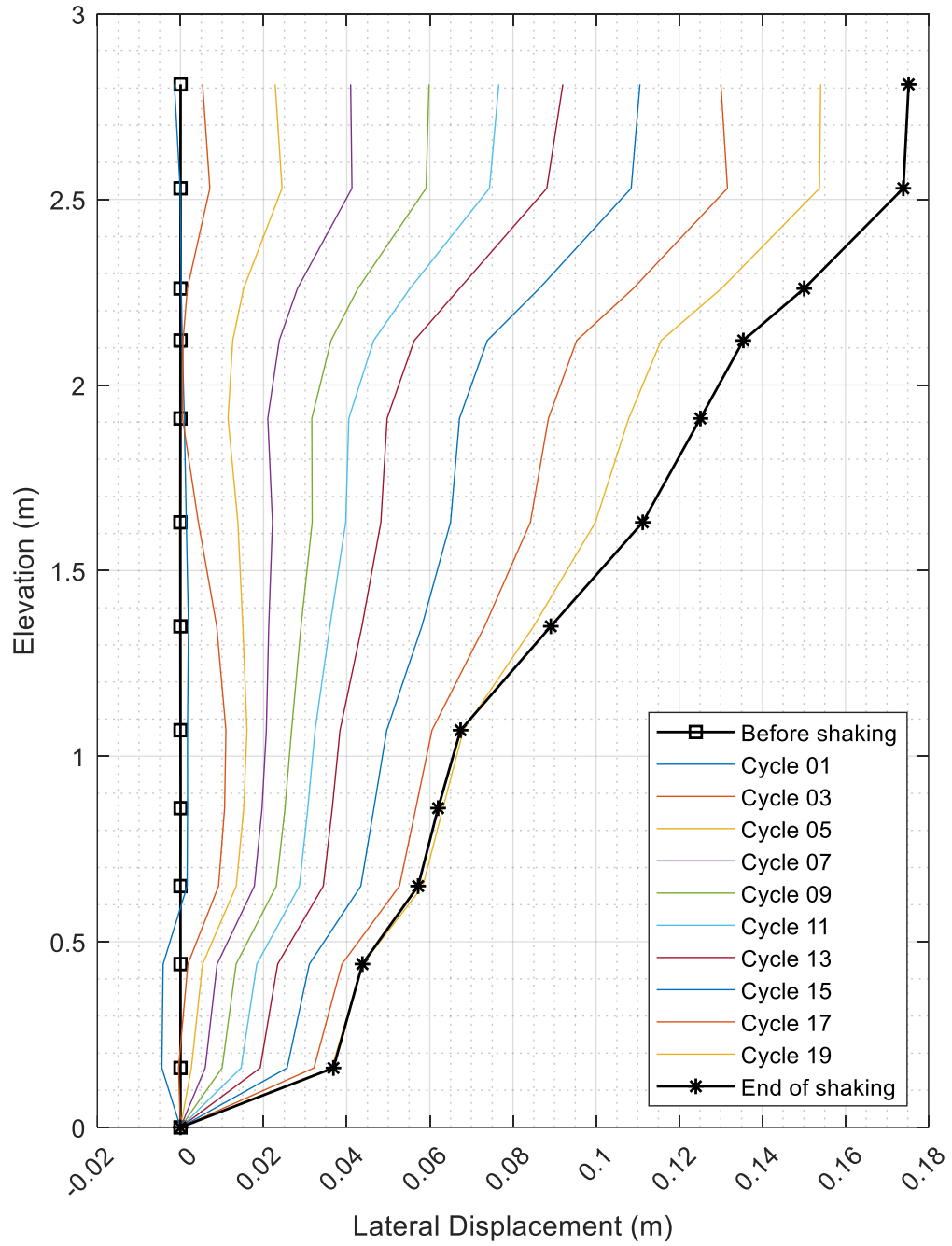


Figure 9-15: Accumulated lateral displacement profiles at different cycles during the shaking event

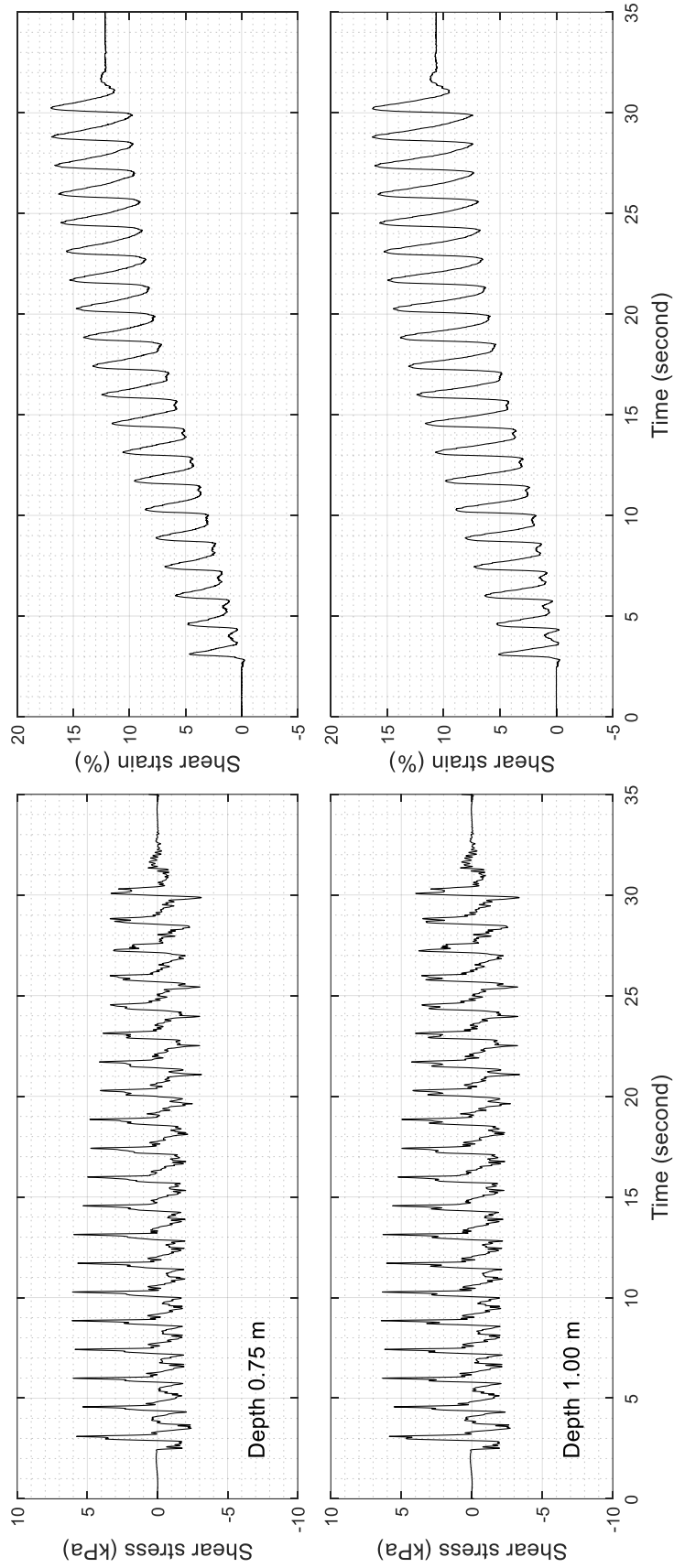


Figure 9-16: Shear stress and strain time histories at 0.75 m, and 1 m depth

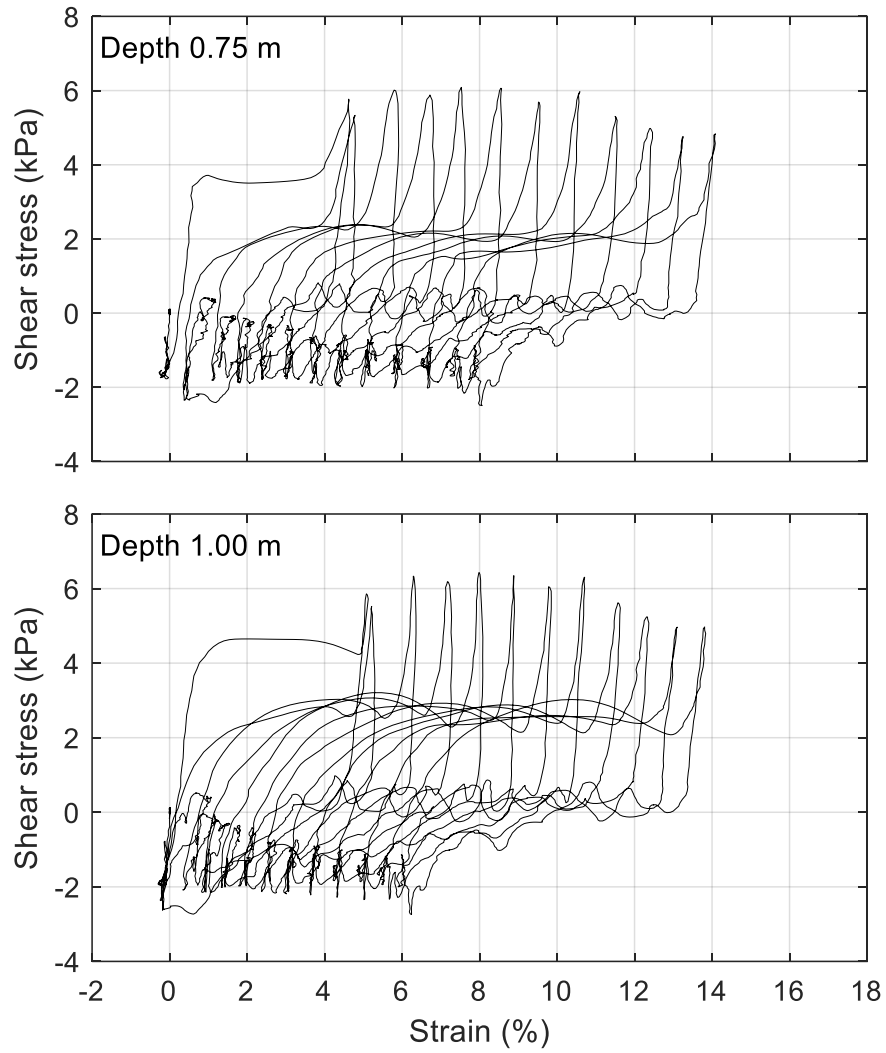
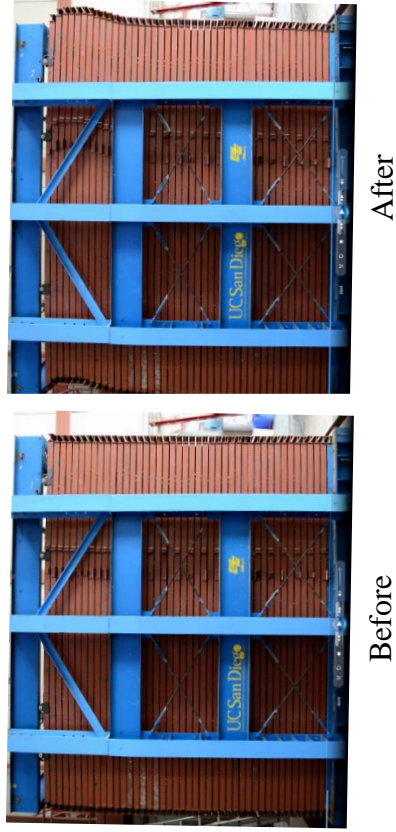
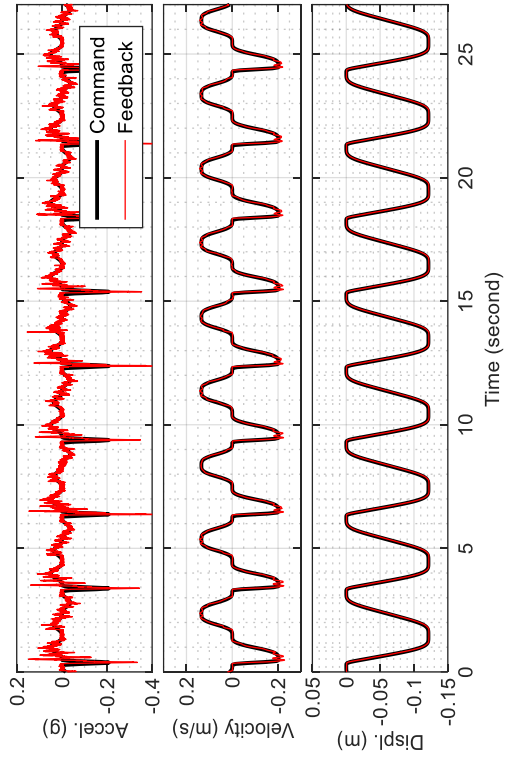


Figure 9-17: Shear stress-strain response during shaking event (within the saturated medium-dense stratum)

**First Shaking Event**



**Second Shaking Event**

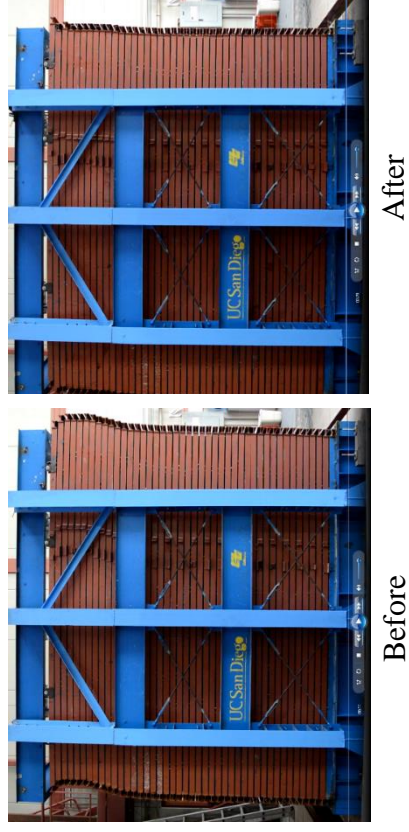
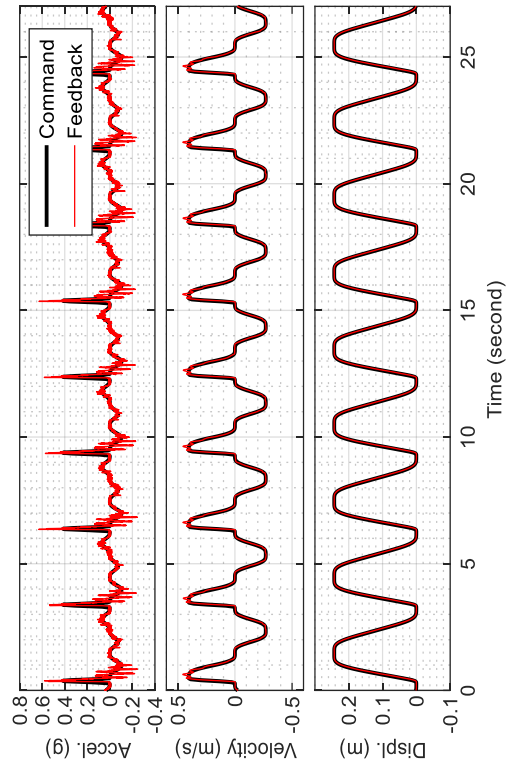


Figure 9-18: Command and feedback of input motion for the two preliminary shaking tests and lateral deformation of soil container

# Chapter 10

## Summary and conclusion

*There is a lesson here and I am not going to be the one  
to figure it out.*

– Rick and Morty: Season 4, Episode 1

### **10.1 Seismic response of bucket foundation for offshore wind turbines**

Motivated by the current expansion of offshore wind projects in seismically active zones, a 1-g shaking table experimental program was conducted on a scaled bucket foundation wind turbine model. The model was tested in a laminar soil container. The documented experimental data was used to calibrate a 3D finite element model. A comparison between the experimental the calibrated numerical results is presented. The calibrated model is further employed to investigate the seismic response of an idealized utility-scale OWT model. Pore pressure response beneath and around the bucket as well as the foundation moment and rotation response were explored. In addition, effect of soil permeability on the soil-bucket system seismic response was investigated. The numerical framework and the insights derived from this study are of general relevance to bucket foundation dynamic response for offshore wind applications. Specific observations and conclusions include:

- Modeling the interface between soil and bucket foundation is crucial towards capturing the measured experimental response. The soil-bucket system showed stiffer response when zeroLength interface elements were not employed.
- In non-seismically active zones, the investigated bucket models can provide sufficient safety margins against stability (overturning and bearing capacity) failures. In addition, these buckets are able to achieve the fundamental frequency requirement specified by the turbine manufacturer under operational loads.
- Accounting for operational wind loads on wind turbines during seismic loading is considered to result in a more realistic response scenario. The initial bucket rotation due to operational wind loads might further result in rotation accumulation during earthquake shaking. No appreciable rotation accumulation resulted in the case of wind loads neglected, which might significantly underestimate the actual system response.
- During seismic excitation, acceleration at the tower top can be of lower amplitude and of different frequency bandwidth than that along the tower.
- Modeling the OWT as a SDOF via a single lumped mass at the tower top might not result in accurate seismic response due to inaccurate representation of the inertial forces. Instead, modeling the tower as discrete masses at the connecting nodes yields a more realistic representation of the super-structure response. As such, the MDOF model resulted in more accumulated rotation at the end of shaking when compared to the SDOF model, which can be critical to the OWT serviceability limit.
- A correlation between the near field pore pressure build-up and the bucket rotation can be observed, resulting in foundation stiffness degradation due to soil softening associated with excess pore pressure build-up.

- Ground motion characteristics have a direct impact on the permanent bucket rotation with the latter also depending on the resulting near field pore pressure response.
- Soil permeability can be of much significance to the bucket moment-rotation response. In this regard, it was noticed that: i) at lower values of  $D_r$ , lower permeability would result in larger rotation due to the greater excess pore-pressure build-up, and ii) For very high  $D_r$ , lower permeability can result in relatively less rotation due to stronger dilative response which results in larger contribution of the suction mechanism to the overall bucket foundation response (as well as minimal excess pore pressure build-up in the free-field).
- For a given bucket size, permanent bucket rotation tends to stabilize at the lower and upper ends of the soil permeability range, reflecting the fully undrained and drained conditions, respectively.
- The observed change in permanent rotation between drained and undrained conditions represents the partially drained scenarios.
- The difference in permanent bucket rotation between undrained and drained conditions tends to decrease with increasing soil stiffness.
- Buckets with different dimensions with essentially identical fundamental frequency of the combined OWT-foundation system, will result in similar seismic response.
- Within the range of investigated scenarios, an essentially linear correlation was noted between the OWT fundamental frequency and the permanent bucket rotation.
- For ground motions similar to 1940 Imperial Valley (El Centro record), 1994 Northridge (Mulholland Drive record), and 1995 Kobe (Takatori record) earthquakes scaled to PGA of about 0.3 g (for medium dense sand -  $D_r$  75%) and 0.4 g (for very dense sand -  $D_r$  90%):

- i. The investigated 3.45 MW OWT with bucket foundation of diameter  $d$  12 m and skirt length  $L$  8 m (model B4) showed adequate response under combined operational wind and earthquake loading in medium-dense and very dense saturated sands, with overall rotation not exceeding the serviceability limit of 0.5 degrees.
  - ii. On the other hand, the bucket foundation of diameter  $d$  12 m and skirt length  $L$  5 m (model B1) showed inadequate response in medium dense and very dense saturated sands with permanent rotation exceeding the serviceability limit.
  - iii. For this bucket (B1 of  $d = 12$  m and  $L = 5$  m) to meet the rotation serviceability limit:
    1. A necessary increase in skirt length of about 60% was required in medium dense sand (about 20% in very dense sand).
    2. Alternatively, an increase in bucket diameter of about 17% in medium dense sand (about 9% in very dense sand) was found to meet the rotation serviceability limit.
    3. Further increase in bucket dimensions would be necessary to withstand stronger ground motions.
- Viscous damping at higher frequencies might have a significant effect on the bucket moment rotation response, such that:
    - i. The damped higher modes resulted in lower moment demand on the bucket foundation as the propagated accelerations along the OWT structure were lower. This also resulted in lower pore pressure build-up which led to less degradation in the foundation rotational stiffness.



- ii. Therefore, employing realistic damping ratios can be of importance to the OWT seismic response. Overdamping can lead to unconservative response while underestimating the damping might result in unrealistic increase in the foundation deformation that might be attributed to larger excess pore pressure build-up.

## **10.2 A high-resolution vertical accelerometer array for tracking shear wave velocity**

A technique was described for estimating the evolution of shear wave velocity  $V_s$  during dynamic or seismic excitation. This technique employs the cross-correlation approach with an overlapping moving time window. For each time window, the delay in shear wave arrival between any two accelerometers is calculated and  $V_s$  is estimated, knowing the distance between them.

Data sets from two different 1-g shake table tests were used to illustrate application of the analysis framework and its outcomes. For each test, evolution of  $V_s$  with time was displayed at different depths within the soil model. The procedure captured a number of response characteristics such as: i) liquefaction and its progression from the top downwards, and ii) the isolation mechanism above the liquefied layer and the related essentially rigid body displacements within overlying strata.

In sampling  $V_s$ , high spatial resolution is achieved via close spacing between the deployed vertical array accelerometers. As such, particularly high sampling rates (small time step) are needed in order to achieve accuracy in the calculated  $V_s$  estimates.

## **10.3 Asymmetric input motion for accumulation of lateral ground deformation in laminar container shake table testing**

Asymmetric motion is proposed as base excitation for laminar container shake table testing to simulate scenarios related to accumulation of lateral deformations. In this context, a biased dynamic 1D shear state of stress is emulated. Using a representative asymmetric input motion, a large-scale shake table laminar container test was conducted to illustrate the underlying response mechanisms. Characteristics of the asymmetric motion along with the soil model response were presented and discussed. This response, including the accumulated cyclic shear strain excursions, provides crucial insights for calibration of numerical models.

The motion presented in this particular study was specifically designed for short stroke actuators, enabling wider applicability and adoption. In general, the concepts involved in tailoring such asymmetric motions were shown to allow versatility in terms of the accumulated deformation direction and amplitude. From a broader perspective, asymmetric input motions may be of interest for a range of earthquake engineering applications, exploring uni-directional 1-DOF as well as multi-directional 6-DOF seismic response under conditions of biased inertial loading.

## **10.4 Recommendations for future research**

### **10.4.1 Physical modeling**

Further experimental work can be conducted as a follow up to the presented bucket foundation research. Buckets of various dimensions can be tested on the shake table facility with the laminar soil container to assess rotational stiffness as well as seismic response of each scenario.

Moreover, larger scale models (i.e., 1:16 and 1:8 scales) are recommended for testing using the large size laminar container on the Large High-Performance Outdoor Shake Table (LHPOST) facility at the Englekirk Structural Engineering Center. In addition, testing bucket foundation models in clay soil will provide valuable data sets. Such data sets can be helpful to further refine and improve the corresponding numerical modeling efforts.

### **10.4.2 Numerical modeling**

Upon conducting the above recommended testing, the collected data can be further used to investigate the numerical model capabilities in estimating the foundation stiffness and dynamic response for different bucket sizes and model scales. Moreover, data collected for bucket foundations tested in clays can be employed to improve the numerical model capabilities in predicting bucket foundation response in cohesive soils.

In addition, further studies may be conducted to assess effect of bucket size on the soil-foundation-structure natural frequencies and the overall dynamic system characteristics. The correlation between near-field pore-pressure build-up and the bucket rotation can be investigated for different soil properties, ground motions and bucket dimensions. Different environmental and extreme loads (wave, hurricane, typhoon, extreme wind) can be considered along with earthquake loading in future studies to investigate the bucket foundation response under these scenarios. The outcomes can then be generalized further within a simplified modeling framework, to predict potential foundation stiffness degradation and accumulated rotation.

## REFERENCES

- Abdoun, T., and R. Dobry. 2002. "Evaluation of pile foundation response to lateral spreading." *Soil Dynamics and Earthquake Engineering* 22 (22):1051-1058.
- Abdoun, T., R. Dobry, T. D. O'Rourke, and S. Goh. 2003. "Pile response to lateral spreads: centrifuge modeling." *Journal of Geotechnical and Geoenvironmental engineering* 129 (10):869-878.
- Abdoun, T., R. Dobry, T. F. Zimmie, and M. Zeghal. 2005. "Centrifuge research of countermeasures to protect pile foundations against liquefaction-induced lateral spreading." *Journal of earthquake engineering* 9 (special issue):105-125.
- Achmus, M., C. Akdag, and K. Thieken. 2013. "Load-bearing behavior of suction bucket foundations in sand." *Applied Ocean Research* 43:157-165.
- Afifi, S., and F. Richart. 1973. "Stress-history effects on shear modulus of soils." *Soils and Foundations* 13 (1):77-95.
- Andrus, R. D., and T. L. Youd. 1987. *Subsurface Investigation of a Liquefaction-Induced Lateral Spread, Thousand Springs Valley, Idaho*. Brigham Young University, Provo, UT: U.S. Department of Energy.
- Arany, L., S. Bhattacharya, J. Macdonald, and S. Hogan. 2017. "Design of monopiles for offshore wind turbines in 10 steps." *Soil Dynamics and Earthquake Engineering* 92:126-152.
- Arany, L., S. Bhattacharya, J. H. Macdonald, and S. J. Hogan. 2016. "Closed form solution of Eigen frequency of monopile supported offshore wind turbines in deeper waters incorporating stiffness of substructure and SSI." *Soil Dynamics and Earthquake Engineering* 83:18-32.
- Arulnathan, R., R. W. Boulanger, B. L. Kutter, and W. K. Sluis. 2000. "New tool for shear wave velocity measurements in model tests." *Geotechnical Testing Journal* 23 (4):444-453.
- Arulnathan, R., R. W. Boulanger, and M. F. Riemer. 1998. "Analysis of bender element tests." *Geotechnical Testing Journal* 21 (2):120-131.

- ASCE/AWEA. 2011. Recommended practice for compliance of large land-based wind turbine support structures. Washington DC: American Society of Civil Engineers and the American Wind Energy Association ....
- Ashford, S., and W. Jakrapiyanun. 2001. Design and verification of the UCSD laminar container. University of California San Diego, Department of Structural Engineering, La Jolla, CA.
- Athanasiau, C., A. Bye, J. Tistel, A. Ribe, K. Arnesen, S. Feizikhanhandi, and E. Sørli. 2015. "Simplified earthquake analysis for wind turbines and subsea structures on closed caisson foundations." *Frontiers in Offshore Geotechnics III*:221.
- AWEA. 2020. Wind Powers America Second Quarter 2020 Report. American Wind Energy Association.
- Bakmar, C. L., K. Ahle, S. A. Nielsen, and L. B. Ibsen. 2009. "The Monopod Bucket Foundation: recent experiences and challenges ahead." The European Offshore Wind Conference & Exhibition.
- Barari, A., K. Glittrup, L. R. Christiansen, L. B. Ibsen, and Y. W. Choo. 2021. "Tripod suction caisson foundations for offshore wind energy and their monotonic and cyclic responses in silty sand: Numerical predictions for centrifuge model tests." *Soil Dynamics and Earthquake Engineering* 149:106813.
- Bartlett, S. F., and T. L. Youd. 1995. "Empirical prediction of liquefaction-induced lateral spread." *Journal of Geotechnical Engineering* 121 (4):316-329.
- Bastidas, A. M. P. 2016a. "Ottawa F-65 Sand Characterization." Ph.D. dissertation, Department of Civil and Environmental Engineering, University of California Davis, Davis, CA.
- Bastidas, A. M. P. 2016b.
- Bathe, K.-J. 2007. "Conserving energy and momentum in nonlinear dynamics: a simple implicit time integration scheme." *Computers & structures* 85 (7-8):437-445.
- Beeston, H., and T. McEvelly. 1977. "Shear wave velocities from down-hole measurements." *Earthquake Engineering & Structural Dynamics* 5 (2):181-190.

- Bendat, J. S., and A. G. Piersol. 1980. "Engineering applications of correlation and spectral analysis." *New York, Wiley-Interscience, 1980. 315 p.*
- Bhattacharya, S. 2019. *Design of foundations for offshore wind turbines*: John Wiley & Sons.
- BOEM. 2021a. Comparison of Environmental Effects from Different Offshore Wind Turbine Foundations. U.S. Department of the Interior, Bureau of Ocean Management.
- BOEM. 2021b. "Renewable Energy - California Activities." BOEM. <https://www.boem.gov/renewable-energy/state-activities/california>.
- Bouckovalas, G. D., Y. Z. Tsiapas, A. I. Theocharis, and Y. K. Chaloulos. 2016. "Ground response at liquefied sites: seismic isolation or amplification?" *Soil Dynamics and Earthquake Engineering* 91:329-339.
- Brandenberg, S., S. Choi, B. Kutter, D. Wilson, and J. Santamarina. 2006. "A bender element system for measuring shear wave velocities in centrifuge models." 6th International Conference on Physical Modeling in Geotechnics.
- Brandenberg, S. J., R. W. Boulanger, B. L. Kutter, and D. Chang. 2005. "Behavior of pile foundations in laterally spreading ground during centrifuge tests." *Journal of Geotechnical and Geoenvironmental Engineering* 131 (11):1378-1391.
- Brandenberg, S. J., R. W. Boulanger, B. L. Kutter, and D. Chang. 2007a. "Liquefaction-induced softening of load transfer between pile groups and laterally spreading crusts." *Journal of Geotechnical and Geoenvironmental Engineering* 133 (1):91-103.
- Brandenberg, S. J., R. W. Boulanger, B. L. Kutter, and D. Chang. 2007b. "Static pushover analyses of pile groups in liquefied and laterally spreading ground in centrifuge tests." *Journal of Geotechnical and Geoenvironmental Engineering* 133 (9):1055-1066.
- Brennan, A., N. Thusyanthan, and S. Madabhushi. 2005. "Evaluation of shear modulus and damping in dynamic centrifuge tests." *Journal of Geotechnical and Geoenvironmental Engineering* 131 (12):1488-1497.
- Brignoli, E. G., M. Gotti, and K. H. Stokoe. 1996. "Measurement of shear waves in laboratory specimens by means of piezoelectric transducers." *Geotechnical Testing Journal* 19 (4):384-397.

- Byrne, B., and G. Houlsby. 2006. "Assessing novel foundation options for offshore wind turbines." World maritime technology conference.
- Byrne, B., G. Houlsby, C. Martin, and P. Fish. 2002. "Suction caisson foundations for offshore wind turbines." *Wind Engineering* 26 (3):145-155.
- Byrne, P. M., S.-S. Park, M. Beaty, M. Sharp, L. Gonzalez, and T. Abdoun. 2004. "Numerical modeling of liquefaction and comparison with centrifuge tests." *Canadian Geotechnical Journal* 41 (2):193-211.
- Carey, T. J., T. Hashimoto, D. Cimini, and B. L. Kutter. 2018. "LEAP-GWU-2015 centrifuge test at UC Davis." *Soil Dynamics and Earthquake Engineering* 113:663-670.
- Cetin, K. O., N. Isik, and B. Unutmaz. 2004. "Seismically induced landslide at Degirmendere Nose, Izmit Bay during Kocaeli (Izmit)-Turkey earthquake." *Soil Dynamics and Earthquake Engineering* 24 (3):189-197.
- Chan, A. H.-C. 1988. "A unified finite element solution to static and dynamic problems of geomechanics." Swansea University.
- Chang, B., and T. Hutchinson. 2012. "Experimental Evaluation of p-y Curves Considering Development of Liquefaction." *Journal of Geotechnical and Geoenvironmental Engineering* 139 (4):577-586.
- Chang, B. J., and T. C. Hutchinson. 2013. "Experimental investigation of plastic demands in piles embedded in multi-layered liquefiable soils." *Soil Dynamics and Earthquake Engineering* 49:146-156.
- Chang, C.-Y., Y. Tang, C. Mok, H. Tang, M. Power, and J. Stepp. 1991. "Development of shear modulus reduction curves based on Lotung downhole ground motion data."
- Chen, F., J. Lian, H. Wang, F. Liu, H. Wang, and Y. Zhao. 2016. "Large-scale experimental investigation of the installation of suction caissons in silt sand." *Applied Ocean Research* 60:109-120. doi: <https://doi.org/10.1016/j.apor.2016.09.004>.
- Choo, Y., S. Yang, K. Lee, Y. Kim, K. Bae, B. Jin, and N. Kim. 2015. "Seismic response of bucket foundations for offshore wind tower using dynamic centrifuge tests." *Frontiers in Offshore Geotechnics III*:233.

- Cozzi, L., and B. Wanner. 2019. *Offshore Wind Outlook*. International Energy Agency.
- Cubrinovski, M., K. Robinson, M. Taylor, M. Hughes, and R. Orense. 2012. "Lateral spreading and its impacts in urban areas in the 2010–2011 Christchurch earthquakes." *New Zealand Journal of Geology and Geophysics* 55 (3):255-269.
- Da Fonseca, A. V., C. Ferreira, and M. Fahey. 2008. "A framework interpreting bender element tests, combining time-domain and frequency-domain methods." *Geotechnical Testing Journal* 32 (2):91-107.
- De Risi, R., S. Bhattacharya, and K. Goda. 2018. "Seismic performance assessment of monopile-supported offshore wind turbines using unscaled natural earthquake records." *Soil Dynamics and Earthquake Engineering* 109:154-172.
- Devriendt, C., W. Weijtjens, M. El-Kafafy, and G. De Sitter. 2014. "Monitoring resonant frequencies and damping values of an offshore wind turbine in parked conditions." *IET Renewable Power Generation* 8 (4):433-441.
- Ding, H., P. Zhang, C. Le, and X. Liu. 2011. "Construction and installation technique of large-scale top-bearing bucket foundation for offshore wind turbine." *Mechanic Automation and Control Engineering (MACE)*, 2011 Second International Conference on.
- DNV-GL. 2018. *DNVGL-ST-0126 - Support structures for wind turbines*. Oslo, Norway: DNV GL.
- DNV. 2004. *Offshore Standard DNV-OS-J101: Design of Offshore Wind Turbine Structures*. Høvik, Norway: Det Norske Veritas.
- DNV/Risø. 2002. *Guidelines for design of wind turbines*. Second ed. Denmark: Jydsk Centraltrykkeri Copenhagen, Denmark.
- Dobry, R. 1994. "Possible lessons from VELACS model No. 2 results." *Int. Conf. Verification of Numerical Procedures for the Analysis of Soil Liquefaction Problems*, Davis, California, USA, 17-20 October 1994.
- Dobry, R., I. Oweis, and A. Urzua. 1976. "Simplified procedures for estimating the fundamental period of a soil profile." *Bulletin of the Seismological Society of America* 66 (4):1293-1321.



- Dobry, R., S. Thevanayagam, C. Medina, R. Bethapudi, A. Elgamal, V. Bennett, T. Abdoun, M. Zeghal, U. El Shamy, and V. Mercado. 2010. "Mechanics of lateral spreading observed in a full-scale shake test." *Journal of geotechnical and geoenvironmental engineering* 137 (2):115-129.
- Ebeido, A. 2019. "Lateral-Spreading Effects on Pile Foundations: Large-scale Testing and Analysis." PhD Dissertation, University of California San Diego, La Jolla, CA.
- Ebeido, A. 2020. "Lateral-Spreading Effects on Pile Foundations: Large-scale Testing and Analysis." Ph.D. dissertation, Department of Structural Engineering, University of California San Diego, La Jolla, CA.
- Ebeido, A., A. Elgamal, and M. Zayed. 2018a. "Pile response during liquefaction-induced lateral spreading: 1-g shake table tests with different ground inclination." 9th International Conference on Physical Modelling in Geotechnics (ICPMG 2018), London, United Kingdom, July 17-20, 2018.
- Ebeido, A., A. Elgamal, and M. Zayed. 2018b. "Pile response during liquefaction-induced lateral spreading: 1-g shake table tests with different ground inclination." In *Physical Modelling in Geotechnics, Volume 2*, 1335-1339. CRC Press.
- El-Sekelly, W., T. Abdoun, and R. Dobry. 2012. "Soil characterization in centrifuge models through measurement of shear wave velocities using bender elements." In *GeoCongress 2012: State of the Art and Practice in Geotechnical Engineering*, 2037-2047.
- El-Sekelly, W., V. Mercado, T. Abdoun, M. Zeghal, and H. El-Ganainy. 2013. "Bender elements and system identification for estimation of Vs." *International Journal of Physical Modelling in Geotechnics* 13 (4):111-121.
- El-Sekelly, W., A. Tessari, and T. Abdoun. 2014. "Shear wave velocity measurement in the centrifuge using bender elements." *Geotechnical Testing Journal* 37 (4):689-704.
- El Ghoraihy, M., H. Park, and M. T. Manzari. 2020. "Physical and mechanical properties of Ottawa F65 sand." In *Model Tests and Numerical Simulations of Liquefaction and Lateral Spreading*, 45-67. Springer.
- El Wakil, A. Z. 2010. "Horizontal capacity of skirted circular shallow footings on sand." *Alexandria Engineering Journal* 49 (4):379-385. doi: <https://doi.org/10.1016/j.aej.2010.07.003>.

- El Wakil, A. Z. 2013. "Bearing capacity of Skirt circular footing on sand." *Alexandria Engineering Journal* 52 (3):359-364. doi: <https://doi.org/10.1016/j.aej.2013.01.007>.
- Elgamal, A.-W., M. Zeghal, E. Parra, R. Gunturi, H. Tang, and J. Stepp. 1996a. "Identification and modeling of earthquake ground response—I. Site amplification." *Soil Dynamics and Earthquake Engineering* 15 (8):499-522.
- Elgamal, A.-W., M. Zeghal, H. Tang, and J. Stepp. 1995. "Lotung downhole array. I: Evaluation of site dynamic properties." *Journal of Geotechnical Engineering* 121 (4):350-362.
- Elgamal, A., L. He, J. Lu, A. Abe, T. Abdoun, R. Dobry, M. Sato, K. Tokimatsu, and T. Shantz. 2006. "Liquefaction-induced lateral load on piles." Fourth international conference on earthquake engineering, Taipei, Taiwan, 12-13 October 2006.
- Elgamal, A., Z. Yang, E. Parra, and A. Ragheb. 2003. "Modeling of cyclic mobility in saturated cohesionless soils." *International Journal of Plasticity* 19 (6):883-905.
- Elgamal, A., M. Zeghal, V. Taboada, and R. Dobry. 1996b. "Analysis of site liquefaction and lateral spreading using centrifuge testing records." *Soils and Foundations* 36 (2):111-121.
- Elnashai, A. S., B. Gencturk, O.-S. Kwon, I. L. Al-Qadi, Y. Hashash, J. R. Roesler, S. J. Kim, S.-H. Jeong, J. Dukes, and A. Valdivia. 2010. Department of Civil Engineering, University of Illinois, Urbana, Champaign.
- ENERGINET. 2015. Technical Project Description for Offshore Wind Farms (200 MW) - Offshore Wind Farms at Vesterhav Nord. Denmark: Energinet.dk.
- Fiegel, G. L., and B. L. Kutter. 1994. "Liquefaction mechanism for layered soils." *Journal of geotechnical engineering* 120 (4):737-755.
- Foglia, A., and L. B. Ibsen. 2014a. "Bucket foundations: a literature review." *Department of Civil Engineering, Aalborg University, Denmark, Technical Report No. 176*.
- Foglia, A., and L. B. Ibsen. 2014b. "Laboratory experiments of bucket foundations under cyclic loading." *Department of Civil Engineering, Aalborg University, Denmark, Technical Report No. 177*.

- Fu, L., G. Liu, and X. Zeng. 2008. "Evaluation of shear wave velocity based soil liquefaction resistance criteria by centrifuge tests." *Geotechnical Testing Journal* 32 (1):39-44.
- Fu, L., X. Zeng, and J. L. Figueroa. 2004. "Shear wave velocity measurement in centrifuge using bender elements." *International journal of physical modelling in geotechnics* 4 (2):01-11.
- Fugro. 2020. Centrifuge Testing - Cyclic Loading of Suction Bucket Foundations in Undrained Sand. United States of America: centrifuge testing suction bucket BOEM.
- Ghalandarzadeh, A., T. Orita, I. Towhata, and F. Yun. 1998. "Shaking table tests on seismic deformation of gravity quay walls." *Soils and foundations* 38 (Special):115-132.
- Ghayoomi, M., and J. S. McCartney. 2011. "Measurement of small-strain shear moduli of partially saturated sand during infiltration in a geotechnical centrifuge." *Geotechnical Testing Journal* 34 (5):503-513.
- Ghosh, B., and S. Madabhushi. 2002. "An efficient tool for measuring shear wave velocity in the centrifuge." Proceedings of the international conference on physical modelling in geotechnics.
- Gohl, W., and W. Finn. 1991. "Use of piezoceramic bender elements in soil dynamics testing." Recent Advances in Instrumentation, Data Acquisition and Testing in Soil Dynamics.
- Gonzalez, L., T. Abdoun, and R. Dobry. 2009. "Effect of soil permeability on centrifuge modeling of pile response to lateral spreading." *Journal of Geotechnical and Geoenvironmental Engineering* 135 (1):62-73.
- Gordon, J. 2020. "Mechanisms of growth in Offshore wind power: Feasibility of 2030 targets in the North Seas Energy Cooperation."
- Haigh, S., and S. Madabhushi. 2002. "Centrifuge modelling of lateral spreading past pile foundations." International Conference on Physical Modelling in Geotechnics (ICPMG'02), St. John's, New Foundland, Canada, 10-12 July 2002.
- Hall, J. F., T. H. Heaton, M. W. Halling, and D. J. Wald. 1995. "Near-source ground motion and its effects on flexible buildings." *Earthquake spectra* 11 (4):569-605.

- Hamada, M., S. Yasuda, R. Isoyama, and K. Emoto. 1986. "Study on liquefaction-induced permanent ground displacements and earthquake damage." *Proceedings of Japan Society of Civil Engineers* III-6 (376):221-229.
- Horikoshi, K., A. Tateishi, and T. Fujiwara. 1998. "Centrifuge modeling of a single pile subjected to liquefaction-induced lateral spreading." *Soils and Foundations* 38 (Special):193-208.
- Houlsby, G. T., and B. W. Byrne. 2000. "Suction Caisson Foundations for Offshore Wind Turbines and Anemometer Masts." *Wind Engineering* 24 (4):249-255. doi: 10.1260/0309524001495611.
- Houlsby, G. T., L. B. Ibsen, and B. W. Byrne. 2005. "Suction caissons for wind turbines." *Frontiers in Offshore Geotechnics: ISFOG, Perth, WA, Australia*:75-93.
- Houlsby, G. T., R. B. Kelly, J. Huxtable, and B. W. Byrne. 2006. "Field trials of suction caissons in sand for offshore wind turbine foundations." *Géotechnique* 56 (1):3-10.
- Hung, L. C., and S. R. Kim. 2012. "Evaluation of vertical and horizontal bearing capacities of bucket foundations in clay." *Ocean Engineering* 52:75-82. doi: <https://doi.org/10.1016/j.oceaneng.2012.06.001>.
- Iai, S., and T. Sugano. 1999. "Soil-structure interaction studies through shaking table tests." *Proceedings of the Second International Conference on Earthquake Geotechnical Engineering, Lisboa, Portugal, June*.
- Ibsen, L. B., and R. Brincker. 2004. "Design of a new foundation for offshore wind turbines." *Proceedings of The 22nd International Modal Analysis Conference (IMAC), Detroit, Michigan*.
- Idriss, I. M., and R. W. Boulanger. 2008. *Soil liquefaction during earthquakes*: Earthquake Engineering Research Institute.
- IRENA. 2019. *Future of wind: Deployment, investment, technology, grid integration and socio-economic aspects (A Global Energy Transformation paper)*. Abu Dhabi: International Renewable Energy Agency.
- Ismail, M., and Y. Hourani. 2003. "An innovative facility to measure shear-wave velocity in centrifuge and 1-g models." *Proceedings of Deformation Characteristics of Geomaterials, Lyon*:21-29.

- Iwan, W. D., M. A. Moser, and C.-Y. Peng. 1984. California Institute of Technology.
- Iwan, W. D., M. A. Moser, and C.-Y. Peng. 1985. "Some observations on strong-motion earthquake measurement using a digital accelerograph." *Bulletin of the Seismological Society of America* 75 (5):1225-1246.
- Jalbi, S., M. Shadlou, and S. Bhattacharya. 2018. "Impedance functions for rigid skirted caissons supporting offshore wind turbines." *Ocean Engineering* 150:21-35.
- Jiang, Z. 2021. "Installation of offshore wind turbines: A technical review." *Renewable and Sustainable Energy Reviews* 139:110576.
- Jonkman, J., S. Butterfield, W. Musial, and G. Scott. 2009. Definition of a 5-MW reference wind turbine for offshore system development. National Renewable Energy Lab.(NREL), Golden, CO (United States).
- Kalkan, E., and S. K. Kunnath. 2006. "Effects of fling step and forward directivity on seismic response of buildings." *Earthquake spectra* 22 (2):367-390.
- Karimi, Z., and S. Dashti. 2016. "Numerical and centrifuge modeling of seismic soil–foundation–structure interaction on liquefiable ground." *Journal of Geotechnical and Geoenvironmental Engineering* 142 (1):04015061.
- Katayama, T., F. Yamazaki, S. Nagata, L. Lu, and T. Turker. 1990. "A strong motion database for the Chiba seismometer array and its engineering analysis." *Earthquake Engineering & Structural Dynamics* 19 (8):1089-1106.
- Kawaguchi, T., T. Mitachi, and S. Shibuya. 2001. "Evaluation of shear wave travel time in laboratory bender element test." Proceedings of the International Conference on Soil Mechanics and Geotechnical Engineering.
- Khosravifar, A., A. Elgamal, J. Lu, and J. Li. 2018. "A 3D model for earthquake-induced liquefaction triggering and post-liquefaction response." *Soil Dynamics and Earthquake Engineering* 110:43-52.
- Kim, N.-R., and D.-S. Kim. 2010. "A shear wave velocity tomography system for geotechnical centrifuge testing." *Geotechnical Testing Journal* 33 (6):434-444.

- Kita, K., T. Shibata, A. Yashima, and S. KOBAYASHI. 1992. "Measurement of shear wave velocities of sand in a centrifuge." *Soils and foundations* 32 (2):134-140.
- Koga, Y., and O. Matsuo. 1990. "Shaking table tests of embankments resting on liquefiable sandy ground." *Soils and Foundations* 30 (4):162-174.
- Kokusho, T. 2014. "Seismic base-isolation mechanism in liquefied sand in terms of energy." *Soil Dynamics and Earthquake Engineering* 63:92-97.
- Kourkoulis, R., P. Lekakakis, F. Gelagoti, and A. Kaynia. 2014. "Suction caisson foundations for offshore wind turbines subjected to wave and earthquake loading: effect of soil-foundation interface." *Géotechnique* 64 (3):171.
- Kramer, S. L. 1996. *Geotechnical Earthquake Engineering*. Upper Saddle River, NJ: Prentice-Hall, Inc.
- Kuhlemeyer, R. L., and J. Lysmer. 1973. "Finite element method accuracy for wave propagation problems." *Journal of the Soil Mechanics and Foundations Division* 99 (5):421-427.
- Lee, C.-J. 2005. "Centrifuge modeling of the behavior of caisson-type quay walls during earthquakes." *Soil Dynamics and Earthquake Engineering* 25 (2):117-131. doi: <https://doi.org/10.1016/j.soildyn.2004.10.011>.
- Lee, C.-J., and H. Huang. 2007. "Wave velocities and their relation to fabric evolution during the shearing of sands." *Soil Dynamics and Earthquake Engineering* 27 (1):1-13.
- Lee, C.-J., C.-R. Wang, Y.-C. Wei, and W.-Y. Hung. 2012. "Evolution of the shear wave velocity during shaking modeled in centrifuge shaking table tests." *Bulletin of Earthquake Engineering* 10 (2):401-420.
- Lee, J., and F. Zhao. 2020. *Global Offshore Wind Report - GWEC*. Brussels, Belgium: Global Wind Energy Council.
- Leite, O. B. 2015. "Review of design procedures for monopile offshore wind structures."
- Leong, E. C., S. H. Yeo, and H. Rahardjo. 2005. "Measuring shear wave velocity using bender elements." *Geotechnical Testing Journal* 28 (5):488-498.

- Li, D., L. Feng, and Y. Zhang. 2014. "Model tests of modified suction caissons in marine sand under monotonic lateral combined loading." *Applied Ocean Research* 48:137-147. doi: <https://doi.org/10.1016/j.apor.2014.08.005>.
- Li, D., Y. Zhang, L. Feng, and Y. Gao. 2015. "Capacity of modified suction caissons in marine sand under static horizontal loading." *Ocean Engineering* 102:1-16. doi: <https://doi.org/10.1016/j.oceaneng.2015.04.033>.
- Liingaard, M. 2006. "Dynamic behaviour of suction caissons." Aalborg University, Department of Civil Engineering, Division of Water and Soil.
- Lin, M.-L., and K.-L. Wang. 2006. "Seismic slope behavior in a large-scale shaking table model test." *Engineering Geology* 86 (2):118-133.
- Lindenberg, S., B. Smith, K. O'Dell, E. DeMeo, and B. Ram. 2009. *20% Wind Energy By 2030: Increasing Wind Energy's Contribution to US Electricity Supply*. Diane Publishing.
- Lutes, L. D., and S. Sarkani. 2004. *Random vibrations: analysis of structural and mechanical systems*: Butterworth-Heinemann.
- Madabhushi, S. G., B. Teymur, S. Haigh, and A. Brennan. 2001. "Modelling of liquefaction and lateral spreading." International Workshop on Earthquake Simulation in Geotechnical Engineering, Cleveland, OH, July 2001.
- Madera, G. A. 1970. *Fundamental period and amplification of peak acceleration in layered systems*: MIT Department of Civil Engineering, Inter-American Program.
- Magenes, G. 1989a. "Design, analysis and calibration of the UCSD shake table." PhD Dissertation, Department of Structural Engineering, University of California San Diego, La Jolla, CA.
- Magenes, G. 1989b. "Design, analysis and calibration of the UCSD shake table." Ph.D. dissertation, Department of Applied Mechanics/Engineering Sciences, University of California San Diego, La Jolla, CA.
- Manzari, M. T., M. El Ghoraihy, B. L. Kutter, M. Zeghal, T. Abdoun, P. Arduino, R. J. Armstrong, M. Beaty, T. Carey, and Y. Chen. 2018. "Liquefaction experiment and analysis projects (LEAP): Summary of observations from the planning phase." *Soil Dynamics and Earthquake Engineering* 113:714-743.

- Mazzoni, S., F. McKenna, M. H. Scott, and G. L. Fenves. 2006. "OpenSees command language manual." *Pacific Earthquake Engineering Research (PEER) Center* 264:137-158.
- McKenna, F., M. H. Scott, and G. L. Fenves. 2010. "Nonlinear finite-element analysis software architecture using object composition." *Journal of Computing in Civil Engineering* 24 (1):95-107.
- Meyerhof, G. G. 1963. "Some recent research on the bearing capacity of foundations." *Canadian geotechnical journal* 1 (1):16-26.
- Motamed, R., and I. Towhata. 2009. "Shaking table model tests on pile groups behind quay walls subjected to lateral spreading." *Journal of Geotechnical and Geoenvironmental Engineering* 136 (3):477-489.
- Motamed, R., I. Towhata, T. Honda, K. Tabata, and A. Abe. 2013. "Pile group response to liquefaction-induced lateral spreading: E-Defense large shake table test." *Soil Dynamics and Earthquake Engineering* 51:35-46.
- Motamed, R., I. Towhata, T. Honda, S. Yasuda, K. Tabata, and H. Nakazawa. 2009. "Behaviour of pile group behind a sheet pile quay wall subjected to liquefaction-induced large ground deformation observed in shaking test in E-defense project." *Soils and foundations* 49 (3):459-475.
- Murillo, C. A., L. Thorel, and B. Caicedo. 2009. "Spectral analysis of surface waves method to assess shear wave velocity within centrifuge models." *Journal of Applied Geophysics* 68 (2):135-145.
- Musial, W. 2007. "Offshore wind electricity: a viable energy option for the coastal United States." *Marine Technology Society Journal* 41 (3):32-43.
- Musial, W., P. Beiter, J. Nunemaker, V. Gevorgian, A. Cooperman, R. Hammond, M. Shields, and P. Spitsen. 2020. 2019 offshore wind technology data update. National Renewable Energy Lab.(NREL), Golden, CO (United States).
- Musial, W., and B. Ram. 2010. Large-scale offshore wind power in the United States: Assessment of opportunities and barriers. National Renewable Energy Lab.(NREL), Golden, CO (United States).



- Musial, W. D., P. C. Beiter, P. Schwabe, T. Tian, and O. Spitsen. 2017. 2016 Offshore Wind Technologies Market Report. National Renewable Energy Lab.(NREL), Golden, CO (United States).
- Musial, W. D., P. C. Beiter, P. Spitsen, J. Nunemaker, and V. Gevorgian. 2019. 2018 Offshore Wind Technologies Market Report. National Renewable Energy Lab.(NREL), Golden, CO (United States).
- Nielsen, S. D. 2016. "Transient monotonic and cyclic load effects on mono bucket foundations." Aalborg Universitetsforlag.
- Ogden, S. 2021. "SO News - Major offshore wind projects to watch in 2021." accessed 12/10/2021. <https://www.spencer-ogden.com/blog/2020/11/number-sonews-major-offshore-wind-projects-to-watch-in-2021>.
- Parra-Colmenares, E. J. 1996. "Numerical modeling of liquefaction and lateral ground deformation including cyclic mobility and dilation response in soil systems." Rensselaer Polytechnic Institute.
- Pennington, D. S., D. F. Nash, and M. L. Lings. 2001. "Horizontally mounted bender elements for measuring anisotropic shear moduli in triaxial clay specimens." *Geotechnical testing journal* 24 (2):133-144.
- Petersen, M. D., A. M. Shumway, P. M. Powers, C. S. Mueller, M. P. Moschetti, A. D. Frankel, S. Rezaeian, D. E. McNamara, N. Luco, and O. S. Boyd. 2020. "The 2018 update of the US National Seismic Hazard Model: Overview of model and implications." *Earthquake spectra* 36 (1):5-41.
- PowerTechnologies. 2021. "Block Island Wind Farm." <https://www.power-technology.com/projects/block-island-wind-farm/>.
- Prowell, I., A. Elgamal, C. M. Uang, J. Enrique Luco, H. Romanowitz, and E. Duggan. 2014. "Shake table testing and numerical simulation of a utility-scale wind turbine including operational effects." *Wind Energy* 17 (7):997-1016.
- Pryor, S. C., R. J. Barthelmie, and T. J. Shepherd. 2021. "Wind power production from very large offshore wind farms." *Joule*.

- Qiu, Z., A. Ebeido, A. Almutairi, J. Lu, A. Elgamal, P. B. Shing, and G. Martin. 2020. "Aspects of bridge-ground seismic response and liquefaction-induced deformations." *Earthquake Engineering & Structural Dynamics* 49 (4):375-393.
- Ramirez, J., A. R. Barrero, L. Chen, S. Dashti, A. Ghofrani, M. Taiebat, and P. Arduino. 2018. "Site response in a layered liquefiable deposit: evaluation of different numerical tools and methodologies with centrifuge experimental results." *Journal of Geotechnical and Geoenvironmental Engineering* 144 (10):04018073.
- Rammah, K., M. Ismail, and M. Fahey. 2006. "Development of a centrifuge seismic tomography system at UWA." 6th International Conference on Physical Modeling in Geotechnics.
- REN21. 2019. Renewables 2019 Global Status Report. REN21 Secretariat, Paris, France: REN21.
- Rodrigues, S., C. Restrepo, E. Kontos, R. T. Pinto, and P. Bauer. 2015. "Trends of offshore wind projects." *Renewable and Sustainable Energy Reviews* 49:1114-1135.
- Sato, M. 1997. "Reproduction of seismic liquefaction damage to caisson type quay wall and its neighboring pile foundation in a centrifuge model." *Proceedings of Japan Society of Civil Engineers* 1997 (582):295-304.
- Seed, H. B., R. T. Wong, I. Idriss, and K. Tokimatsu. 1986. "Moduli and damping factors for dynamic analyses of cohesionless soils." *Journal of geotechnical engineering* 112 (11):1016-1032.
- Shakal, A., and C. Petersen. 1992. "Downhole strong-motion accelerometry: Objectives and techniques." *Seismological Research Letters* 63 (1):30.
- Shirley, D. J., and L. D. Hampton. 1978. "Shear-wave measurements in laboratory sediments." *The Journal of the Acoustical Society of America* 63 (2):607-613.
- Sims, J. D., and C. D. Garvin. 1995. "Recurrent liquefaction induced by the 1989 Loma Prieta earthquake and 1990 and 1991 aftershocks: implications for paleoseismicity studies." *Bulletin of the Seismological Society of America* 85 (1):51-65.
- Sonmez, B., R. Ulusay, and H. Sonmez. 2008. "A study on the identification of liquefaction-induced failures on ground surface based on the data from the 1999 Kocaeli and Chi-Chi earthquakes." *Engineering Geology* 97 (3-4):112-125.

- Stapelfeldt, M., B. Bienen, and J. Grabe. 2021. "Influence of Low-Permeability Layers on the Installation and the Response to Vertical Cyclic Loading of Suction Caissons." *Journal of Geotechnical and Geoenvironmental Engineering* 147 (8):04021076.
- Su, L., J. Lu, A. Elgamal, and A. K. Arulmoli. 2017. "Seismic performance of a pile-supported wharf: Three-dimensional finite element simulation." *Soil Dynamics and Earthquake Engineering* 95:167-179.
- Taboada-Urtuzuastegui, V. M., and R. Dobry. 1998. "Centrifuge modeling of earthquake-induced lateral spreading in sand." *Journal of geotechnical and geoenvironmental engineering* 124 (12):1195-1206.
- Taboada, V. 1995. "Centrifuge modeling of earthquake-induced lateral spreading using a laminar box." PhD dissertation.
- Tang, L., X. Zhang, X. Ling, L. Su, and C. Liu. 2014. "Response of a pile group behind quay wall to liquefaction-induced lateral spreading: a shake-table investigation." *Earthquake Engineering and Engineering Vibration* 13 (4):741-749.
- Thevanayagam, S., T. Kanagalingam, A. Reinhorn, R. Tharmendhira, R. Dobry, M. Pitman, T. Abdoun, A. Elgamal, M. Zeghal, and N. Ecmis. 2009. "Laminar box system for 1-g physical modeling of liquefaction and lateral spreading." *Geotechnical Testing Journal* 32 (5):438-449.
- Tokimatsu, K., S. Tamura, H. Suzuki, and K. Katsumata. 2012. "Building damage associated with geotechnical problems in the 2011 Tohoku Pacific Earthquake." *Soils and Foundations* 52 (5):956-974.
- Trautner, C., Y. Zheng, J. S. McCartney, and T. Hutchinson. 2018. "An approach for shake table performance evaluation during repair and retrofit actions." *Earthquake Engineering & Structural Dynamics* 47 (1):131-146.
- van der Tempel, J., and D.-P. Molenaar. 2002. "Wind turbine structural dynamics—a review of the principles for modern power generation, onshore and offshore." *Wind engineering* 26 (4):211-222.
- Versteijlen, W. G., A. Metrikine, J. Hoving, E. Smidt, and W. De Vries. 2011. "Estimation of the vibration decrement of an offshore wind turbine support structure caused by its interaction with soil." Proceedings of the EWEA Offshore 2011 Conference, Amsterdam, The Netherlands, 29 November-1 December 2011.

- Vestas. 2021. "4 MW Platform - V117-3.45 MW Facts & figures." accessed 29 August. <https://nozebra.ipapercms.dk/Vestas/Communication/4mw-platform-brochure/?page=12>.
- Vigny, C., A. Socquet, S. Peyrat, J.-C. Ruegg, M. Métois, R. Madariaga, S. Morvan, M. Lancieri, R. Lacassin, and J. Campos. 2011. "The 2010 Mw 8.8 Maule megathrust earthquake of central Chile, monitored by GPS." *Science* 332 (6036):1417-1421.
- Villalobos, F. A., B. W. Byrne, and G. T. Houlsby. 2005. "Moment loading of caissons installed in saturated sand." Proceedings of international symposium on frontiers in Geotechnics, ISFOG. University of Western.
- Villalobos, F. A., B. W. Byrne, and G. T. Houlsby. 2010. "Model testing of suction caissons in clay subjected to vertical loading." *Applied Ocean Research* 32 (4):414-424. doi: <https://doi.org/10.1016/j.apor.2010.09.002>.
- Wang, X., X. Yang, and X. Zeng. 2017a. "Lateral response of improved suction bucket foundation for offshore wind turbine in centrifuge modelling." *Ocean Engineering* 141:295-307.
- Wang, X., X. Yang, and X. Zeng. 2017b. "Seismic centrifuge modelling of suction bucket foundation for offshore wind turbine." *Renewable energy* 114:1013-1022.
- Wang, X., X. Zeng, and J. Li. 2019. "Vertical performance of suction bucket foundation for offshore wind turbines in sand." *Ocean Engineering* 180:40-48.
- Wang, X., X. Zeng, J. Li, X. Yang, and H. Wang. 2018. "A review on recent advancements of substructures for offshore wind turbines." *Energy Conversion and Management* 158:103-119.
- Wang, X., X. Zeng, H. Yu, and H. Wang. 2015. "Centrifuge modeling of offshore wind turbine with bucket foundation under earthquake loading." In *IFCEE 2015*, 1741-1750.
- Wang, Z.-L., C.-Y. Chang, and C. M. Mok. 2001. "Evaluation of site response using downhole array data from a liquefied site."
- Wiser, R., E. Lantz, T. Mai, J. Zayas, E. DeMeo, E. Eugeni, J. Lin-Powers, and R. Tusing. 2015. "Wind vision: A new era for wind power in the United States." *The Electricity Journal* 28 (9):120-132.

- Yamazaki, H., Y. Morikawa, and F. Koike. 2003. "Study on design method of suction foundation using model tests." *PPSoft Ground Engineering in Coastal Areas. LisseNetherlands: Swets & Zeitlinger BV*:419-422.
- Yang, Z. 2000. *Numerical modeling of earthquake site response including dilation and liquefaction*: Columbia University.
- Yang, Z., and A. Elgamal. 2002. "Influence of permeability on liquefaction-induced shear deformation." *Journal of Engineering Mechanics* 128 (7):720-729.
- Yin, Z.-Y., J.-C. Teng, Z. Li, and Y.-Y. Zheng. 2020. "Modelling of suction bucket foundation in clay: From finite element analyses to macro-elements." *Ocean Engineering* 210:107577.
- Yu, H., X. Zeng, and J. Lian. 2014. "Seismic behavior of offshore wind turbine with suction caisson foundation." *Geo-Congress 2014: Geo-characterization and Modeling for Sustainability*.
- Zafeirakos, A., and N. Gerolymos. 2014. "Towards a seismic capacity design of caisson foundations supporting bridge piers." *Soil Dynamics and Earthquake Engineering* 67:179-197.
- Zayed, M., A. Ebeido, A. Prabhakaran, K. Kim, Z. Qiu, and A. Elgamal. 2020. "Shake Table Testing: A High-Resolution Vertical Accelerometer Array for Tracking Shear Wave Velocity." *Geotechnical Testing Journal* 44 (4).
- Zayed, M., A. Ebeido, A. Prabhakaran, Z. Qiu, and A. Elgamal. 2021. "Asymmetric input motion for accumulation of lateral ground deformation in laminar container shake table testing." *Canadian Geotechnical Journal* 58 (2):210-223.
- Zeghal, M., and A.-W. Elgamal. 1994a. "Analysis of site liquefaction using earthquake records." *Journal of geotechnical engineering* 120 (6):996-1017.
- Zeghal, M., A.-W. Elgamal, H. Tang, and J. Stepp. 1995. "Lotung downhole array. II: Evaluation of soil nonlinear properties." *Journal of geotechnical engineering* 121 (4):363-378.
- Zeghal, M., A.-W. Elgamal, X. Zeng, and K. Arulmoli. 1999. "Mechanism of liquefaction response in sand-silt dynamic centrifuge tests." *Soil Dynamics and Earthquake Engineering* 18 (1):71-85.

- Zeghal, M., and A. W. Elgamal. 1994b. "Analysis of Site Liquefaction Using Earthquake Records." *Journal of Geotechnical Engineering* 120 (6):996-1017.
- Zeghal, M., N. Goswami, B. L. Kutter, M. T. Manzari, T. Abdoun, P. Arduino, R. Armstrong, M. Beaty, Y.-M. Chen, and A. Ghofrani. 2018. "Stress-strain response of the LEAP-2015 centrifuge tests and numerical predictions." *Soil Dynamics and Earthquake Engineering* 113:804-818.
- Zhang, J., L. Zhang, and X. Lu. 2007. "Centrifuge modeling of suction bucket foundations for platforms under ice-sheet-induced cyclic lateral loadings." *Ocean engineering* 34 (8-9):1069-1079.
- Zhang, P., Y. Han, H. Ding, and S. Zhang. 2015. "Field experiments on wet tows of an integrated transportation and installation vessel with two bucket foundations for offshore wind turbines." *Ocean Engineering* 108:769-777.
- Zhou, Y.-G., and Y.-M. Chen. 2007. "Laboratory investigation on assessing liquefaction resistance of sandy soils by shear wave velocity." *Journal of Geotechnical and Geoenvironmental Engineering* 133 (8):959-972.
- Zhu, F. Y., B. Bienen, C. O'Loughlin, M. J. Cassidy, and N. Morgan. 2019. "Suction caisson foundations for offshore wind energy: cyclic response in sand and sand over clay." *Géotechnique* 69 (10):924-931.

# APPENDIX A

## System identification of bucket foundation wind turbine model in shake table testing

This appendix includes results of shake table tests conducted on the bucket foundation wind turbine model using the white noise excitations described in Table 3.4. Results of tests WN1 and WN2 are presented as time histories of the following records:

- Acceleration of shake table input excitation,
- Lateral soil accelerations,
- Lateral soil displacements,
- Soil excess pore water pressures,
- Excess pore water pressure around bucket foundation,
- Vertical displacement of bucket foundation,
- Lateral accelerations of wind turbine tower,
- Tower lateral displacement, and
- Tower bending moments.

The contents of this appendix are directly related to Chapter 3 and Chapter 4.

# A.1 Test WN1

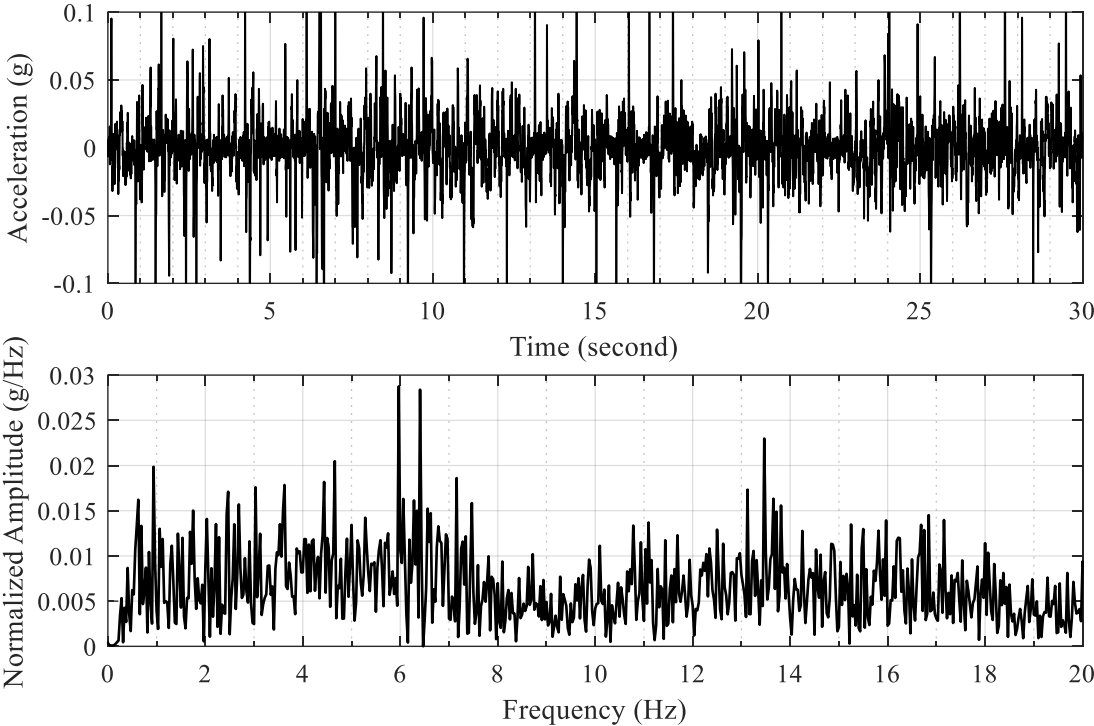


Figure A-1: Acceleration time history of shake table input excitation and the corresponding frequency spectrum for test WN1



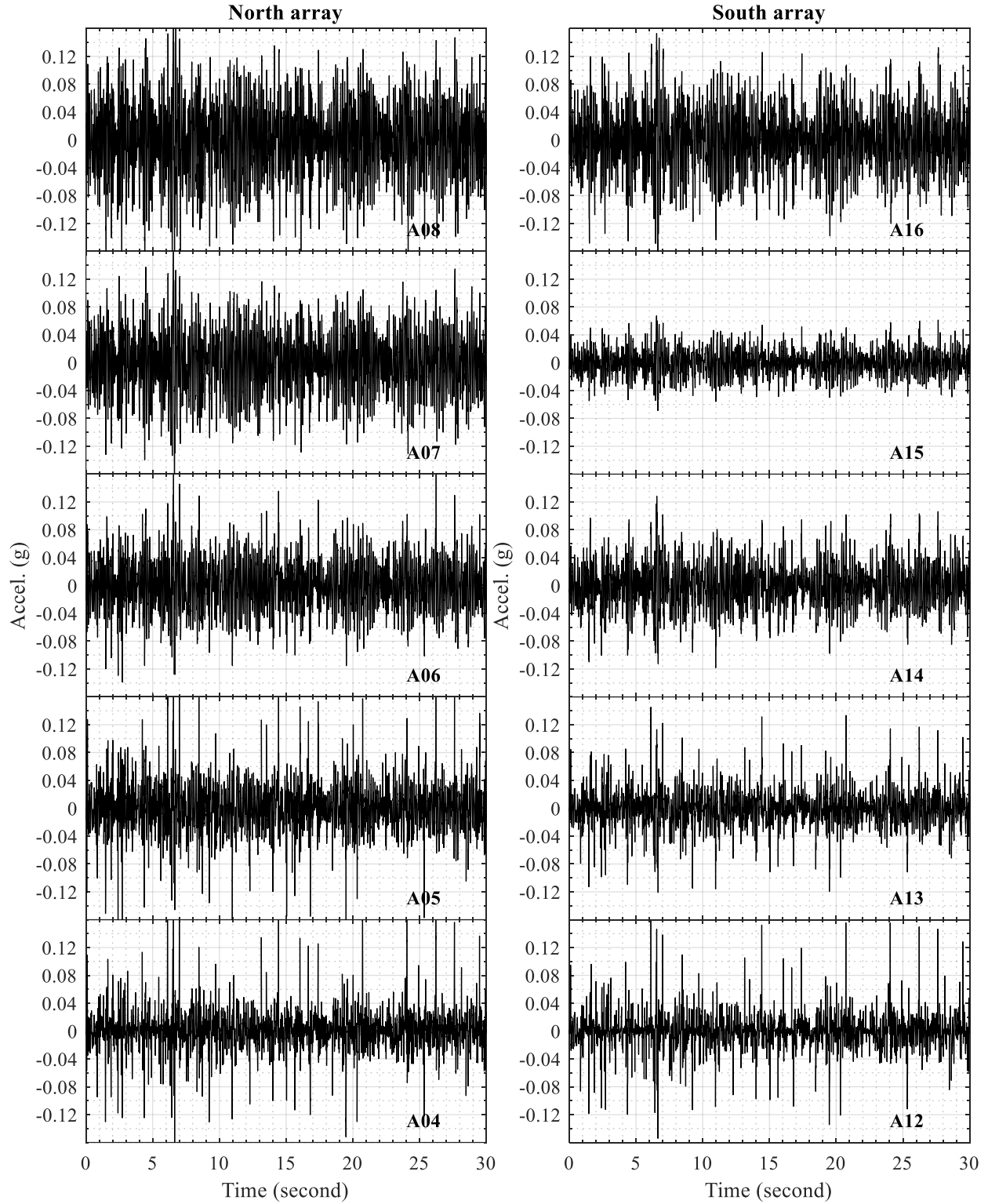


Figure A-2: Time histories of lateral soil acceleration in north and south arrays for test WN1

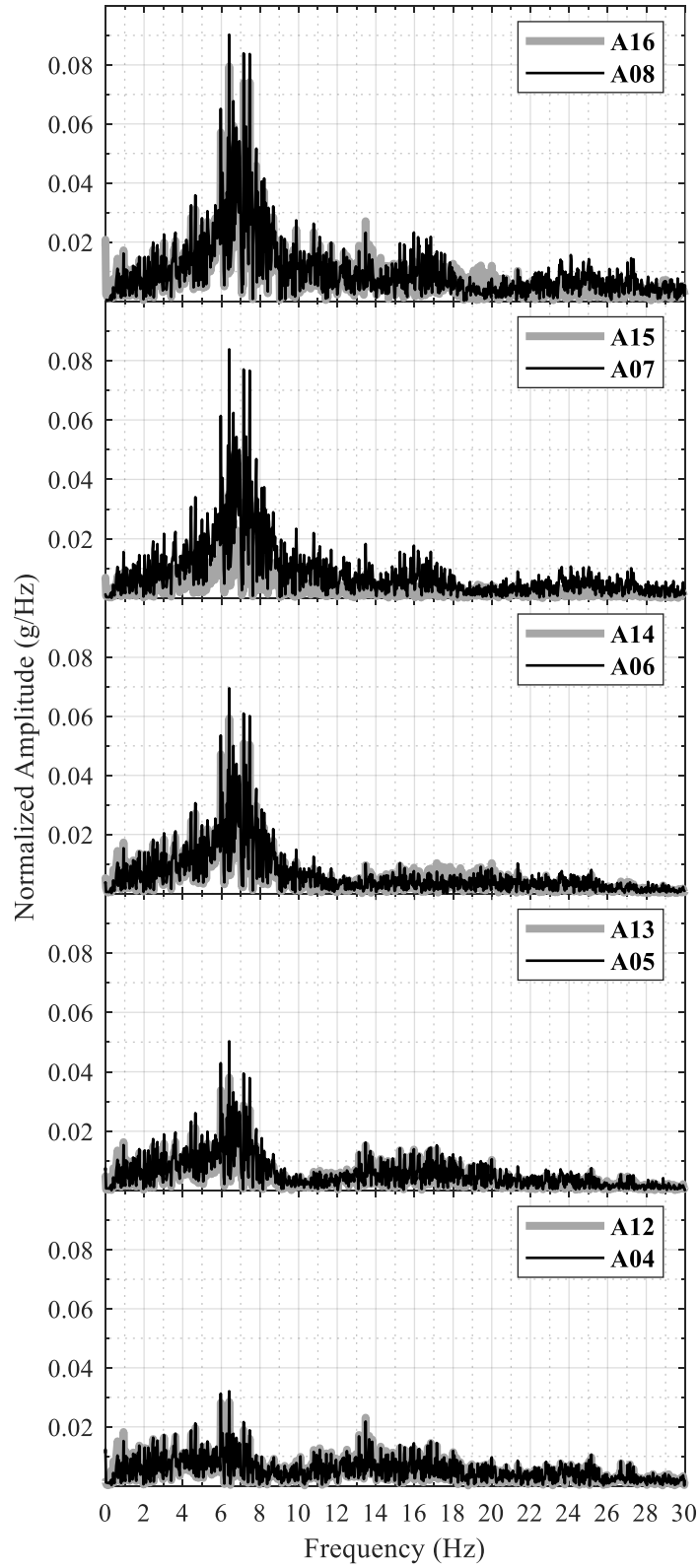


Figure A-3: Frequency spectra of lateral soil acceleration in north and south arrays for test WN1

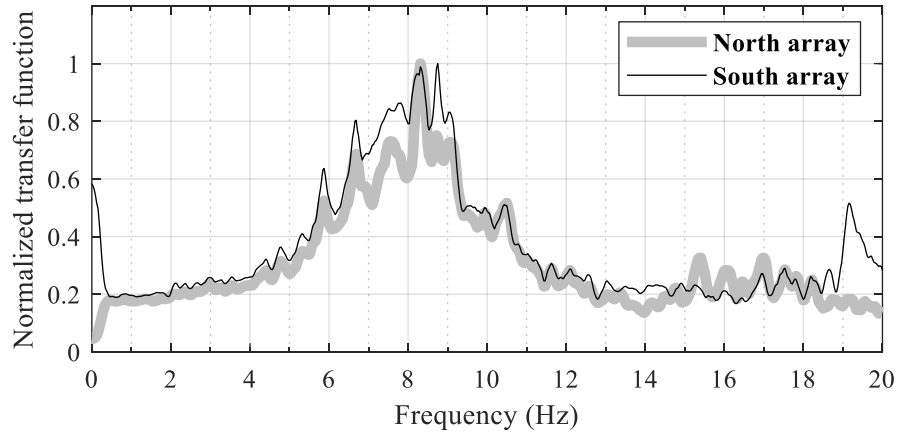


Figure A-4: Transfer function between uppermost and lowermost soil acceleration records for test WN1

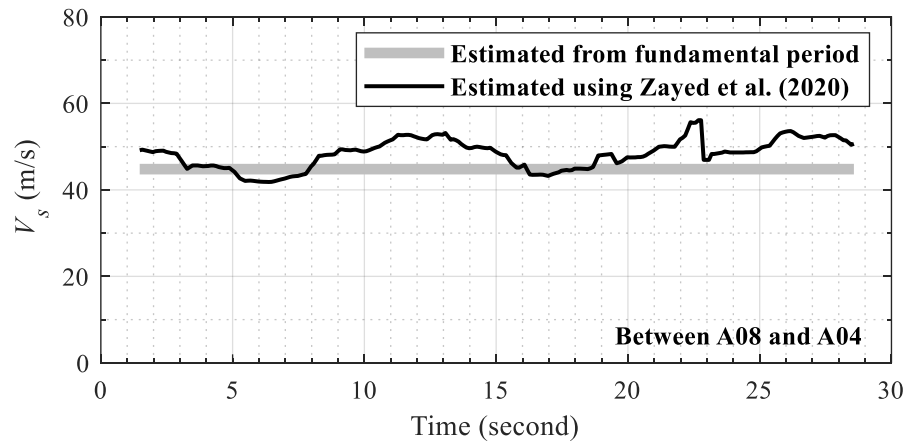


Figure A-5: Change in soil  $V_s$  with time during test WN1

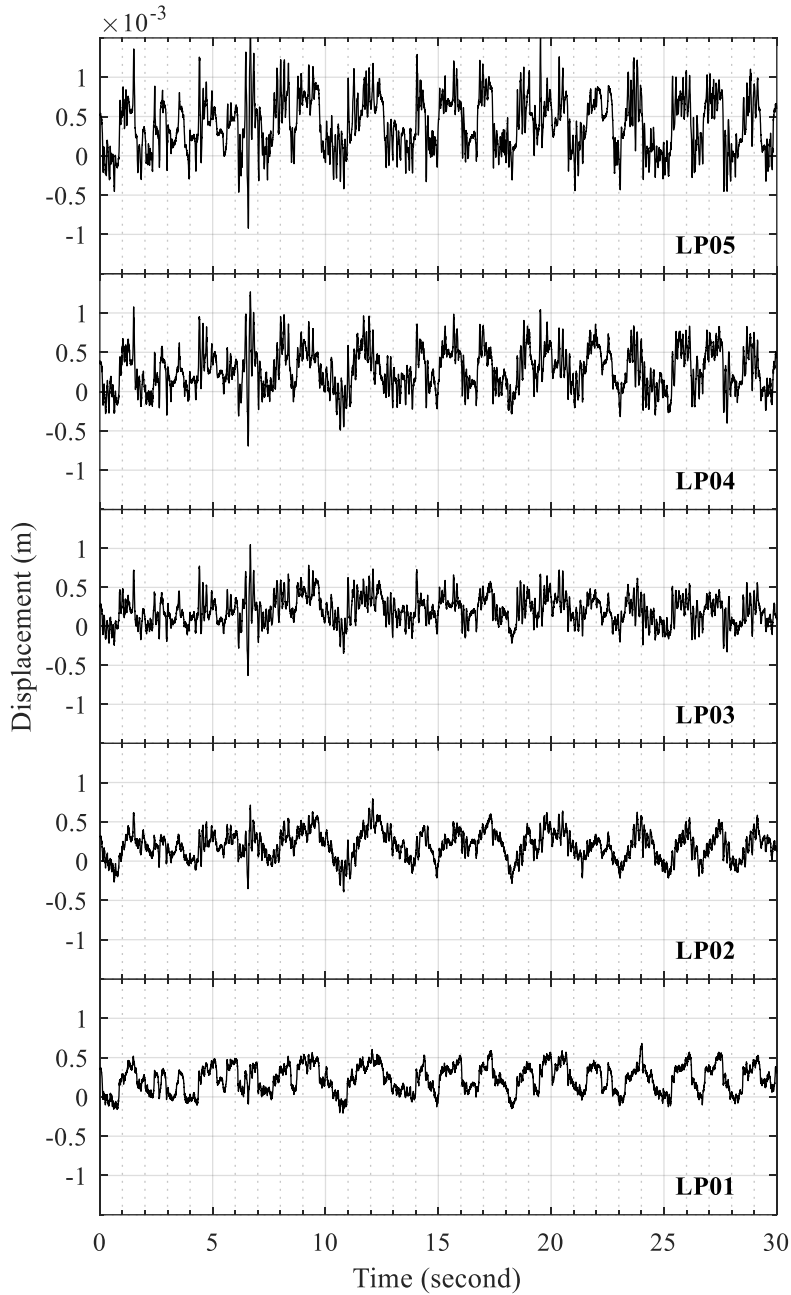


Figure A-6: Time histories of lateral soil displacement relative to laminar container base for test WN1

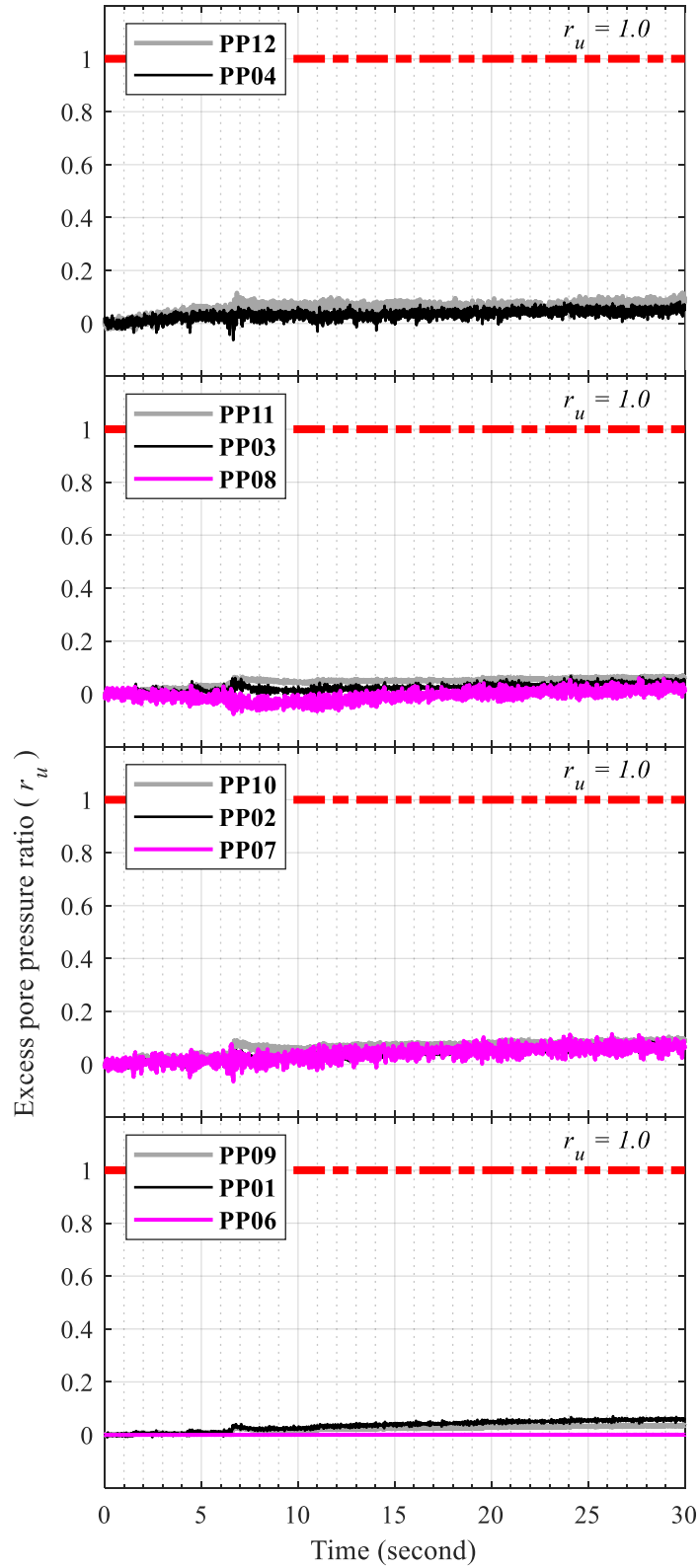


Figure A-7: Time histories of soil excess pore pressure for test WN1

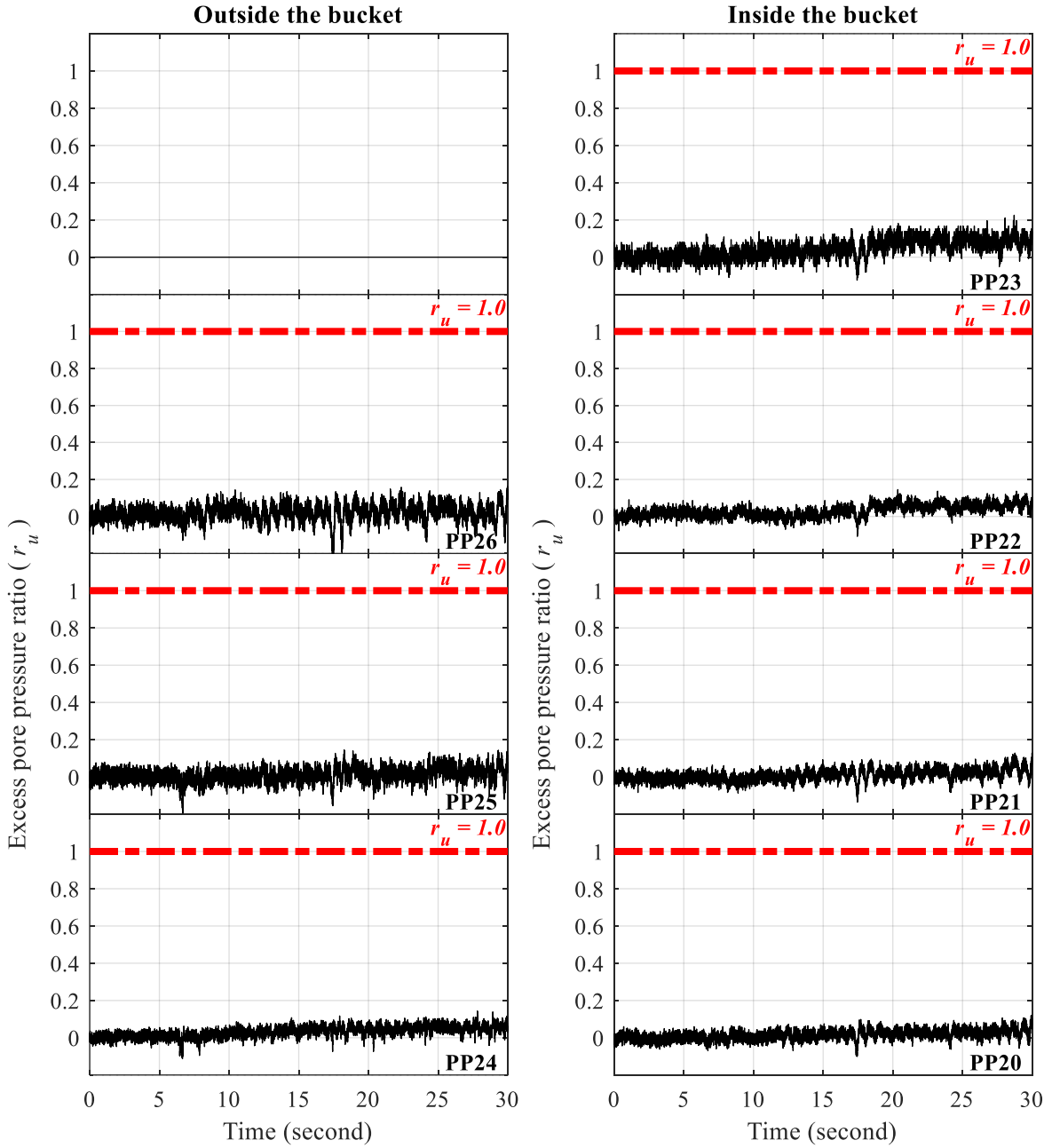


Figure A-8: Time histories of excess pore pressure at north edge of suction bucket for test WN1

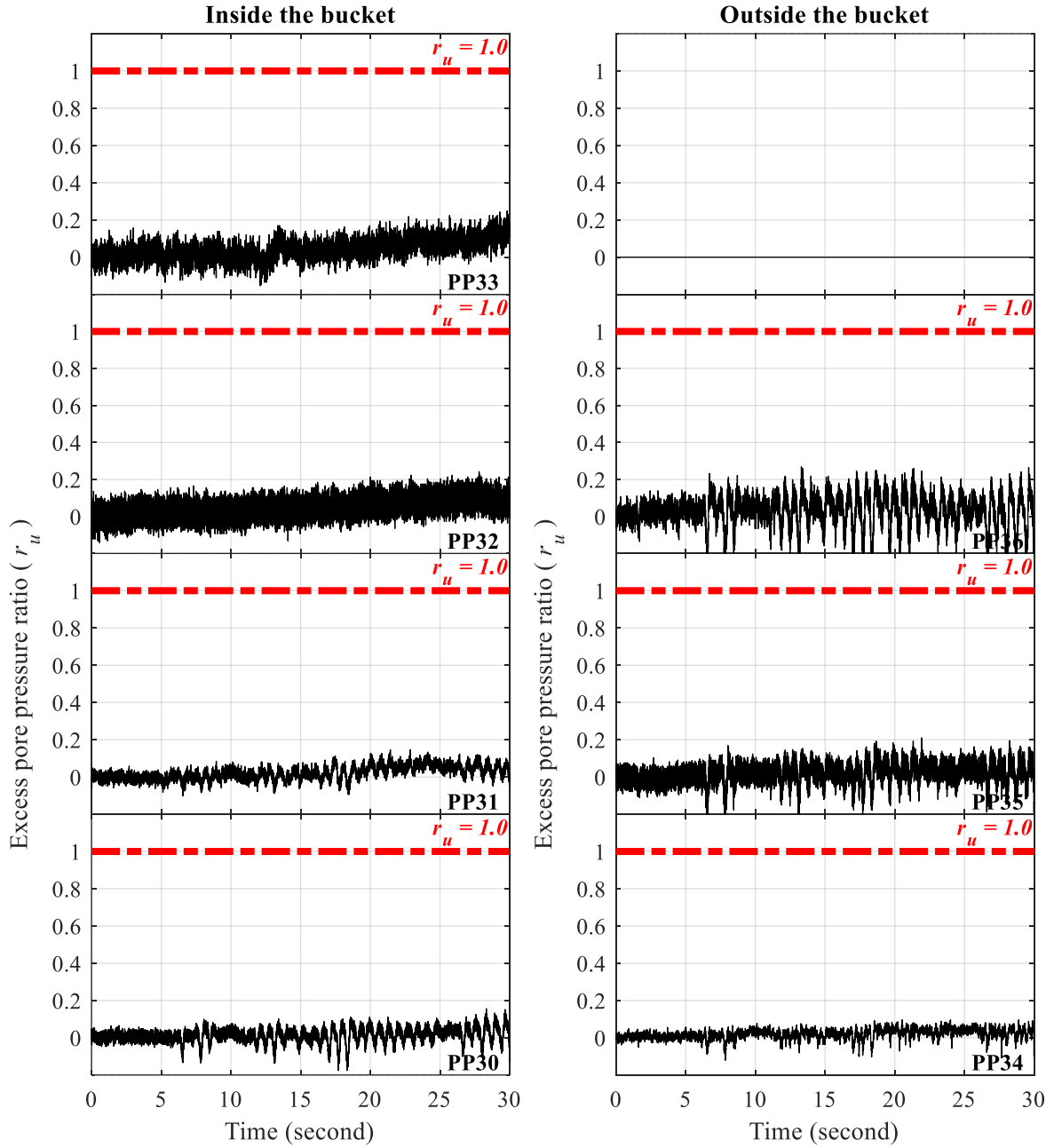


Figure A-9: Time histories of excess pore pressure at south edge of suction bucket for test WN1



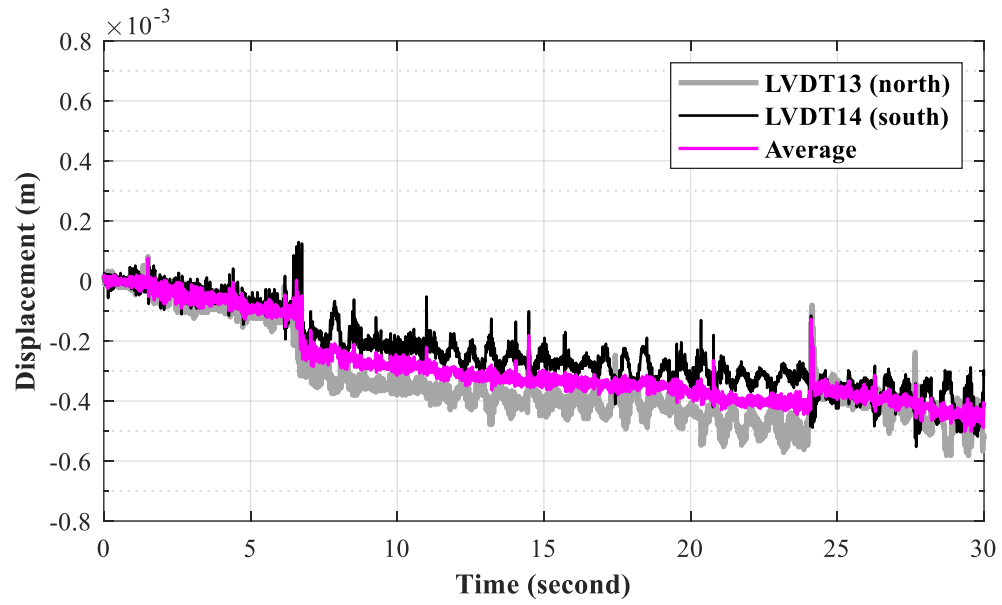


Figure A-10: Time histories of vertical bucket displacement for test WN1

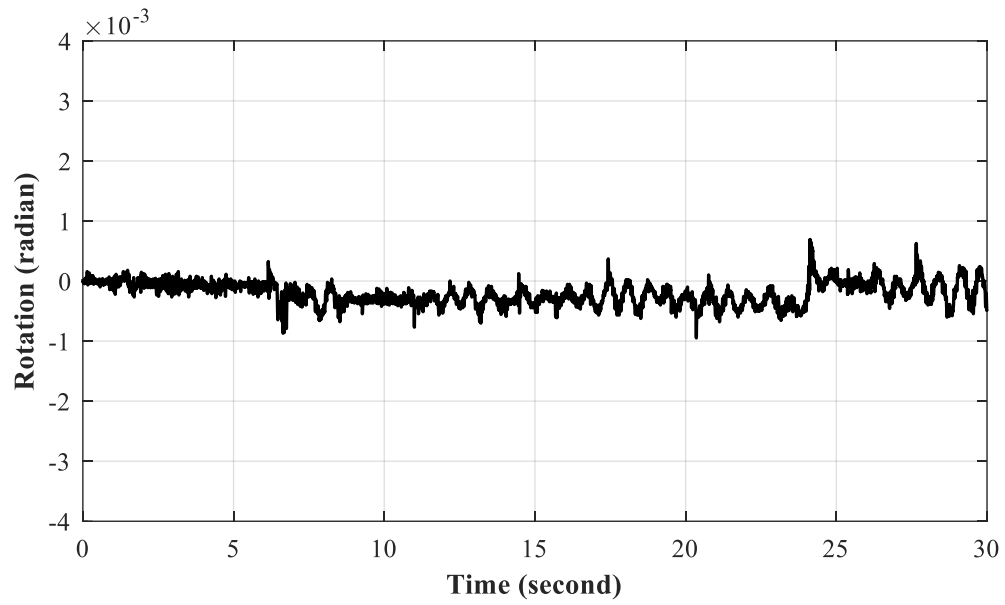


Figure A-11: Time history of bucket rotation for test WN1

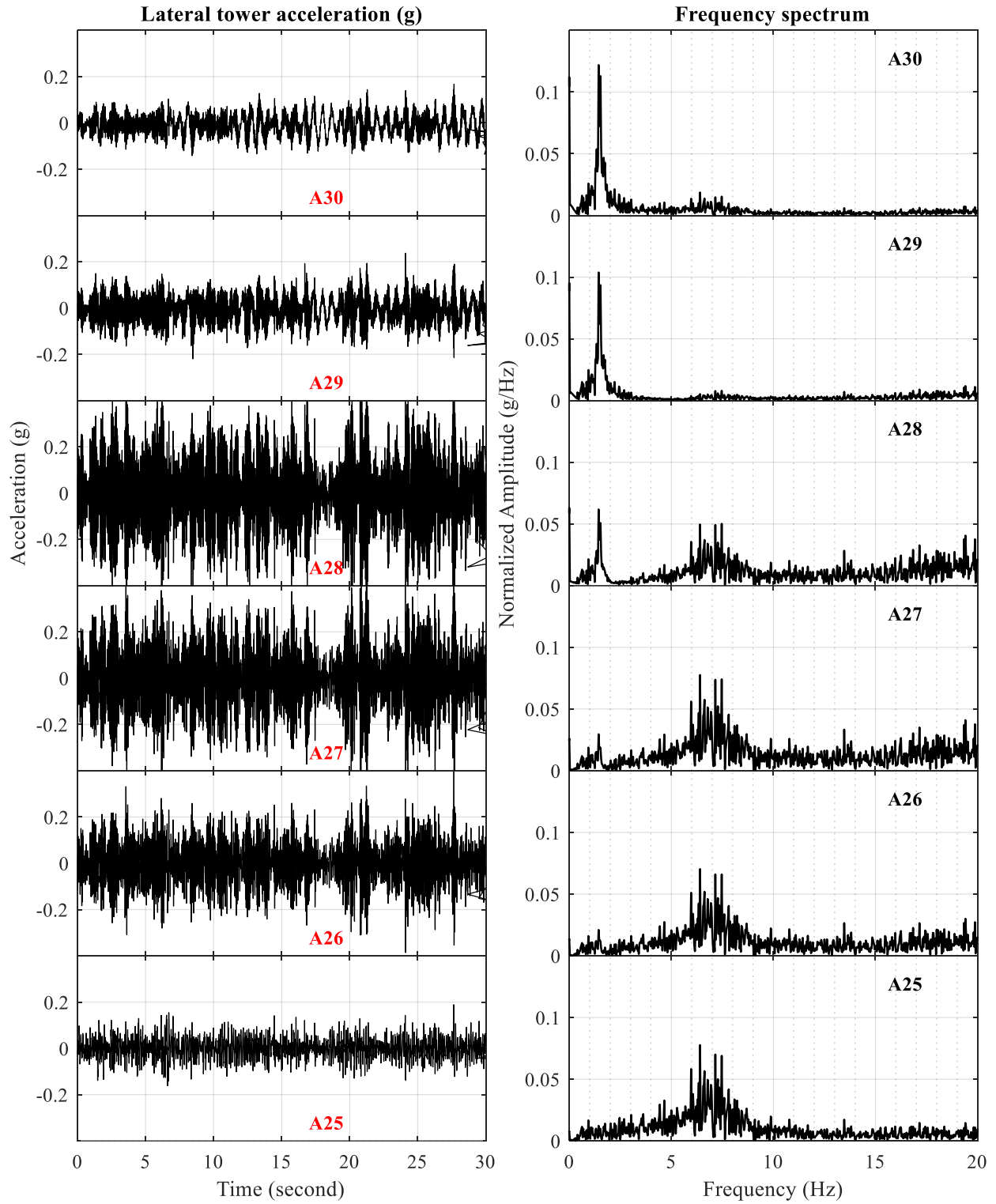


Figure A-12: Time histories of lateral tower acceleration for test WN1

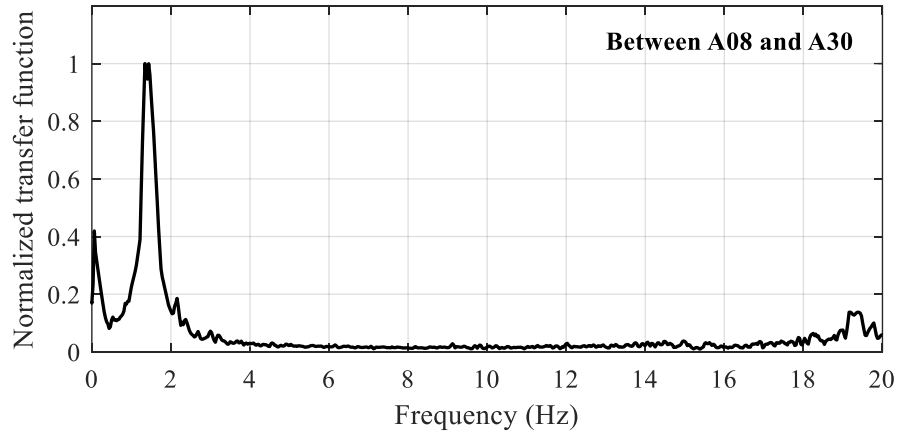


Figure A-13: Transfer function between acceleration records at the tower top (A30) and soil top near the suction bucket foundation (A08) for test WN1

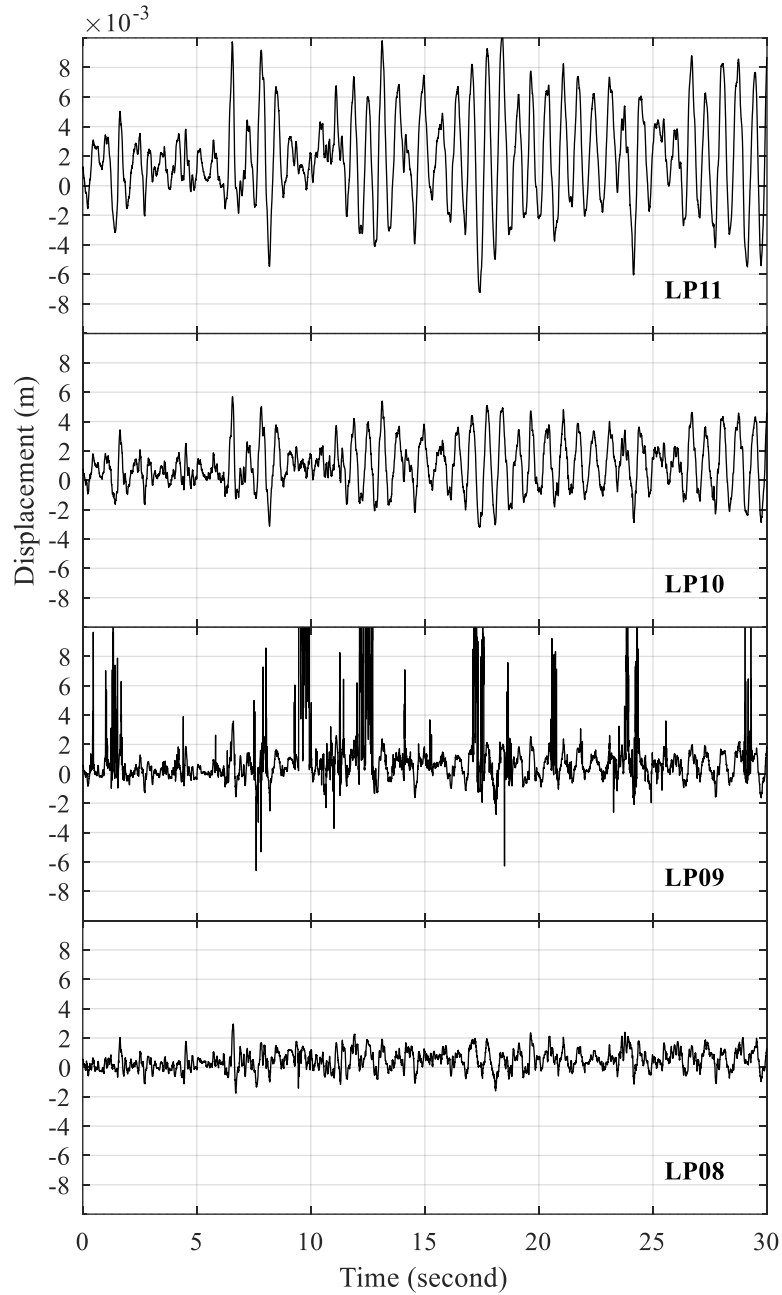


Figure A-14: Time histories of lateral tower displacement relative to lateral soil displacement at the foundation level (LP05) for test WN1

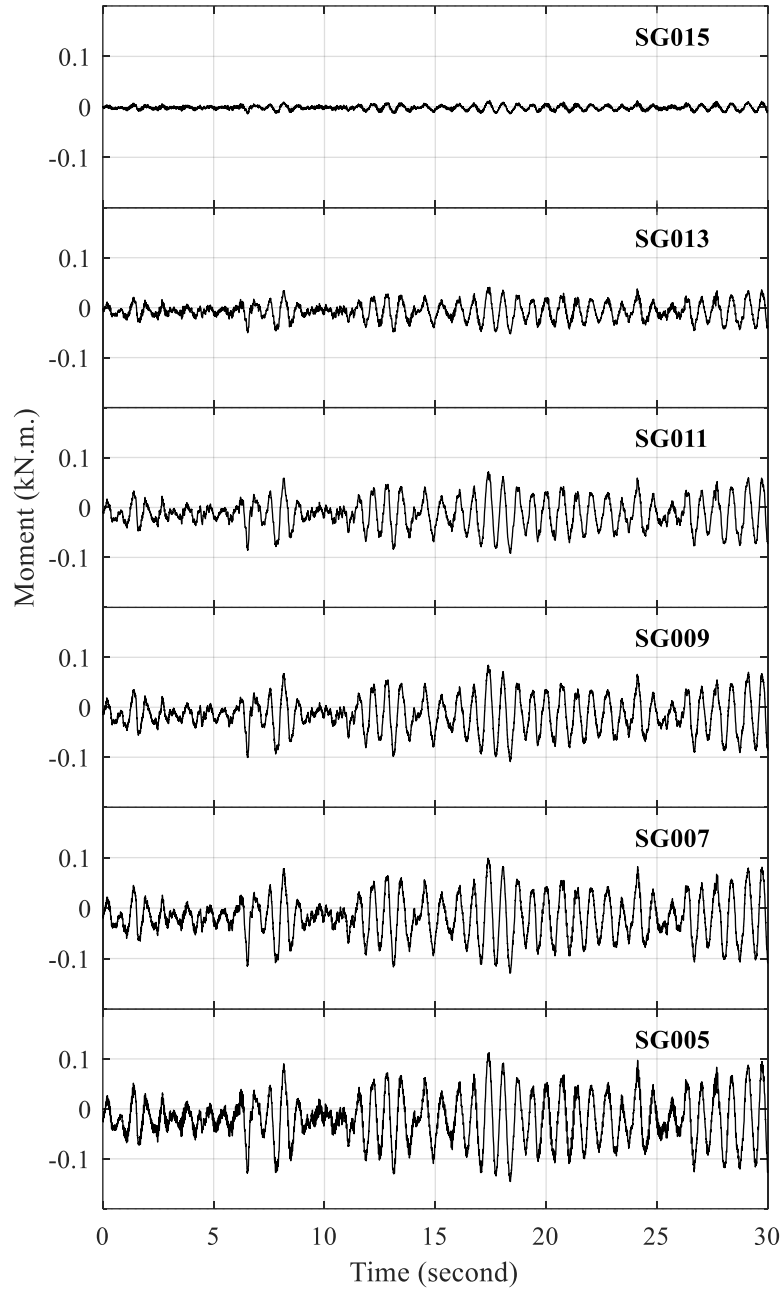


Figure A-15: Time histories of tower bending moment for test WN1

## A.2 Test WN2

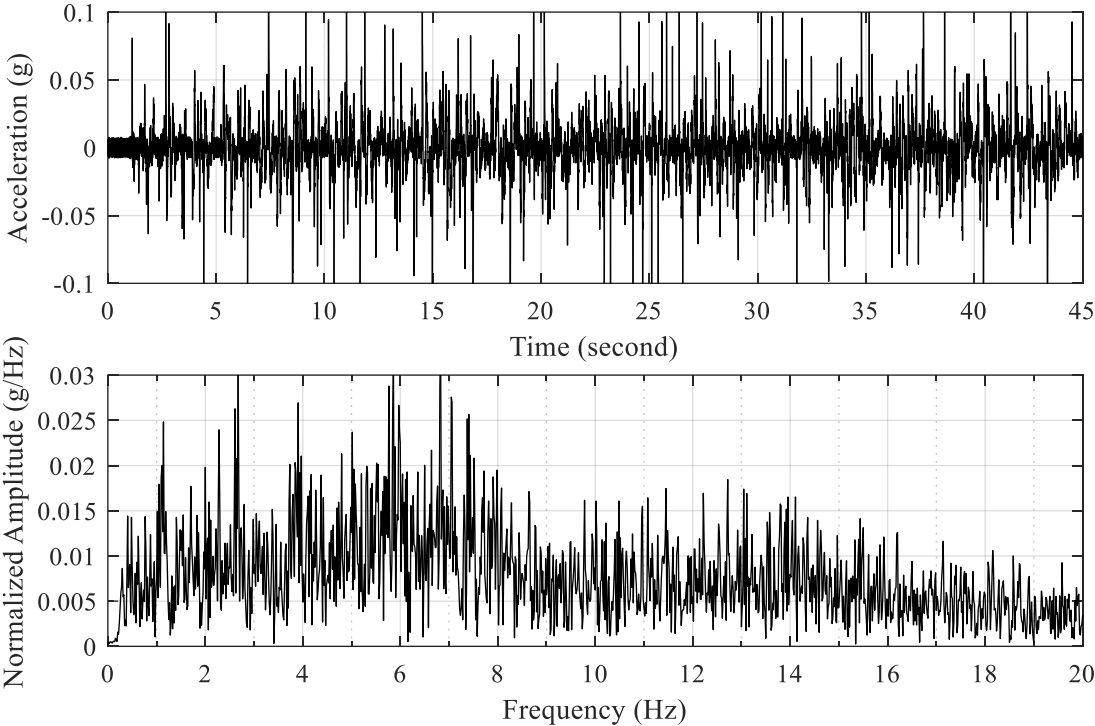


Figure A-16: Acceleration time history of shake table input excitation and the corresponding frequency spectrum for test WN2

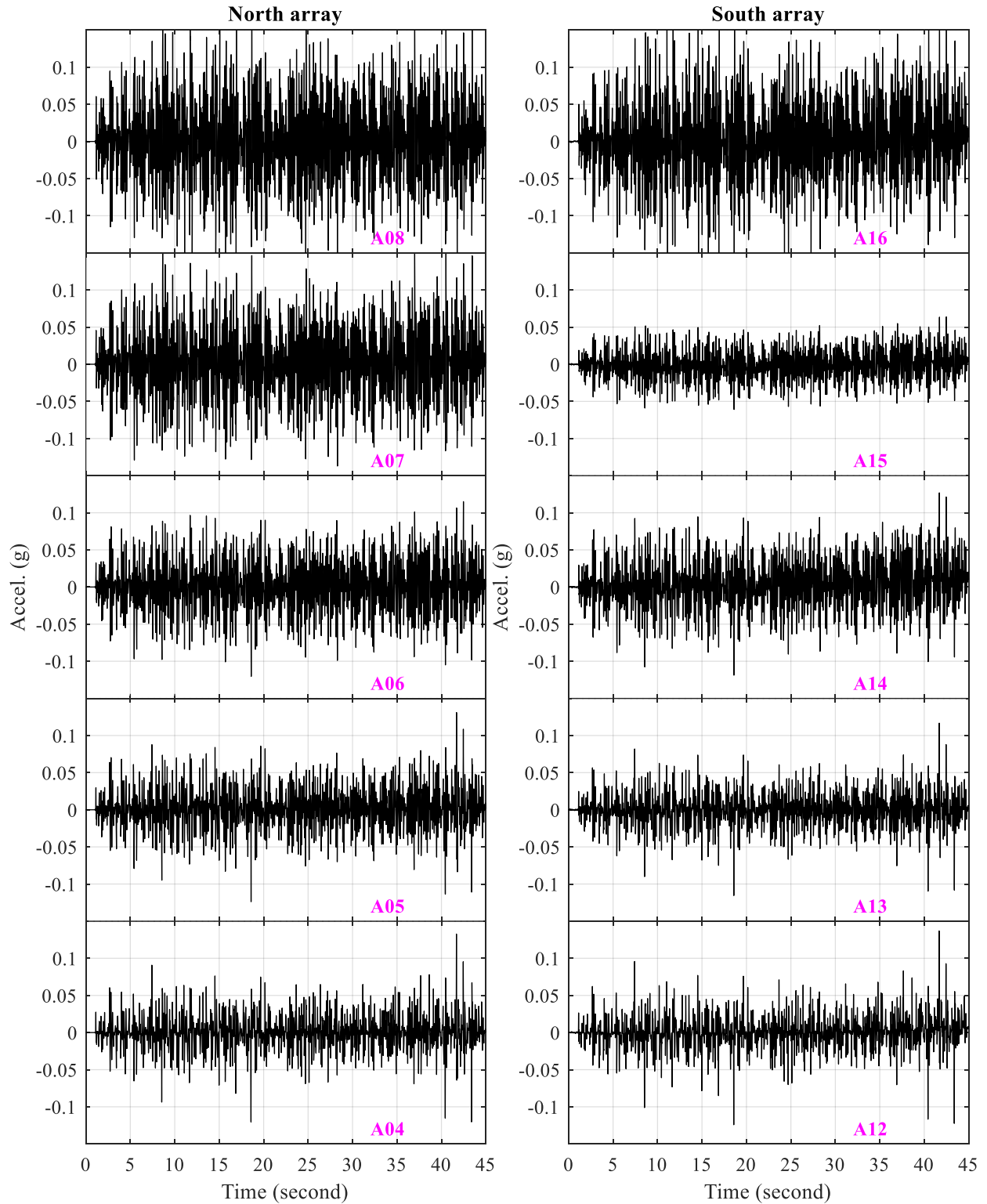


Figure A-17: Time histories of lateral soil acceleration in north and south arrays for test WN2



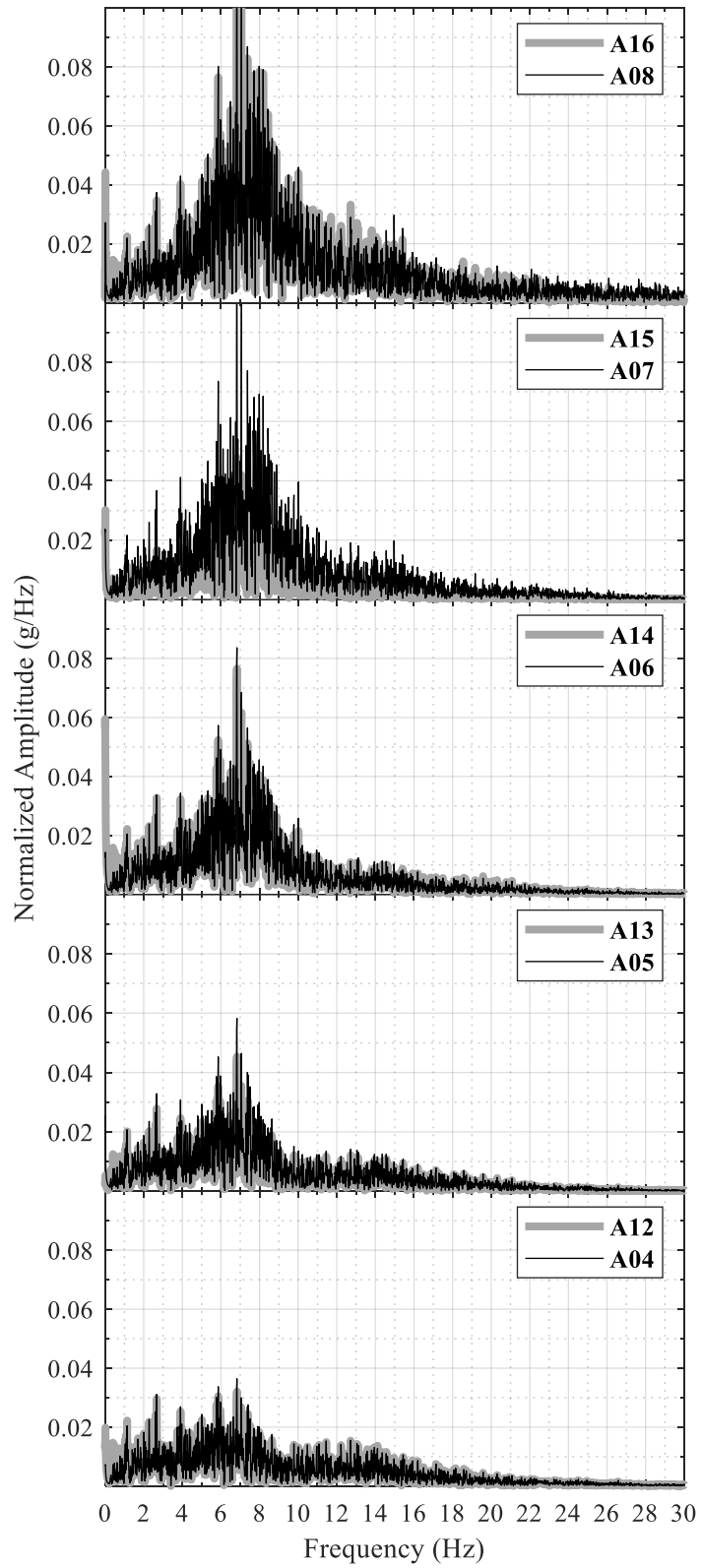


Figure A-18: Frequency spectra of lateral soil acceleration in north and south arrays for test WN2

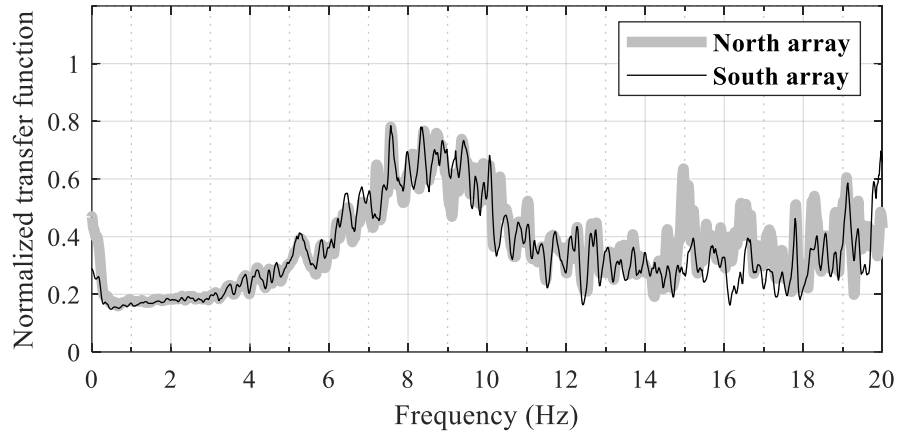


Figure A-19: Transfer function between uppermost and lowermost soil acceleration records for test WN2

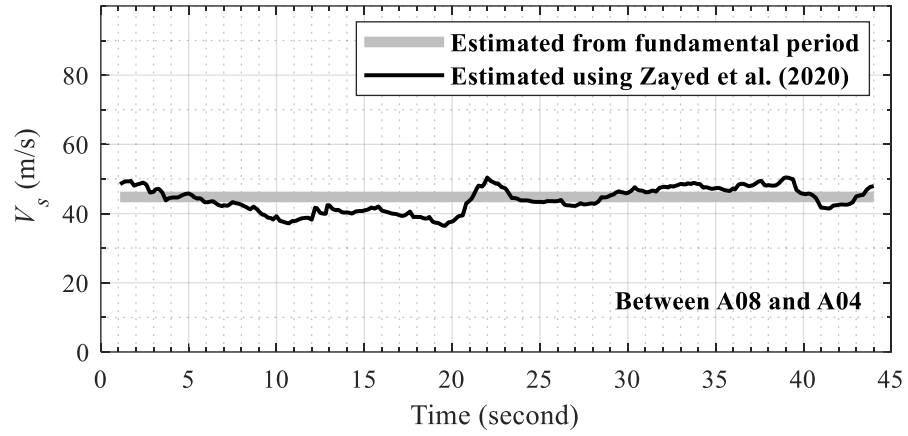


Figure A-20: Change in soil  $V_s$  with time during test WN2

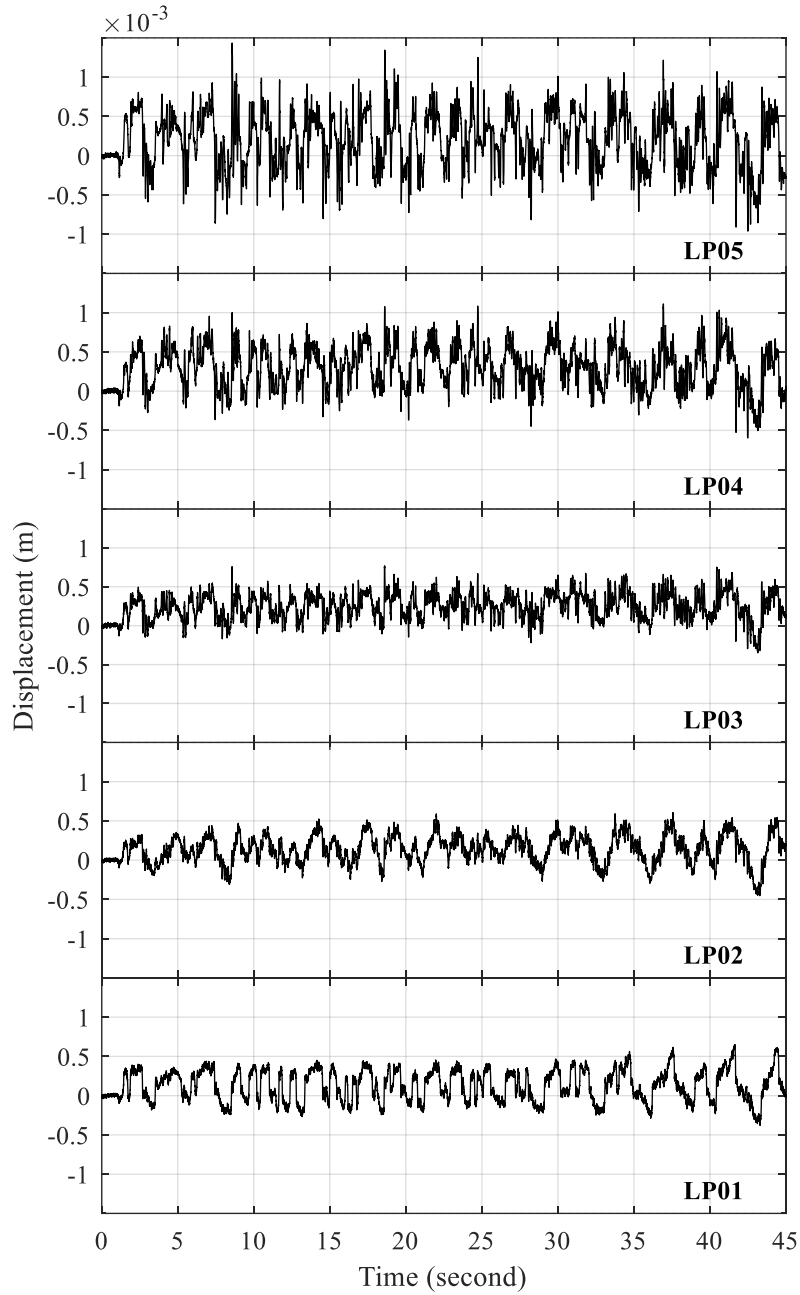


Figure A-21: Time histories of lateral soil displacement relative to laminar container base for test WN2

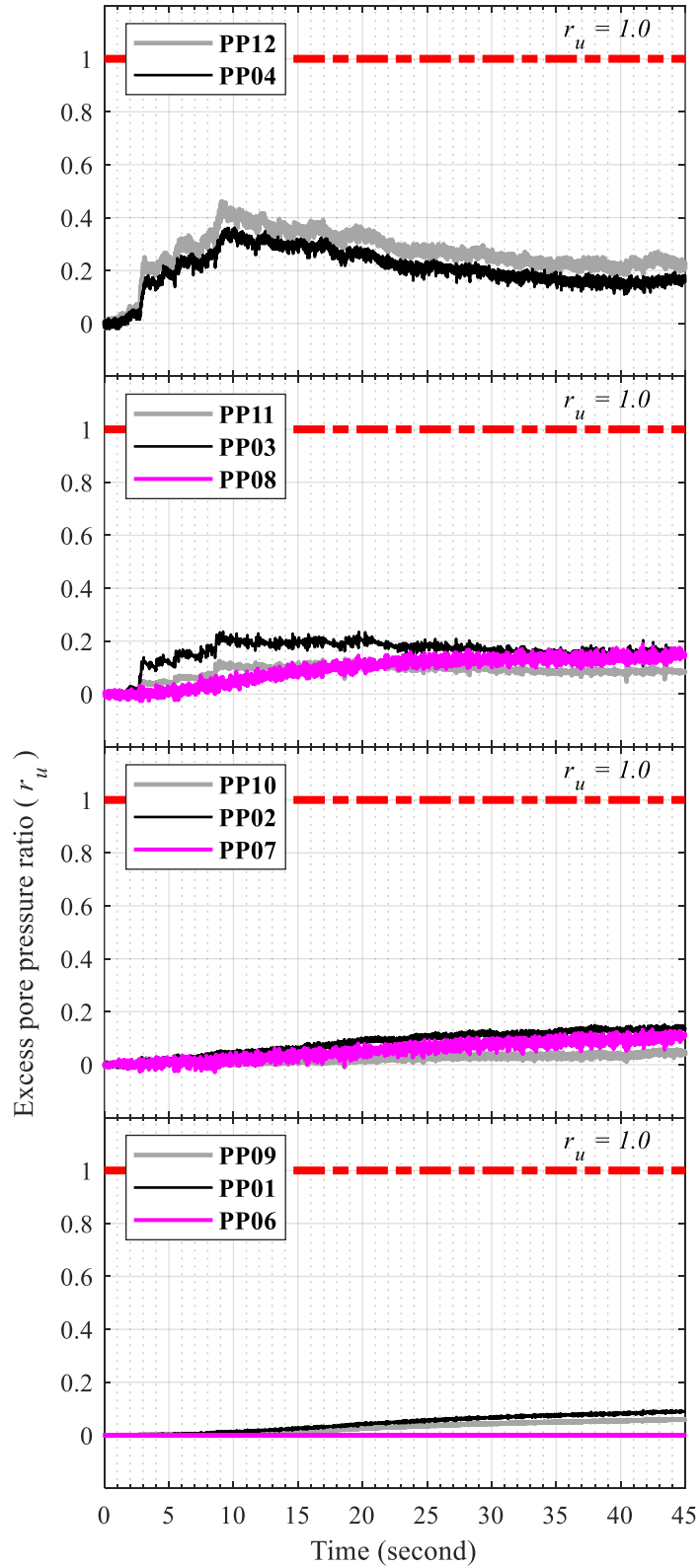


Figure A-22: Time histories of soil excess pore pressure for test WN2

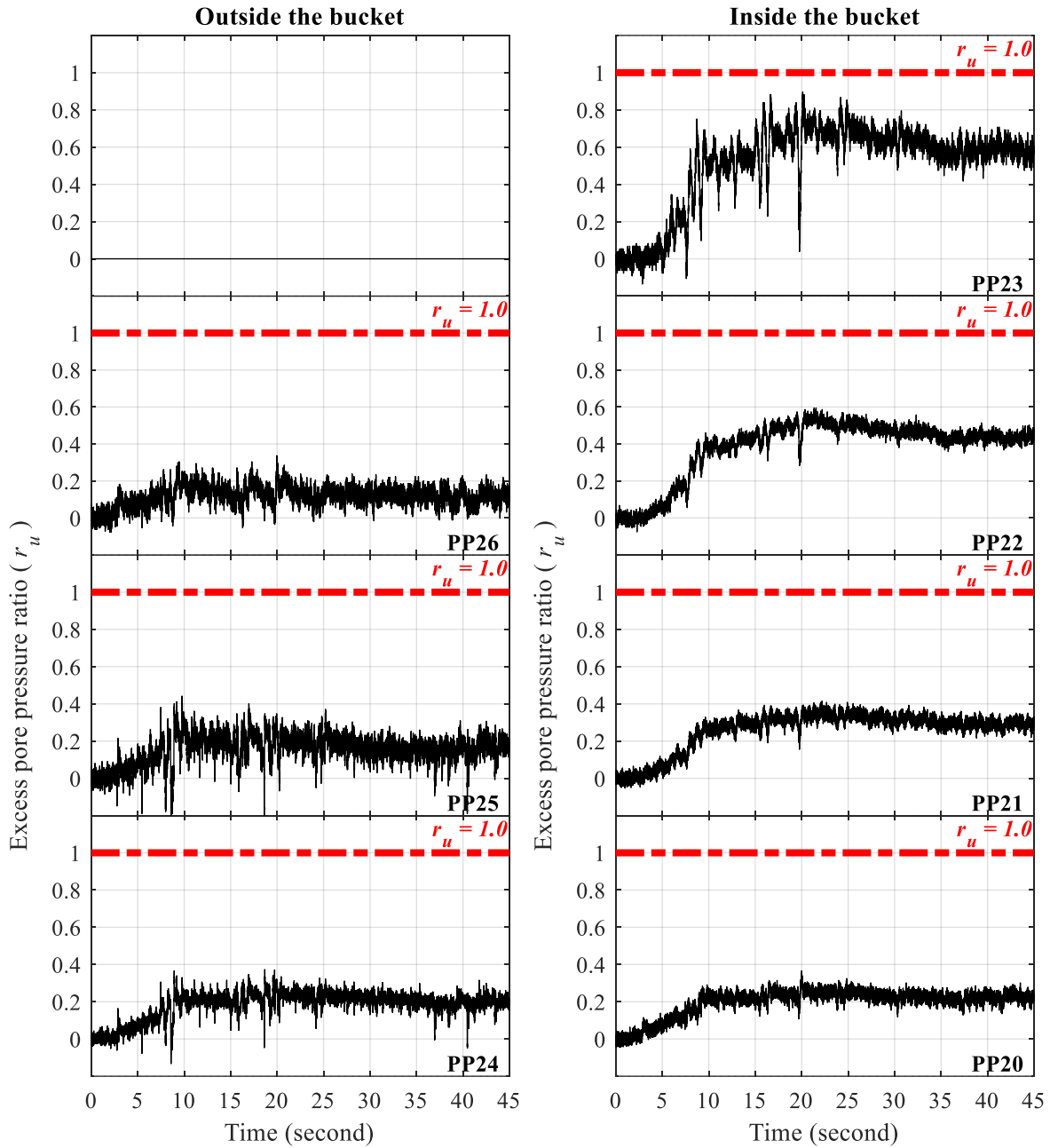


Figure A-23: Time histories of excess pore pressure at north edge of suction bucket for test WN2

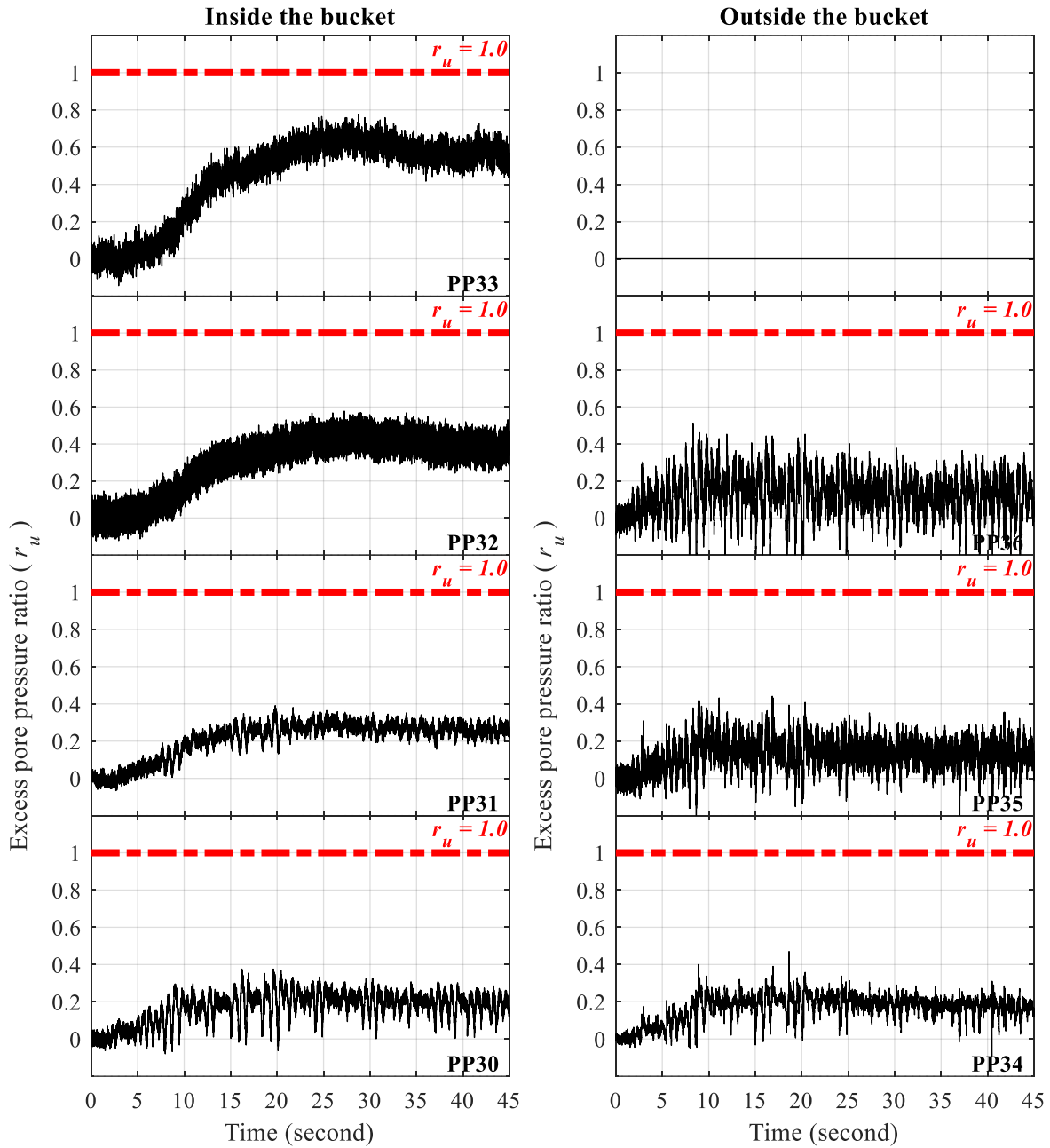


Figure A-24 Time histories of excess pore pressure at south edge of suction bucket for test WN2

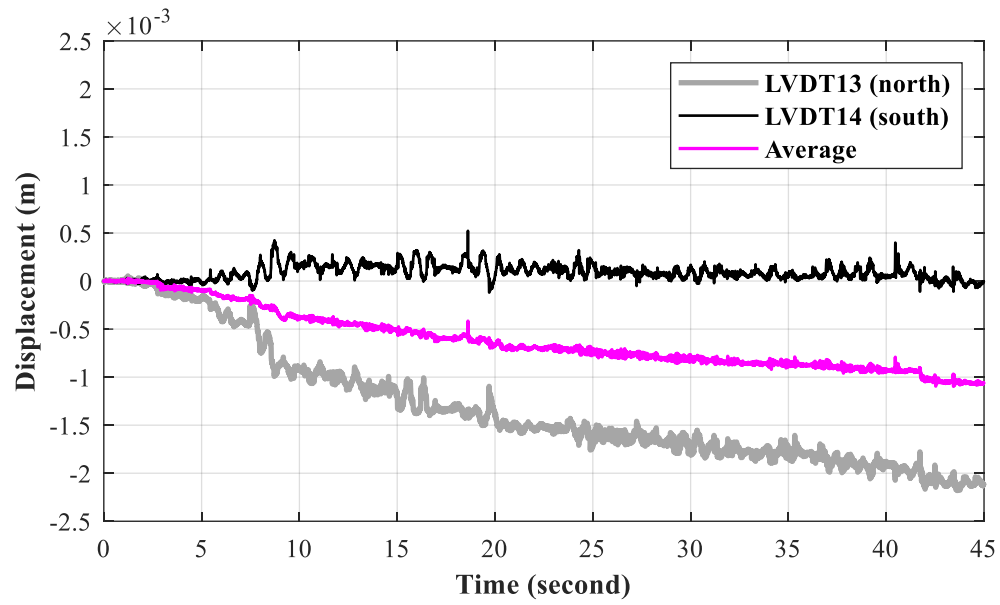


Figure A-25: Time histories of vertical bucket displacement for test WN2



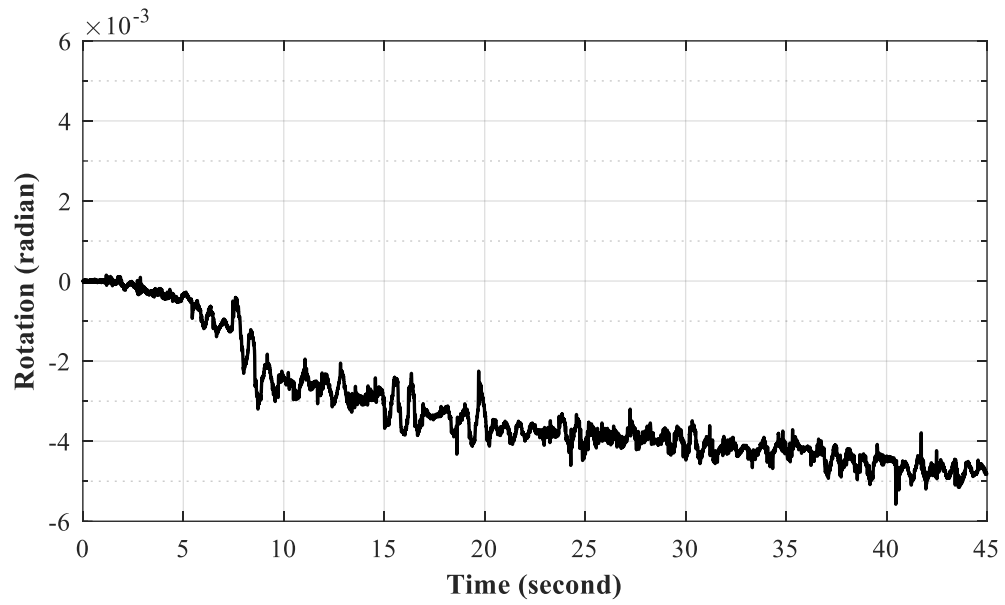


Figure A-26: Time history of suction bucket rotation for test WN2

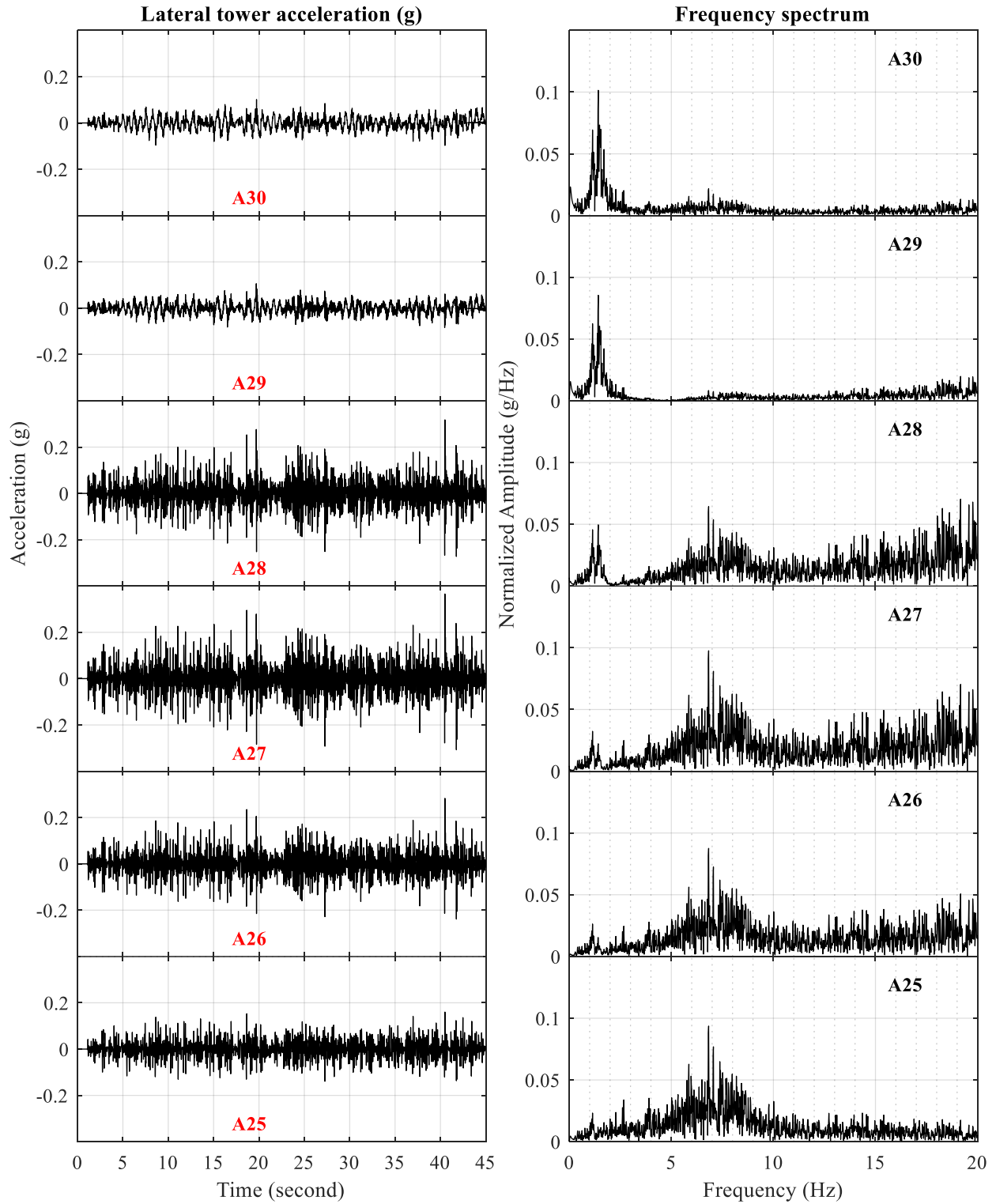


Figure A-27: Time histories of lateral tower acceleration for test WN2

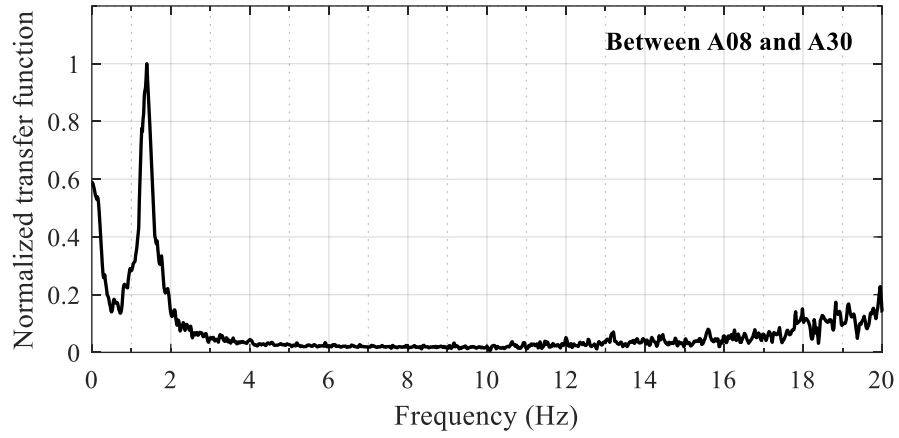


Figure A-28: Transfer function between acceleration records at the tower top (A30) and soil top near the suction bucket foundation (A08) for test WN2

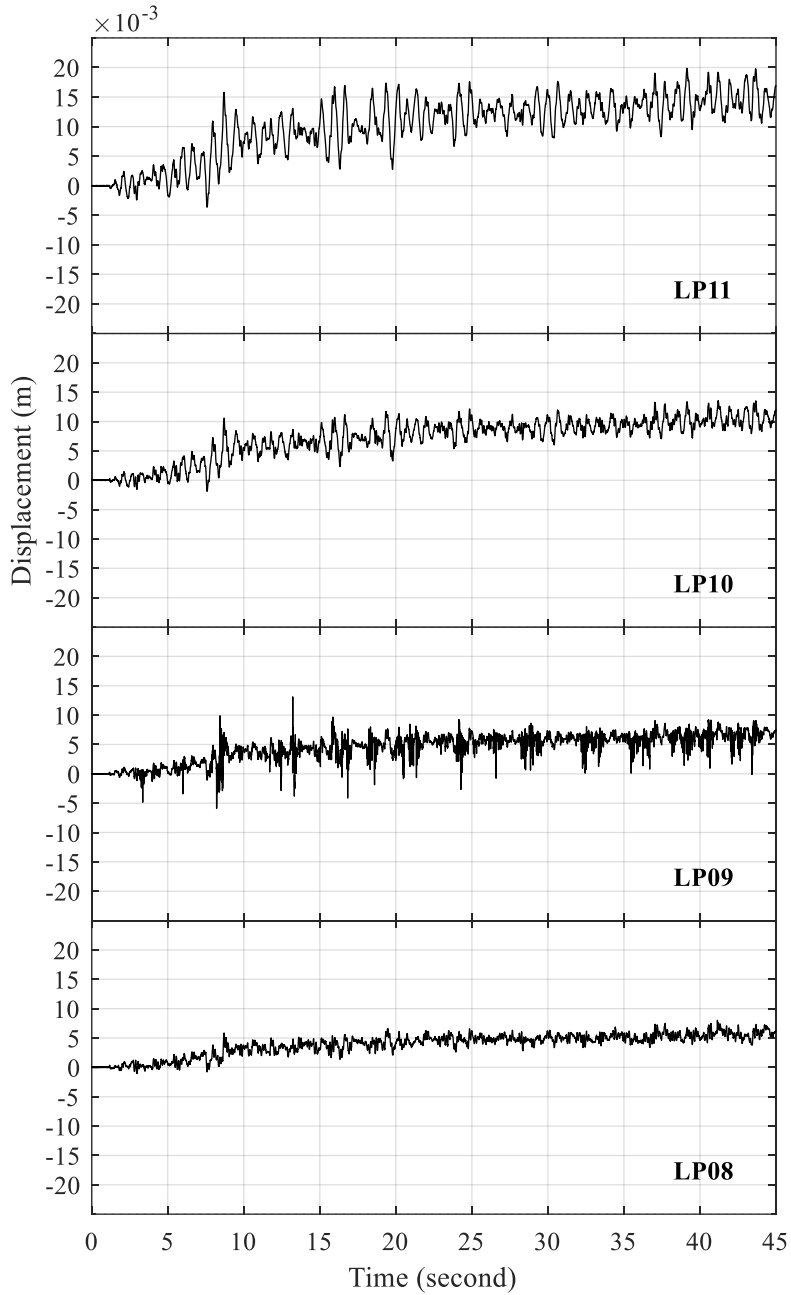


Figure A-29: Time histories of lateral tower displacement relative to lateral soil displacement at the foundation level (LP05) for test WN2

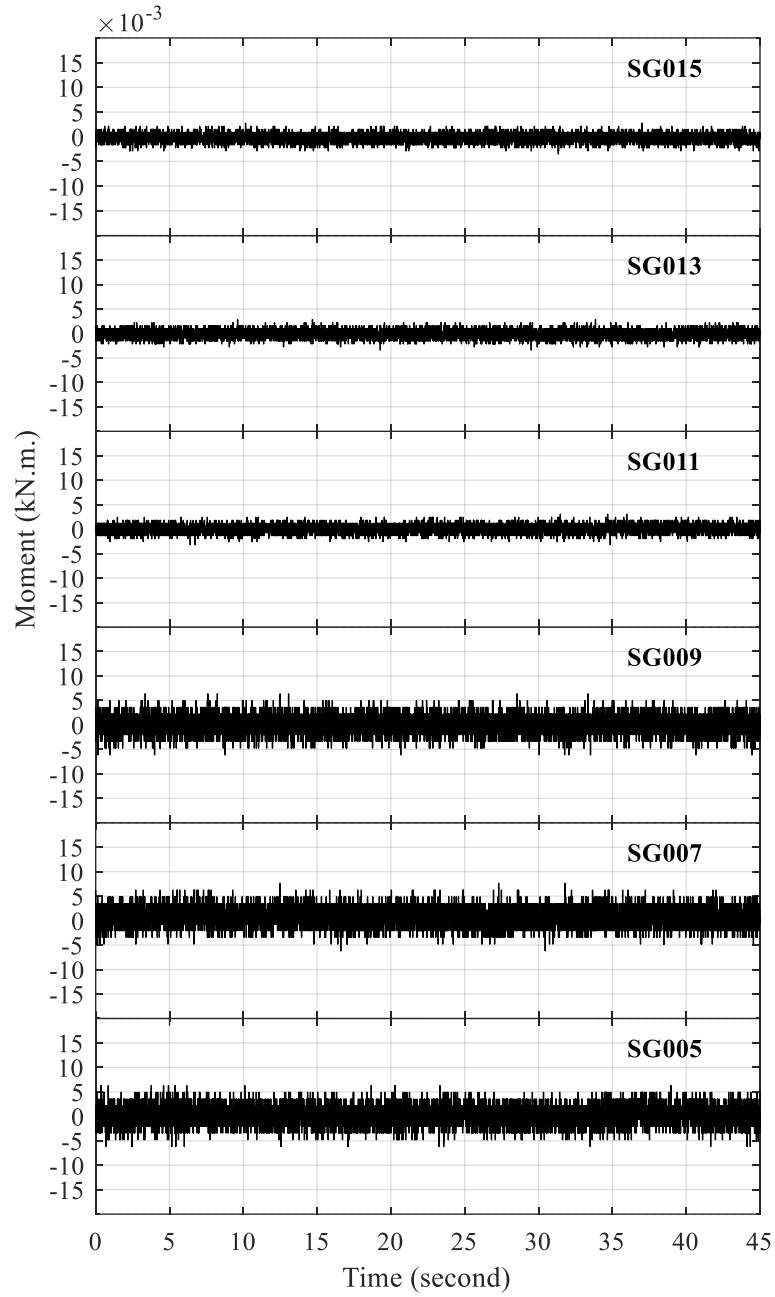


Figure A-30: Time histories of tower bending moment for test WN2

## **APPENDIX B**

### **Bucket foundation wind turbine shake table testing results**

This appendix includes results of shake table tests conducted on the bucket foundation wind turbine model using the harmonic excitations and scaled earthquake record excitations described in Table 3-4. Results of test H1 to H10 as well as T1 to T3 are presented as time histories of the following records:

- Acceleration of shake table input excitation,
- Lateral soil accelerations,
- Lateral soil displacements,
- Soil excess pore water pressures,
- Excess pore water pressure around bucket foundation,
- Vertical displacement of bucket foundation,
- Lateral accelerations of wind turbine tower,
- Tower lateral displacement, and
- Tower bending moments.

The contents of this appendix are directly related to Chapter 3 and Chapter 4.

# B.1 Test H1

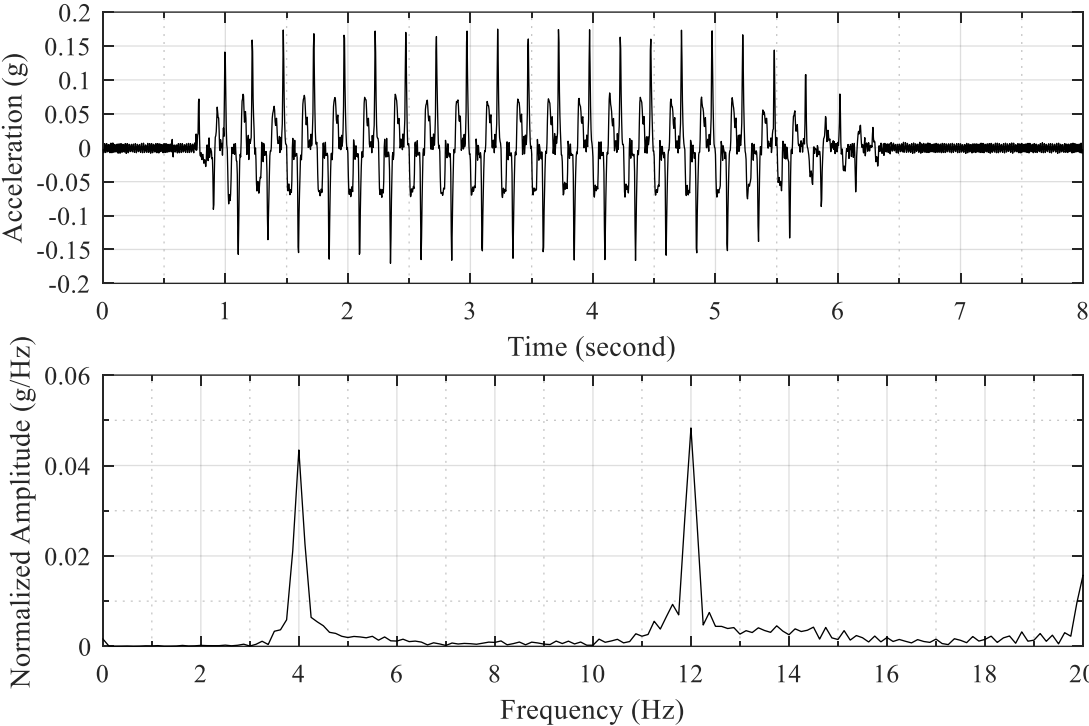


Figure B-1: Acceleration time history of shake table input excitation and the corresponding frequency spectrum for test H1

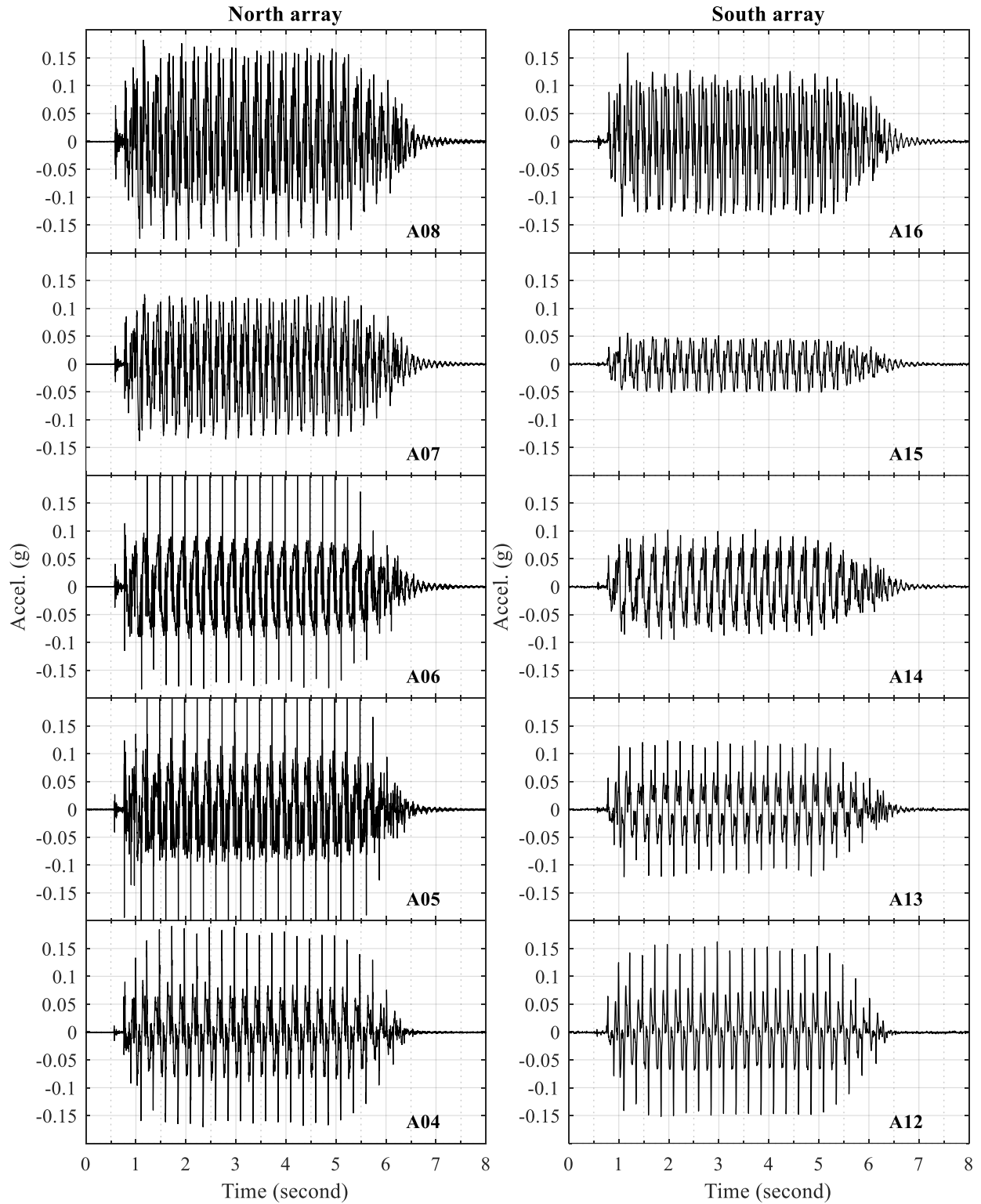


Figure B-2: Time histories of lateral soil acceleration in north and south arrays for test H1



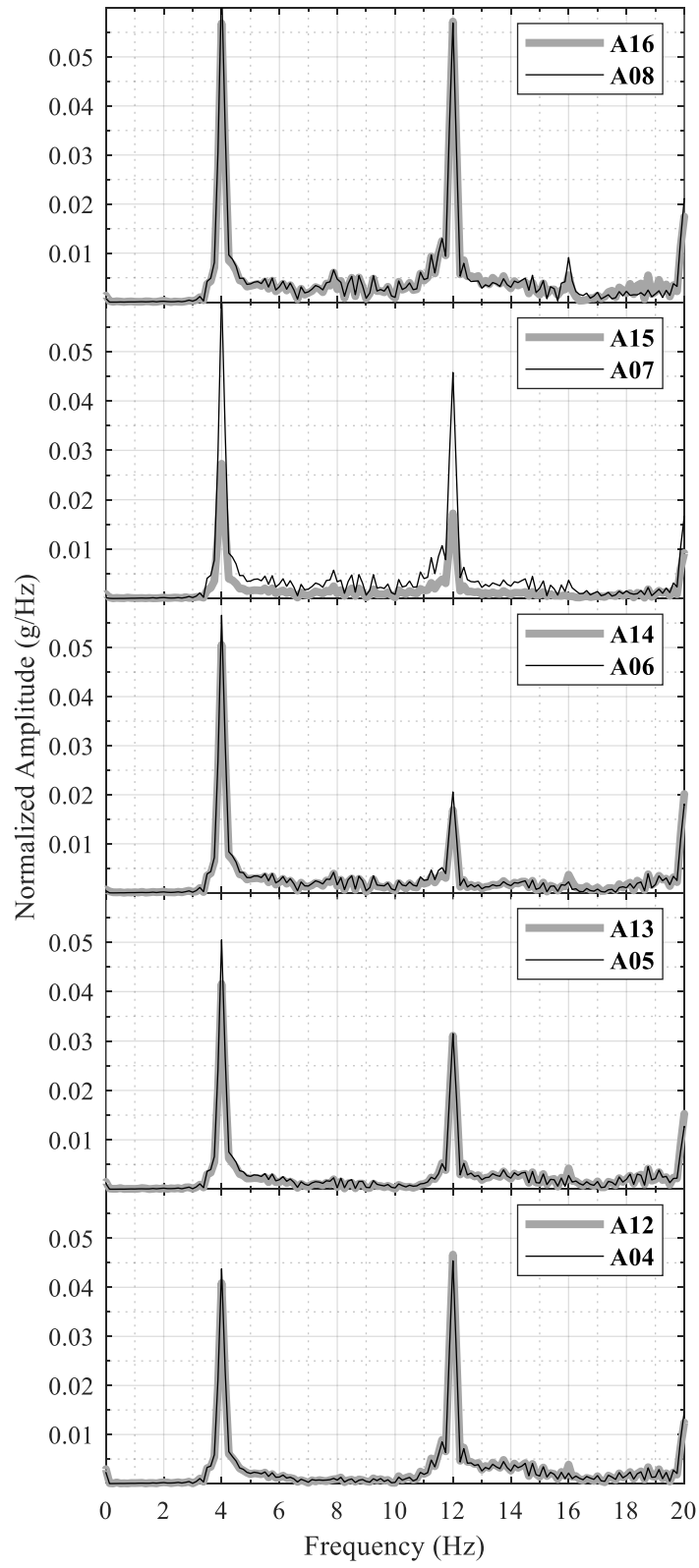


Figure B-3: Frequency spectra of lateral soil acceleration in north and south arrays for test H1

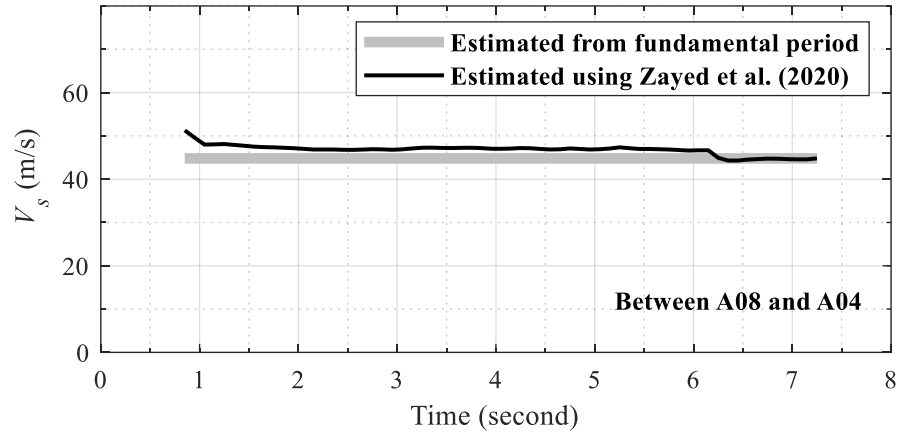


Figure B-4: Change in soil  $V_s$  with time during test H1

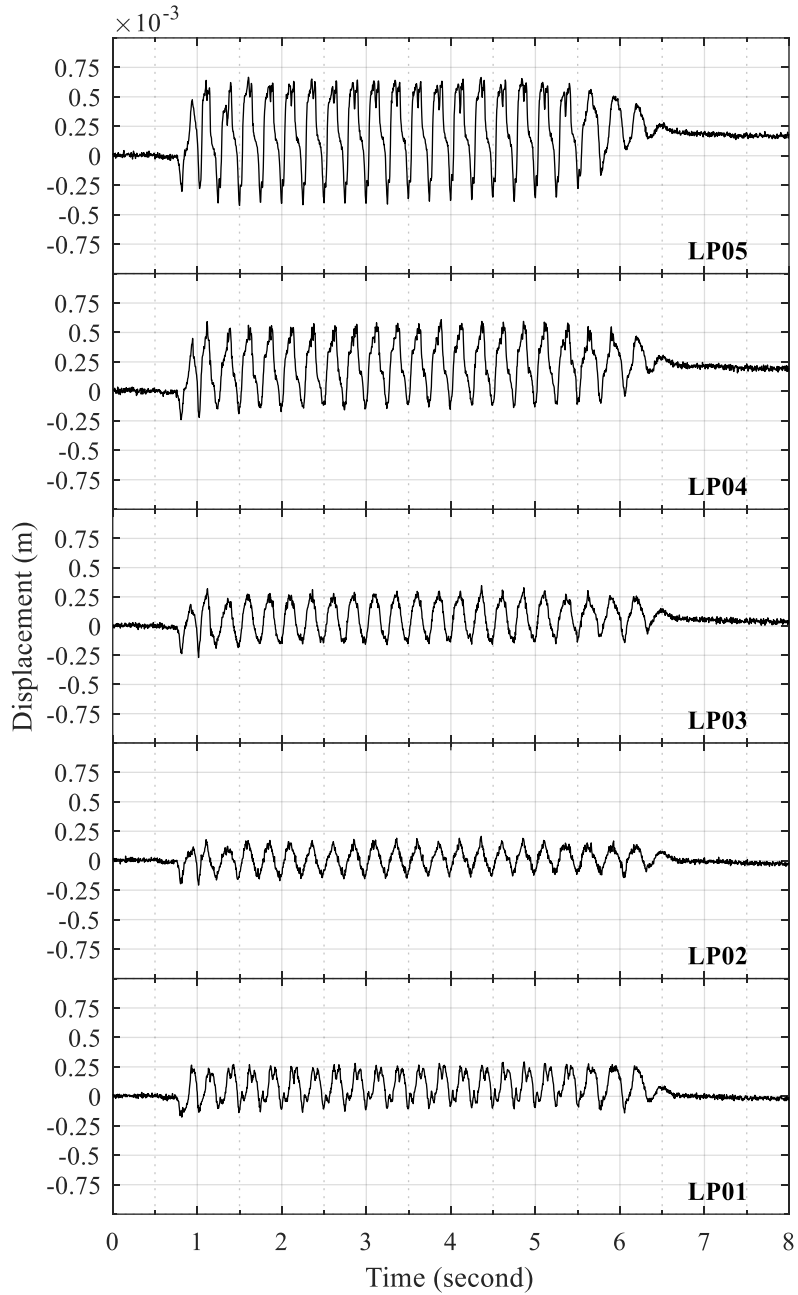


Figure B-5: Time histories of lateral soil displacement relative to laminar container base for test H1

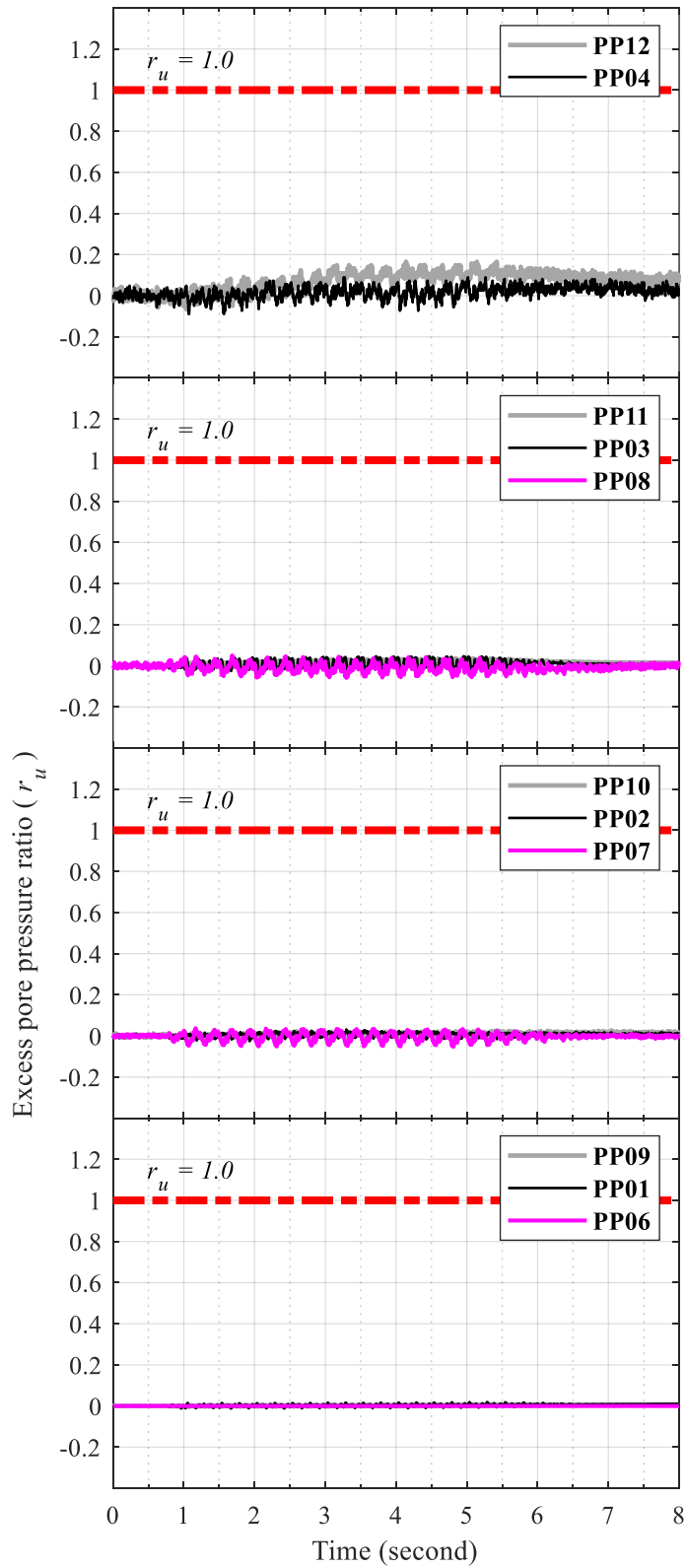


Figure B-6: Time histories of soil excess pore pressure for test H1

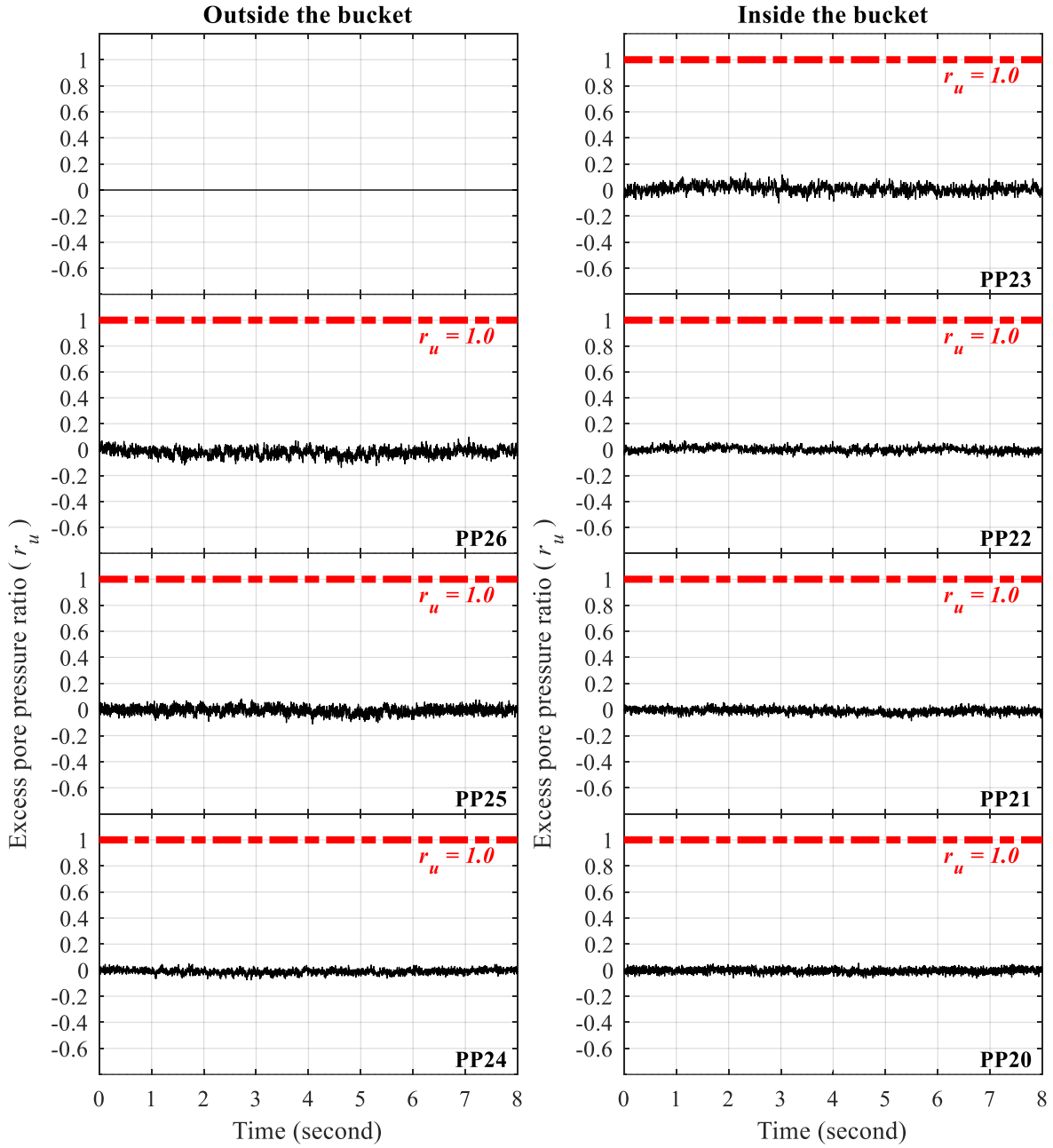


Figure B-7: Time histories of excess pore pressure at north edge of suction bucket for test H1

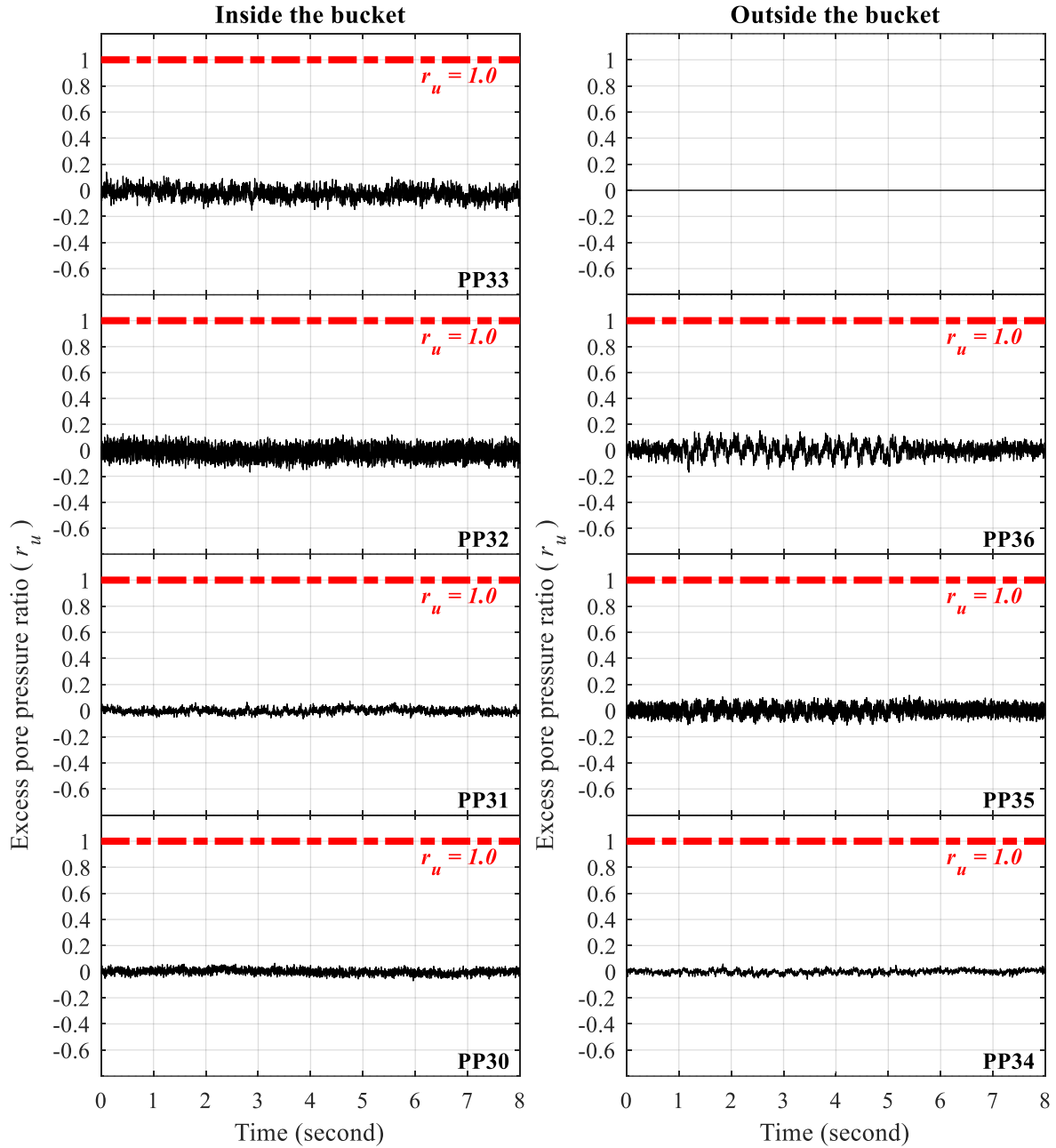


Figure B-8: Time histories of excess pore pressure at south edge of suction bucket for test H1

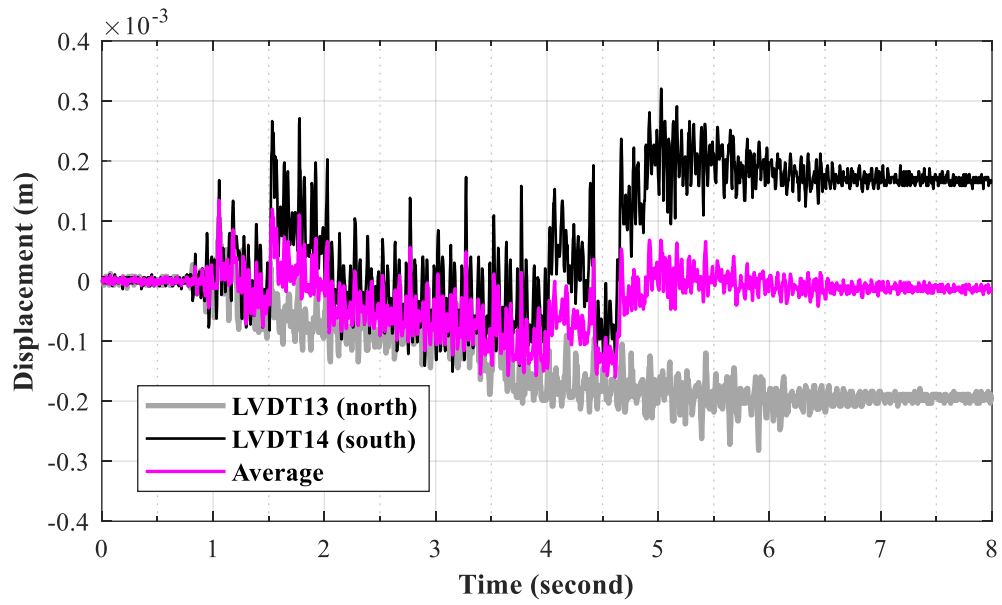


Figure B-9: Time histories of vertical bucket displacement for test H1

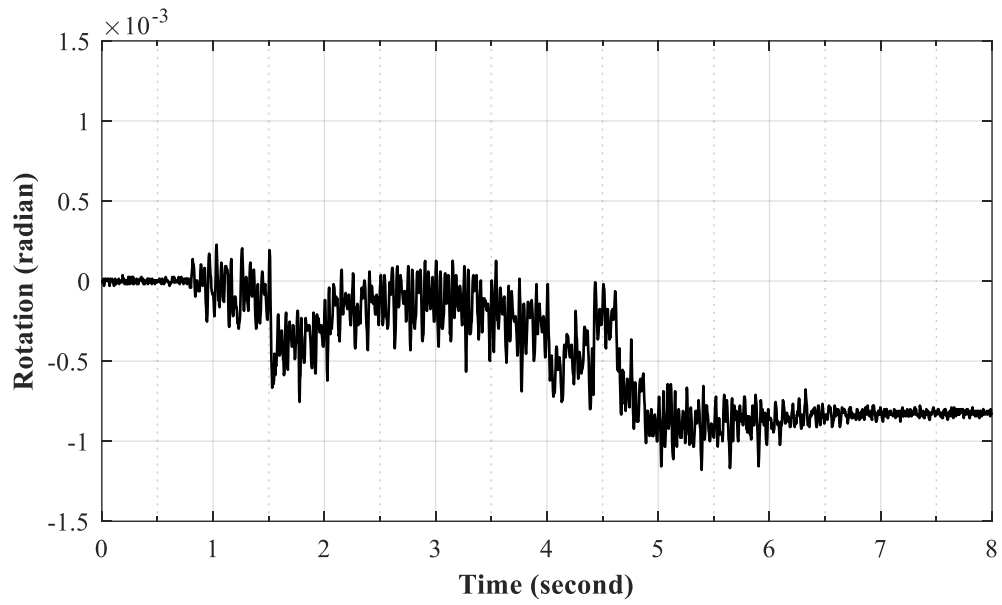


Figure B-10: Time history of suction bucket rotation for test H1



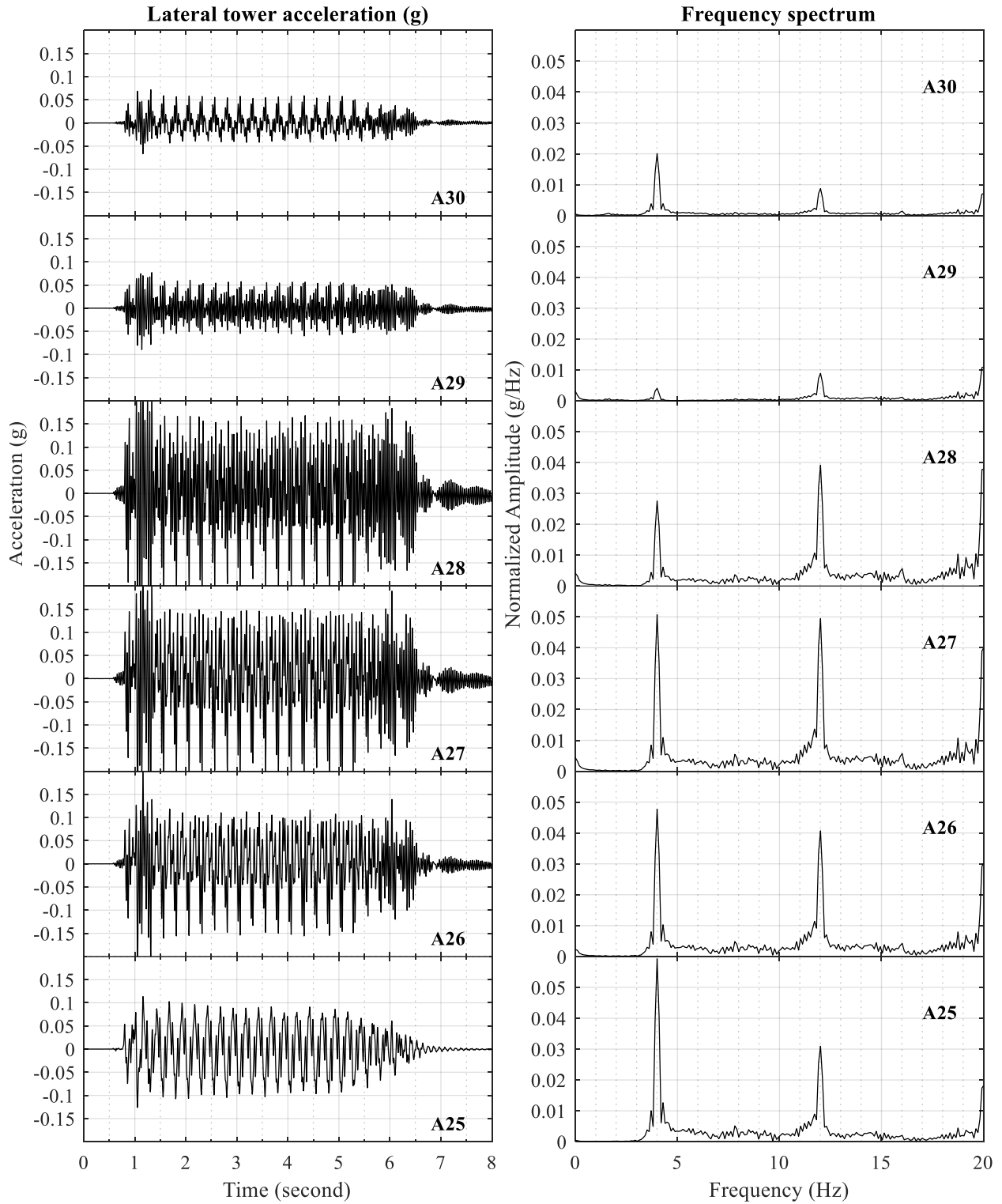


Figure B-11: Time histories of lateral tower acceleration for test H1

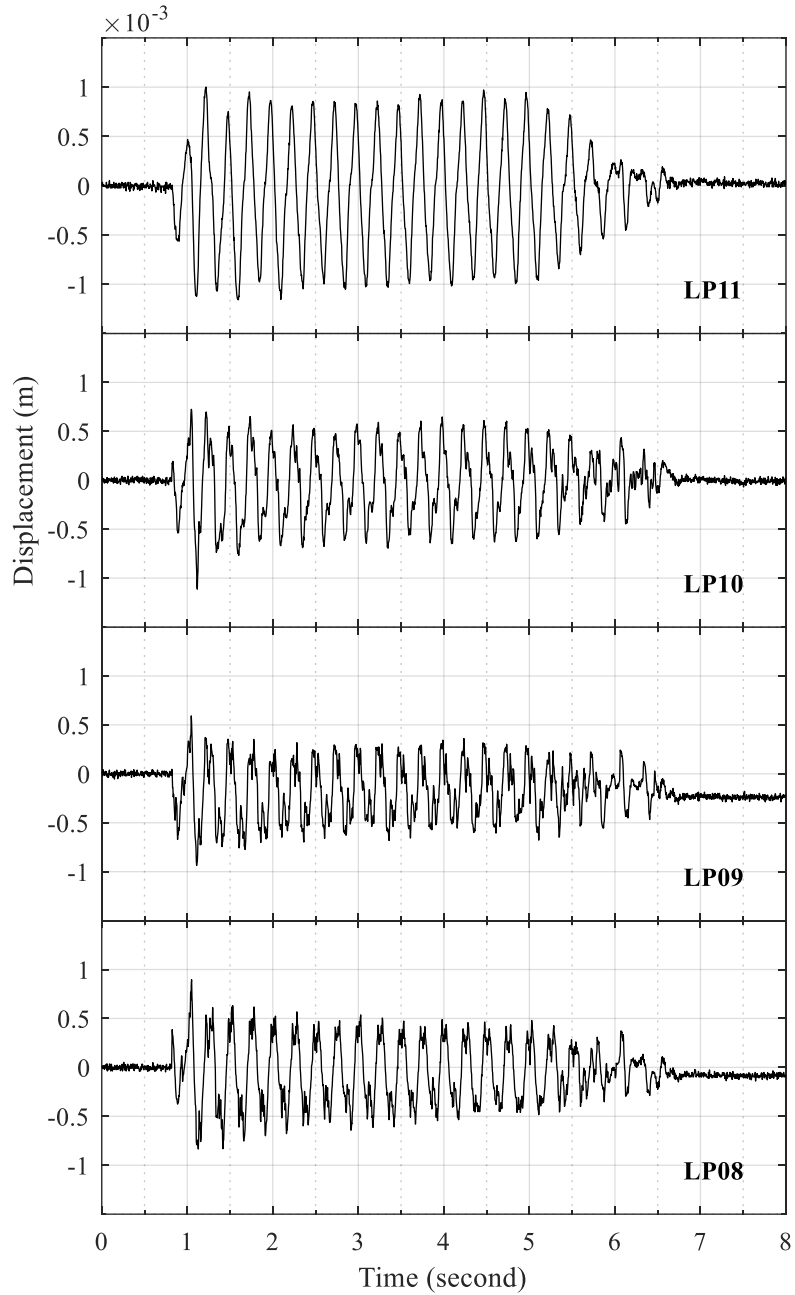


Figure B-12: Time histories of lateral tower displacement relative to lateral soil displacement at the foundation level (LP05) for test H1

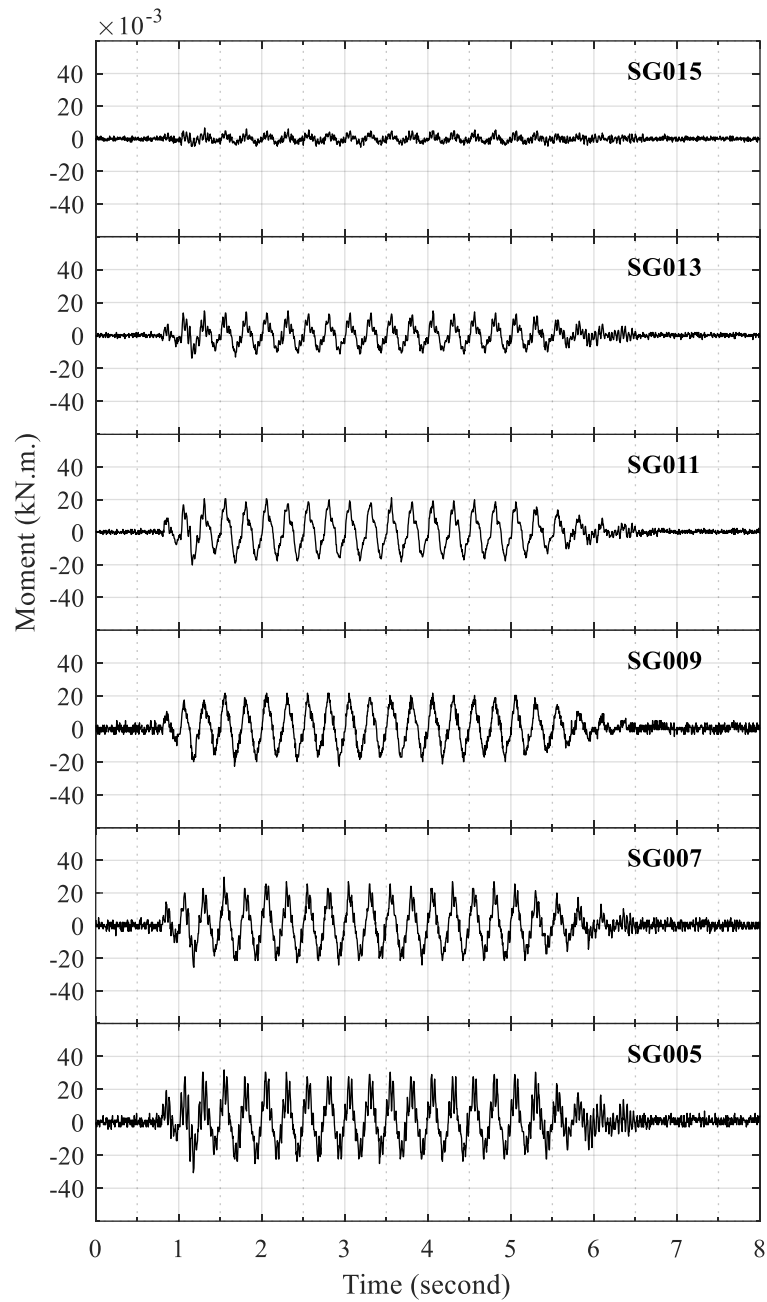


Figure B-13: Time histories of tower bending moment for test H1

## B.2 Test H2

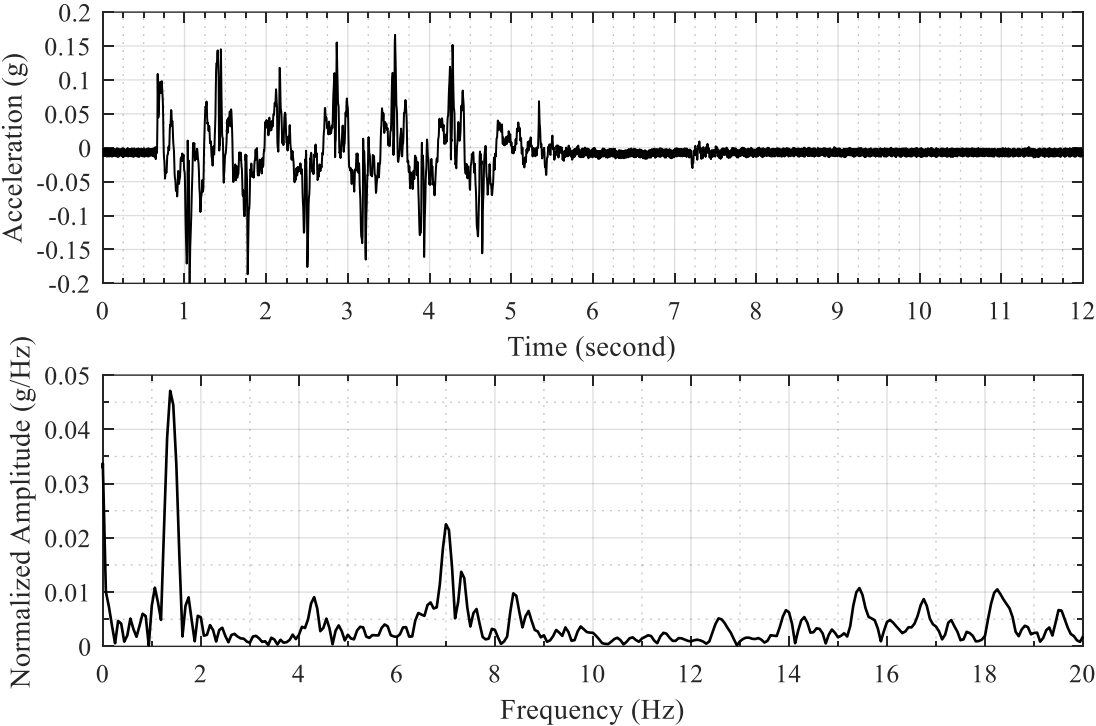


Figure B-14: Acceleration time history of shake table input excitation and the corresponding frequency spectrum for test H2

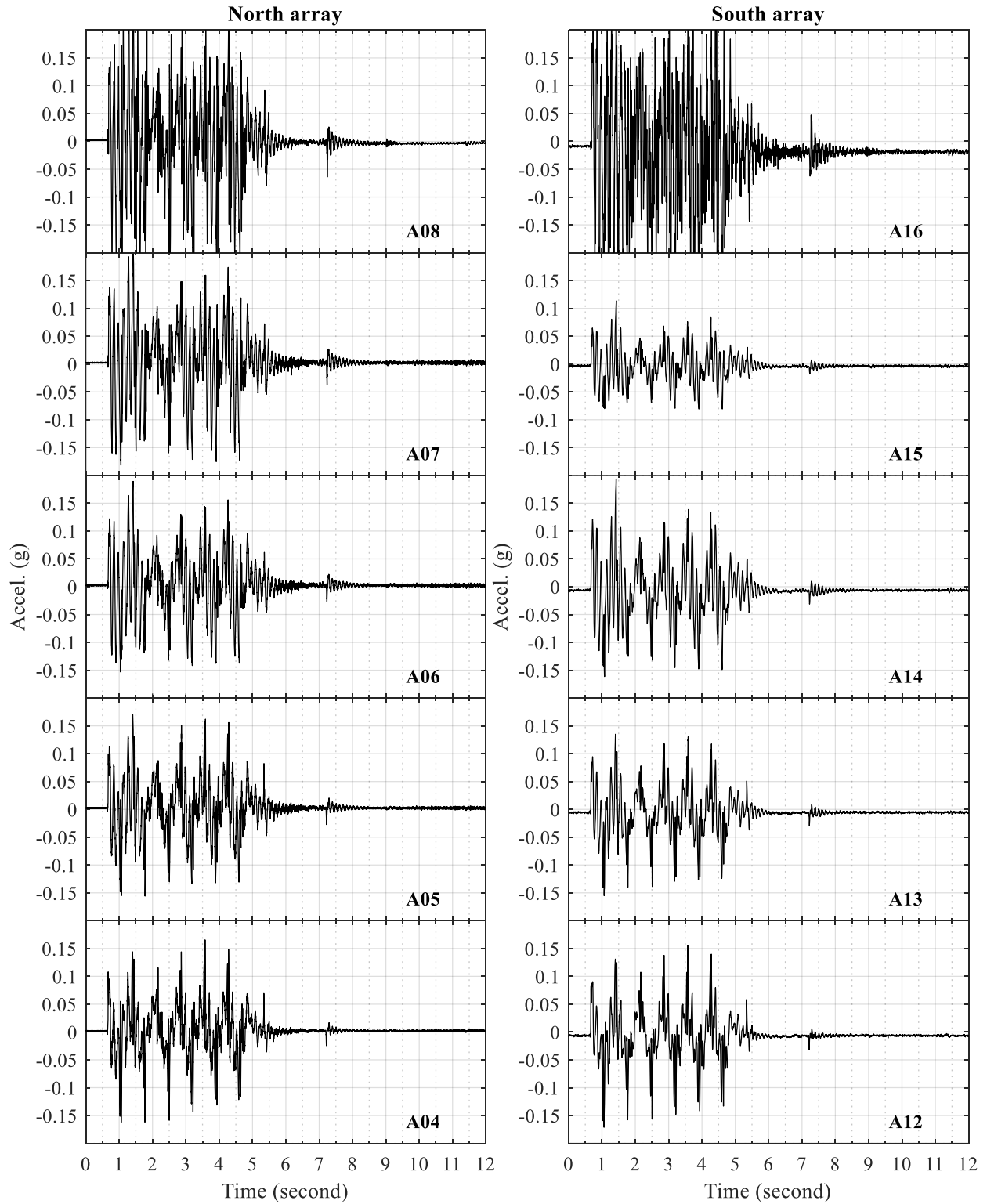


Figure B-15: Time histories of lateral soil acceleration in north and south arrays for test H2

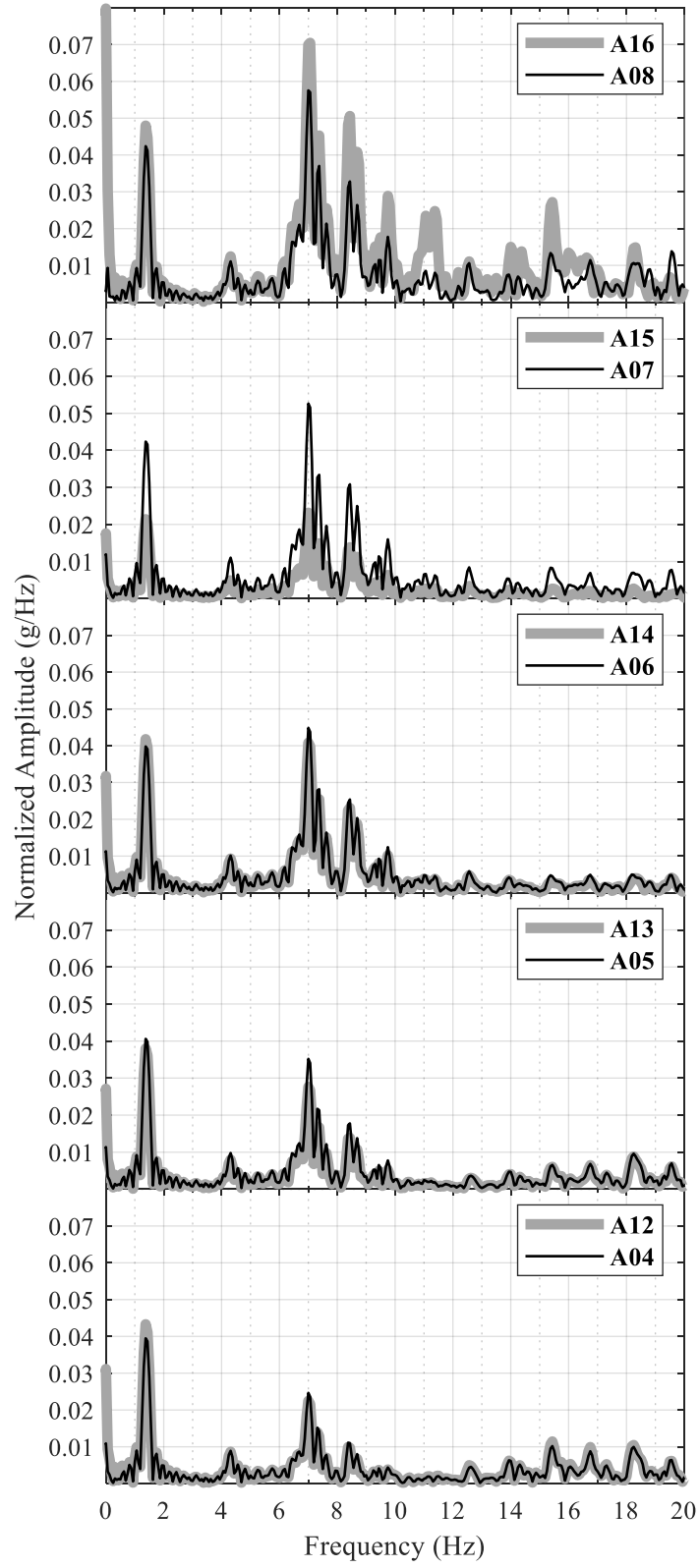


Figure B-16: Frequency spectra of lateral soil acceleration in north and south arrays for test H2

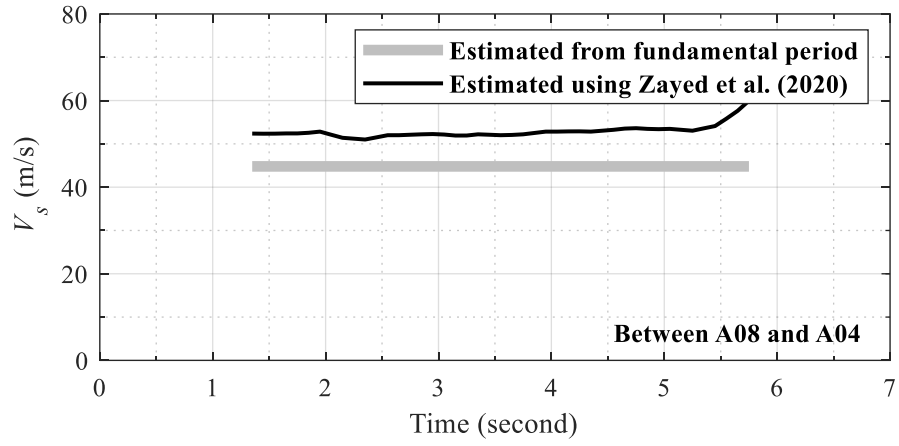


Figure B-17: Change in soil  $V_s$  with time during test H2

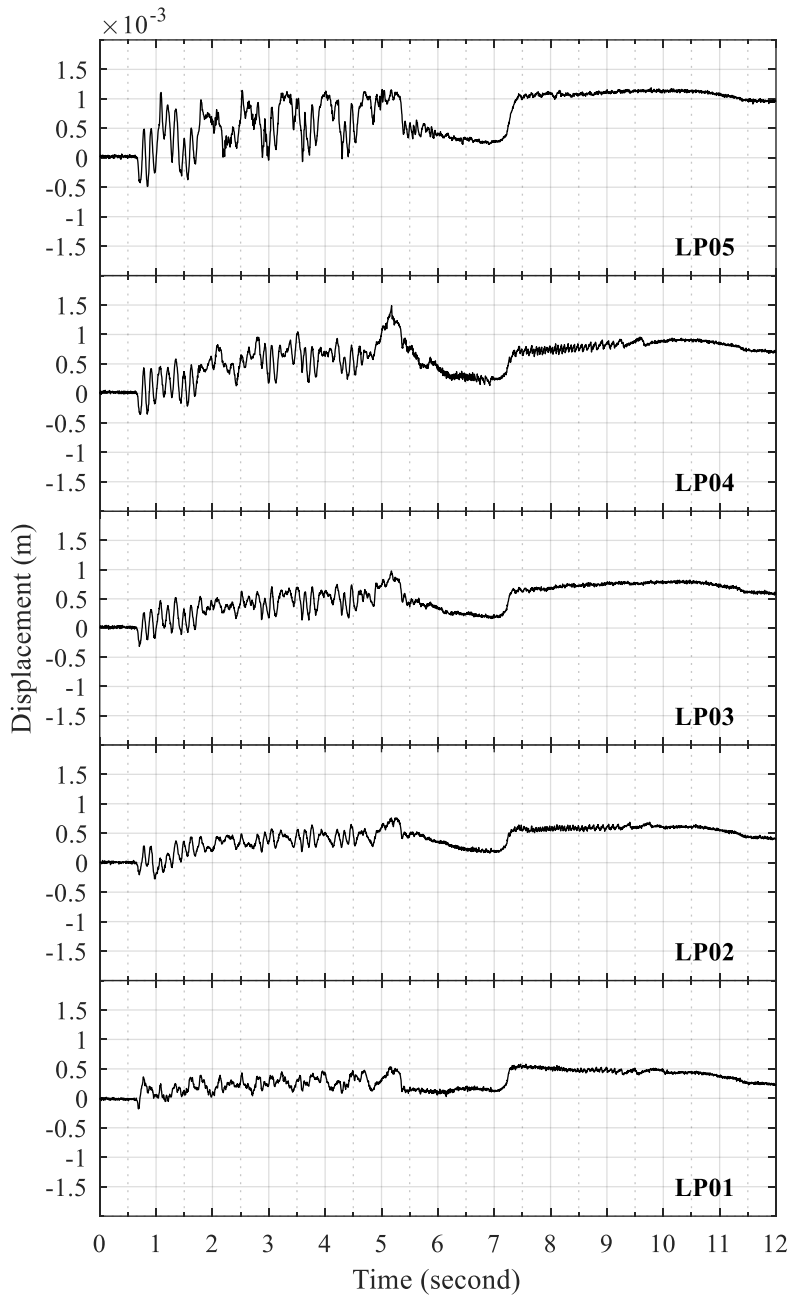


Figure B-18: Time histories of lateral soil displacement relative to laminar container base for test H2



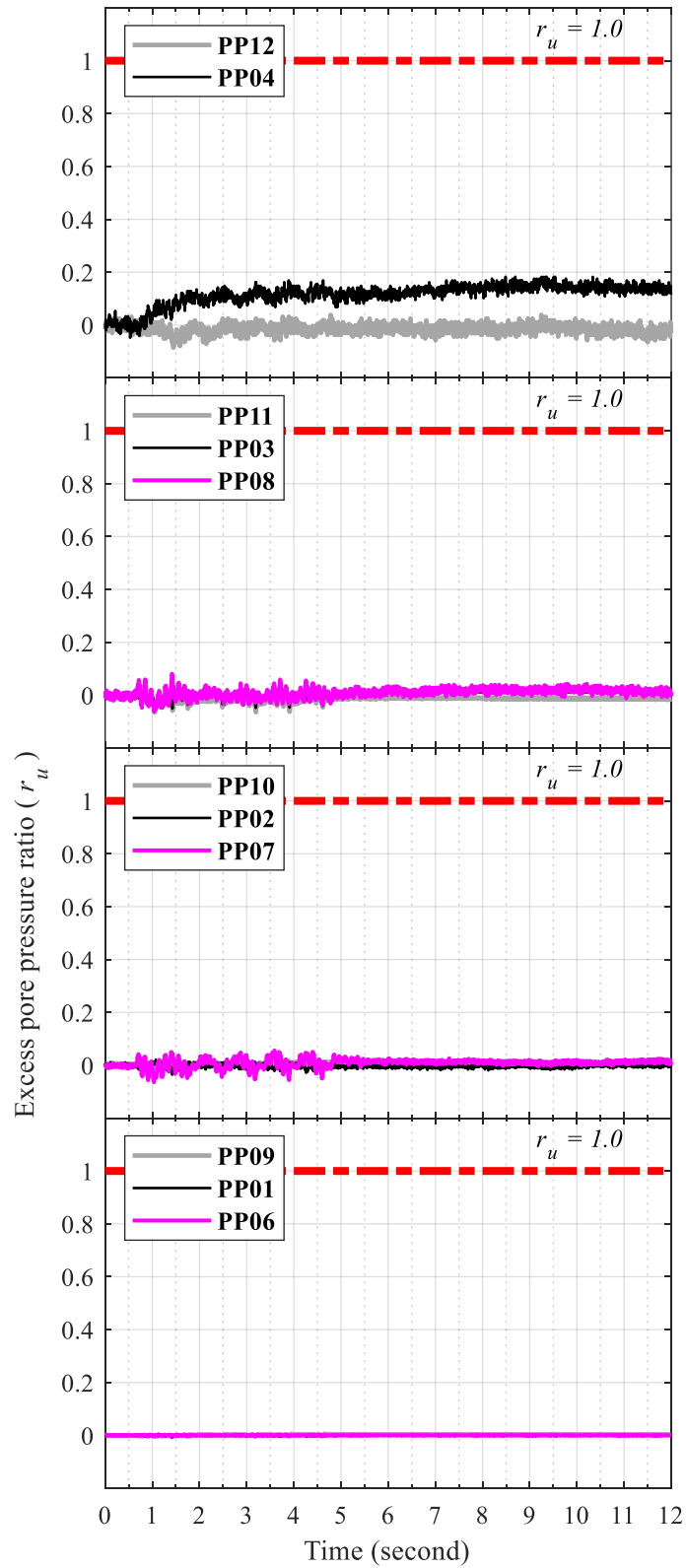


Figure B-19: Time histories of soil excess pore pressure for test H2

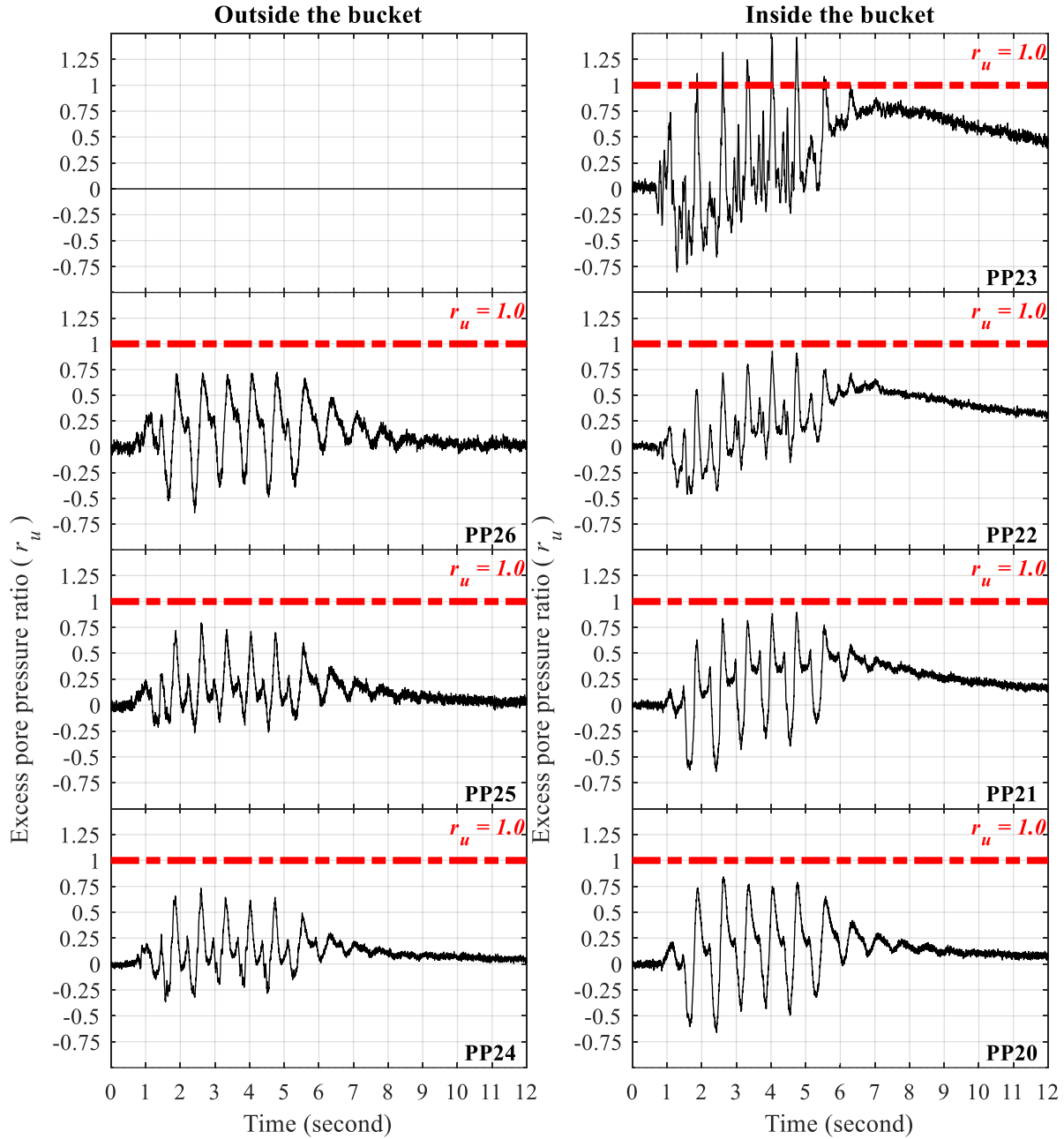


Figure B-20: Time histories of excess pore pressure at north edge of suction bucket for test H2

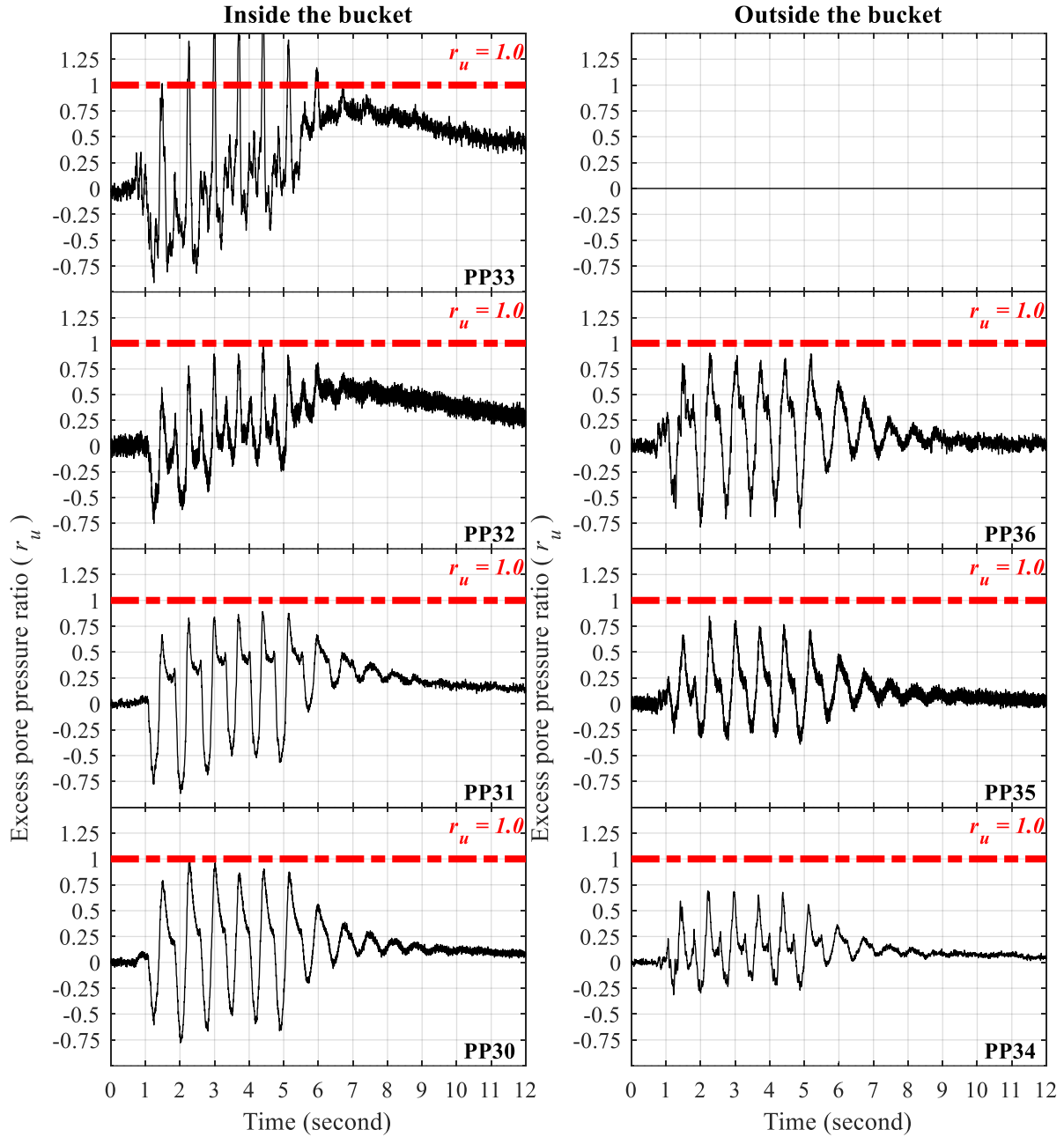


Figure B-21: Time histories of excess pore pressure at south edge of suction bucket for test H2

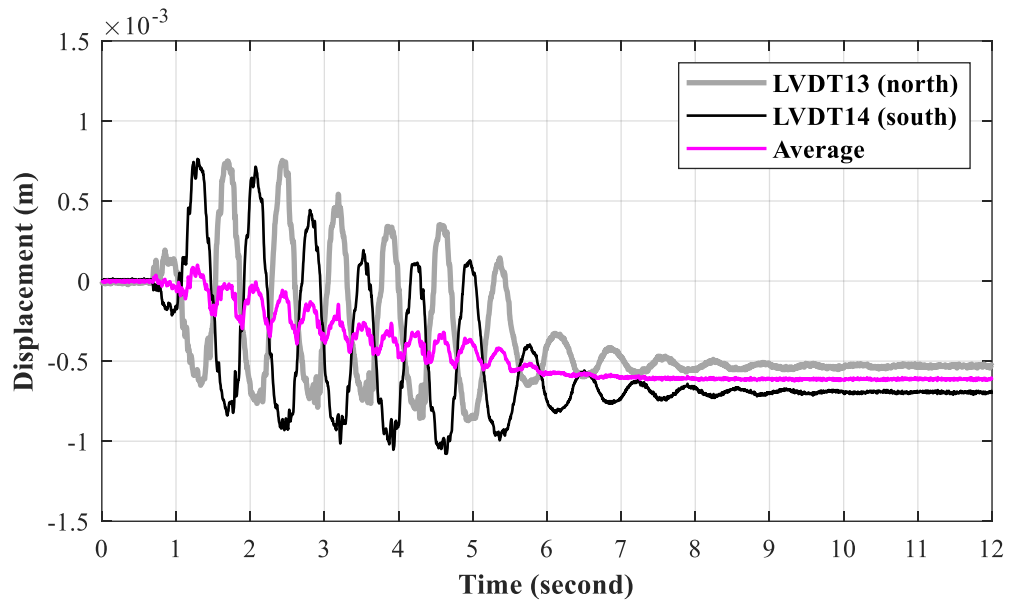


Figure B-22: Time histories of vertical bucket displacement for test H2

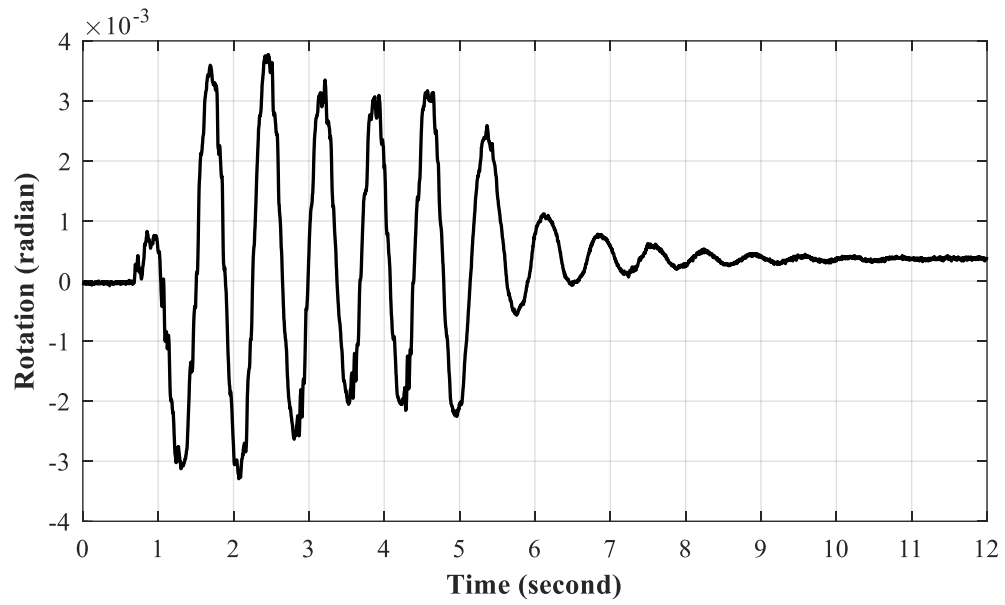


Figure B-23: Time history of suction bucket rotation for test H2

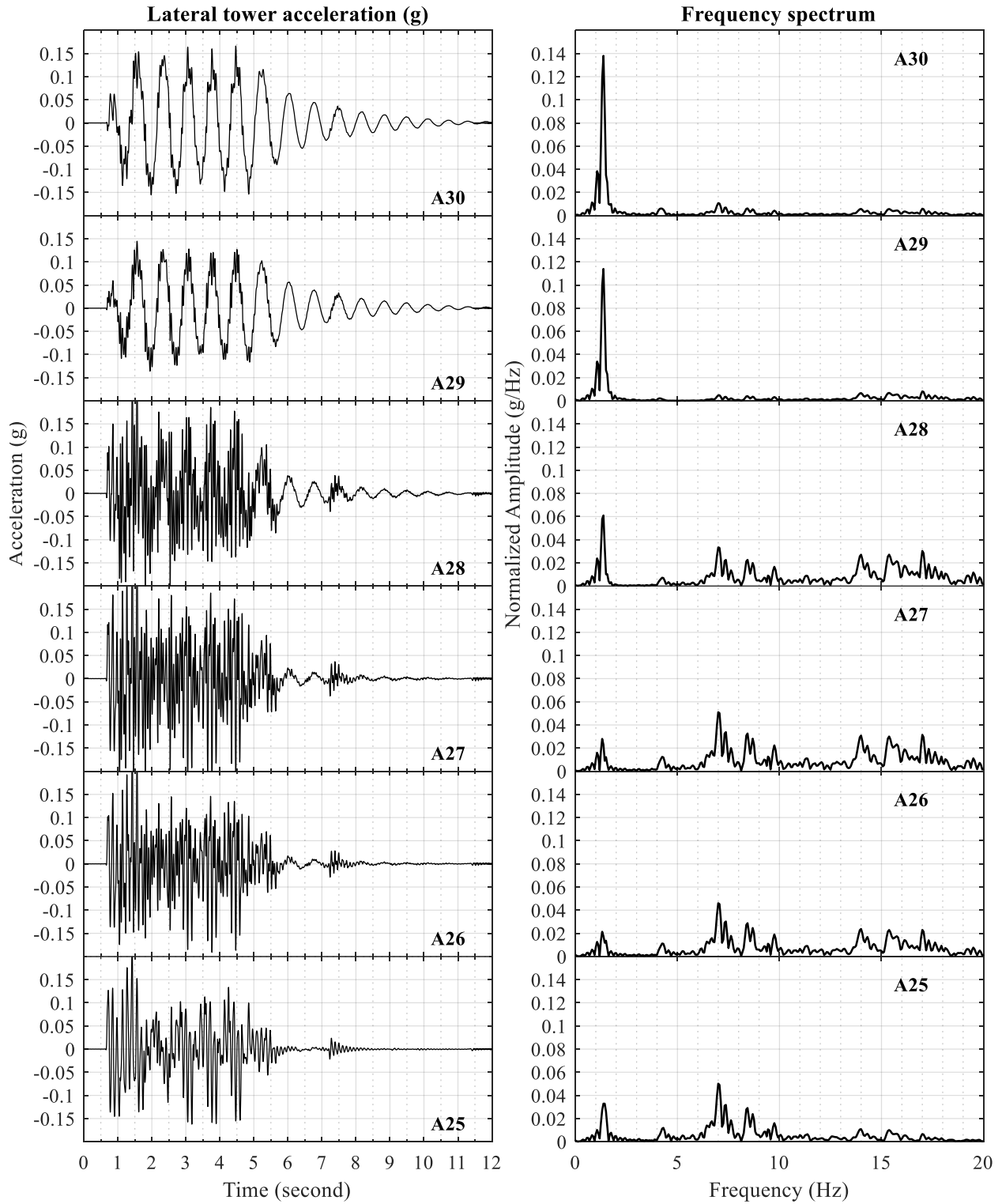


Figure B-24: Time histories of lateral tower acceleration for test H2

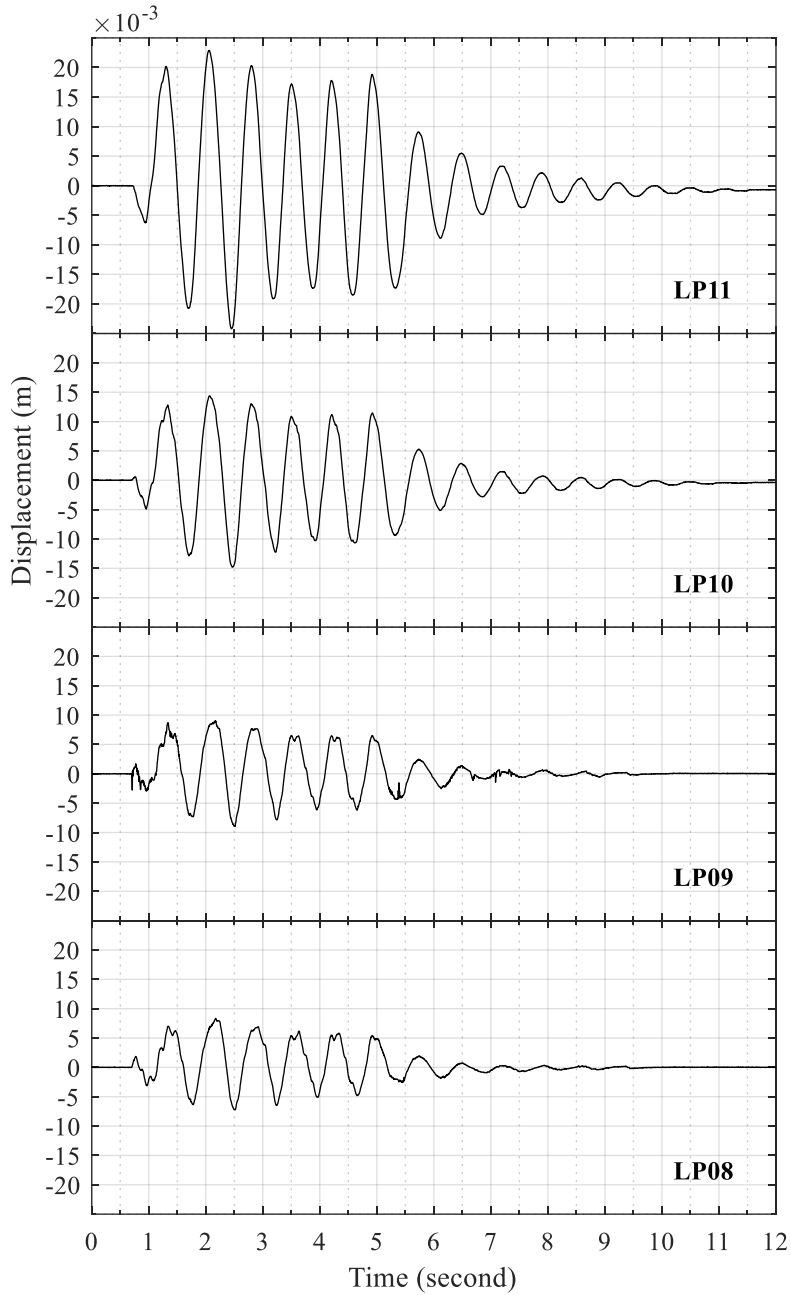


Figure B-25: Time histories of lateral tower displacement relative to lateral soil displacement at the foundation level (LP05) for test H2

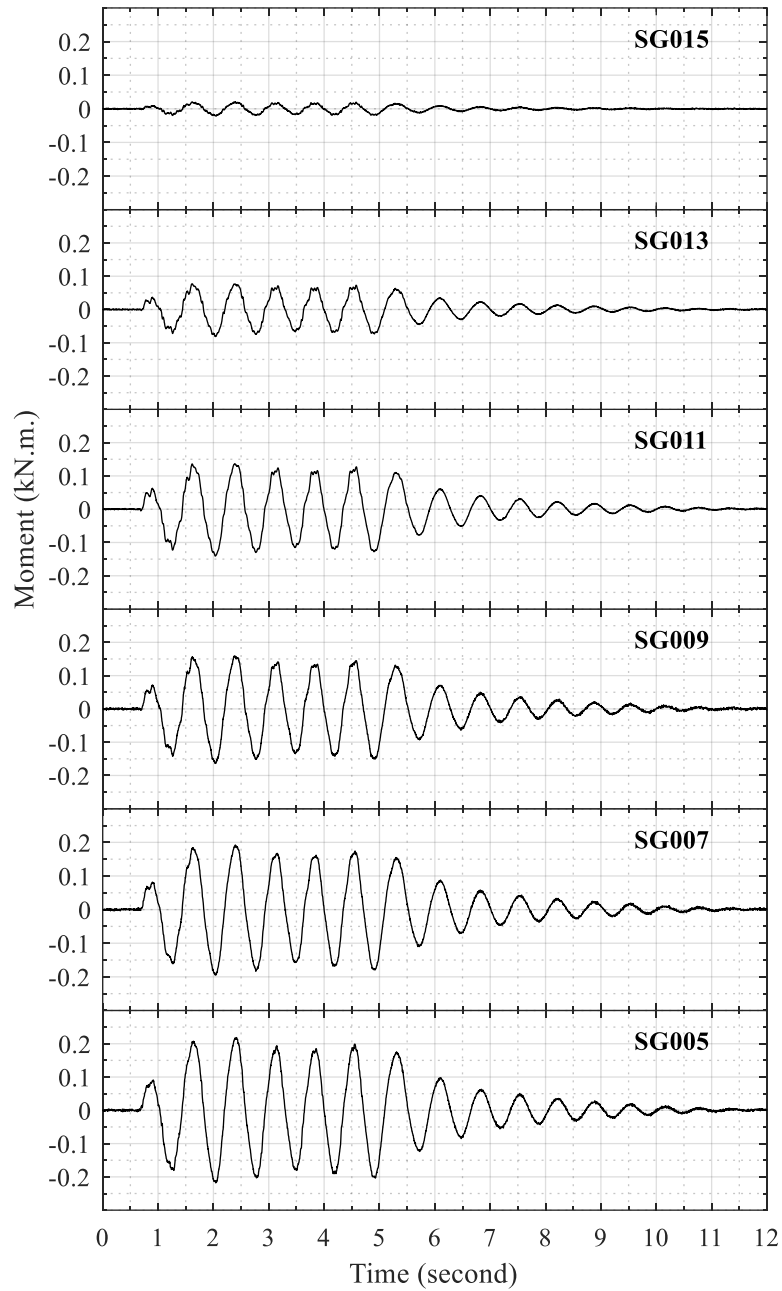


Figure B-26: Time histories of tower bending moment for test H2



### B.3 Test H3

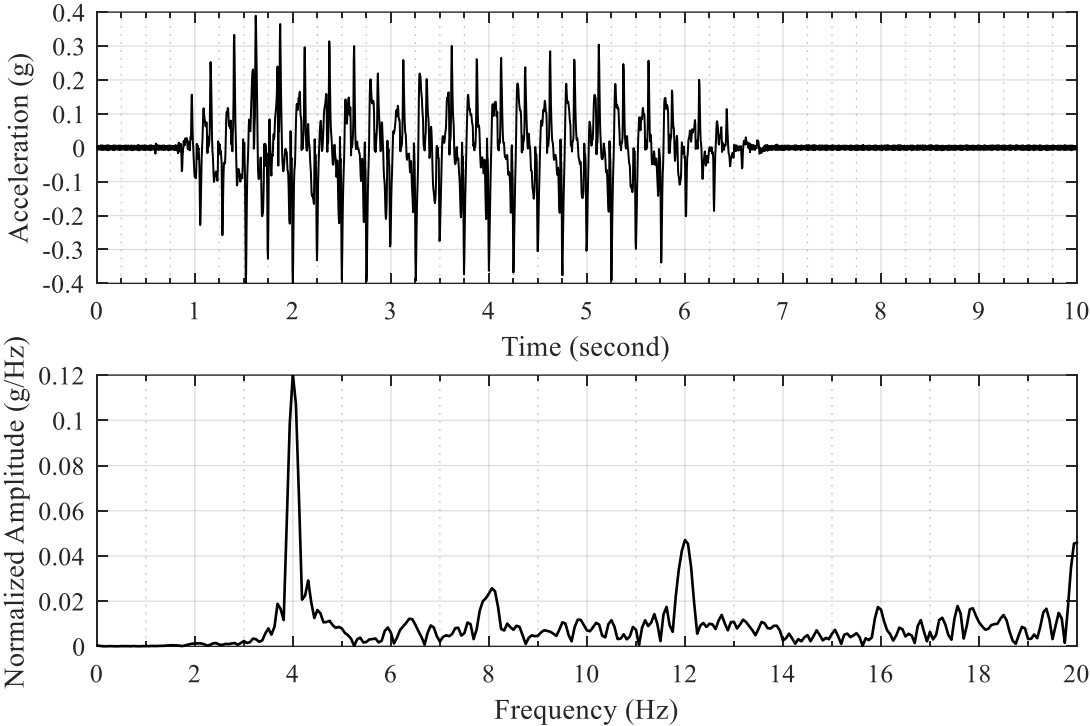


Figure B-27: Acceleration time history of shake table input excitation and the corresponding frequency spectrum for test H3

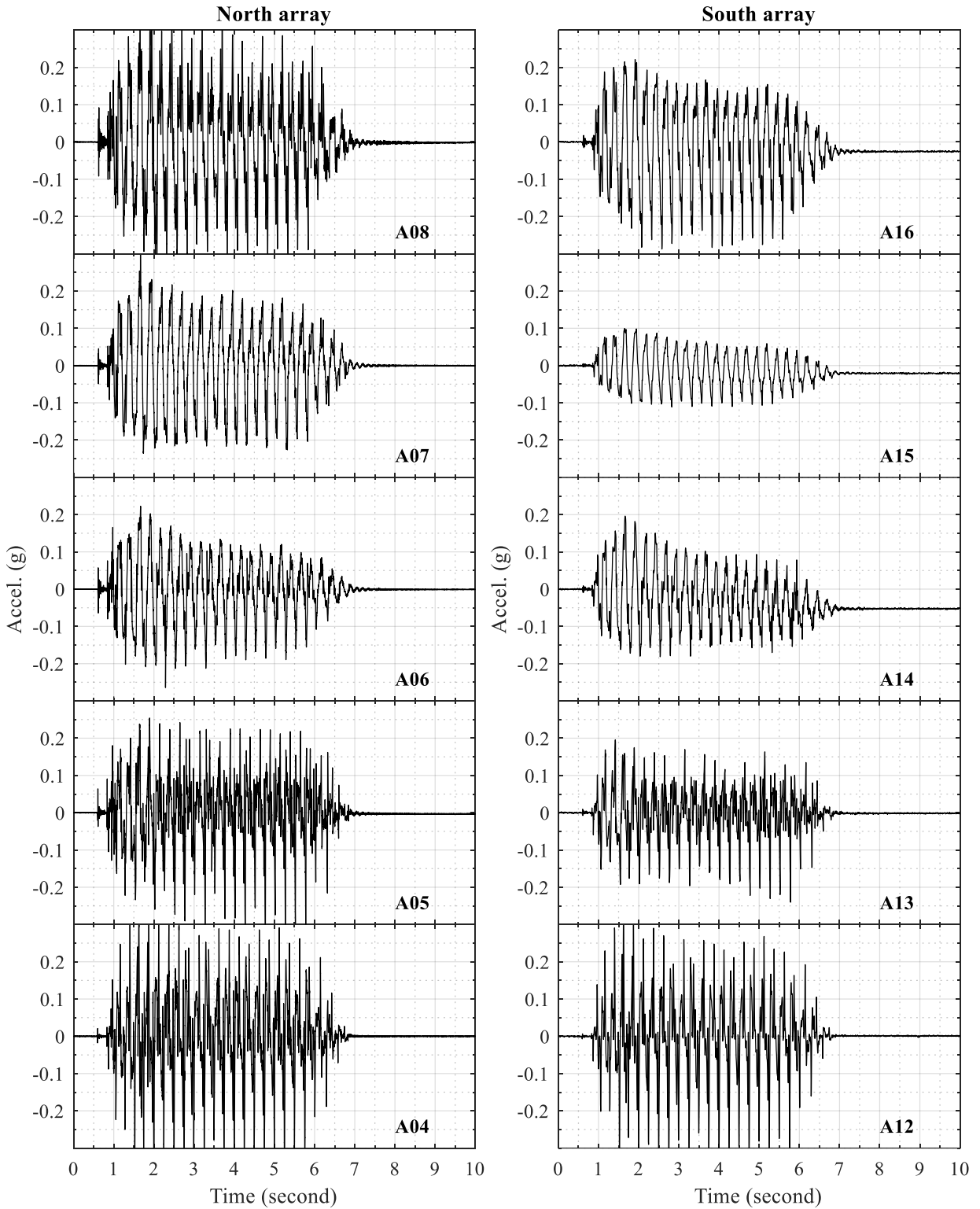


Figure B-28: Time histories of lateral soil acceleration in north and south arrays for test H3

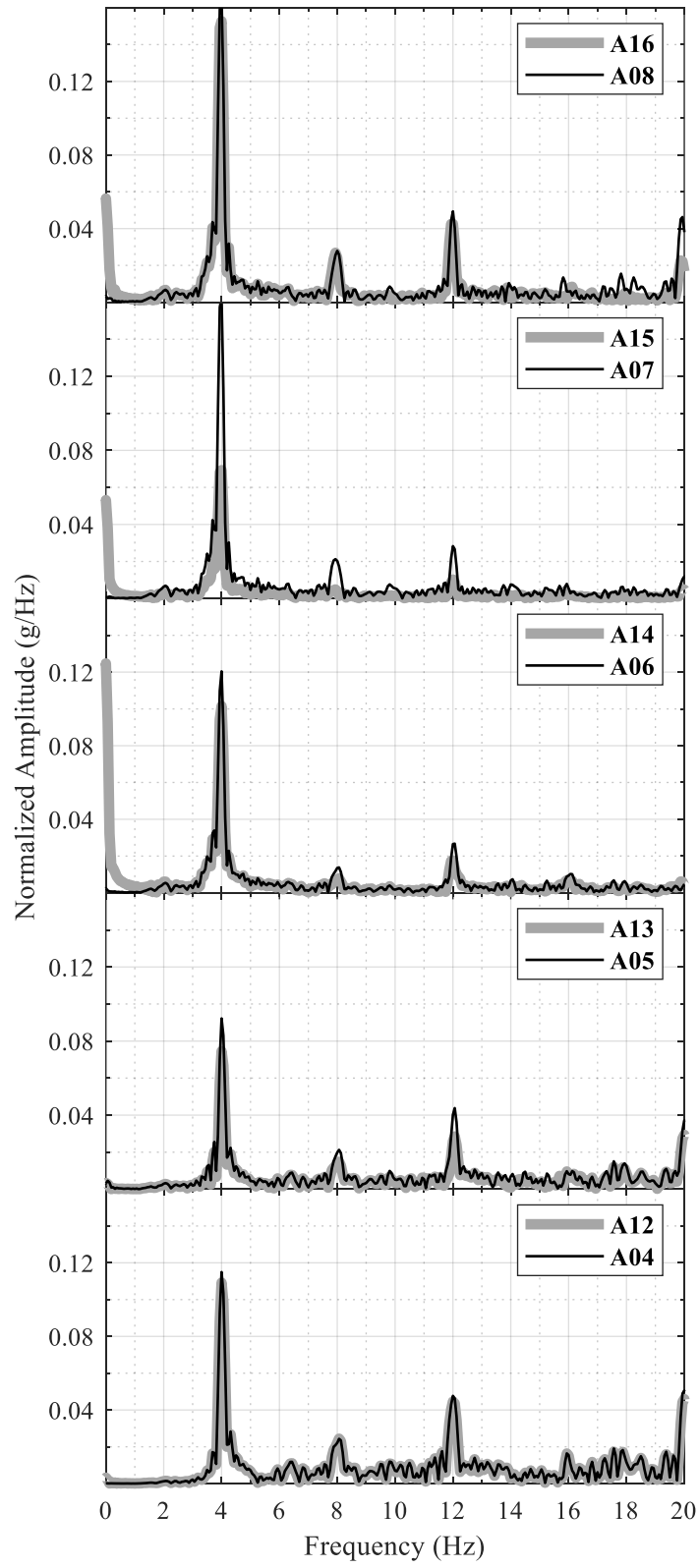


Figure B-29: Frequency spectra of lateral soil acceleration in north and south arrays for test H3

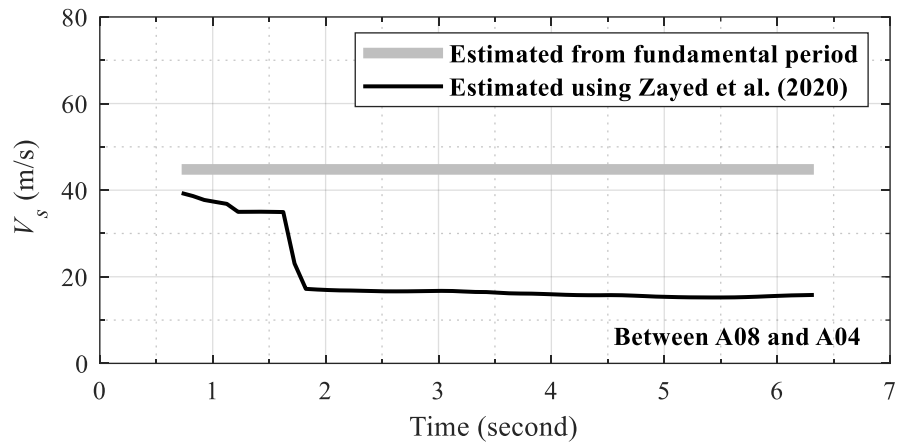


Figure B-30: Change in soil  $V_s$  with time during test H3

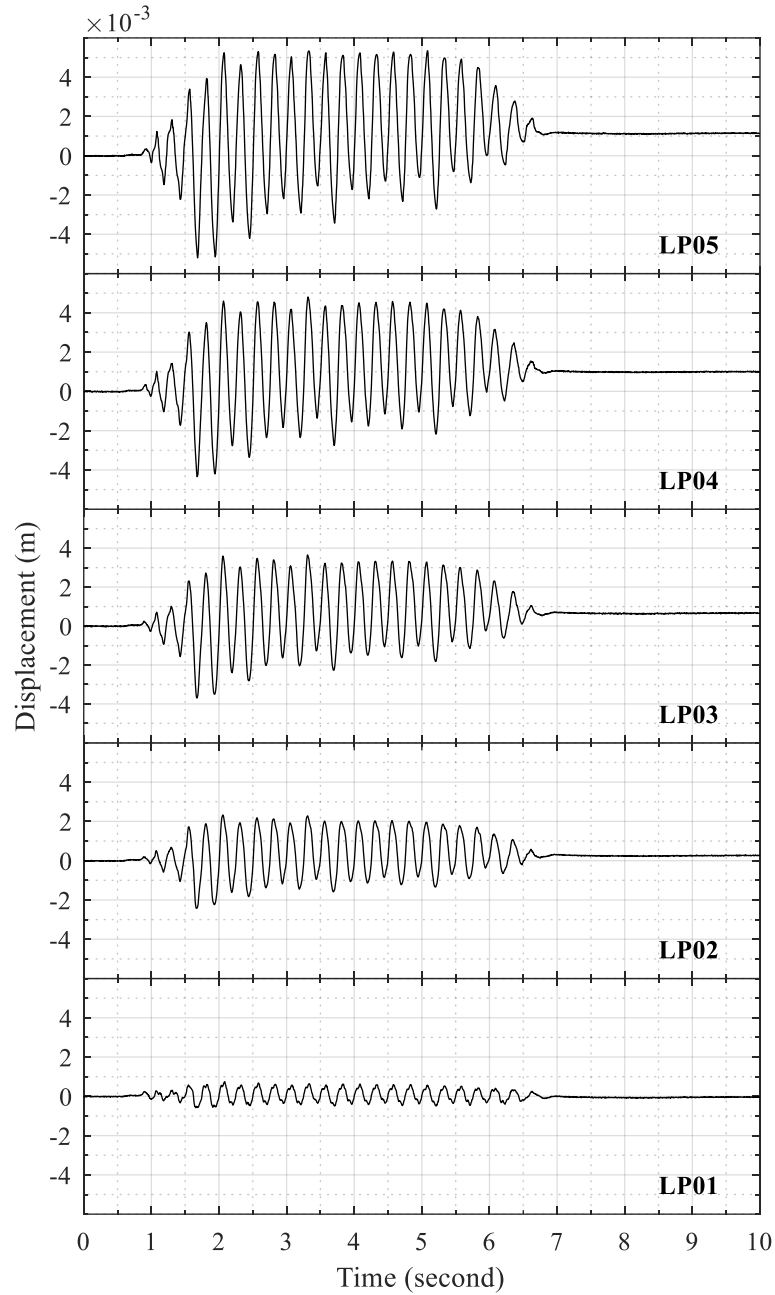


Figure B-31: Time histories of lateral soil displacement relative to laminar container base for test H3

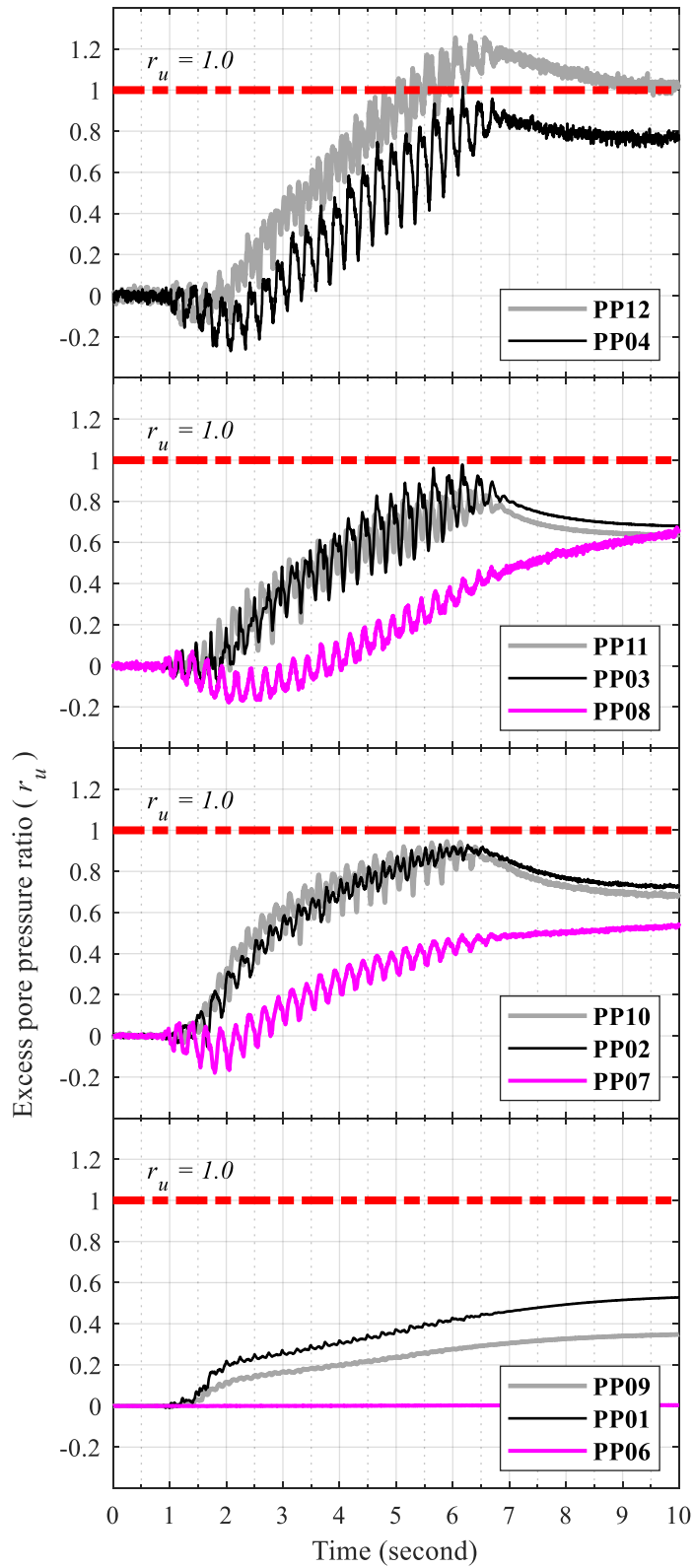


Figure B-32: Time histories of soil excess pore pressure for test H3

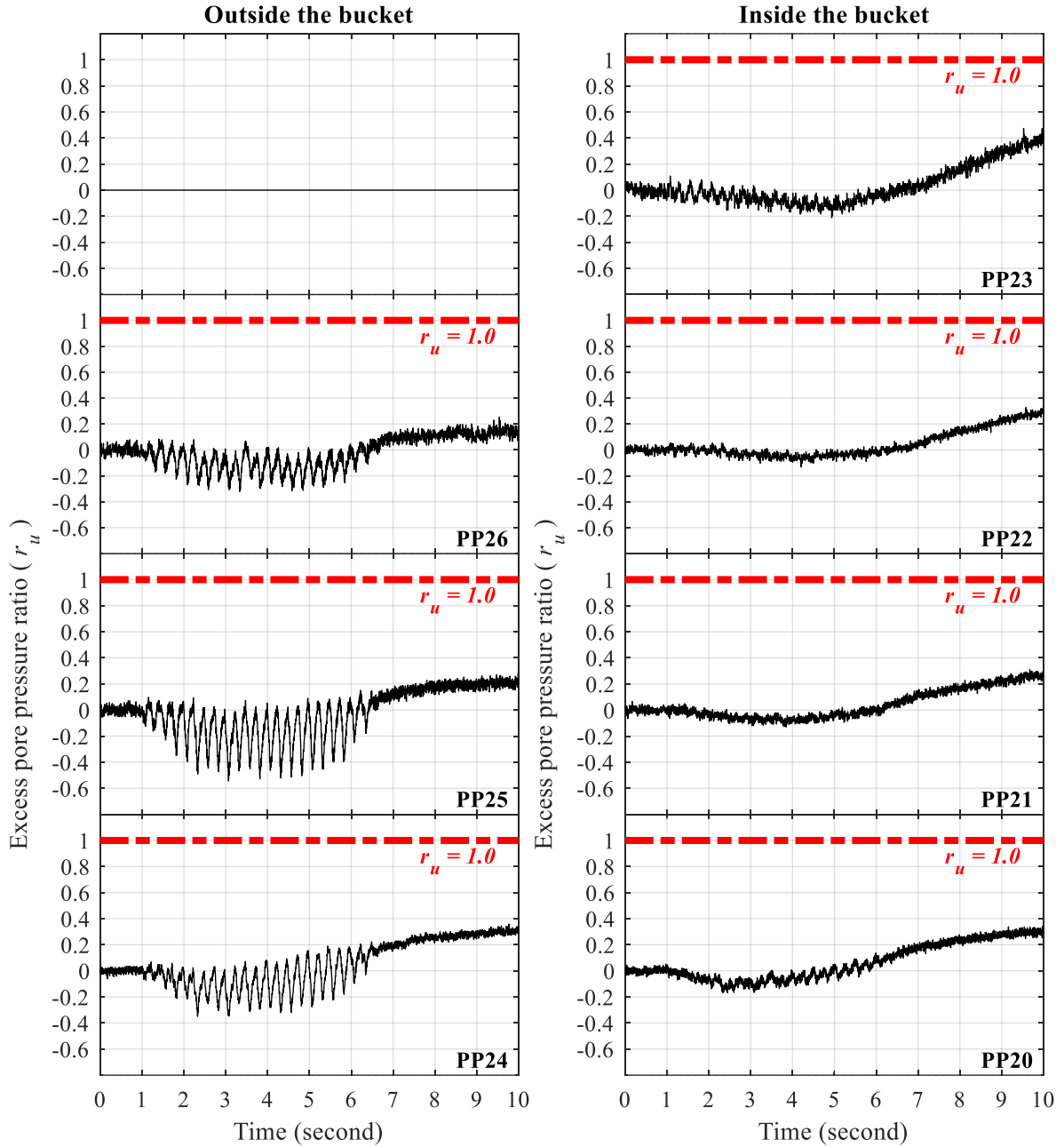


Figure B-33: Time histories of excess pore pressure at north edge of suction bucket for test H3

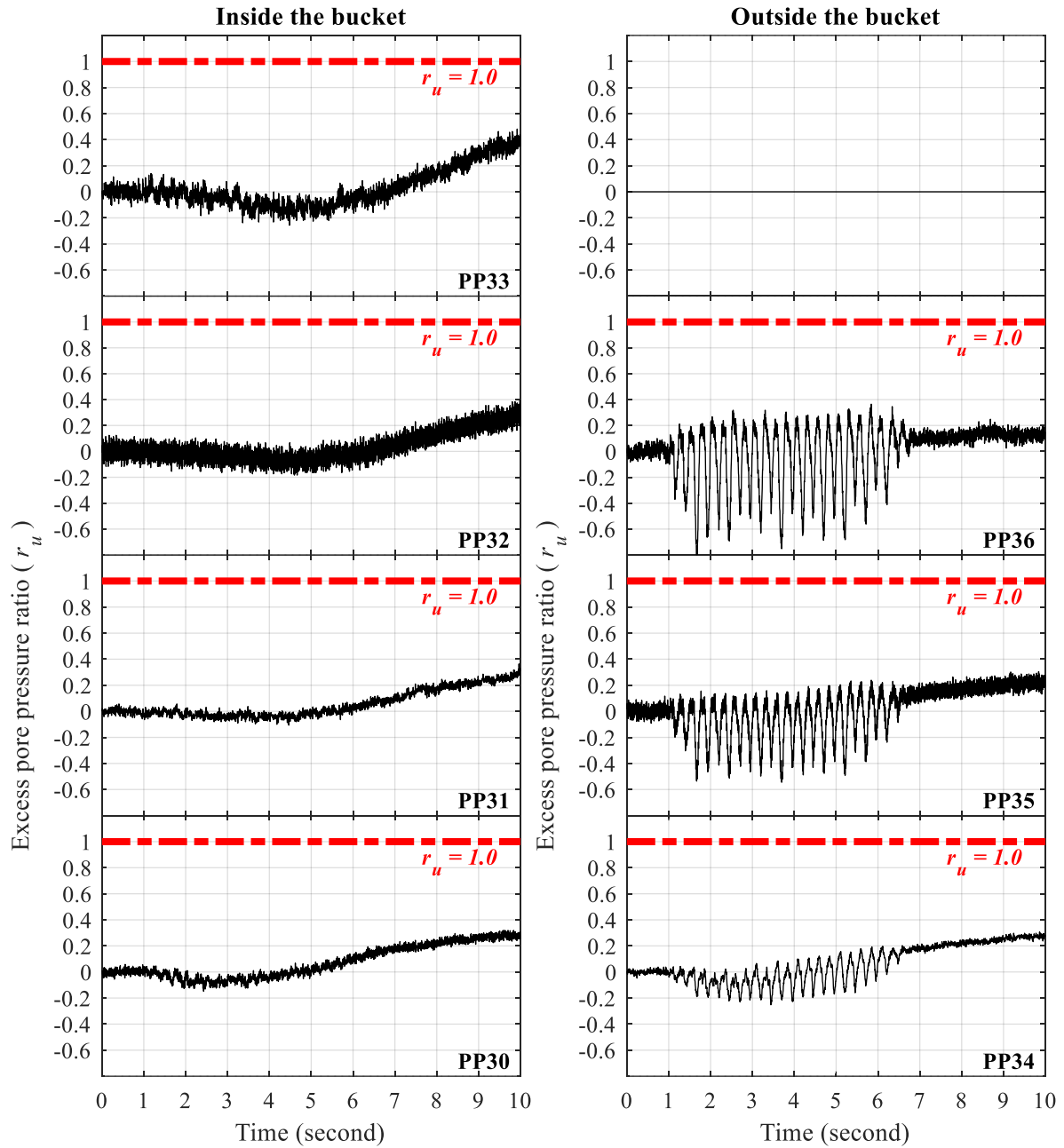


Figure B-34: Time histories of excess pore pressure at south edge of suction bucket for test H3



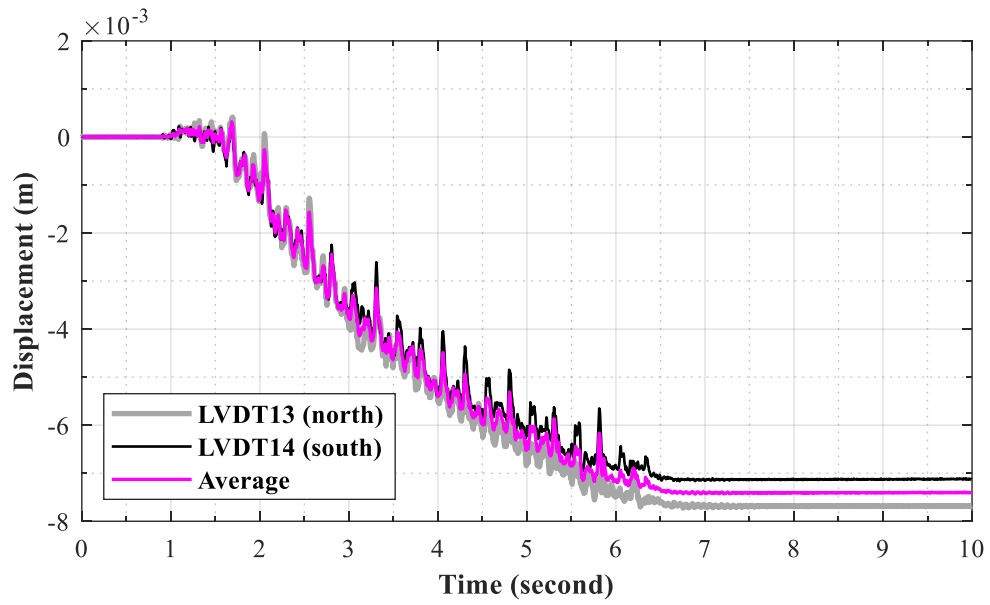


Figure B-35: Time histories of vertical bucket displacement for test H3

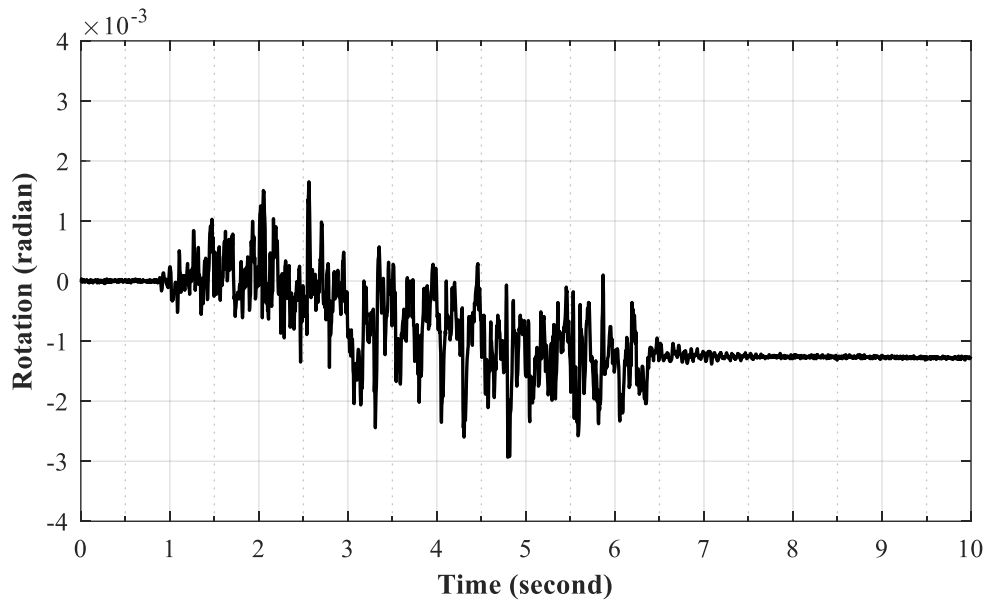


Figure B-36: Time history of suction bucket rotation for test H3

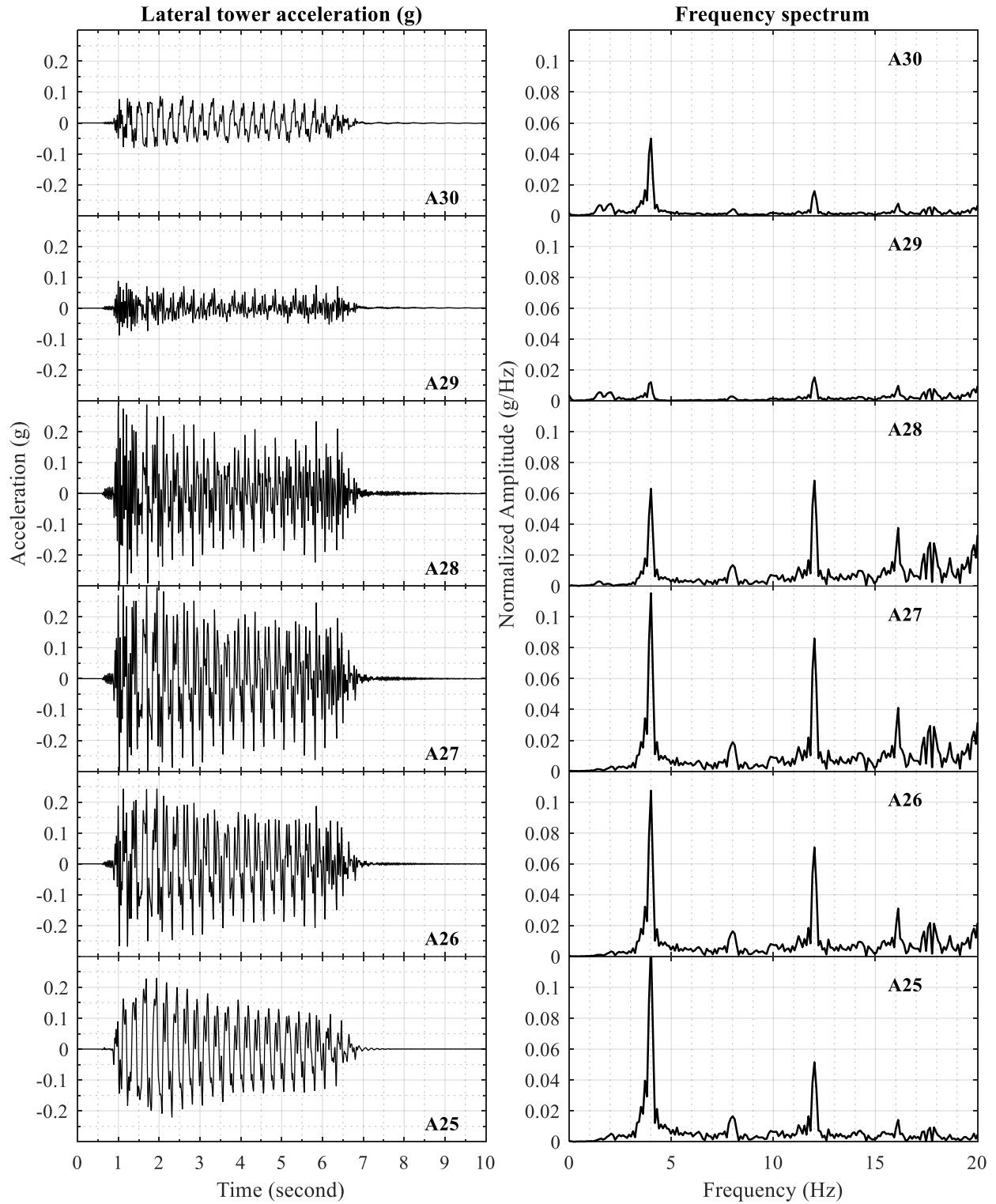


Figure B-37: Time histories of lateral tower acceleration for test H3

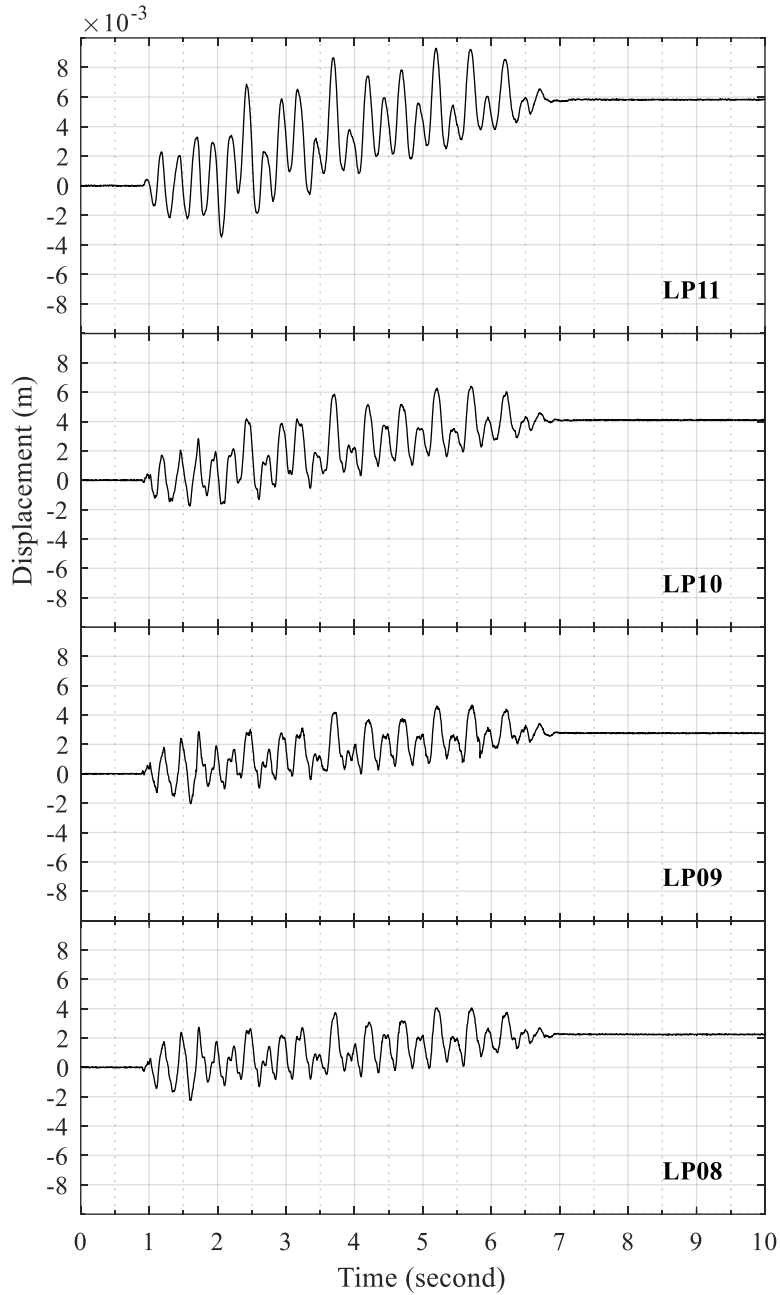


Figure B-38: Time histories of lateral tower displacement relative to lateral soil displacement at the foundation level (LP05) for test H3

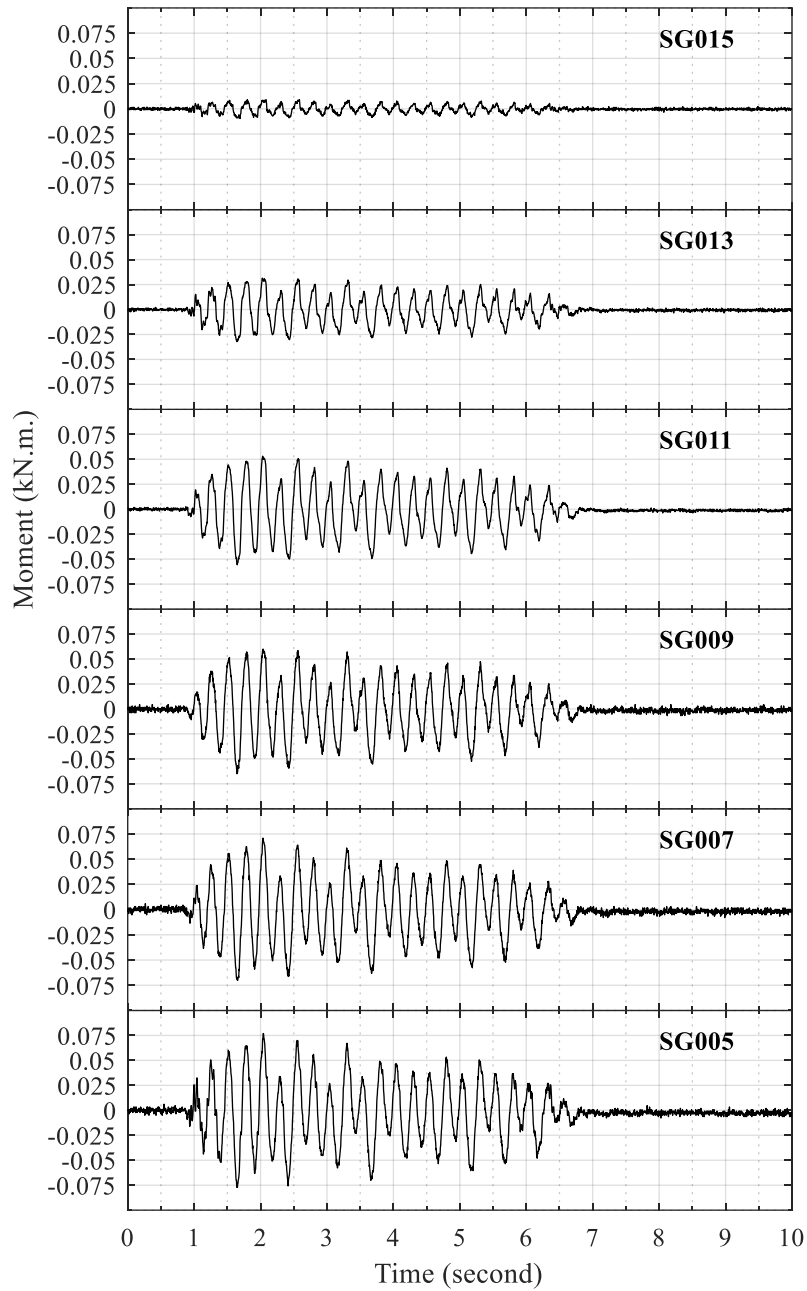


Figure B-39: Time histories of tower bending moment for test H3

### B.4 Test H4

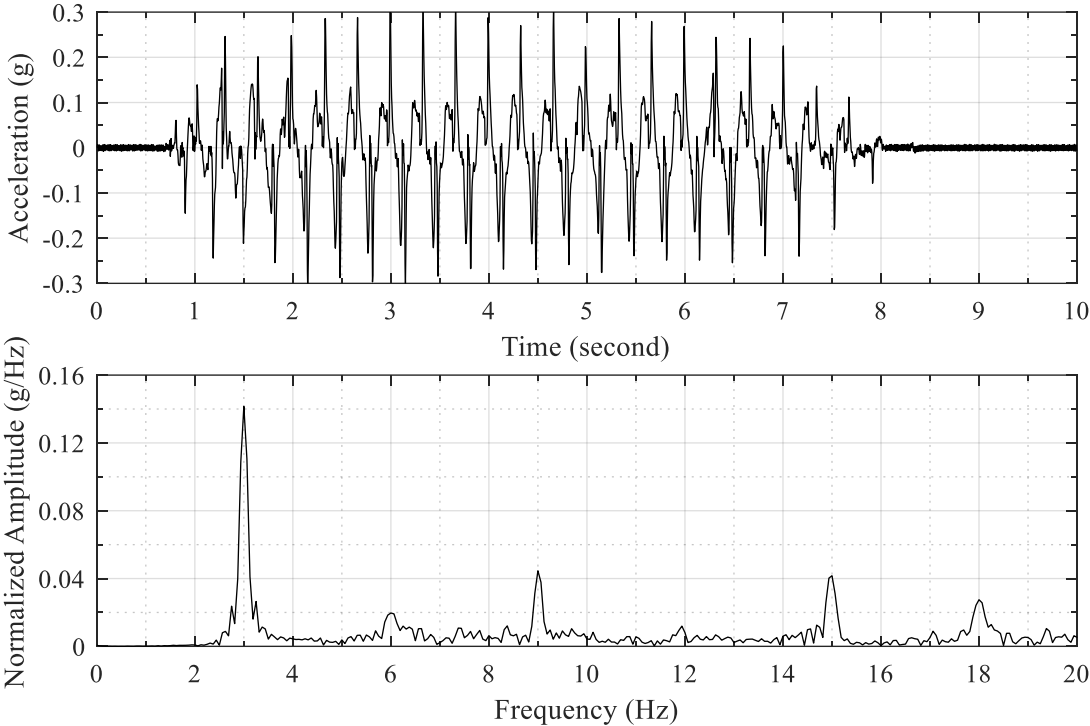


Figure B-40: Acceleration time history of shake table input excitation and the corresponding frequency spectrum for test H4

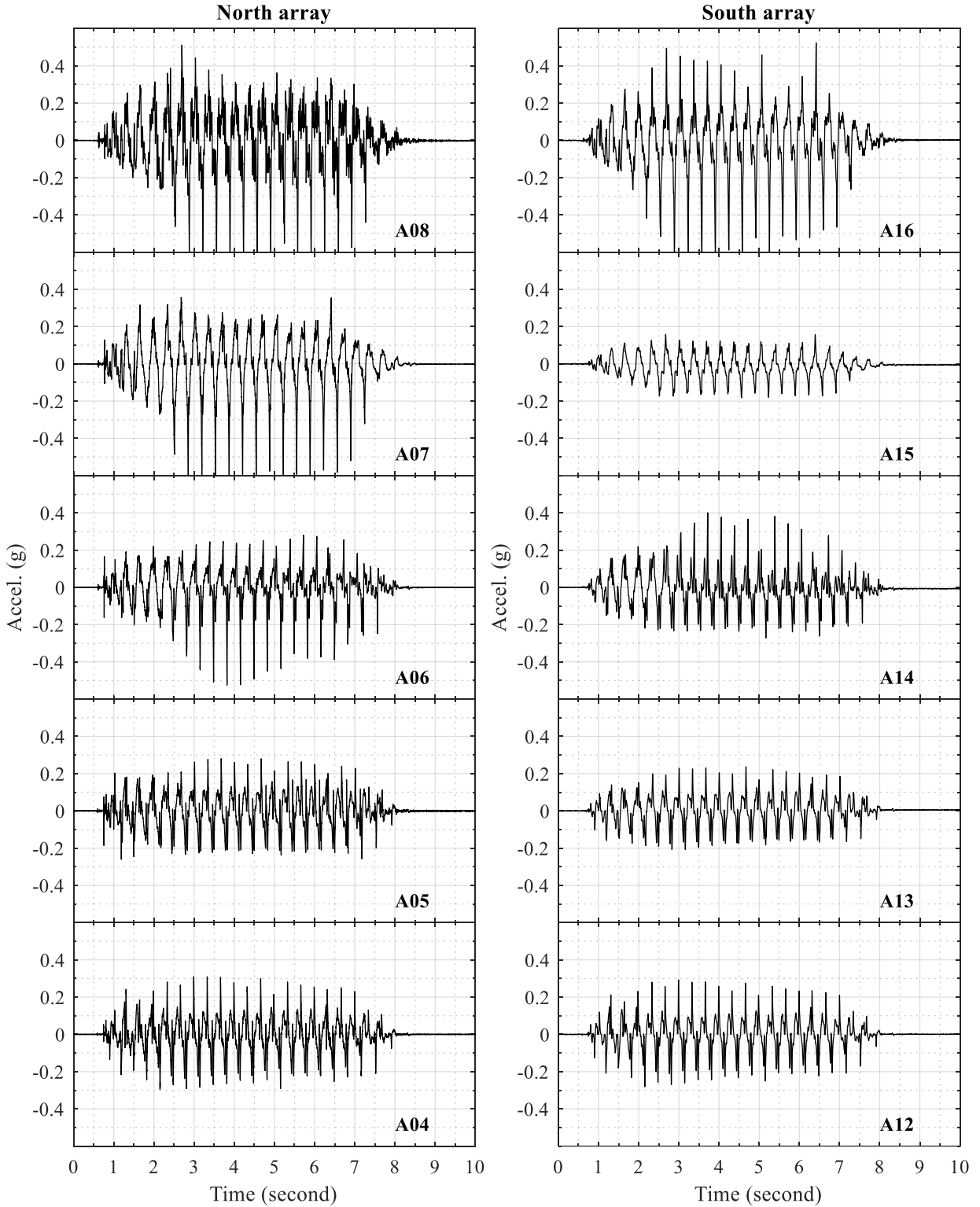


Figure B-41: Time histories of lateral soil acceleration in north and south arrays for test H4

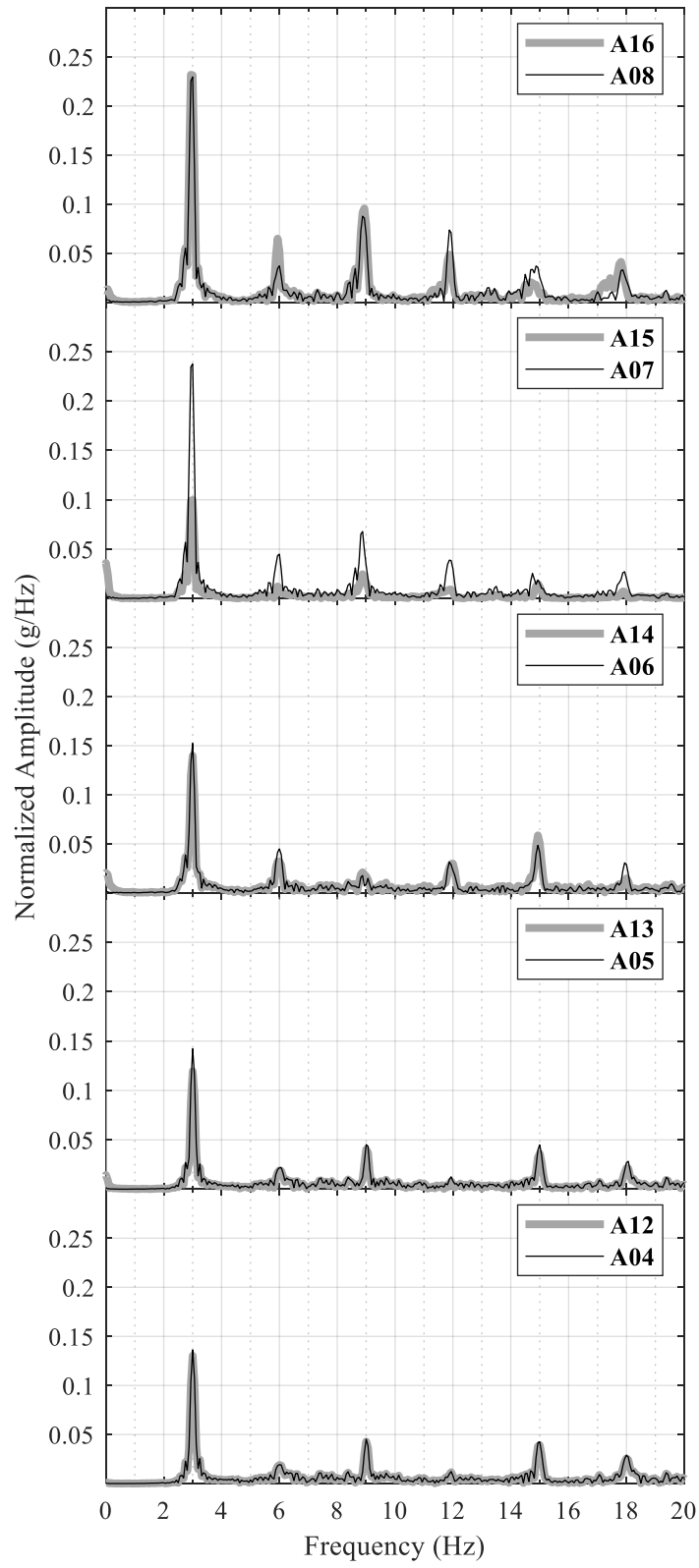


Figure B-42: Frequency spectra of lateral soil acceleration in north and south arrays for test H4



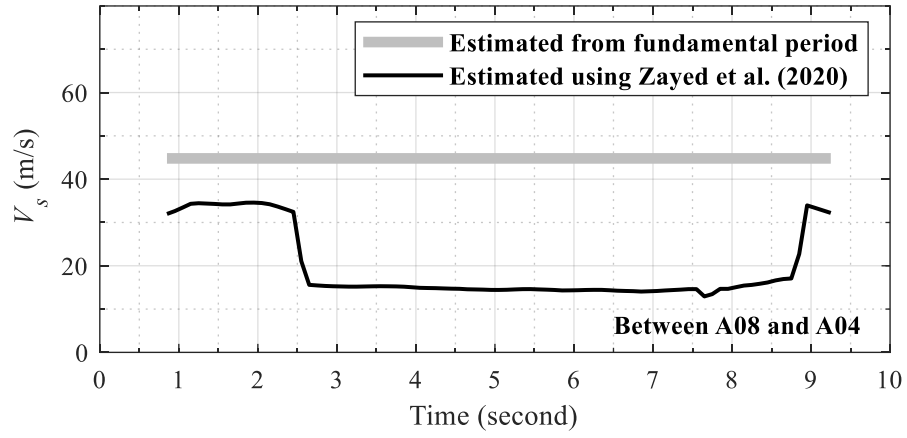


Figure B-43: Change in soil  $V_s$  with time during test H4

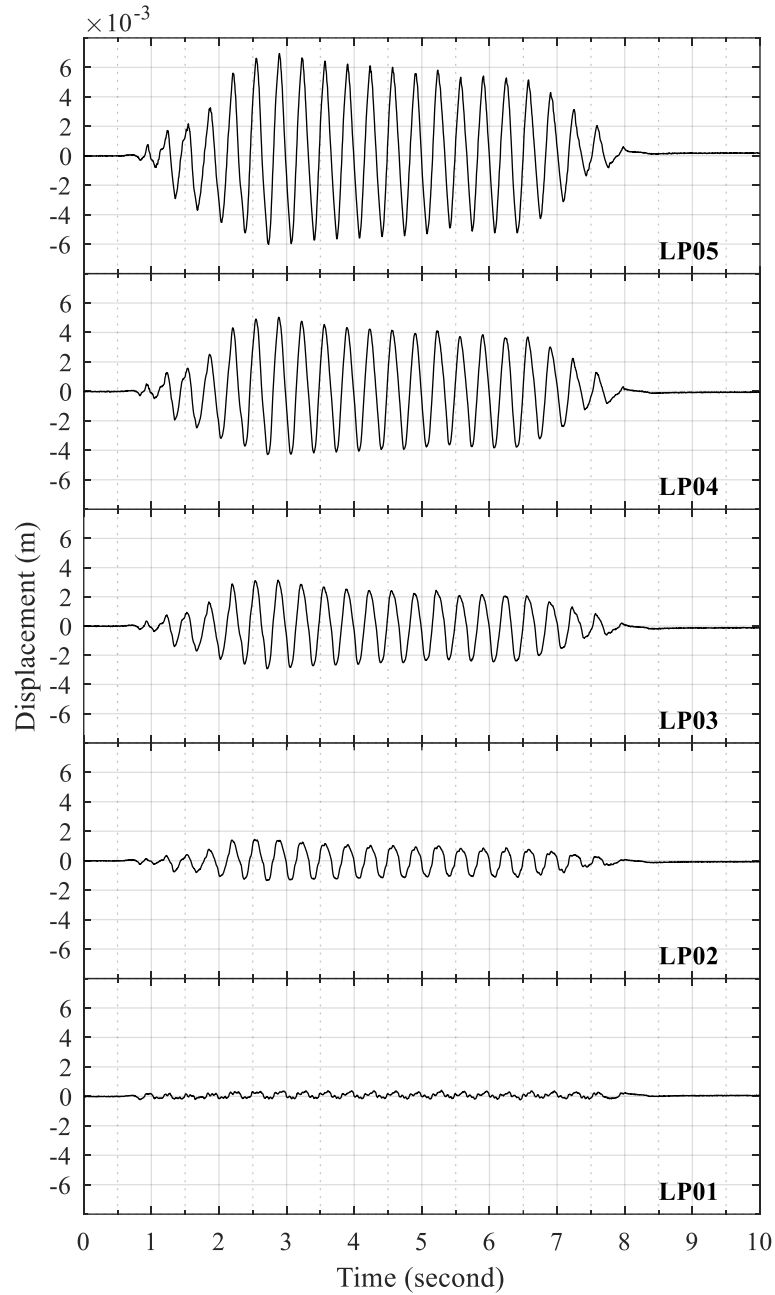


Figure B-44: Time histories of lateral soil displacement relative to laminar container base for test H4

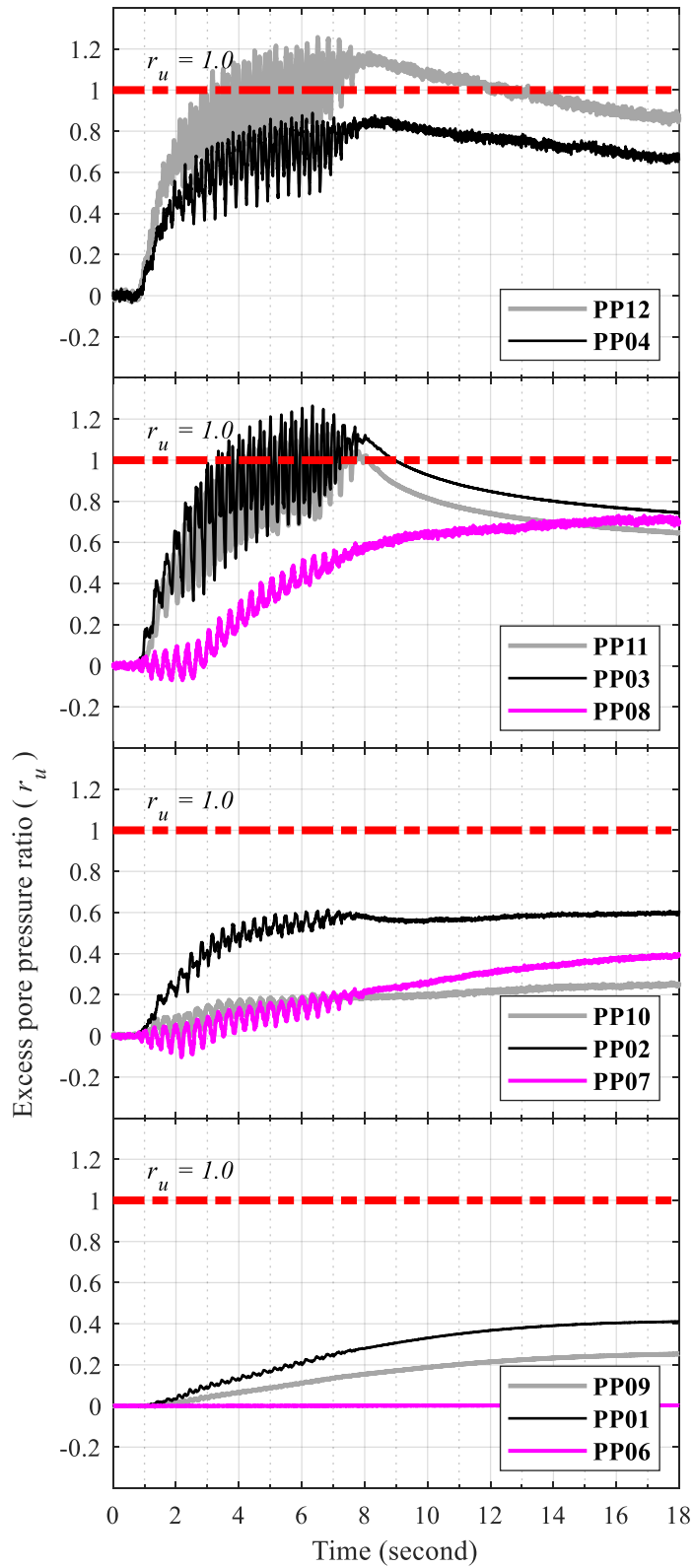


Figure B-45: Time histories of soil excess pore pressure for test H4

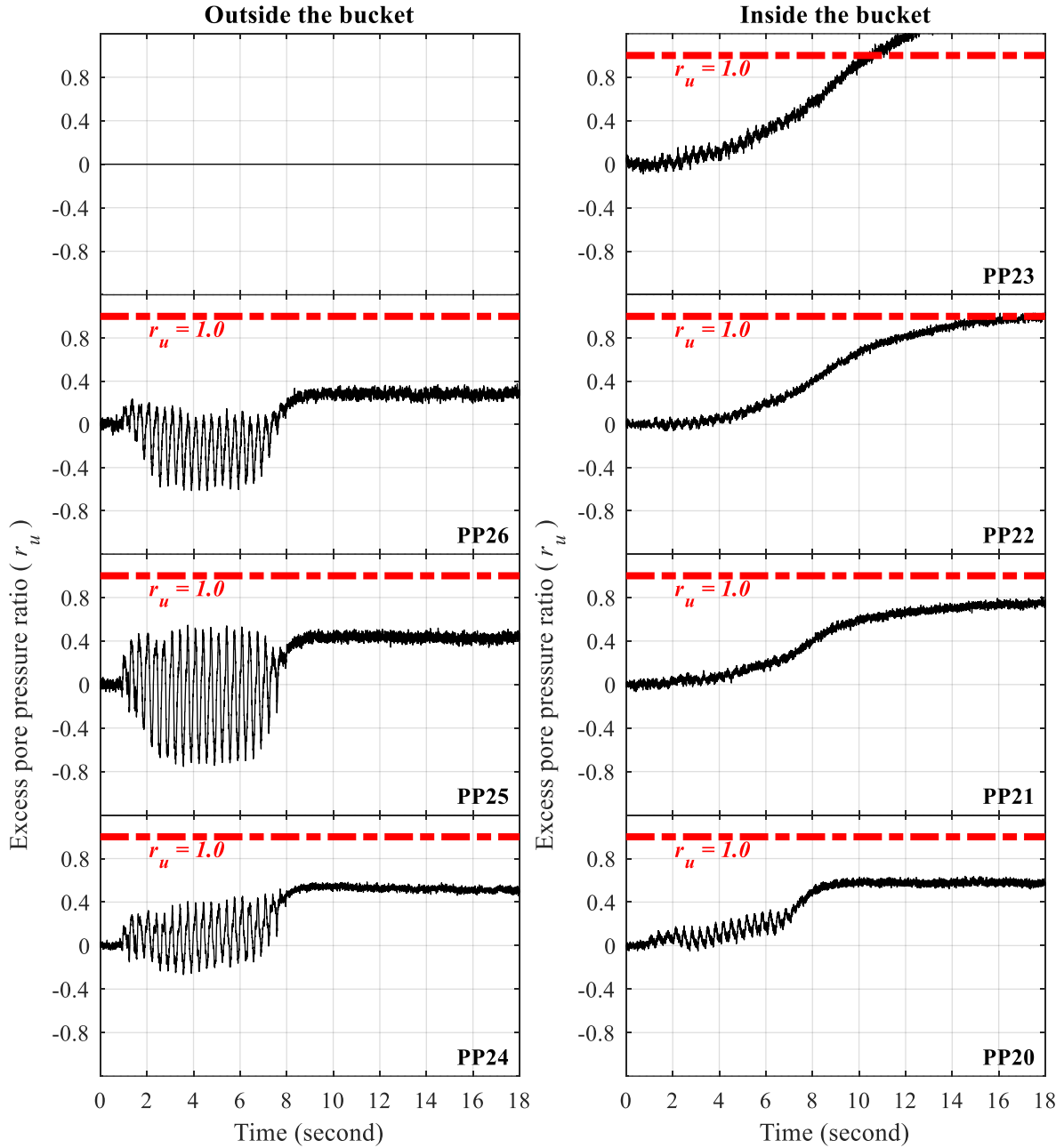


Figure B-46: Time histories of excess pore pressure at north edge of suction bucket for test H4

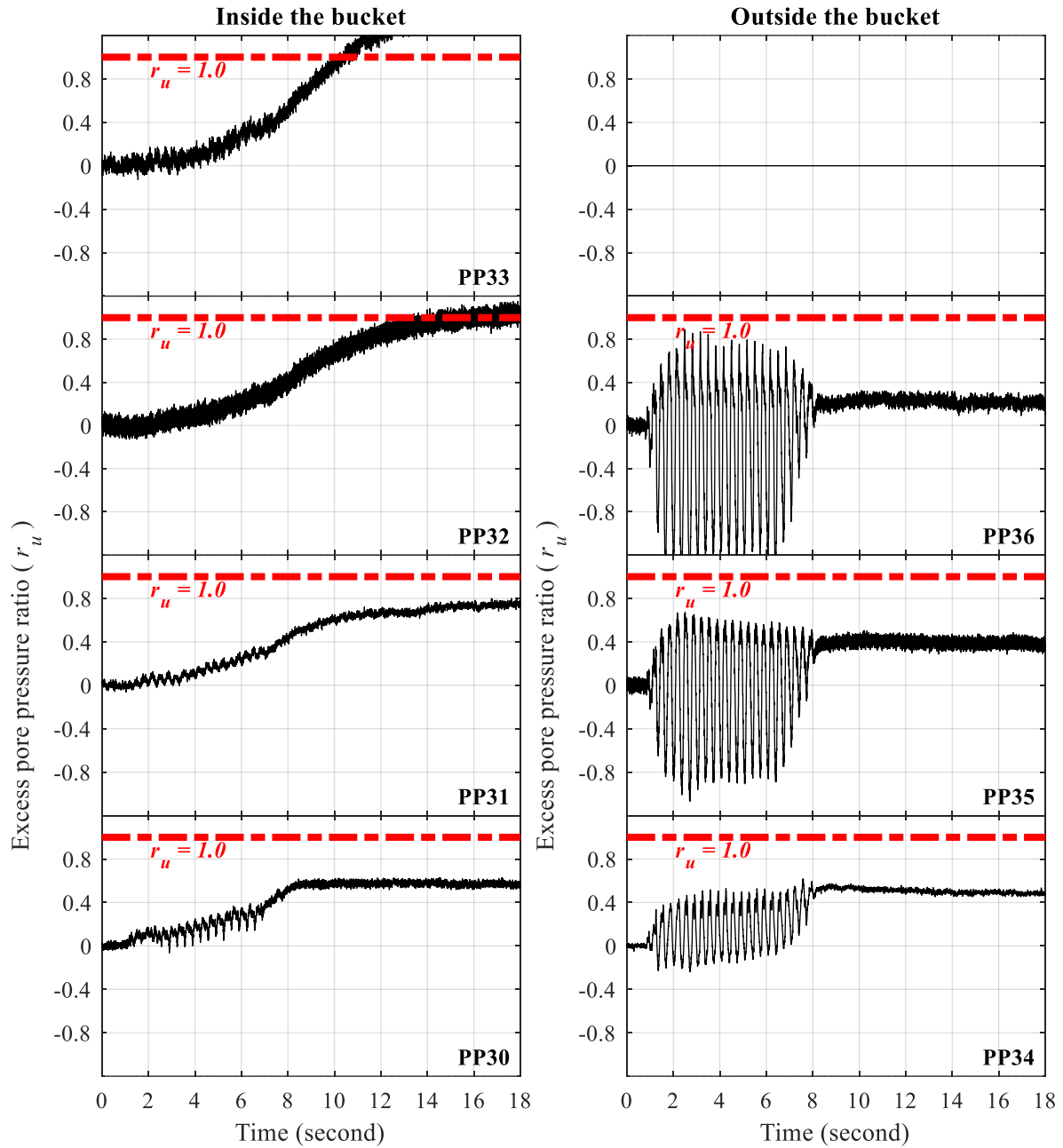


Figure B-47: Time histories of excess pore pressure at south edge of suction bucket for test H4

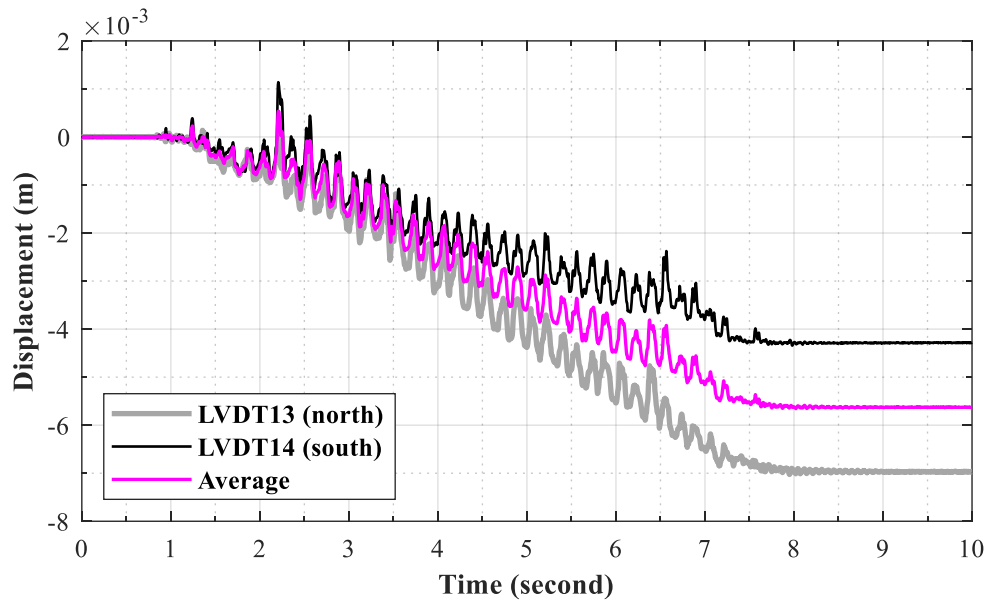


Figure B-48: Time histories of vertical bucket displacement for test H4

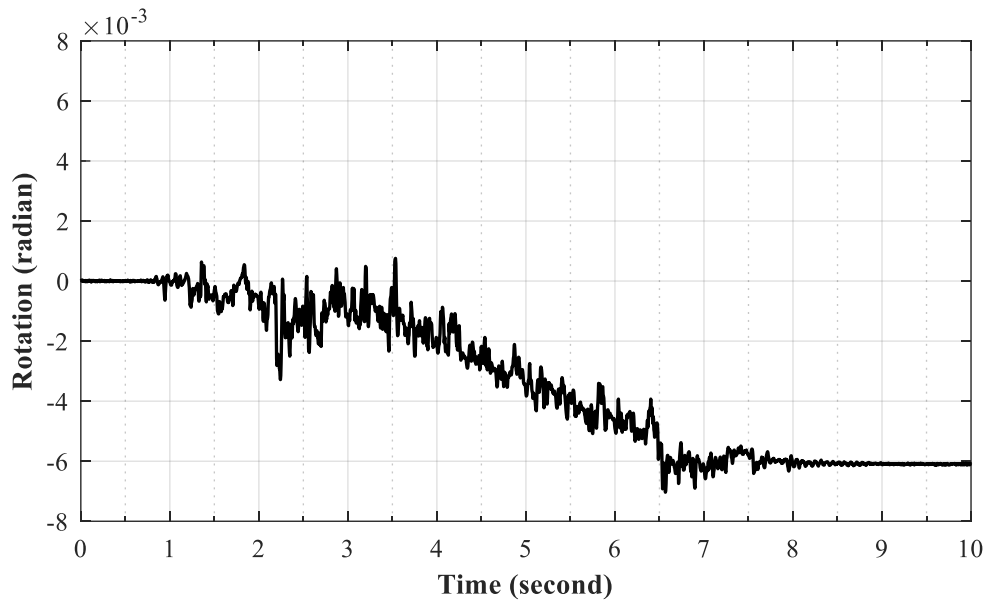


Figure B-49: Time history of suction bucket rotation for test H4

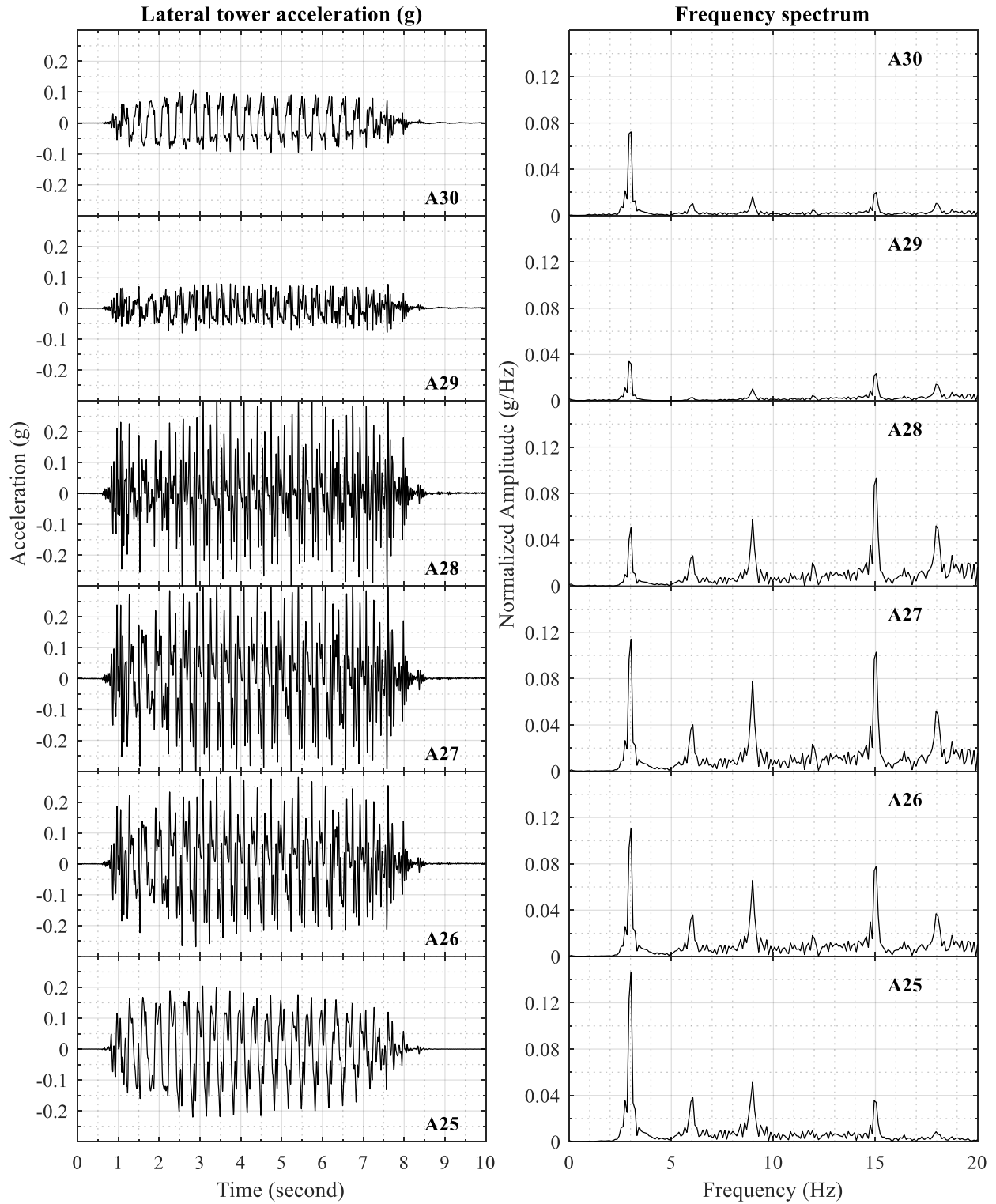


Figure B-50: Time histories of lateral tower acceleration for test H4



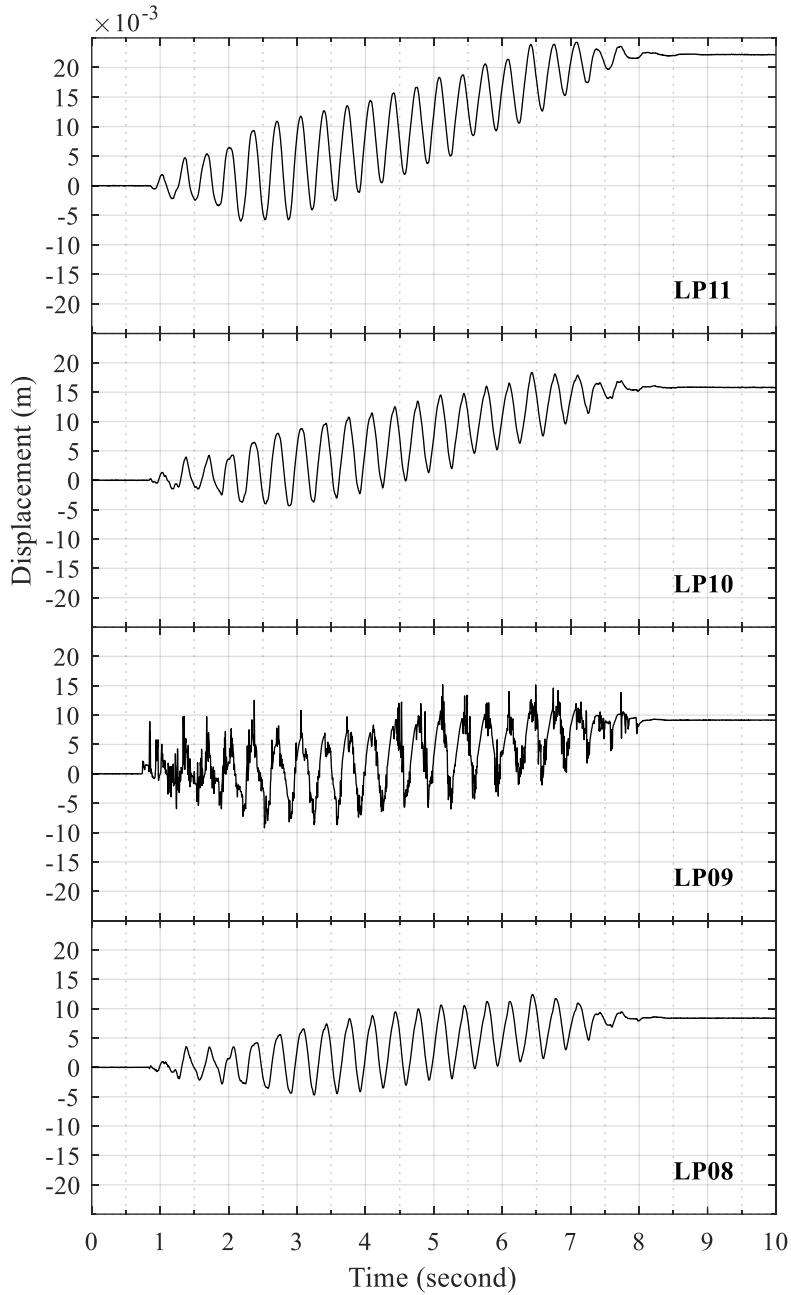


Figure B-51: Time histories of lateral tower displacement relative to lateral soil displacement at the foundation level (LP05) for test H4

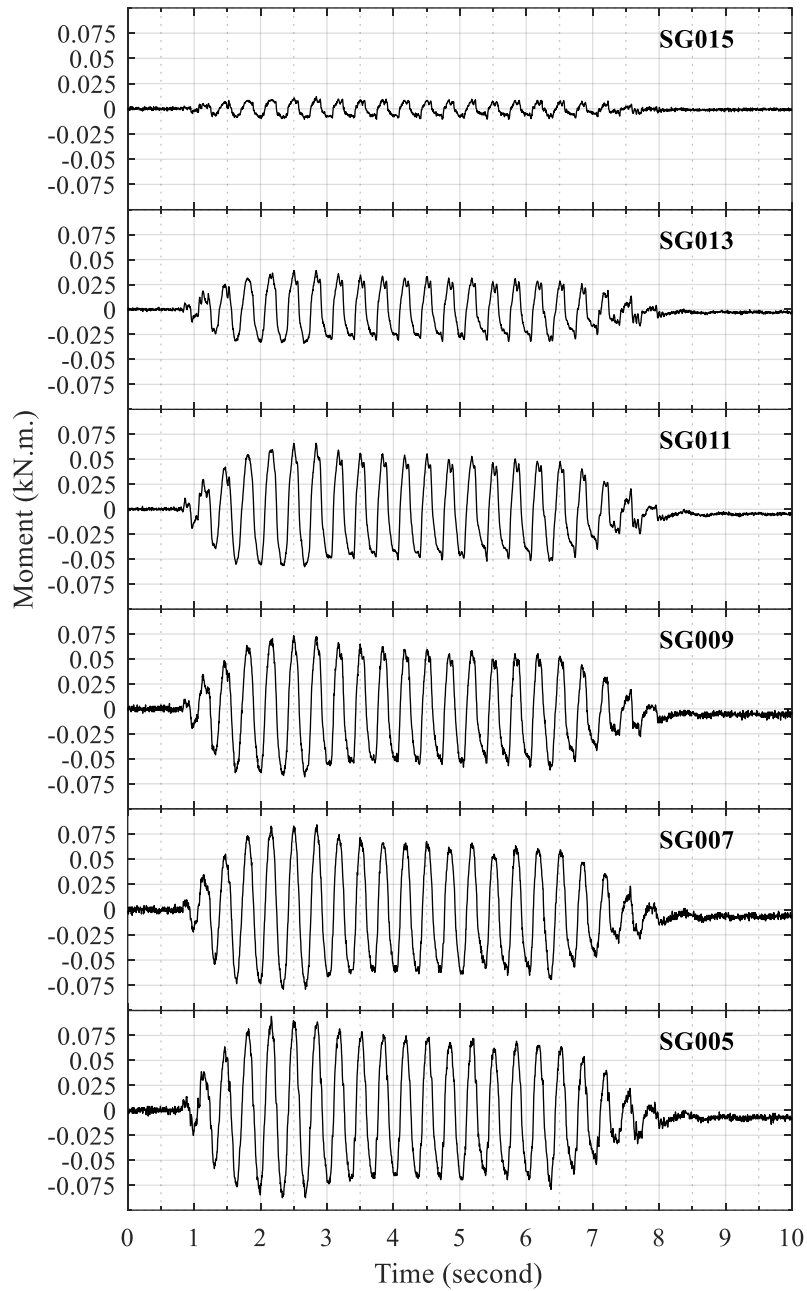


Figure B-52: Time histories of tower bending moment for test H4

### B.5 Test H5

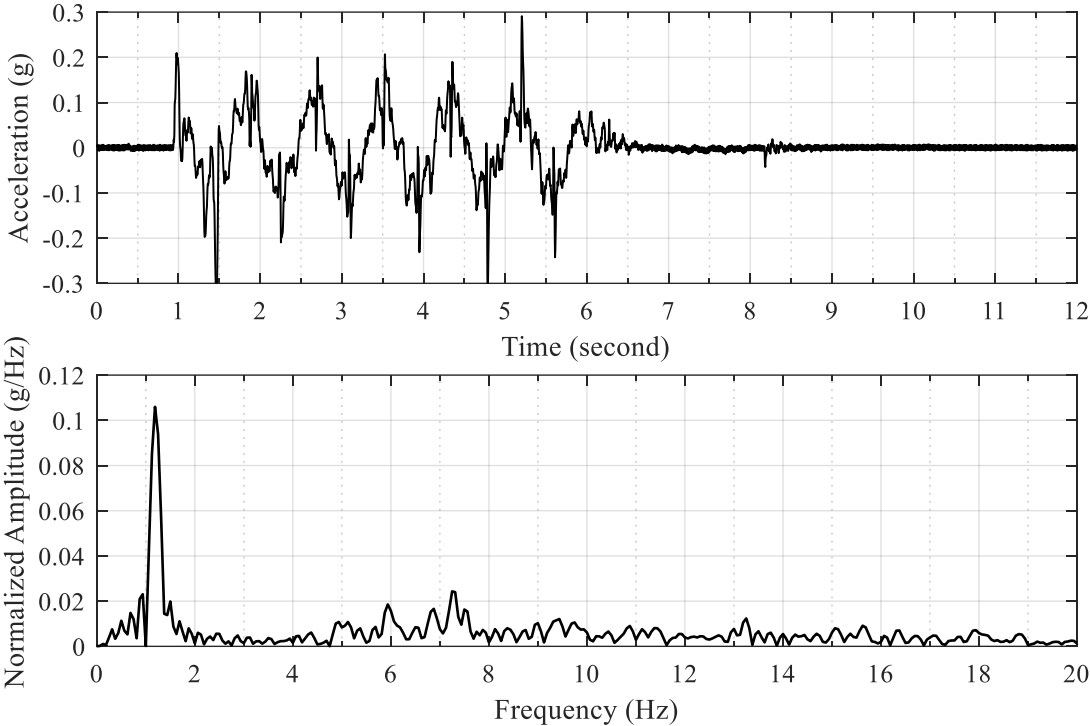


Figure B-53: Acceleration time history of shake table input excitation and the corresponding frequency spectrum for test H5

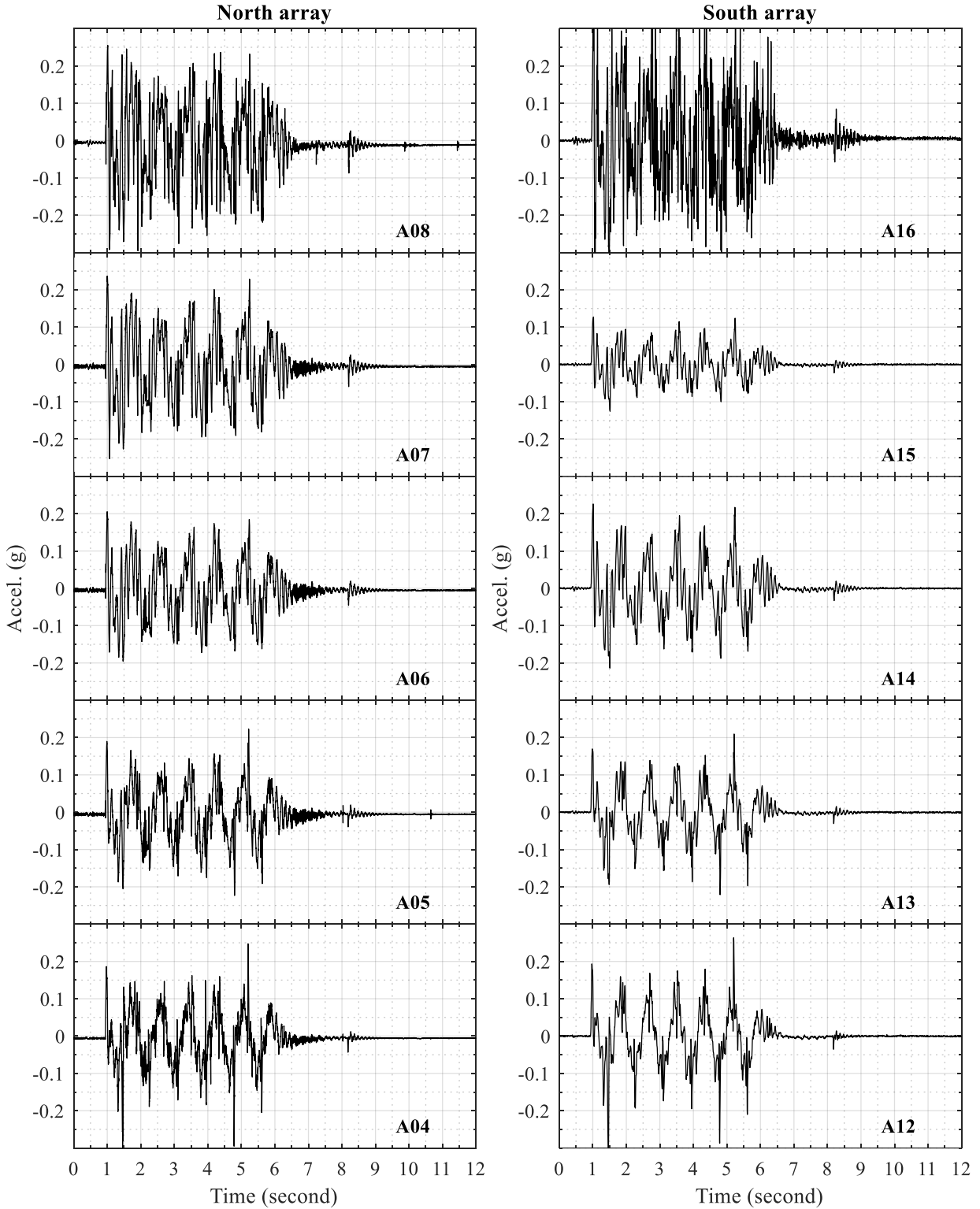


Figure B-54: Time histories of lateral soil acceleration in north and south arrays for test H5

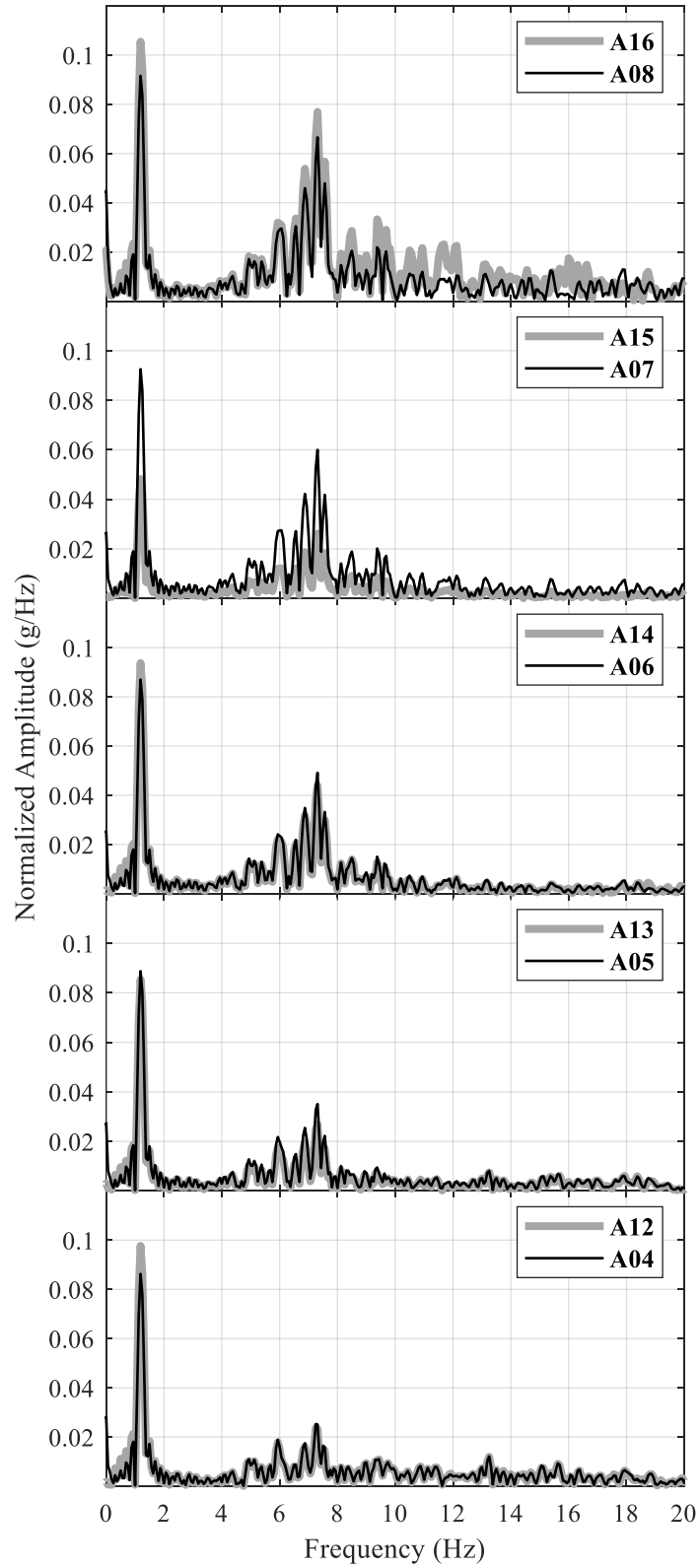


Figure B-55: Frequency spectra of lateral soil acceleration in north and south arrays for test H5

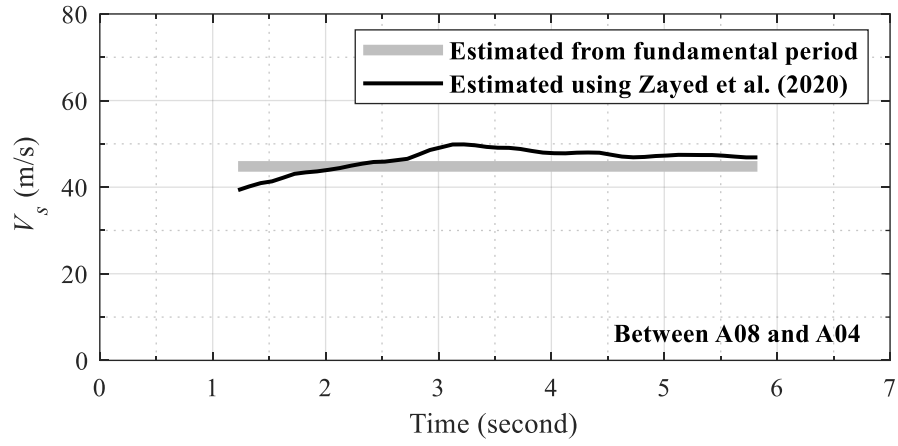


Figure B-56: Change in soil  $V_s$  with time during test H5

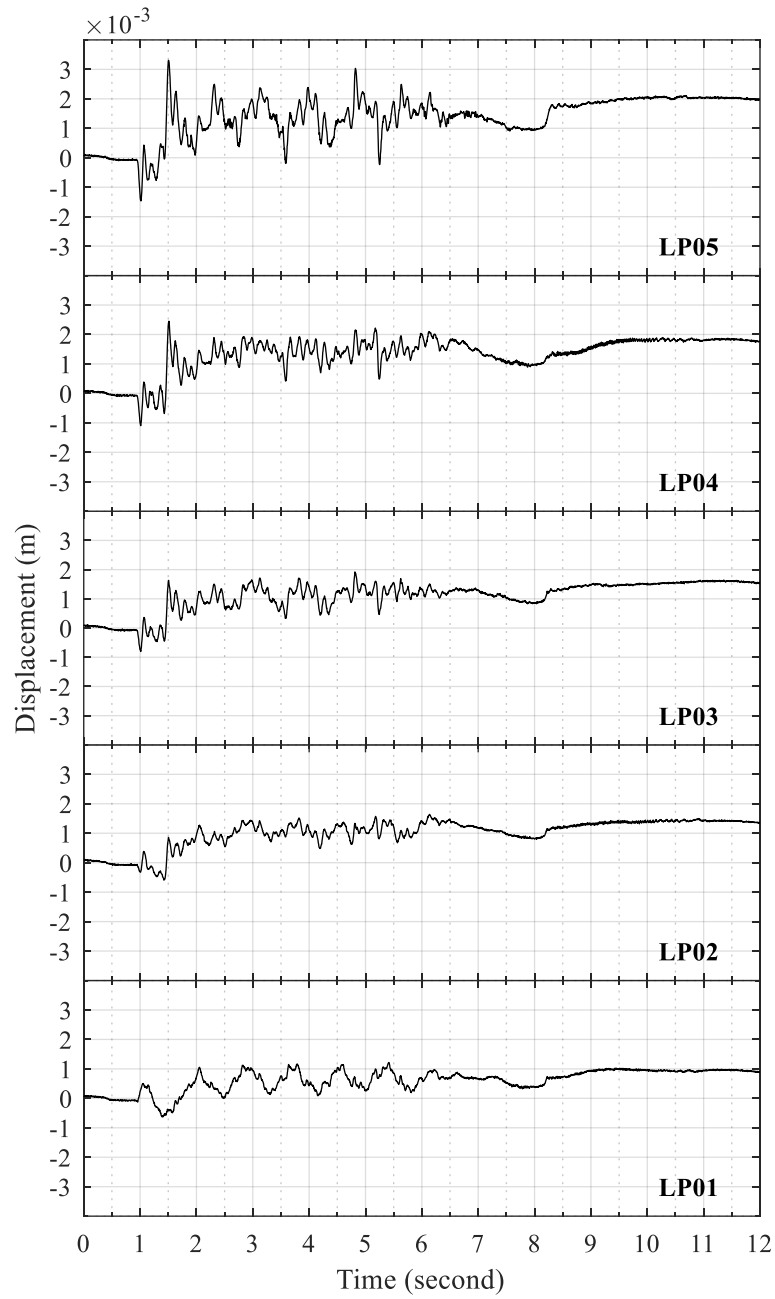


Figure B-57: Time histories of lateral soil displacement relative to laminar container base for test H5

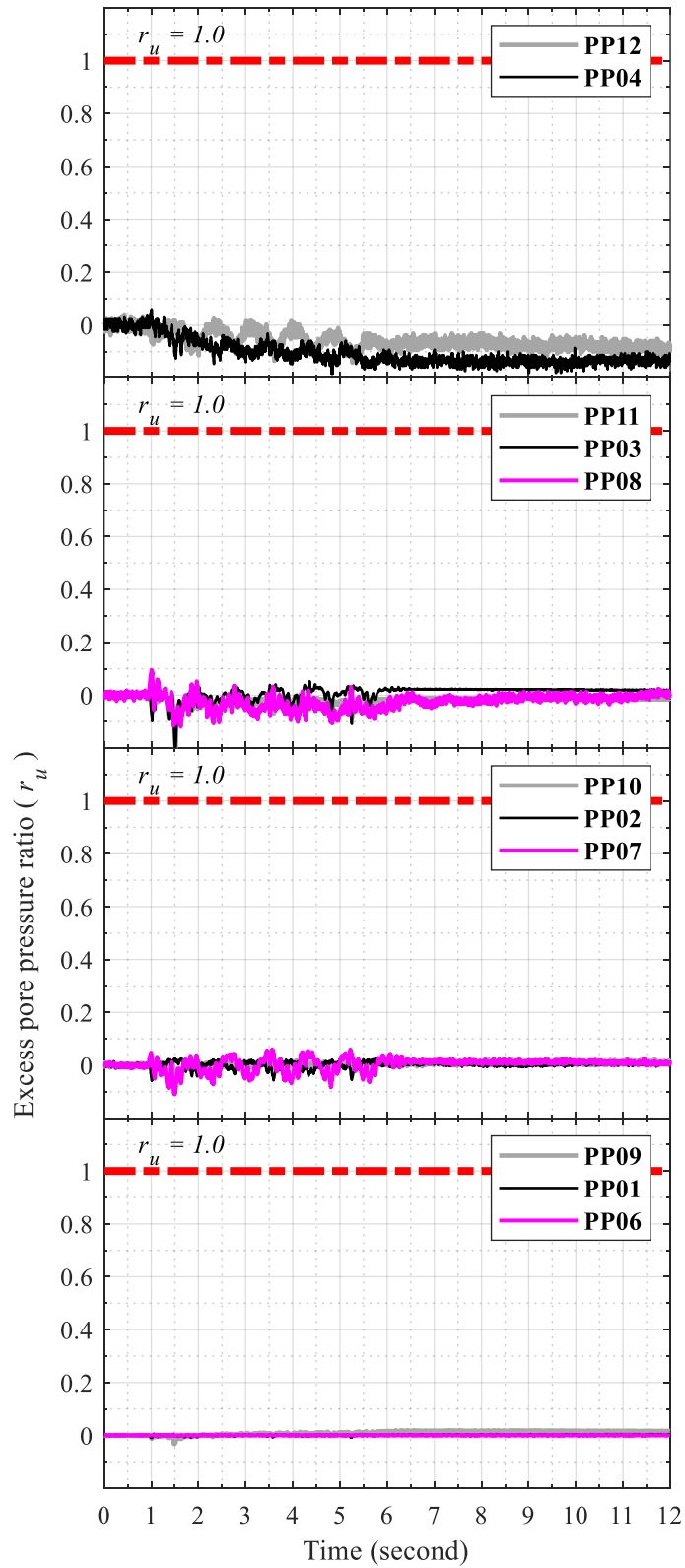


Figure B-58: Time histories of soil excess pore pressure for test H5



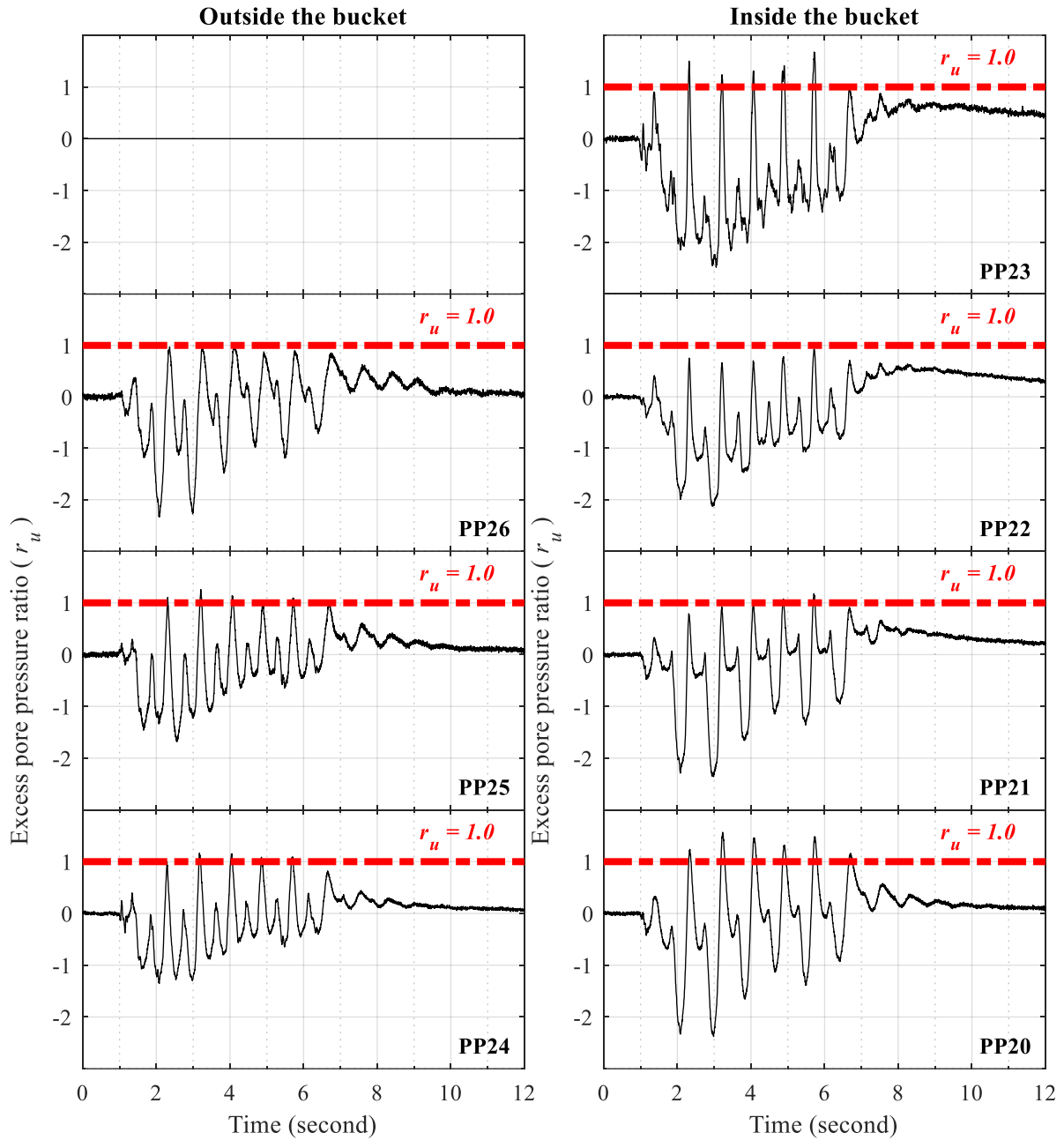


Figure B-59: Time histories of excess pore pressure at north edge of suction bucket for test H5

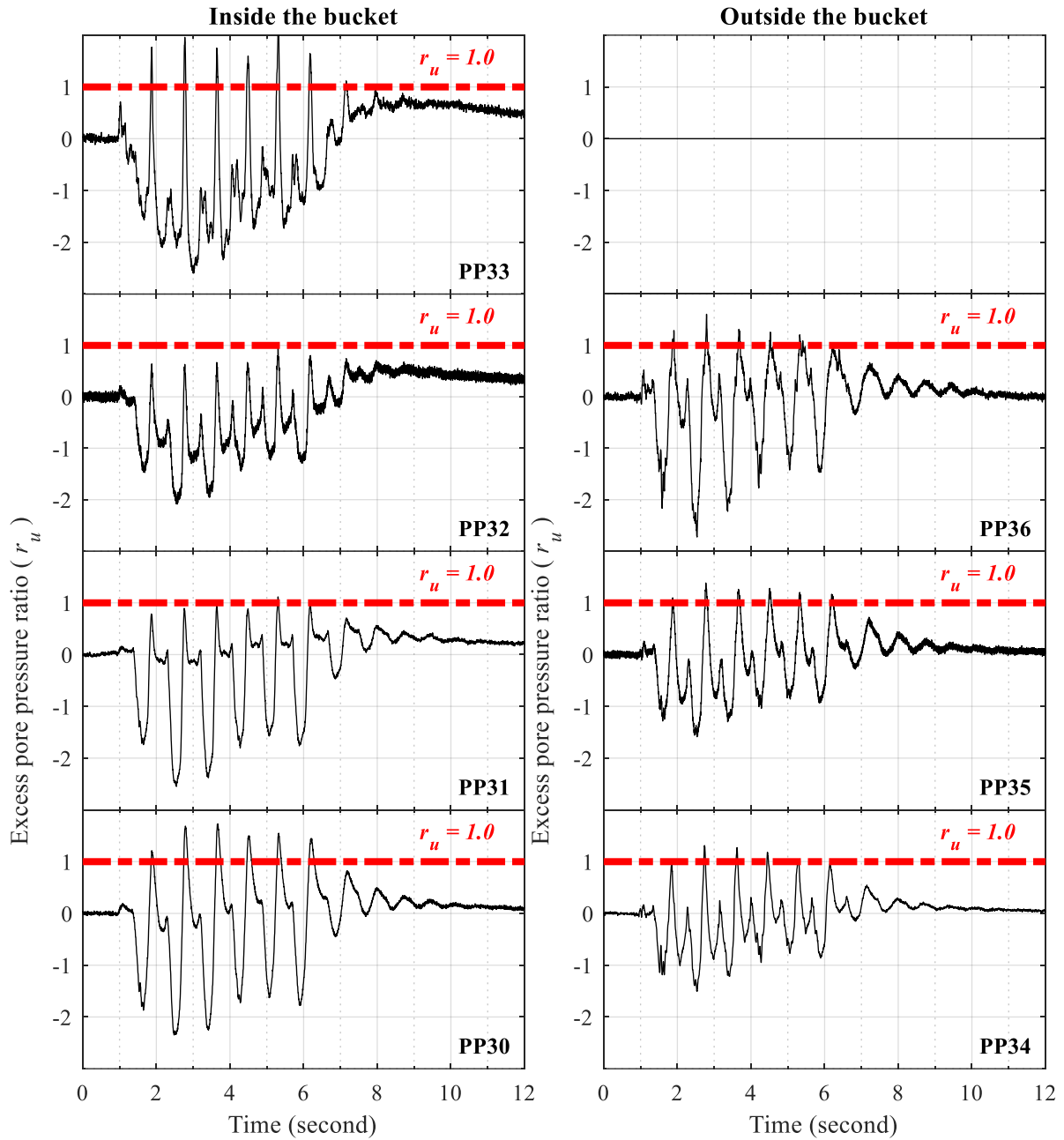


Figure B-60: Time histories of excess pore pressure at south edge of suction bucket for test H5

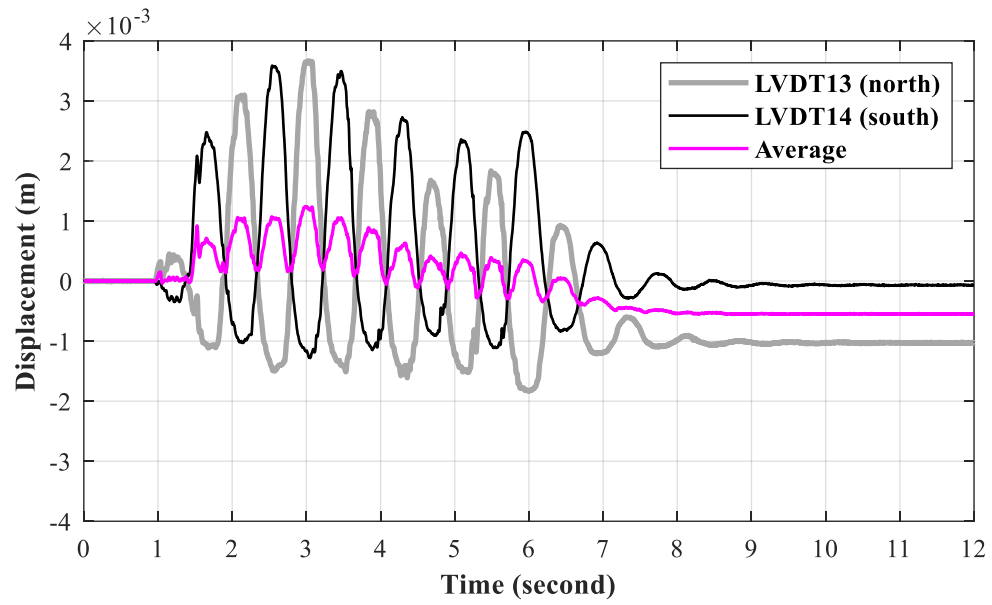


Figure B-61: Time histories of vertical bucket displacement for test H5

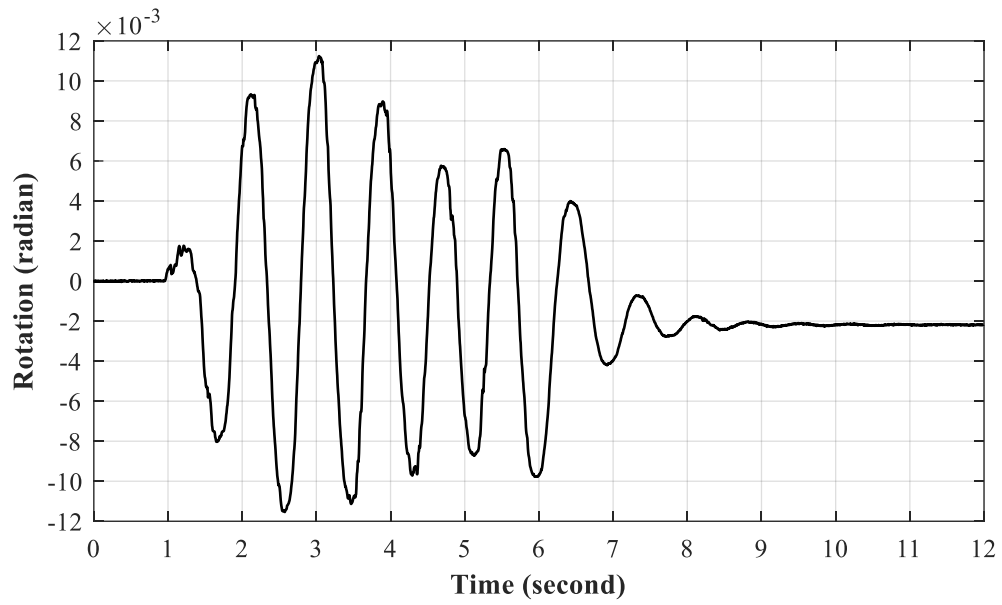


Figure B-62: Time history of suction bucket rotation for test H5

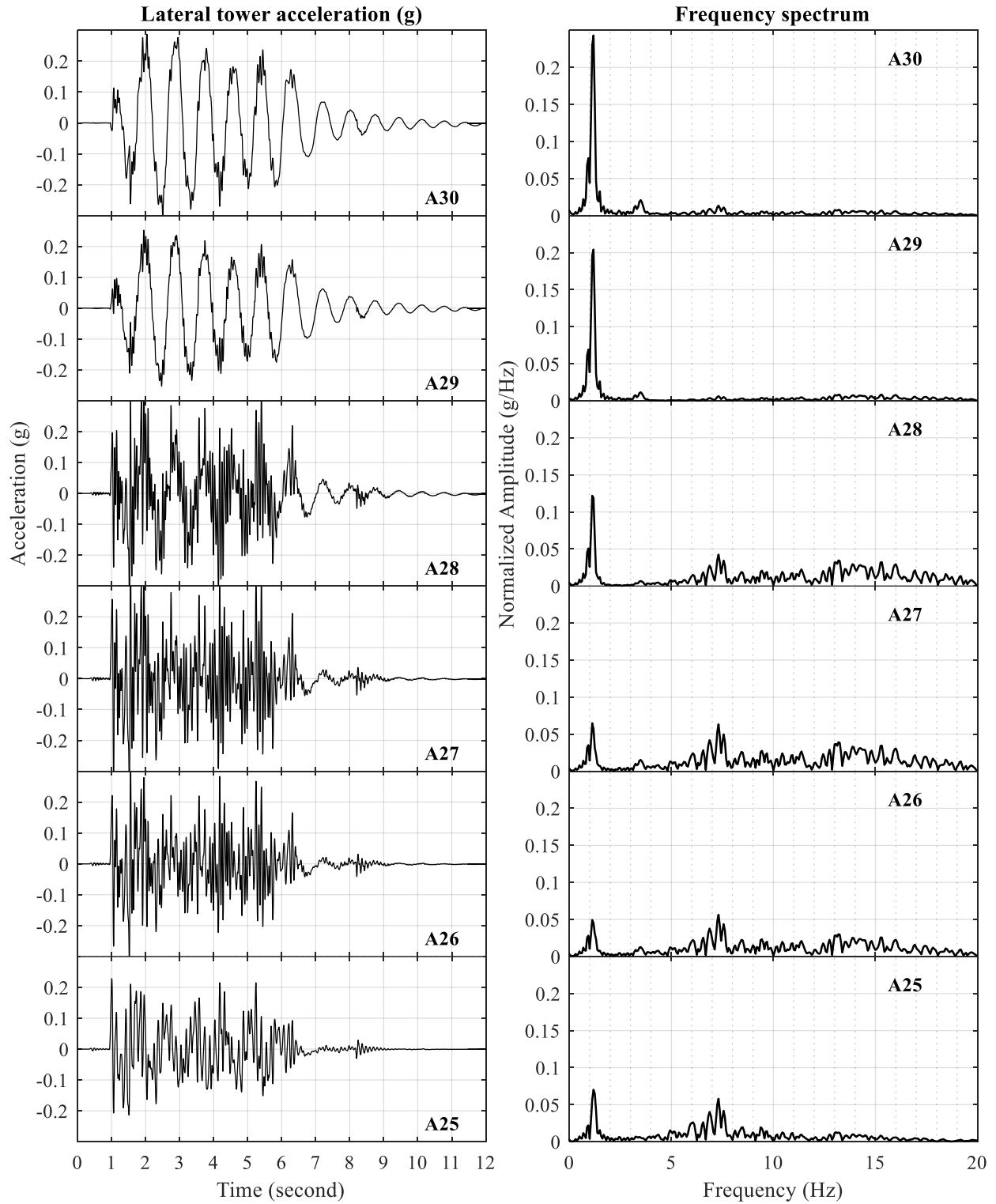


Figure B-63: Time histories of lateral tower acceleration for test H5

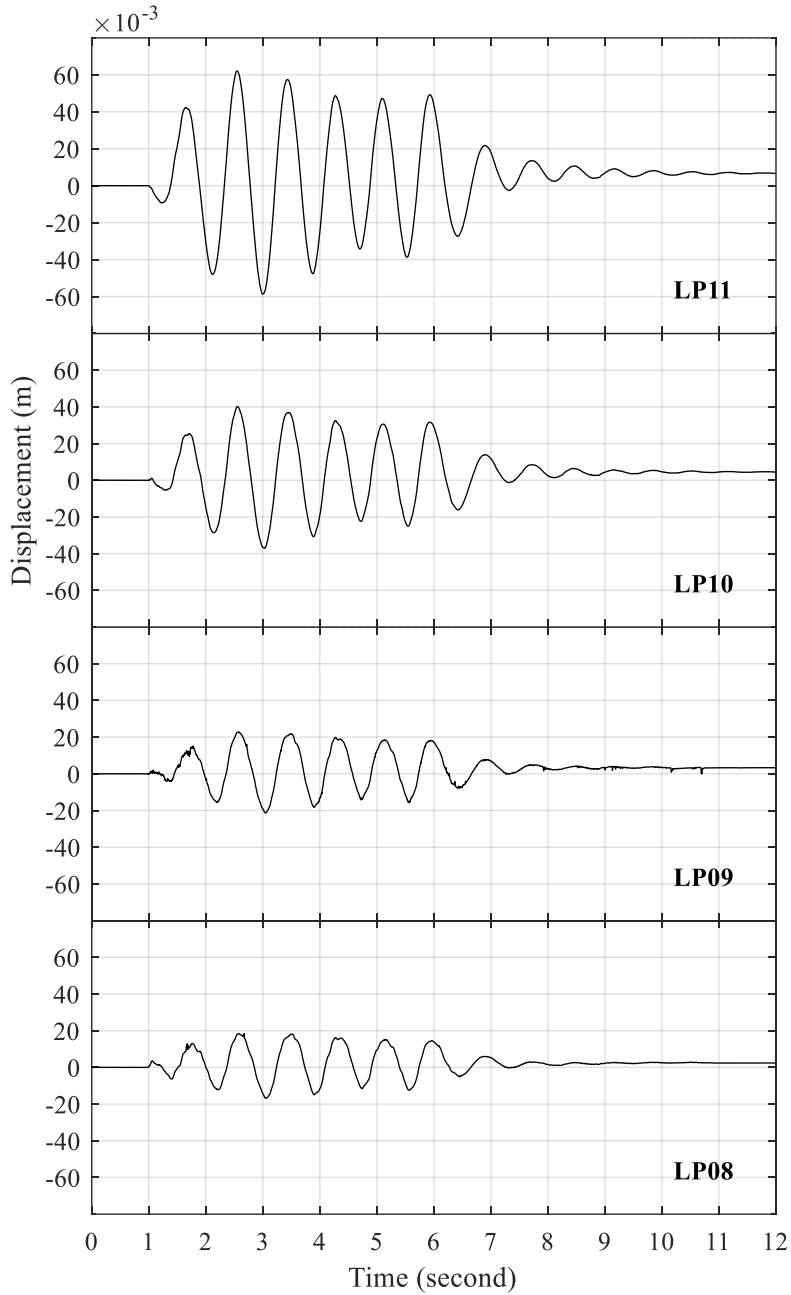


Figure B-64: Time histories of lateral tower displacement relative to lateral soil displacement at the foundation level (LP05) for test H5

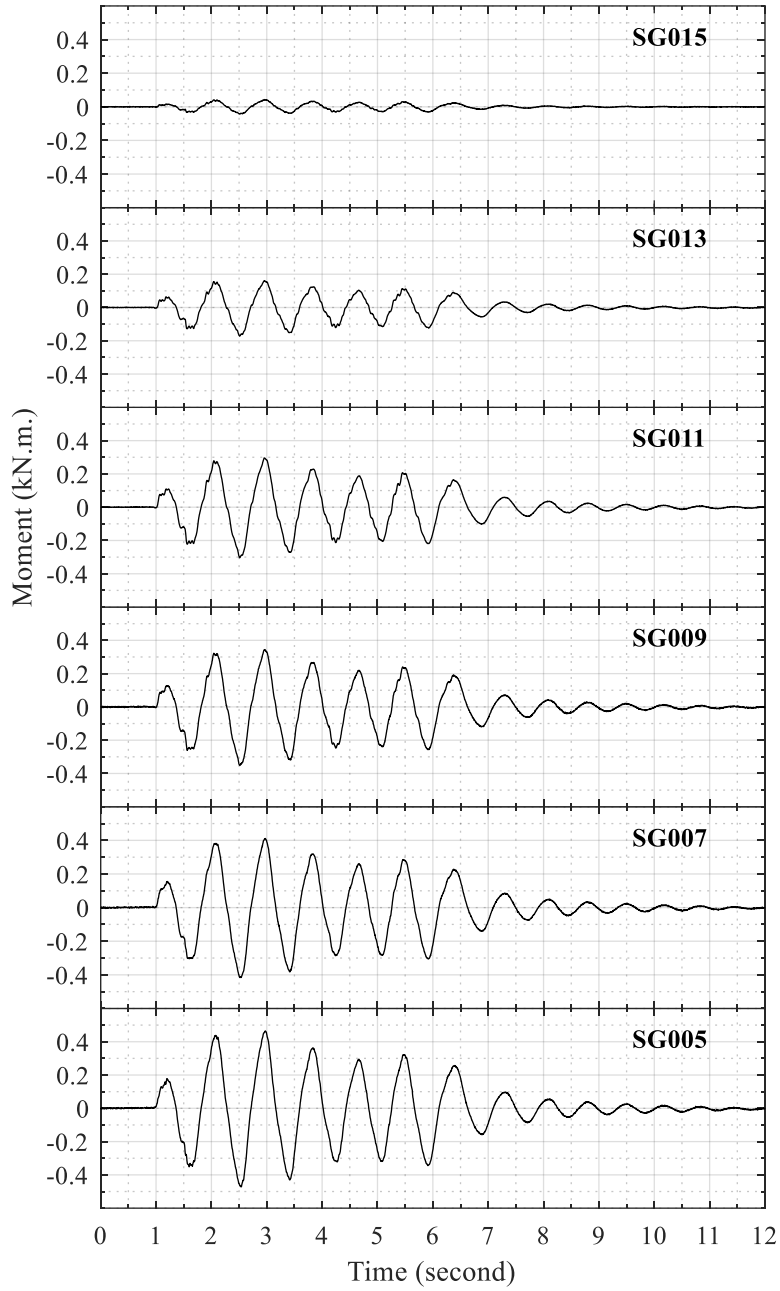


Figure B-65: Time histories of tower bending moment for test H5

### B.6 Test H6

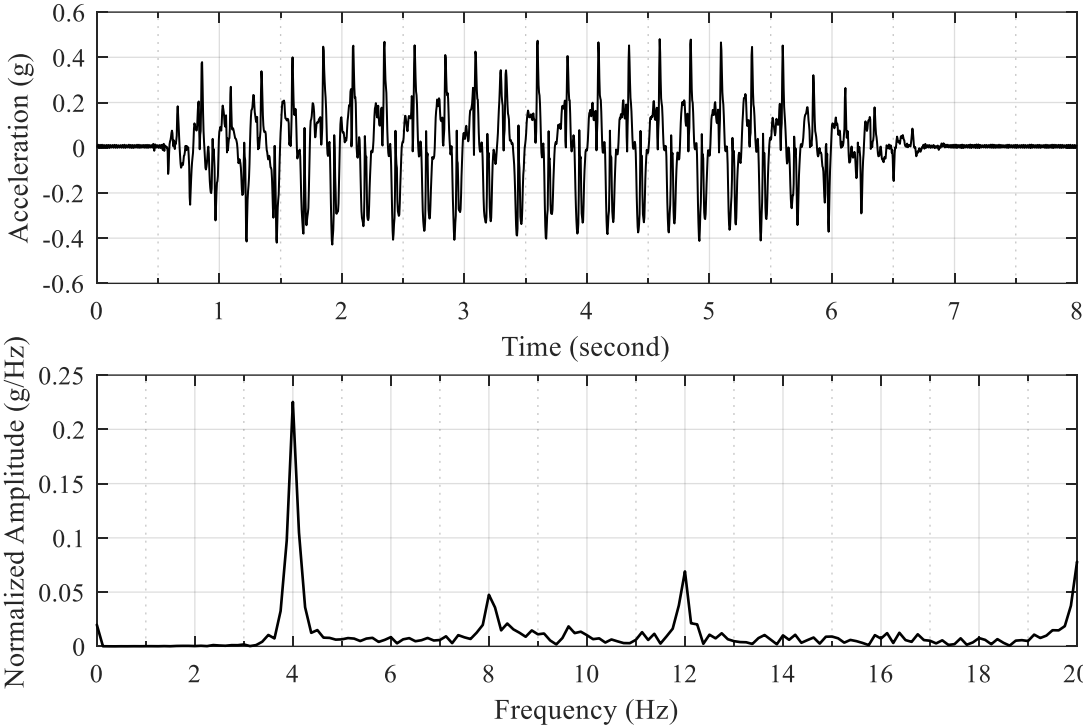


Figure B-66: Acceleration time history of shake table input excitation and the corresponding frequency spectrum for test H6



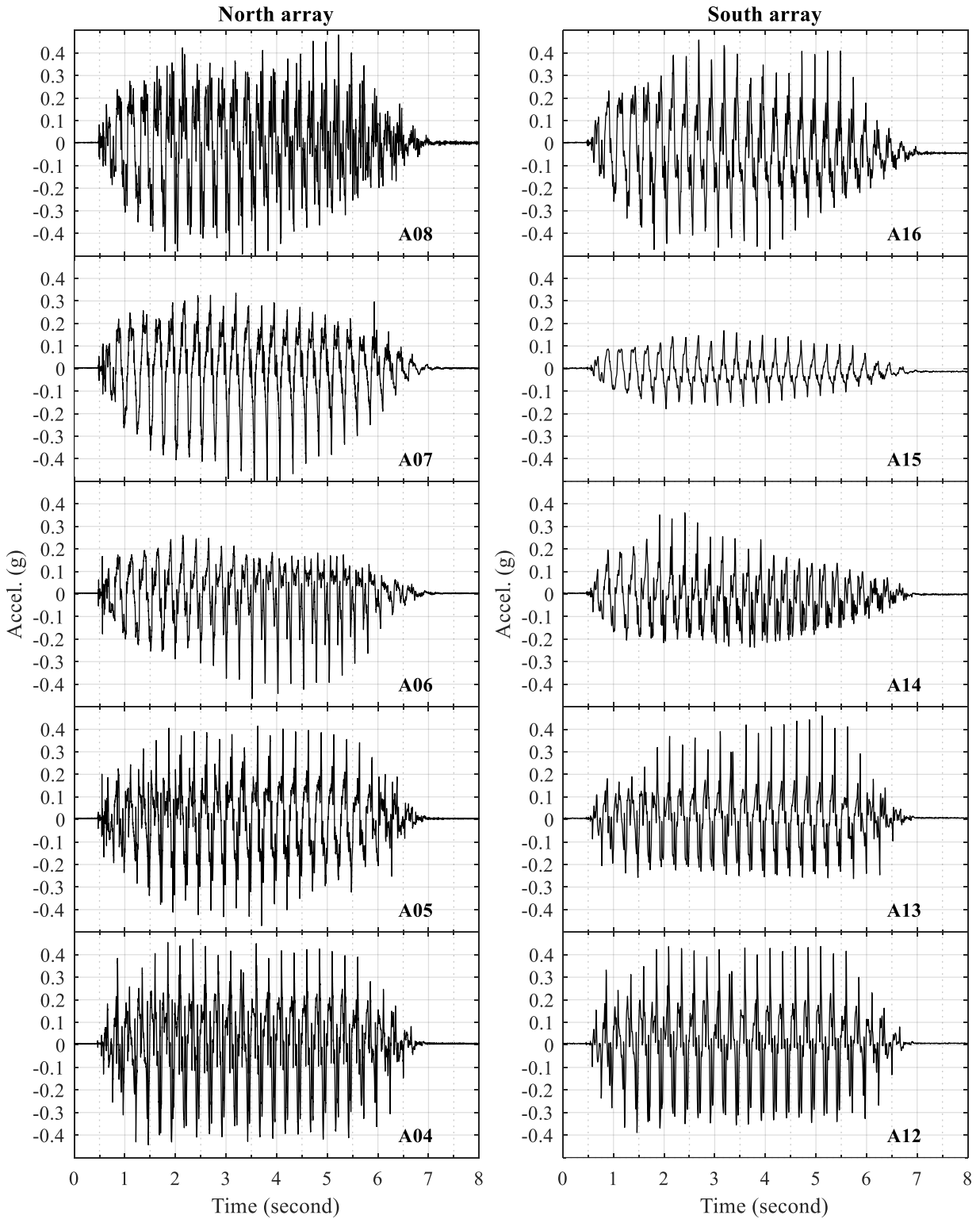


Figure B-67: Time histories of lateral soil acceleration in north and south arrays for test H6

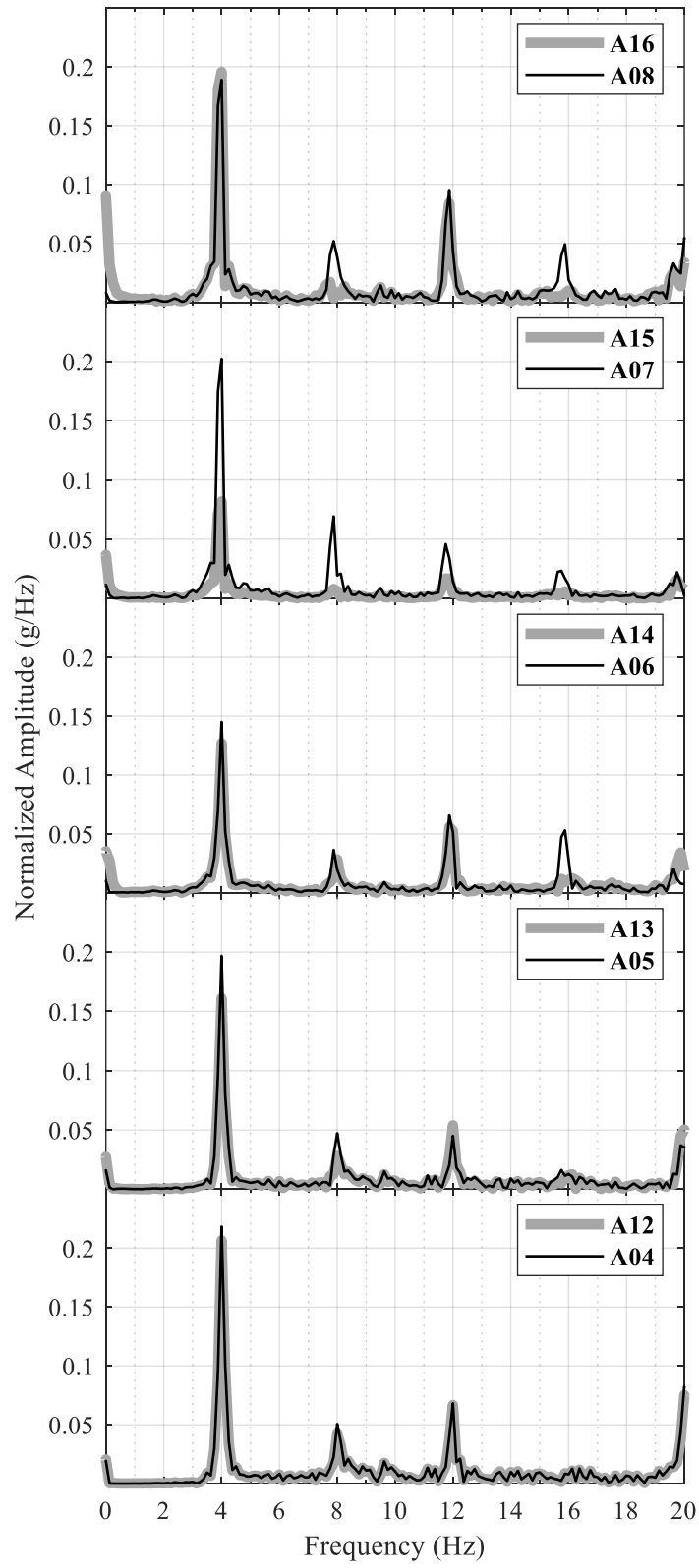


Figure B-68: Frequency spectra of lateral soil acceleration in north and south arrays for test H6

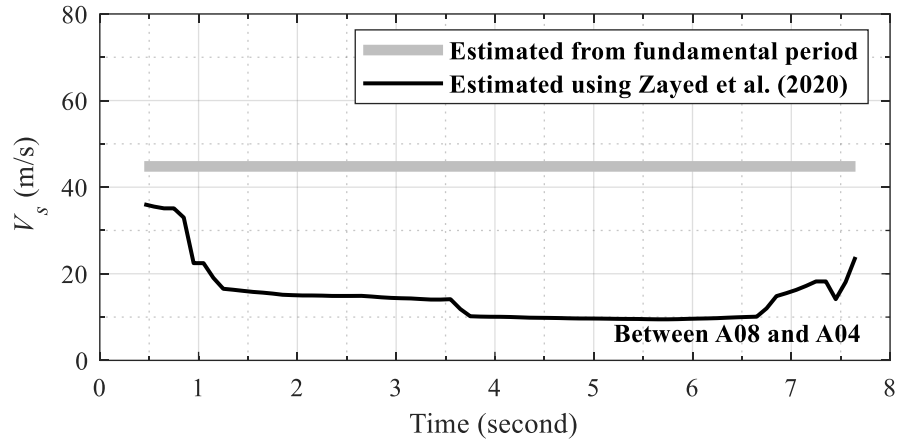


Figure B-69: Change in soil  $V_s$  with time during test H6

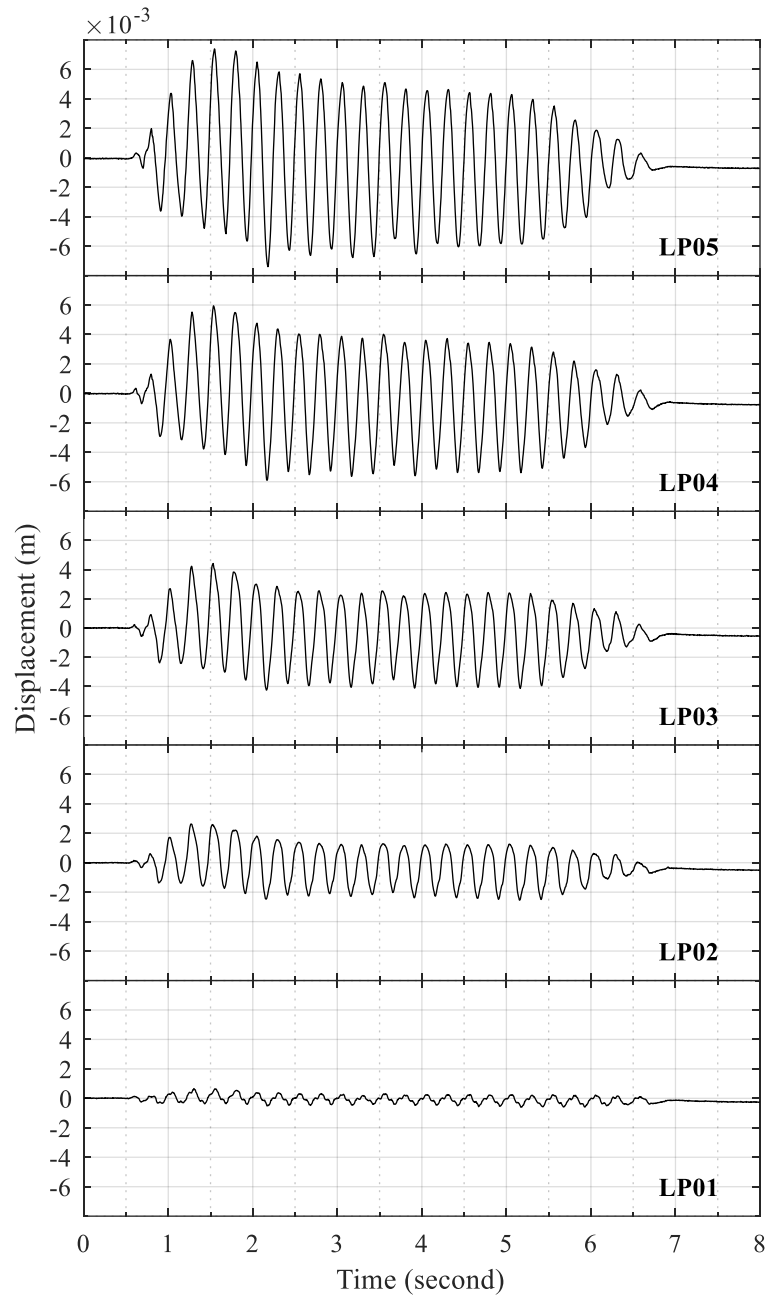


Figure B-70: Time histories of lateral soil displacement relative to laminar container base for test H6

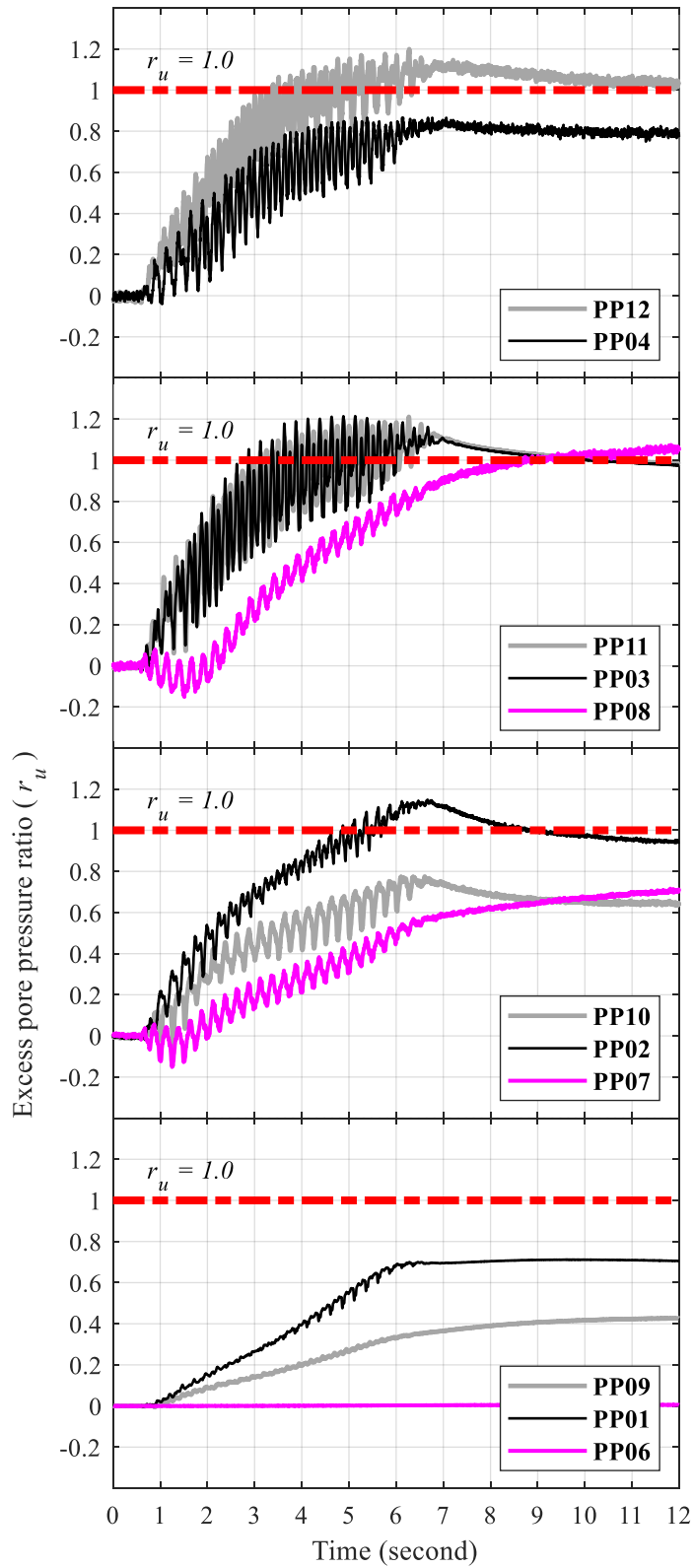


Figure B-71: Time histories of soil excess pore pressure for test H6

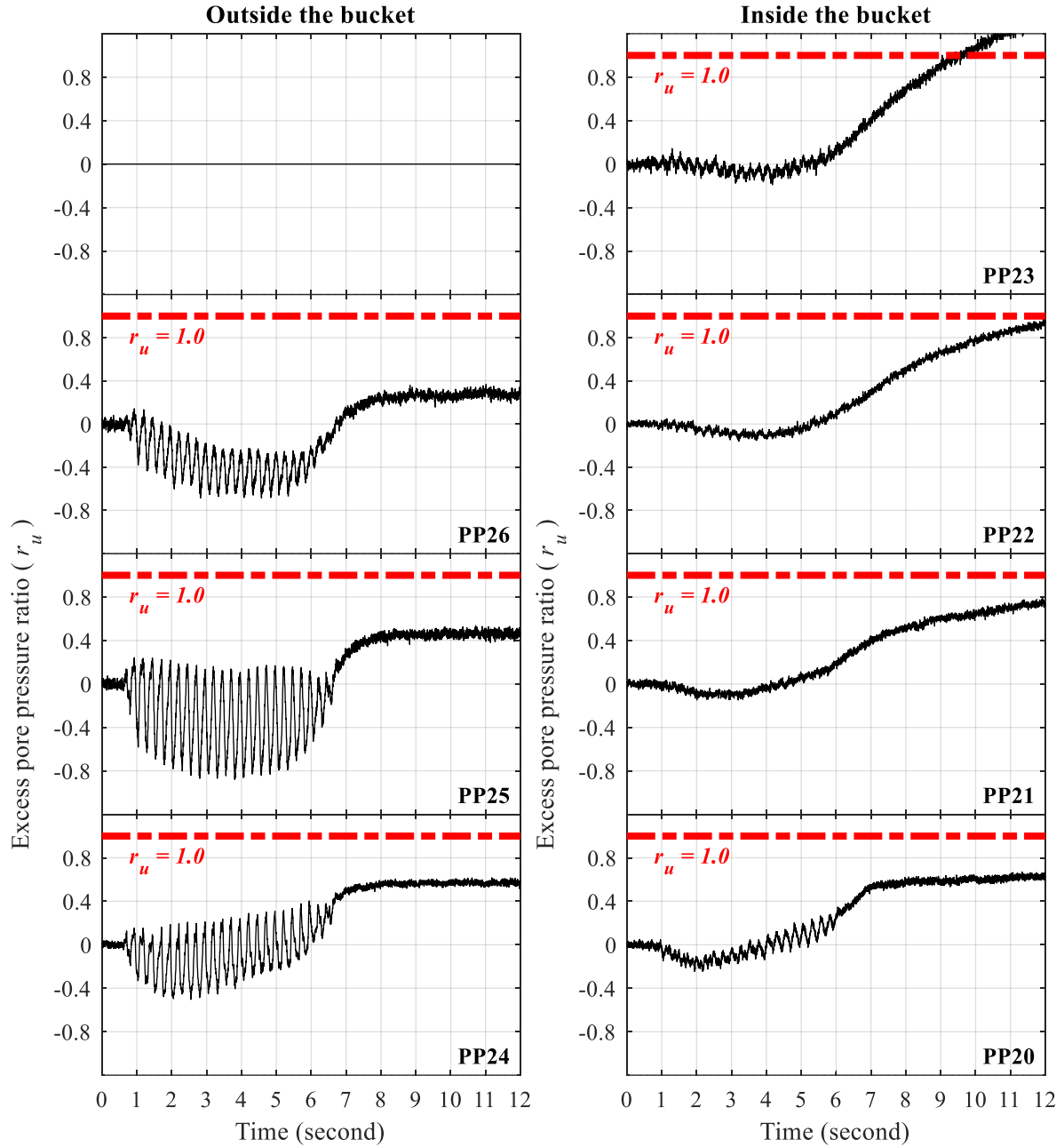


Figure B-72: Time histories of excess pore pressure at north edge of suction bucket for test H6

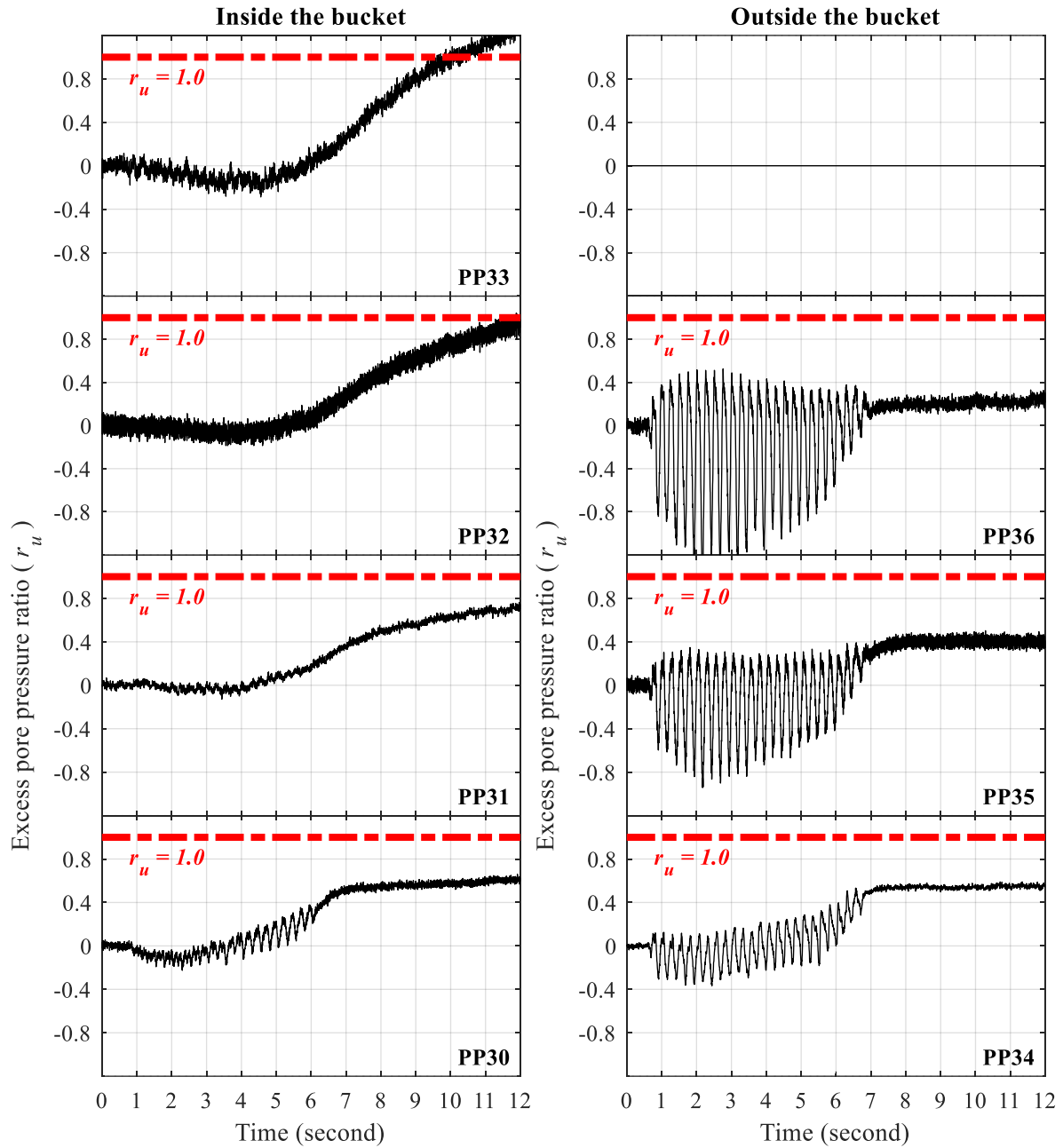


Figure B-73: Time histories of excess pore pressure at south edge of suction bucket for test H6

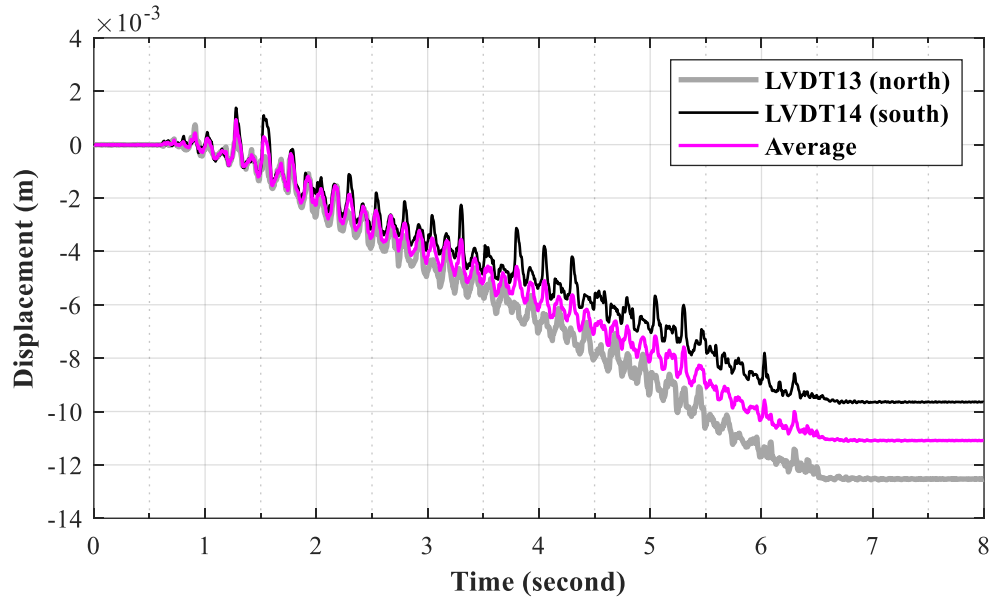


Figure B-74: Time histories of vertical bucket displacement for test H6



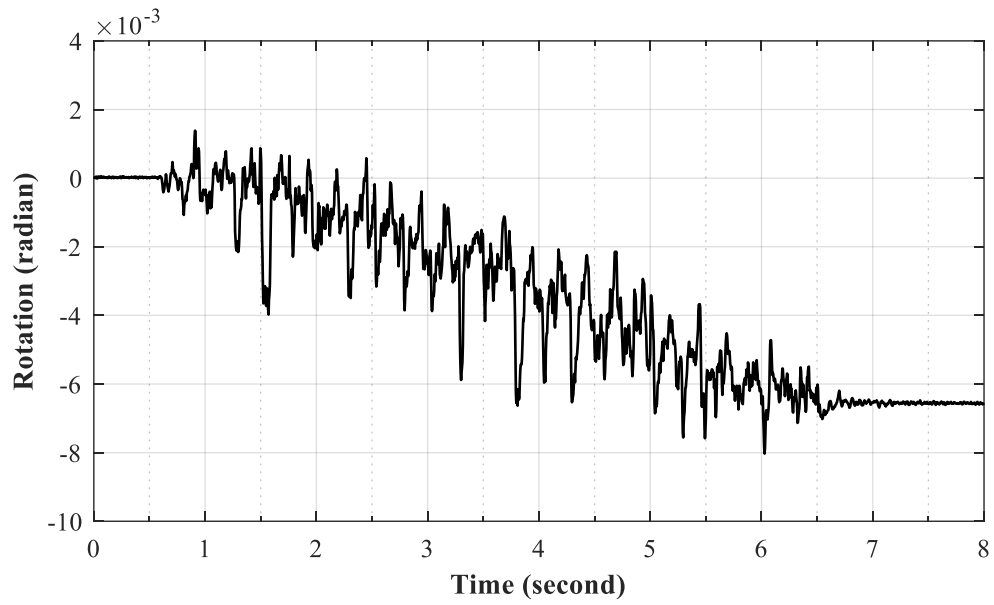


Figure B-75: Time history of suction bucket rotation for test H6

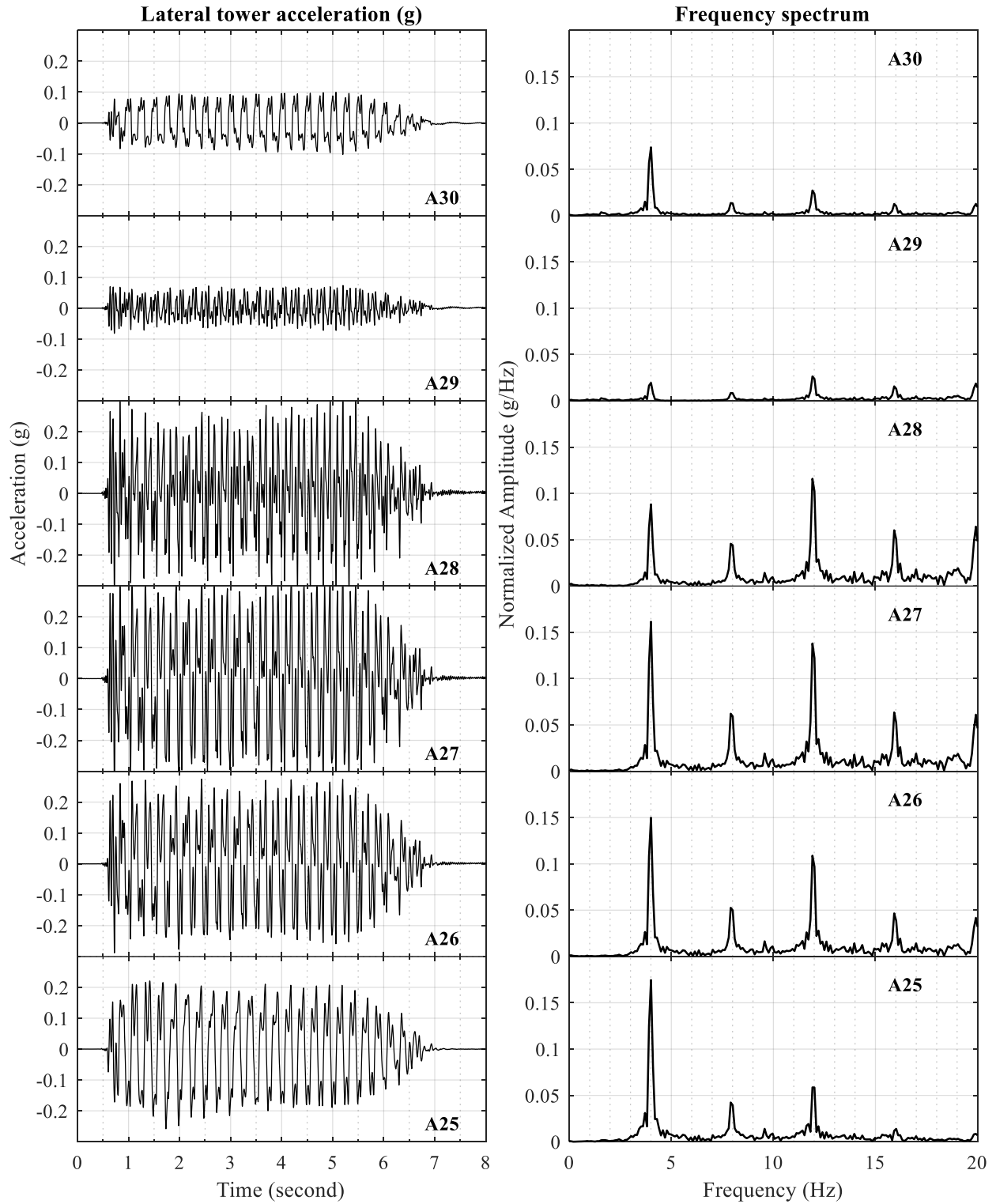


Figure B-76: Time histories of lateral tower acceleration for test H6

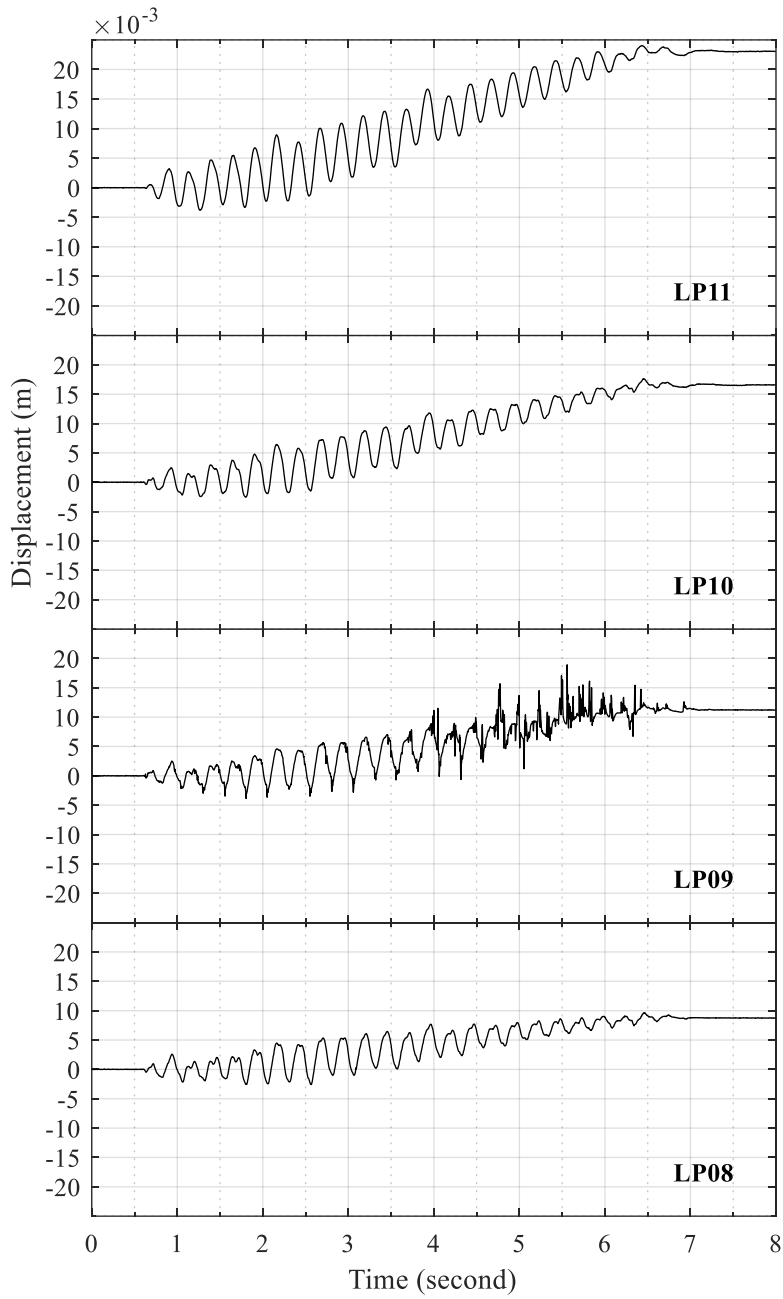


Figure B-77: Time histories of lateral tower displacement relative to lateral soil displacement at the foundation level (LP05) for test H6

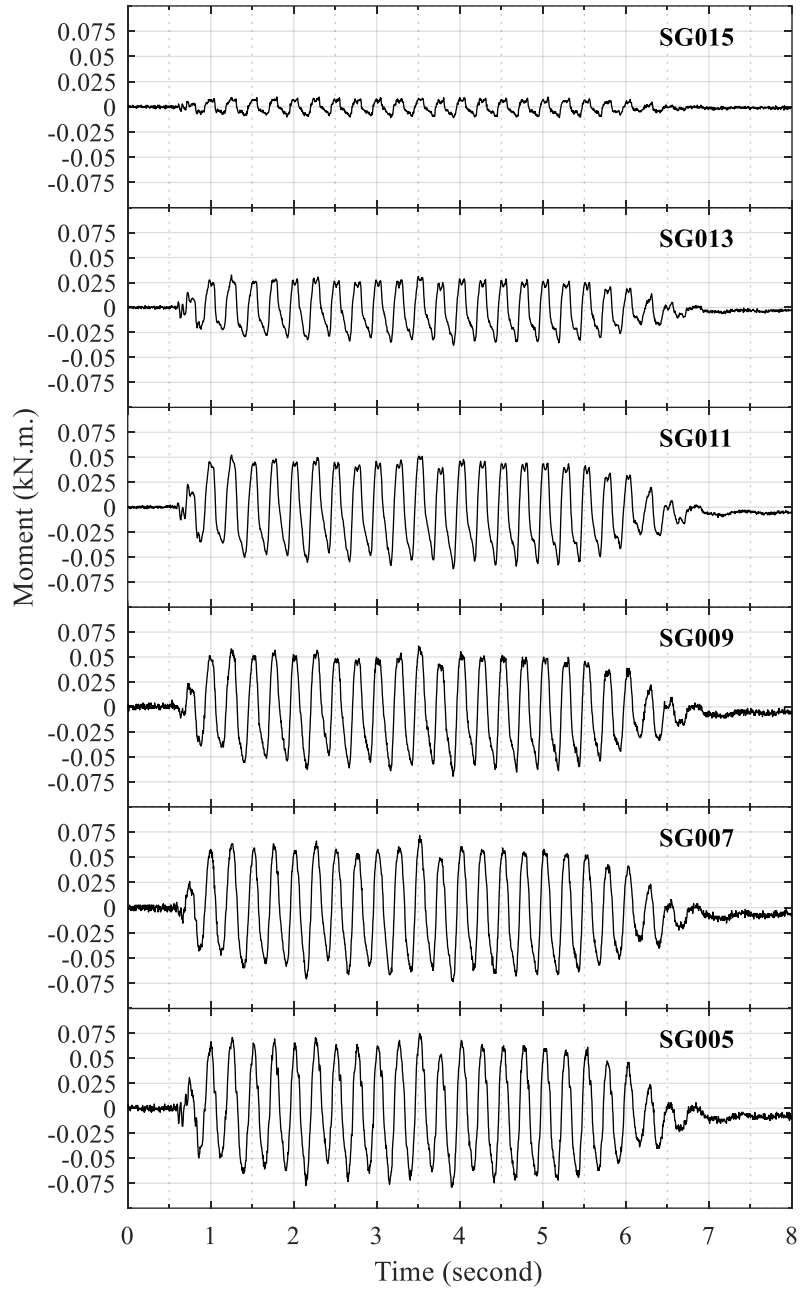


Figure B-78: Time histories of tower bending moment for test H6

### B.7 Test H7

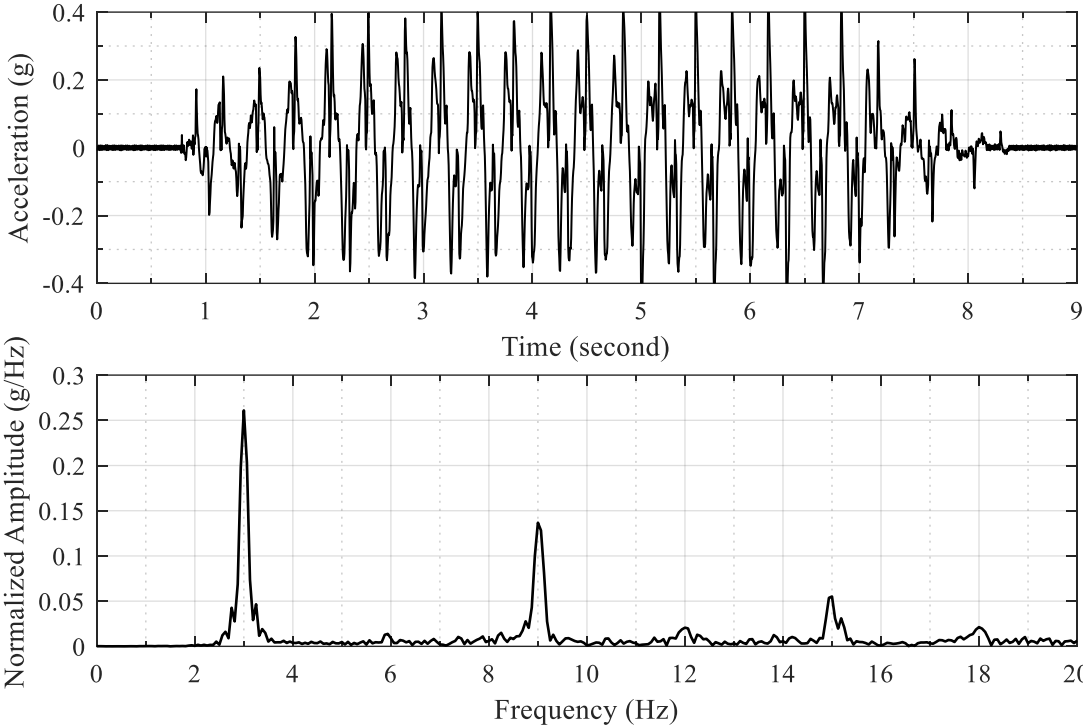


Figure B-79: Acceleration time history of shake table input excitation and the corresponding frequency spectrum for test H7

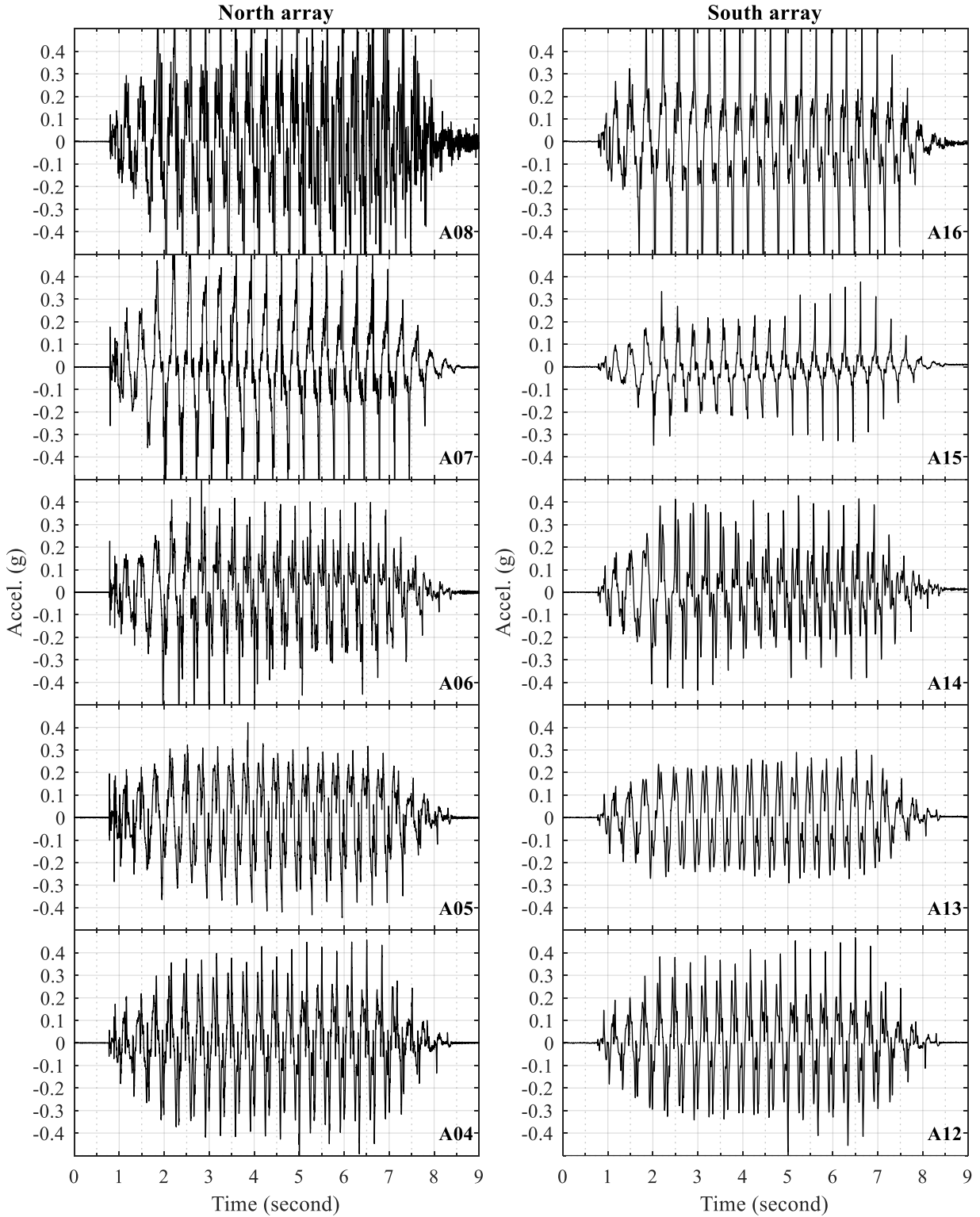


Figure B-80: Time histories of lateral soil acceleration in north and south arrays for test H7

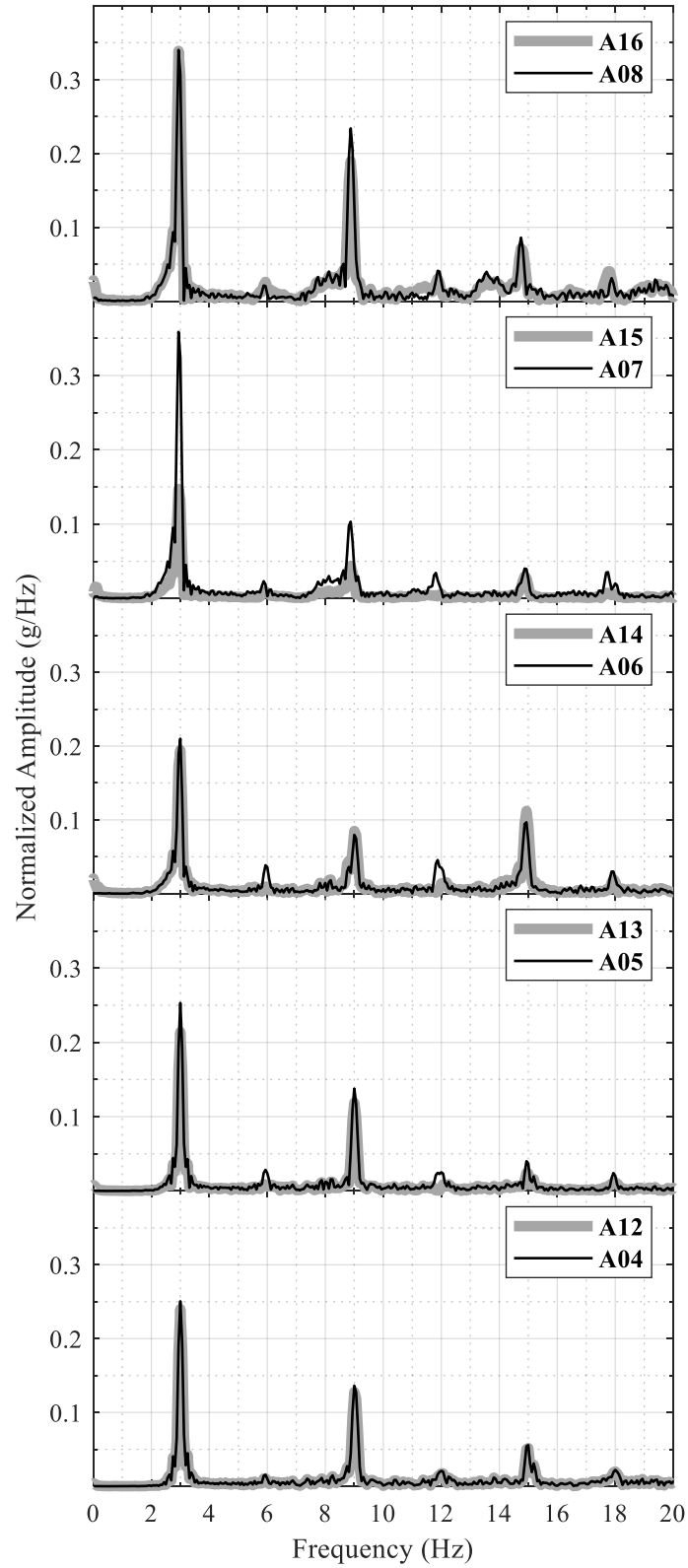


Figure B-81: Frequency spectra of lateral soil acceleration in north and south arrays for test H7

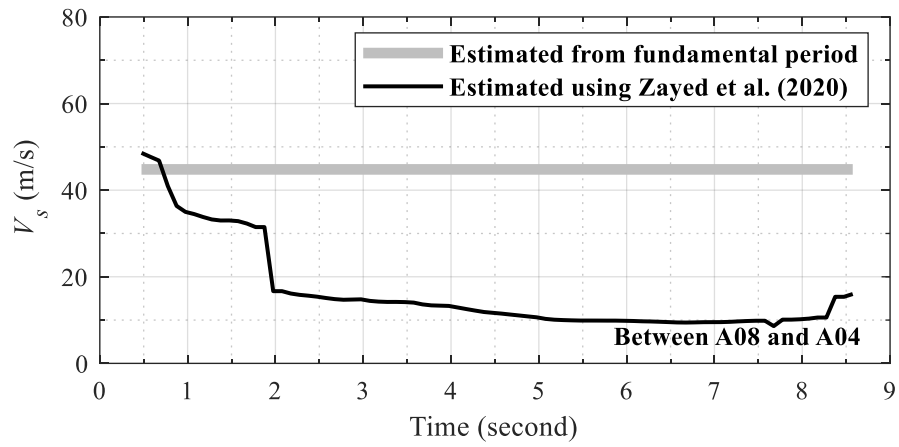


Figure B-82: Change in soil  $V_s$  with time during test H7



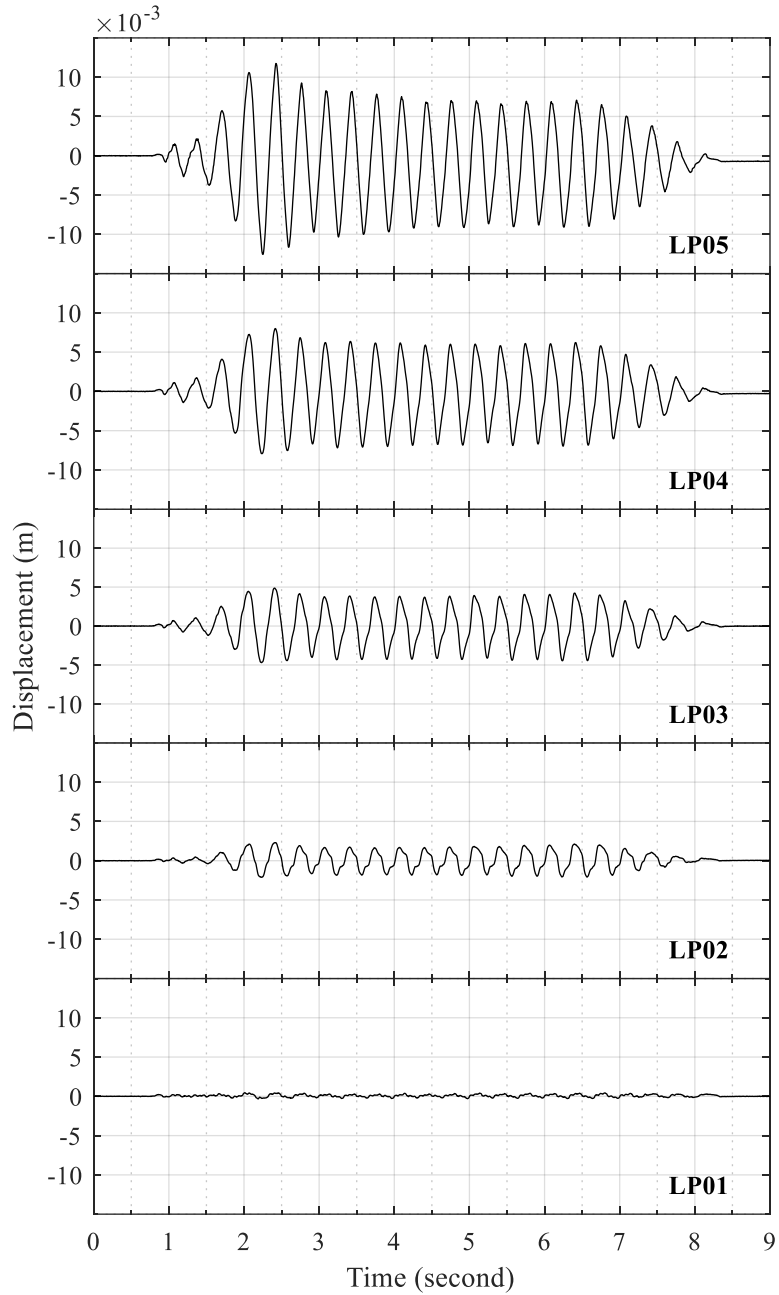


Figure B-83: Time histories of lateral soil displacement relative to laminar container base for test H7

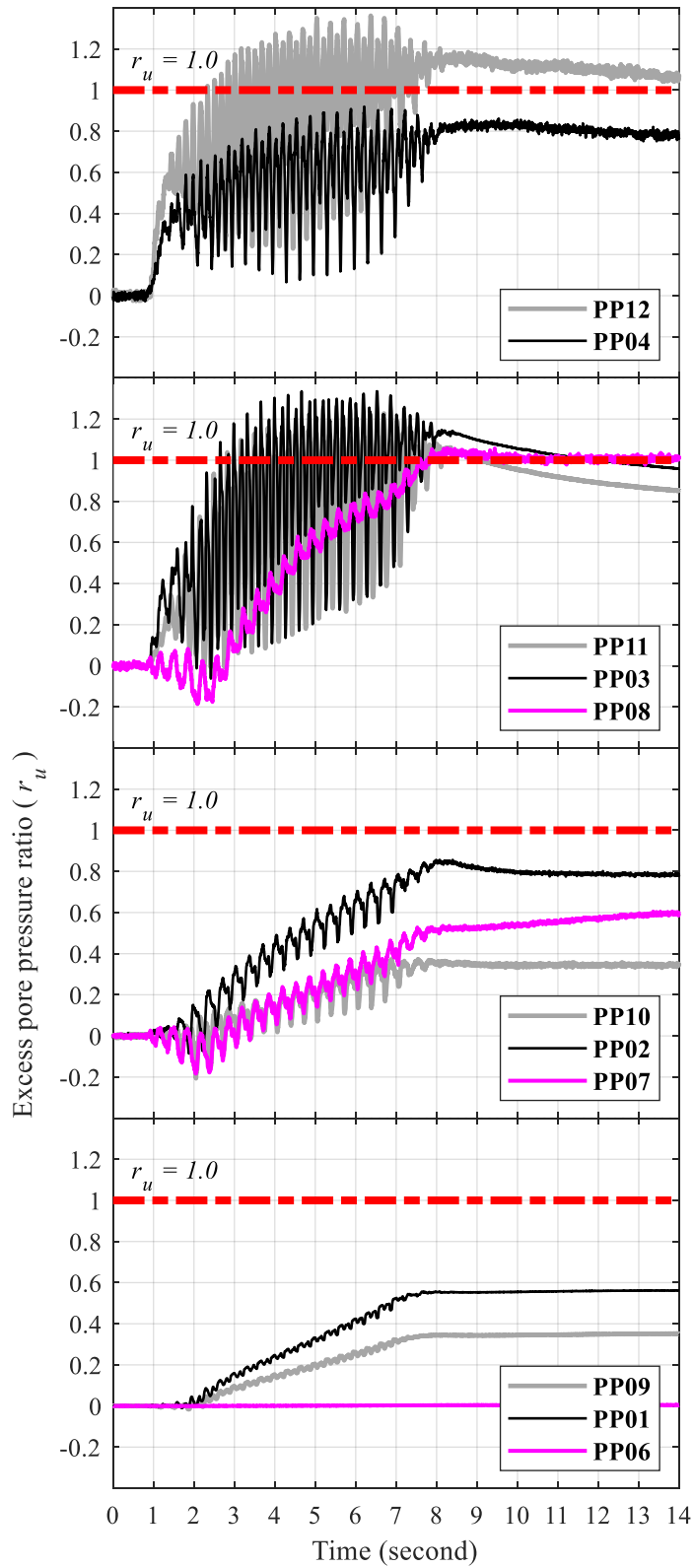


Figure B-84: Time histories of soil excess pore pressure for test H7

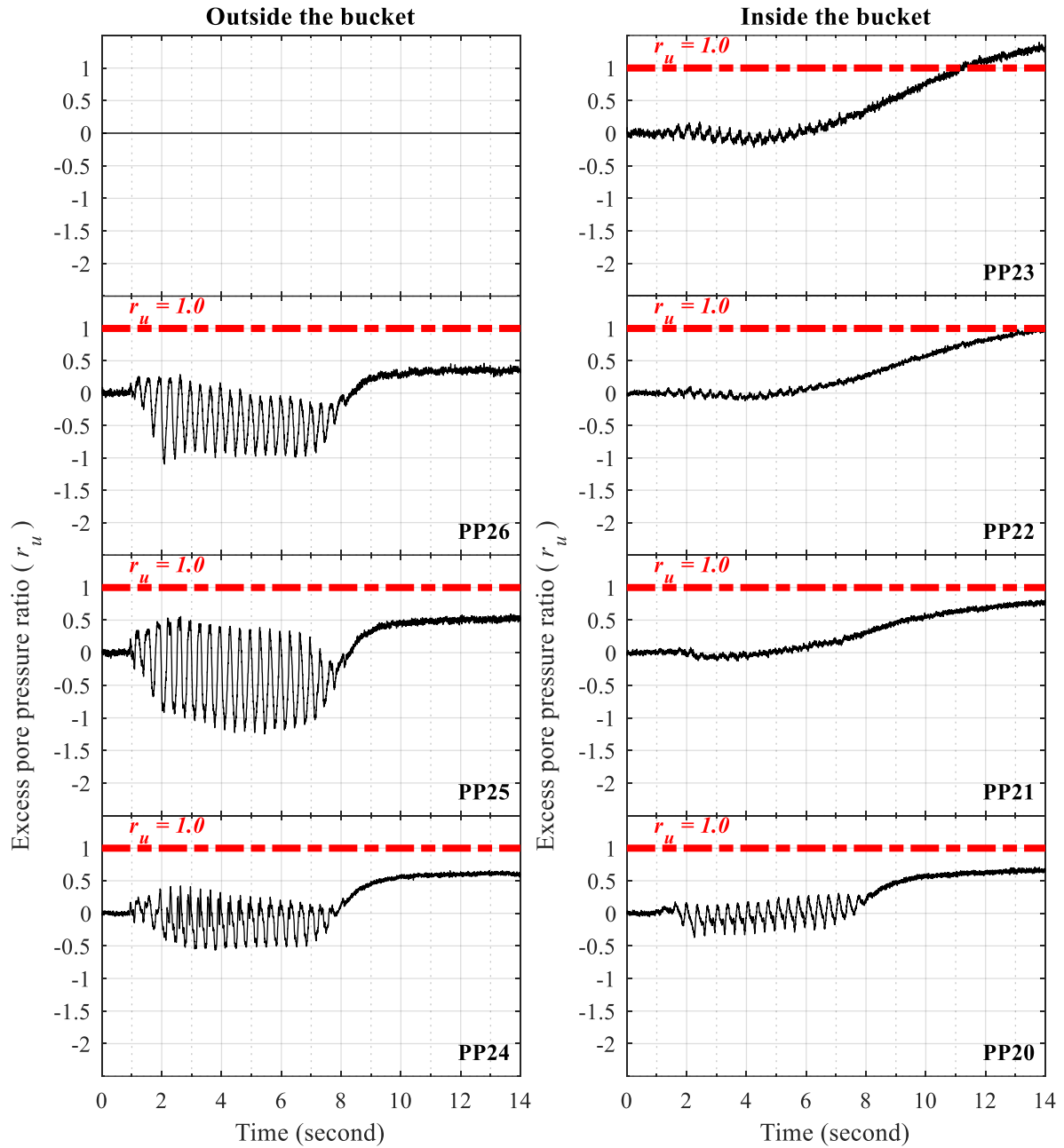


Figure B-85: Time histories of excess pore pressure at north edge of suction bucket for test H7

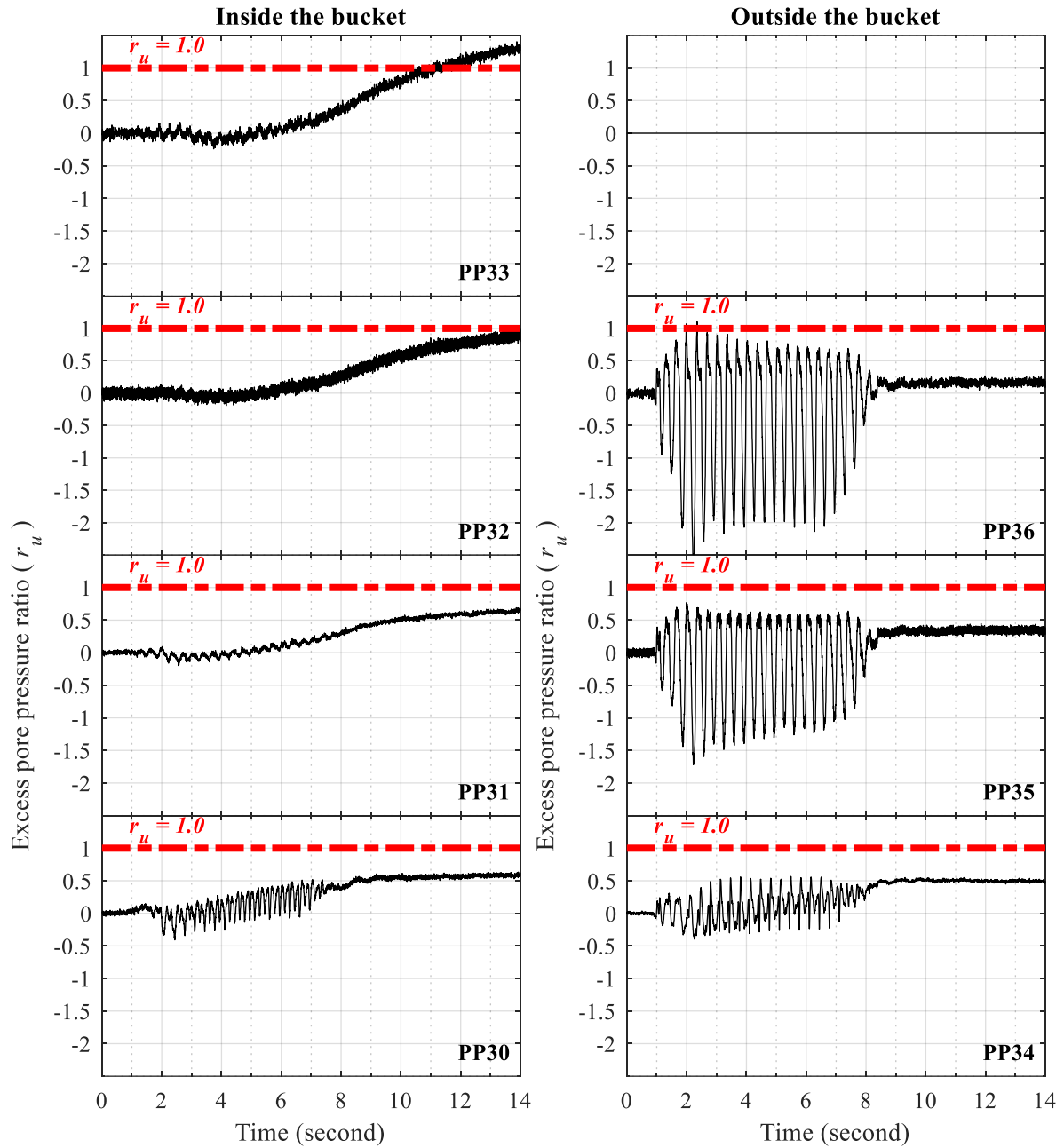


Figure B-86: Time histories of excess pore pressure at south edge of suction bucket for test H7

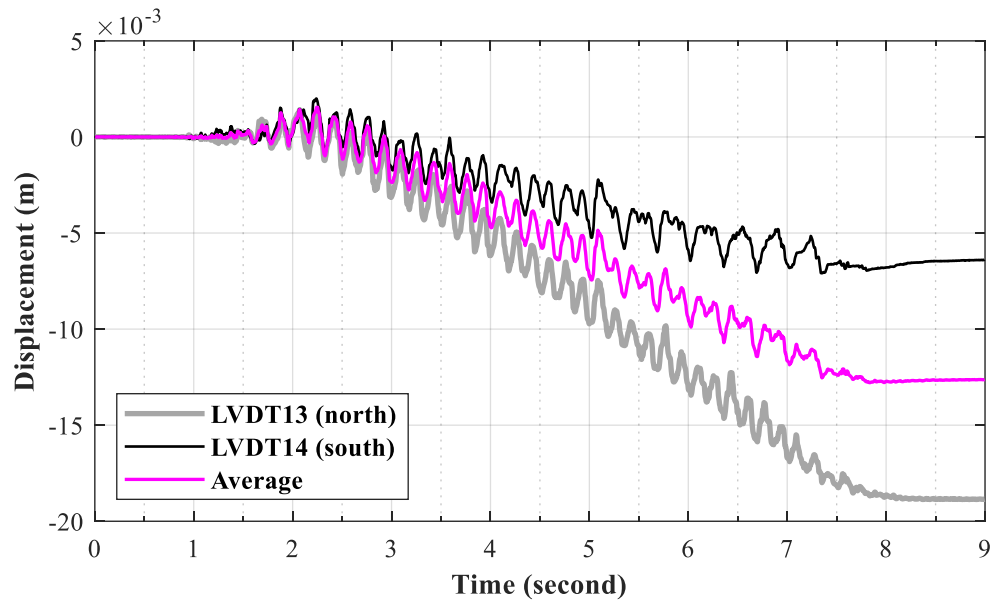


Figure B-87: Time histories of vertical bucket displacement for test H7

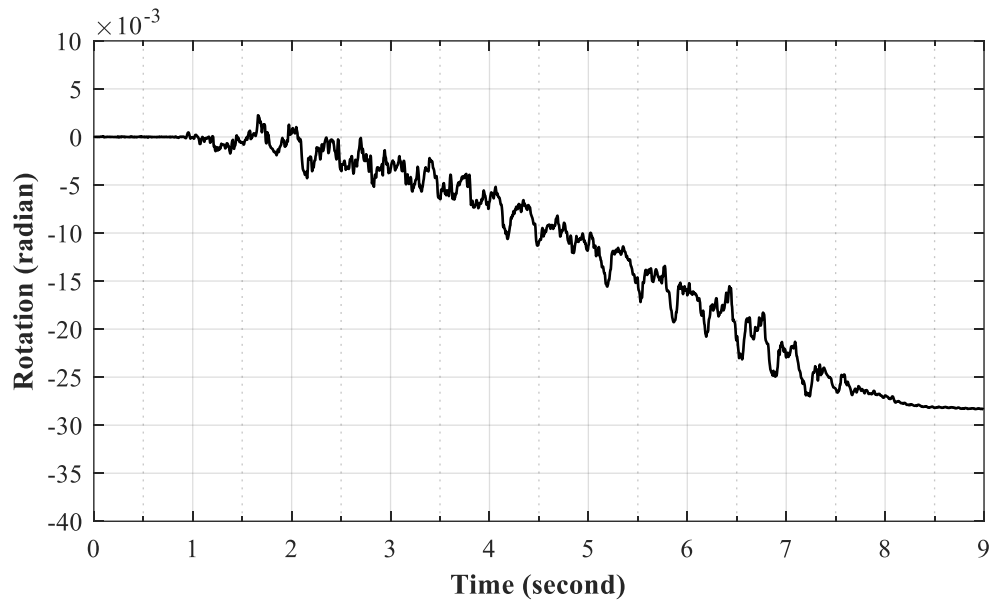


Figure B-88: Time history of suction bucket rotation for test H7

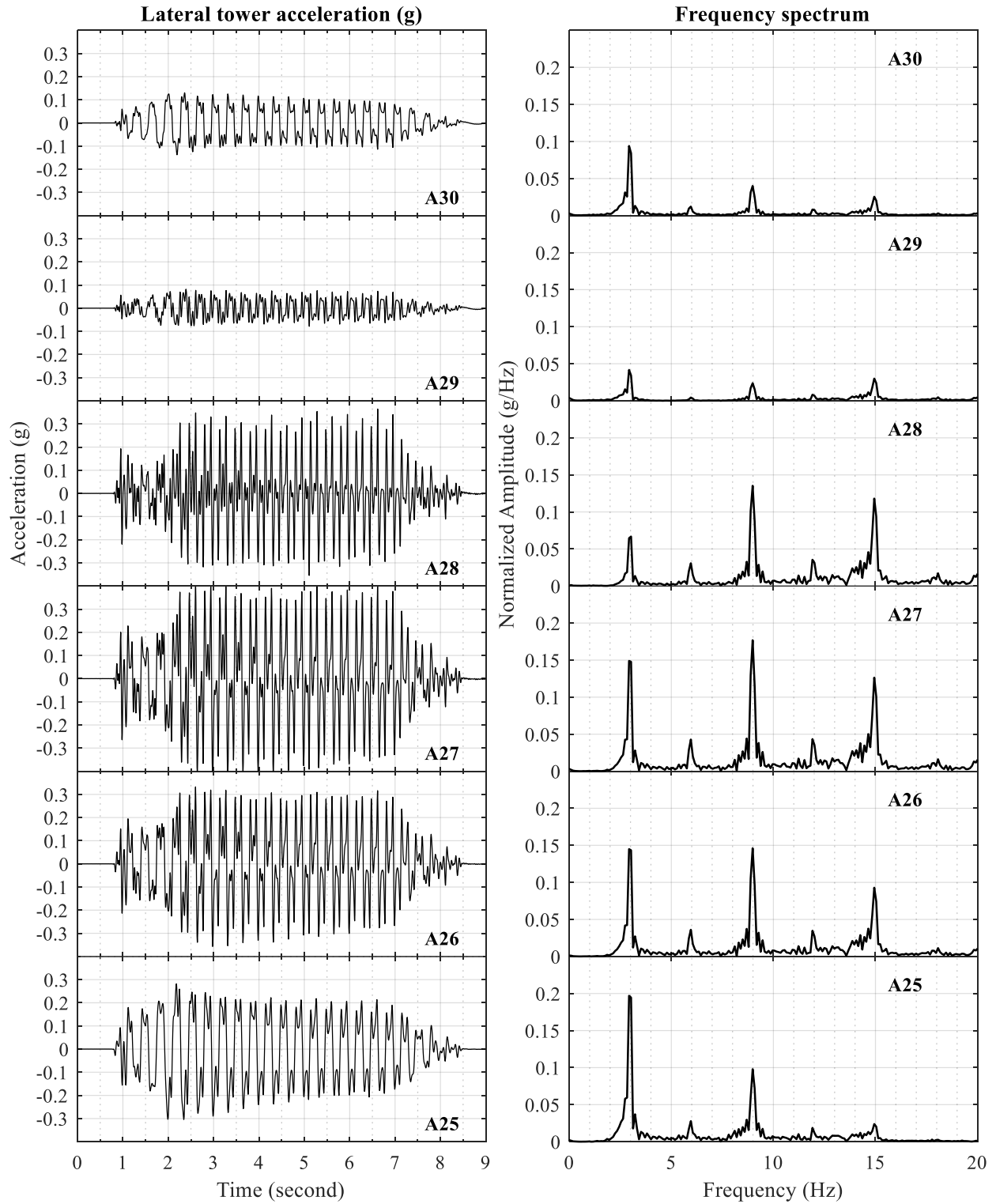


Figure B-89: Time histories of lateral tower acceleration for test H7

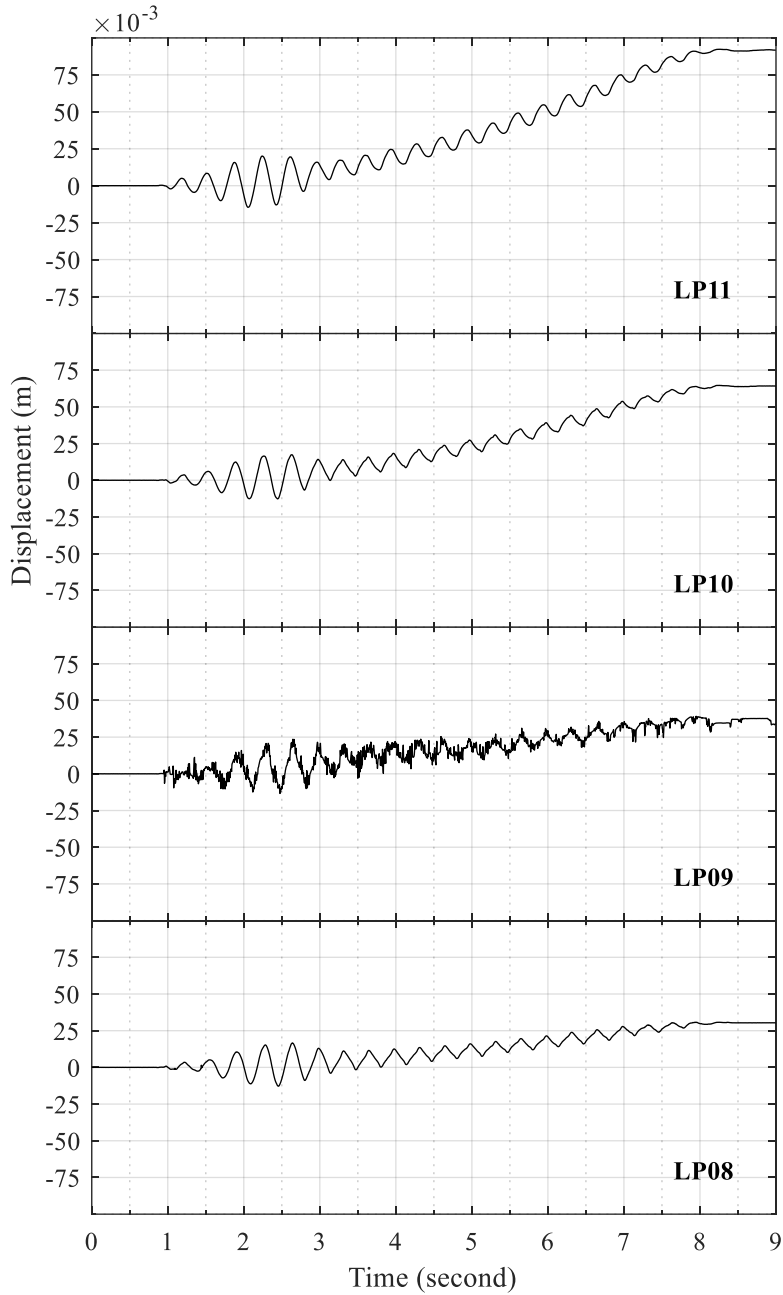


Figure B-90: Time histories of lateral tower displacement relative to lateral soil displacement at the foundation level (LP05) for test H7



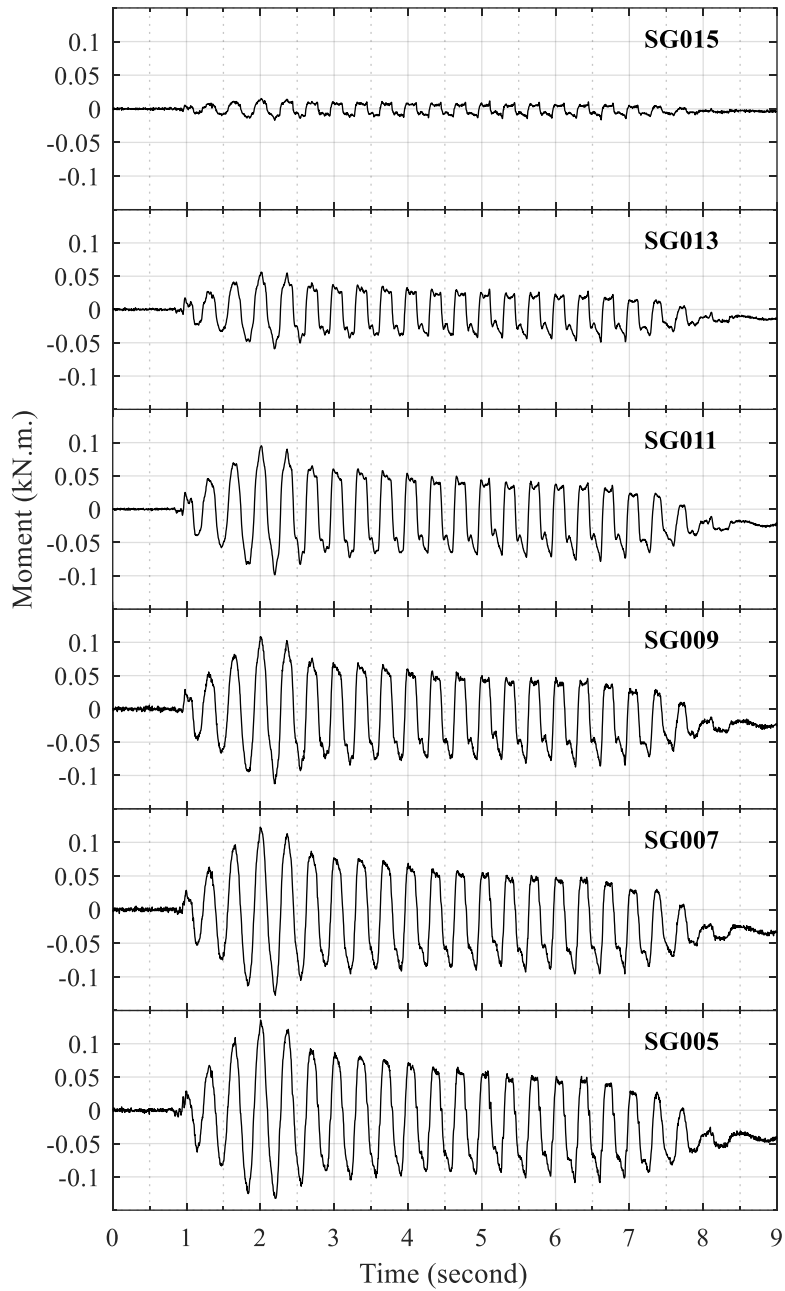


Figure B-91: Time histories of tower bending moment for test H7

### B.8 Test H8

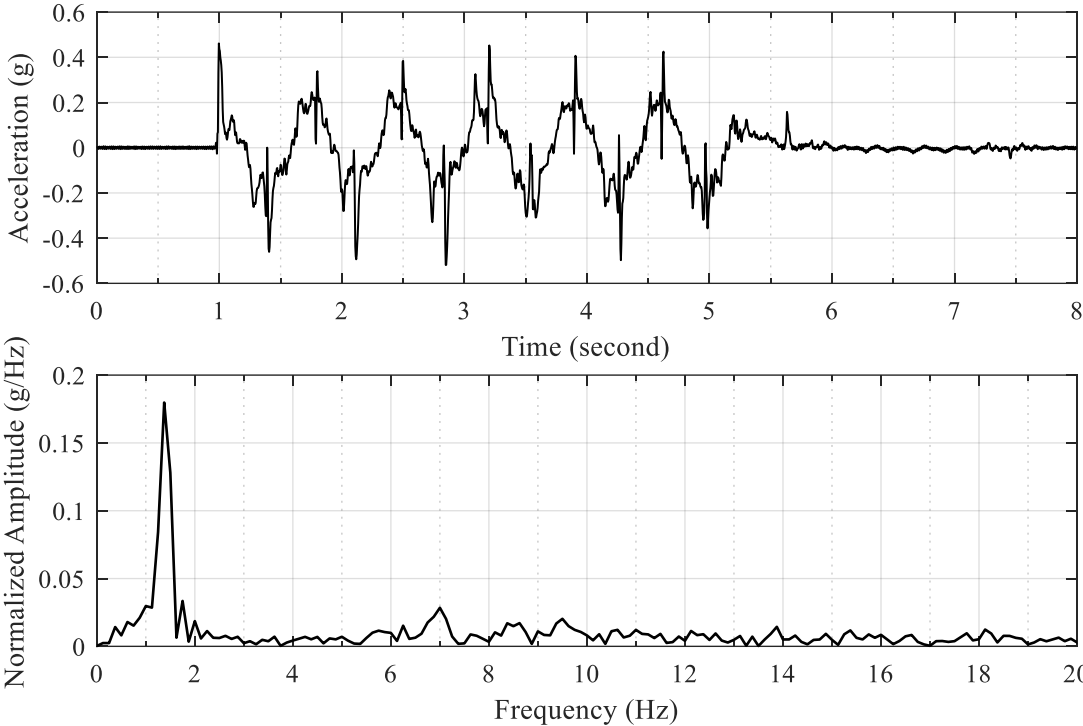


Figure B-92: Acceleration time history of shake table input excitation and the corresponding frequency spectrum for test H8

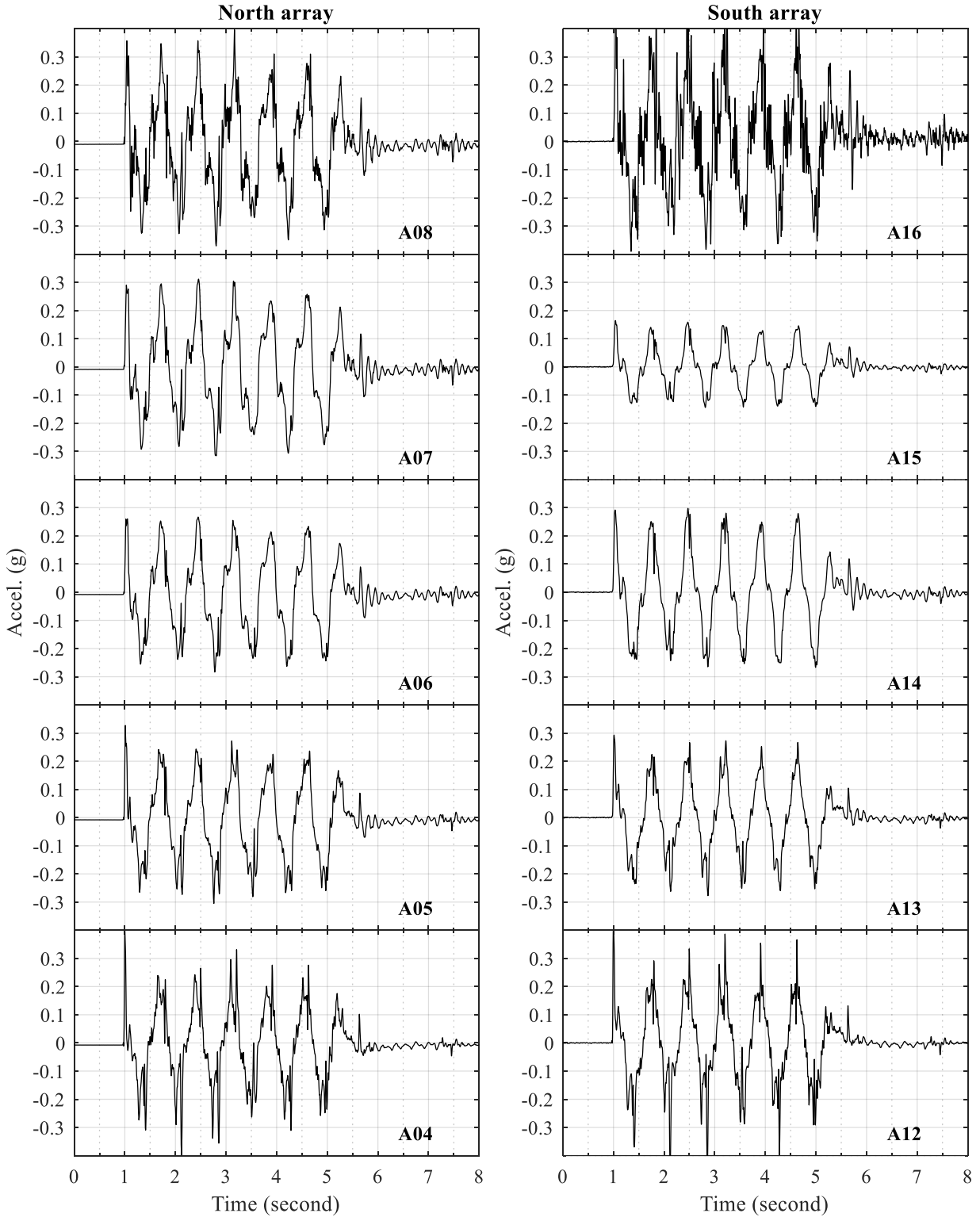


Figure B-93: Time histories of lateral soil acceleration in north and south arrays for test H8

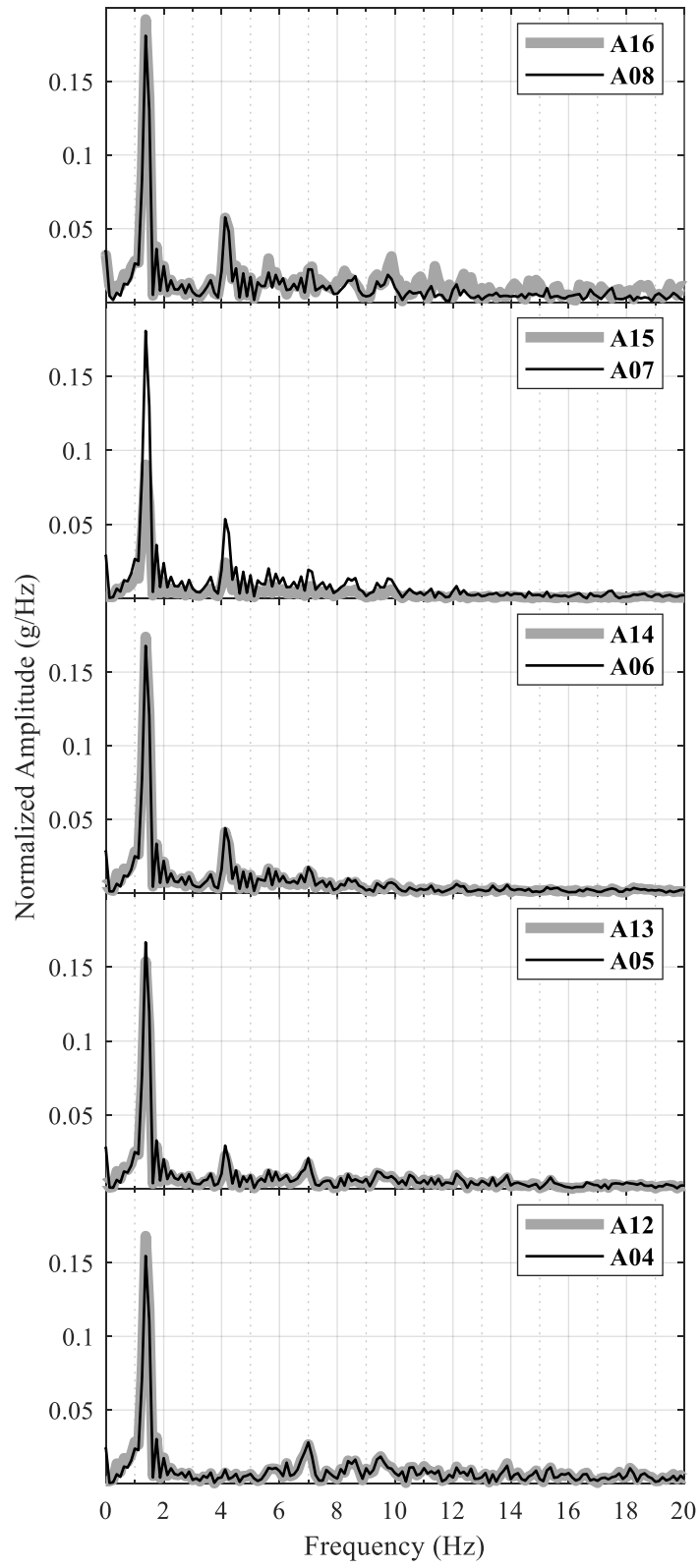


Figure B-94: Frequency spectra of lateral soil acceleration in north and south arrays for test H8

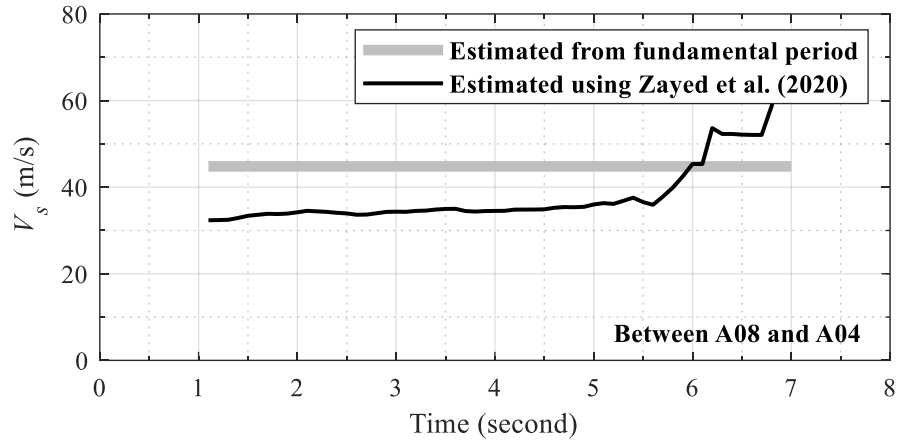


Figure B-95: Change in soil  $V_s$  with time during test H8

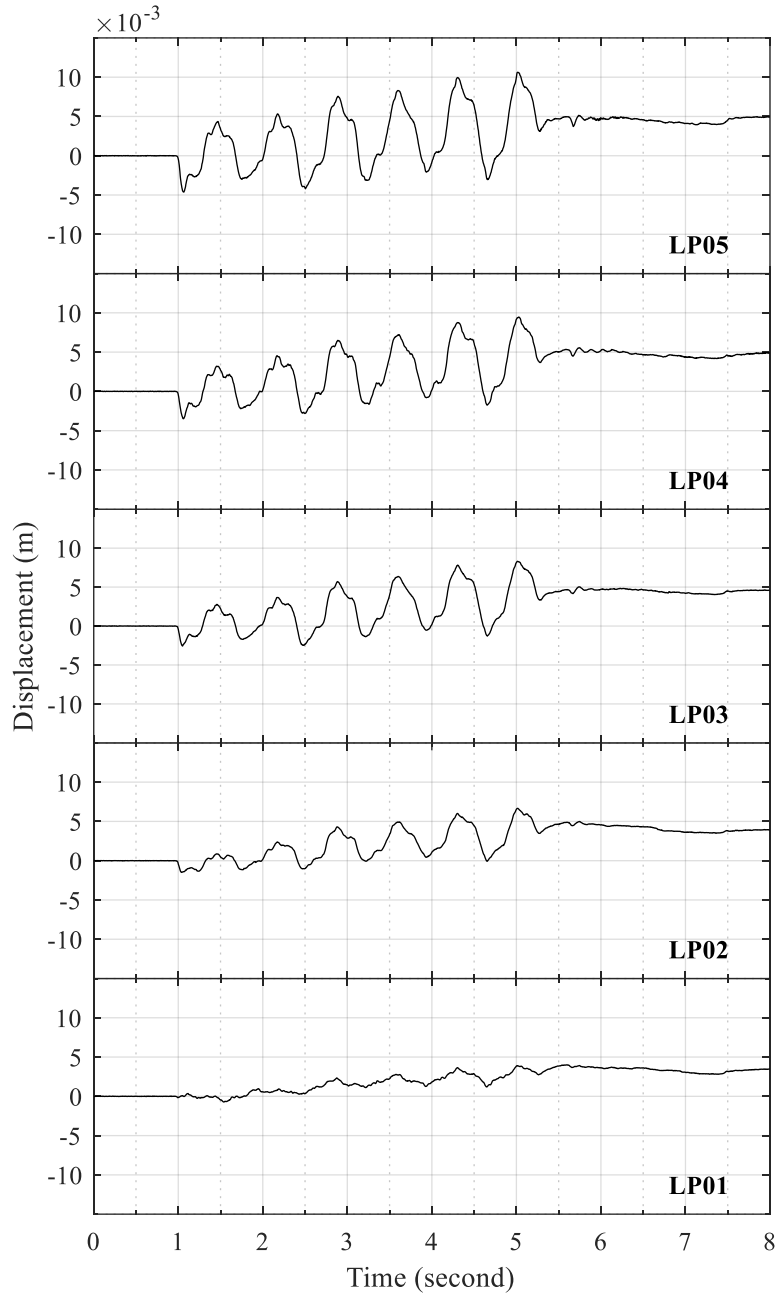


Figure B-96: Time histories of lateral soil displacement relative to laminar container base for test H8

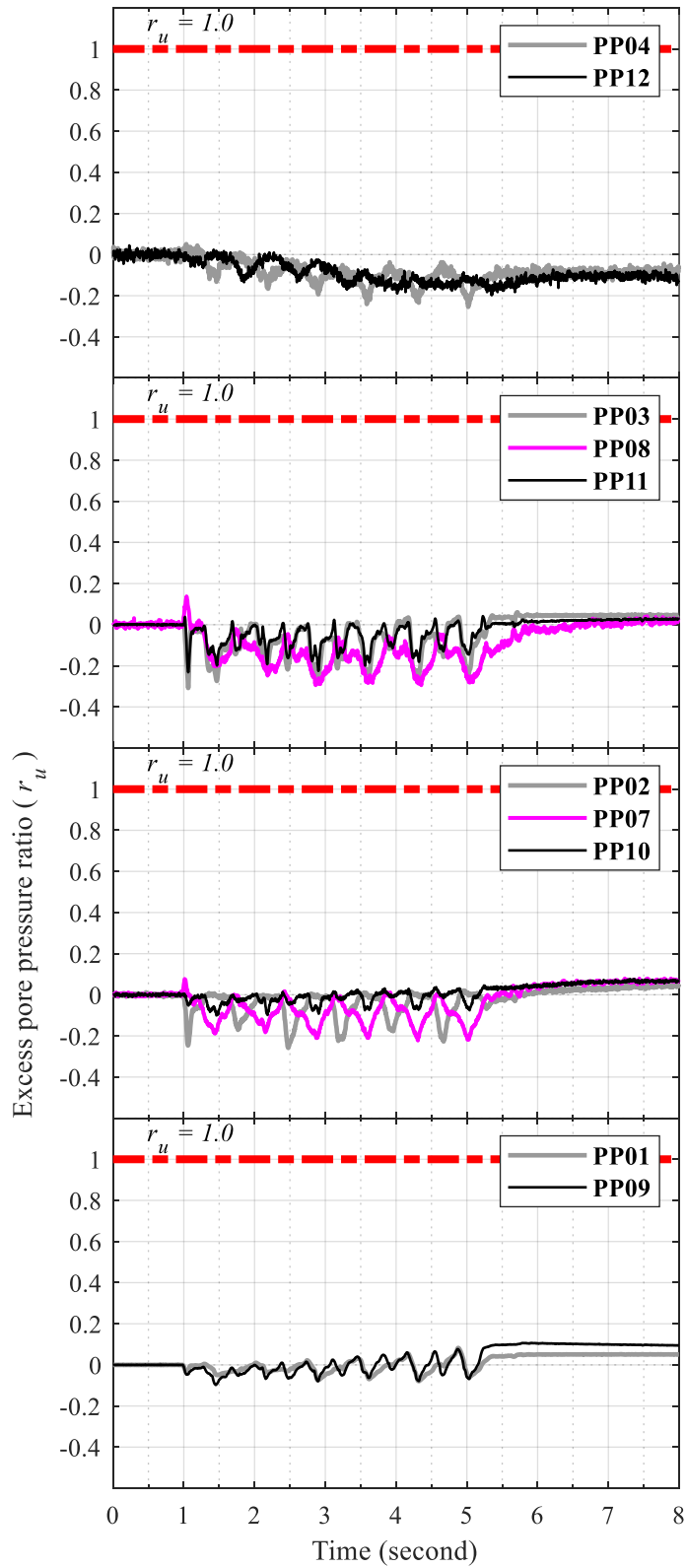


Figure B-97: Time histories of soil excess pore pressure for test H8

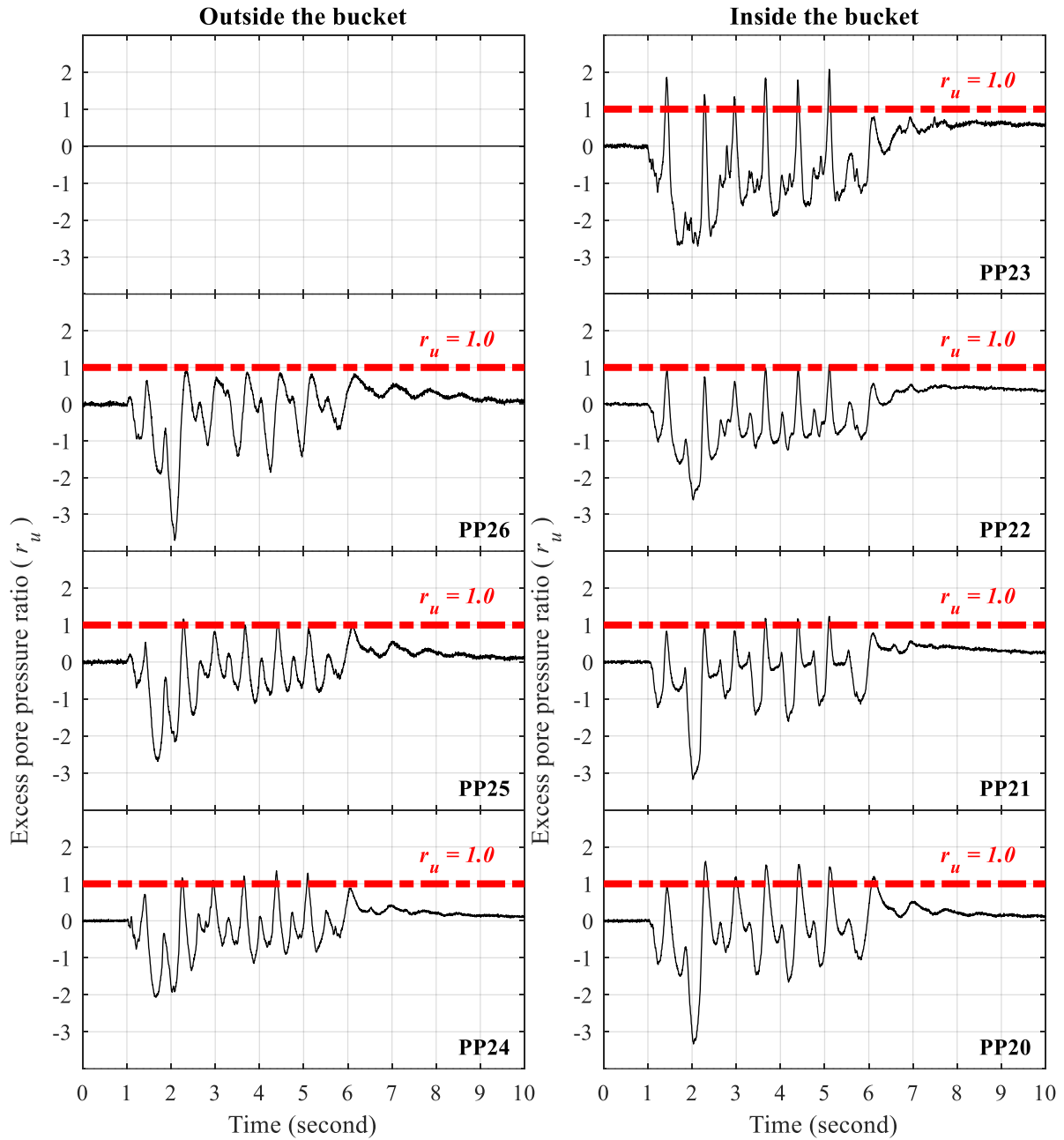


Figure B-98: Time histories of excess pore pressure at north edge of suction bucket for test H8



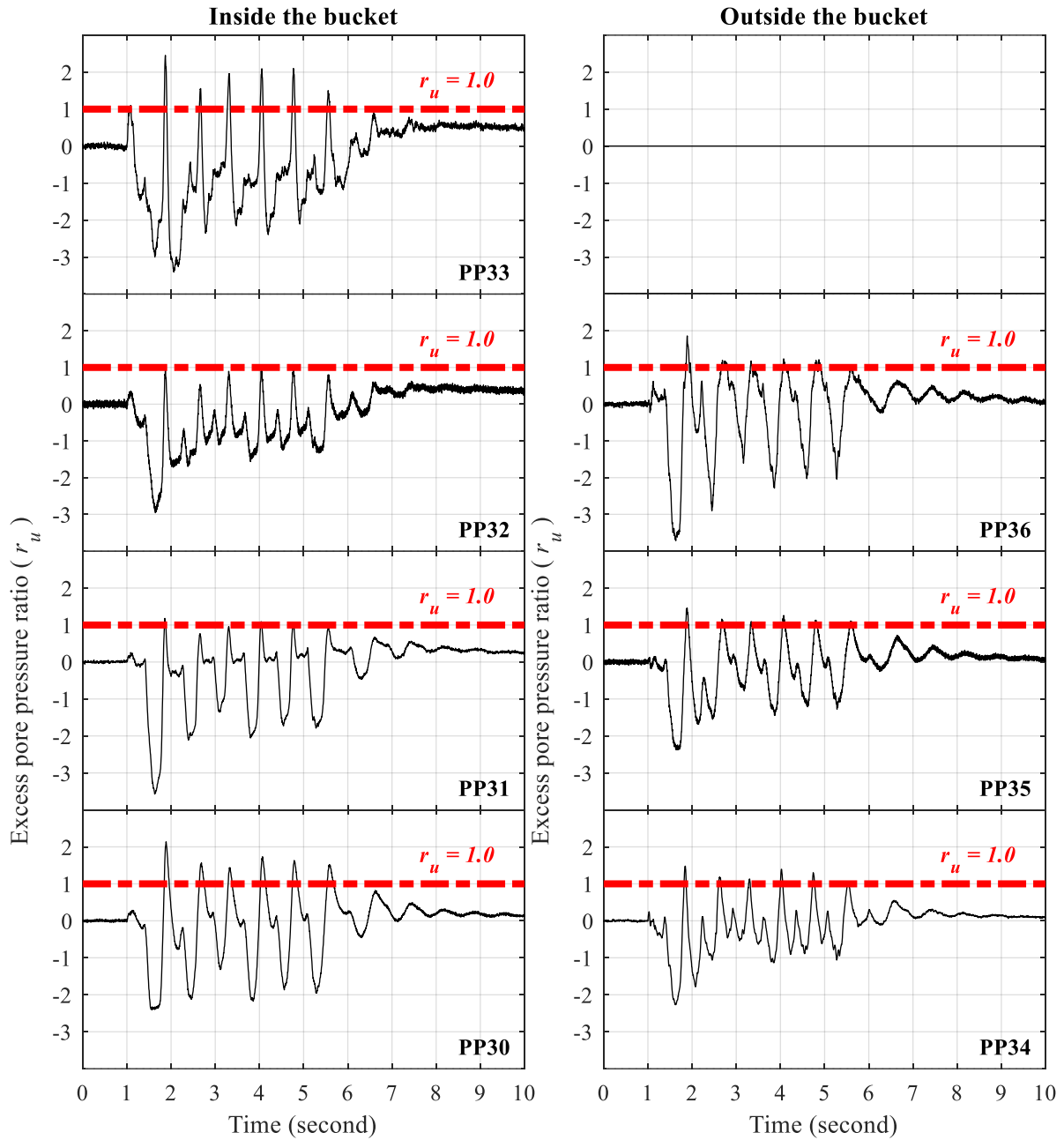


Figure B-99: Time histories of excess pore pressure at south edge of suction bucket for test H8

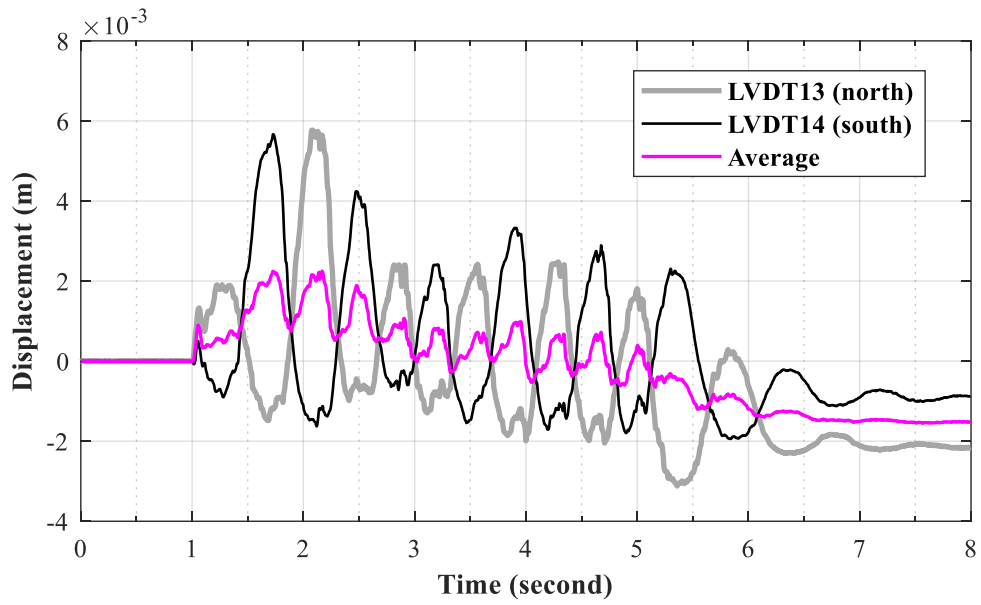


Figure B-100: Time histories of vertical bucket displacement for test H8

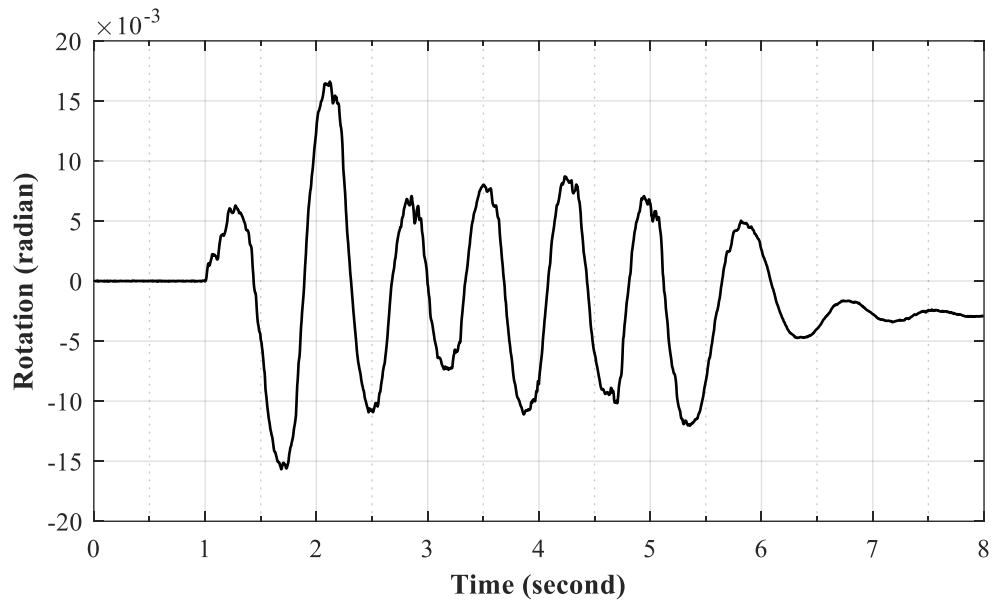


Figure B-101: Time history of suction bucket rotation for test H8

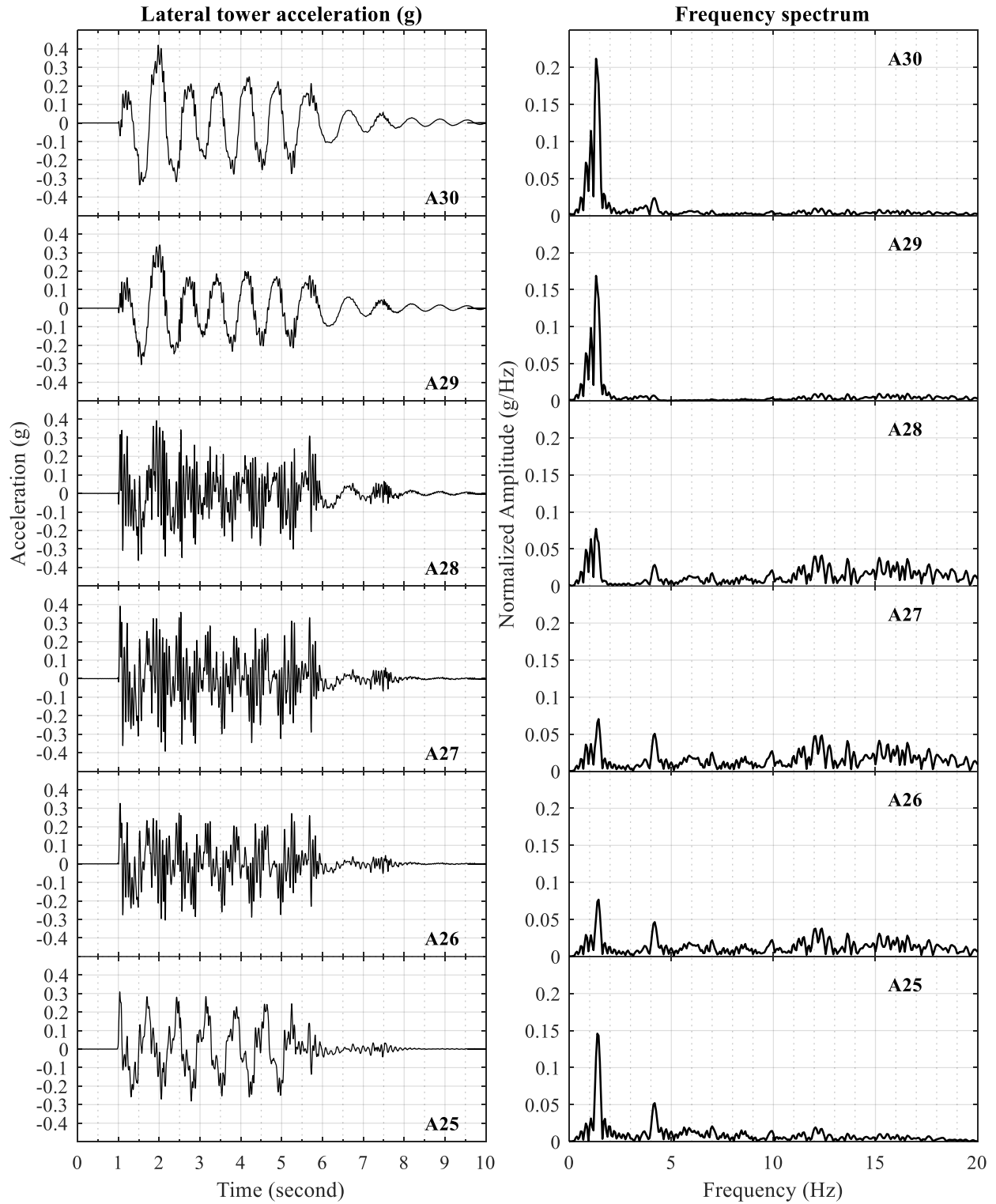


Figure B-102: Time histories of lateral tower acceleration for test H8

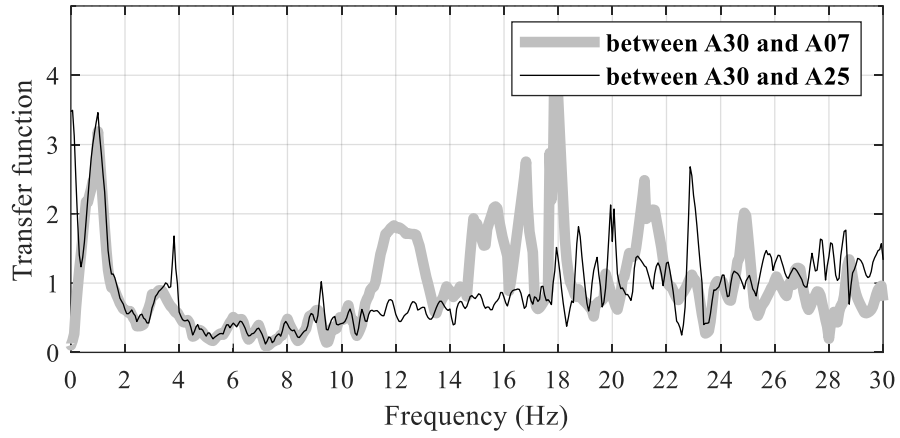


Figure B-103: Transfer function between accelerations at tower top (A30) and at soil top near the suction bucket foundation (A08) for test H8

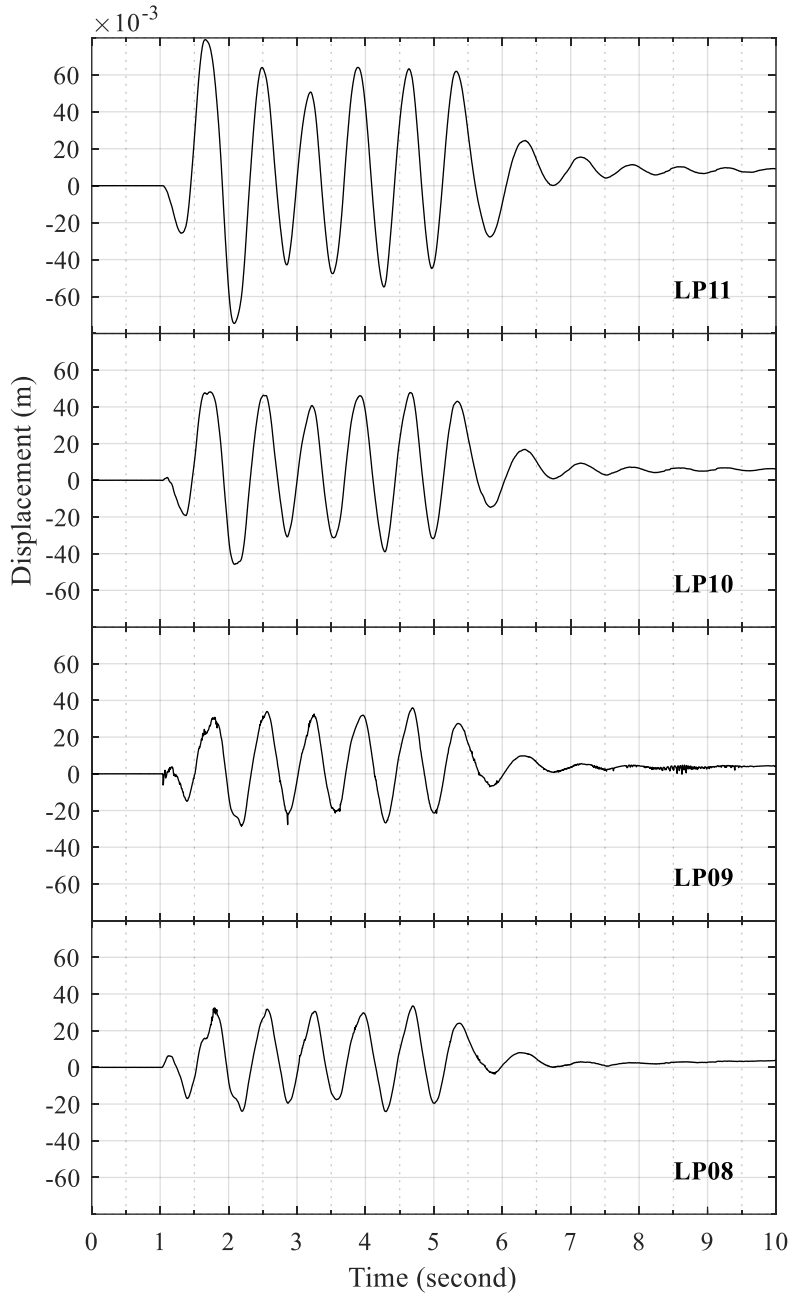


Figure B-104: Time histories of lateral tower displacement relative to lateral soil displacement at the foundation level (LP05) for test H8

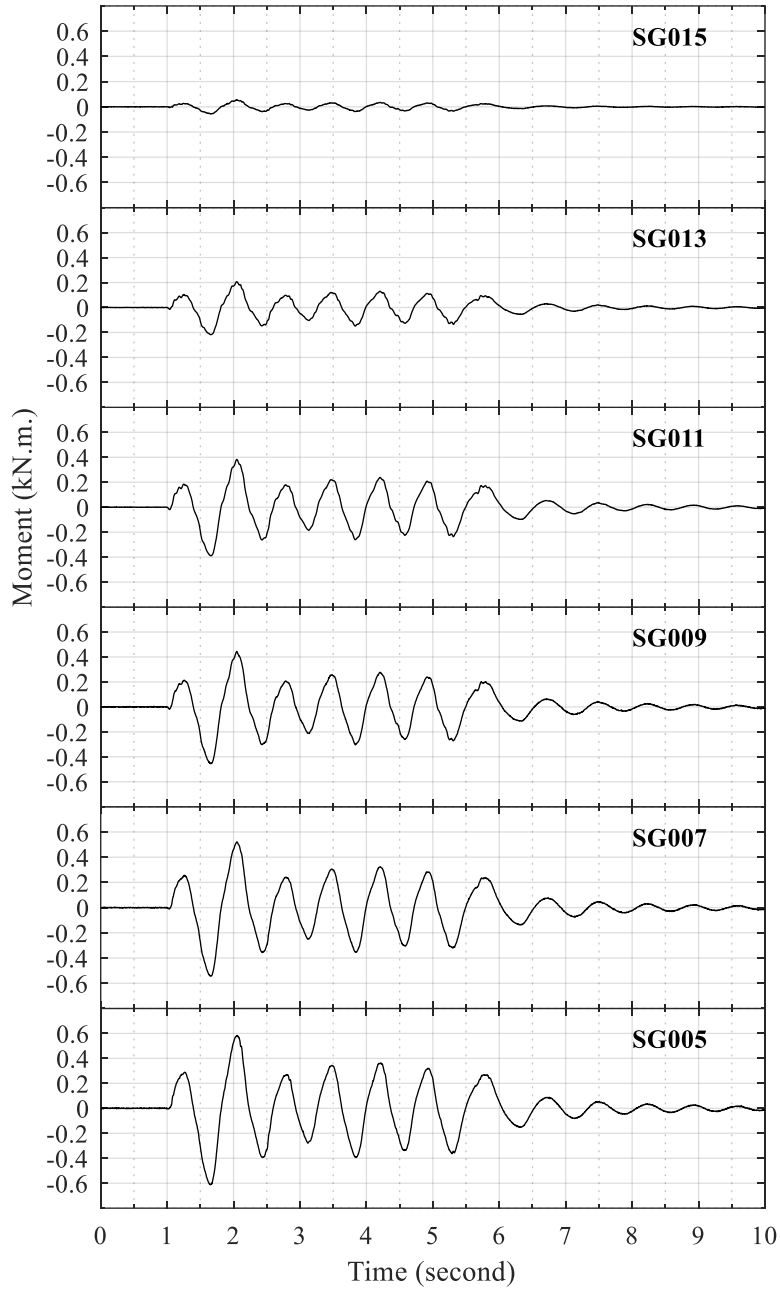


Figure B-105: Time histories of tower bending moment for test H8

### B.9 Test H9

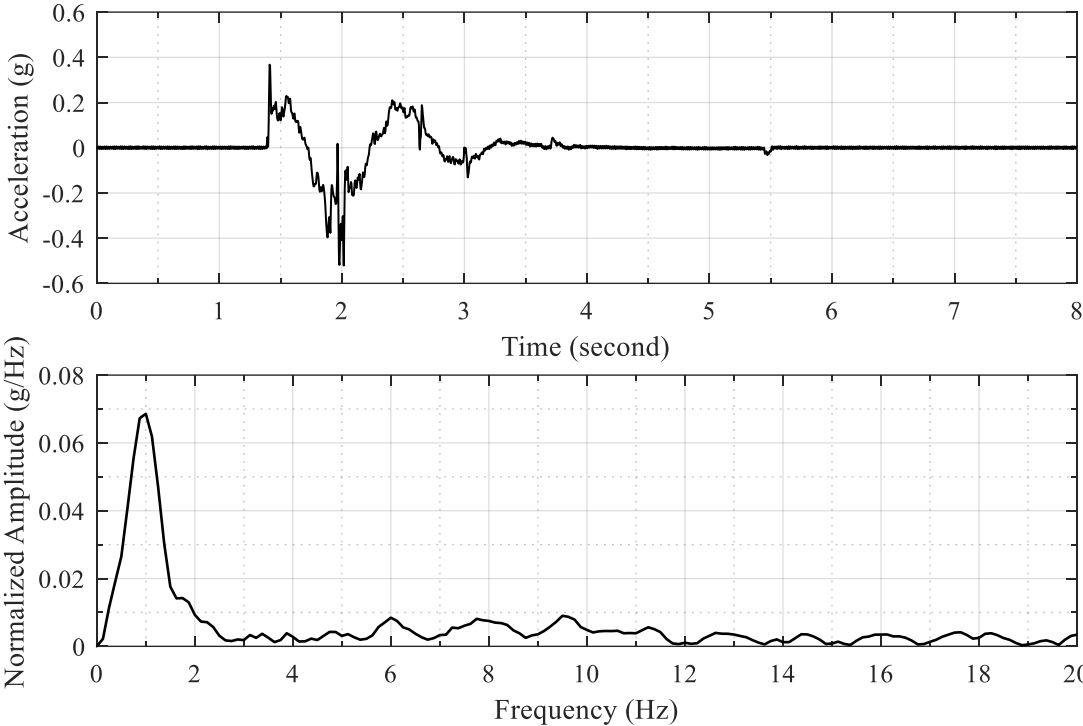


Figure B-106: Acceleration time history of shake table input excitation and the corresponding frequency spectrum for test H9



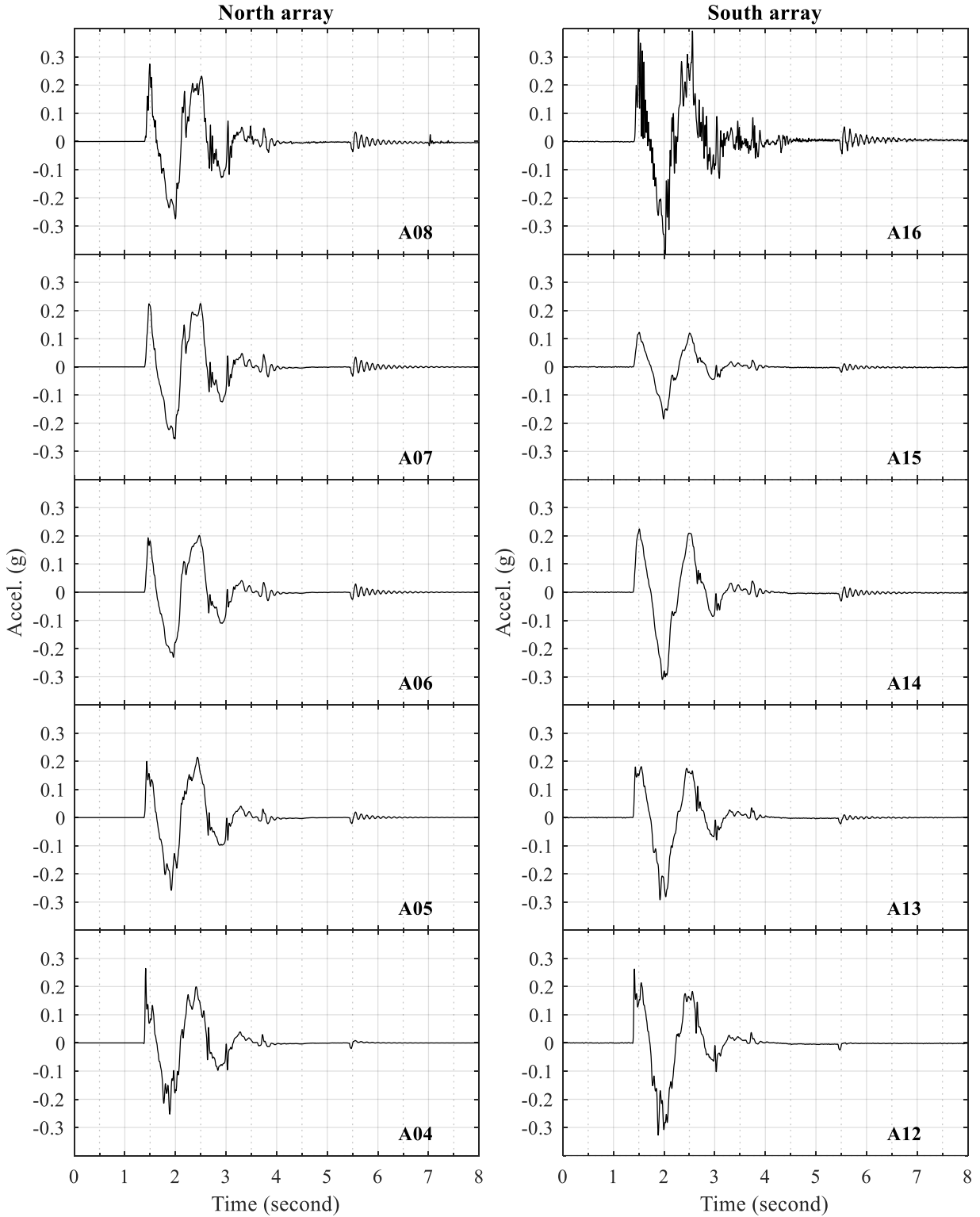


Figure B-107: Time histories of lateral soil acceleration in north and south arrays for test H9

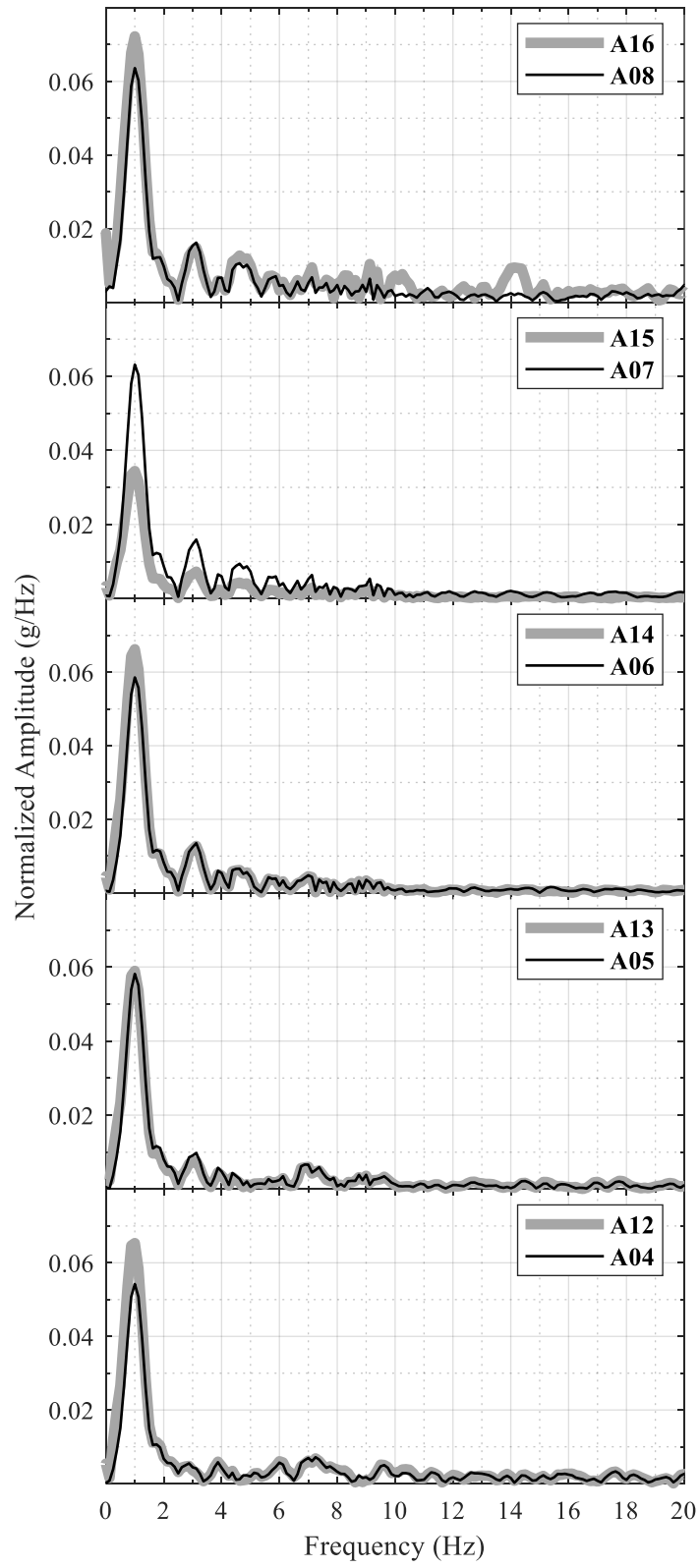


Figure B-108: Frequency spectra of lateral soil acceleration in north and south arrays for test H9

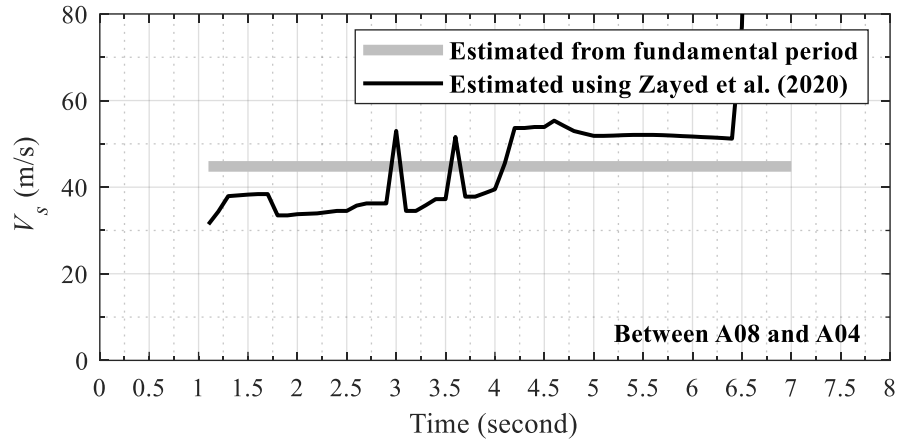


Figure B-109: Change in soil  $V_s$  with time during test H9

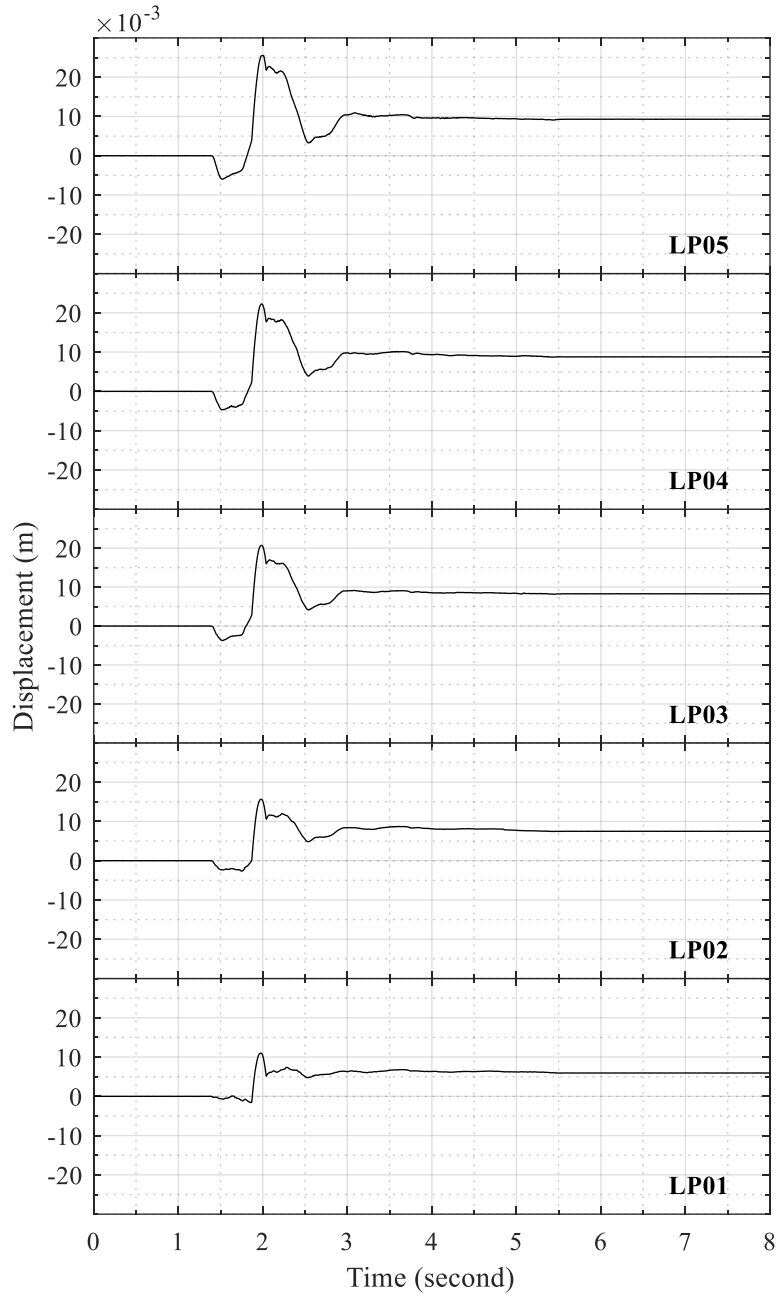


Figure B-110: Time histories of lateral soil displacement relative to laminar container base for test H9

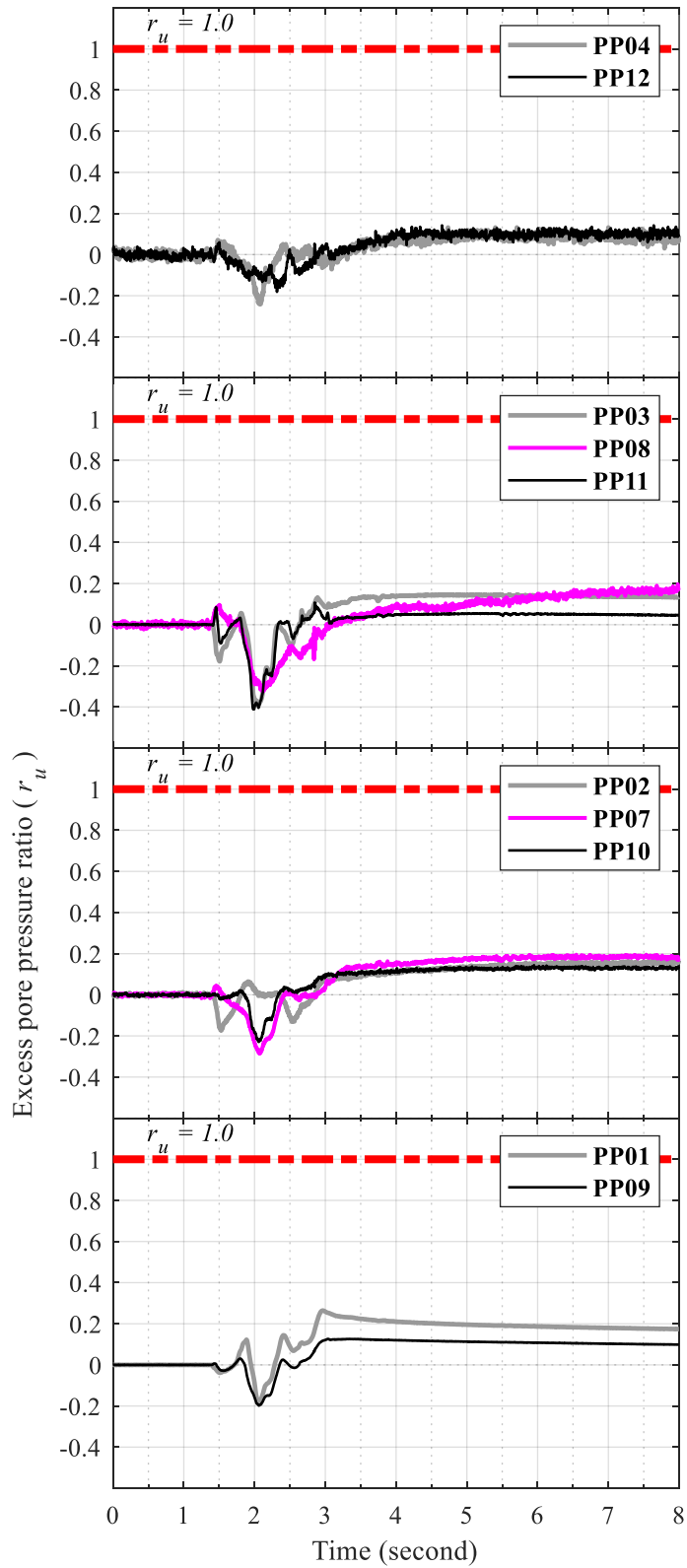


Figure B-111: Time histories of soil excess pore pressure for test H9

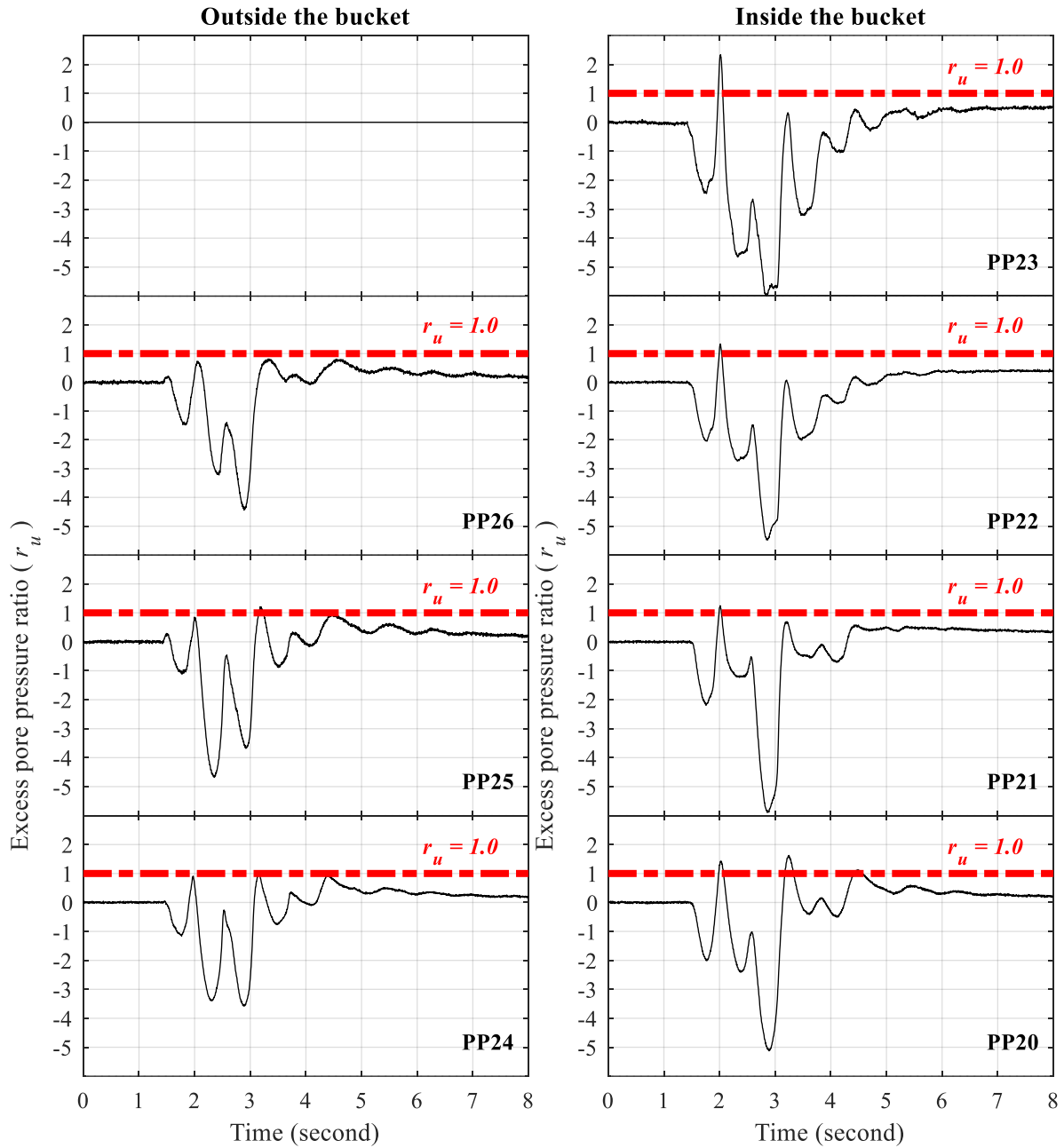


Figure B-112: Time histories of excess pore pressure at north edge of suction bucket for test H9

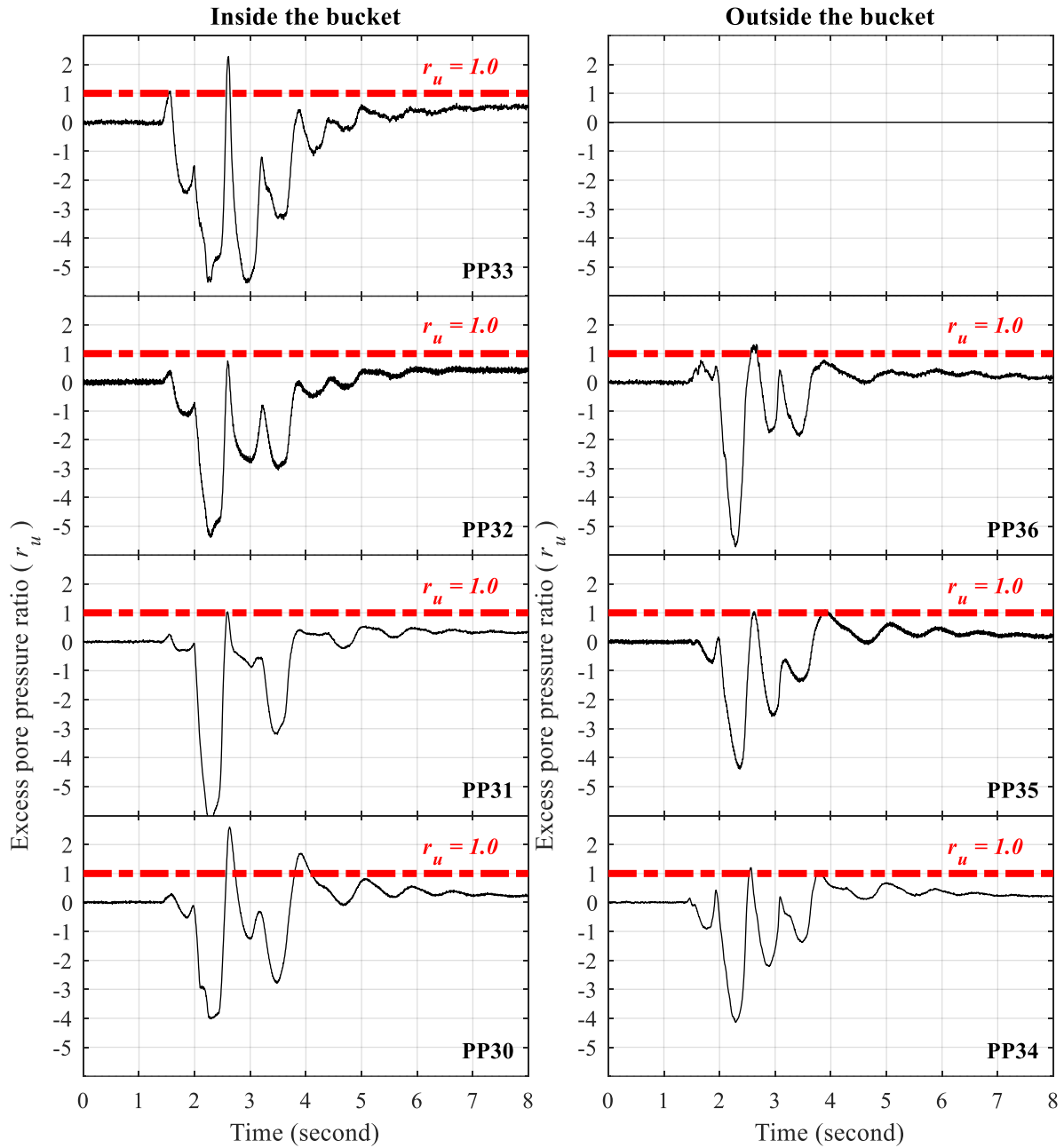


Figure B-113: Time histories of excess pore pressure at south edge of suction bucket for test H9

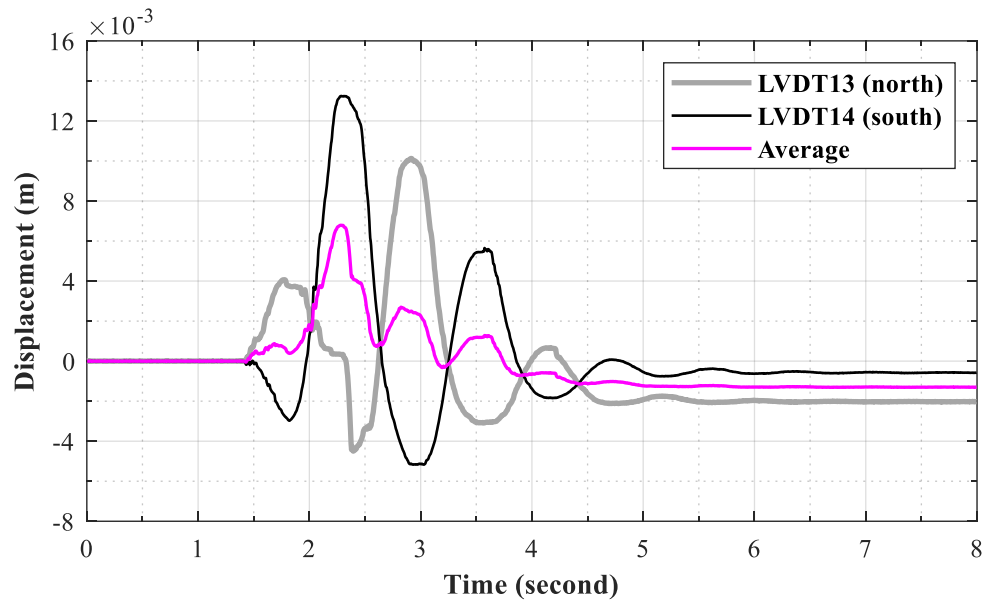


Figure B-114: Time histories of vertical bucket displacement for test H9



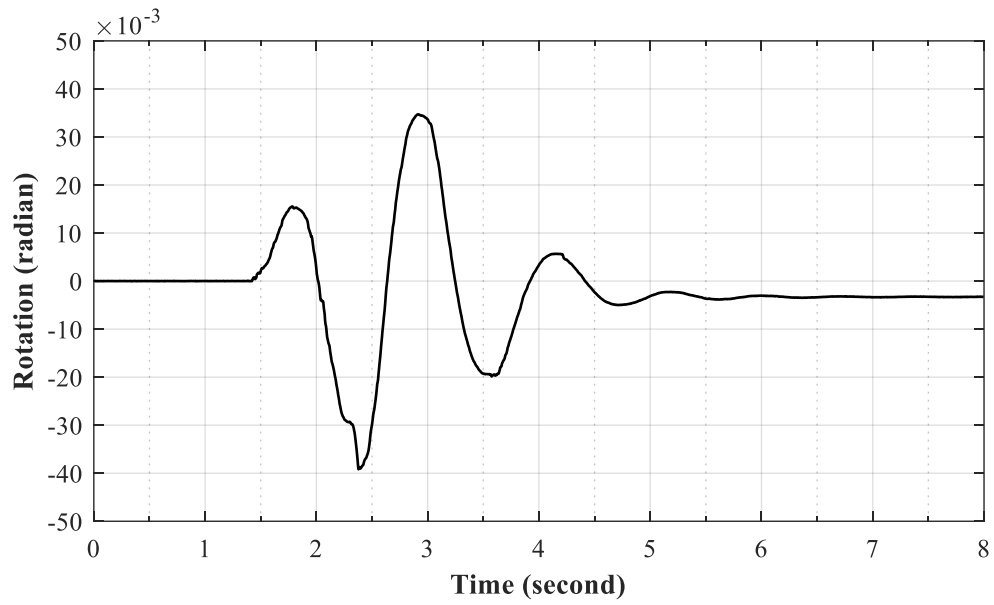


Figure B-115: Time history of suction bucket rotation for test H9

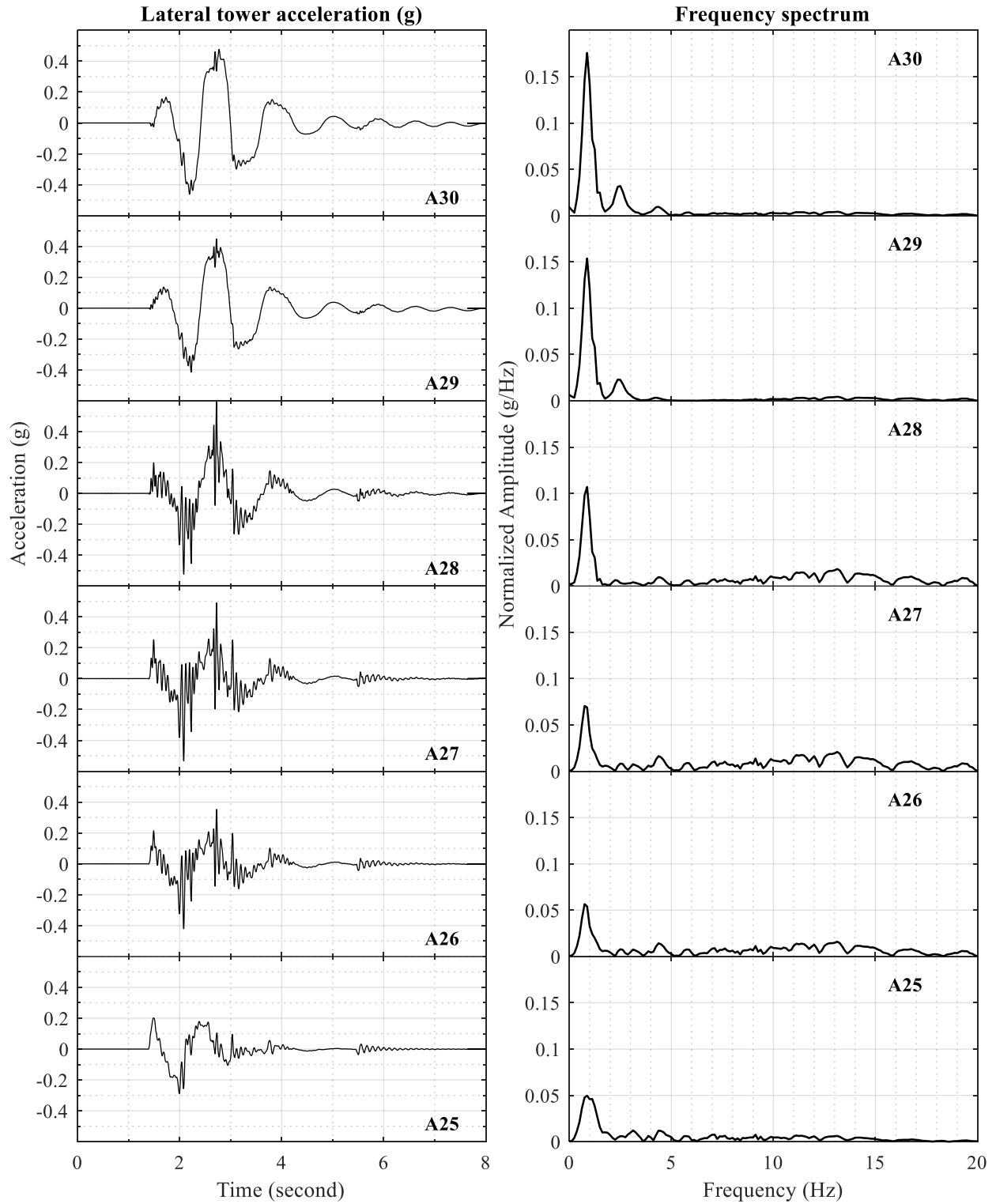


Figure B-116: Time histories of lateral tower acceleration for test H9

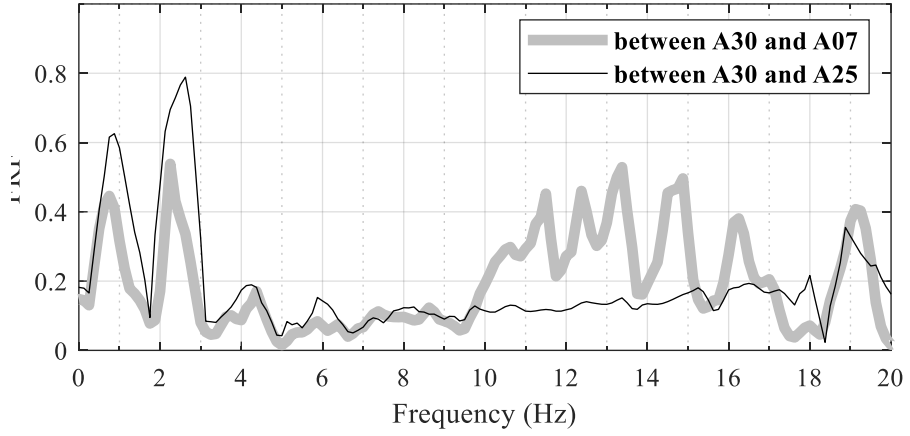


Figure B-117: Transfer function between accelerations at tower top (A30) and at soil top near the suction bucket foundation (A08) for test H9

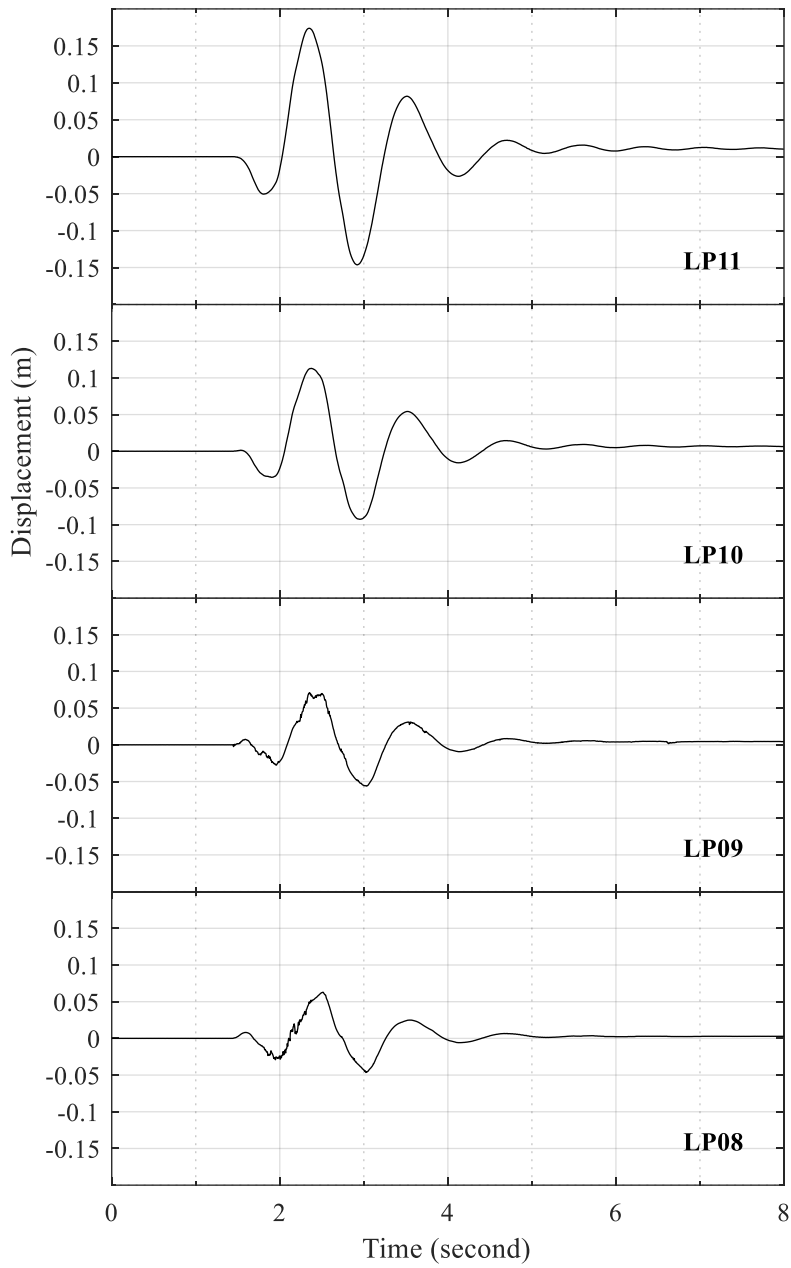


Figure B-118: Time histories of lateral tower displacement relative to lateral soil displacement at the foundation level (LP05) for test H9

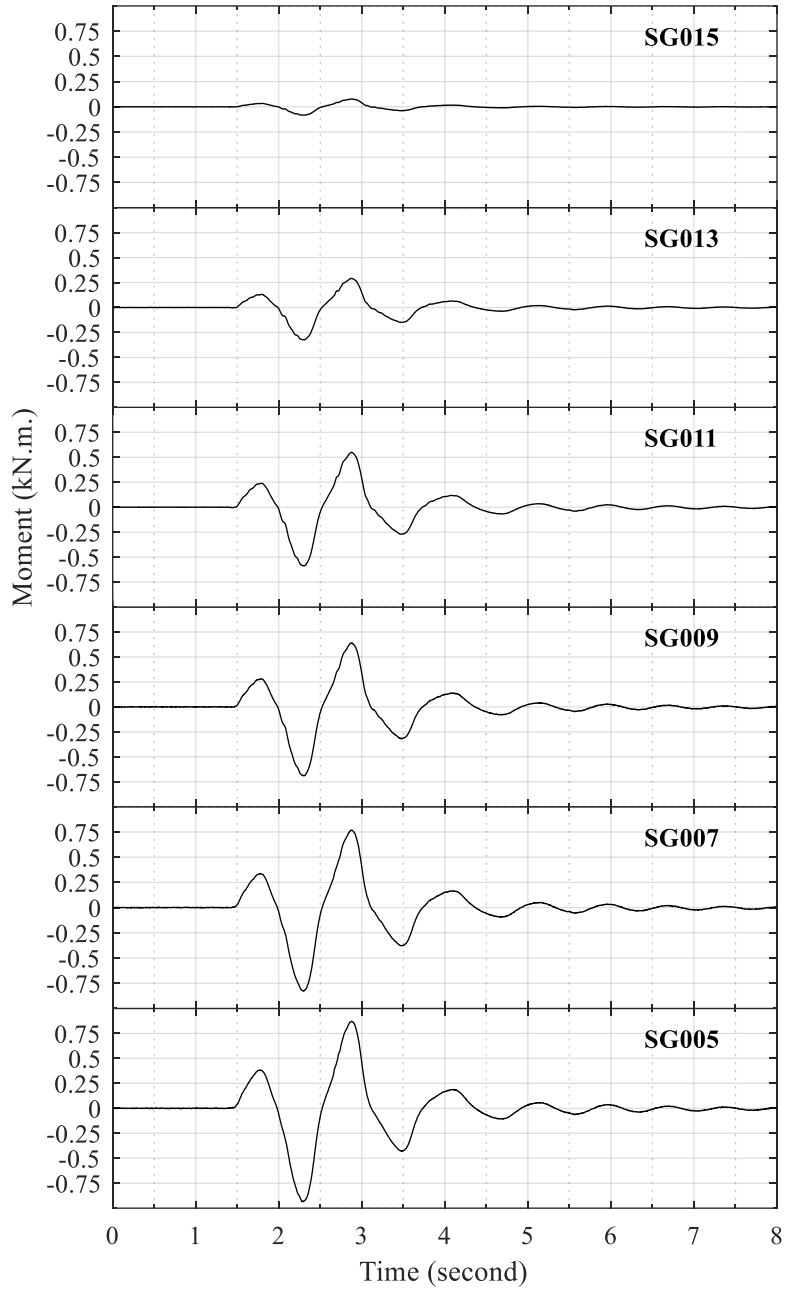


Figure B-119: Time histories of tower bending moment for test H9

### B.10 Test H10

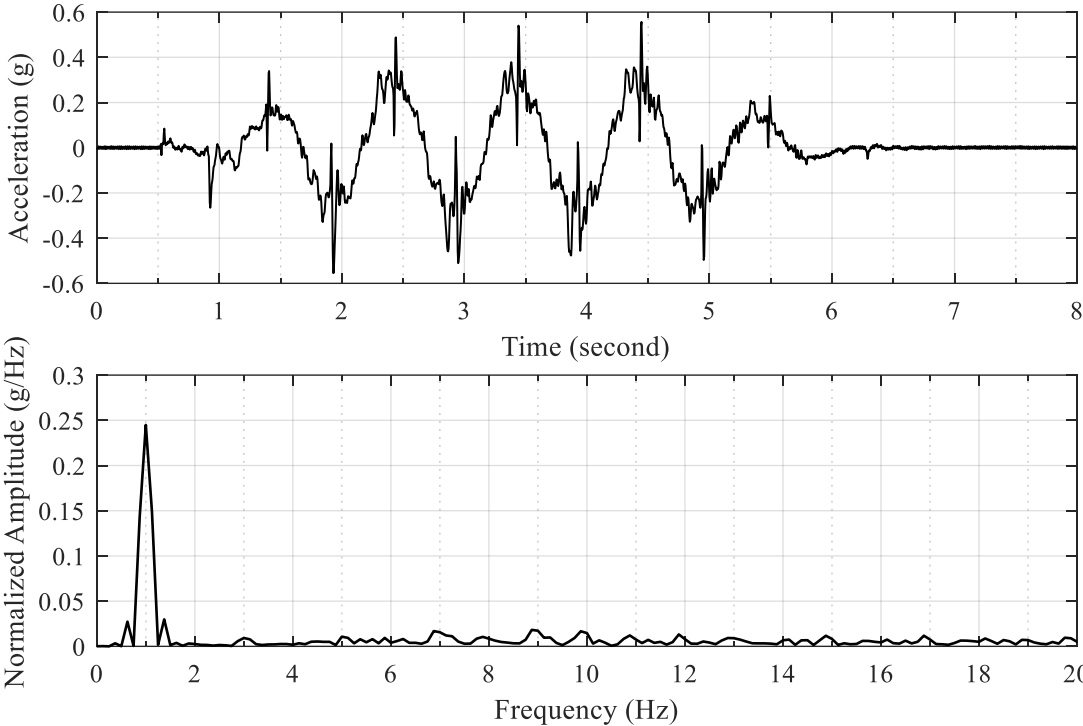


Figure B-120: Acceleration time history of shake table input excitation and the corresponding frequency spectrum for test H10

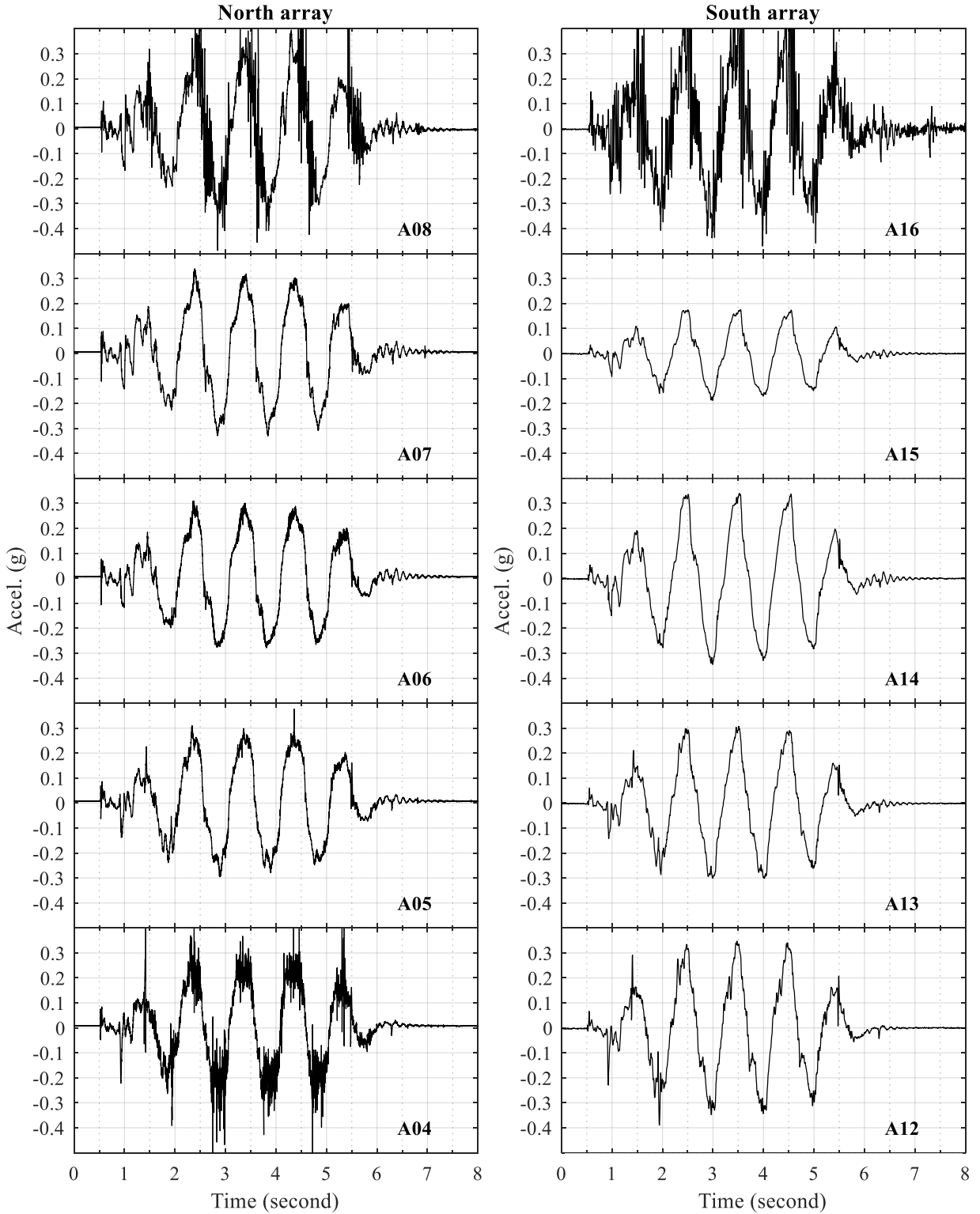


Figure B-121: Time histories of lateral soil acceleration in north and south arrays for test H10

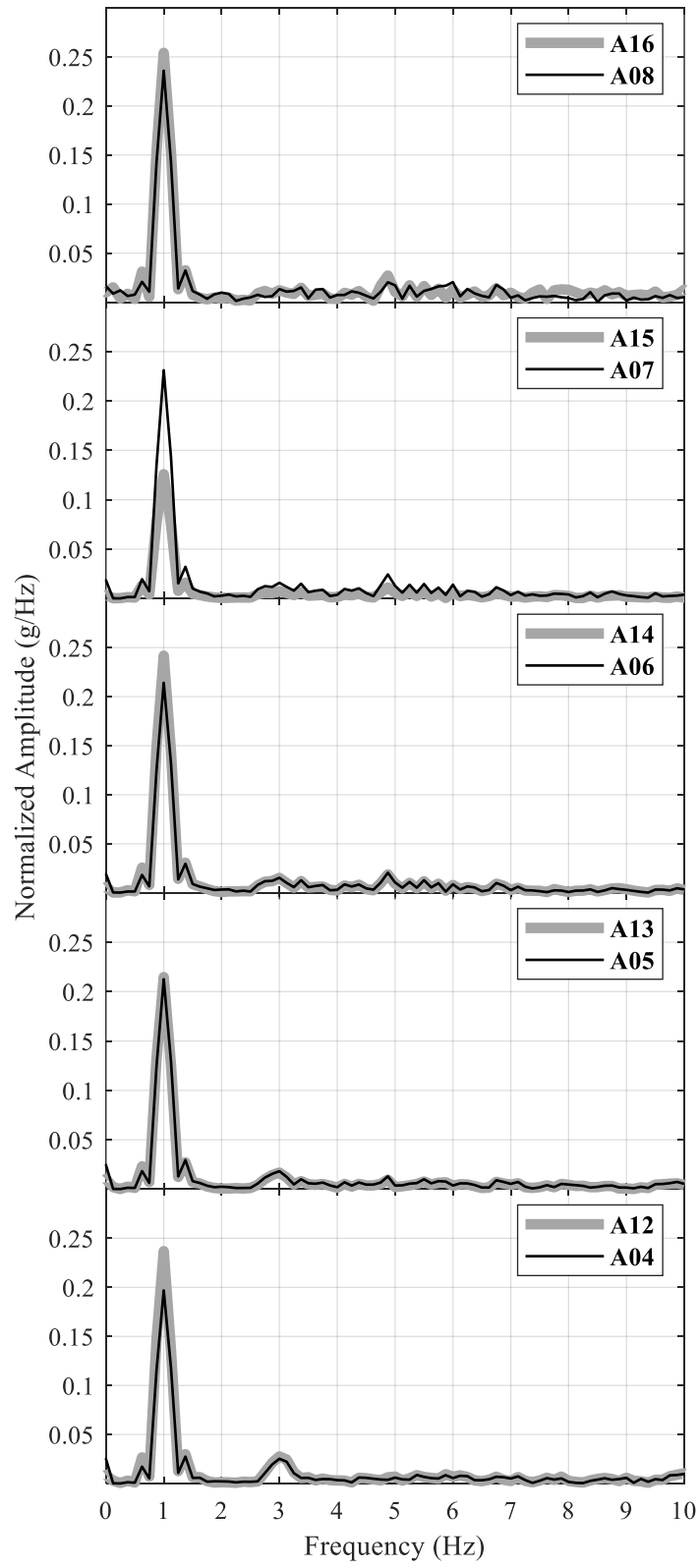


Figure B-122: Frequency spectra of lateral soil acceleration in north and south arrays for test H10



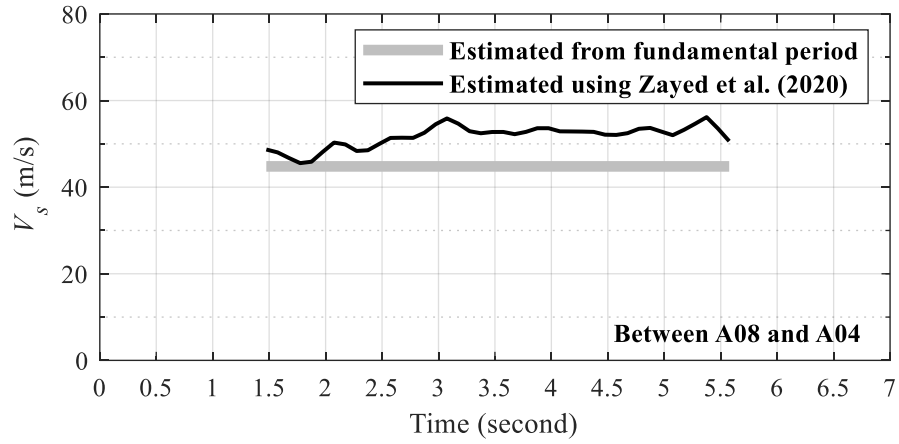


Figure B-123: Change in soil  $V_s$  with time during test H10

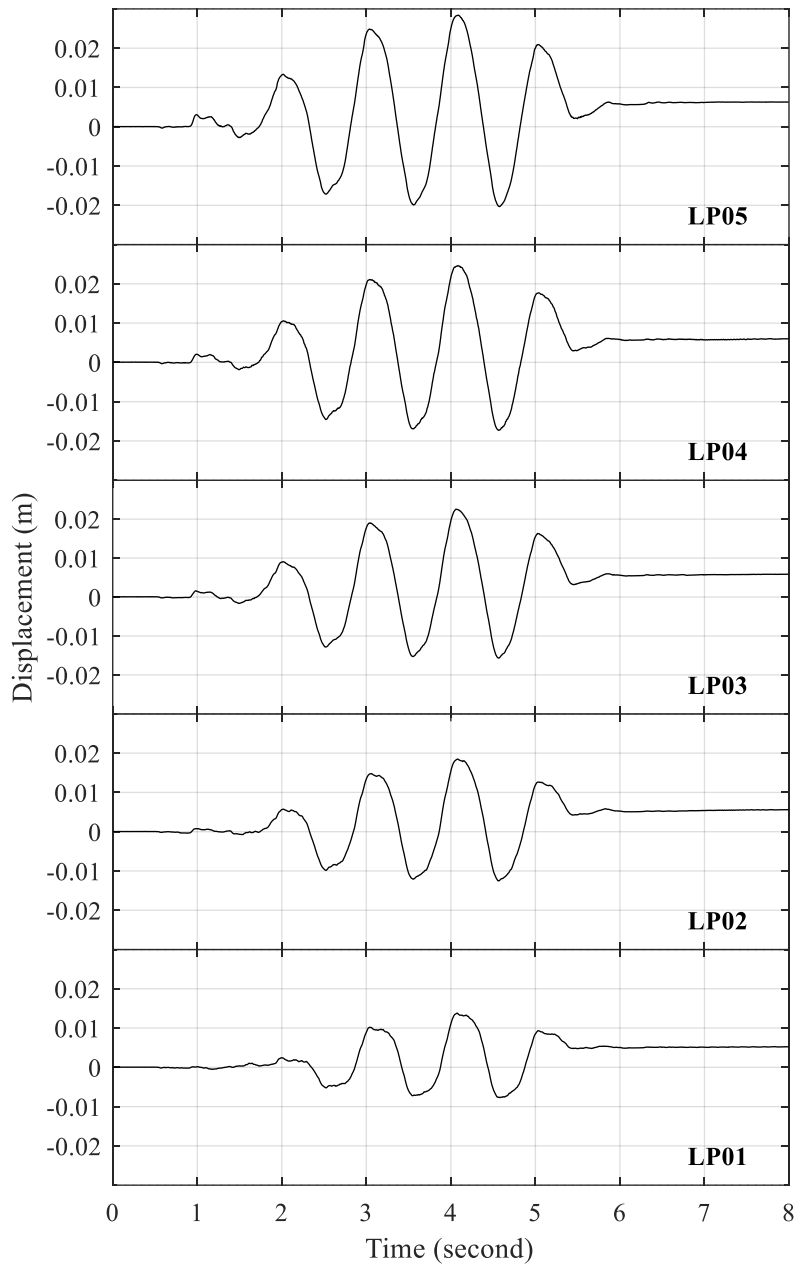


Figure B-124: Time histories of lateral soil displacement relative to laminar container base for test H10

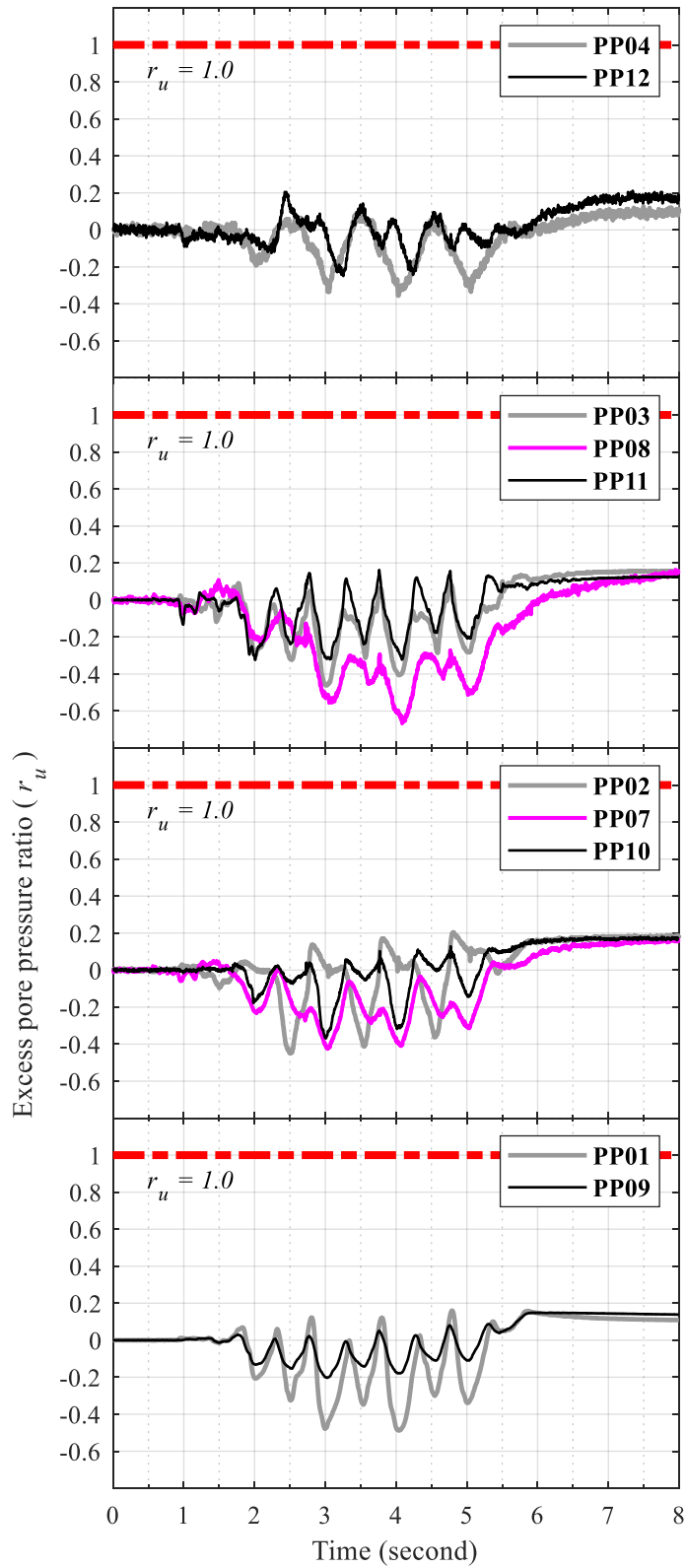


Figure B-125: Time histories of soil excess pore pressure for test H10

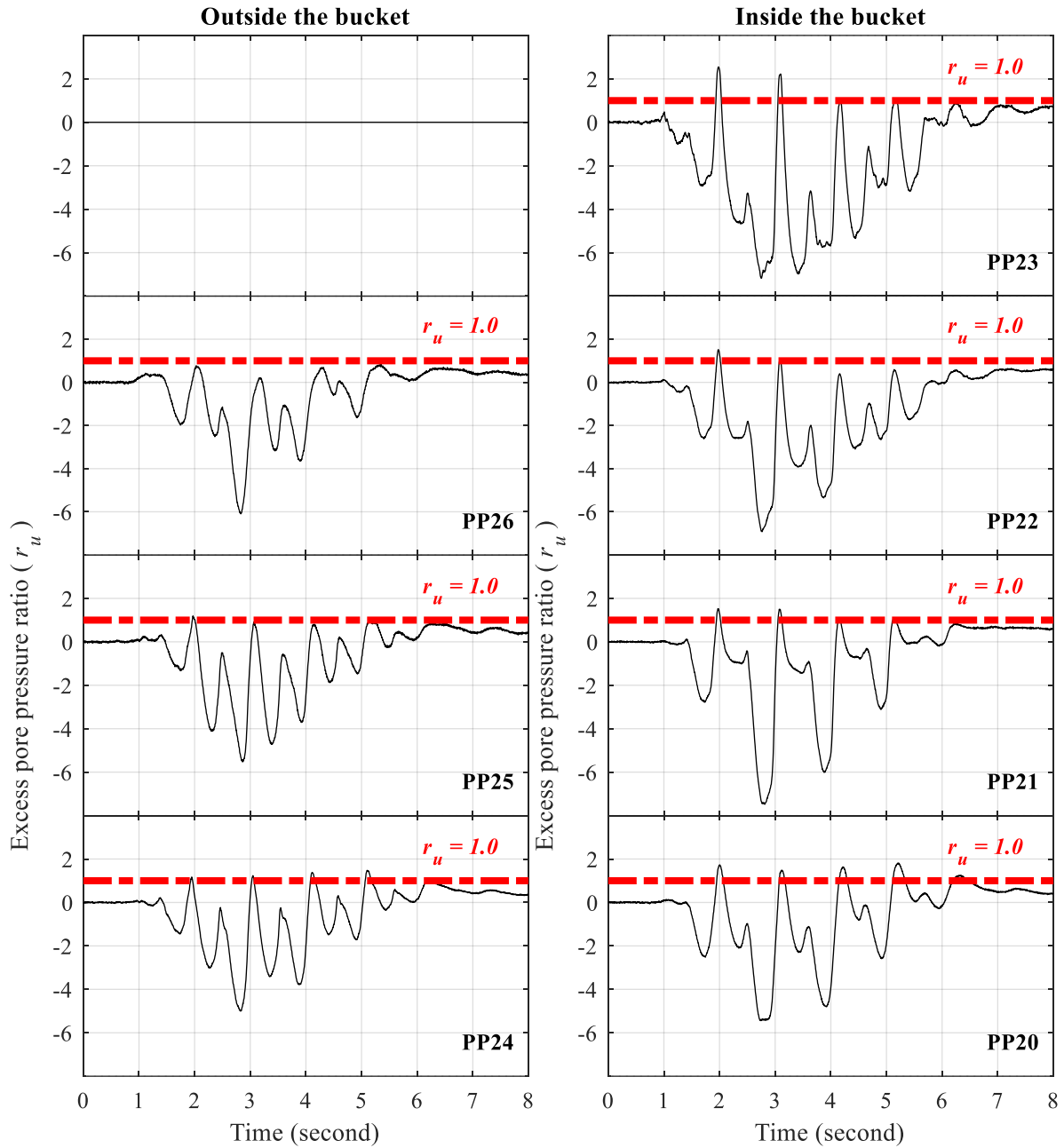


Figure B-126: Time histories of excess pore pressure at north edge of suction bucket for test H10

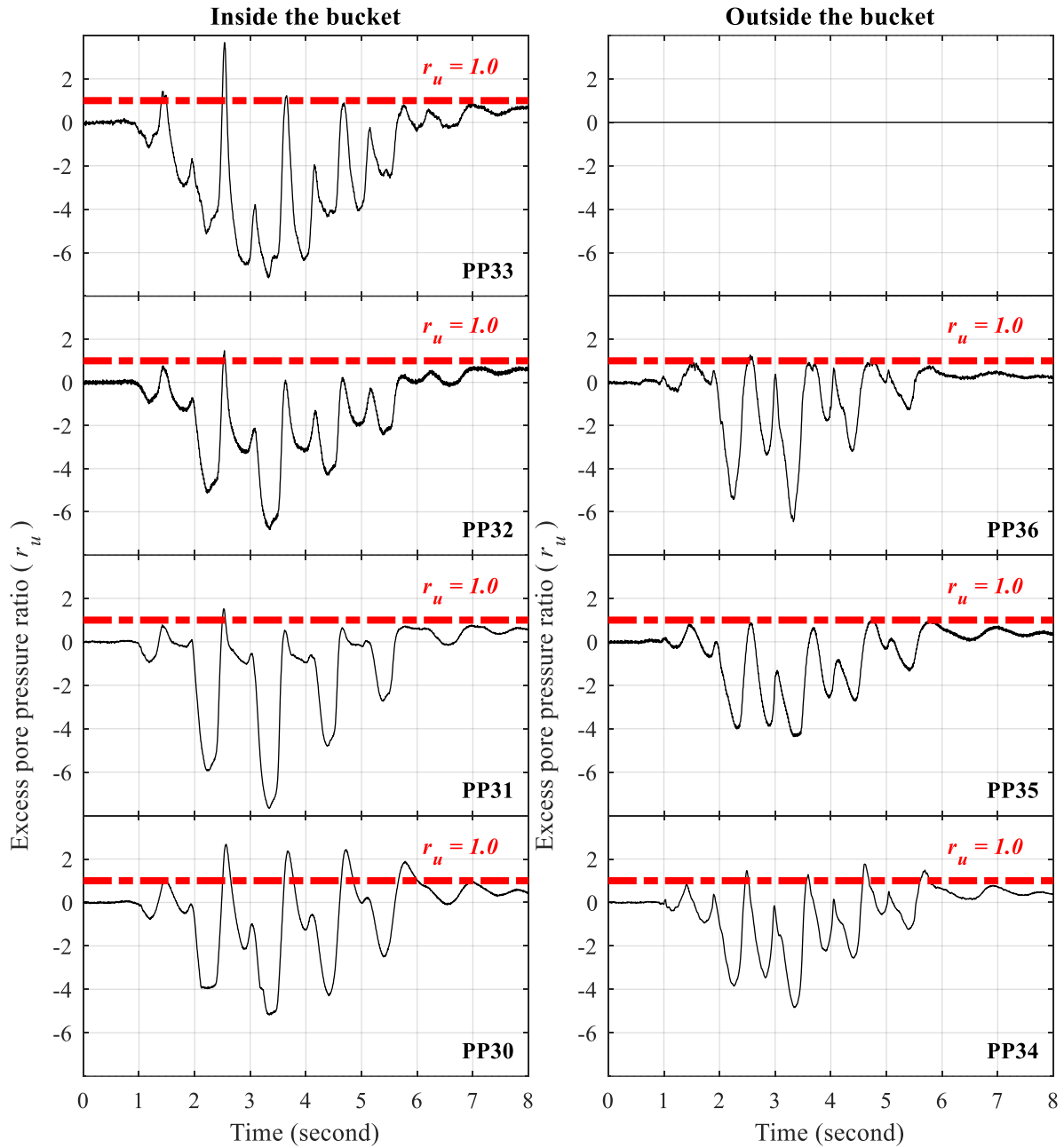


Figure B-127: Time histories of excess pore pressure at south edge of suction bucket for test H10

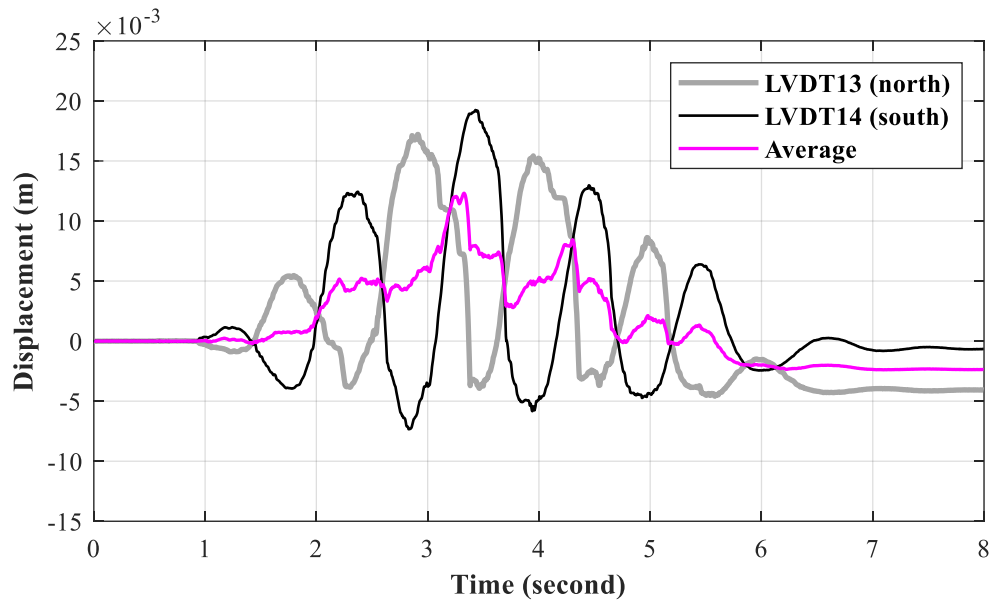


Figure B-128: Time histories of vertical bucket displacement for test H10

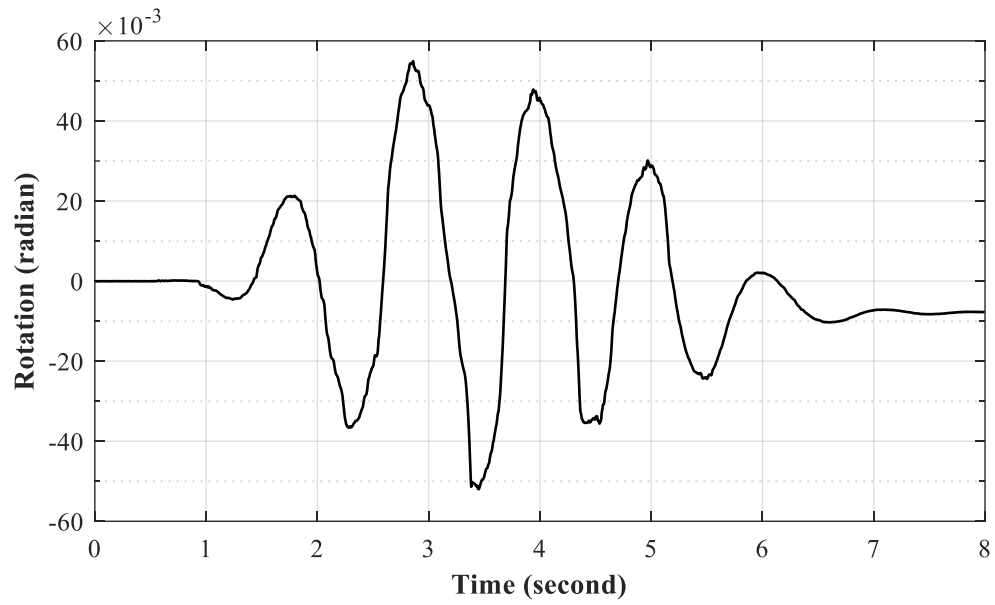


Figure B-129: Time history of suction bucket rotation for test H10

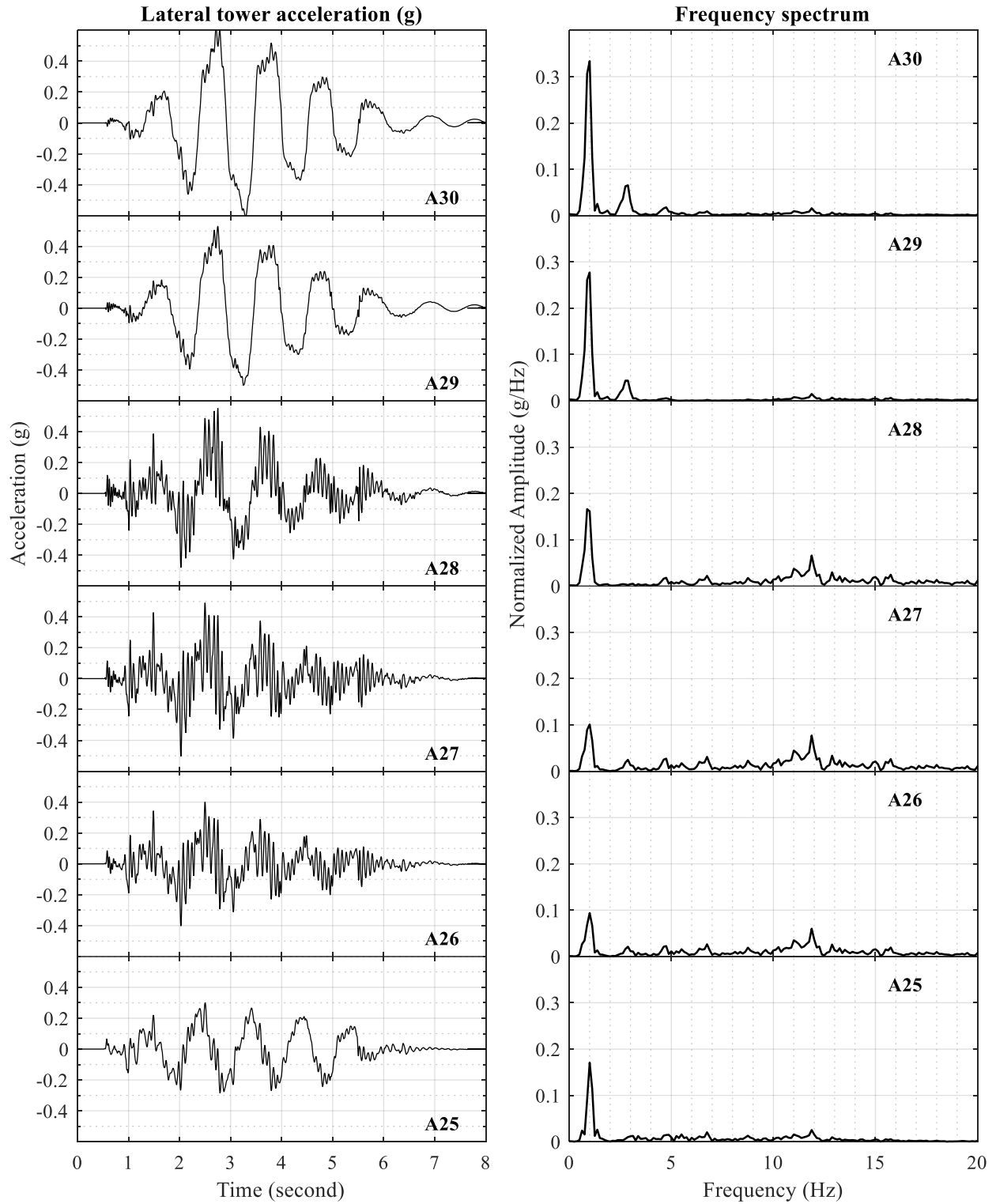


Figure B-130: Time histories of lateral tower acceleration for test H10



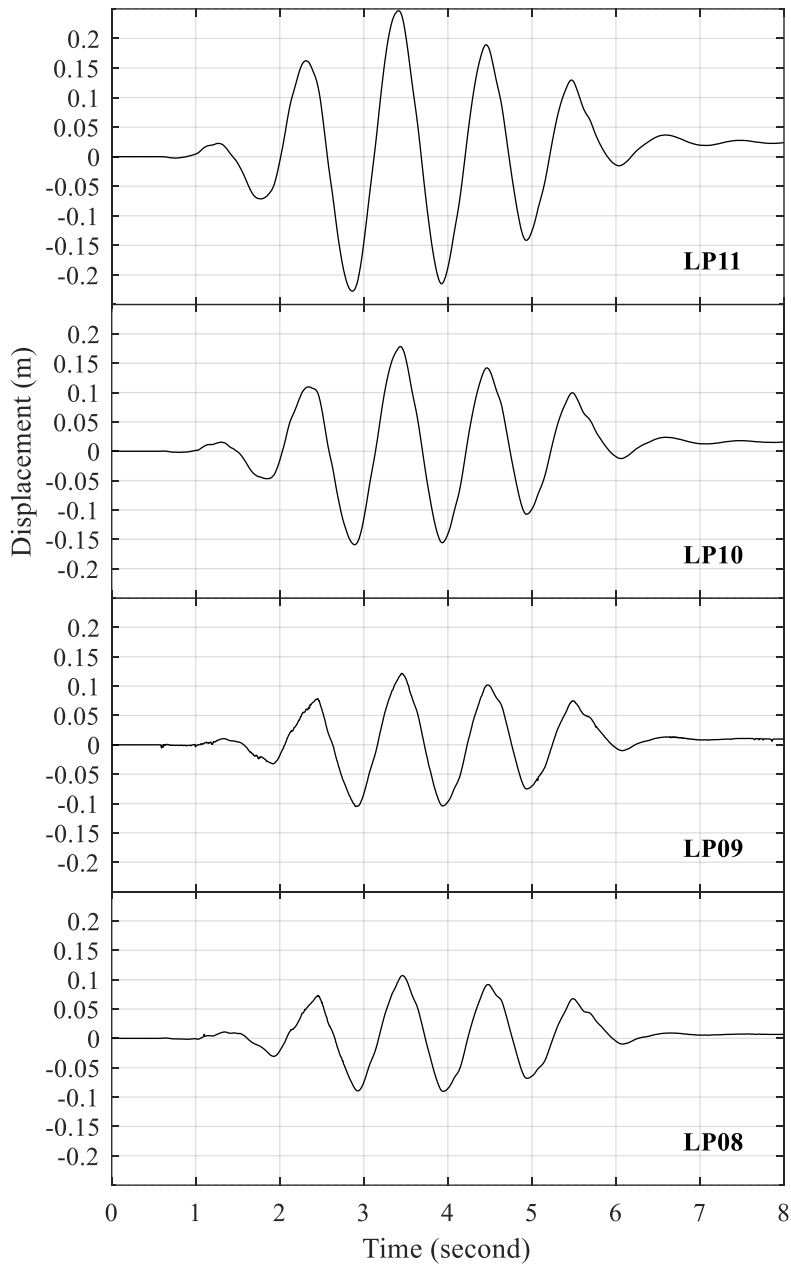


Figure B-131: Time histories of lateral tower displacement relative to lateral soil displacement at the foundation level (LP05) for test H10

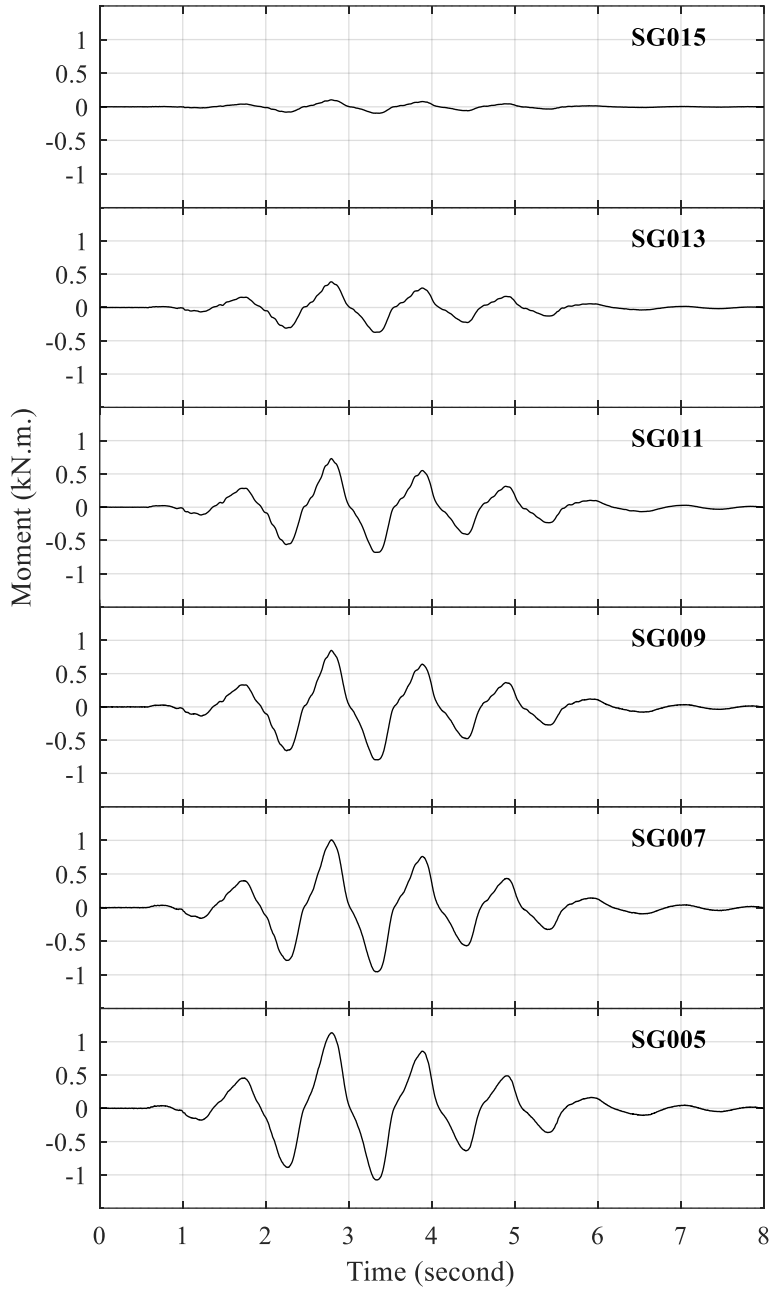


Figure B-132: Time histories of tower bending moment for test H10

## B.11 Test T1

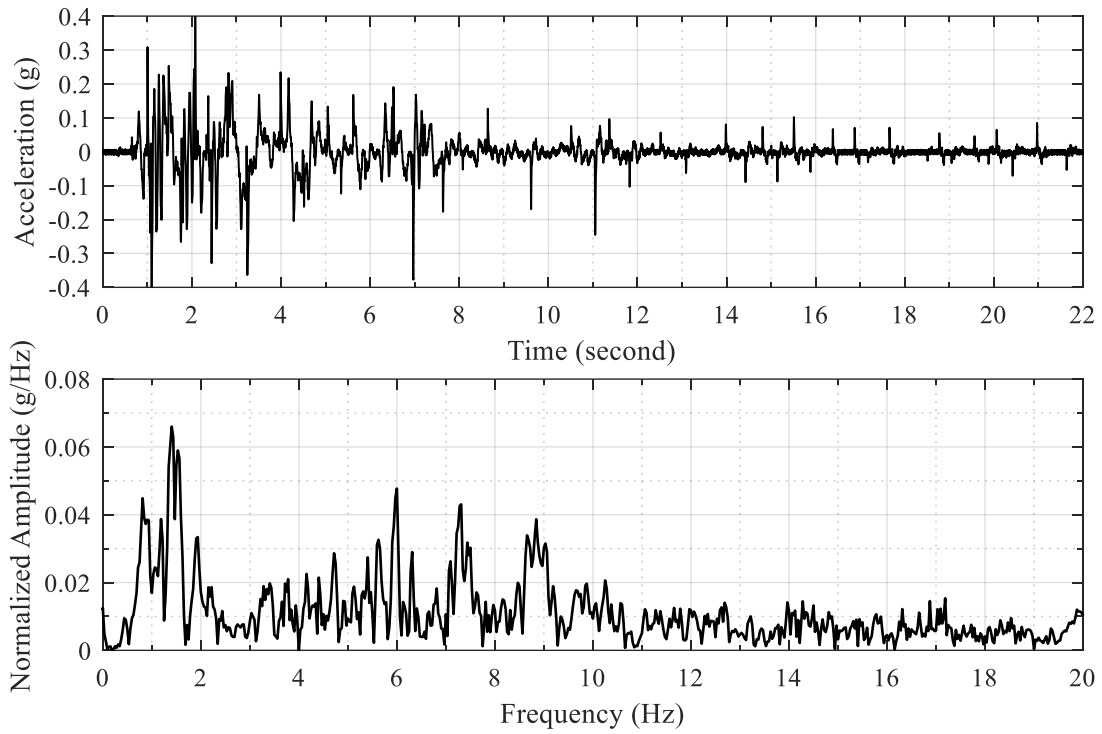


Figure B-133: Acceleration time history of shake table input excitation and the corresponding frequency spectrum for test T1

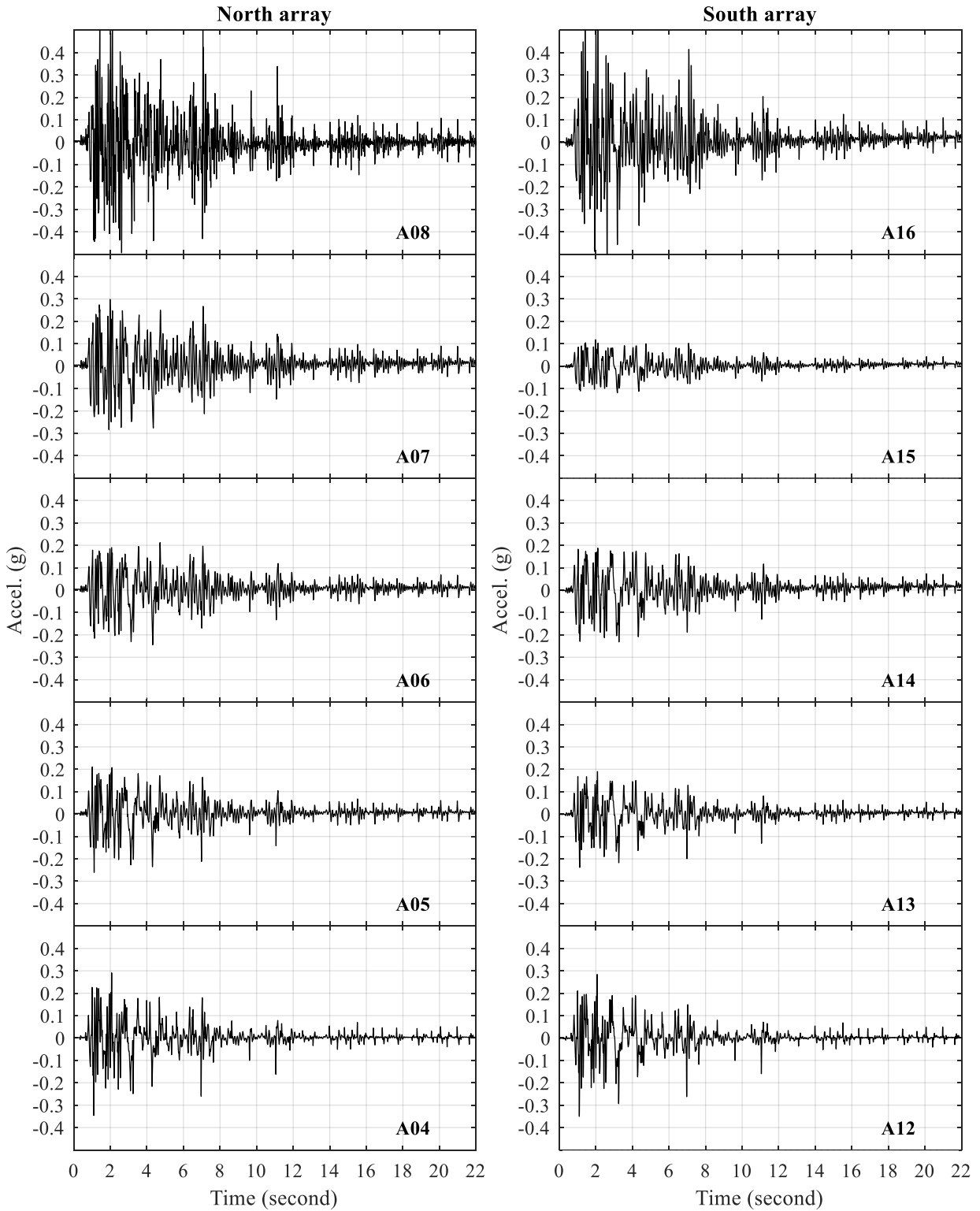


Figure B-134: Time histories of lateral soil acceleration in north and south arrays for test T1

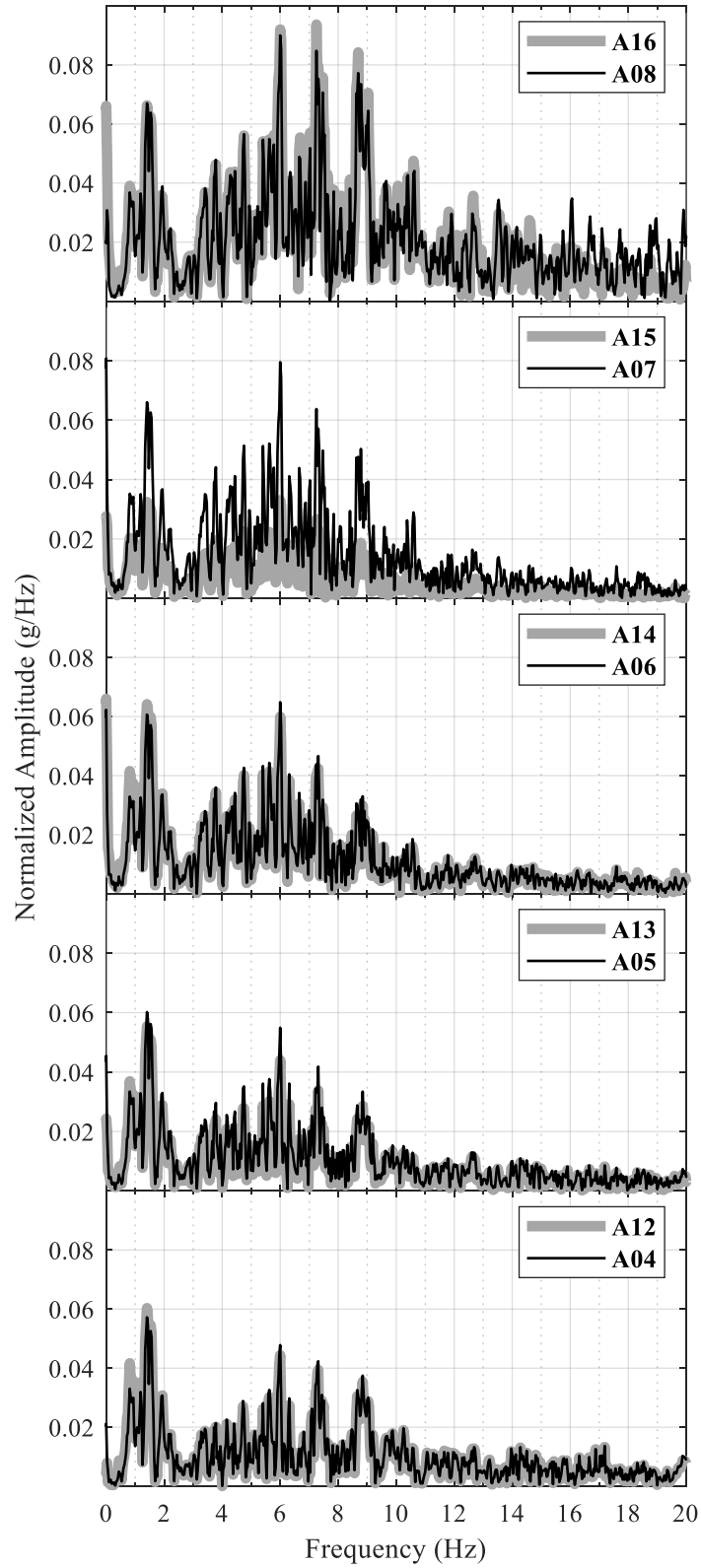


Figure B-135: Frequency spectra of lateral soil acceleration in north and south arrays for test T1

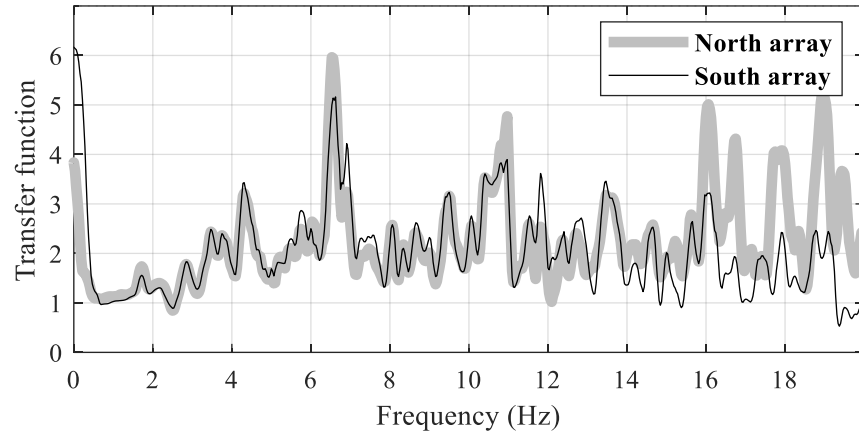


Figure B-136: Transfer function between soil acceleration at uppermost and lowermost sensor locations for test T1

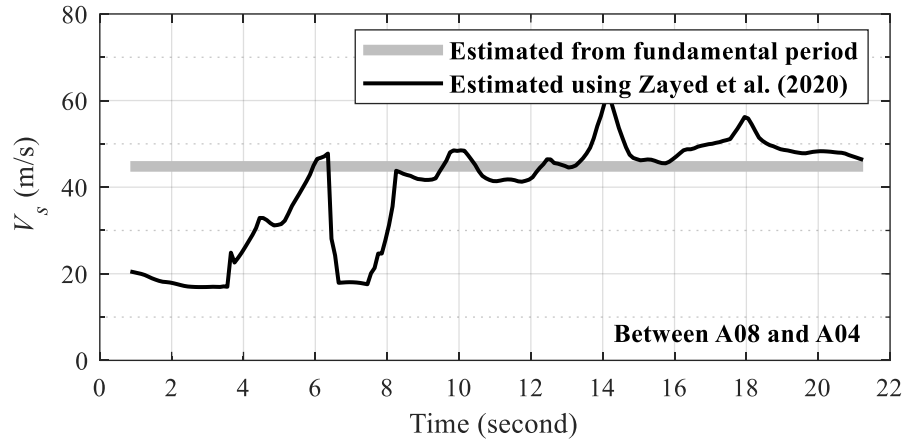


Figure B-137: Change in soil  $V_s$  with time during test T1

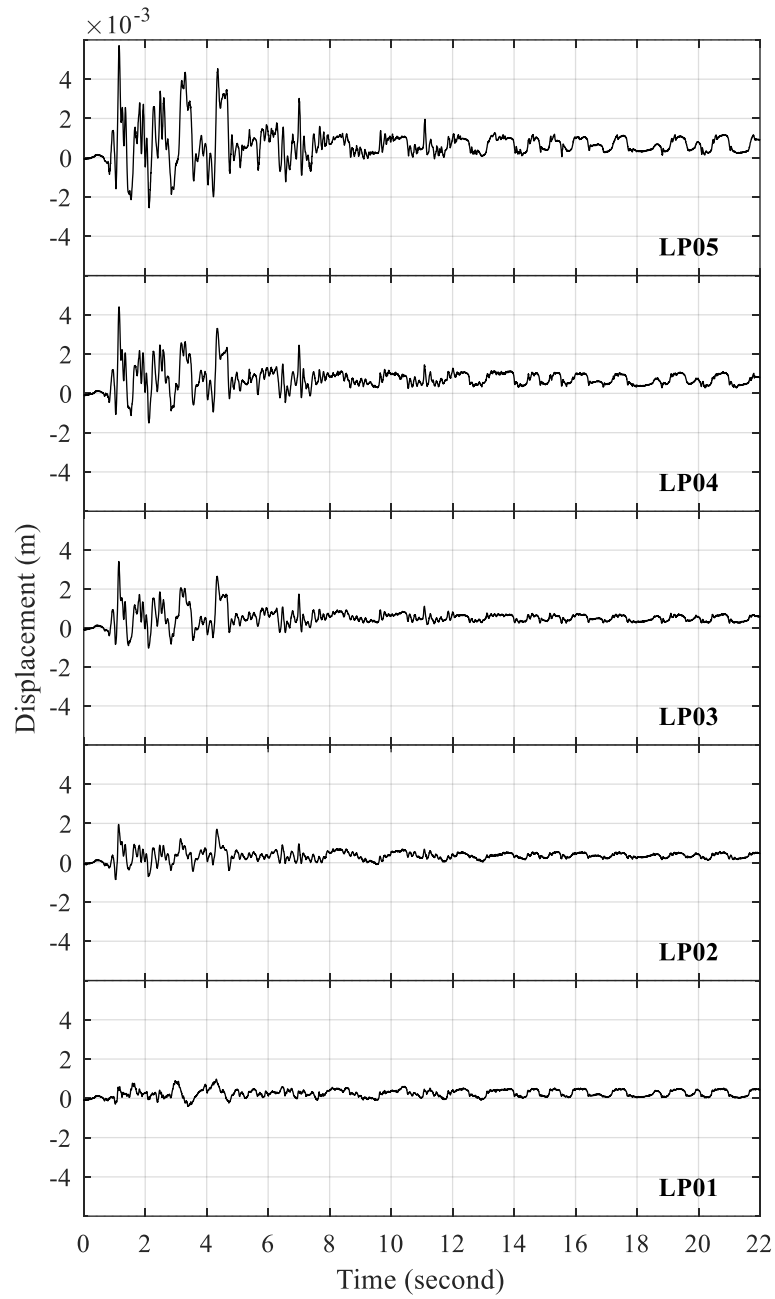


Figure B-138: Time histories of lateral soil displacement relative to laminar container base for test T1



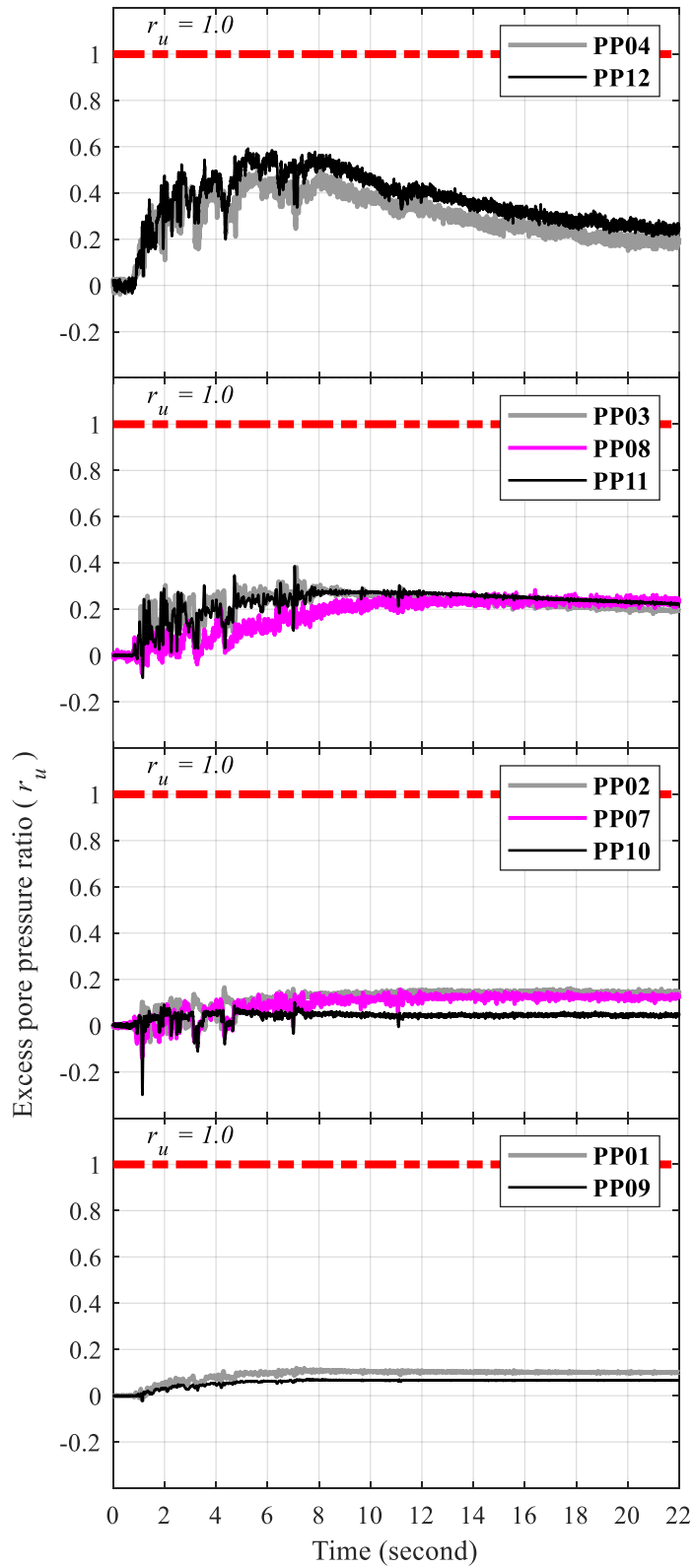


Figure B-139: Time histories of soil excess pore pressure for test T1

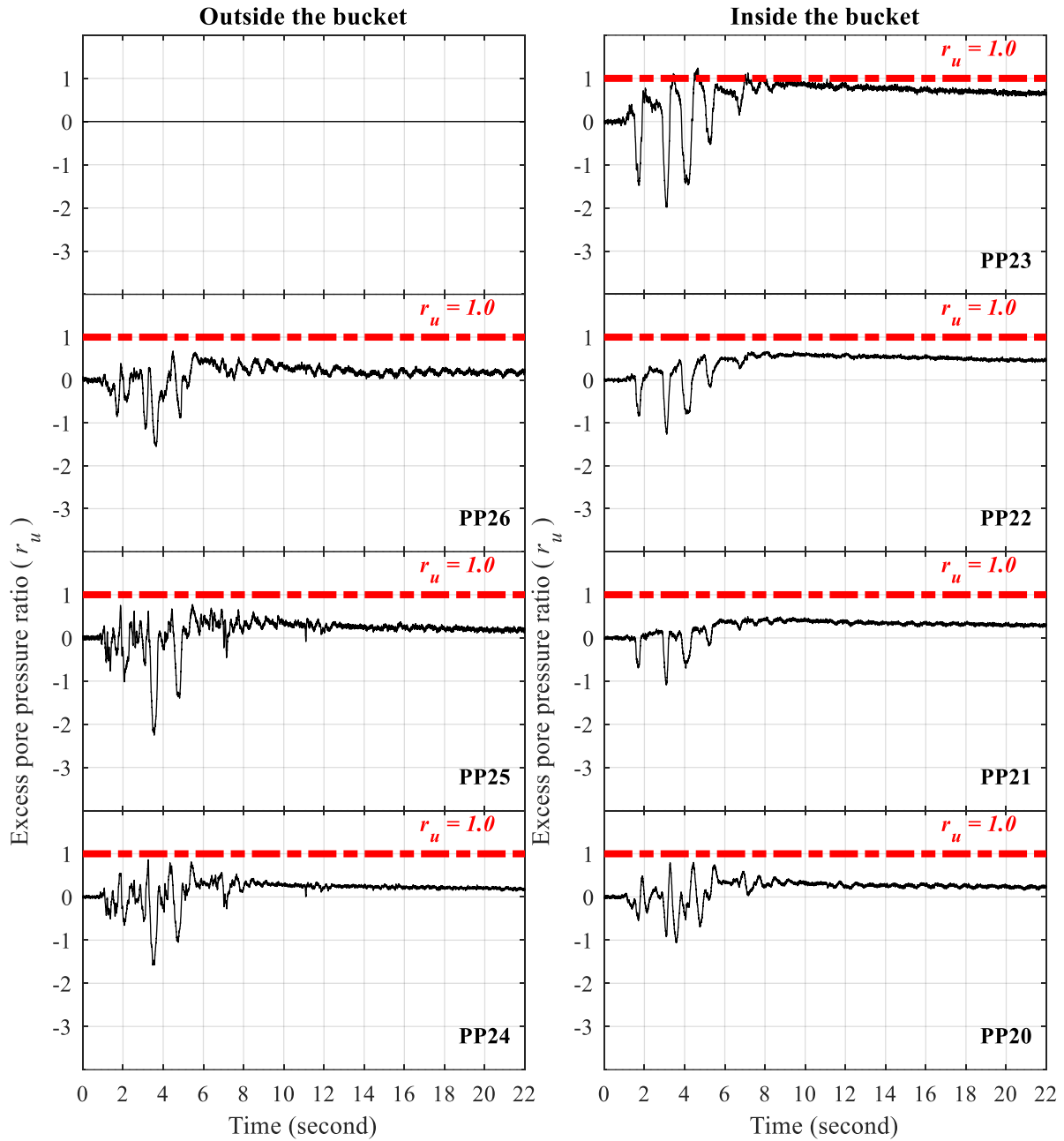


Figure B-140: Time histories of excess pore pressure at north edge of suction bucket for test T1

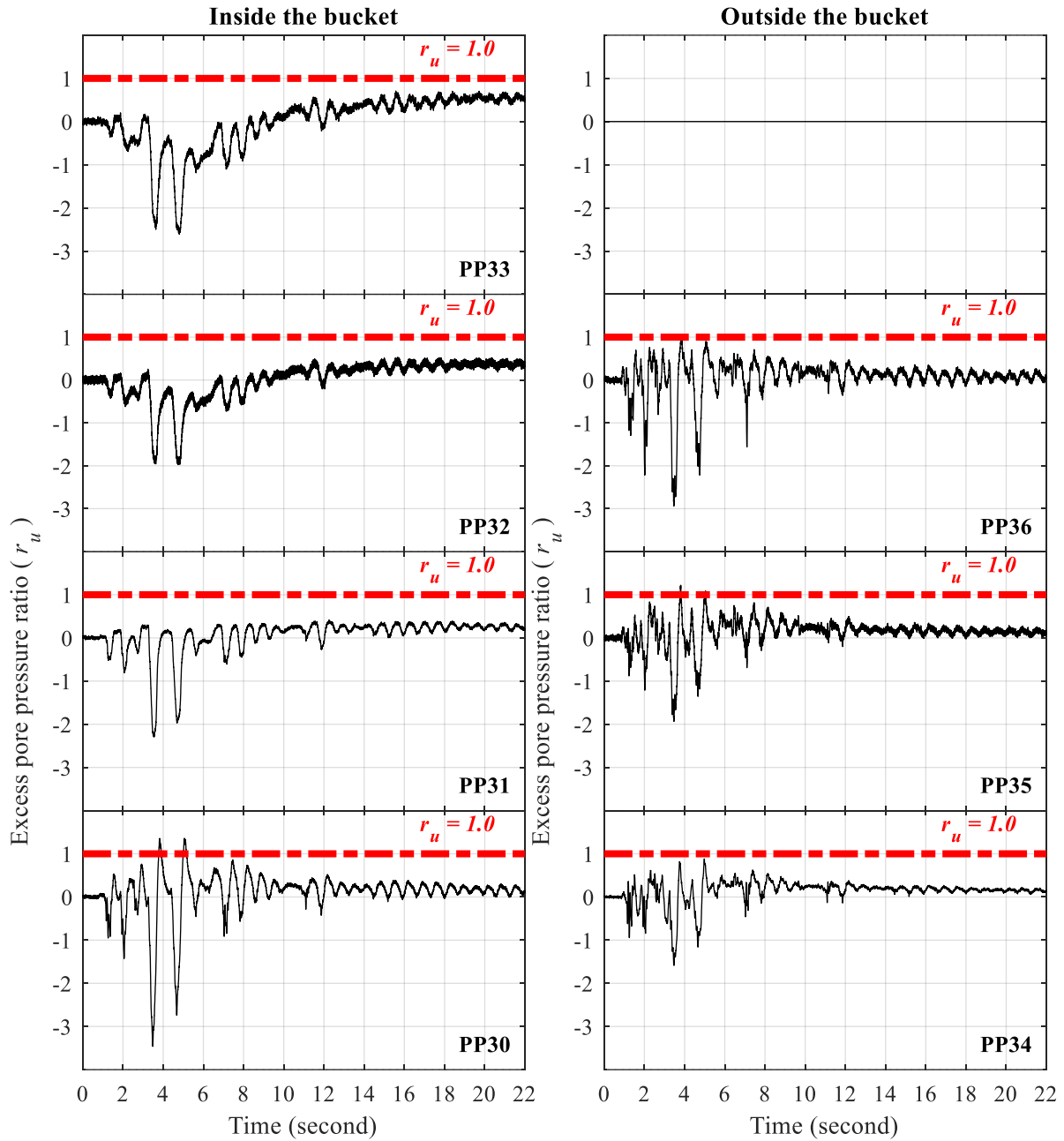


Figure B-141: Time histories of excess pore pressure at south edge of suction bucket for test T1

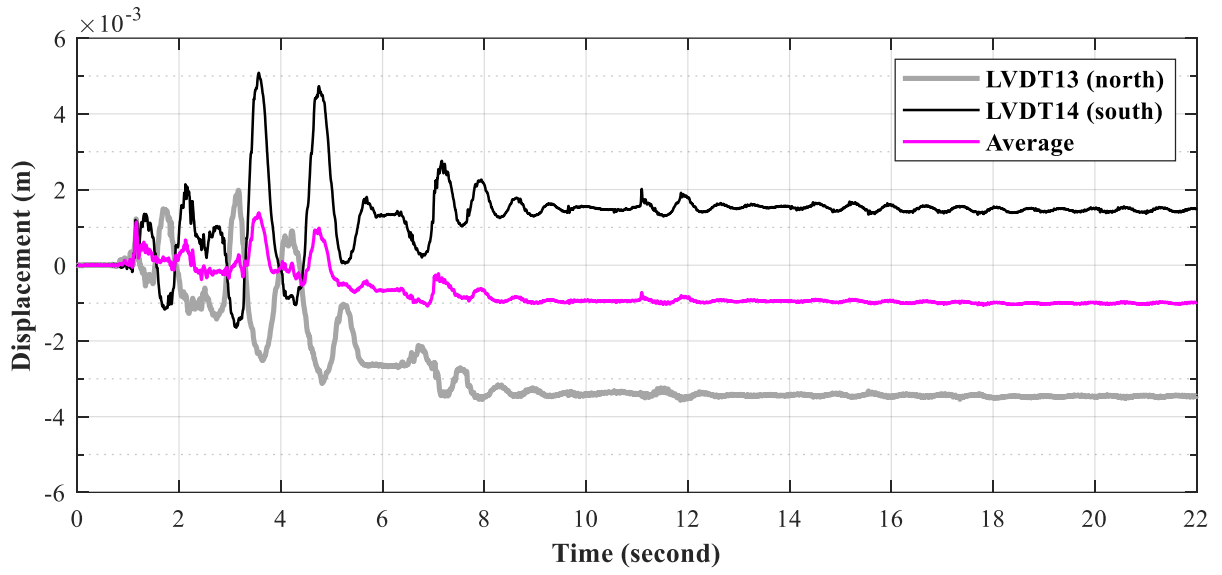


Figure B-142: Time histories of vertical bucket displacement for test T1

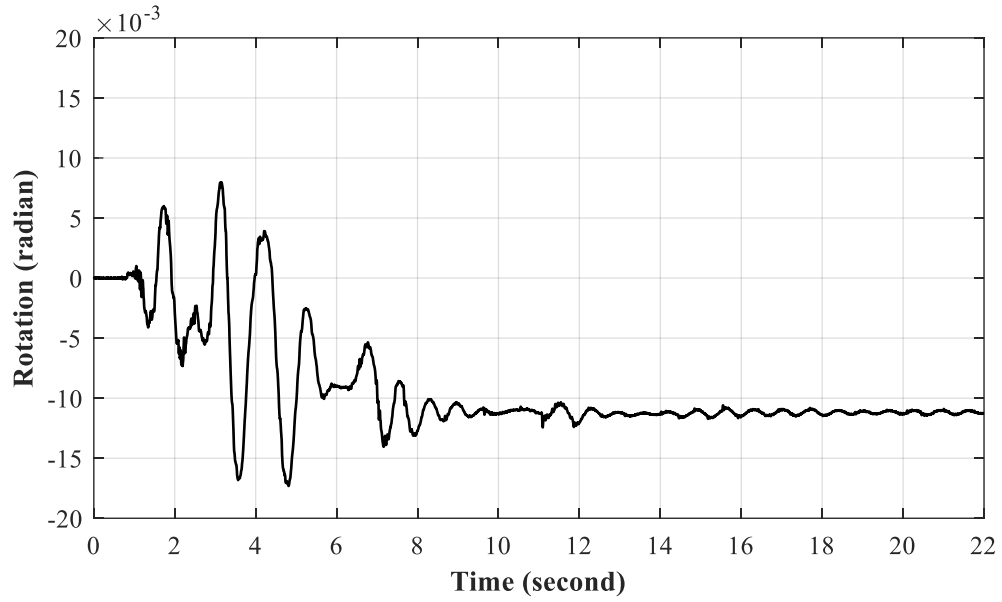


Figure B-143: Time history of suction bucket rotation for test T1

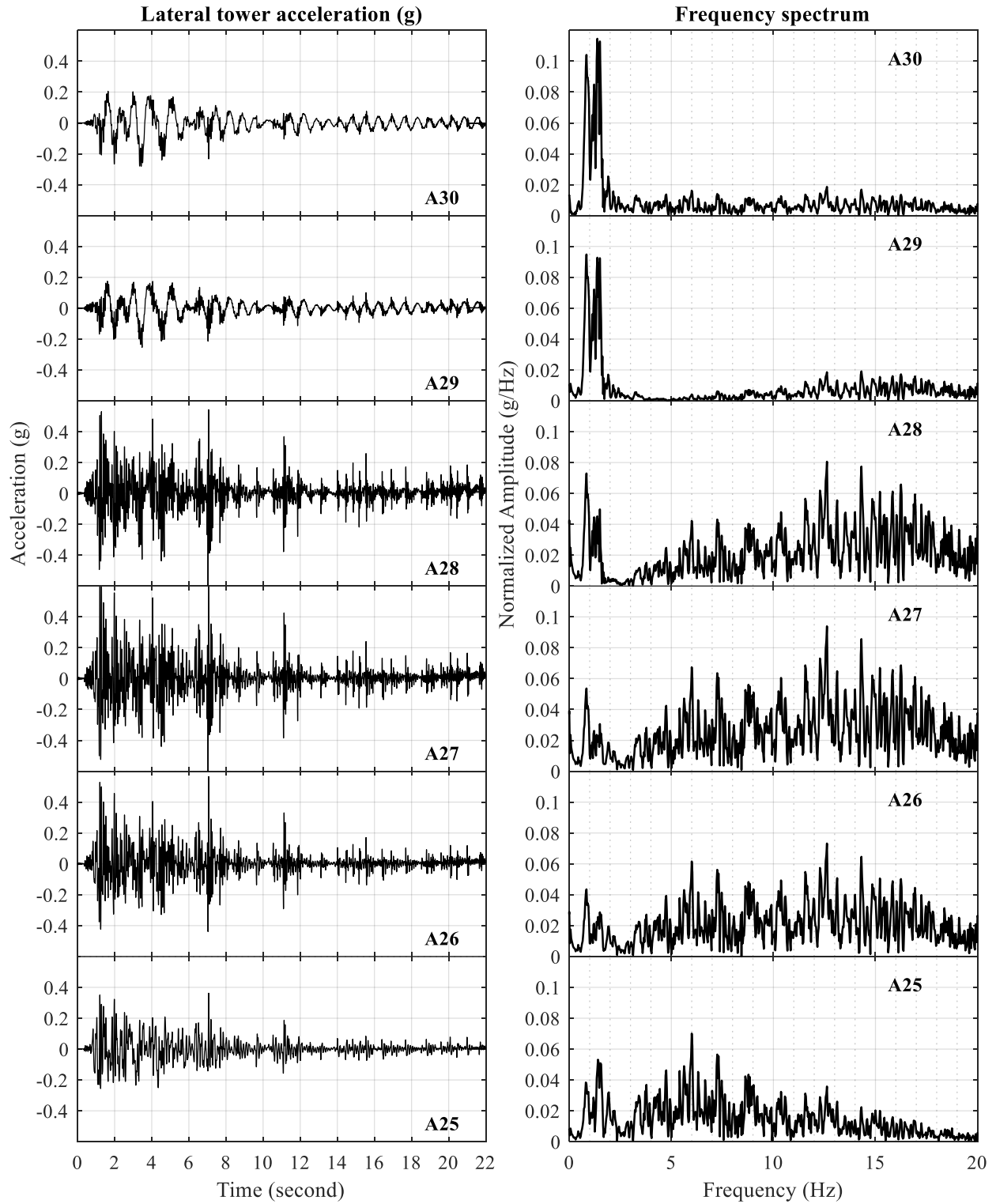


Figure B-144: Time histories of lateral tower acceleration for test T1

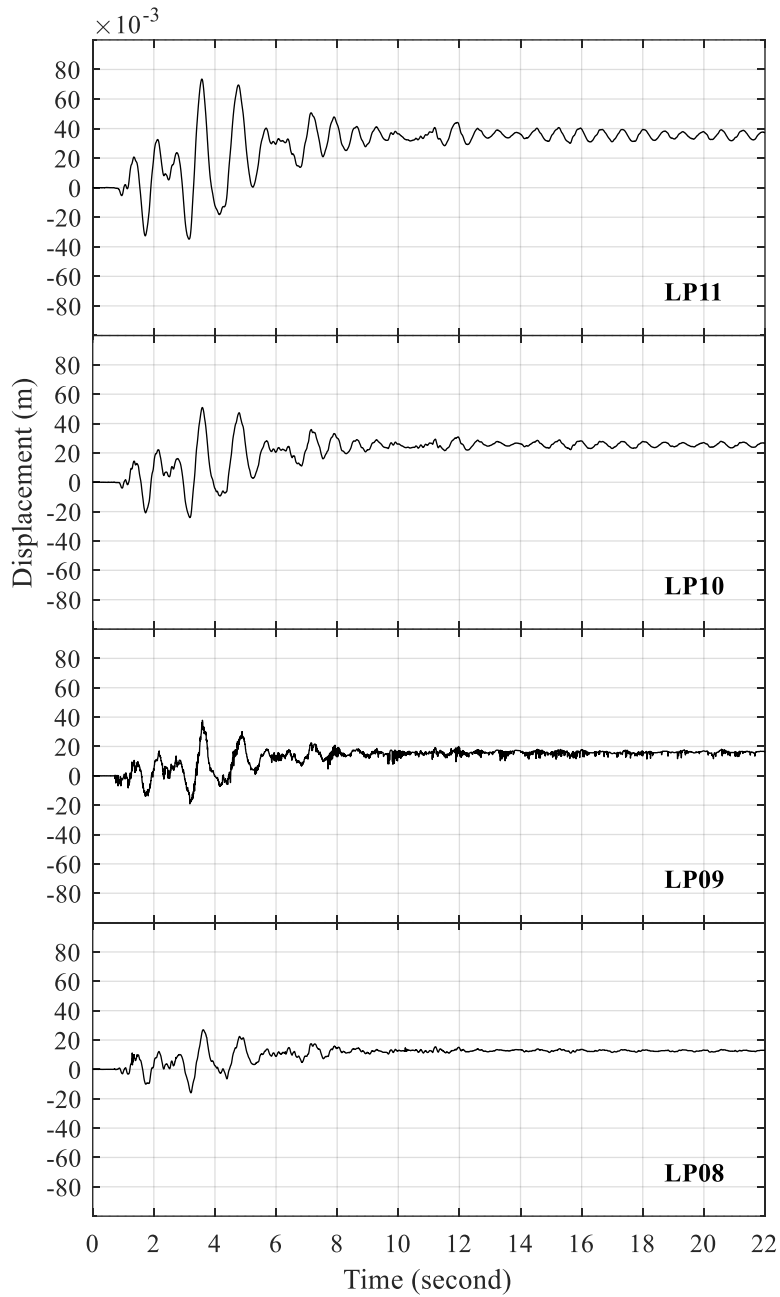


Figure B-145: Time histories of lateral tower displacement relative to lateral soil displacement at the foundation level (LP05) for test T1

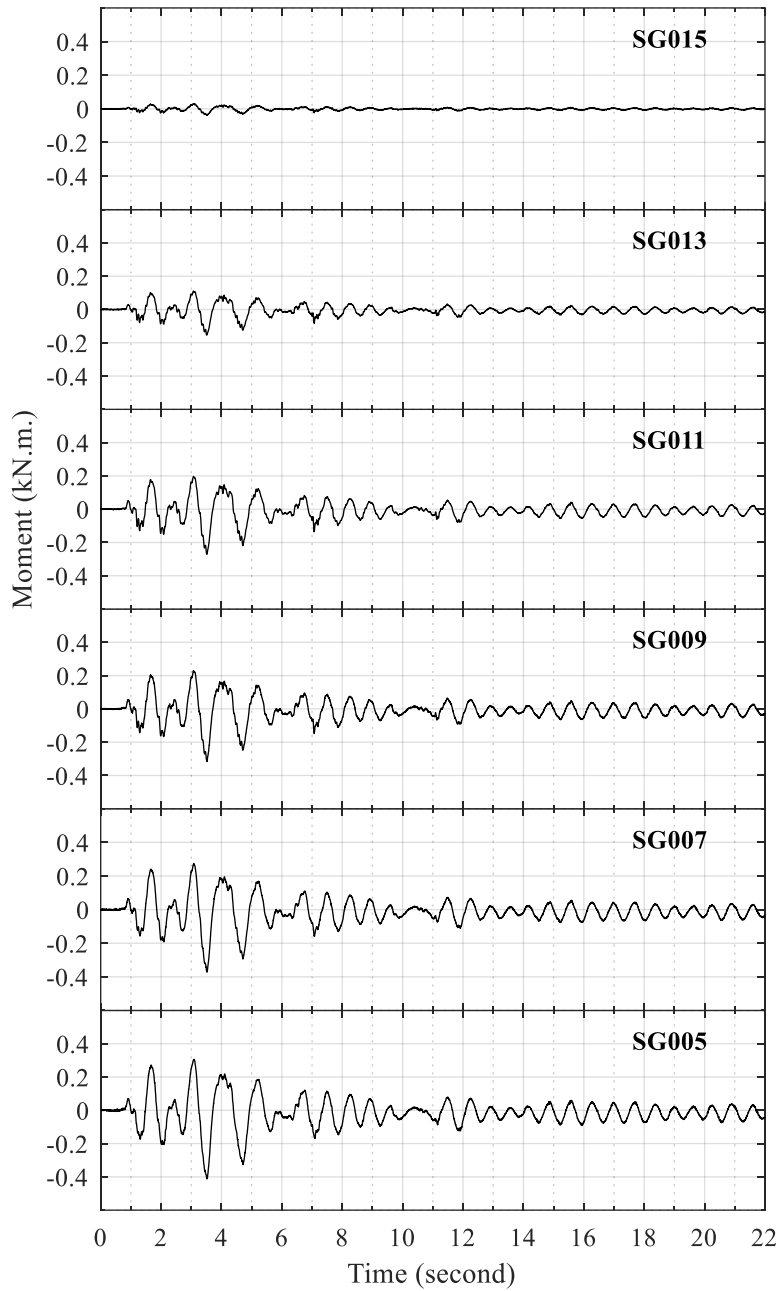


Figure B-146: Time histories of tower bending moment for test T1



## B.12 Test T2

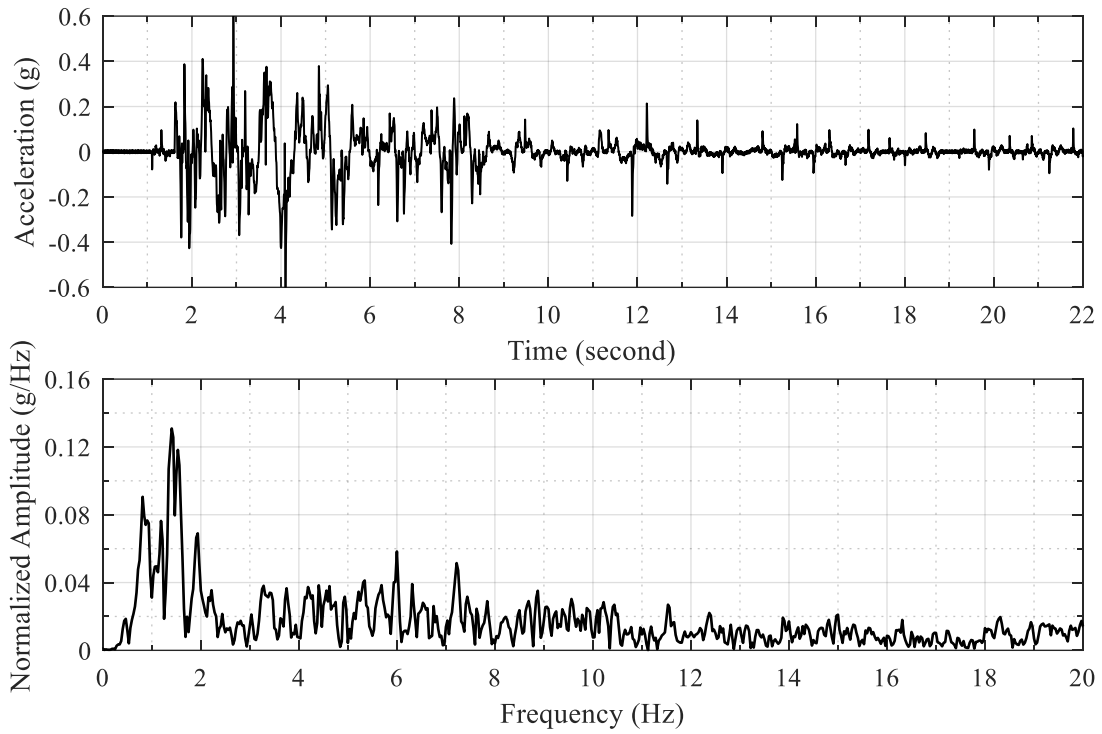


Figure B-147: Acceleration time history of shake table input excitation and the corresponding frequency spectrum for test T2

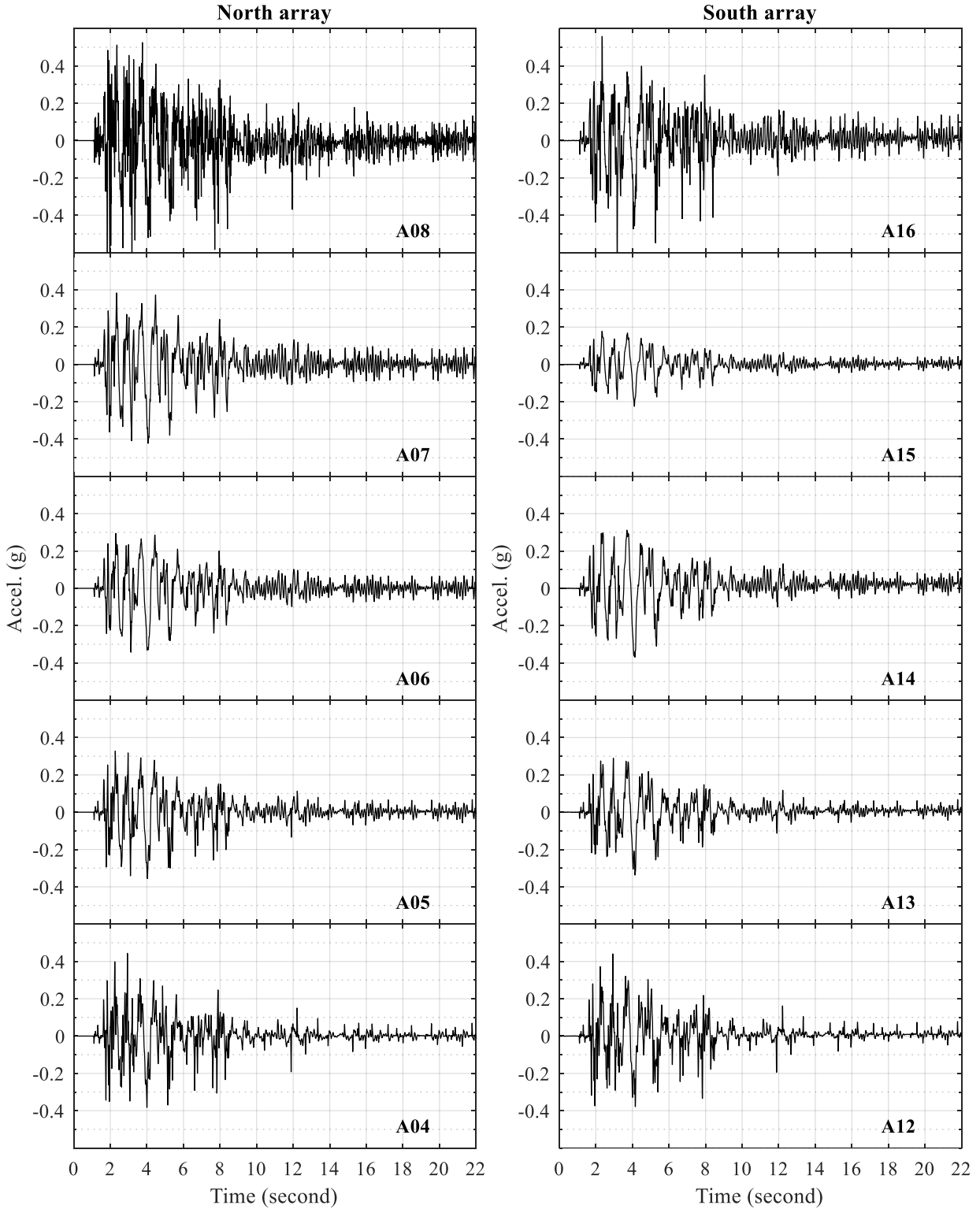


Figure B-148: Time histories of lateral soil acceleration in north and south arrays for test T2

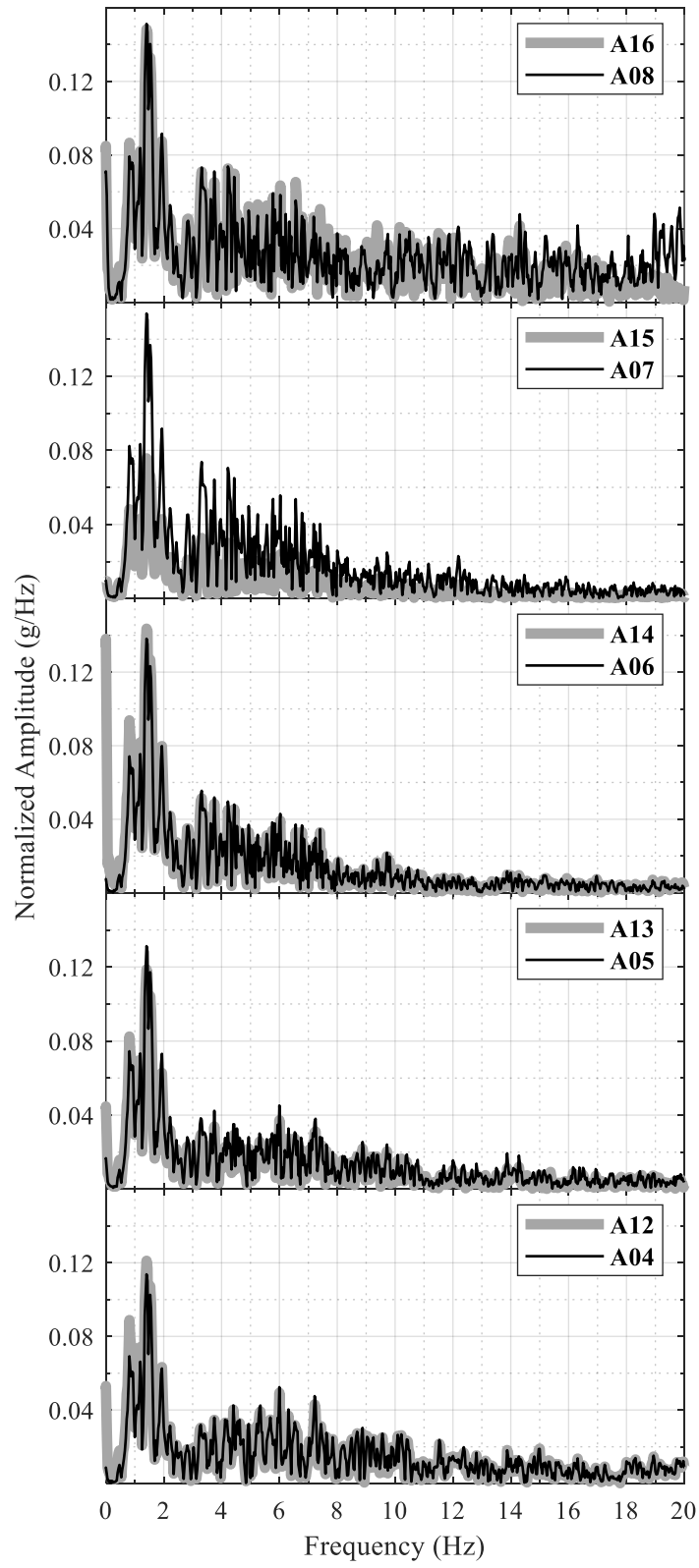


Figure B-149: Frequency spectra of lateral soil acceleration in north and south arrays for test T1

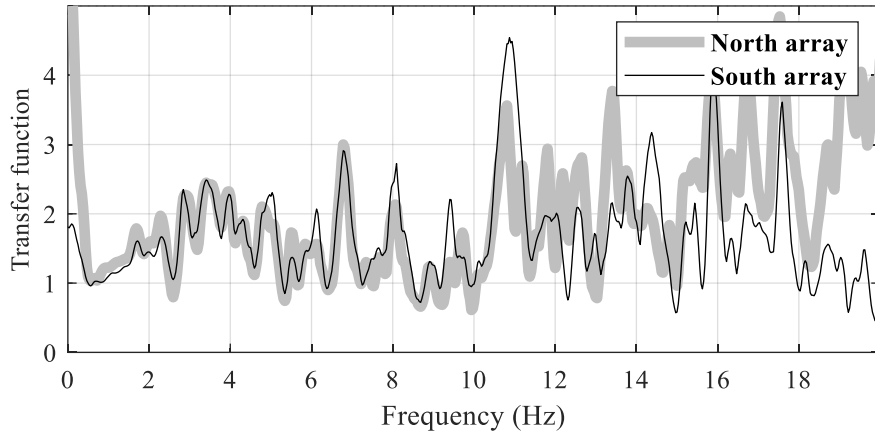


Figure B-150: Transfer function between soil acceleration at uppermost and lowermost sensor locations for test T2

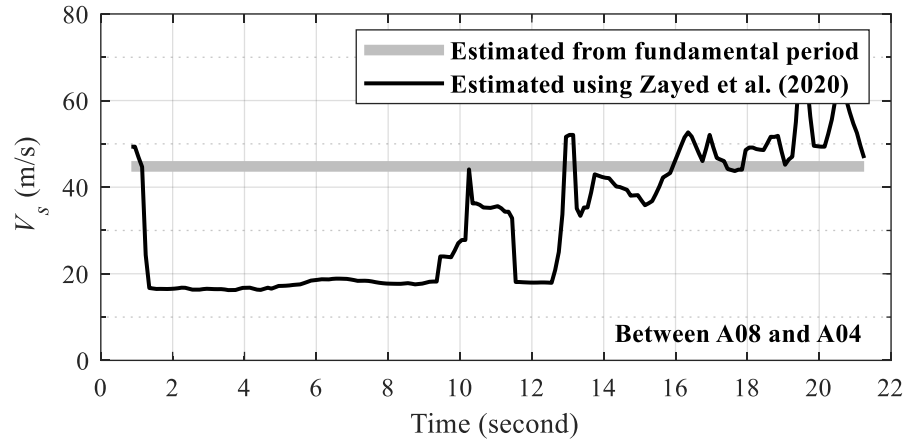


Figure B-151: Change in soil  $V_s$  with time during test T2

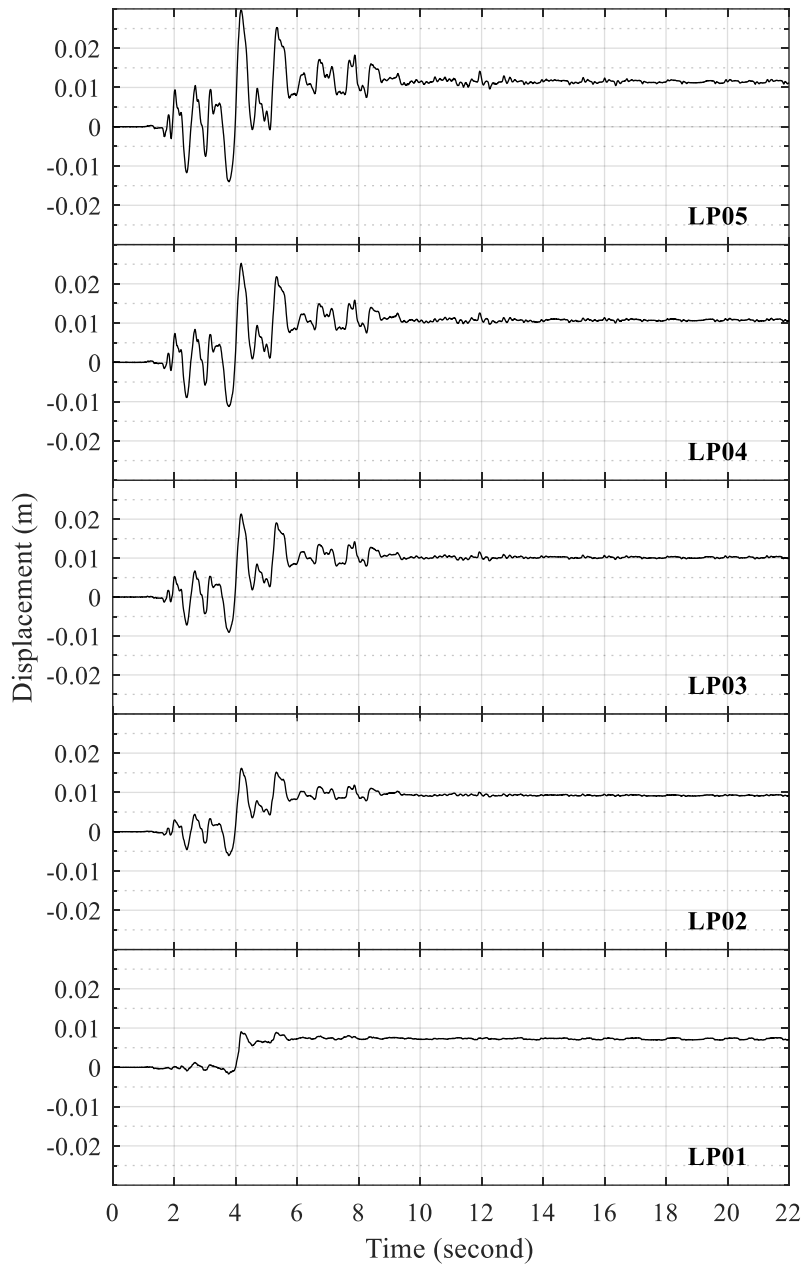


Figure B-152: Time histories of lateral soil displacement relative to laminar container base for test T2

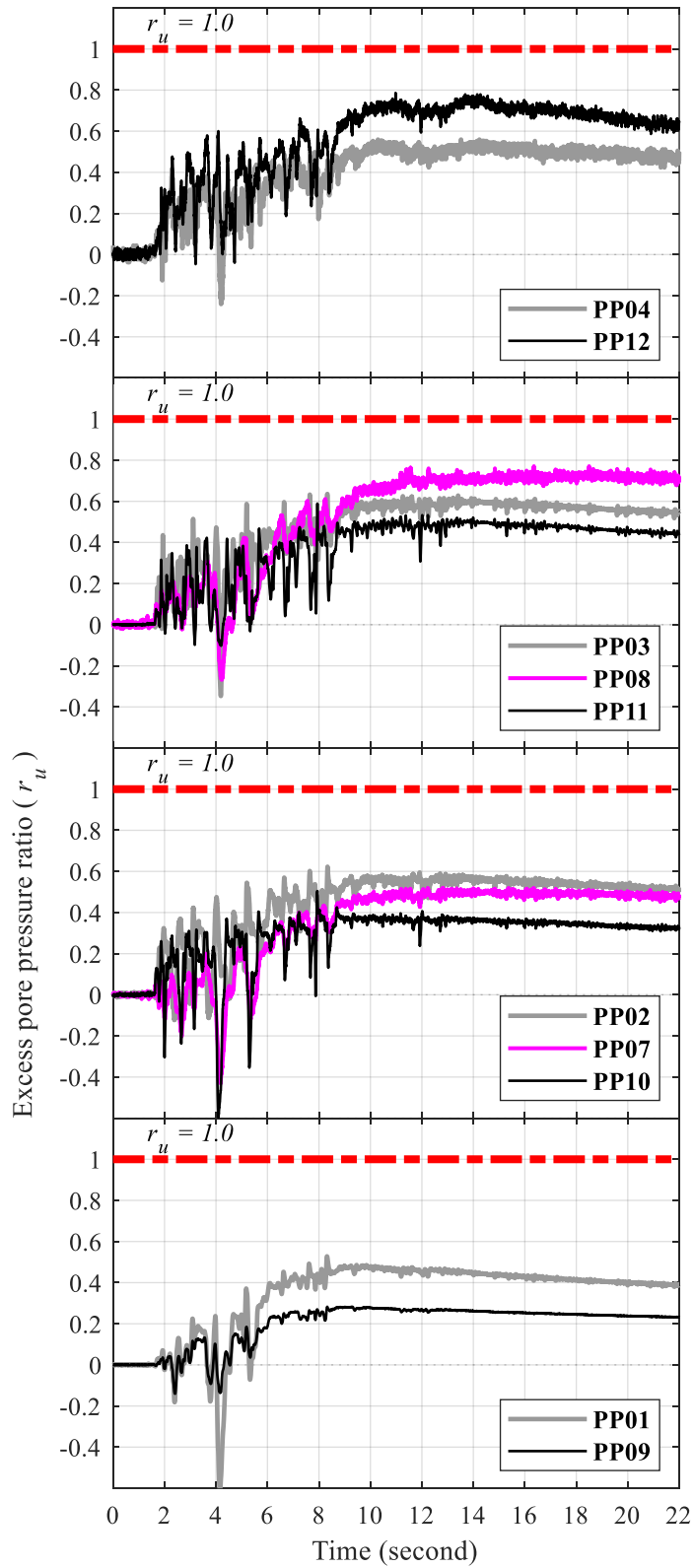


Figure B-153: Time histories of soil excess pore pressure for test T2

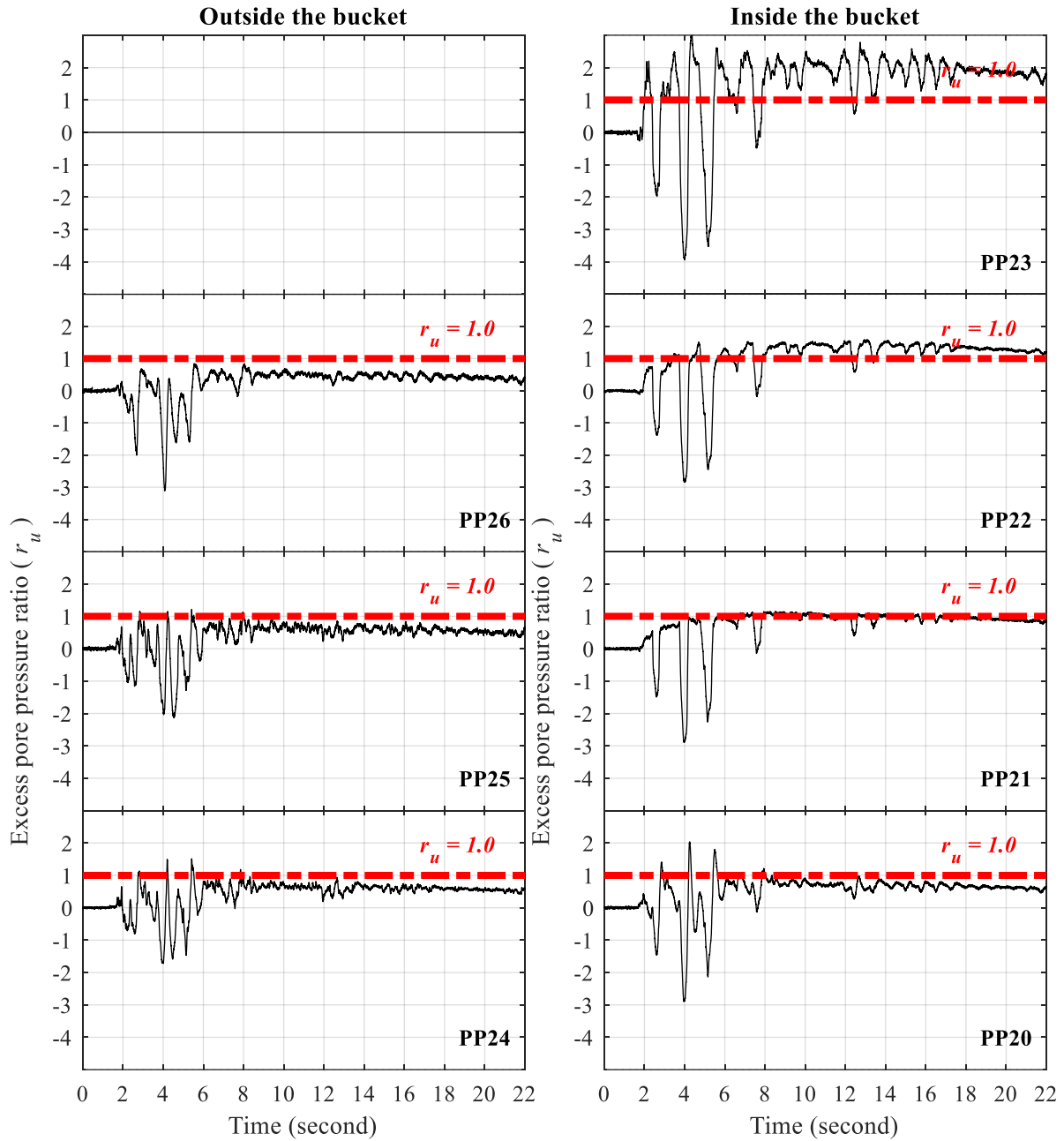


Figure B-154: Time histories of excess pore pressure at north edge of suction bucket for test T2



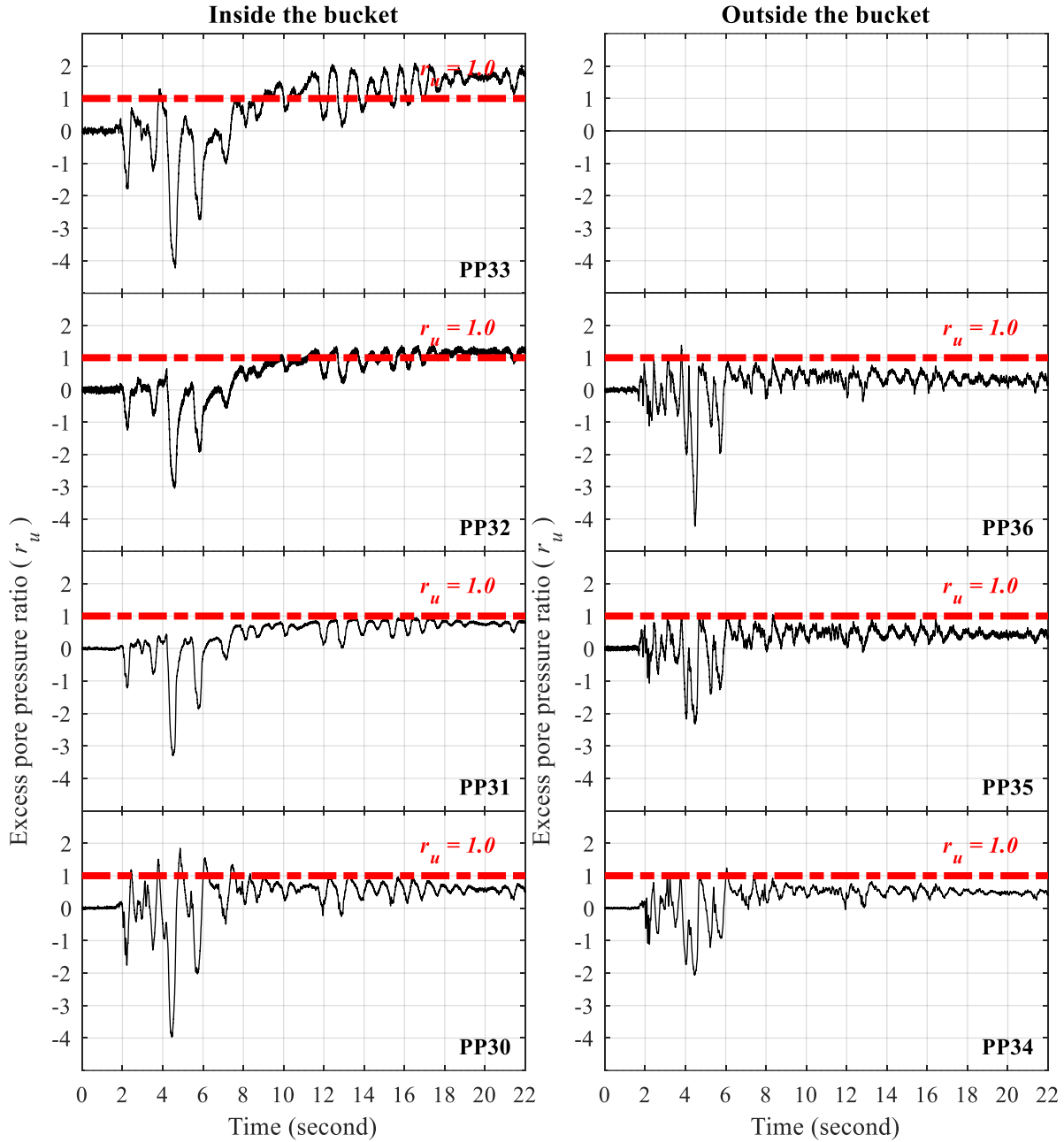


Figure B-155: Time histories of excess pore pressure at south edge of suction bucket for test T2

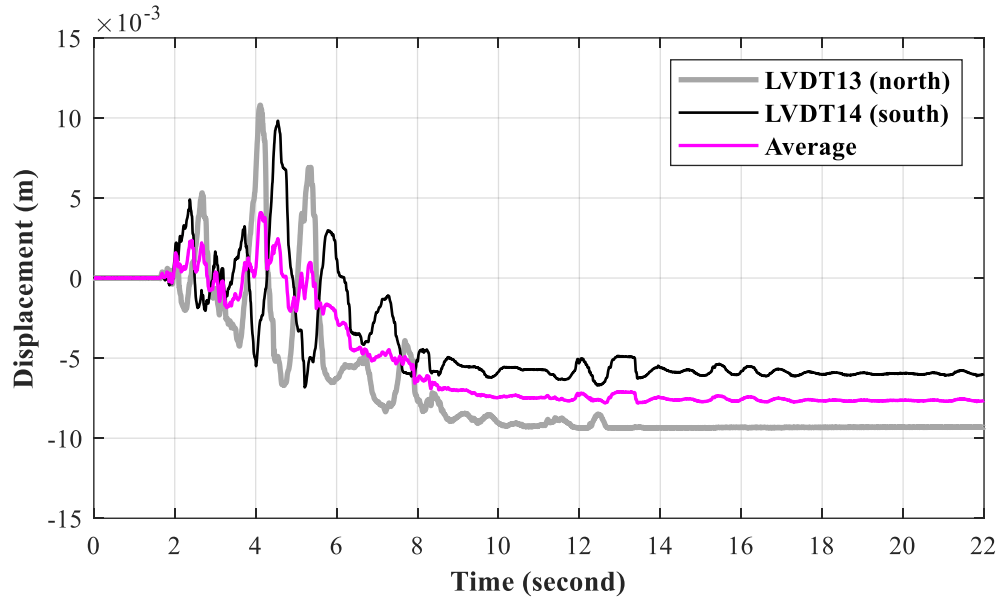


Figure B-156: Time histories of vertical bucket displacement for test T2

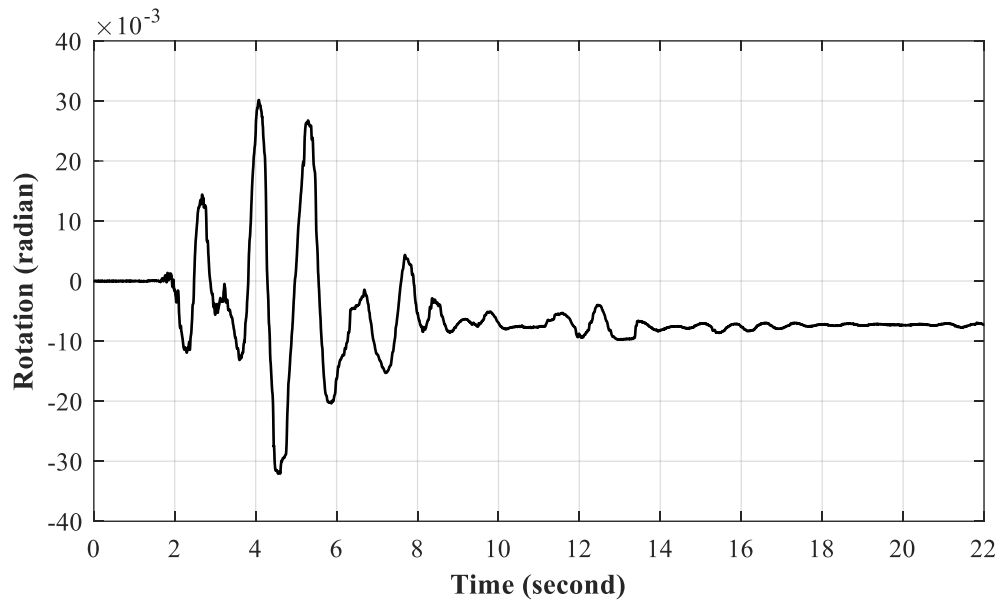


Figure B-157: Time history of suction bucket rotation for test T2

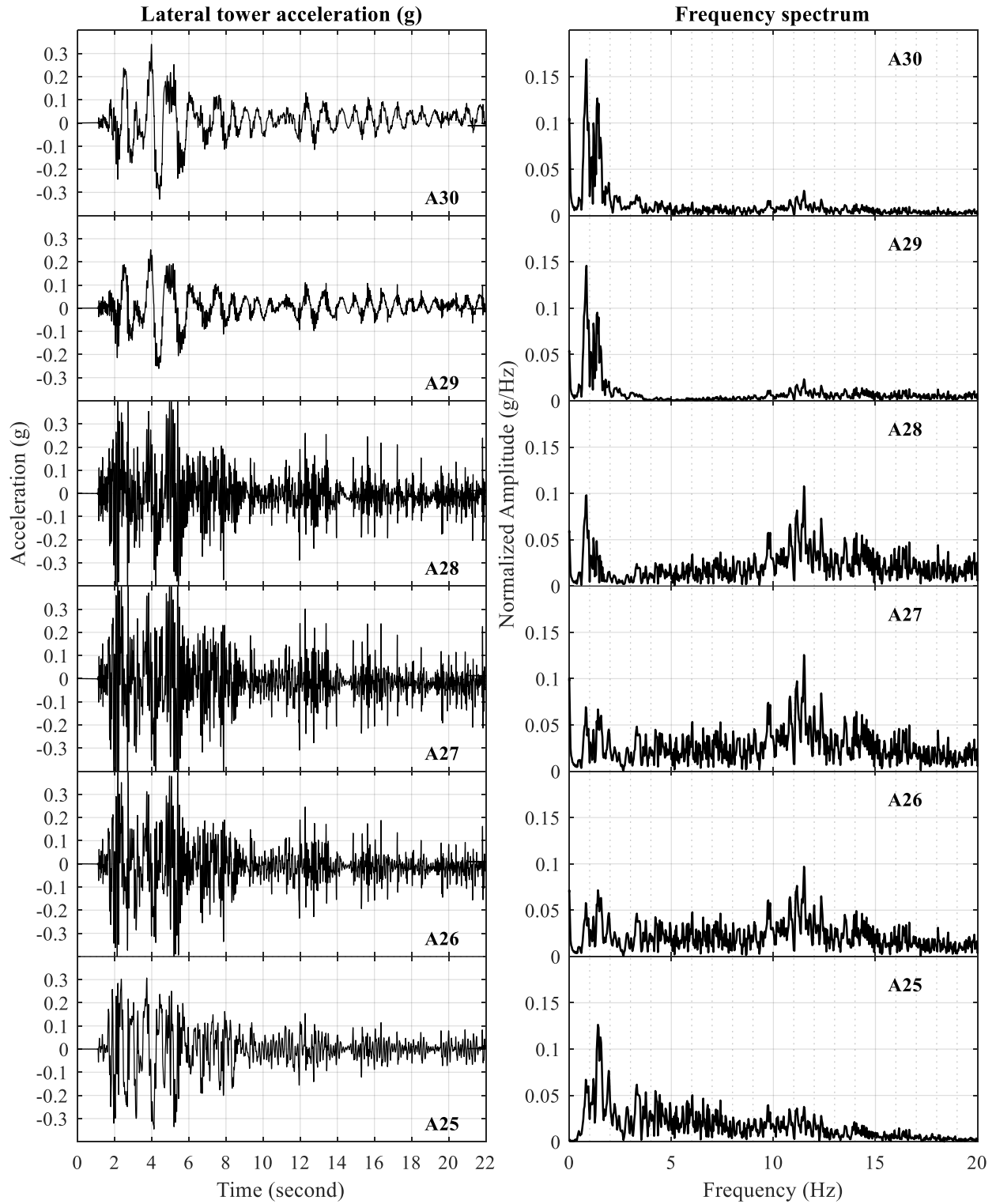


Figure B-158: Time histories of lateral tower acceleration for test T2

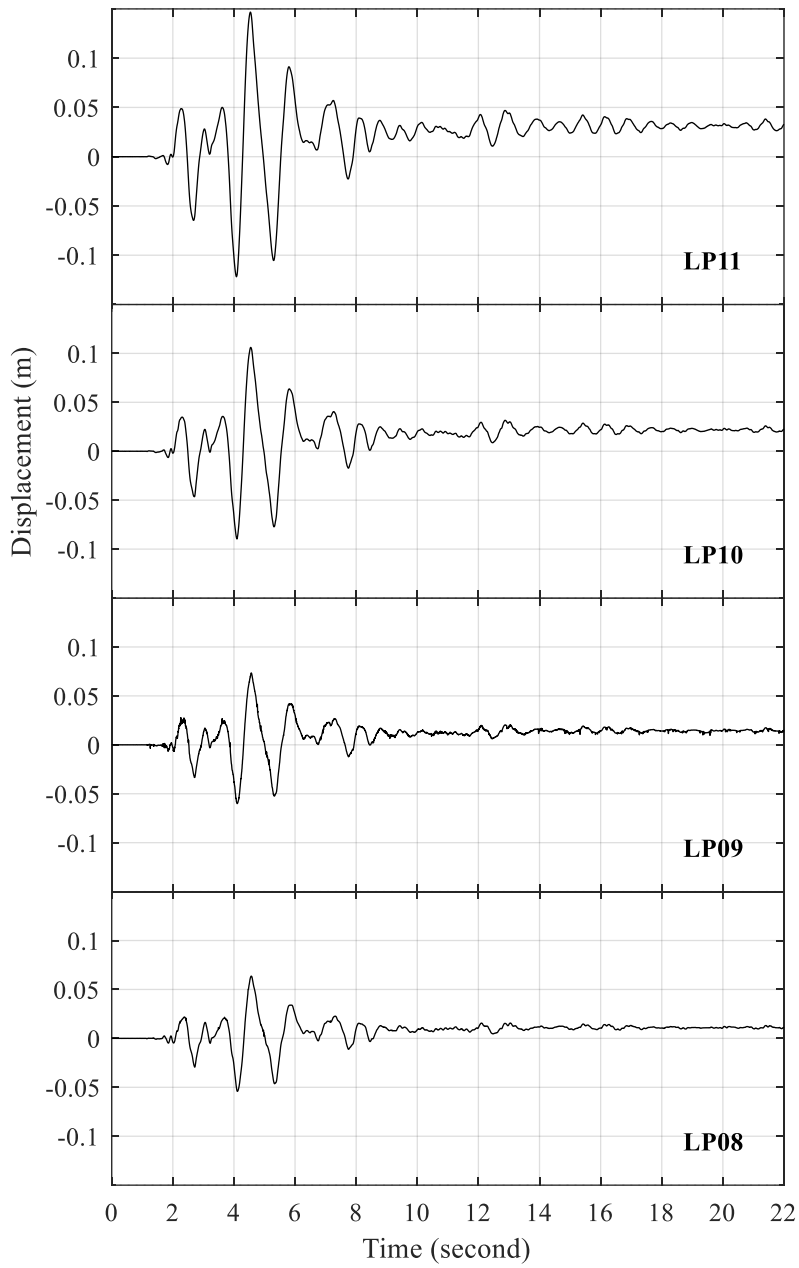


Figure B-159: Time histories of lateral tower displacement relative to lateral soil displacement at the foundation level (LP05) for test T2

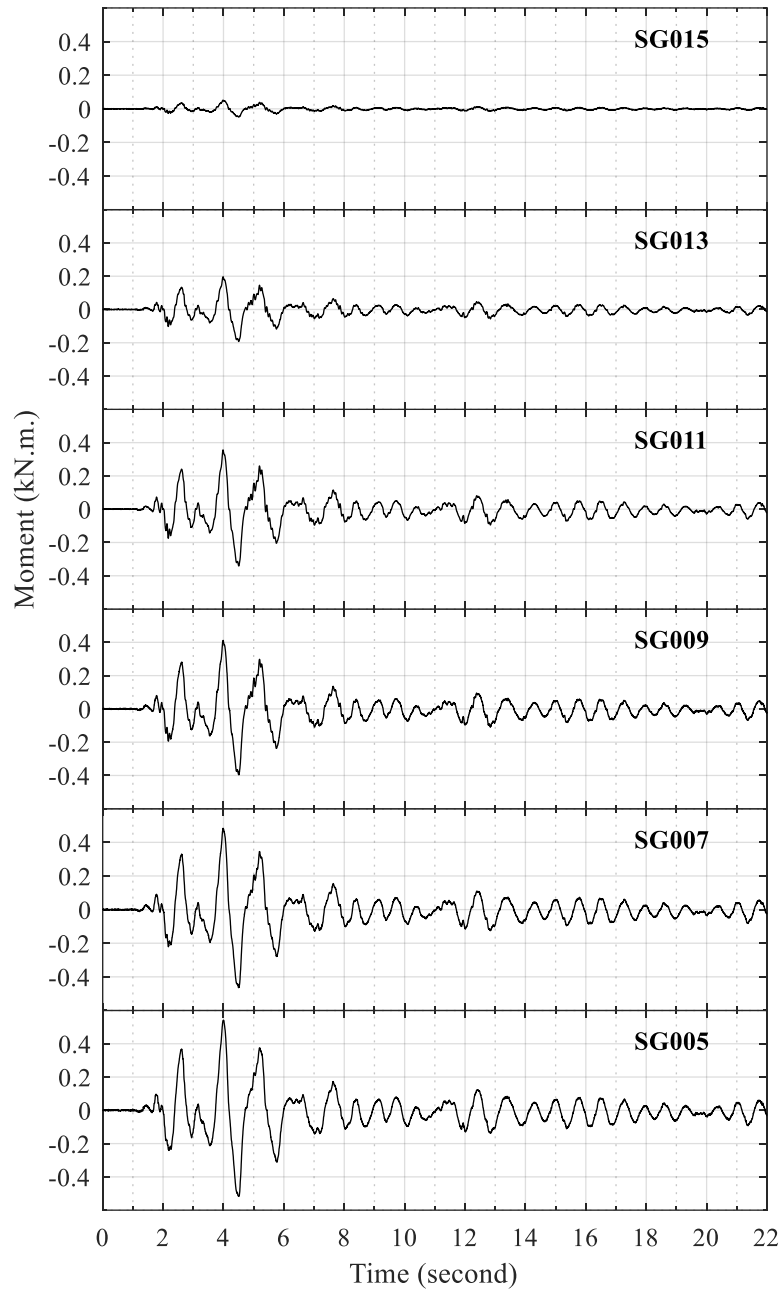


Figure B-160: Time histories of tower bending moment for test T2

### B.13 Test T3

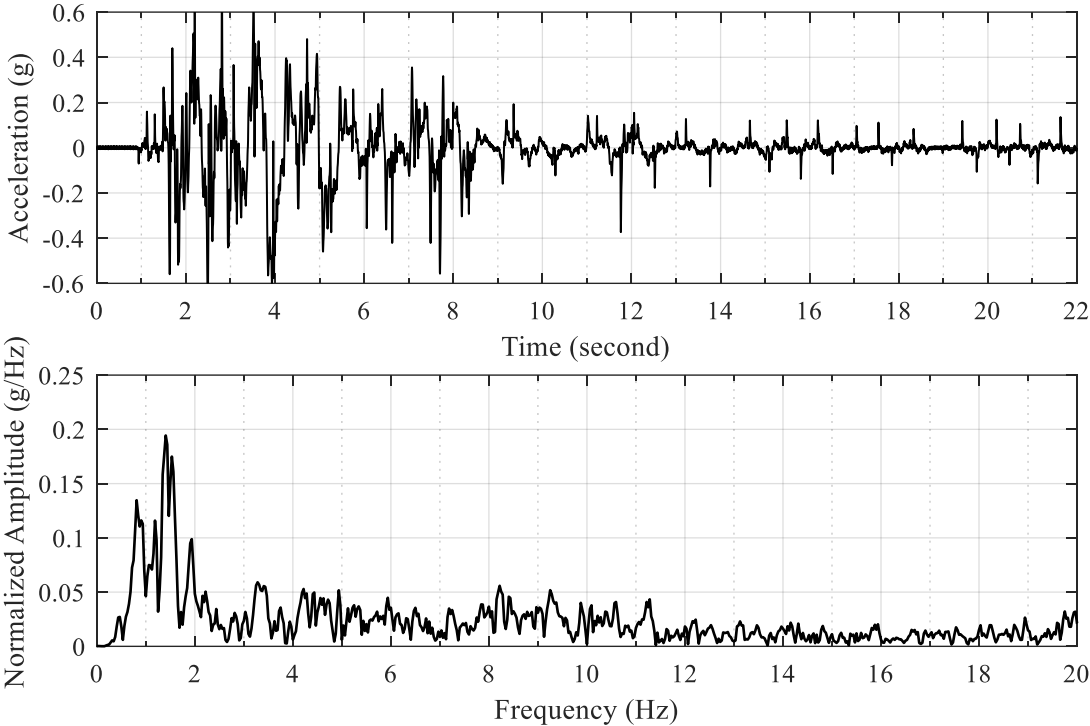


Figure B-161: Acceleration time history of shake table input excitation and the corresponding frequency spectrum for test T3

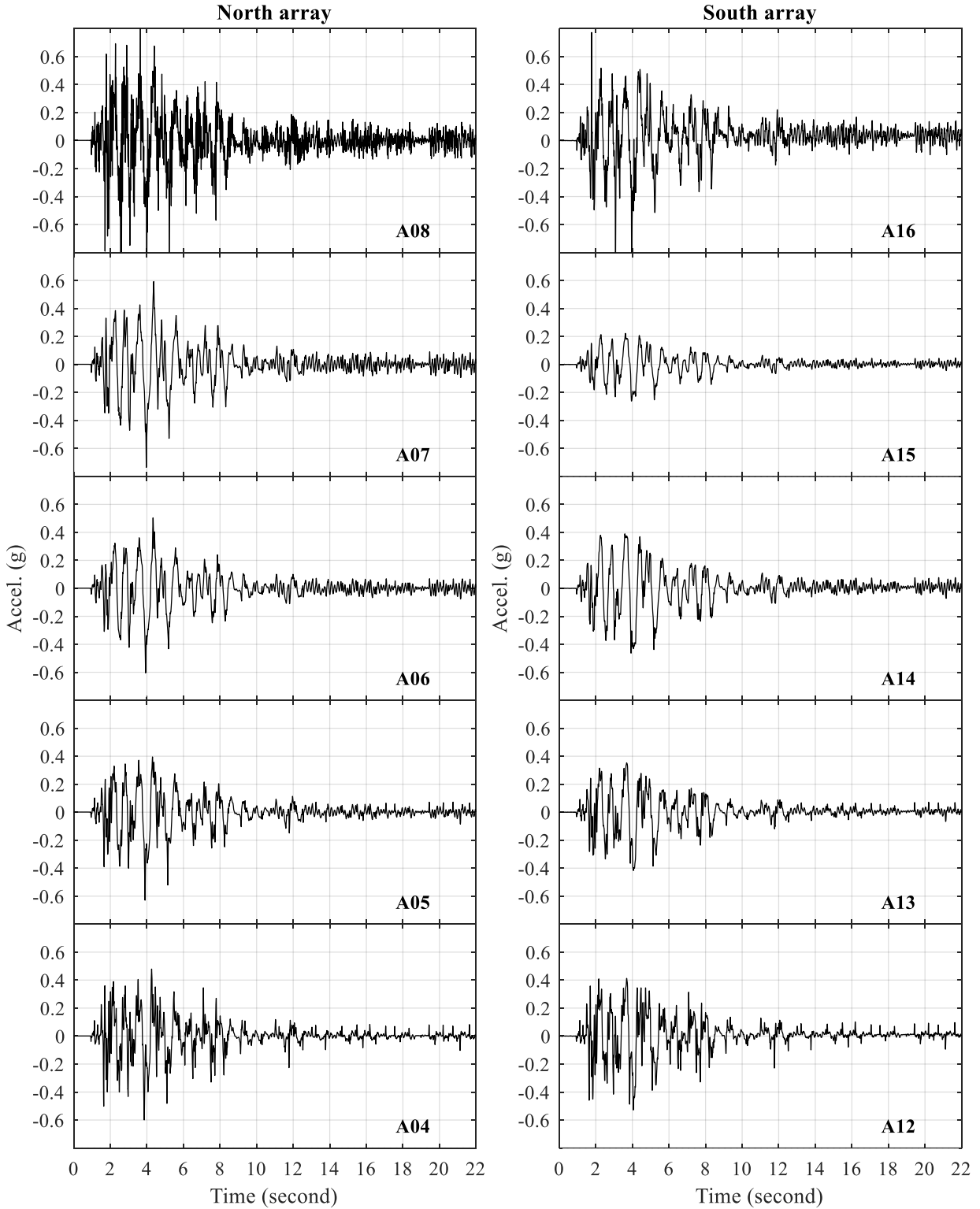


Figure B-162: Time histories of lateral soil acceleration in north and south arrays for test T3



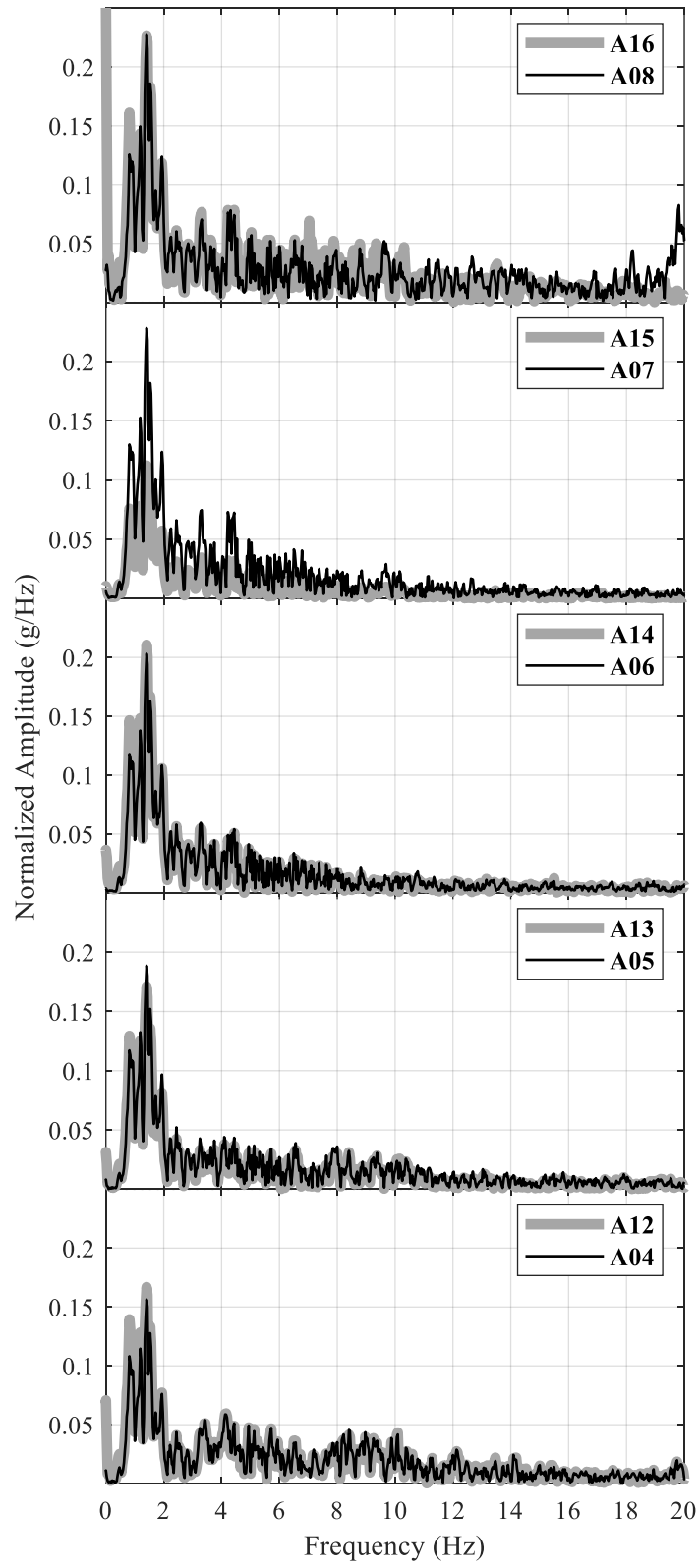


Figure B-163: Frequency spectra of lateral soil acceleration in north and south arrays for test T3

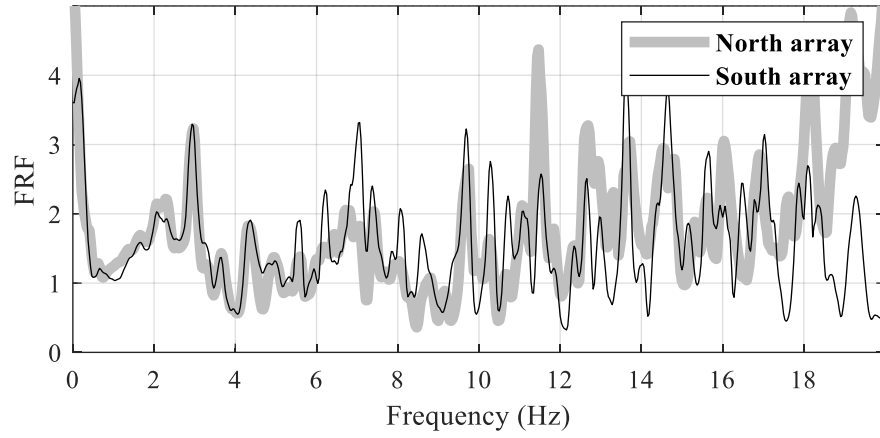


Figure B-164: Transfer function between soil acceleration at uppermost and lowermost sensor locations for test T3

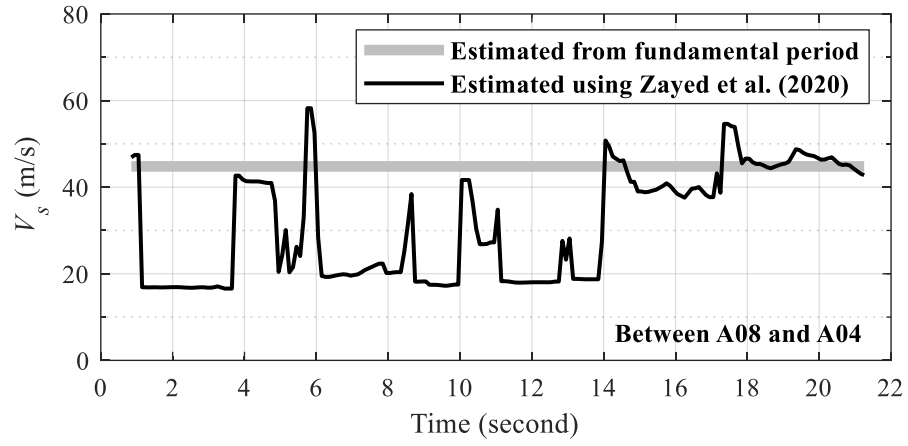


Figure B-165: Change in soil  $V_s$  with time during test T3

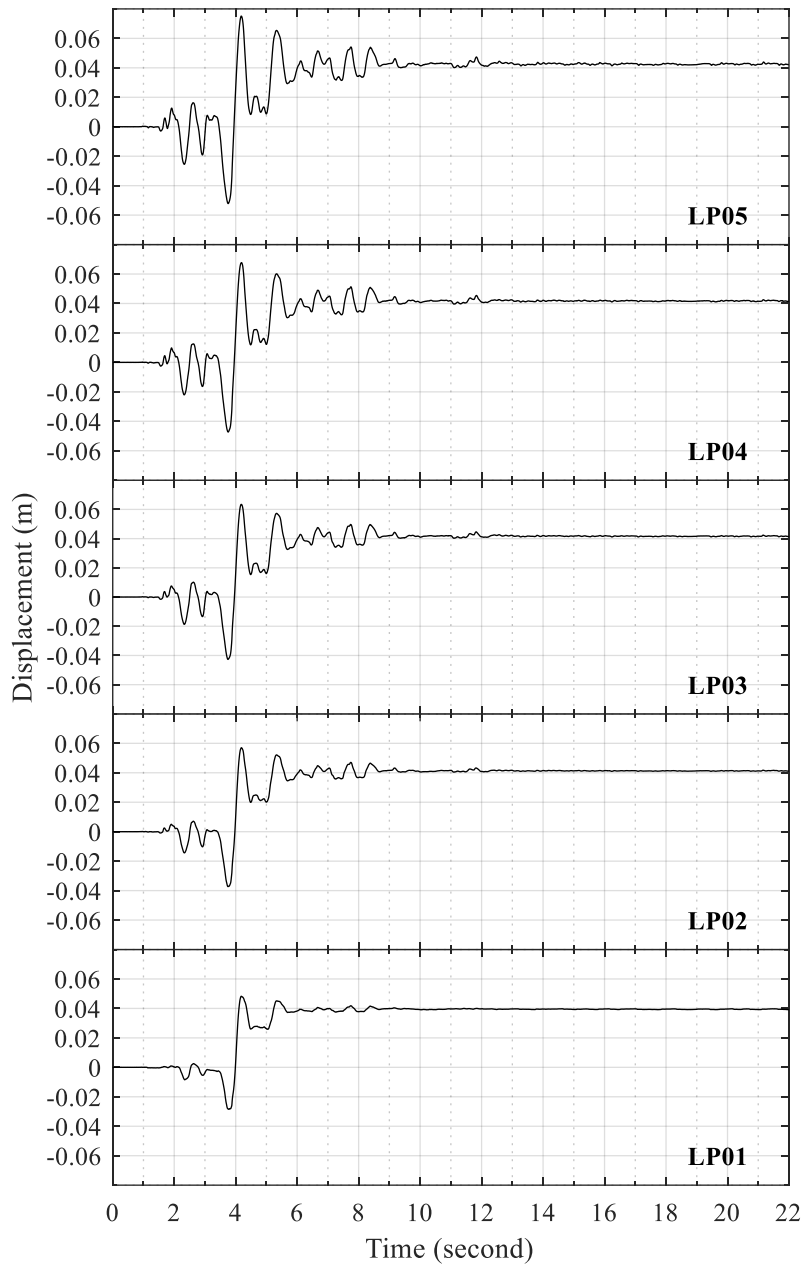


Figure B-166: Time histories of lateral soil displacement relative to laminar container base for test T3

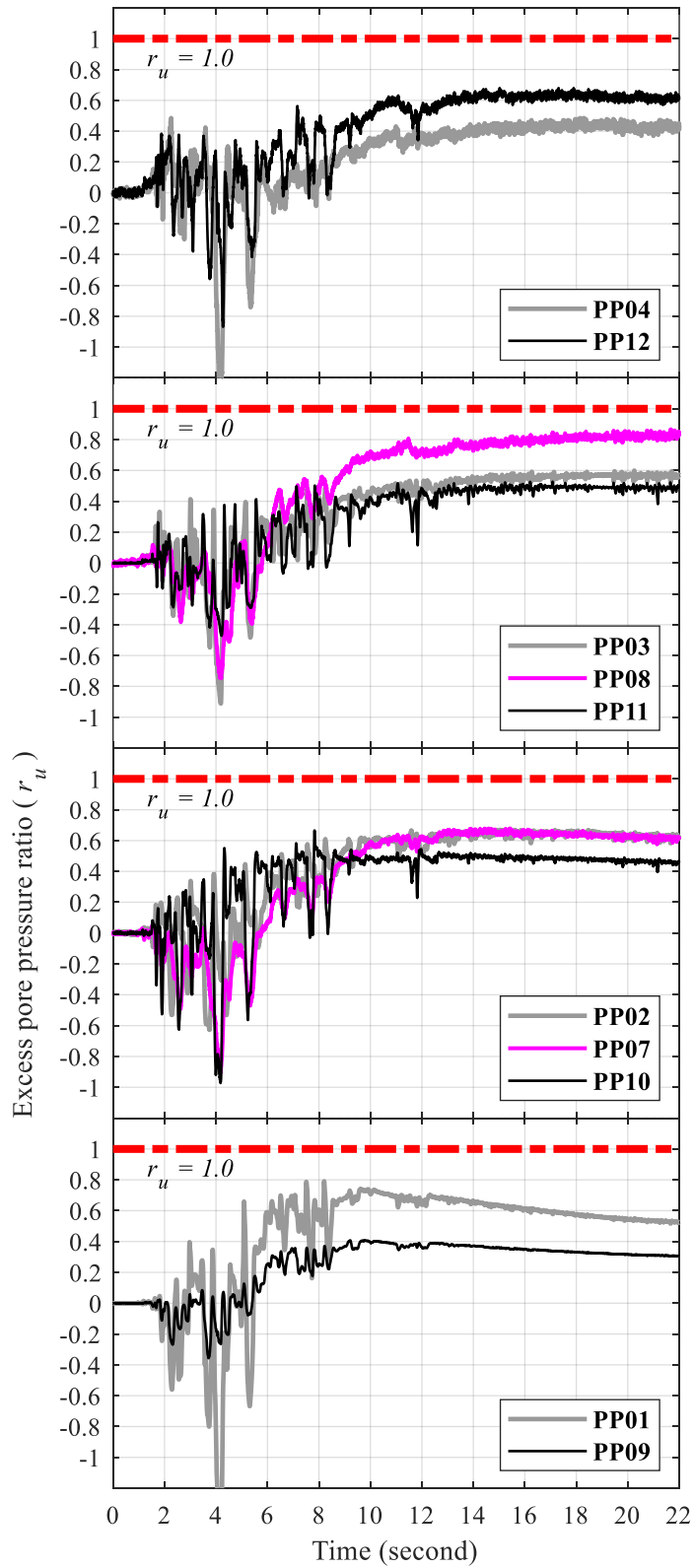


Figure B-167: Time histories of soil excess pore pressure for test T3

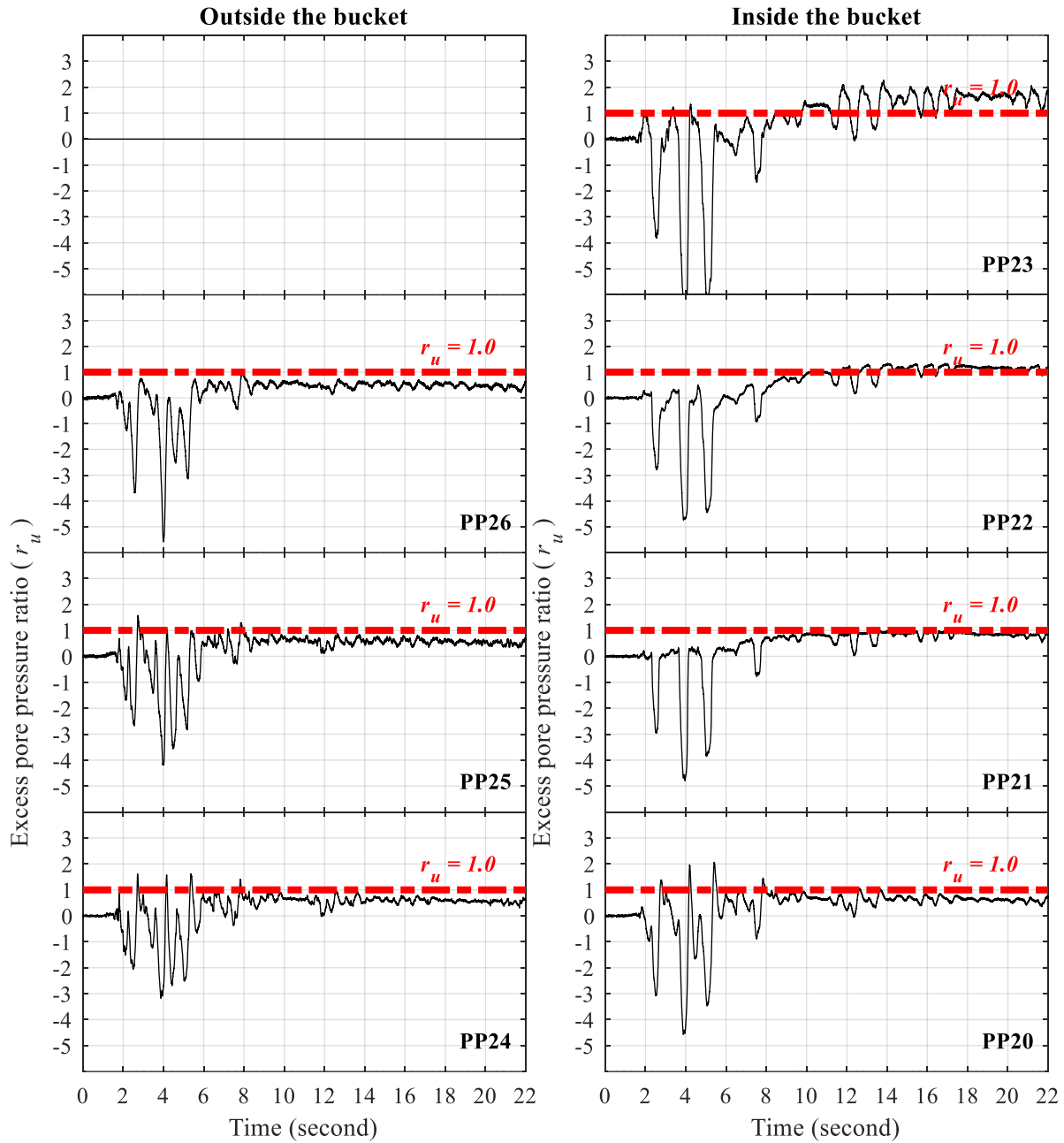


Figure B-168: Time histories of excess pore pressure at north edge of suction bucket for test T3

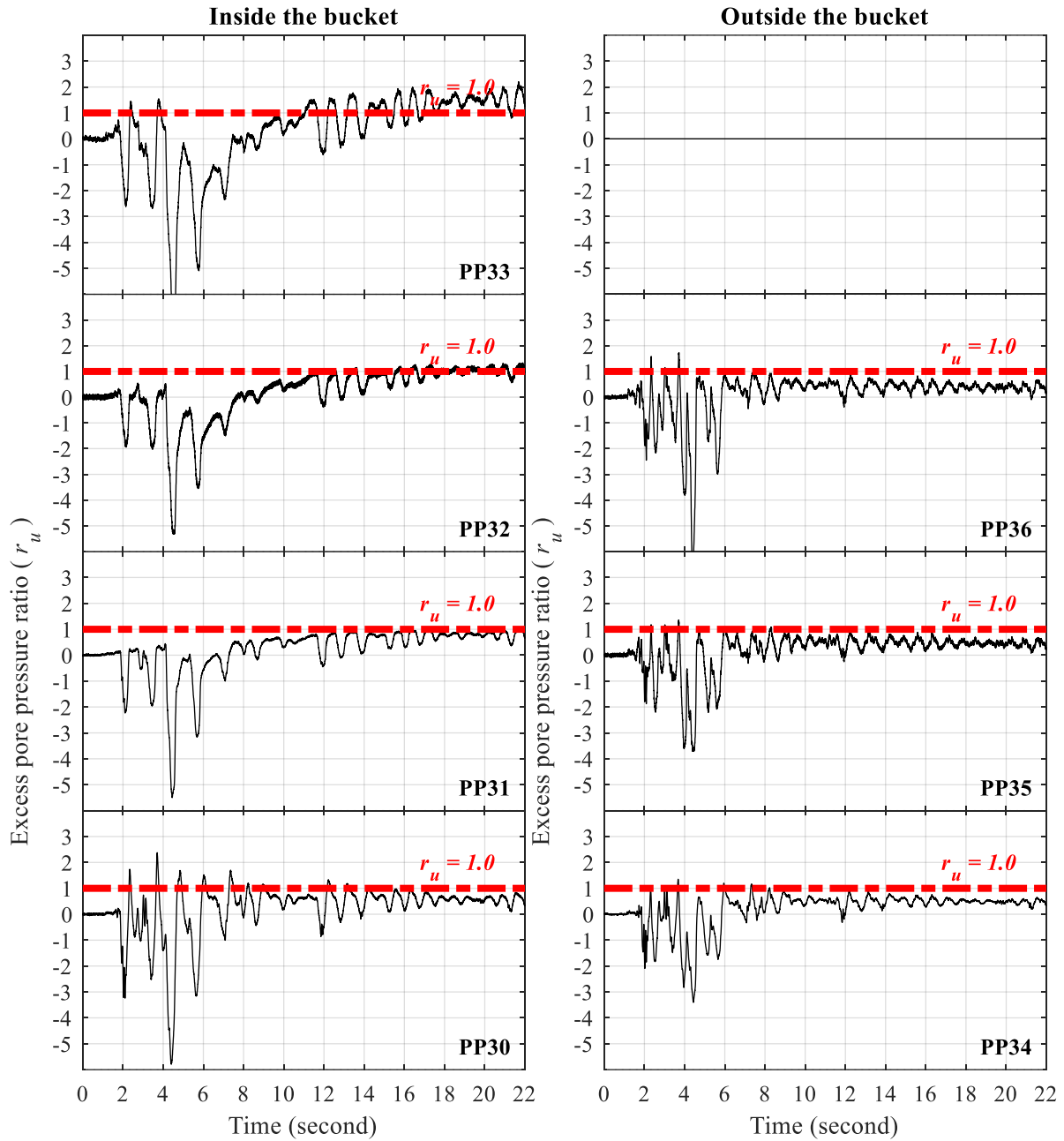


Figure B-169: Time histories of excess pore pressure at south edge of suction bucket for test T3

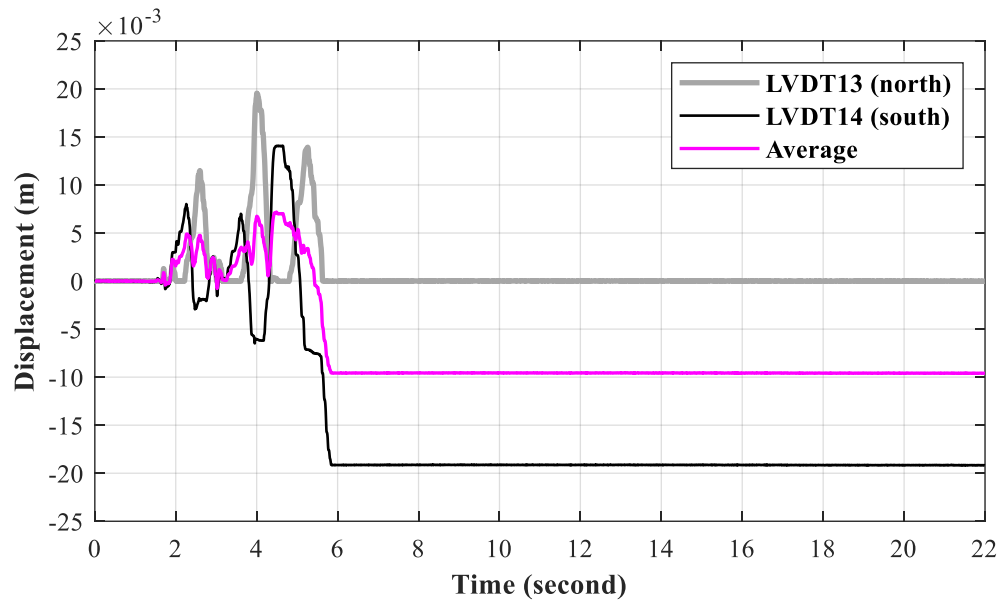


Figure B-170: Time histories of vertical bucket displacement for test T3



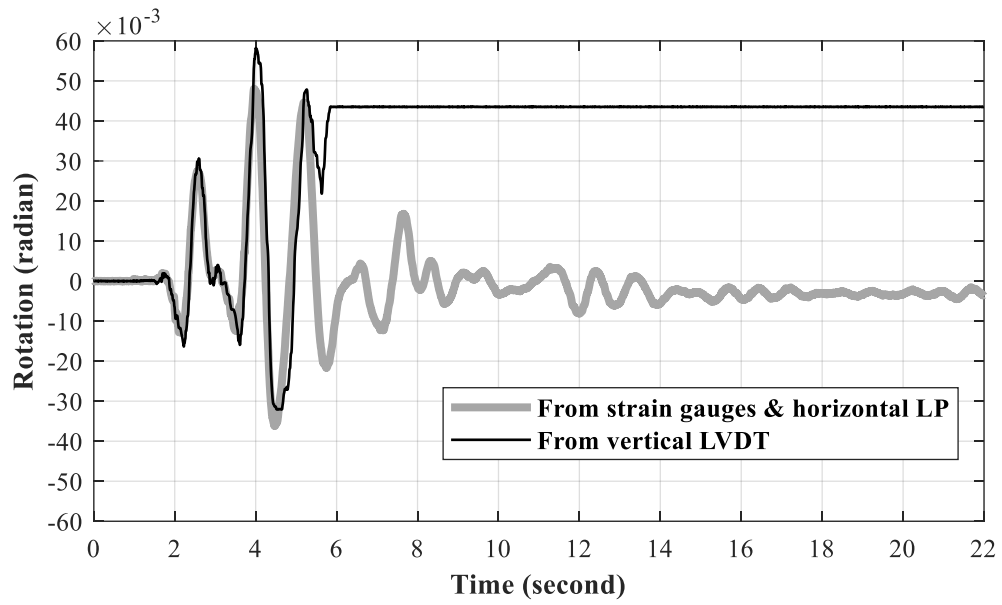


Figure B-171: Time history of suction bucket rotation for test T3

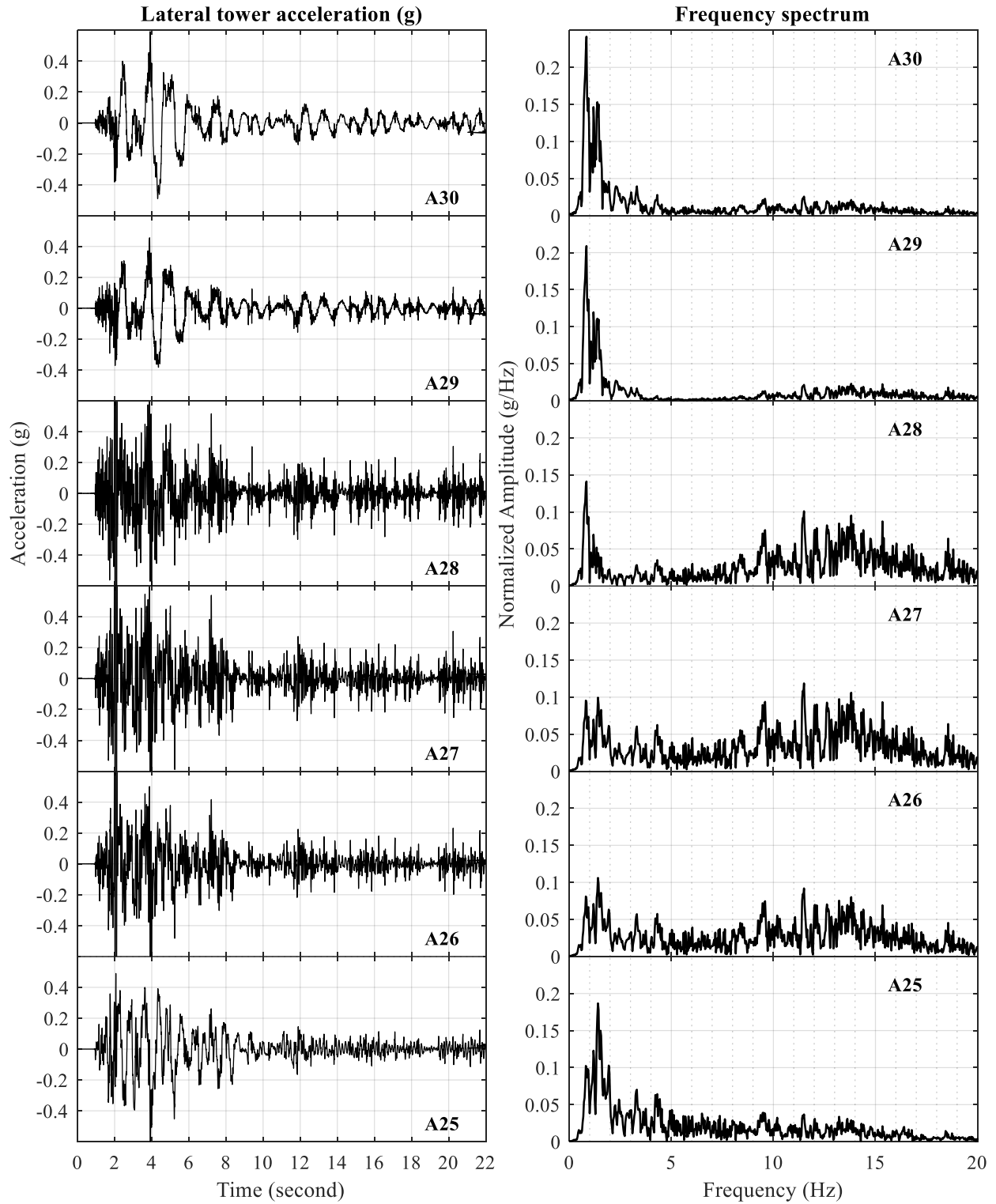


Figure B-172: Time histories of lateral tower acceleration for test T3

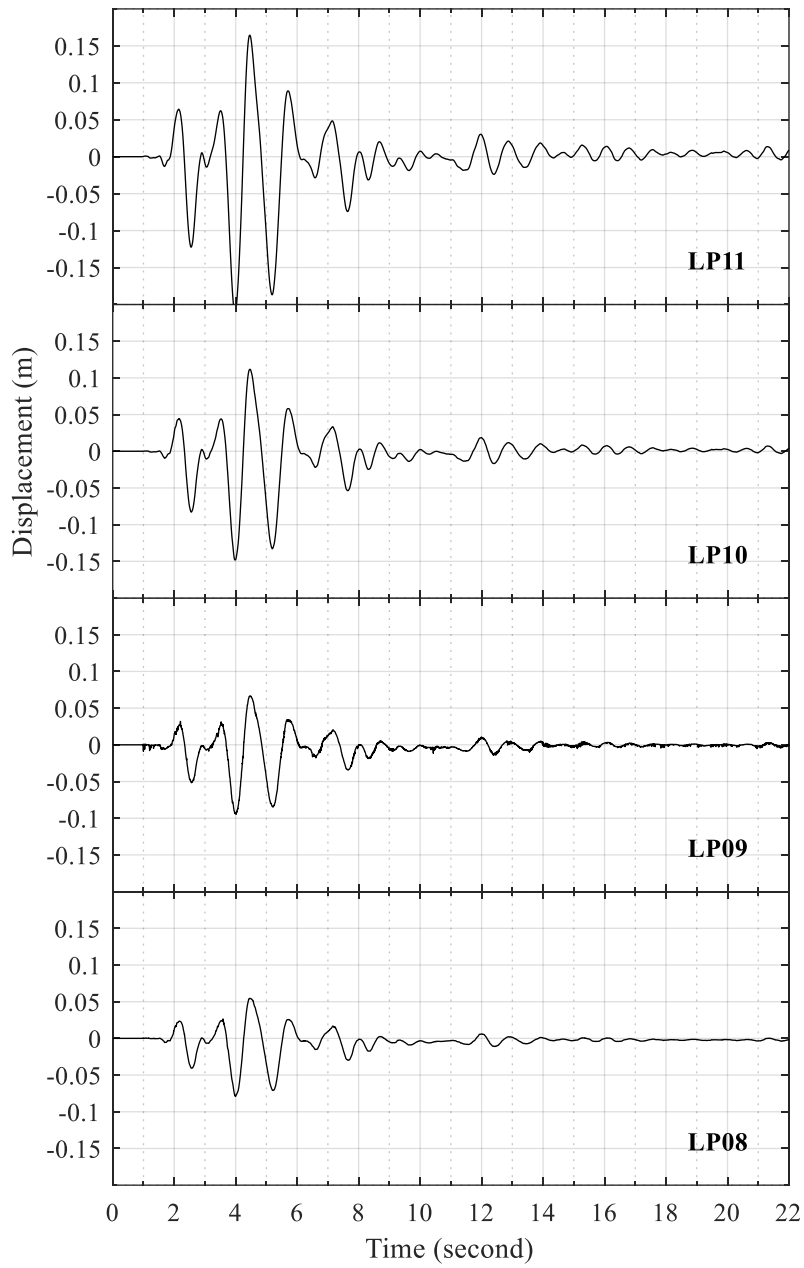


Figure B-173: Time histories of lateral tower displacement relative to lateral soil displacement at the foundation level (LP05) for test T3

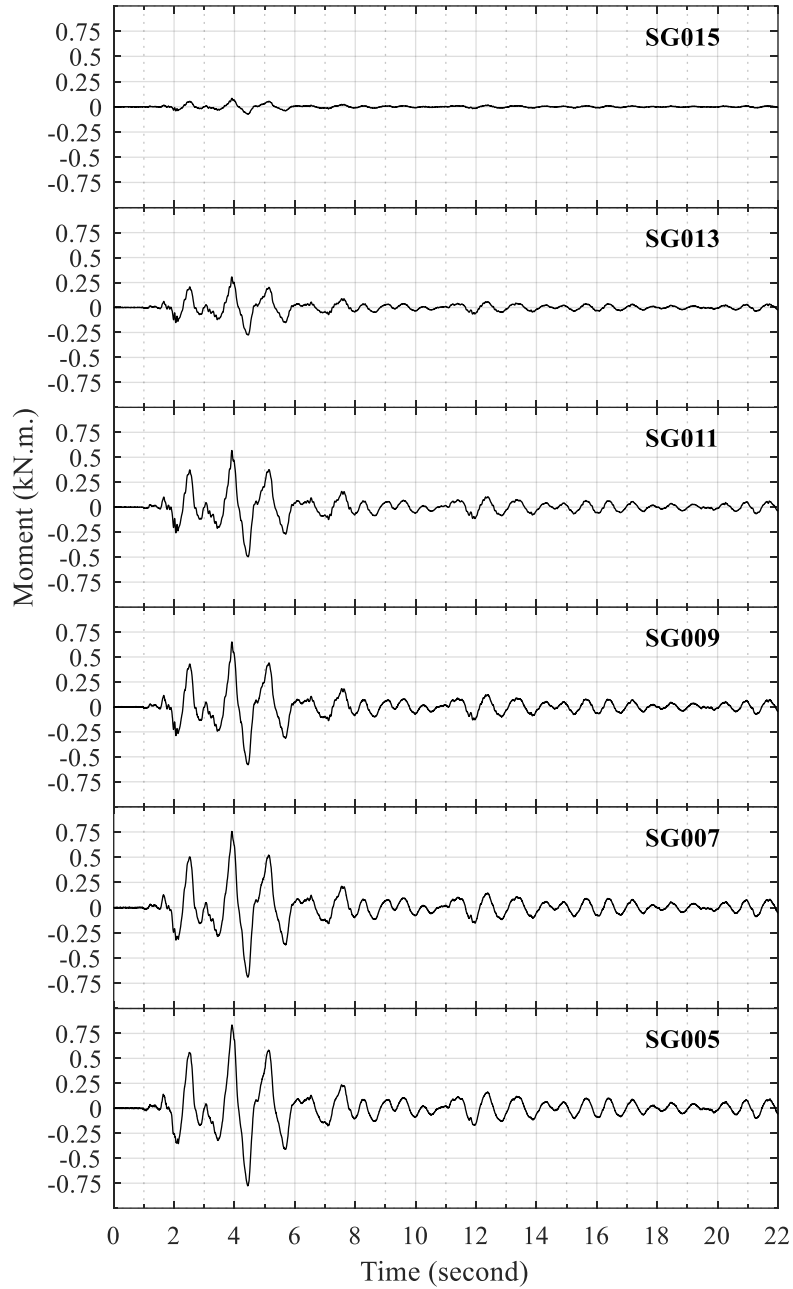


Figure B-174: Time histories of tower bending moment for test T3